Jeffrey T. Freymueller
Laura Sánchez   *Editors*

International Symposium on Earth and Environmental Sciences for Future Generations

Proceedings of the IAG General Assembly, Prague, Czech Republic, June 22-July 2, 2015

🐎 Springer

International Association of Geodesy Symposia

International Association of Geodesy Symposia

Jeffrey T. Freymueller, Series Editor
Laura Sánchez, Series Assistant Editor

More information about this series at http://www.springer.com/series/1345

International Symposium on Earth and Environmental Sciences for Future Generations

Proceedings of the IAG General Assembly, Prague, Czech Republic, June 22-July 2, 2015

Edited by

Jeffrey T. Freymueller, Laura Sánchez

Springer

Series Editor

Jeffrey T. Freymueller
Geophysical Institute and Department of Geosciences
University of Alaska Fairbanks
903 Koyukuk Dr.
Fairbanks, AK 99775
United States of America

Assistant Editor

Laura Sánchez
Deutsches Geodätisches Forschungsinstitut
Technische Universität München
Arcisstr. 21
DE-80333 Munich
Germany

Preface

The quadrennial General Assembly of the International Association of Geodesy (IAG) was held together with the 26th General Assembly of the International Union of Geodesy and Geophysics (IUGG) from June 22 to July 2 in Prague, Czech Republic. The theme of the General Assembly was "Earth and Environmental Sciences for Future Generations." More than 4,000 participants registered for the IUGG General Assembly, 542 of those as IAG associates. This is the largest number of participants since the General Assembly 1995 in Boulder, USA. The IAG organized one Union Symposium (of 11 in total), three Joint Symposia with other IUGG Associations (of 27 in total), and eight IAG Symposia, amounting to 52 sessions across the 8 days of the meeting. IAG co-conveners were involved in all the other Union Symposia and in 10 other Joint Symposia. Five hundred and forty-five presentations (of 5,378 in total) were given in the IAG Symposia, and 65 (of 711 in total) in the IAG lead Joint Symposia, nearly half of those as posters.

The eight IAG Symposia were structured according to the four IAG Commissions and the three GGOS Focus Areas:

1. Reference Frames
2. Static Gravity Field Models and Observations
3. Variations of the Gravity Field
4. Earth Rotation and Geodynamics
5. GNSS++: Emerging Technologies and Applications
6. Unified Height Systems
7. Geohazards Monitoring
8. Sea-Level Observation and Modelling

The joint symposia supported by the IAG were:

- Joint Inversion and Mutually Constrained Inversion of Geophysical Observations
- Results from SWARM, Ground-Based Data and Earlier Satellite Missions
- Data on the Edge: Preservation and Utilization of Historical Data in the Geosciences
- Dynamics of the Cryosphere from Geometric and Gravimetric Observations
- Modelling the Atmosphere and Ionosphere by Space Measurements
- Variations of the Hydrosphere from Satellite Gravity Missions
- Extreme Hydrological Events
- Earth Systems Dynamics, Predictability and Probabilistic Forecasting
- Data Assimilation in Geophysical Sciences
- Sea Level Change and Variability: Past, Present and Future
- Satellite Oceanography and Climatology
- Geophysical Imaging of Natural Resources
- Deformation of the Lithosphere: Integrating Seismology and Geodesy Through Modelling

This volume contains selected papers from all of the symposia related to IAG. All published papers were peer-reviewed, and we warmly recognize the contributions and support of the Associated Editors and reviewers (see the list in later pages).

Technology marches onward, and the IAG Symposia series is evolving with it. This is the final volume in the series that will be published as a paper book, as all future volumes will be electronic books. The papers for this book, once accepted, were made available online,

and the same will be true in the future. Eventually, the series may become Open Access, if the economics of that publishing model work out. We are excited to see this volume finally complete, and we will be working to ensure that the time to publication for future volumes becomes shorter and more competitive with other publication venues.

Fairbanks, AK, USA   Jeffrey T. Freymueller
Munich, Germany   Laura Sánchez

Contents

Part III   Detection and Modelling of Gravity Field Variations

Part IV   Earth Rotation and Geodynamics

Part I

Geodetic Reference Systems and Frames

Simulation of VLBI Observations to Determine a Global TRF for GGOS

Susanne Glaser, Dimitrios Ampatzidis, Rolf König, Tobias Nilsson, Robert Heinkelmann, Frank Flechtner, and Harald Schuh

Abstract

In this study, we present a global terrestrial reference frame (TRF) from simulated very long baseline interferometry (VLBI) observations. In the time span from 2008 until 2014, 695 standard VLBI rapid turnaround (R1, R4) 24 h-sessions were simulated using a network of 28 globally distributed stations. Within the software VieVS@GFZ, we apply different measurement noise at the observation level and investigate the impact on the TRF and on the Earth rotation parameters. We find that the effect of varying only the noise applied within the simulation is not proportional to the changes in the estimates and their uncertainties. For instance, increasing the noise level from 15 ps to 300 ps increases the uncertainty of the station positions by a factor of 3.5, of station velocities by 5, of polar motion by 3.4, and of UT1-UTC by 1.5. A comparison with the VLBI-TRF derived from real observations within the same time span shows that the solution simulated with a noise level based on the formal errors of real observations is still too optimistic.

Keywords

GGOS • Simulation • TRF • VLBI

1   Introduction

A global terrestrial reference frame (TRF) with highest accuracy, consistency and stability is necessary for the correct interpretation of geodetic products associated with Earth system sciences (Rummel 2000). This is of paramount importance in times of climate change. In order to make reliable statements about the changes within the Earth's system the uncertainties of the underlying TRF should be minimized.

For instance, uncertainties of the applied TRF are one of the most limiting factors for the determination of global sea-level rise from satellite altimeter data (Morel and Willis 2005). In the framework of the Global Geodetic Observing System (GGOS) a TRF should have an accuracy and a stability of 1 mm and 0.1 mm/year, respectively (Gross et al. 2009).

The most recent official realization of the conventional ITRS is called ITRF2014 and was derived from the combination of the following space geodetic techniques: Doppler Orbitography and Radiopositioning Integrated by Satellite (DORIS), Global Navigation Satellite System (GNSS), Satellite Laser Ranging (SLR) and Very Long Baseline Interferometry (VLBI). The accuracy of the predecessor of ITRF2014, ITRF2008, was estimated to be 1 cm for the origin and 1.2 ppb for the scale (corresponding to 8 mm at the Earth's surface) (Altamimi et al. 2011). Thus, the GGOS goals have not been met yet. Consequently, technique-specific and combination related issues have to be investigated thoroughly.

S. Glaser (✉) • H. Schuh • F. Flechtner
Institute of Geodesy and Geoinformation Science, Technische
Universität Berlin, Berlin, Germany
e-mail: susanne.glaser@tu-berlin.de

D. Ampatzidis • R. König • F. Flechtner
GFZ German Research Centre for Geosciences, Oberpfaffenhofen,
Wessling, Germany

H. Schuh • T. Nilsson • R. Heinkelmann
GFZ German Research Centre for Geosciences, Potsdam, Germany

Within the project GGOS-SIM ("Simulation of the Global Geodetic Observing System", Schuh et al. 2016) observations of DORIS, GNSS, SLR and VLBI are simulated and rigorous combination strategies are applied. This allows to comprehend the error sources contributing to TRF accuracy since the constituents of the simulated observations are completely understood as they are artificially generated.

The purpose of this study is to initially simulate VLBI observations which are close to real data and to determine a simulated VLBI-TRF. Furthermore, the effect of different simulation strategies on the TRF concerning accuracy and stability is investigated.

In this paper the strategy of the simulation (see Sect. 2.2) and combination (see Sect. 2.3) of VLBI observations by using the software VieVS@GFZ (Boehm et al. 2012; Nilsson et al. 2015) is described. In Sect. 3, our results (station positions, station velocities, Earth rotation parameters) are presented and compared to a VLBI-TRF obtained from real data, the ITRF2008, and the IERS 08 C04 series of Earth orientation parameters (EOP; Bizouard and Gambis 2011). Finally, the study is summarized by a discussion and conclusions in Sect. 4.

2   Strategy

2.1   Data

The input data comprise the standard VLBI rapid turnaround R1 and R4 sessions. Since R1 sessions are regularly starting on Monday and R4 on Thursday, the availability of these sessions is twice a week. In the time span from 2008 until 2014 in total 695 24 h-sessions were simulated. Each session uses a network of 7–11 stations. In total, 28 globally distributed stations were used, see Fig. 1. The selection of the observing stations and observing schedules were the same as used for the real observations of the same time span. In addition, real observations (R1 and R4 sessions of the International VLBI Service for Geodesy and Astrometry, Schuh and Behrend 2012) were used as well in order to compare with the simulated observations.

2.2   Simulation

The simulation strategy is based on a Monte Carlo Simulator (Pany et al. 2011) which allows to simulate the most prominent random error sources in VLBI data analysis: station clock and wet tropospheric delay. Furthermore, baseline dependent white noise can be added to the simulated data within the software VieVS@GFZ. The module vie_sim was used to obtain the reduced observation vector $\mathbf{l} = (\mathbf{o} - \mathbf{c})$ ("observed minus computed from a priori values") following:

$$(o - c) = (zwd_2 \cdot wmf_2(e) + clk_2) \tag{1}$$
$$- (zwd_1 \cdot wmf_1(e) + clk_1) + wn_{bsl},$$

where zwd_1, zwd_2 denote the simulated equivalent zenith wet delays based on the turbulence model of Nilsson and
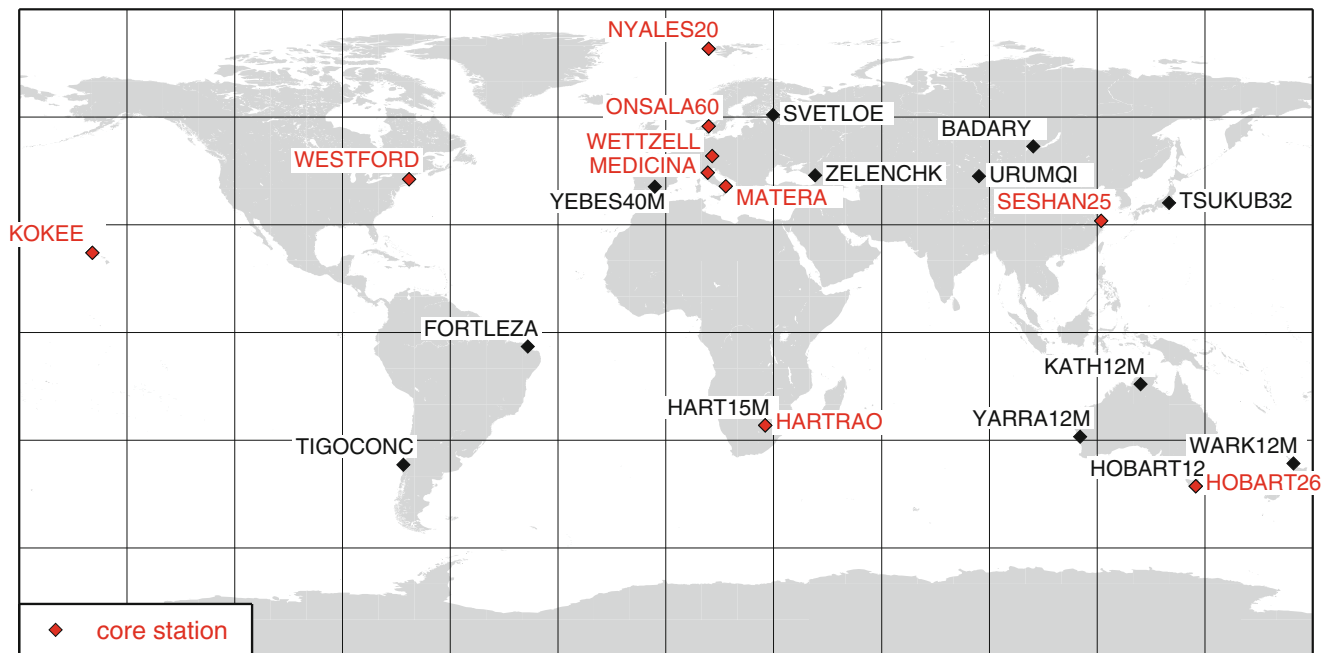
Fig. 1 Network with 23 stations used for the determination of the simulated VLBI-TRF. Ten core stations for datum definition are indicated with *red*. Five reduced stations (see Sect. 2.3) are not shown

Haas ([2010](#)) together with the mapping functions $wmf_1(e)$, $wmf_2(e)$ depending on the elevation angle e. clk_1, clk_2 are the simulated clock offsets (Boehm et al. [2006](#)) at station 1 and 2 of the baseline. The clocks are modeled as random walk plus an integrated random walk process (Herring et al. [1990](#)) with an Allan standard deviation $ASD = 1 \cdot 10^{-14}@50$ min which represents the accuracy of a high-performance maser system used at present VLBI sites. By tuning the white noise wn_{bsl} of the baseline bsl, different accuracy levels of the observations can be investigated. As far as the simulated zenith wet delays are concerned, the most important input parameters are the structure constant for the refractive index fluctuations which is based on the Kolmogorov turbulence theory (Tatarski [1961](#); Treuhaft and Lanyi [1987](#)) and the effective height of the troposphere. All input parameters for the simulation of the troposphere (e.g. north and east component of wind vector) are the same for all stations and assumed to be constant over the entire time span.

In order to derive simulated observations **o** the a priori computed values **c** known from reduction models have to be added to the simulated reduced observation vector $(\mathbf{o} - \mathbf{c})$ which leads to: $\mathbf{o} = (\mathbf{o} - \mathbf{c}) + \mathbf{c}$. Here, the solutions adhere to the IERS Conventions 2010 (Petit and Luzum [2010](#)). It is important to mention that the same reduction models (e.g. mapping functions $wmf_{1,2}$, cf. Eq. ([1](#))) were applied for the simulations as well as for the analysis of the observations. Therefore, it can be expected that no modeling effects propagate into the estimated parameters. Furthermore, no discontinuities due to earthquakes or antenna repairs were introduced neither within the simulations nor in the estimation of the parameters. This was done in order to get continuous observations and parameters without breaks. On the contrary, since stations in reality can be affected by earthquakes or antenna repairs, discontinuities[1] were introduced within the analysis of the real observations.

Finally, we end up with artificial observation files per session containing the simulated group delays as the main observable in geodetic VLBI data analysis. The simulated observations are of the same design as those which actually took place. These observations can then be analyzed also session-wise and combined to a VLBI-TRF, see Sect. [2.3](#).

2.3 Combination

The simulated observations were analyzed using the least squares module vie_lsm within VieVS@GFZ. The resulting datum-free session-wise normal equation systems (NEQs) were then combined by using the module vie_glob in order to determine a VLBI-only TRF. The NEQs contain sta-

tion positions, station velocities, station clock estimates, parameters concerning the troposphere (zenith wet delay, gradients in north-south and east-west), EOP (terrestrial pole coordinates, UT1-UTC, celestial pole offsets), and source positions (right ascension, declination). Within the combination these parameters have either been estimated, session-wise reduced, or fixed. As a TRF is usually based on a linear motion model consisting of station positions at a reference epoch and station velocities, these parameters were estimated together with Earth Rotation Parameters (ERP: pole coordinates and UT1-UTC). All other parameters were reduced from the NEQs besides the source positions. Source coordinates were fixed to their catalog values of the ICRF2 (Fey et al. [2015](#)) defining sources[2] with the exception of three having a structure index[3] of 4 which indicate a rather unstable position. These three sources and all non-defining sources (including special handling sources) were session-wise reduced from the NEQs. The rationale behind this is, that the estimated EOP derived within the TRF determination should be consistent with the celestial reference frame.

At some sites, the short observation time span did not allow to estimate reliable station velocities. Therefore, the coordinates of the stations AIRA, KASHIM11, and KASHIM34 (observed just few months within 2008–2014), TIANMA65 (one session) and PARKES (four sessions) were reduced from the NEQs. The geodetic datum of the VLBI-TRF was then realized in the following way:

– Origin and its temporal change: no-net translation condition w. r. t. ITRF2008 using 10 core stations (cf. Fig. [1](#))
– Scale and its temporal change: inherently from the VLBI observations
– Orientation and its temporal change: no-net rotation condition w. r. t. ITRF2008 using the same 10 core stations

3 Results

Four different solution types concerning the specification of white noise within the observation simulation process have been performed, see Table [1](#). One optimistic solution has

Table 1 Solution types of the simulated VLBI-TRF w. r. t. different amplitudes of white noise wn per baseline and type of noise (constant (c) or individual (i) for all observations and stations)

Solution	Amplitude of white noise	Type of noise
S003	$wn = 3$ ps ≈ 0.9 mm	c
S015c	$wn = 15$ ps ≈ 4.5 mm	c
S015i	$wn = 15$ ps ≈ 4.5 mm	i
S300	$wn = 300$ ps ≈ 89.9 mm	c

[1] http://lupus.gsfc.nasa.gov/files_IVS-AC/discontinuities.txt.

[2] http://hpiers.obspm.fr/webiers/icrf2/icrf2-defining.dat.
[3] http://vlbi.obs.u-bordeaux1.fr/index.php.

a relatively small uncertainty where the amplitude of white noise is about 1 mm (*S003*) and one pessimistic solution has a relatively large uncertainty of almost 10 cm (*S300*). In between, the solution *S015c* has an uncertainty of about 5 mm. All these solutions have a constant amplitude of white noise for all observations and stations. In contrast, the fourth solution *S015i* is based on the formal errors of the delays of the real observations with an average of 15 ps. The amplitude of white noise in this solution was set individually for every observation and station taken from real observations (formal delay error) in the same time span. The motivation for the solution *S015i* was to approach as close as possible the real data.

Between the four simulated VLBI-TRFs (sim-VLBI-TRF) and the VLBI-TRF determined from real observations (real-VLBI-TRF) 14-parameter Helmert transformations (three translations, three rotations, one scale offset and the respective rates) were computed w. r. t. the ITRF2008 at the reference epoch 2005.0 considering all stations of the network, see Table 2. Stations with residuals larger than 3σ were eliminated (URUMQI in this case). The differences of the transformation parameters within the simulated VLBI-TRFs are not significant for the noise levels of 3 ps and 15 ps. In case of the simulated TRF with noise level of 300 ps the values and uncertainties of the transformation parameters increased significantly by about a factor of 2 compared to the other sim-VLBI-TRFs. The transformation parameters for all solutions attest an agreement with ITRF2008 of several sub-mm up to a few mm. The differences are relatively small since the datum of the sim-TRFs and the real-TRF are realized by NNT/NNR w. r. t. the ITRF2008 positions and velocities and the simulated observations only

consist of random error sources. The largest values in the transformation parameters appear in T_x of the *S300* (1.6 mm) and the *real* (−1.6 mm) solution and in R_z of the *real* (50 µas ≈ 1.5 mm) solution w. r. t. ITRF2008. Furthermore, comparing the standard deviations of the transformation parameters between the real-VLBI-TRF and ITRF2008 are about 2–6 times larger compared to the sim-VLBI-TRFs (depending on the used white noise amplitude). A potential explanation could be that the simulated observations are still too optimistic. However, the nature of the real observations is not of white noise character (as applied in the simulation). In addition, the real observations are influenced by station events, e.g. due to earthquakes which may cause shorter observation time spans due to discontinuities in the station time series. In contradiction, the simulated observations are based on continuous stochastic processes. Overall, it should be noted that the standard deviations indicate that the transformation parameters could not be estimated significantly in the statistical sense.

The velocity differences in the north, east and up component between 17 stations with ITRF2008 coordinates of the sim-VLBI-TRF *S015i* and the real-VLBI-TRF compared to ITRF2008 are illustrated in Fig. 2 as well as the mean and standard deviation of all solutions (cf. Table 1). The largest differences in the station velocities occur at station URUMQI which was eliminated due to residuals larger than 3σ within the Helmert transformations. The differences at the other stations in case of the sim-TRF are in almost all cases below 1 mm/year. In case of the real-VLBI-TRF the differences are larger compared to the sim-VLBI-TRFs. A reason could be that the simulated observations with measurement noise taken from real observations are still too optimistic. Another

Table 2 The 14-parameter Helmert transformations (translation T_x, T_y, T_z, rotation R_x, R_y, R_z, scale D, and their temporal changes with their corresponding standard deviations) at reference epoch 2005.0 of a VLBI-TRF from simulated observations (different solution types Table 1) and a VLBI-TRF from real observations with standard deviation s_0 of the transformation w.r.t. ITRF2008

	T_x [mm]	T_y [mm]	T_z [mm]	R_x [µas]	R_y [µas]	R_z [µas]	D [ppb]	s_0 [mm]
S003								
pos	0.7 ± 0.6	-0.7 ± 0.6	-0.1 ± 0.6	27 ± 24	8 ± 22	-2 ± 24	-0.12 ± 0.09	2.0
vel [/year]	-0.1 ± 0.1	0.1 ± 0.1	-0.0 ± 0.1	-3 ± 3	-2 ± 3	0 ± 3	0.02 ± 0.01	0.3
S015i								
pos	-0.0 ± 0.7	-1.2 ± 0.8	-0.5 ± 0.7	23 ± 30	16 ± 28	-28 ± 30	0.10 ± 0.11	2.5
vel [/year]	-0.0 ± 0.1	0.2 ± 0.1	0.1 ± 0.1	-3 ± 4	-2 ± 4	4 ± 4	-0.01 ± 0.02	0.3
S015c								
pos	0.1 ± 0.7	-0.3 ± 0.7	-0.1 ± 0.6	20 ± 26	-16 ± 25	13 ± 26	-0.16 ± 0.10	2.2
vel [/year]	0.0 ± 0.1	0.0 ± 0.1	-0.0 ± 0.1	-2 ± 4	3 ± 4	-2 ± 4	0.03 ± 0.01	0.3
S300								
pos	1.6 ± 1.5	-0.9 ± 1.5	0.3 ± 1.4	34 ± 58	27 ± 55	10 ± 58	-0.01 ± 0.22	5.0
vel [/year]	-0.3 ± 0.2	0.1 ± 0.2	-0.1 ± 0.2	-2 ± 10	-4 ± 9	-0 ± 10	0.01 ± 0.04	0.8
real								
pos	-1.6 ± 2.3	0.2 ± 2.4	-0.9 ± 2.3	5 ± 93	3 ± 87	50 ± 92	0.10 ± 0.35	7.7
vel [/year]	0.3 ± 0.5	-0.2 ± 0.5	0.0 ± 0.5	-2 ± 20	1 ± 19	-24 ± 20	0.04 ± 0.08	1.7

Fig. 2 Velocity differences in [mm/year] in the north, east and up component between stations of the sim-VLBI-TRF with 15 ps individual noise level (*S015i*, in *red*), the real-VLBI-TRF (*blue*) and the ITRF2008 at reference epoch 2005.0. Numbers indicate mean ± standard deviation and [min max] value of all solutions, see Table 1

Table 3 Standard deviations σ of the estimated station positions and velocities (average over all stations) of a VLBI-TRF from simulated observations (different solution types cf. Table 1) and a VLBI-TRF from real observations

	σ_x [mm]	σ_y [mm]	σ_z [mm]
S003			
pos	6.0	5.8	6.3
vel [/year]	0.6	0.4	0.6
S015i			
pos	6.2	5.9	6.4
vel [/year]	0.6	0.5	0.6
S015c			
pos	5.2	5.4	5.7
vel [/year]	0.5	0.4	0.5
S300			
pos	19.7	16.6	21.1
vel [/year]	2.4	2.0	2.6
real			
pos	9.3	10.2	9.9
vel [/year]	1.1	1.2	1.2

Table 4 Mean and standard deviation of estimated ERP (pole coordinates x_p, y_p, and UT1-UTC) from VLBI-TRF determination based on simulated and real observations (different solution types cf. Table 1) w.r.t. IERS 08 C04 EOP series

	x_p [mas]	y_p [mas]	UT1-UTC [ms]
S003	0.004 ± 0.144	0.002 ± 0.148	-0.001 ± 0.015
S015i	0.000 ± 0.145	0.003 ± 0.149	0.000 ± 0.015
S015c	-0.000 ± 0.109	0.001 ± 0.126	-0.001 ± 0.014
S300	-0.001 ± 0.382	0.040 ± 0.421	-0.002 ± 0.021
real	0.022 ± 0.309	0.048 ± 0.646	0.000 ± 0.026

real-VLBI-TRF are tabulated in Table 3. As anticipated, the standard deviations of the estimated positions and velocities increase when more noise has been introduced in the simulated observations. There is a significant increase of the uncertainty by a factor of about 3.5 in case of station positions and of about 5 in case of station velocities when going from a noise level of 15 ps to 300 ps. Compared to the real observations, the solution *S015i* which was supposed to be closest to the real data, seems still too optimistic.

The mean and standard deviation of the estimated ERP (pole coordinates x_p, y_p and UT1-UTC) w.r.t. the IERS 08 C04 EOP series of all solutions are presented in Table 4. As far as the different VLBI-TRFs from simulated observations are concerned, the standard deviations indicate that the noise level significantly affects the estimated ERP. As expected, the more noise is included in the simulated observations, the larger is the scatter of the estimates. However, changing from 3 ps to 15 ps does not drastically impact the ERPs, indeed the scatter actually decreases. When increasing noise from 15 ps to 300 ps, both pole components and UT1-UTC have more

reason could be errors in ITRF2008. Considering the means and standard deviations of all solutions indicate that the sim-VLBI-TRF based on 300 ps noise level is closest to the velocity estimates from real observations.

The standard deviations of the estimated station positions and velocities of the sim-VLBI-TRFs and the

scatter, by a factor of 3.4 for the pole components and of 1.5 for the UT1-UTC results.

4 Discussion and Conclusion

The impact of different noise levels in simulated VLBI observations on the parameters of a TRF was investigated by using 695 24 h-sessions within 2008–2014. The estimated parameters such as station positions, velocities and ERP as well as their standard deviations do not significantly differ in case of the investigated noise levels of 3 ps and 15 ps. However, increasing the noise level from 15 ps to 300 ps results in larger standard deviations of the estimates. For the station positions by a factor of about 3.5 and for the station velocities by about 5. The uncertainty of the pole coordinates increases by 3.4 while in the case of UT1-UTC by 1.5. This shows that uncertainties of the estimates do not change according to the white noise applied. The reason is that besides white noise, zenith wet delays and station clocks are simulated as well and seem to dominate the simulations.

The simulation of white noise according to the formal error of the real observations is out of the investigated noise levels the best approximation of the real observations. However, the standard deviations of the estimated station positions and velocities and of the ERP indicate that the white noise amplitude of 15 ps on average seems to be too optimistic. In further studies other noise types, e.g. colored noise can be used in addition. The noise level should be in total less then 300 ps in order to get simulated observations close to reality.

Since the TRF GGOS goals have not been met so far for a TRF based on real observations, different observation scenarios have to be investigated as well. For instance, the simulation of artificial stations, e.g. on the southern hemisphere can show how much a better global distribution of the station network can improve the TRF.

Moreover, it should be emphasized that the evaluation of the resulting TRF is not a trivial task. The accuracy of the ITRF2008 is assessed by comparisons to previous realizations via Helmert transformations. External evaluation with geodetic data should be considered as well, e.g. post-glacial rebound models, tectonic plate motion models, absolute gravity observations (Collilieux et al. 2014), which have not been used for the TRF determination.

Further studies within project "GGOS-SIM" will include the combination of the NEQs from other techniques, e.g. SLR. Within the combinations we can investigate the impact of different combination strategies, e.g. the co-location points of the techniques: local ties at the stations, space ties (e.g. SLR to GNSS satellites, Geodetic Reference Antenna in Space: GRASP), global ties (like ERPs) or also tropospheric ties. Important to note is that the same simulation strategy and the same reduction models together with the same software (EPOS-OC, Zhu et al. 2004) will be used in order to prevent the introduction of inconsistencies between the solutions of the different techniques into the combination.

References

Altamimi Z, Collilieux X, Métivier L (2011) ITRF2008: an improved solution of the international terrestrial reference frame. J Geod 85(8):457–473. doi:10.1007/s00190-011-0444-4

Bizouard C, Gambis D (2011) The combined solution C04 for Earth orientation parameters consistent with international terrestrial reference frame 2008. http://hpiers.obspm.fr/iers/eop/eopc04/C04.guide.pdf

Boehm J, Wresnik J, Pany A (2006) Simulation of wet zenith delays and clocks. Technical report, IVS Memorandum 2006-013v03. ftp://ivscc.gsfc.nasa.gov/pub/memos/ivs-2006-013v03.pdf

Boehm J, Boehm S, Nilsson T, Pany A, Plank L, Spicakova H, Teke K, Schuh H (2012) The New Vienna VLBI software VieVS. In: Kenyon S, Pacino MC, Marti U (eds) Geodesy for planet Earth. International Association of Geodesy Symposia, vol 136. Springer, Berlin/Heidelberg, pp 1007–1011. doi:10.1007/978-3-642-20338-1_126

Collilieux X, Altamimi Z, Argus D, Boucher C, Dermanis A, Haines B, Herring T, Kreemer C, Lemoine F, Ma C, MacMillan D, Mäkinen J, Métivier L, Ries J, Teferle F, Wu X (2014) External evaluation of the terrestrial reference frame: report of the task force of the IAG sub-commission 1.2. In: Rizos C, Willis P (eds) Earth on the edge: science for a sustainable planet. International Association of Geodesy Symposia, vol 139, Springer, Berlin/Heidelberg, pp 197–202. doi:10.1007/978-3-642-37222-3_25

Fey AL, Gordon D, Jacobs CS, Ma C, Gaume RA, Arias EF, Bianco G, Boboltz DA, Böckmann S, Bolotin S, Charlot P, Collioud A, Engelhardt G, Gipson J, Gontier AM, Heinkelmann R, Kurdubov S, Lambert S, Lytvyn S, MacMillan DS, Malkin Z, Nothnagel A, Ojha R, Skurikhina E, Sokolova J, Souchay J, Sovers OJ, Tesmer V, Titov O, Wang G, Zharov V (2015) The second realization of the international celestial reference frame by very long baseline interferometry. Astron J 150(2):58. http://stacks.iop.org/1538-3881/150/i=2/a=58

Gross R, Beutler G, Plag HP (2009) Integrated scientific and societal user requirements and functional specifications for the GGOS. In: Global geodetic observing system: meeting the requirements of a global society on a changing planet in 2020. Springer, Berlin/Heidelberg, pp 209–224. doi:10.1007/978-3-642-02687-4_7

Herring TA, Davis JL, Shapiro II (1990) Geodesy by radio interferometry: the application of Kalman filtering to the analysis of very long baseline interferometry data. J Geophys Res Solid Earth 95(B8):12,561–12,581. doi:10.1029/JB095iB08p12561

Morel L, Willis P (2005) Terrestrial reference frame effects on global sea level rise determination from TOPEX/Poseidon altimetric data. Adv Space Res 36(3):358–368. http://dx.doi.org/10.1016/j.asr.2005.05.113

Nilsson T, Haas R (2010) Impact of atmospheric turbulence on geodetic very long baseline interferometry. J Geophys Res Solid Earth 115(B3):b03407. doi:10.1029/2009JB006579

Nilsson T, Soja B, Karbon M, Heinkelmann R, Schuh H (2015) Application of Kalman filtering in VLBI data analysis. Earth Planets Space 67(1):1–9. doi:10.1186/s40623-015-0307-y

Nothnagel A, International VLBI Service for Geodesy and Astrometry (IVS) et al (2015) The IVS data input to ITRF2014. International VLBI Service for Geodesy and Astrometry, GFZ Data Services. doi:10.5880/GFZ.1.1.2015.002

Pany A, Boehm J, MacMillan D, Schuh H, Nilsson T, Wresnik J (2011) Monte Carlo simulations of the impact of troposphere, clock and measurement errors on the repeatability of VLBI positions. J Geod 85(1):39–50. doi:10.1007/s00190-010-0415-1

Petit G, Luzum B (eds) (2010) IERS Conventions (2010). IERS Technical note, vol 36. Verlag des Bundesamts für Kartographie und Geodäsie, Frankfurt am Main, Germany

Rummel R (2000) Global integrated geodetic and geodynamic observing system (GIGGOS). In: Towards an integrated global geodetic observing system (IGGOS). International Association of Geodesy Symposia, vol 120. Springer, Berlin/Heidelberg, pp 253–260. doi:10.1007/978-3-642-59745-9_53

Schuh H, Behrend D (2012) VLBI: a fascinating technique for geodesy and astrometry. J Geodyn 61:68–80. doi:http://dx.doi.org/10.1016/j.jog.2012.07.007

Schuh H, König R, Ampatzidis D, Glaser S, Flechtner F, Heinkelmann R, Nilsson TJ (2016) GGOS-SIM: simulation of the reference frame for the global geodetic observing system. Springer, Berlin/Heidelberg, pp 1–6. doi:10.1007/1345_2015_217

Tatarski VI (1961) Wave propagation in a turbulent medium. Translated by R.A. Silverman. McGraw-Hill, New York, 285 pp. Science 134(3475):324–325. doi:10.1126/science.134.3475.324-b

Treuhaft RN, Lanyi G (1987) The effect of the dynamic wet troposphere on radio interferometric measurements. Radio Sci 22(2):251–265

Zhu S, Reigber C, König R (2004) Integrated adjustment of CHAMP, GRACE, and GPS data. J Geod 78(1–2):103–108. doi:10.1007/s00190-004-0379-0

The Assessment of the Temporal Evolution of Space Geodetic Terrestrial Reference Frames

Dimitrios Ampatzidis, Rolf König, Susanne Glaser, and Harald Schuh

Abstract

The assessment of the accuracy and the stability of the global Terrestrial Reference Frames (TRFs) is a matter of great importance for the geodetic community. The classical Helmert transformation plays a crucial role in terms of evaluating the datum related parameters of global TRFs (origin, scale, and orientation, and their associated rates). We discuss a new alternative approach for the assessment of TRFs temporal evolution and we compare it with the Helmert transformation. Our concept relies on the splitting of the velocities into two specified parts. The first one is referred to the reference system effect and the latter one to the deformation, respectively. This separation is done in order to create the necessary mathematical tools for the TRF assessment. The new approach is tested on the single-technique TRFs (VLBI, SLR, GPS and DORIS, respectively) of the DTRF2008. The novelty of the new methodology is its ability to treat individually the systematic errors of each TRF. This feature detects systematic effects that the Helmert transformation cannot. The results reveal that the new approach and the Helmert transformation show almost the same results in terms of rates of the datum parameters with an uncertainty of 0.1–0.3 mm/year for the four space geodetic techniques TRFs. The uncertainty refers to the estimated rate differences standard deviation between the new approach and the Helmert one.

Keywords

DTRF2008 • Helmert transformation • Reference system • Space geodetic techniques • Temporal evolution

D. Ampatzidis (✉) • R. König
German Research Center for Geosciences (GFZ), Oberpfaffenhofen, 82234 Wessling, Germany
e-mail: ampatzi@gfz-potsdam.de

S. Glaser
Technical University of Berlin (TUB), Straße des 17. Juni 135, 10623 Berlin, Germany

H. Schuh
German Research Center for Geosciences (GFZ), Oberpfaffenhofen, 82234 Wessling, Germany

Technical University of Berlin (TUB), Straße des 17. Juni 135, 10623 Berlin, Germany

1   Introduction

The quality assessment of global Terrestrial Reference Frames (TRFs) is mainly based on the well known Helmert type transformation (Helmert 1880). For example, the internal assessment of the origin and its time variation of a global TRF is realized through the comparison of the Helmert translation parameters between the SLR-only and the final combined global TRF (Altamimi et al. 2011; Seitz et al. 2012). The scale and its rate are evaluated through the comparison of the SLR- and VLBI-only TRFs (e.g. Altamimi et al. 2011). However, none of the space geodetic techniques provides any orientation information with respect

to the TRF (just VLBI senses the orientation with respect to the celestial frame). The estimated Helmert type parameters (origin and scale) assess the consistency and agreement of the global TRF relative to the different space-technique TRFs (e.g. VLBI-TRF and SLR-TRF) and therefore its accuracy. Thus it is necessary to judge the Helmert transformation itself, checking its ability to detect all possible systematic effects in terms of origin, scale and orientation of the global TRF solution. This is achieved through the suggested new approach. In this paper, we present it for the assessment of the temporal evolution of the associated space technique-wise TRFs of the DTRF2008 (Seitz et al. 2012) and we compare it with the classical Helmert transformation.

2   The Mathematical Model

Let us assume that the 3D velocity vector $\mathbf{v}$ of any point i can be divided into two parts: (a) The artificial quantity $\mathbf{v}^{tr}$ which refers to the reference system effect and is directly connected to the datum choice (through the constraints) and (b) the deformation part δv which reflects the tectonic motion or/and the post glacial rebound. The mathematical expression yields (Dermanis, 2015, personal communication; Schuh et al. 2016):

$$\mathbf{v}_i = \mathbf{v}_i^{tr} + \delta\tilde{\mathbf{v}}_i \tag{1}$$

where the term $\delta\tilde{\mathbf{v}}_i = \delta\mathbf{v}_i + \mathbf{e}_i$ represents the real deformation and the associated error term $\mathbf{e}_i$. The straightforward linear relation between the 3D coordinate vector $\mathbf{x}$ in two different epochs t_0 and t is:

$$\begin{aligned} \mathbf{x}_i(t) &= \mathbf{x}_i(t_0) + \mathbf{v}_i^{tr} \cdot (t - t_0) + \delta\tilde{\mathbf{v}}_i \cdot (t - t_0) \Rightarrow \\ \mathbf{x}_i(t) &= \mathbf{x}_i(t_0) + \delta\mathbf{x}_i(t) + \delta\tilde{\mathbf{v}}_i \cdot (t - t_0) \end{aligned} \tag{2}$$

The term $\delta\mathbf{x}_i^t$ corresponds to a spatial change between the two epochs. This spatial change is related to the reference system effect and it can be expressed by the Helmert transformation as follows:

$$\delta\mathbf{x}_i(t) = \mathbf{v}_i^{tr} \cdot (t - t_0) = \mathbf{E}_i \boldsymbol{\theta}(t) \tag{3}$$

where $\mathbf{E}_i$ is the design matrix (see e.g. Altamimi et al. 2002, Eq. A6) and $\boldsymbol{\theta}(t) = \begin{bmatrix} t_x(t) & t_y(t) & t_z(t) & \delta s(t) & r_x(t) & r_y(t) & r_z(t) \end{bmatrix}^T$ the seven time dependent Helmert parameters (translations, scale, and orientations, respectively). Combining Eqs. (2) and (3) we finally get:

$$\mathbf{x}_i(t) - \mathbf{x}_i(t_0) = \mathbf{E}_i \boldsymbol{\theta}(t) + \delta\tilde{\mathbf{v}}_i \cdot (t - t_0) \tag{4}$$

After dividing by the time difference term $(t - t_0)$ and since $\mathbf{x}_i(t) - \mathbf{x}_i(t_0) / (t - t_0) = \mathbf{v}_i$ we get:

$$\mathbf{v}_i = \mathbf{E}_i \boldsymbol{\theta}(t) / (t - t_0) + \delta\tilde{\mathbf{v}}_i \tag{5}$$

For the selected network points of a specified TRF Eq. (5) becomes:

$$\mathbf{v} = \mathbf{E}\dot{\boldsymbol{\theta}} + \delta\tilde{\mathbf{v}} \tag{6}$$

where $\dot{\boldsymbol{\theta}}$ is the vector of the estimated rates of the Helmert transformation parameters', $\mathbf{v} = \begin{bmatrix} \mathbf{v}_i^T & \cdots & \mathbf{v}_n^T \end{bmatrix}^T$ the vector of the observed 3D velocities, and $\mathbf{E} = \begin{bmatrix} \mathbf{E}_i^T & \cdots & \mathbf{E}_n^T \end{bmatrix}^T$ the total design matrix. Applying the least squares principle $\delta\tilde{\mathbf{v}}^T \mathbf{C}^{-1} \delta\tilde{\mathbf{v}} = \min$ we estimate the rates of the parameters (using the classical Least Squares approach):

$$\widehat{\dot{\boldsymbol{\theta}}} = \left(\mathbf{E}^T \mathbf{C}^{-1} \mathbf{E}\right)^{-1} \mathbf{E}^T \mathbf{C}^{-1} \mathbf{v} \tag{7}$$

where $\mathbf{C}$ is the error covariance matrix of the observed velocities. As an additional comment, we should note that the norm minimization refers not only to the deformation part $\delta\mathbf{v}$; it contains inevitably the error effects of the observed velocities. However, the random errors of the velocities – for the majority of the stations – are relatively much smaller than the deformation signal itself and it can be assumed that their effects do not change significantly the interpretation of the results. The latter is achieved by carefully selecting stations of good quality, namely stations with relatively small uncertainties of the velocities (e.g. velocities with uncertainty equal or better than 1 mm/year).

The artificial part of the velocities (Eq. 2) expresses a global trend of the velocities and does not have any geophysical interpretation. Furthermore, we should note that the suggested methodology is applicable only in a relative sense, as we describe in the next section. This practically means that the estimated parameters from an individual TRF do not provide any geometric or physical meaning.

2.1   The Relation with the Helmert Transformation

The two approaches, the new one and the Helmert transformation coincide if and only if: (a) They are applied only to common stations and (b) They share a common error covariance matrix of the observations. Then, the difference of the estimated parameters between two different frames A and B is expressed as follows:

$$\begin{aligned} \Delta\widehat{\dot{\boldsymbol{\theta}}}_{AB} &= \widehat{\dot{\boldsymbol{\theta}}}_B - \widehat{\dot{\boldsymbol{\theta}}}_A = \left(\mathbf{E}^T \mathbf{C}^{-1} \mathbf{E}\right)^{-1} \mathbf{E}^T \mathbf{C}^{-1} \left(\mathbf{v}_B - \mathbf{v}_A\right) \Rightarrow \\ \Delta\widehat{\dot{\boldsymbol{\theta}}}_{AB} &= \left(\mathbf{E}^T \mathbf{C}^{-1} \mathbf{E}\right)^{-1} \mathbf{E}^T \mathbf{C}^{-1} \mathbf{v}_{AB} \end{aligned} \tag{8}$$

Fig. 1 The single-technique TRFs of DTRF2008, used for this study
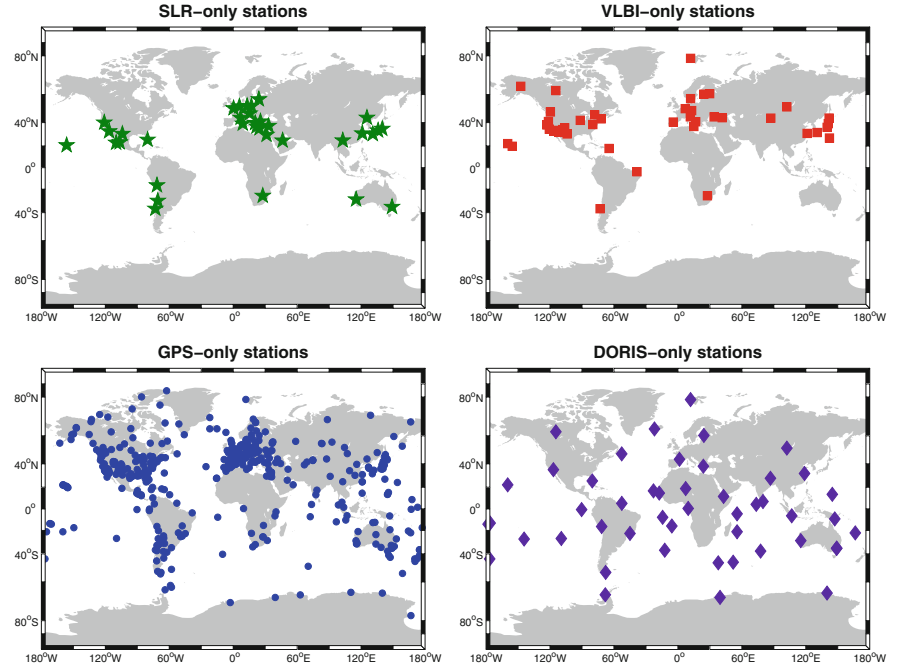
where $\Delta\hat{\boldsymbol{\theta}}_{AB}, \mathbf{v}_{AB}$ are the differences of the parameters and velocities, respectively. Equation (8) can be used as an assessment tool for the temporal evaluation of the TRF. Since the estimated rates are strongly correlated with the reference system choice, this approach can be used for the comparison of: (a) Different TRFs, (b) The same TRF using different constraint choices and (c) a space geodetic technique-wise TRFs versus the final combined solution.

If the aforementioned conditions are fulfilled but the numerical results of the two methodologies differ, it is rather possible that there exist some systematic errors undetectable by the Helmert transformation. Let us assume that there are some undetected and unknown systematic errors of the observed TRF velocities which can be represented with the additional vector $\boldsymbol{\psi}$. The classical Helmert transformation velocity differences are expressed as follows:

$$\mathbf{v}_{AB}^{Helmert} = \mathbf{v}_B - \mathbf{v}_A + \mathbf{B}\left(\boldsymbol{\psi}_B - \boldsymbol{\psi}_A\right) \tag{9a}$$

In the case of the new approach the corresponding term becomes:

$$\mathbf{v}_{AB}^{new\ approach} = \mathbf{v}_B - \mathbf{v}_A + \mathbf{B}_B\boldsymbol{\psi}_B - \mathbf{B}_A\boldsymbol{\psi}_A \tag{9b}$$

where $\mathbf{B}$ is the matrix which is associated to the undetected systematic errors of the velocities, relating them to the observed velocities. The subscript refers to each of the examined frames. We can imply that in the case of the new approach each undetected systematic error refers to the specified frame only and they do not have necessarily the same effect as in the case of the classical Helmert

transformation. Indeed, the new approach treats separately each velocity set which carries its own systematic errors. On the contrary, the Helmert transformation uses only the velocity differences and the possible biases have a relative sense. Hence, any parameters' differences between the two methodologies will reflect the undetected systematic errors.

3 Numerical Application: The DTRF2008 Technique-Wise TRFs

For the numerical tests we use the associated technique-wise TRFs of the DTRF2008. We apply our methodology to the single-technique TRFs and then we applied the Helmert transformation of these TRFs w.r.t the DTRF2008. Figure 1 depicts the four space technique TRFs of the DTRF2008. The error covariance matrices practically coincide for the case of the single-technique TRFs and the final combined solution. In the first step, we exclude stations if at least one of the uncertainties of the velocity components is larger than 1 mm/year. This criterion is imposed in order to minimize the effect of problematic stations to the final results. Then, we apply the least square adjustment for the Helmert transformation and we remove stations if at least one of its 3D residual components is larger than three times residuals' standard deviation. The residual RMS of the Helmert transformations between each space technique TRF and the DTRF2008 are: 0.25 mm/year for VLBI (42 stations) and GPS (441 stations), 0.35 mm/year for SLR (34 stations), and 0.84 mm/year for DORIS (49 stations). Tables 1 and 2 compile to the parameters and their standard deviations for the new approach

Table 1 The estimated parameters for single-technique TRF versus DTRF2008 using the new approach [Eq. (8) ibid.]

Parameters	VLBI	SLR	GPS	DORIS
$\dot{t}_x$	-0.41 ± 0.04	-0.07 ± 0.04	-0.01 ± 0.08	-0.13 ± 0.10
$\dot{t}_y$	-0.29 ± 0.03	0.15 ± 0.04	0.11 ± 0.08	0.32 ± 0.10
$\dot{t}_z$	-0.10 ± 0.04	0.08 ± 0.04	-0.08 ± 0.08	0.75 ± 0.10
$\delta\dot{s}$	-0.03 ± 0.03	-0.07 ± 0.03	0.22 ± 0.08	-0.20 ± 0.08
$\dot{r}_x$	1.12 ± 0.06	-0.09 ± 0.07	0.00 ± 0.07	-0.93 ± 0.08
$\dot{r}_y$	-0.39 ± 0.06	-0.03 ± 0.07	0.00 ± 0.07	0.18 ± 0.10
$\dot{r}_z$	-0.47 ± 0.07	-0.37 ± 0.08	0.03 ± 0.08	0.13 ± 0.10

Units are in mm/year

Table 2 The estimated parameters for the single-technique TRF versus DTRF2008 using the Helmert transformation w.r.t DTRF2008

Parameters	VLBI	SLR	GPS	DORIS
$\dot{t}_x$	-0.35 ± 0.09	-0.05 ± 0.07	-0.04 ± 0.08	-0.10 ± 0.24
$\dot{t}_y$	-0.35 ± 0.09	0.12 ± 0.07	0.10 ± 0.08	0.40 ± 0.24
$\dot{t}_z$	0.02 ± 0.09	0.06 ± 0.07	-0.05 ± 0.08	0.80 ± 0.23
$\delta\dot{s}$	-0.05 ± 0.05	-0.10 ± 0.05	0.18 ± 0.01	-0.15 ± 0.24
$\dot{r}_x$	1.22 ± 0.13	0.06 ± 0.12	-0.03 ± 0.03	-0.95 ± 0.31
$\dot{r}_y$	-0.33 ± 0.13	-0.06 ± 0.12	-0.03 ± 0.03	0.08 ± 0.31
$\dot{r}_z$	-0.39 ± 0.13	-0.28 ± 0.12	0.06 ± 0.03	0.03 ± 0.31

Units are in mm/year

Table 3 The differences between the two approaches (new approach minus Helmert)

Parameters	VLBI	SLR	GPS	DORIS
$\dot{t}_x$	-0.06 ± 0.10	-0.02 ± 0.08	0.03 ± 0.09	-0.03 ± 0.26
$\dot{t}_y$	0.06 ± 0.09	0.03 ± 0.08	0.01 ± 0.09	-0.08 ± 0.26
$\dot{t}_z$	0.12 ± 0.10	0.02 ± 0.08	-0.03 ± 0.09	-0.05 ± 0.26
$\delta\dot{s}$	0.02 ± 0.06	0.03 ± 0.06	0.04 ± 0.08	-0.05 ± 0.25
$\dot{r}_x$	-0.10 ± 0.14	-0.15 ± 0.14	0.03 ± 0.08	0.02 ± 0.32
$\dot{r}_y$	-0.06 ± 0.14	0.03 ± 0.14	0.03 ± 0.08	0.10 ± 0.33
$\dot{r}_z$	-0.08 ± 0.14	-0.09 ± 0.14	-0.03 ± 0.09	0.10 ± 0.33

Units are in mm/year

and for the Helmert transformation (single-technique TRF versus DTRF2008), respectively, while Table 3 refers to the differences of the two methods.

The standard deviations of the parameters of the new proposed methodology are smaller than in the case of the classical Helmert transformation. However, we find relatively large differences though not significant differences at the 95% confidence level for the translation rate of the z axis for VLBI and for the orientation rate about the x axis for SLR, respectively. We have already mentioned that VLBI is insensitive to origin and orientation and SLR to orientation, respectively. The differences reveal that there could exist some undetected systematic errors which the Helmert transformation cannot detect. Nevertheless, these differences are insignificant due to their associated uncertainties. The large values could be caused by different constraint choices for the single-techniques TRFs (VLBI and SLR, respectively) and the final combined DTRF2008 solution.

The scale rates of the SLR and VLBI TRFs do not show any significant discrepancies. In addition, the SLR translation rates do not display inconsistencies. The GPS only TRF presents the best consistency between the two methodologies. The uncertainty is found at the level of 0.1 mm/year for VLBI, SLR and GPS and 0.3 mm/year for DORIS, respectively. The uncertainty refers to the standard deviation of the differences between the two methodologies.

One immediately finds that the results of the new methodology do not differ significantly from those of Helmert transformation. The straightforward question will be: does the suggested methodology offer anything new to the assessment of the temporal variation of the TRFs? In fact, the new methodology judges the results of the Helmert transformation. As we mentioned and proved before the new methodology treats the systematic effects of each TRF separately. This is the greatest advantage of the suggested strategy; it provides

a rigorous assessment of the TRFs temporal variation. If the two methodologies give the same results this fairly ensures that the Helmert transformation does not miss systematic errors.

4 Summary and Future Work

We presented an alternative approach for the assessment of the temporal evolution of a global TRF. The comparison of the new methodology with the classical Helmert transformation gives an additional option for the evaluation of global TRFs. The major advantage of the new methodology is the treatment of the systematic errors individually for each TRF. This offers a robust assessment of single-technique TRF temporal variation. On the contrary, the classical Helmert transformation is unable to separate systematic effects in each frame, since it handles the velocity differences only. The results for the DTRF2008 imply that the two methodologies (the new one and the Helmert transformation) are consistent to better than 0.1 mm/year in terms of the origin and scale rates. For the case of GPS and DORIS TRFs we found the same results with uncertainty of 0.1 and 0.3 mm/year, respectively.

One should be careful when applying and comparing the two methodologies. Any undetected blunder could distort significantly the results and their interpretation. Thus, a proper data evaluation should be initially applied to the Helmert transformation results. In addition, the two different methodologies should be applied to a common set of stations, sharing also the same covariance matrix of the observation errors. This approach can be considered as an alternative tool for the validation of the results of the classical Helmert transformation. As a final comment, the new approach could also be applied to a variety of reference frames like regional and local ones.

References

Altamimi Z, Sillard P, Boucher C (2002) ITRF2000: a new release of the International Terrestrial Reference Frame for earth science applications. J Geophys Res 107:B10. doi:10.1029/2001JB000561

Altamimi Z, Collilieux X, Métivier L (2011) ITRF2008: an improved solution of the International terrestrial reference frame. J Geodesy 85:457–473. doi:10.1007/s00190-011-0444-4

Helmert FR (1880) Die mathematischen und physikalischen Theorieen der Höheren Geodäsie, Band I. Verlag Teubner, Leipzig

Schuh H, König R, Ampatzidis D, Flechtner F, Glaser S, Heinkelmann R, Nilsson T (2016) GGOS-SIM: Simulation of the Reference Frame for the Global Geodetic Observing System. In: International Association of Geodesy Symposia [online]. http://doi.org/10.1007/1345_2015_217

Seitz M, Angermann D, Bloßfeld M, Drewes H, Gerstl M (2012) The 2008 DGFI realization of the ITRS: DTRF2008. J Geodesy 86(12):1097–1123. doi:10.1007/s00190-012-0567-2

Analysis Strategies for the Densification of the ICRF with VLBA Calibrator Survey Sources

Hana Krásná, David Mayer, and Johannes Böhm

Abstract

Six campaigns with a total of twenty-four Very Long Baseline Array Calibrator Survey (VCS) observing sessions were carried out with ten radio telescopes located on U.S. territory from 1994 to 2007. The aim of those astrometric sessions was to estimate source positions and to make snapshot images of compact radio sources. Coordinates of about two thirds of the sources in the ICRF2 catalogue are estimated from VCS sessions, most of them from two scans in one session only. Moreover, there are systematic errors due to the deficiencies of a continent-wide network for the estimation of Earth orientation parameters (EOP) and the linking between the celestial and terrestrial frame. We investigate the impact of EOP estimation on source positions for those sessions and we use polar motion estimates from the analysis of Global Navigation Satellite Systems (GNSS) observations to strengthen the solution. We find that there is a systematic effect up to 1 mas in the estimated source coordinates between a solution with fixed EOP coming from the GNSS techniques and a solution where the EOP are estimated in the Very Long Baseline Interferometry analysis. Furthermore, we discuss analysis strategies for these sessions including the proper use of datum or "transfer sources".

Keywords

Celestial reference frames • Earth orientation parameters • ICRF • VLBI

1 Introduction

The current fundamental realization of the international celestial reference system is the second realization of the International Celestial Reference Frame (ICRF2) by Very Long Baseline Interferometry (VLBI) which is based on positions of 295 compact extragalactic radio sources selected on the basis of positional stability and the lack of extensive intrinsic source structure (Fey et al. 2009, 2015). In addition to the defining sources ICRF2 contains positions of another 3119 extragalactic radio sources. The majority of the sources

(2197) was observed in the so-called Very Long Baseline Array (VLBA) Calibrator Survey (VCS) observing sessions. The network of these sessions consists of ten VLBA 25-m radio telescopes located on U.S. territory (eight in North America, one in the Pacific, and one in the Caribbean (Fig. 1)). The primary goal of the VCS sessions was to obtain precise positions and snapshot maps of compact radio sources to increase the number of calibrator sources available for VLBI phase referencing (Fey et al. 2009). Since the VCS sessions were available when the ICRF2 was generated, the VCS sources were used for its densification. Twenty-four VCS sessions were carried out from 1994 to 2007 with a separation in six campaigns VCS1–VCS6 (Beasley et al. 2002; Fomalont et al. 2003; Kovalev et al. 2007; Petrov et al. 2005, 2006, 2008). Since the observing time was limited, most of the radio sources (about 2100) were observed in one session only. In 2014/2015 the VCS-II

H. Krásná (✉) • D. Mayer • J. Böhm
Department of Geodesy and Geoinformation, Technische Universität Wien, Gußhausstraße 27-29, A-1040 Wien, Austria
e-mail: hana.krasna@tuwien.ac.at
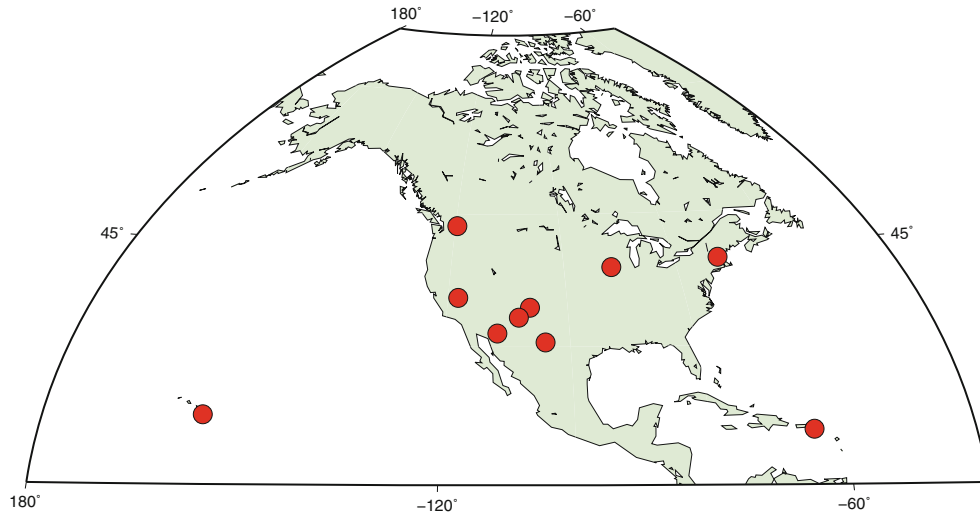
Fig. 1 Distribution of the ten VLBA radio telescopes
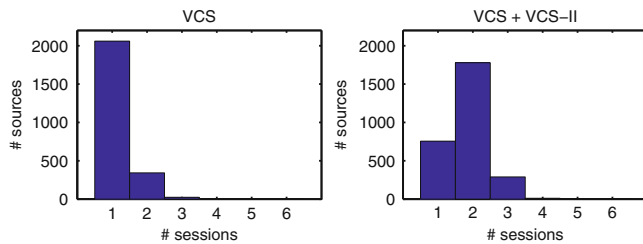
Fig. 2 Histogram of sources observed in the respective number of sessions during the VCS campaign only (left hand side) and after the re-observation during VCS-II (right hand side)

Fig. 3 Right ascension and declination of observed sources in a typical schedule of the VCS2–VCS6 sessions plotted from the beginning to the end of the session. *Black crosses* depict the VCS sources, the *grey crosses* show the non-VCS sources

campaign (Gordon et al. 2016) was carried out which re-observed most of the single epoch sources. Figure 2 shows number of sources observed in the respective number of sessions during the VCS campaign only (left hand side) and after the re-observation during VCS-II (right hand side).[1] The number of one-session-only sources decreased to about 700 and most of the VCS sources (about 1800) are observed in two sessions now. The VCS sessions, primarily designed for astrometry, focused on making short observations of many new sources. They were not optimised in the geodetic sense, i.e., they did not concentrate on a full sky coverage where observations at different elevation angles and azimuths help to separate station dependent parameters (clock, height and tropospheric parameters). The VCS sessions were scheduled using two different approaches. The first VCS campaign was scheduled for sources in narrow declination strips. Typically the new sources were observed twice in a session, once shortly after becoming mutually visible at all ten telescopes and for the second time shortly before

they ceased to be visible at all antennas. This scheme was interrupted every 2 h to observe non-VCS sources spread over the sky to determine tropospheric delays and to link to the small geodetic catalogue available at the time. The next VCS campaigns (VCS2–VCS6) observed sources with declination spread over the whole observable sky, i.e., down to 45° southern declination. The linking to the ICRF was ensured through the observations of the non-VCS sources which were included in the general scheduling strategy (Fig. 3). In the VCS-II campaign the sources were observed in clusters, i.e., sources with similar position on the sky were observed successively. In the analysis of the VCS sessions systematic errors also due to the deficiencies of a non-ideal continent-wide network can occur which causes uncertainties

---

[1]In this paper we analyse eight VCS-II sessions which were made freely available until March 2016.

in the estimation of Earth Orientation Parameters (EOP), i.e., by the link between the celestial and terrestrial frame. In this paper we focus on the impact of the EOP estimation on source positions and we discuss the proper use of datum or "transfer sources".

2 Estimation of Source Coordinates from VCS Sessions

We analysed the VCS sessions with the Vienna VLBI Software (VieVS Böhm et al. 2012) varying the parameterisation of EOP and assessing the impact on the estimated source coordinates. We computed four session-wise solutions. In each solution, zenith wet delays, tropospheric gradients, clock parameters (Table 1), station coordinates (using no-net-rotation (NNR) and no-net-translation (NNT) condition w.r.t. VTRF2008 Böckmann et al. 2010) and source coordinates (NNR w.r.t. non-VCS sources in ICRF2 with equal weights) were estimated. Sources with less than three observations were removed from the analysis. The remaining observations were weighted with a diagonal matrix consisting of squared formal errors provided by the correlator plus an error floor of $1\,cm^2$. The different handling of EOP in each of the solutions is summarized in Table 2. In the first three solutions the IERS C04 08 time series was used as a priori which is obtained from a combination of EOP series derived from various astro-geodetic techniques (Bizouard and Gambis 2009; Gambis 2004). In Solution 1 the EOP were estimated as offsets per session, in Solution 2 the rates of the Earth rotation parameters were estimated additionally, and in Solution 3 the EOP were fixed. In the fourth solution the a priori values for polar motion were taken from the Global Positioning System (GPS) final solution[2] provided by the International Global Navigation Satellite Systems (GNSS) Service and those were fixed in the VLBI analysis. As an example of the achieved typical results we show the estimated correction to the source coordinates from the session 04APR30XV with respect to the ICRF2 (Fig. 4, left hand side) and with respect to the Solution 1 where the EOP were estimated as offsets per session (Fig. 4, right hand side). The NNR condition

Table 1 Interval lengths between the piece-wise linear offsets of auxiliary parameters and relative constraints added as pseudo-observations to the Jacobian matrix of the least-squares adjustment in all four solutions

Parameter	Interval (min)	Relative constraints
Clock	60	1.3 cm after 60 min
zwd	60	1.5 cm after 60 min
Trop. gradients	360	0.05 cm after 360 min

[2]http://hpiers.obspm.fr/eop-pc/index.php?index=analysis&lang=en#GPS(April2016).

Table 2 Parameterisation of the Earth orientation parameters in the four solutions. Statistic WRMS and χ^2 values are given for session 04APR30XV

	Colour in Fig. 4	A priori EOP	Parameterisation of EOP estimates	WRMS w.r.t. ICRF2 RA/De [mas]	χ^2 w.r.t. ICRF2 RA/De [-]
Sol. 1	Black	C04 08	1 set of offsets per session	0.243/0.549	0.485/1.374
Sol. 2	Blue	C04 08	1 set of offsets per session + 3 ERP rates	0.269/0.580	0.583/1.490
Sol. 3	Red	C04 08	EOP fixed	0.252/0.474	0.752/1.087
Sol. 4	Green	Polar motion from GPS solution UT1 + nutation from C04 08	EOP fixed	0.269/0.476	0.855/1.096
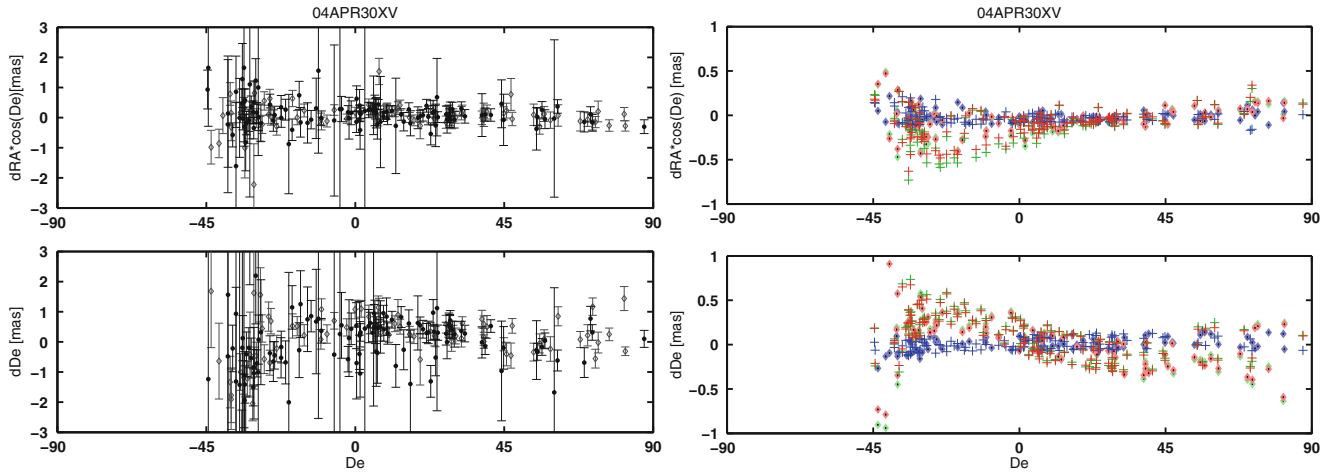
Fig. 4 Estimated source coordinate corrections with formal errors from Solution 1 w.r.t. ICRF2 (left hand side). Right hand side plots show differences between the Solutions 2-4 w.r.t. Solution 1 (*blue, red and green* colour, respectively). The crosses show the VCS sources, diamonds depict the non-VCS sources. Session 04APR30XV

was applied on 75 non-VCS sources and 114 VCS sources were estimated as free parameters. Table 2 contains statistics such as the Weighted Root Mean Square (WRMS) variations about the weighted mean w.r.t. the ICRF2 (column 5) and χ^2 per degree of freedom w.r.t. ICRF2 (column 6). The difference between the one-session-only sources from our Solution 1 and the ICRF2 can be also caused by the fact that ICRF2 was created in a common global adjustment of all suitable VLBI data observed between 1979 and 2009 (as described in Fey et al. 2009) where the station positions of the VLBA telescopes were estimated from a larger number of sessions. Because of the large systematic effect up to 1 mas in the estimated source coordinates which is seen between solutions with fixed EOP and solutions where the EOP were estimated in the VLBI analysis (Fig. 4, right hand side) we recommend fixing the EOP in the single session analysis to the values given in the combined C04 08 time series or to the values provided by the GNSS techniques.

2.1 Investigations on CRF Datum Definition

To illustrate the effect of the CRF datum definition on the estimated source coordinates and on the EOP, we estimated the source coordinates from Solution 1, i.e., NNR condition on non-VCS sources (hereafter referred to as "NNR solution"), and compared them with a solution where the non-VCS sources were fixed to their a priori coordinates from the ICRF2 catalogue (hereafter referred to as "fixed solution"). Furthermore, we computed a solution similar to Solution 1 but we fixed the station coordinates to VTRF2008. The estimates of the EOP from all VCS and VCS-II sessions are plotted in Fig. 5. On the left hand side, results obtained from a single session adjustment are shown and on the right

hand side EOP estimates from a common adjustment of all VCS and VCS-II sessions are plotted, where a common adjustment of coordinates of the ten VLBA telescopes was computed. The WRMS and weighted mean for all three solutions w.r.t. the a priori C04 08 values are summarized in Table 3. The largest deviations from the a priori C04 08 values are found for the "NNR solution". The larger WRMS and offset of y pole corrections vanish in the solution with fixed TRF which points to the geometry and regional distribution of the VLBA telescopes. The lower standard deviations of the EOP, especially of the Earth rotation parameters (ERP, i.e., polar motion and dUT1), from the solutions with the common adjustment of the observing sessions show that a stabilisation of the terrestrial reference frame strengthens the estimation of the VCS source coordinates. Furthermore, the comparison of the first two solutions with a single session adjustment indicates, that also the fixing of the well-known non-VCS source coordinates leads to a more stable ERP estimation which implicates a more reliable determination of the VCS source coordinates.

Corrections to the VCS source positions w.r.t. ICRF2 values have a random direction distribution and the size of most of the arrows lies below 1 mas. Figure 6 contains differences in the estimated source coordinates between the solutions "NNR" minus "fixed". On the left hand side the estimates are sorted by the Right Ascension (RA) and on the right hand side by the declination of the source positions. The corrections estimated in the common adjustment of the VCS sessions are plotted with red crosses, corrections from an adjustment of VCS sessions together with VCS-II are plotted in green. The WRMS and weighted mean of the differences are summarized in Table 4. Lower values are found for a common adjustment of VCS and VCS-II sessions which is caused by the higher number of observations to most of the
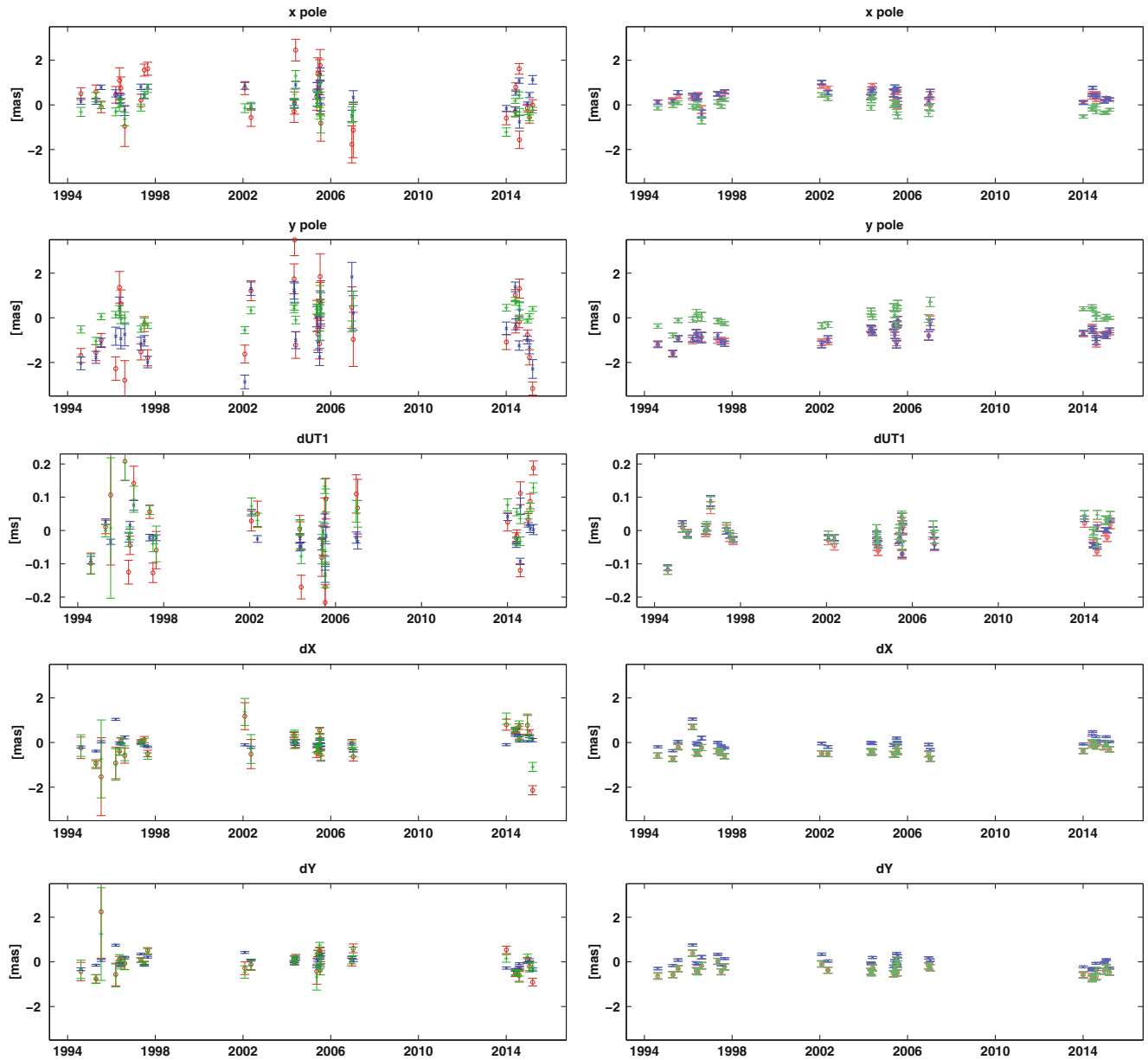
Fig. 5 EOP estimates from solution with CRF datum definition by an NNR condition on non-VCS sources (*red colour*) and by fixing the non-VCS sources to the ICRF2 values (*blue colour*). The *green colour* shows an NNR-solution with fixed TRF. Plots on the left hand side depict the results obtained from a single session solution, on the right hand side plots show estimates from the common adjustment of all VCS and VCS-II sessions

Table 3 WRMS and weighted mean of the EOP estimates with respect to the a priori C04 08 time series

WRMS (session-wise adjustment/global solution) weighted mean (session-wise adjustment/global solution)	x pole [mas]	y pole [mas]	dUT1 [ms]	dX [mas]	dY [mas]
	0.82/0.21	1.24/0.30	0.09/0.06	0.54/0.26	0.35/0.24
NNR on non-VCS sources	0.34/0.38	−0.69/−0.77	0.00/−0.01	0.07/−0.34	−0.03/−0.35
	0.42/0.24	1.10/0.30	0.06/0.06	0.26/0.26	0.26/0.24
Fixed non-VCS sources	0.38/0.41	−0.75/−0.78	−0.01/−0.01	0.02/0.04	0.03/−0.02
	0.43/0.24	0.45/0.30	0.06/0.06	0.47/0.27	0.34/0.24
NNR on non-VCS sources + TRF fixed	−0.09/−0.10	0.11/0.05	0.03/0.01	0.09/−0.34	−0.02/0.36
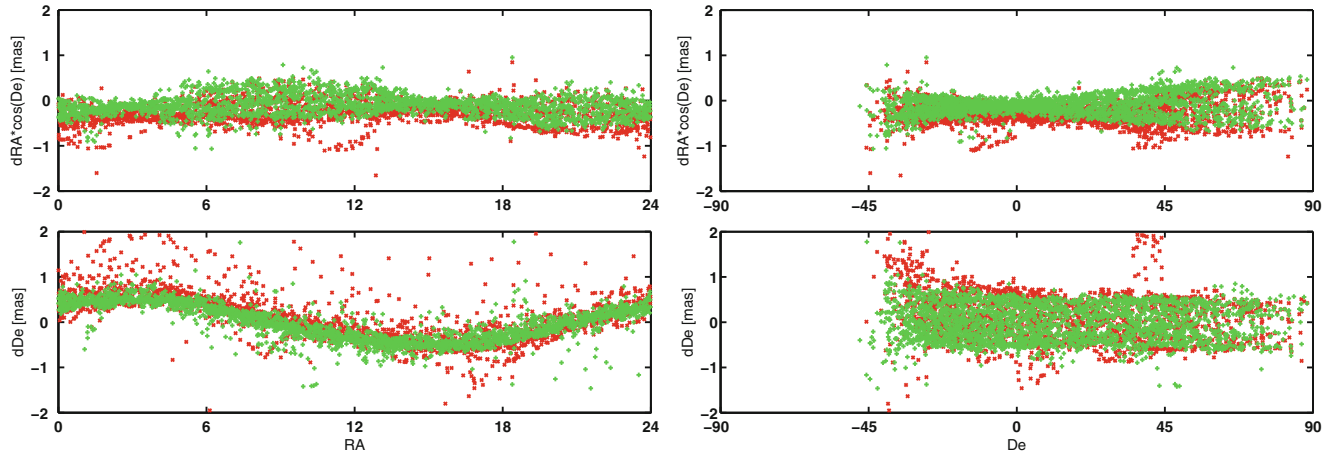
Fig. 6 Differences in estimated VCS source positions between solutions: "NNR" minus "fixed" from all VCS sessions (*red crosses*) and from all VCS plus VCS-II sessions (*green crosses*). On the left hand side the differences are sorted by RA, on the right hand side by declination of the source positions

Table 4 WRMS and weighted mean of the differences in source coordinates between solutions "NNR" minus "fixed" from VCS sessions and from VCS+VCS-II sessions

	VCS sessions dRA/dDe [mas]	VCS + VCS-II sessions dRA/dDe [mas]
WRMS	0.27/0.49	0.27/0.37
Weighted mean	−0.30/0.06	−0.07/−0.03

Table 5 Weighted rotation parameters and their formal errors between solutions "NNR" minus "fixed" from VCS sessions and from VCS+VCS-II sessions

Parameter	VCS sessions	VCS + VCS-II sessions
A1 [mas]	−0.424 ± 0.007	−0.354 ± 0.004
A2 [mas]	0.357 ± 0.006	0.379 ± 0.004
A3 [mas]	0.351 ± 0.005	0.128 ± 0.003

VCS sources. An offset of −0.30 mas in RA for the common adjustment of VCS sessions is found. Rotations of the whole celestial reference frame appear in the differences from both adjustments. The weighted rotation parameters computed between the solutions "NNR" minus "fixed" are summarized in Table 5.

2.2 Difference in Arc-Length

In order to examine whether the systematic errors propagate into the relative position of sources, the difference in arc-length for each source to each other source was calculated for the observing sessions. We show results from session 07JAN11XV in Fig. 7 as an example. The upper plot contains the differences in arc-length w.r.t. ICRF2 for solution with the NNR condition on non-VCS sources (red dots) and for solution with the fixed non-VCS sources (blue dots). The few large differences (up to 40 mas) are due to the large estimated corrections to the ICRF2 source coordinates. The difference in arc-length between our two solutions ("NNR" minus "fixed") is plotted in the lower plot. The differences reach several milliarcseconds and there is a systematic shift in the estimated arc-length of nearly 2 mas. We will concentrate on this phenomenon in our future work.

3 Conclusions

The application of the NNR condition on non-VCS sources compared to the fixing of their position on a priori coordinates changes the estimated source positions by up to several milliarcseconds. If EOP are estimated within the VCS sessions, systematic effects up to 1 mas in the estimated source coordinates occur. Therefore we recommend fixing the EOP in the VLBI analysis to the IERS C04 08 values or to the values provided by the GNSS techniques. Common adjustment of the VCS sessions strengthens the estimation of ERP via stabilisation of the terrestrial frame, but it can change the inner geometry and change the arc-length.
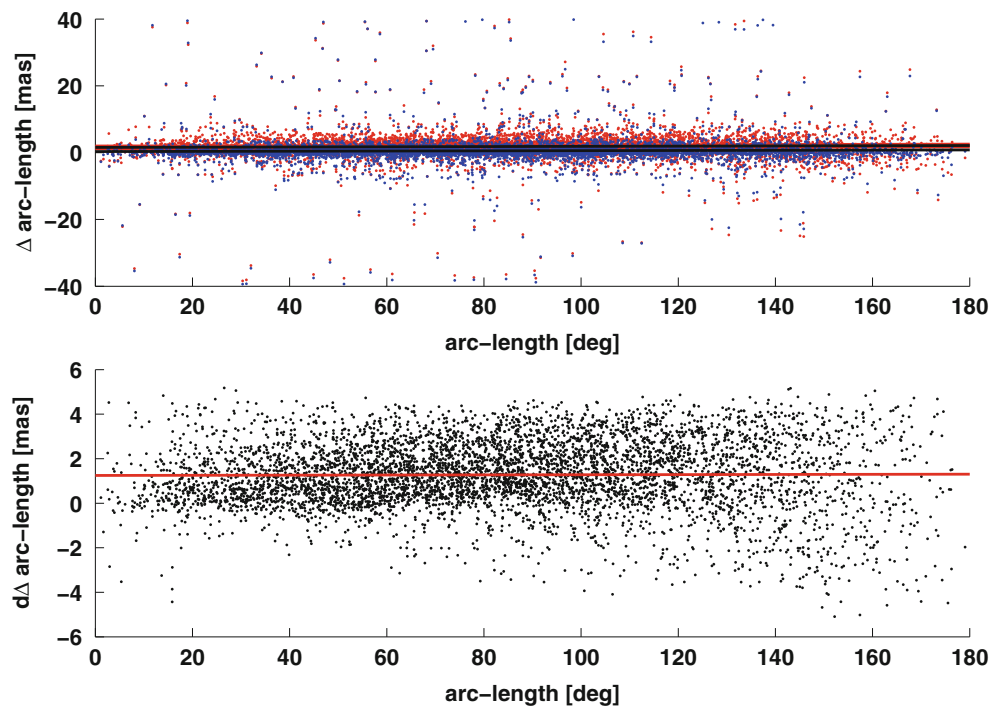
Fig. 7 *Upper plot* shows the difference in arc-length w.r.t. ICRF2 for the solution with the NNR condition on non-VCS sources (*red dots*) and for the solution with the fixed non-VCS sources (*blue dots*) computed from the session 07JAN11XV. The differences between the two solutions ("NNR" minus "fixed") are plotted in the *lower plot*. The *red line* indicates the best fit linear curve

References

Beasley AJ, Gordon D, Peck AB, Petrov L, MacMillan DS, Fomalont EB, Ma C (2002) The VLBA calibrator survey-VCS1. Astrophys J Suppl Ser 141:13–21. doi:10.1086/339806

Bizouard C, Gambis D (2009) The combined solution C04 for Earth orientation parameters consistent with international terrestrial reference frame 2005. In: IAG Symposium Series, vol 134, pp 265–270. doi:10.1007/978-3-642-00860-341.

Böckmann S, Artz T, Nothnagel A (2010) VLBI terrestrial reference frame contributions to ITRF2008. J Geod 84:201–219. doi:10.1007/s00190-009-0357-7

Böhm J, Böhm S, Nilsson T, Pany A, Plank L, Spicakova H, Teke K, Schuh H (2012) The new Vienna VLBI software VieVS. IAG Symposium Series, vol 136, pp 1007–1011. doi:10.1007/978-3-642-20338-1_126

Fey A, Gordon D, Jacobs CS (eds) (2009) The second realization of the international celestial reference frame by very long baseline interferometry, presented on behalf of the IERS/IVS working group. IERS Technical Note, No. 35. Verlag des Bundesamtes für Kartographie und Geodäsie, Frankfurt am Main, Germany, 204 p. ISBN 3-89888-918-6

Fey A, Gordon D, Jacobs CS, Ma C, Gaume RA et al (2015) The second realization of the international celestial reference frame by very long baseline interferometry Astron J 150:58

Fomalont EB, Petrov L, MacMillan DS, Gordon D, Ma C (2003) The second VLBA calibrator survey: VCS2. Astron J 126:2562–2566. doi:10.1086/378712

Gambis D (2004) Monitoring Earth orientation using space-geodetic techniques: state-of-the-art and prospective. J Geod 78:295–303. doi:10.1007/s00190-004-0394-1

Gordon D, Jacobs C, Beasley A, Peck A, Gaume R, Charlot P, Fey A, Ma C, Titov O, Boboltz D (2016) Second epoch VLBA calibrator survey observations: VCS-II. Astron J 151:154. doi:10.3847/0004-6256/151/6/154

Kovalev YY, Petrov L, Fomalont EB, Gordon D (2007) The fifth VLBA calibrator survey: VCS5. Astron J 133:1236–1242. doi:10.1086/511157

Nothnagel A, International VLBI Service for Geodesy and Astrometry (IVS) et al (2015) The IVS data input to ITRF2014. International VLBI Service for Geodesy and Astrometry, GFZ Data Services. doi:10.5880/GFZ.1.1.2015.002. http://doi.org/10.5880/GFZ.1.1.2015.002

Petrov L, Kovalev YY, Fomalont E, Gordon D (2005) The third VLBA calibrator survey: VCS3. Astron J 129:1163–1170. doi:10.1086/426920

Petrov L, Kovalev YY, Fomalont E, Gordon D (2006). The fourth VLBA calibrator survey: VCS4. Astron J 131:1872–1879. doi:10.1086/499947

Petrov L, Kovalev YY, Fomalont E, Gordon D (2008). The sixth VLBA calibrator survey: VCS6. Astron J 136:580–585. doi:10.1088/0004-6256/136/2/580

Towards the Definition and Realization of a Global Absolute Gravity Reference System

H. Wilmes, L. Vitushkin, V. Pálinkáš, R. Falk, H. Wziontek, and S. Bonvalot

Abstract

For many years, there has been a recognized discrepancy between the accuracies of absolute gravity determination and the hitherto valid gravity reference system of the International Association of Geodesy (IAG), the International Gravity Standardization Net 1971 (IGSN71).

Scientists from metrology and geosciences agreed on a proposal to base a new absolute gravity reference upon repeated instrument comparisons under metrological rules for traceability to SI quantities. In a strategy paper, which originated from the lively discussion of a mixed working group in metrology and geodesy with the objective to define and harmonize the measurements at the highest accuracy level, it was proposed to continue the comparisons under the International Committee for Weights and Measures (CIPM) every four years at alternating locations with the aim to distribute comparison results over a global network of carefully observed gravity reference and comparison sites. Their gravity variations are recorded by a combination of repeated absolute gravity measurements and continuously operating superconducting gravimeters. The results of comparisons and the gravity variations of the reference stations will be documented in a registry, part of the AGrav database, maintained jointly by the International Gravimetric Bureau (BGI) and the Federal Agency for Cartography and Geodesy (BKG).

By means of this network of comparison and gravity reference stations it will be possible to establish a global gravity reference system covering the needs of the geodetic and metrological communities and with capabilities to integrate observations of any new kind of absolute gravimeters including that based on cold atoms. Recorded gravity variations in an absolute reference system complement the Global Geodetic Reference Frame and will be used for combination with other geoscientific data and the investigation of mass transports and global change processes in the context of the Global Geodetic Observing System, GGOS. The implementation of the new gravity reference system will be based upon the international standards and conventions of the IAG. During the IUGG General Assembly in Prague 2015, the IAG adopted Resolution No. 2 and initiated the *Establishment of a Global Absolute Gravity Reference System*.

H. Wilmes (✉) • R. Falk • H. Wziontek
Federal Agency for Cartography and Geodesy, Frankfurt/M and Leipzig, Germany
e-mail: wilmes.herbert@gmail.com

L. Vitushkin
D.I. Mendeleyev Institute for Metrology, St. Petersburg, Russia

V. Pálinkáš
Research Institute of Geodesy, Topography and Cartography, Geodetic Observatory Pecny, Ondrejov, Czech Republic

S. Bonvalot
International Gravimetric Bureau, GET (IRD, CNRS, UPS, CNES), Toulouse, France

1 Introduction

The international geoscientific community needs accurate and reliable measurements of absolute gravity acceleration *g*. This follows from the requirement of modern geodesy to provide long-term stable global reference frames for gravity and height necessary for monitoring global change processes and investigating their causes. It is a basic precondition for monitoring the three fundamental geodetic observables: Earth shape, Earth gravity field and Earth rotation. Hence, the Global Geodetic Observing System (GGOS) of the International Association of Geodesy (IAG) recommends maintaining a global accurate reference frame which ensures a long-term monitoring of the geodetic observables, provides consistency of geometric and gravimetric products and guarantees clear and consistent standards and conventions for geometry and gravimetry (Drewes 2012). The activity is supported by the International Gravity Field Service (IGFS) and the International Gravimetric Bureau of the IAG (BGI). Absolute gravity has a high value for providing an accurate and unified global gravity reference as well as for the observation and investigation of post-glacial uplift (Timmen et al. 2012), tectonic height changes (Van Camp et al. 2011), mass transports of the geophysical fluids and other effects (Forsberg et al. 2005)

In metrology, similar importance is placed upon the watt balance experiment (Jiang et al. 2013), the consistent definition of fundamental physical constants and the integration of new measurement principles like the cold atom interferometry or the use of ultraprecise clocks for the determination of the gravity potential (Robinson 2012; Pereira dos Santos and Bonvalot 2016).

At present the desirable target uncertainty in absolute *g* measurements for geodetic and metrological questions is estimated to $\pm (1\text{-}2) \times 10^{-8}$ m s^{-2} or $\pm (1\text{-}2)\,\mu$Gal.

2 Development of the Gravity Reference Systems

Until today, gravity reference systems have been based upon one or more reference sites which were assumed to be stable. The classical realization of such a system was the Potsdam Gravity Datum of 1909. The uncertainty of the gravity values derived with one absolute pendulum apparatus and distributed with relative pendulum observations was estimated with ± 1 mGal. Some decades later, stationary absolute pendulum observations in Europe and U.S.A. indicated discrepancies in the order of 14 mGal to the Potsdam Gravity Datum. With the appearance of new, ballistic absolute gravimeters in the 1960'ies the systematic offset of the Potsdam datum was confirmed. In the meantime, relative spring gravity measurements were also used for a global densification of the network.

Consequently the global gravity reference system had to be improved: In 1971 the IUGG general assembly in Moscow adopted the International Gravity Standardization Net (IGSN71) (Morelli et al. 1974). The IGSN71 station uncertainty is ± 0.1 mGal and basis for the determination of location-dependent gravity variations. But in the sixties and seventies of the last century time-variable absolute gravity variations of less than ± 0.1 mGal mostly were covered by instrumental uncertainties.

Due to the advances in technical development and first mobility of the instruments, absolute gravimeter comparisons were started at the International Bureau for Weights and Measures (BIPM) in 1981 (Boulanger et al. 1983). During this period as well, an International Absolute Gravity Base station Network (IAGBN) was proposed (Boedecker and Fritzer 1986).

With a scientific manufacturing of a small series of freefall absolute gravimeters and later the industrial production of commercial instruments, the consistency and reliability of the absolute gravimeters improved at the end of the twentieth century to a few microgals. Today about 100 transportable instruments exist, the majority come from one manufacturer. As showed in Van Camp et al. (2016) and Pálinkáš et al. (2013), the offsets between instruments have to be known to detect subtle geodynamic signal at microgal level.

The comparisons between instruments thus became crucial for estimating the overall accuracy and sensitivity of absolute gravimeters and checking each individual instrument. An absolute gravimeter relies upon its instrumental measurement standards for time and frequency units. The necessity of a careful calibration of laser and frequency generator underlines the need for a successful cooperation between metrology and geoscience specialists. Improved transportable absolute gravimeters and the participation in the comparisons allow the establishment of independent national gravity networks and networks for scientific applications because the absolute gravimeter has the capability to realize its own gravity reference (Wilmes et al. 2003).

3   Cooperation of Metrology and Geosciences

Comparisons of absolute gravimeters have been carried out since 1981 and were hosted by the BIPM in Sèvres (France). The participating institutions represent geodetic stakeholders, scientific institutions and institutions representing the national metrology institutes.

In 2003, advanced comparison rules were introduced in metrology with the "Mutual Recognition Arrangement" (BIPM 2003). As a consequence, the international comparisons of absolute gravimeters were developed to key comparisons (KC). The new Working Group on Gravimetry of the Consultative Committee for Mass and Related Quantities (CCM-WGG) prepared the following comparisons and evaluations. The implementation of KCs improved the procedures and consistency of the comparisons and results (Jiang et al. 2012). Also these procedures specify the correction models, procedures and algorithms of the comparisons. Comparisons are guided under the partnership of a regional metrological organization like e.g. EURAMET (European Association of National Metrology Institutes). However, a consequence of this cooperation under metrological rules was that only the absolute gravimeters from the national metrology institutes and designated metrology institutes (NMI/DIs) contribute to the key comparison result. Therefore the discussion started about a satisfactory solution for the remaining institutions.

The members of the CCM-WGG together with the representatives of IAG Commission 2 (Gravity Field) and two IAG working groups: JWG 2.1 (Techniques and metrology in absolute gravimetry) and JWG 2.2 (Absolute gravimetry and absolute gravity reference system) managed to prepare a formal document about the "CCM - IAG Strategy for Metrology in Absolute Gravimetry" (CCM 2015). The objective of this document is to connect and balance the official rules in metrology with the needs of the non-metrological institutions, mainly from the geodetic community. It is understood as an important contribution for the geodetic community, because for the first time a formal agreement has been reached on the traceability of absolute gravity measurements to SI units at the uncertainty level of a few parts in 10^{-9} through comparison and calibration of the absolute gravimeters. Further, it connects terminologies and conventions used in metrology and geodesy for the observations, correction models and evaluations procedures. This mutual recognition of the gravity standards is an extremely important precondition for the realization and maintenance of a global consistent and homogeneous absolute gravity reference system. It prepares and explains the conditions and rules how the comparisons shall be continued under CIPM in the future.

The document was submitted to the IAG Executive Committee which agrees with the initiative between the geodetic and metrological community in the field of absolute gravimetry. The IAG Executive Committee accepts the document as most relevant, and important, as it will assist in the establishment of a global absolute gravity reference system. Furthermore it is a contribution to the Global Geodetic Observing System (GGOS).

4   Realization of a New Absolute Gravity Reference System

Based upon this agreement and the continuation of absolute gravimeter comparisons under the International Committee for Weights and Measures (CIPM), the series of CIPM comparisons will define the measurement standards in gravimetry (absolute gravimeters) (Vitushkin 2011) and gravity standards (gravimetry sites) for metrology and geodesy as from now. The participating absolute gravimeters represent, strictly speaking, the measurement standards of acceleration unit in gravimetry and it makes it possible to establish the metrological traceability of other gravity measurement instruments and the sites of a distributed reference network to measurement standards in gravimetry. Some groups of the international community already make use of such gravity standards for monitoring the gravity variations at a given site by combining a very sensitive continuous recording gravimeter and an absolute gravimeter previously checked at international comparisons (Crossley et al. 2013).

A gravity reference function is generated by the combination of absolute gravity data with the continuous record of the superconducting gravimeter. Visiting instruments can connect to this gravity standard or verify their own results. The gravity reference function is an important dataset for the combination with other geosciences time series under the context of GGOS. The reference stations form the basis for the realization of the new absolute gravity reference system. Absolute gravity measurements are supposed to support the new time series with reference and scale. Reversely, the superconducting data provide a comparison reference function and offer the interpolation between the epochs of CIPM comparisons.

While the current repetition rate of the international CIPM comparisons of 4 years and the regional comparisons on continental scale between the CIPM comparisons are presently a matter of discussion, it seems adequate for the present instruments and teams and for the realization of an absolute gravity reference system. With such a four-yearly repetition rate it should be possible to detect changes related to the specific sensors and to provide enough opportunity for new teams and instruments to participate in the comparisons. With changing

locations of the CIPM comparisons the gravity reference system is distributed to a global coverage.

The international absolute gravity database AGrav (http://agrav.bkg.bund.de/; http://bgi.obs-mip.fr/) (Wilmes et al. 2009; Wziontek et al. 2012) will be used as registry for the comparison results. Similar to the key comparison database of the BIPM it will store all observations from the metrological community. However, for its function as registry of the absolute gravity reference system it will also store the comparison results of the geoscientific instruments of the four-yearly CIPM comparisons. In addition it will take the results of all additional comparisons intermediate to the CIPM comparisons.

At the IUGG General Assembly in Prague 2015 an IAG resolution was passed on the subject of the establishment of a global absolute gravity reference system (IAG Resolutions 2015). The adoption of this resolution encourages continuing the work necessary for a state-of-the-art terrestrial gravity system and the replacement of the IGSN71. This objective will be also greatly facilitated by the increasing number of absolute gravimeters who are contributing in many countries since the last decade to the establishment of national absolute gravity networks.

5 Outlook

The IAG resolution 2015, No. 2 now provides the opportunity to realize the intended global gravity reference system. What are the next steps?

1. The next CIPM Key Comparison, for the first time in Asia at Changping Campus, Beijing, China in 2017 (CCM.G-K3), will be prepared under guidance of the CIPM, which defines the absolute gravity standard for metrology and geodesy over the following years.
2. A network of distributed gravity reference stations with superconducting gravimeters and repeated absolute gravimeter measurements is defined which have the ability to preserve the absolute gravity standard and realize an absolute gravity reference function. This will enable and support additional comparisons.
3. The comparison result of the participating absolute gravimeters will be transferred to additional instruments and reference stations; see document "CCM - IAG Strategy for Metrology in Absolute Gravimetry (CCM 2015)".
4. Records of all comparison results will be kept in the AGrav database operated by BKG and BGI. The documentation in the BIPM Key Comparison Database is limited to the CIPM comparison results.

5. Standard models and corrections (like tidal system, geometrical reference frame) will be defined in cooperation with the GGOS Bureau of Standards and Conventions.
6. Finally the participation in the CIPM comparisons will be agreed with the National Metrology Institutes.

In detail subsequent steps are the following:

A new working group with the subject "Establishment of a global absolute gravity reference system" in IAG Commission 2 will be installed to replace the working group JWG 2.2 which was closed at the IUGG/IAG General Assembly due to the IAG rules. The new working group will contact the CCM-WGG and work cooperatively.

The AGrav database will be extended to work as registry for the global absolute gravity reference system. This is an addition to the present function to document the absolute gravity measurements of the international community. The database is well prepared for observations with new measurement principles like cold atom gravimeters or ultra precise clocks which develop quickly and soon will have an influence upon the absolute gravimeter comparisons and the gravity field observations.

Close cooperation is foreseen with the new IAG service "IGETS: International Geodynamics and Earth Tide Service" (former Global Geodynamics Project, GGP, operating a global network of superconducting gravimeters) for the realization of the gravity reference and comparison stations.

To reach all these goals, continued support will be necessary from the international community working in gravimetry and metrology. Advanced absolute gravimeters, which are well compared and using consistent models, parameters and corrections models will make it possible to determine reliable time-variable gravity changes for the investigation of global change processes. The initiated new Global Absolute Gravity Reference System will provide the framework for it.

References

BIPM (2003) International equivalence of measurements: the CIPM MRA. http://www.bipm.org/en/cipm-mra/

Boedecker G, Fritzer T (1986) International absolute gravity basestation network. IAG-SSG 3.87 Status Report March 1986. Veröff. Bayer. Komm. f. d. Int. Erdmessung d. Bayer. Akad. d. Wiss., Astron.-Geod. Arb, 47, München

Boulanger YD, Arnautov GP, Scheglov SN (1983) Results of comparison of absolute gravimeters, Sèvres, 1981. Bull Inf BGI 52:99–124

CCM (2015) CCM – IAG strategy for metrology in absolute gravimetry. http://www.bipm.org/wg/CCM/CCM-WGG/Allowed/2015-meeting/CCM_IAG_Strategy.pdf, http://iag.dgfi.tum.de/fileadmin/IAG-docs/Travaux2015/02_Travaux_Comm_2_2015.pdf

Crossley D, Hinderer J, Riccardi U (2013) The measurement of surface gravity. Rep Prog Phys 76(4):046101. doi:10.1088/0034-4885/76/4/046101

Drewes H (2012) The Geodesist's handbook 2012. J Geodesy 86(10):787–974. doi:10.1007/s00190-012-0584-1

Forsberg R, Sideris MG, Shum CK (2005) The gravity field and GGOS. J Geodynamics 40(4–5):387–393. doi:10.1016/j.jog.2005.06.014

IAG Resolutions (2015) No. 1 (International Height Reference System) and No. 2 (Establishment of a Global Absolute Gravity Reference System), 2015. http://iag.dgfi.tum.de/fileadmin/IAG-docs/IAG_Resolutions_2015.pdf

Jiang Z, Pálinkáš V, Arias FE, Liard J, Merlet S, Wilmes H, Vitushkin L, Robertsson L, Tisserand L, Pereira dos Santos F, Bodart Q, Falk R, Baumann H, Mizushima S, Mäkinen J, Bilker-Koivula M, Lee C, Choi IM, Karaboce B, Ji W, Wu Q, Ruess D, Ullrich C, Kostelecký J, Schmerge D, Eckl M, Timmen L, Le Moigne N, Bayer R, Olszak T, Ågren J, Del Negro C, Greco F, Diament M, Deroussi S, Bonvalot S, Krynski J, Sekowski M, Hu H, Wang LJ, Svitlov S, Germak A, Francis O, Becker M, Inglis D, Robinson I (2012) The 8th international comparison of absolute gravimeters 2009: the first Key comparison (CCM.G-K1) in the field of absolute gravimetry. Metrologia 49:666–684. doi:10.1088/0026-1394/49/6/666

Jiang Z, Pálinkáš V, Francis O, Baumann H, Makinen J, Vitushkin L, Merlet S, Tisserand L, Jousset J, Rothleitner C, Becker M, Robertsson L, Arias EF (2013) On the gravimetric contribution to watt balance experiments. Metrologia 50:452–471. doi:10.1088/0026-1394/50/5/452

Morelli C, Gantar C, Honkasalo T, McConnell RK, Tanner JG, Szabo B, Uotila U, Whalen CT (1974) The International Gravity Standardization Net 1971 (IGSN71), I.U.G.G.-I.A.G.-Publ. Spec. 4, Paris

Pálinkáš V, Lederer M, Kostelecký J, Šimek J, Mojzeš M, Ferianc D, Csapó G (2013) Analysis of the repeated absolute gravity measurements in the Czech Republic, Slovakia and Hungary from the period 1991–2010 considering instrumental and hydrological effects. J Geodesy 87:29–42. doi:10.1007/s00190-012-0576-1

Pereira dos Santos F, Bonvalot S (2016) Cold atom absolute gravimetry. In: Grafarend EW (ed) Encyclopedia of geodesy. Springer International Publishing, Switzerland. doi:10.1007/978-3-319-02370-0_30-1

Robinson IA (2012) Towards the redefinition of the kilogram: a measurement of the Planck constant using the NPL Mark II watt balance. Metrologia 49:113–156. doi:10.1088/0026-1394/49/1/016

Timmen L, Gitlein O, Klemann V, Wolf D (2012) Observing gravity change in the Fennoscandian uplift area with the Hanover absolute gravimeter. Pure Appl Geophys 169(8):1331–1342. doi:10.1007/s00024-011-0397-9

Van Camp M, de Viron O, Scherneck HG, Hinzen KG, Williams SDP, Lecocq T, Quinif Y, Camelbeeck T (2011) Repeated absolute gravity measurements for monitoring slow intraplate vertical deformation in Western Europe. J Geophys Res 116, B08402. doi:10.1007/s00024-011-0397-9

Van Camp M, De Viron O, Avouac JP (2016) Separating climate-induced mass transfers and instrumental effects from tectonic signal in repeated absolute gravity measurements. Geophys Res Lett 43:4313–4320. doi:10.1007/s00024-011-0397-9

Vitushkin L (2011) Measurement standards in gravimetry. Gyroscopy Navigation 2(3):184–191. doi:10.1134/S2075108711030126

Wilmes H, Richter B, Falk R (2003) Absolute gravity measurements: a system by itself. In: Tziavos IN (ed) Gravity and Geoid 2002, 3rd Meeting of the International Gravity and Geoid Commission. ZITI Editions, Thessaloniki, pp 19–25

Wilmes H, Wziontek H, Falk R, Bonvalot S (2009) AGrav – the new absolute gravity database and a proposed cooperation with the GGP project. J Geodynamics 48:305–309. doi:10.1016/j.jog.2009.09.035

Wziontek H, Wilmes H, Bonvalot S (2012) AGrav: an international database for absolute gravity measurements. In: Geodesy for the Planet Earth. Proceedings of the 2009 IAG Symposium, Buenos Aires, Argentina, 31 August–4 September 2009. International Association of Geodesy Symposia, vol 136. Springer, Berlin, Heidelberg, pp 1037–1042, doi:10.1007/978-3-642-20338-1_130

Part II

Static Gravity Field Observations and Modelling

The Linearized Fixed Gravimetric Boundary Value Problem and Its Solution in Spheroidal Approximation

Georgios Panou and Romylos Korakitis

Abstract

In this work, the linearized fixed gravimetric boundary value problem and its solution in spheroidal approximation is discussed. Input to the problem are gravity disturbances, using the known Earth's topography as a boundary, so this corresponds to an oblique derivative problem. From the physical viewpoint, it has many advantages and can serve as the basis in establishing a world height system that supports geometrical and physical heights worldwide with high precision. Adopting the spheroidal approximation, an integral equation results which can be solved using successive approximations. The mathematical model becomes simpler and can be solved more easily by neglecting the Earth's topography. On the other hand, adopting the spherical approximation, the solution corresponds to a normal derivative problem plus suitable corrections which include the topography. We conclude that the spheroidal approximation should be taken into account in order to achieve higher accuracy.

Keywords

Fixed gravimetric boundary value problem • Gravity disturbance • Height datum problem • Spheroidal approximation • Surface layer potential in boundary value problem

1 Introduction

The determination of the external gravity field of the Earth using gravity data can be related to the solution of a free boundary value problem (BVP) which is based on the theory of Stokes (1849) and Molodensky et al. (1962). In order to enhance the theoretical completeness and to improve the expected accuracy, this theory was extended in spheroidal approximation, e.g. Molodensky et al. (1962), Koch (1969) and Zhu (1981). However, using global navigation satellite systems (GNSS), we may assume nowadays that the Earth's topography is completely known, thus a commonly used BVP is the fixed gravimetric boundary value problem.

This problem has two main advantages: Firstly, its solution contains the first order terms of spherical harmonic series, which means that the Earth's mass center can be derived from it. Secondly, because the Earth's topography is known, it avoids the computational difficulties from different height bases, as in the Molodensky BVP (Yu and Zhang 2005). A Molodensky-type solution was presented in detail by Stock (1983) and a Brovar-type solution by Heck (2011) in spherical approximation. Also, a numerical solution on the basis of the boundary element method has been applied by Čunderlík et al. (2008).

In this work we discuss an analytical solution of the linearized fixed gravimetric BVP in spheroidal approximation, which can provide a basis for establishing a world height system. It is adopted from the approach introduced by Koch (1969) for the Molodensky problem in spheroidal approximation using gravity anomalies. Our solution provides the gravity potential W on the Earth's physical surface and through the geopotential numbers, one can obtain the

G. Panou (✉) • R. Korakitis
Department of Surveying Engineering, National Technical University of Athens, Zografou Campus, 15780 Athens, Greece
e-mail: geopanou@survey.ntua.gr

physical heights. Using this concept, it is no longer required to carry out time-consuming levellings (Heck 2011). A recent work along these lines can be found in Grombein et al. (2015). Also, from the theoretical point of view, the proposed solution has a relative error of the order of e'^4, where $e' = (a^2 - b^2)^{1/2}/b$ is the second eccentricity of the reference spheroid having semiaxes a, b $(a > b)$. This corresponds to an accuracy less than one centimeter for the geoid height, provided there are gravimetry values available at equivalent accuracy, i.e. about 1 μgal (Yu and Zhang 2005).

2 The Problem Under Consideration

Let W be the Earth's gravity potential and U the normal potential. Then, the disturbing potential T is given by

$$T = W - U. \tag{1}$$

The disturbing potential can be regarded as a harmonic function in the outer space of the Earth (Ω). The fixed gravimetric boundary value problem is a mathematical model for the determination of T from gravity disturbances $\delta g = g - \gamma$, obtained from gravity measurements on the surface of the Earth (S). The tie between T and the gravity disturbance δg is represented by an oblique derivative boundary condition. Moreover, we assume that T is regular at infinity, see Holota (1997). Hence, the linearized fixed gravimetric boundary value problem is given by:

$$\Delta T = 0 \, in \, \Omega, \tag{2}$$

$$\langle s, grad\, T \rangle = -\delta g \, on \, S, \tag{3}$$

$$T = O\left(|\boldsymbol{x}|^{-1}\right) \, as \, x \to +\infty, \tag{4}$$

where Δ means Laplace's operator, $\langle \cdot, \cdot \rangle$ means the inner product, $s = (-1/\gamma)\,grad\,U$, $g = |grad\,W|$ and $\gamma = |grad\,U|$. The existence, uniqueness and stability of a weak solution of the above problem have been studied by Holota (1997). Our aim is to work out the solution of the problem (2)–(4), with a relative error of the order of e'^4. Thus, the boundary condition must be given with an equivalent accuracy. Using Eq. (1) we have (Koch 1969)

$$\frac{\partial T}{\partial h_P} = \frac{\partial W}{\partial h_P} - \frac{\partial U}{\partial h_P} = -\delta g_P + \frac{1}{2}g_P \varepsilon_P^2, \tag{5}$$

where h_P is the ellipsoidal height and ε_P is the angle between g_P and h_P, i.e. the deflection of the vertical, see Fig. 1. The last term in the right-hand side of Eq. (5) involves additional data to the problem, necessary in order to fulfill the stated accuracy requirements. We note that this term is of some
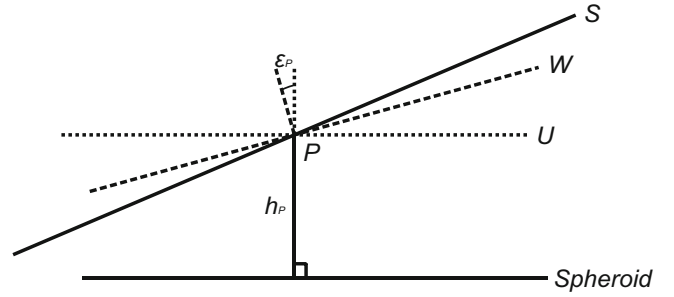
Fig. 1 Surfaces relevant to the fixed GBVP
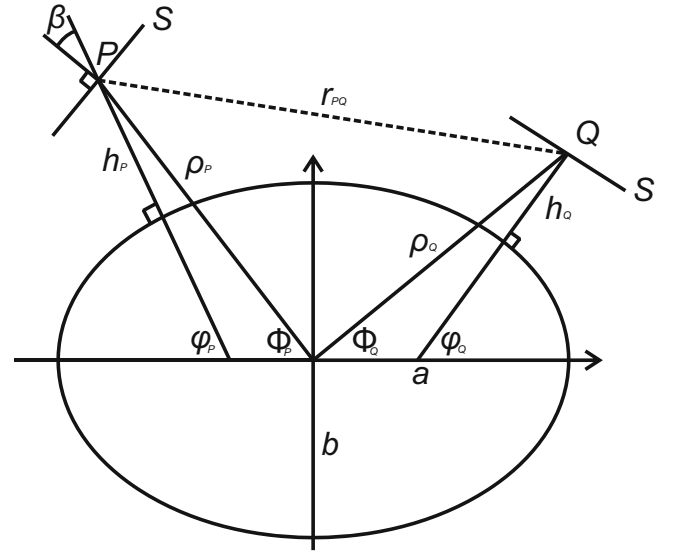
Fig. 2 Geometrical quantities of the integral equation

significance only in areas with large values of the deflection of the vertical.

3 Integral Equation for the Surface Layer

We assume that the Earth's topography is smooth under the assumptions discussed by Holota (1997). Then, the disturbing potential T at some point P can be represented as the potential of a surface layer on S with a surface density σ:

$$T_P = \iint_S \frac{\sigma_Q}{r_{PQ}} dS_Q, \, P \in S, \tag{6}$$

where r_{PQ} is the distance between the fixed point P and the variable point Q of the integration, and dS_Q the surface element at Q, see Fig. 2. The derivative of a surface layer potential is

$$\frac{\partial T}{\partial h_P} = \iint_S \sigma_Q \frac{\partial}{\partial h_P}\left(\frac{1}{r_{PQ}}\right) dS_Q - 2\pi\sigma_P cos\beta_P, \tag{7}$$

where β_P is the angle between h_P and the normal n_P to the surface S at P (inclination angle of S in P) (Heiskanen and Moritz 1967).

Changing the variables with the auxiliary substitutions $\sigma = t \cos \beta$ and $dE = dS \cos \beta$, where dE is the projection of the surface element dS onto the plane perpendicular to the normal h of the reference spheroid (Koch 1969), Eq. (7) using Eq. (5) reads

$$2\pi t_P cos^2\beta_P - \iint\limits_E t_Q \frac{\partial}{\partial h_P}\left(\frac{1}{r_{PQ}}\right) dE_Q = \delta g_P - \frac{1}{2}g_P \varepsilon_P^2. \tag{8}$$

According to Molodensky et al. (1962):

$$\frac{\partial}{\partial h_P}\left(\frac{1}{r_{PQ}}\right)$$
$$= \frac{1}{r_{PQ}^3}\left[\begin{array}{l} (N_Q + h_Q) \cos \varphi_P \cos \varphi_Q \cos (\lambda_Q - \lambda_P) \\ - (N_P + h_P) \cos^2\varphi_P \\ + \left(\frac{b^2}{a^2}N_Q + h_Q\right) \sin \varphi_P \sin \varphi_Q \\ - \left(\frac{b^2}{a^2}N_P + h_P\right) \sin^2\varphi_P \end{array}\right], \tag{9}$$

where

$$\begin{array}{c} r_{PQ}^2 = (N_P + h_P)^2 + (N_Q + h_Q)^2 \\ -2(N_P + h_P)(N_Q + h_Q)\left[\sin \varphi_P \sin \varphi_Q \\ + \cos \varphi_P \cos \varphi_Q \cos (\lambda_Q - \lambda_P)\right] \\ -\frac{a^4-b^4}{a^4}(N_Q \sin \varphi_Q - N_P \sin \varphi_P)^2 \\ -2\frac{a^2-b^2}{a^2}(N_Q \sin \varphi_Q - N_P \sin \varphi_P) \\ \times (h_Q \sin \varphi_Q - h_P \sin \varphi_P) \end{array}, \tag{10}$$

and

$$dE_Q = (M_Q + h_Q)(N_Q + h_Q) \cos \varphi_Q d\varphi_Q d\lambda_Q, \tag{11}$$

where φ, λ are the geodetic coordinates and M, N the principal radii of curvature of the reference spheroid. Equation (8) is the integral equation for the fixed gravimetric BVP in the case of a reference spheroid. The corresponding integral equation in the case of a reference sphere is presented by Stock (1983). Inserting Eqs. (9) and (11) into Eq. (8), the resulting integral equation can be solved by successive approximations in order to obtain t and then the disturbing potential T. Examples of the application of the method of successive approximations for the solution of some BVP can be found in Moritz (1980) and Holota (1992). Also, a formulation of the process of successive approximations within the concept of the weak solution and variational principles for the fixed gravimetric BVP was presented by Holota (2005).

4 Integral Equation in the Geocentric System

In order to solve the integral equation (8), we express it in a geocentric coordinate system (ρ, Φ, λ), where ρ is the distance from the center of the spheroid, Φ is the geocentric latitude and λ the longitude. With a relative error of the order of e'^4 we have the following approximate formulas (Koch 1969)

$$M = a\left(1 - e'^2 + \frac{3}{2}e'^2\sin^2\Phi\right), \tag{12}$$

$$N = a\left(1 + \frac{1}{2}e'^2\sin^2\Phi\right), \tag{13}$$

$$\sin \varphi = \sin \Phi \left(1 + e'^2\cos^2\Phi\right), \tag{14}$$

$$\cos \varphi = \cos \Phi \left(1 - e'^2\sin^2\Phi\right), \tag{15}$$

$$b^2 = a^2\left(1 - e'^2\right). \tag{16}$$

Also, we make the reasonable assumption: $e'^2h/a < e'^4$. Then using $\tan \varphi = (a^2/b^2)\tan \Phi$, Eq. (11) is replaced by

$$dE_Q = (a + h_Q)^2\left(1 - e'^2\sin^2\Phi_Q\right) \cos \Phi_Q d\Phi_Q d\lambda_Q. \tag{17}$$

Hence, Eq. (10) can be written as

$$r_{PQ}^2 = \bar{r}_{PQ}^2 - a^2 e'^2\left(\sin^2\Phi_P + \sin^2\Phi_Q\right)(1 - \cos \omega), \tag{18}$$

where

$$\bar{r}_{PQ}^2 = (a + h_P)^2 + (a + h_Q)^2 \\ - 2(a + h_P)(a + h_Q)\cos \omega, \tag{19}$$

and

$$\cos \omega = \sin \Phi_P \sin \Phi_Q + \cos \Phi_P \cos \Phi_Q \cos (\lambda_Q - \lambda_P). \tag{20}$$

Finally, Eq. (9) is written as

$$\frac{\partial}{\partial h_P}\left(\frac{1}{r_{PQ}}\right)$$
$$= \frac{1}{r_{PQ}^3}\left\{\begin{array}{l} -(a + h_P) + (a + h_Q)\cos \omega \\ + ae'^2\left[\begin{array}{l}\sin \Phi_P \left(\frac{1}{2}\sin \Phi_P + \sin \Phi_Q\right) \\ - \cos \omega \left(\sin^2\Phi_P + \frac{1}{2}\sin^2\Phi_Q\right)\end{array}\right]\end{array}\right\}. \tag{21}$$

Now we insert Eqs. (17) and (21) into Eq. (8) and obtain the integral equation of our problem in the geocentric system with a relative error of the order of e'^4:

$$2\pi t_P \cos^2 \beta_P$$

$$-\iint_E \frac{t_Q}{\overline{r}_{PQ}^3} \left\{ \begin{array}{l} -(a+h_P)+(a+h_Q)\cos\omega \\ +ae'^2 \left[\begin{array}{l} \sin\Phi_P \left(\frac{1}{2}\sin\Phi_P + \sin\Phi_Q\right) \\ -\cos\omega \left(\sin^2\Phi_P + \frac{1}{2}\sin^2\Phi_Q\right) \end{array} \right] \end{array} \right\} \cdot$$

$$(a+h_Q)^2 \left(1 - e'^2\sin^2\Phi_Q\right)\cos\Phi_Q d\Phi_Q d\lambda_Q$$

$$= \delta g_P - \frac{1}{2}g_P \varepsilon_P^2 \tag{22}$$

5 Solution of the Integral Equation

In order to solve the integral equation (22) we use a series expansion for r and $\cos^2\beta$. Then Eq. (19) is written as

$$\overline{r}_{PQ}^2 = 4a^2\sin^2\frac{\omega}{2}\left(1+k\right), \tag{23}$$

where

$$k = \frac{(h_Q - h_P)^2}{4a^2\sin^2\omega/2} + \frac{1}{a}\left(h_P + h_Q + \frac{h_P h_Q}{a}\right). \tag{24}$$

Also, Eq. (19) can be written as

$$\frac{1}{\overline{r}_{PQ}^3}\left[-(a+h_P)+(a+h_Q)\cos\omega\right]$$

$$= \frac{h_Q - h_P}{\overline{r}_{PQ}^3} + \frac{(h_Q - h_P)^2}{2(a+h_P)\overline{r}_{PQ}^3} - \frac{1}{2(a+h_P)\overline{r}_{PQ}}. \tag{25}$$

We expand the quantities r_{PQ}^2, $1/r_{PQ}$ and $1/r_{PQ}^3$ in series of powers of k (with $k<1$) with a relative error of the order of e'^4. Also, we use the series expansion $1/(a+h_P) = (1/a)(1 - h_P/a + \ldots)$ and $\cos^2\beta_P = 1 - \tan^2\beta_P + \ldots$ with $\tan^2\beta_P < 1$.

Then, the solution can be obtained by successive approximations

$$t = t_0 + t_1 + t_2 + \ldots, \tag{26}$$

introducing all series expansions as above in Eq. (22).

Now we assume that: $t = t_0 + t_1$, where t_0 is the spherical solution without considering topography and t_1 is a linear function of e'^2 and the height differences $h_Q - h_P$. Remaining terms of the solution contain higher powers of e'^2 and the height difference $h_Q - h_P$, so we can neglect them, according to our original assumption i.e., relative error of the

order of e'^4. This leads to the following system of integral equations:

$$2\pi t_0 + \frac{a}{2}\iint_E \frac{t_0}{2a\sin\omega/2}\cos\Phi_Q d\Phi_Q d\lambda_Q = \delta g_P - \frac{1}{2}g_P \varepsilon_P^2, \tag{27}$$

$$2\pi t_1 + \frac{a}{2}\iint_E \frac{t_1}{2a\sin\omega/2}\cos\Phi_Q d\Phi_Q d\lambda_Q = F, \tag{28}$$

where

$$F = ae'^2 \iint_E \frac{t_0}{2a\sin\omega/2}\left[\frac{1}{2}\sin^2\Phi_P\right.$$

$$+ \frac{3}{4}\sin^2\Phi_Q - \frac{(\sin\Phi_P - \sin\Phi_Q)^2}{8\sin^2\omega/2}\right]\cos\Phi_Q d\Phi_Q d\lambda_Q$$

$$+ a^2 \iint_E t_0 \frac{h_Q - h_P}{8a^3\sin^3\omega/2}\cos\Phi_Q d\Phi_Q d\lambda_Q. \tag{29}$$

Equation (29) contains integrals with well-known singularities demanding appropriate methods of numerical evaluation, which are beyond the scope of our work.

Special Cases
Neglecting the Earth's topography i.e. $h_P = h_Q = 0$ and $\beta_P = 0$, the solution is given by the system of Eqs. (27) and (28) where

$$F = ae'^2 \iint_E \frac{t_0}{2a\sin\omega/2}\left[\frac{1}{2}\sin^2\Phi_P + \frac{3}{4}\sin^2\Phi_Q \right.$$

$$\left. - \frac{(\sin\Phi_P - \sin\Phi_Q)^2}{8\sin^2\omega/2}\right]\cos\Phi_Q d\Phi_Q d\lambda_Q. \tag{30}$$

On the other hand, in the spherical approximation (i.e. $e'^2 = 0$) and retaining the topography, we get the system of Eqs. (27) and (28) where

$$F = a^2 \iint_E t_0 \frac{h_Q - h_P}{8a^3\sin^3\omega/2}\cos\Phi_Q d\Phi_Q d\lambda_Q. \tag{31}$$

6 Conclusions

The linearized fixed gravimetric boundary value problem and its solution in spheroidal approximation have been presented. This problem is simpler, both formally and mathematically, than the Molodensky problem, which is a free BVP and requires the vertical gradient of the normal gravity. The presented approach is based on the surface layer and includes some approximations. The solution of the integral equation is

also discussed considering some special cases, like neglecting the Earth's topography and a spherical approximation. The derivation is analogous to the solutions of Stock (1983) and Heck (2011) who solved the same problem in spherical approximation. Our approach provides a mathematical model for the determination of the disturbing potential. However, its application for establishing a world height system critically depends on the availability of accurate gravimetric data with satisfactory global coverage of the Earth's surface.

References

Čunderlík R, Mikula K, Mojzeš M (2008) Numerical solution of the linearized fixed gravimetric boundary-value problem. J Geod 82:15–29

Grombein T, Seitz K, Heck B (2015) Height system unification based on the fixed GBVP approach. In: Proceedings of the IAG General Assembly 2013, 1–6 September 2013, Potsdam. International Association of Geodesy Symposia 143, Springer

Heck B (2011) A Brovar-type solution of the fixed geodetic boundary-value problem. Stud Geophys Geod 55:441–454

Heiskanen WA, Moritz H (1967) Physical geodesy. WH Freeman and Co., San Francisco

Holota P (1992) Integral representation of the disturbing potential: effects involved, iteration technique and its convergence. In: Proceedings of the first continental workshop on the geoid in Europe, Prague, 11–14 May 1992. Research Institute of Geodesy, Topography and Cartography, Prague, in co-operation with IAG-Subcommission for the Geoid in Europe, Prague, pp 402–419

Holota P (1997) Coerciveness of the linear gravimetric boundary-value problem and a geometrical interpretation. J Geod 71:640–651

Holota P (2005) Successive approximations in the solution of a weakly formulated geodetic boundary-value problem. In: Proceedings of the IAG General Assembly 2003, Sapporo, June 30 – July 11, 2003. International Association of Geodesy Symposia 128, pp 452–458, Springer

Koch KR (1969) Solution of the geodetic boundary value problem for a reference ellipsoid. J Geophys Res 74:3796–3803

Molodensky MS, Eremeev VF, Yurkina MI (1962) Methods for study of the external gravitational field and figure of the earth. Israel Program for Scientific Translations, Jerusalem

Moritz H (1980) Advanced physical geodesy. Herbert Wichmann Verlag, Karlsruhe

Stock B (1983) A Molodenskii-type solution of the geodetic boundary value problem using the known surface of the earth. Manuscripta Geodaetica 8:273–288

Stokes GG (1849) On the variation of gravity at the surface of the earth. Trans Camb Philos Soc 8:672–695

Yu J, Zhang C (2005) The GPS-gravimetry boundary value problem. Sci China Ser D Earth Sci 48:398–405

Zhu ZW (1981) The Stokes problem for the ellipsoid using ellipsoidal kernels. Report 319, Department of Geodetic Science and Surveying, The Ohio State University, Columbus

On the Convergence of the h-p Finite Element Method for Solving Boundary Value Problems in Physical Geodesy

David Mráz, Milan Bořík, and Jaroslav Novotný

Abstract

A geopotential model of the Earth is usually calculated using the Stokes coefficients. As computational power has increased, research is focusing more on new ways of gravity field modelling. The objective of this work is to study an application of the h-p finite element method for solving boundary value problems in physical geodesy. For the purpose of studying this method, we have formulated model boundary value problems with different boundary conditions. The algorithm for solving these test problems was designed and was subsequently implemented by the program. We derived a weak formulation for each model boundary value problem and also the corresponding finite element discretization. We used isoparametric reference elements with linear and quadratic shape functions. The authors present the application of the h and p methodologies for increasing the rate of convergence of our solution, discuss mesh generation for large domains, and also solve the model boundary value problem, which is similar to the geodetic boundary value problem.

1   Introduction

Nowadays global solutions of the boundary value problems (BVPs) in physical geodesy are mostly solved using expansion into a series of spherical harmonics (Hofmann-Wellenhof and Moritz 2005). On the other hand, in regional studies, other methods, like the Fast Fourier Transform or the least square collocation, are also successfully used (Sansò and Sideris 2013).

We can also solve the BVP in a way that allows us to look for the so-called weak solution (Rektorys 1980) and solve the BVP with some variational methods. The first work published on the application of the finite element method (FEM) in geodesy was done by Meissl (1981), followed by Shaofeng and Dingbo (1991). Recently, FEM and also the Galerkin method were discussed in Holota (2000, 2001, 2005), Holota and Nesvadba (2007), Nesvadba et al. (2007) and in Fašková et al. (2010). In Šprlák et al. (2011), the application of the so-called couple finite-infinite element method was discussed. Additionally, the boundary element method (Klees 1995; Klees et al. 2001; Čunderlík et al. 2008) and the finite volume method in Minarechová et al. (2015) were also used efficiently. The aim of this paper is to study the application and convergence of the h-p FEM (Babuška and Suri 1990) for the different boundary value problems on differently sized domains. We focused on solving the BVPs for the exterior of the Earth.

In our numerical experiments, we solved the model BVPs with the Neumann and the Dirichlet boundary conditions (BCs). The input data for the model BVPs are the values of the gravity potential W, or the gravitational potential V. These values were obtained from the analytical

D. Mráz (✉) • M. Bořík • J. Novotný
Department of Mathematics, Faculty of Civil Engineering, Czech Technical University in Prague, Prague, Czech Republic
e-mail: david.mraz@fsv.cvut.cz

solution. In order to solve the BVPs, which are analogical to the geodetic boundary value problem (GBVP), the input data for the Earth's surface in the last model BVP were chosen as the magnitudes of the gravity acceleration $g = |\mathbf{g}|$.

In geodesy, we distinguish between several types of GBVPs. The free nonlinear and gravimetric GBVPs were discussed in Grafarend and Niemeier (1971), Grafarend et al. (1985), Grafarend (1989) and Heck (1989). When solving GBVPs, we have to deal with the so-called oblique derivative BVP. If the direction of the derivative is normal to the boundary surface, the oblique derivative effect is transformed to the Neumann problem. For our purposes of studying FEM convergence, the oblique derivative effect was neglected.

2 Weak Formulation

Denote Ω as an open domain in R^3. The domain Ω is supposed to be bounded with the Lipschitzian boundary $\partial\Omega = \Gamma_N \cup \Gamma_D$, where Γ_N is the Neumann boundary and Γ_D is the Dirichlet boundary. For the purpose of the generality of the weak formulation, we considered the Poisson equation for the potential $V(x, y, z)$ in the general form

$$\left(\frac{\partial^2 V}{\partial x^2} + \frac{\partial^2 V}{\partial y^2} + \frac{\partial^2 V}{\partial z^2} \right) = -f(x, y, z), \qquad (1)$$

where $f \in L_2(\Omega)$. In our case, we solved the problem with the Newtonian BCs.

$$\begin{aligned} V(x, y, z) &= k(x, y, z) \quad \text{on } \Gamma_D, \\ \frac{\partial V(x, y, z)}{\partial \mathbf{n}} &= l(x, y, z) \quad \text{on } \Gamma_N, \end{aligned} \qquad (2)$$

where $k(x, y, z)$ is a function representing values on the Dirichlet boundary Γ_D, $l(x, y, z)$ is a function representing values on the Neumann boundary Γ_N, $\mathbf{n}$ is a direction of the outward unit normal with respect to $\partial\Omega$, and $\rho = \sqrt{x^2 + y^2 + z^2}$ is an Euclidean distance from the source of gravity to the potential point P. The potential V was assumed to be regular as $\rho \to \infty$. Now consider a test function v from the Sobolev space $W^{1,2}(\Omega)$. We assumed that the test function v was equal to zero on the Dirichlet boundary

$$\vartheta_M = \{v \in W^{1,2}(\Omega), v = 0 \text{ on } \Gamma_D\}. \qquad (3)$$

We multiplied (1) by the test function v, integrated both sides of the equation, and used the Gauss-Green theorem. With respect to the BCs (3), we obtained the weak formulation
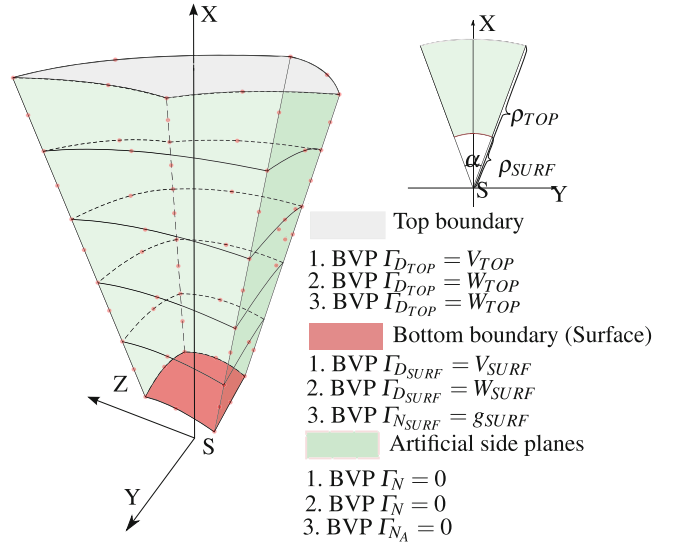
Fig. 1 Finite element mesh for five elements with quadratic shape functions and depicted boundaries for different model BVPs

in this form: find $V \in W^{1,2}(\Omega)$ that

$$\begin{aligned} \int_\Omega \left(\frac{\partial V}{\partial x}\frac{\partial v}{\partial x} + \frac{\partial V}{\partial y}\frac{\partial v}{\partial y} + \frac{\partial V}{\partial z}\frac{\partial v}{\partial z} \right) dx\,dy\,dz = \\ = \int_\Omega f(x, y, z) v \, d\Omega + \int_{\Gamma_N} l(x, y, z) v \, dS, \end{aligned} \qquad (4)$$

for each $v \in \vartheta_M$.

3 Weak Formulations for the Model Boundary Value Problems

In the first case, we solved the boundary value problem for the gravitational potential $V(x, y, z)$ with the mixed boundary conditions. The problem led to the Laplace equation

$$\left(\frac{\partial^2 V}{\partial x^2} + \frac{\partial^2 V}{\partial y^2} + \frac{\partial^2 V}{\partial z^2} \right) = 0. \qquad (5)$$

On the Earth's surface, and also on the top boundary, the Dirichlet conditions were chosen; see Fig. 1. The Dirichlet condition on the top boundary was prescribed as V_{TOP}. On the artificial boundaries, the Neumann conditions were prescribed as zero. Considering (4), we obtained the weak formulation

$$\int_\Omega \left(\frac{\partial V}{\partial x}\frac{\partial v}{\partial x} + \frac{\partial V}{\partial y}\frac{\partial v}{\partial y} + \frac{\partial V}{\partial z}\frac{\partial v}{\partial z} \right) dx\,dy\,dz = 0. \qquad (6)$$

Table 1 Used constants for the model BVPs

Parameter	Value	Units
$GM_\oplus$	$3.986004418 \times 10^{14}$	$[m^3 s^{-2}]$
ω	$7,292,115 \times 10^{-11}$	$[rad\, s^{-1}]$
ρ_{SURF}	$6,371,000$	$[m]$
ρ_{SAT}	$6,671,000$	$[m]$
ρ_{DEMO}	10^9	$[m]$
ρ_∞	10^{17}	$[m]$
α	$\frac{\pi}{180}$	$[rad]$
Longitude λ	$< -\alpha; \alpha >$	$[rad]$
Latitude φ	$< -\alpha; \alpha >$	$[rad]$
ρ_{THR}	0.55×10^8	$[m]$

The analytic solution for the problem is

$$V(x, y, z) = \frac{GM_\oplus}{\rho}, \tag{7}$$

where $GM_\oplus$ is the geocentric gravitational constant; see Table 1.

In the second case, we solved the BVP for the gravity potential W. This problem led to the Poisson equation, where the Laplacian was equal to $2\omega^2$. In this case, ω denoted the angular velocity of the Earth; see Table 1. Using the general form (1), we obtained

$$\left(\frac{\partial^2 W}{\partial x^2} + \frac{\partial^2 W}{\partial y^2} + \frac{\partial^2 W}{\partial z^2} \right) = -2\omega^2. \tag{8}$$

Choosing the analogical BCs as in the first case, we prescribed the Dirichlet condition as W_{SURF} for the bottom boundary and W_{TOP} for the top boundary. The Neumann BCs were again equal to zero from the definition of the equipotential surface for a spherically symmetrical body. Using an analogical method, as we did in the first case, we obtained the weak formulation

$$\int_\Omega \left(\frac{\partial W}{\partial x} \frac{\partial v}{\partial x} + \frac{\partial W}{\partial y} \frac{\partial v}{\partial y} + \frac{\partial W}{\partial z} \frac{\partial v}{\partial z} \right) dx\,dy\,dz = \\ = \int_\Omega 2\omega^2 v \, d\Omega. \tag{9}$$

and the corresponding analytical solution

$$W(x, y, z) = \frac{GM_\oplus}{\rho} + \frac{1}{2}\omega^2 \rho^2 \cos \varphi. \tag{10}$$

The last BVP was also based on solving the Poisson equation (8), but the BCs were chosen in a way that made the model BVP more similar to the GBVP. Instead of using the Dirichlet condition W_{SURF}, we prescribed the Neumann condition on the bottom boundary as the magnitude of the gravity acceleration

$$|\mathbf{g}| = |\mathbf{grad}W|. \tag{11}$$

The Neumann boundary Γ_N was split into two boundaries Γ_{N_A} for the artificial sides, and $\Gamma_{N_{SURF}}$ for the bottom boundary. The surface integral, which refers to Γ_{N_A}, was again equal to zero, so we got the weak formulation for the third BVP in the form

$$\int_\Omega \left(\frac{\partial W}{\partial x} \frac{\partial v}{\partial x} + \frac{\partial W}{\partial y} \frac{\partial v}{\partial y} + \frac{\partial W}{\partial z} \frac{\partial v}{\partial z} \right) dx\,dy\,dz = \\ = \int_\Omega 2\omega^2 v \, d\Omega + \int_{\Gamma_{N_{SURF}}} |\mathbf{g}| v\,dS. \tag{12}$$

4 h-p FEM, h and p Convergence, Error Estimates and FEM Algorithm

In the h-p FEM, we find the solution $V(x, y, z)$ as a linear combination

$$V(x, y, z) = \sum_{i=1}^n \alpha_i \varphi_i (x, y, z), \tag{13}$$

where α_i are coefficients of linear combinations and φ_i are basis functions for $i = 1, 2 \cdots, n$. Substituting (13) for $V(x, y, z)$ or $W(x, y, z)$ to model BVPs weak formulations and also the basis function φ_j for the test function v for $j = 1, 2, \cdots, n$, we got a linear system

$$\mathbf{Au} = \mathbf{f}, \tag{14}$$

where $\mathbf{A}$ is the stiffness matrix, $\mathbf{f}$ is the right-hand side, $\mathbf{u}$ is the solution vector, and n is the number of basis functions, or nodes.

In the finite element analysis, the weak solution can be improved in several different ways. In our model problems, we studied h and p convergence (Babuška and Szabo 1982). As for h convergence, the basis functions for each element were fixed, and the maximum radial size of the element h_{max} approached zero. For p convergence, the mesh was fixed and the order of the shape functions p_{min} approached p_∞. For the purpose of evaluating the results, we used a relative error e_{rel} and an absolute error e_{abs}; see Babuška and Dorr (1981). Let's say that $\tilde{u}_i$ for every $i = 1, \cdots, n$ was the approximated solution obtained at the node i and u_i^A for $i = 1, \cdots, n$ was the analytical solution at the node i. Then the relative error would be given by

$$e_{rel} = \frac{\sqrt{\sum_{i=1}^n (\tilde{u}_i - u_i^A)^2}}{\sqrt{\sum_{i=1}^n (u_i^A)^2}} \tag{15}$$

and the absolute error would be

$$e_{abs} = |\tilde{u}_i - u_i^A|. \tag{16}$$
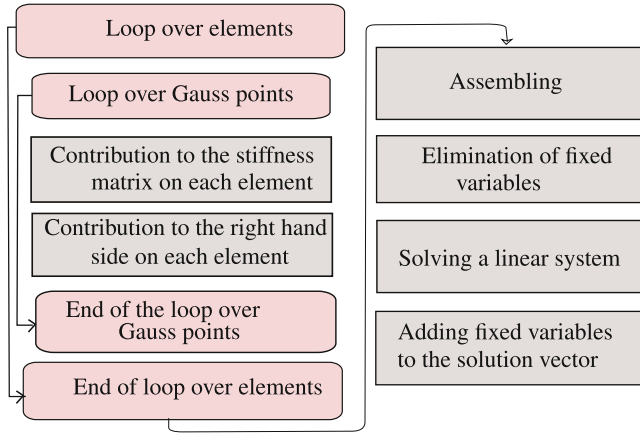
Fig. 2 Simplified scheme of the potential calculation

We have developed a program to solve the model BVPs. The program is split into two main parts. The first part represents generation of the finite element mesh. The second part is the FEM algorithm. The FEM algorithm uses the procedures from Bathe (1999). For the numerical evaluation of the integrals, we used the Gauss-Legendre quadrature with 27 Gauss points on each element for the triple integrals and 9 Gauss points on each side of the element for the surface integrals. First, the stiffness matrices and the right-hand sides of each element were composed. After that, the global stiffness matrix and the global right-hand side were assembled. We solved the linear system using Gaussian elimination (GE) with the prescription of the fixed variables. The solution vector u represents the potential at each node i. A simplified diagram of the computational process is in Fig. 2.

5   Numerical Experiments, h and p Convergence, Methods of Mesh Generation

In our numerical experiments, we solved the model BVPs only with constant values on Dirichlet and Neumann boundaries. These values were obtained from the analytical solutions, so that we could compare the weak solution with the analytical solution. Then the results would be much more valuable for studying radial convergence, and it would also be much easier to compute the relative and absolute errors. Although the analytical solution is known only for some special cases, we could use the convergence tendencies for solving the real GBVP with the measured data.

The geometry of a domain is similar for every numerical experiment. The shape of the domain is defined by the values of the radial distance ρ, the longitude λ, and the latitude φ; see Table 1. The size of the domain for each

numerical experiment differs only in the radial direction. The surface of the Earth is represented by a sphere with the mean radius of the Earth; see Table 1. The upper and lower boundaries are of spherical shape, and the rest of the artificial boundaries are of plane shape; see Fig. 1. For the purpose of studying radial convergence, we discretized the domain only in the radial direction by *NEL* elements, where *NEL* is the number of elements in the domain. Discretization was done by the isoparametric elements (IRE) with linear (LSF) or quadratic shape functions (QSF) (Ergatoudis et al. 1968); see Fig. 3.

In this model BVP we solved the Laplace equation (5). The mesh was only discretized in the radial direction by *NEL* elements. We discretized the domain with 30, 60, 120, 240 and 480 elements. The size of each element in the radial direction was constant. The differences between the different discretizations and the analytical solution are in Fig. 4.

The reference element was an 8-noded IRELSF; see Fig. 3a. The size of the domain in the radial direction was
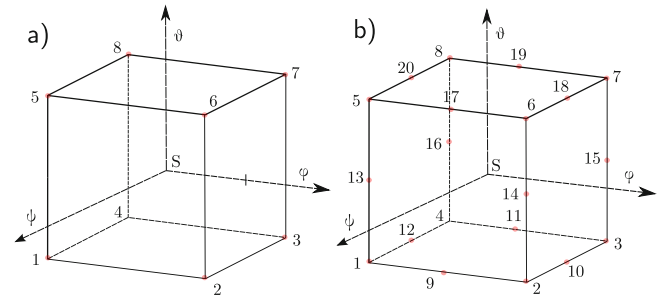
Fig. 3 Reference elements in local coordinates ψ, φ, ϑ. (**a**) Isoparametric reference element with linear shape functions (IRELSF). (**b**) Isoparametric reference element with quadratic shape functions (IRE-QSF)
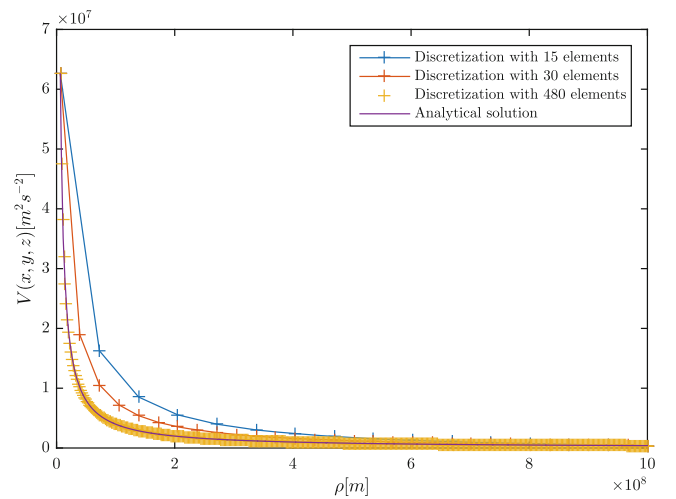
Fig. 4 Increasing convergence with the h methodology. The IRELSF is used. The meshes are generated with the constant radial size of each element. The domain is bounded with the top boundary $\rho_{TOP} = \rho_{DEMO}$

bounded by ρ_{SURF} and ρ_{DEMO}. The value V_{TOP} cannot be represented by real data in this height, but for illustrative purposes, it was computed from the analytical solution (7).

In the first set of meshes, the radial size of each element was constant, but we also generated meshes in which the radial size of the element was dependent on the rate of change of the potential. The principle of mesh generation for the model BVP (8) is that we substituted ρ_{SURF} and ρ_{TOP} into the relation for the magnitude of the gravity acceleration (11). From this relation, we obtained the values g_{SURF} and g_{TOP}. The interval was defined by these values, and we could compute the values

$$g_i = g_{SURF} + i \frac{g_{TOP} - g_{SURF}}{NEL}, \qquad (17)$$

where $i = 0, \cdots, NEL$. By rearranging (11) and substituting values g_i into this relation, we obtained the radial distance ρ_i for each equipotential surface. The relative error e_{rel}^E for the h methodology, with each element having the same radial size, and the relative error for the h methodology with the mesh generation dependent on the potential change e_{rel}^D, is depicted in Fig. 5. The numerical values are in Table 2.
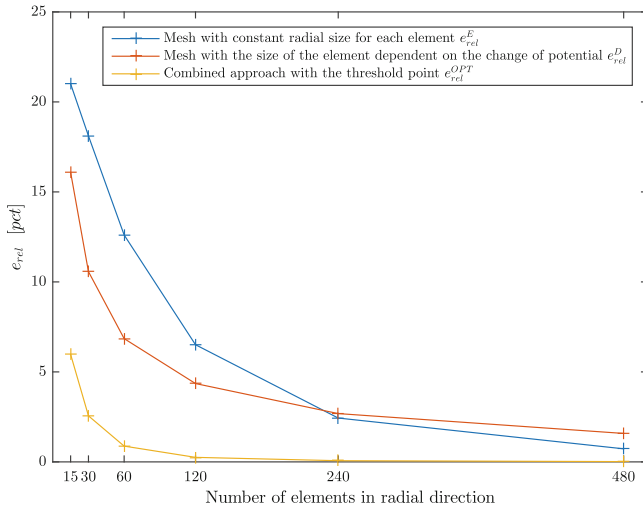
Fig. 5 The relative error for different mesh generation. The domain is bounded by $\rho_{TOP} = \rho_{DEMO} = 10^9$. In these cases, we solve the Laplace equation with the IRELSF

Table 2 Relative errors for different mesh generation with the dependence on the number of elements in radial direction

NEL	e_{rel}^E [pct]	e_{rel}^D [pct]	e_{rel}^{OPT} [pct]
15	21.09	16.09	5.97
30	18.11	10.57	2.56
60	12.61	6.85	0.88
120	6.51	4.35	0.25
240	2.44	2.68	0.066
480	0.73	1.58	0.017
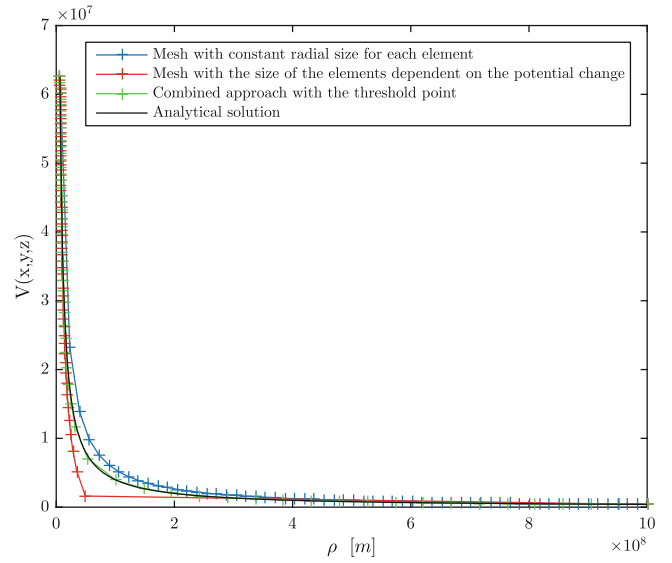
Fig. 6 Different methods for the mesh generation for large domains. Every solution is for the Laplace equation (5) and is discretized with 60 elements with LSF. The top boundary is in radial distance $\rho_{TOP} = 10^9$

This method of mesh generation is not suitable for the type of the domain where the radial size of the domain is too large: $\rho_{TOP} \geq 10^8$; see Fig. 6.

As seen in Fig. 5, a better way to generate the mesh is to combine both approaches. We split the domain into two parts. In the first part, where the rate of change is fast, we used the mesh generation with the dependence on the potential change, and in the second part, we generated a mesh with a constant radial size of the element. The threshold point for splitting the domain should be close to the saddle point. We found that the best point for splitting the domain was $\rho_{THR} \approx 0.55 \times 10^8$, and also that the distribution of the elements in the ratio $\frac{2}{3}NEL$, where $\rho \leq \rho_{THR}$ and $\frac{1}{3}NEL$, where $\rho \geq \rho_{THR}$, was optimal. These values were found by running a number of numerical experiments for different thresholds and for different distributions of the elements. In these experiments, we used relative errors as a determining parameter for choosing the optimal threshold and the optimal distribution of the elements; see Fig. 7a, b. For illustration we found the threshold points for different parameters ρ_{SURF} on the domain, where $\rho_{TOP} = \rho_{DEMO}$; see Fig. 7c.

However, we could also use the p methodology to increase the rate of convergence. In our numerical experiments, we used LSF or QSF to solve the problem, which is similar to the GBVP; see Fig. 3. We solved the model BVP (12), where the input data were equal to the magnitude of gravity acceleration g. Absolute errors are depicted in Fig. 8.

The largest differences were close to the Dirichlet boundary. The most accurate solution was obtained in the centre of the domain Ω. The overall absolute differences were decreasing with the increased number of elements.
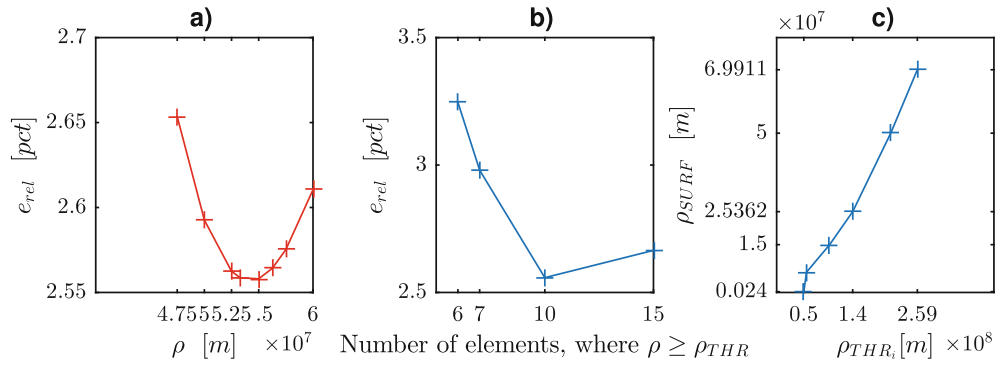
Fig. 7 (**a**) Finding the threshold point with the minimum e_{rel} on the mesh with 30 elements; (**b**) finding the distribution of the elements in the radial direction with the minimum relative error on the mesh with 30 elements; (**c**) relationship between different values ρ_{SURF} and the approximated value of the threshold point ρ_{THR}
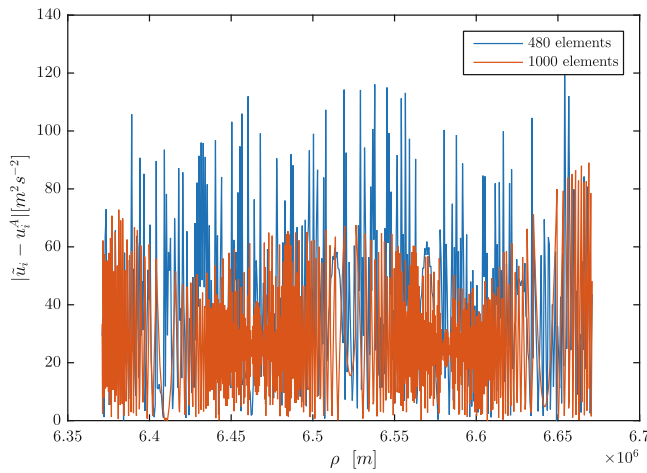
Fig. 8 The overall absolute differences are for the solution of the model BVP (12) with the Dirichlet condition W_{SURF} on the bottom boundary. The domain is in the radial direction bounded by ρ_{SURF} and ρ_{SAT}. The mesh was generated with the constant radial size of the element. The IRELSF is used

6 Conclusion

The main aim of this paper was to study convergence and the application of the h-p FEM in problems of physical geodesy. For that purpose, the weak formulations for the model BVPs were derived, and the hp-FEM algorithm for solving these model BVPs was implemented in the program. We have performed a number of numerical experiments with different meshes and differently sized domains. The main goal of these experiments was to study the rate of convergence for the h and p methodologies and also to find the optimal method for mesh generation. We found that the best way to generate meshes was to split the domain into two parts. In the first part, we used the mesh generation that was dependent on the potential change. In the second part, we used the mesh generation with the same radial size for each element.

In order to decide which methodology to choose, we had to take into account the difficulty of the programming for the p methodology and also the fact that the computation with the IRELSF was more efficient. When the mesh was discretized only in the radial direction, the linear system for QSF had $12NEL + 8$ equations and only $4NEL + 4$ equations for LSF. In general, the improvement with the p methodology was not worth the increased computational power. We could obtain much better results using the h methodology with the mesh generation using the threshold point. If we used this combined approach, the linear system had the same number of equations as with the h methodology with the constant radial size of the element, but the rate of convergence increased much faster than with the p methodology.

In the future, we want to apply the FEM algorithm and convergence tendencies to precise local and global gravity field modelling. The challenges are to implement a priori and a posteriori error estimates, and adaptive mesh refinements, to use the tools of numerical analysis to diminish errors close to the Dirichlet boundary and also to study the effect of the terrain deformations on the weak solution. In precise local and global gravity field modelling, we can use the convergence tendencies that we found and can solve the GBVP much more efficiently and precisely.

References

Babuška I, Dorr MR (1981) Error estimates for the combined h and p version of finite element method. Numer Math 37:252–277

Babuška I, Suri M (1990) The p- and h-p versions of the finite element method an overview. In: Canuto C, Quarteroni A (eds) Spectral and high order methods for partial differential equations. North-Holland, Amsterdam, pp 5–26

Babuška I, Szabo B (1982) On the rates of convergence of the finite element method. Int J Numer Methods Eng 18:323–341. doi:10.1002/nme.1620180302

Bathe K (1999) Finite element procedures. Prentice Hall, Prentice

Čunderlík R, Mikula K, Mojzeš M (2008) Numerical solution of the linearized fixed gravimetric boundary-value problem. J Geod 82(1):15–29

Ergatoudis J, Irons B, Zienkiewicz O (1968) Curved, isoparametric, quadrilateral elements for finite element analysis. Int J Solids Struct 4:31–42

Fašková Z, Čunderlík, Mikula K (2010) Finite element method for solving geodetic boundary value problems. J Geod 84(2):135–144

Grafarend E (1989) The geoid and the gravimetric boundary value problem, Report No 18. The Royal Institute of Technology (Dep of Geod), Stockholm

Grafarend E, Niemeier W (1971) The free nonlinear boundary value problem of physical geodesy. Bull Geod 101:243–261

Grafarend E, Heck B, Knickmeyer E (1985) The free versus fixed geodetic boundary value problem for different combinations of geodetic observables. Bull Geod 59(1):11–32

Hofmann-Wellenhof B, Moritz H (2005) Physical geodesy. Springer, New York

Holota P (2000) Direct methods in physical geodesy. In: Schwarz K-P (ed) Geodesy beyond 2000 - the challenges of the first decade. IAG general assembly, Birmingham, July 19–30, 1999, IAG symposia, vol 121. Springer, Berlin, pp 163–170

Holota P (2001) Variational methods in geoid determination and function bases. Phys Chem Earth Solid Earth Geod 24(1):3–14

Holota P (2005) Neumann's boundary-value problem in studies on Earth gravity field: weak solution. In: Holota P, Slaboch V (eds) 50 years of Research Institute of Geodesy, Topography and Cartography, Prague, vol 50, No 36. Research Institute of Geodesy, Topography and Cartography, Prague, pp 49–69

Holota P, Nesvadba O (2007) Model refinements and numerical solutions of weakly formulated boundary-value problems in physical geodesy. In: Xu P, Liu J, Dermanis A (eds) VI Hotine-Marussi symposium of theoretical and computational geodesy, Wuhan, 29 May–2 June, 2006. IAG symposia, vol 132. Springer, Berlin, pp 314–320

Heck B (1989) On the non-linear geodetic boundary value problem for a fixed boundary surface. Bull Geod 63(1):57–67

Klees R (1995) Boundary value problems and approximation of integral equations by finite elements. Manuscr Geodaet 20:345–361

Klees R, van Gelderen M, Lage C, Schwab C (2001) Fast numerical solution of the linearized Molodensky problem. J Geodesy 75:349–362

Meissl P (1981) The use of finite elements in physical geodesy. Report 313, Geodetic Science and Surveying, The Ohio State University

Minarechová Z, Macák M, Čunderlík R, Mikula K (2015) High-resolution global gravity field modelling by the finite volume method. Stud Geophys Geod 59(1):1–20

Nesvadba O, Holota P, Klees R (2007) A direct method and its numerical interpretation in the determination of the Earth's gravity field from terrestrial data. In: Tregoning P, Rizos C (eds) Dynamic planet. International association of geodesy symposia, vol 130. Springer, Heidelberg, pp 370–376

Rektorys K (1980) Variational methods in mathematics, science and engineering. D. Reidel Publishing Company, Dordrecht

Sansò F, Sideris M (2013) Geoid determination - theory and methods. Lecture notes in earth system sciences. Springer, Heidelberg

Shaofeng B, Dingbo C (1991) The finite element method for the geodetic boundary value problem. Manuscr Geod 16:353–359

Šprlák M, Fašková Z, Mikula K (2011) On the application of the coupled finite-infinite element method to the geodetic boundary value problem. Stud Geophys Geod 55:479–487

Domain Transformation and the Iteration Solution of the Linear Gravimetric Boundary Value Problem

P. Holota

Abstract

The aim of this paper is to discuss the solution of the simple gravimetric boundary value problem by means of the method of successive approximations. A transformation of coordinates is used to express the relation between the description of the boundary of the solution domain and the structure of Laplace's operator. The solution domain is carried onto the exterior of a sphere and the original oblique derivative boundary condition is given the form of Neumann's boundary condition. Laplace's operator expressed in terms of new coordinates involves topography-dependent coefficients. Effects caused by the topography of the physical surface of the Earth are treated as perturbations. Their internal structure is analyzed and modified by using integration by parts. As a result of the transformation a spherical mathematical apparatus may be applied at each iteration step, including the spherical form of Green's function of the second kind, i.e. Neumann's function, in the integral representation of the successive approximations.

1 Introduction

The physical surface of the Earth is rather complex. In gravity field studies and in physical geodesy the experience confirms that if the surface (even in an idealized form) is taken for the boundary in the formulation of boundary value problems, it makes the practical solution of the problems and thus also the determination of the gravity or the disturbing potential rather demanding and numerically complex. This indicates that the relation between the description of the surface of the Earth and the structure of Laplace's operator is an important aspect. Similarly as in other branches of engineering and mathematical physics also here a transformation of coordinates may be used to solve an alternative between the boundary complexity and the complexity of the coefficients of the partial differential equation governing the solution. Laplace's operator has a relatively simple structure in terms of spherical coordinates which are frequently used in geodesy. However, the physical surface of the Earth substantially differs from a (geocentric) sphere of (even optimally chosen) radius R. The situation may be more convenient in a system of curvilinear coordinates such that the physical surface of the Earth is imbedded in the family of coordinate surfaces. However, the structure of Laplace's operator is more complicated in this case and in a sense it represents the topography of the physical surface of the Earth.

P. Holota (✉)

Research Institute of Geodesy, Topography and Cartography, 250 66 Zdiby 98, Praha-východ, Czech Republic

e-mail: petr.holota@pecny.cz

In this paper we will discuss the solution of the simple gravimetric boundary value problem. We use this term for the problem to find a function T such that

$$\Delta T = div \ \mathbf{grad} \ T = 0 \quad \text{in} \quad \Omega, \tag{1}$$

$$\frac{\partial T}{\partial |\mathbf{x}|} = - \ \delta g \quad \text{on} \quad \partial \Omega. \tag{2}$$

see Hofmann-Wellenhof and Moritz (2005). Here $\mathbf{x}$ is a point of rectangular Cartesian coordinates x_i, $i = 1, 2, 3$, in three dimensional Euclidean space $\mathbb{R}^3$, $|\mathbf{x}| = \left(x_1^2 + x_2^2 + x_3^2\right)^{1/2}$, Δ means Laplace's operator, δg is the gravity disturbance, Ω represents an unbounded solution domain and $\partial \Omega$ is its boundary. We suppose that Ω is star-shaped at the origin of the system of coordinates x_i, $i = 1, 2, 3$, and about as irregular as the physical surface of the Earth.

Note in particular that here the simple gravimetric problem is taken for an important theoretical and practical representative of the linear form of the general gravimetric boundary value problem, see e.g. Holota (1997). The problem is seen as an analogue to the notion of the so called simple Molodensky problem, which is well-known and related to the linear form of the general Molodensky problem, see Moritz (1980) and Borre (2006). The definition of the simple gravimetric problem as well as of the simple Molodensky problem involves the concept of spherical approximation. Recall also that within the adopted idealization Ω represents the exterior of the Earth and T is taken for the disturbing potential.

2 Transformation of the Problem: Boundary Condition

We first put $\overline{\Omega}$ for the closure of the solution domain $\Omega \subset \mathbb{R}^3$, i.e., $\overline{\Omega} = \Omega \cup \partial \Omega$. Under this notation our starting point is a transformation of $\overline{\Omega}$ given by

$$x_1 = [\ r + h \ (B, L) \ ] \cos B \cos L,$$
$$x_2 = [\ r + h \ (B, L) \ ] \cos B \sin L, \tag{3}$$
$$x_3 = [\ r + h \ (B, L) \ ] \sin B.$$

The curvilinear coordinates B (geocentric latitude), L (longitude) are the usual spherical coordinates of the point $\mathbf{x} \equiv (x_1, x_2, x_3) \in \overline{\Omega}$,

$$|\mathbf{x}| = r + h \ (B, L) \tag{4}$$

and h is the height of the boundary point $(x_1, x_2, x_3) \in \partial \Omega$ above a geocentric sphere of radius R. Moreover, $\partial |\mathbf{x}| / \partial r = 1$, so that we immediately see that the

transformation is a one-to-one mapping between the original solution domain Ω and the outer space of the (geocentric) sphere of radius R. Obviously the transformation carries the boundary $\partial \Omega$ described by the placement vector of length $R + h$ into a sphere of radius R in the space of curvilinear coordinates r, B, L.

In addition the transition of the coordinates changes also the representation of our boundary value problem. Indeed, we can easily see that the boundary condition turns into

$$\frac{\partial T}{\partial r} = - \delta g \quad \text{for} \quad r = R. \tag{5}$$

On the other hand, however, it is somewhat more complicated to express Laplace's operator of T in terms of the curvilinear coordinates r, B, L, which do not form an orthogonal system.

3 Laplace Operator and Topography-Dependent Coefficients

Here we will use the tensor calculus. Putting (merely for technical reasons)

$$y_1 = r, \quad y_2 = B, \quad y_3 = L, \tag{6}$$

we easily deduce that the Jacobian (Jacobian determinant)

$$D = \left| \frac{\partial x_i}{\partial y_j} \right| = - (r + h)^2 \cos B \tag{7}$$

of the transformation is negative in the closed domain $\overline{\Omega}$ (apart from its zero values for $B = -\pi/2$ and $B = \pi/2$). Moreover, through an elementary calculation we obtain the components of the metric tensor

$$g_{ij}(y) = \frac{\partial x_k}{\partial y_i} \frac{\partial x_k}{\partial y_j} \tag{8}$$

in the coordinates y_i. Going back to the original notation, we have

$$g_{11} = 1, \tag{9}$$

$$g_{12} = \frac{\partial h}{\partial B}, \tag{10}$$

$$g_{13} = \frac{\partial h}{\partial L}, \tag{11}$$

$$g_{22} = (r + h)^2 + \left(\frac{\partial h}{\partial B}\right)^2, \tag{12}$$

$$g_{23} = \frac{\partial h}{\partial B} \frac{\partial h}{\partial L}, \tag{13}$$

$$g_{33} = (r + h)^2 \cos^2 B + \left(\frac{\partial h}{\partial L}\right)^2. \tag{14}$$

Now we are ready to express Laplace's operator applied on T. In terms of the curvilinear coordinates y_i it has the following general form

$$\Delta T = \frac{1}{\sqrt{g}} \frac{\partial}{\partial y_i} \left(\sqrt{g} \, g^{ij} \frac{\partial T}{\partial y_j}\right)$$

$$= g^{ij} \frac{\partial^2 T}{\partial y_i \partial y_j} + \frac{1}{\sqrt{g}} \frac{\partial \sqrt{g} \, g^{ij}}{\partial y_i} \frac{\partial T}{\partial y_j}, \tag{15}$$

where $g^{ij} = G^{ij}/g$ is the associate (or conjugate) metric tensor and G^{ij} is the cofactor of g_{ij} in the determinant $g = |g_{ij}|$, see Sokolnikoff (1971). After some algebra and using our results above, we can write

$$\Delta T = \left(1 + \frac{h}{r}\right)^{-2} [\Delta_S T - \delta(T, h)], \tag{16}$$

where

$$\Delta_S T = \frac{2}{r} \frac{\partial T}{\partial r} + \frac{\partial^2 T}{\partial r^2} + \frac{1}{r^2} \frac{\partial^2 T}{\partial B^2}$$

$$- \frac{\sin B}{r^2 \cos B} \frac{\partial T}{\partial B} + \frac{1}{r^2 \cos^2 B} \frac{\partial^2 T}{\partial L^2}, \tag{17}$$

$$\delta(T, h) = A_1 \frac{\partial T}{\partial r} + A_2 \frac{\partial^2 T}{\partial r^2}$$

$$+ A_3 \frac{1}{r} \frac{\partial^2 T}{\partial r \partial B} + A_4 \frac{1}{r \cos B} \frac{\partial^2 T}{\partial r \partial L} \tag{18}$$

and A_i are topography dependent coefficients given by

$$A_1 = \frac{1}{r^2} [-2h + \Delta_1 h], \tag{19}$$

$$A_2 = -\frac{2h}{r} - \left(\frac{h}{r}\right)^2 - \frac{1}{r^2} |\mathbf{grad}_1 h|^2, \tag{20}$$

$$A_3 = \frac{2}{r} \frac{\partial h}{\partial B}, \tag{21}$$

$$A_4 = \frac{2}{r \cos B} \frac{\partial h}{\partial L} \tag{22}$$

with

$$|\mathbf{grad}_1 h|^2 = \left(\frac{\partial h}{\partial B}\right)^2 + \frac{1}{\cos^2 B} \left(\frac{\partial h}{\partial L}\right)^2 \tag{23}$$

and

$$\Delta_1 h = \frac{1}{\cos B} \frac{\partial}{\partial B} \left(\cos B \frac{\partial h}{\partial B}\right) + \frac{1}{\cos^2 B} \frac{\partial^2 h}{\partial L^2}. \tag{24}$$

Note that $|\mathbf{grad}_1 h|^2$ is the first and $\Delta_1 h$ is the second Beltrami's differential operator referred to the unit sphere.

4 Simple Gravimetric Boundary Value Problem in Curvilinear Coordinates and Neumann's Function

The disturbing potential T is a harmonic function in the original solution domain Ω. In consequence T satisfies Laplace's equation

$$\Delta T = 0 \quad \text{for} \quad r > R, \tag{25}$$

which results in

$$\Delta_S T = \delta(T, h) \quad \text{for} \quad r > R. \tag{26}$$

in view of Eq. (16). Thus the simple gravimetric boundary value problem in terms of the curvilinear coordinates r, B, L attains the form

$$\Delta_S T = f \quad \text{for} \quad r > R, \tag{27}$$

$$\frac{\partial T}{\partial r} = -\delta g \quad \text{for} \quad r = R, \tag{28}$$

where $f = \delta(T, h)$.

Neglecting the fact that f depends on T, we can represent the solution of the problem formally by means of a classical apparatus of mathematical physics. Indeed, it is relatively easy to find the respective Green's function of the second kind N, usually called Neumann's function, which solves the boundary value problem in question. Thus

$$T_P = \frac{1}{4\pi} \int_{r=R} \delta g \, N (r_P, \psi, r) \, dS$$

$$- \frac{1}{4\pi} \int_{r>R} f \, N (r_P, \psi, r) \, dV, \tag{29}$$

where dS and dV are the surface and the volume element, respectively. The quantities with and without the subscript P are referred to the computation and the variable point of the integration. Similarly, ψ is the angle between the placement vector of the computation point and the variable point of the integration. Referring to Holota (2003, 2004), we can immediately write that the function N is given by

$$N = J - H, \qquad (30)$$

where

$$J = \left(r^2 + r_P^2 - 2rr_P \cos \psi\right)^{-1/2} \qquad (31)$$

is the fundamental solution of Laplace's equation and H is a harmonic function

$$H = \frac{1}{R}\sum_{n=0}^{\infty} \frac{n}{n+1} \left(\frac{R^2}{rr_P}\right)^{n+1} P_n \left(\cos \psi\right) \qquad (32)$$

with P_n denoting the usual Legendre polynomial of degree n.

Moreover, referring to Holota (2003, 2004) again, we have even a closed form expression for the function N. Its structure is as follows

$$\begin{aligned} N\left(\boldsymbol{x}, \boldsymbol{x}_P\right) = \frac{1}{|\boldsymbol{x} - \boldsymbol{x}_P|} &+ \frac{R}{|\boldsymbol{x}|}\frac{1}{|\overline{\boldsymbol{x}} - \boldsymbol{x}_P|} \\ &- \frac{1}{R} \ln \frac{|\overline{\boldsymbol{x}} - \boldsymbol{x}_P| + |\overline{\boldsymbol{x}}| - |\boldsymbol{x}_P| \cos \psi}{|\boldsymbol{x}_P|\ (1 - \cos \psi)}, \end{aligned} \qquad (33)$$

where $\overline{\boldsymbol{x}}$ is an image of $\boldsymbol{x}$ given by a transformation of space known as inversion in a sphere (Kelvin's transform), i.e. $|\boldsymbol{x}|\,|\overline{\boldsymbol{x}}| = R^2$.

5   Iteration Process

Neumann's function can also be used to solve the transformed simple gravimetric boundary value problem, where f depends on T. In this case the integral formula (29) represents an integro-differential equation for T and an iteration approach has to be applied. For this purpose we put

$$F_P = \frac{1}{4\pi} \int\limits_{r=R} \delta g\, N\left(r_P, \psi, r\right)\, dS, \qquad (34)$$

which is a harmonic function such that

$$\frac{\partial F}{\partial r} = -\delta g \quad \text{for} \quad r = R \qquad (35)$$

and

$$(KT)_P = -\frac{1}{4\pi} \int\limits_{r>R} f\, N\left(r_P, \psi, r\right)\, dV, \qquad (36)$$

is an integro-differential operator applied on T such that

$$\Delta_S(KT) = \delta\left(T, h\right) \quad \text{for} \quad r > R \qquad (37)$$

and

$$\frac{\partial KT}{\partial r} = 0 \quad \text{for} \quad r = R. \qquad (38)$$

Recall that the above mentioned properties of F and KT are the consequences of the general principles in constructing Neumann's function.

Our aim is to find T from $T = F + KT$ by means of the method of successive approximations

$$T = \lim_n T_n, \quad T_n = F + KT_{n-1}, \qquad (39)$$

where $n = 1, 2, \ldots \infty$ and T_0 is the starting approximation, e.g. $T_0 = F$.

The crucial point is to show that K is a contraction mapping which as a sufficient condition guarantees the convergence of the iteration procedure (39) according to Banach's fixed point theorem, see e.g. Lyusternik and Sobolev (1965). The contractivity of K has been discussed already in Holota (1985, 1986, 1989, 1992a, b) though in the case of Green's function constructed for the simple Molodensky problem. The principal steps of the reasoning can be applied also here. However, for the page limit it is not possible to reproduce them completely. Therefore, we will confine ourselves just to the main points. The contractivity of K has been investigated in Sobolev's weight space $W_2^{(2)}(D)$ equipped by the norm

$$\begin{aligned} &\|u\|_{2,2} \\ &= \left[\int\limits_D \left(|u|^2 + R^2\,|\boldsymbol{grad}\,u|^2 + R^4 \sum_{i,j=1}^{3}\left|\partial^2 u/\partial x_i \partial x_j\right|^2\right) dV\right]^{1/2}, \end{aligned} \qquad (40)$$

where $D \equiv [\boldsymbol{x},\ R < |\boldsymbol{x}|]$. The most intricate step to estimate the second order derivatives of Ku has been done by means of a special case of the Calderon-Zygmund inequality, which belongs to the concept of the so-called L_p estimates for Poisson's equation (analogous to Chauder's theory in Hölder spaces), see Gilbarg and Trudinger (1983).

Banach's theorem has a constructive nature and the constant α such that

$$\|Ku - Kv\|_{2,2} \le \alpha\,\|u - v\|_{2,2} \qquad (41)$$

for all $u, v \in W_2^{(2)}(D)$ depends on the coefficients A_i, i.e., it essentially depends on the topography of the boundary of the original solution domain Ω. In particular α derived in Holota (1986) depends on essential supreme values

$$\operatorname*{supess}_{D} |A_i| \qquad (42)$$

of A_i, $i = 1, 2, 3, 4$ and the inequality $\alpha < 1$ (which is sufficient for K to be a contractive mapping) has been proved for the topography of a realistic range of heights and relatively gentle slopes. Since α depends on the essential supreme values (42) we can expect that the contraction nature of K will be kept also for larger slopes, provided that they do not occur too frequently.

The problem which still deserves attention is the question whether F is an element of $W_2^{(2)}(D)$. Here the theory of regularity of weak solutions has to be applied. We believe that for δg being sufficiently smooth also F has the necessary degree of regularity. In analogy to Holota (1986) one can show that δg has to be at least an element of the Sobolev-Slobodeckii space $W_2^{(1/2)}$ (with fractional derivative) of functions defined on the surface of a sphere, see Nečas (1967) or Kufner et al. (1977).

6 Modification of *KT* and a Linear Theory

For practical computation it is convenient to give the term KT a somewhat different form which is more applicable. Starting with $\delta(T, h)$, we immediately see that

$$f = a_1 \frac{\partial T}{\partial r} + A_2 \frac{\partial^2 T}{\partial r^2} + \frac{1}{r^2} \frac{\partial}{\partial r} \left(T \Delta_1 h + 2 \langle grad_1 T, grad_1 h \rangle \right), \quad (43)$$

where $\langle , \rangle$ means the scalar product and

$$a_1 = A_1 - \frac{1}{r^2} \Delta_1 h = -\frac{2h}{r^2}. \quad (44)$$

In the next step we recall that

$$\Delta_1(Th) = T \Delta_1 h + 2 \langle grad_1 T, grad_1 h \rangle + h \Delta_1 T, \quad (45)$$

which enables us to write

$$\frac{1}{r^2} \frac{\partial}{\partial r} \left(T \Delta_1 h + 2 \langle grad_1 T, grad_1 h \rangle \right)$$
$$= \frac{1}{r} \left[\Delta_S \left(hr \frac{\partial T}{\partial r} \right) - h \Delta_S \left(r \frac{\partial T}{\partial r} \right) \right]. \quad (46)$$

Here

$$\Delta_S \left(r \frac{\partial T}{\partial r} \right) = 2 \Delta_S T + r \frac{\partial}{\partial r} \Delta_S T, \quad (47)$$

so that one arrives at

$$\left(1 + \frac{2h}{r} \right) f + h \frac{\partial f}{\partial r} = Q, \quad (48)$$

which is an elementary differential equation for the function f, where on the right hand side

$$Q = a_1 \frac{\partial T}{\partial r} + A_2 \frac{\partial^2 T}{\partial r^2} + \frac{1}{r} \Delta_S \left(hr \frac{\partial T}{\partial r} \right). \quad (49)$$

Its general solution is

$$f = \frac{1}{r^2} e^{-r/h} \left[C(B, L) + \frac{1}{h} \int r^2 Q \, e^{r/h} dr \right], \quad (50)$$

while $C(B, L)$ is an arbitrary function of the coordinates B and L and e means the base of natural logarithm. The solution makes it possible to display the structure of individual approximations more explicitly. Indeed, using the integration by parts and comparing this solution with Eq. (43), one can show that $C(B, L) = 0$ and that

$$f = Q - \frac{h}{r^2} \frac{\partial}{\partial r} \left(r^2 Q \right) + \frac{h^2}{r^2} \frac{\partial^2}{\partial r^2} \left(r^2 Q \right)$$
$$- \frac{h^2}{r^2} e^{-r/h} \frac{1}{h} \int e^{r/h} \frac{\partial^3}{\partial r^3} \left(r^2 Q \right) dr. \quad (51)$$

In the sequel we will confine ourselves to a linear theory in h/r and also in $|grad_1 h| / r$ (which in second power appears in the coefficient A_2). In this case we have $f = Q^{(1)}$, where

$$Q^{(1)} = -\frac{2h}{r^2} \frac{\partial T}{\partial r} - \frac{2h}{r} \frac{\partial^2 T}{\partial r^2} + \frac{1}{r} \Delta_S \left(hr \frac{\partial T}{\partial r} \right). \quad (52)$$

In the linear theory our integro-differential equation turns into

$$T^{(1)} = F + K^{(1)} T^{(1)} \quad (53)$$

and by analogy the iteration process applied for the solution is

$$T^{(1)} = \lim_n T_n^{(1)}, \quad T_n^{(1)} = F + K^{(1)} T_{n-1}^{(1)}, \quad (54)$$

where $T_0^{(1)}$ is the starting approximation, e.g. $T_0^{(1)} = F$. In the following we first will use the integration by parts to modify the integral

$$\left(K^{(1)} T \right)_P = -\frac{1}{4\pi} \int_{r>R} Q^{(1)} N \left(r_P, \psi, r \right) \, dV. \quad (55)$$

We easily deduce that

$$-\int_{r>R} \frac{h}{r} \frac{\partial^2 T}{\partial r^2} N \, dV = \frac{1}{R} \int_{r=R} h \frac{\partial T}{\partial r} N dS + \int_{r>R} \frac{h}{r^2} \frac{\partial T}{\partial r} N dV$$
$$+ \int_{r>R} \frac{h}{r} \frac{\partial T}{\partial r} \frac{\partial N}{\partial r} dV. \quad (56)$$

Similarly, using Green's second identity, we obtain

$$\int\limits_{r>R} \frac{1}{r}\, \Delta_S \left(hr\frac{\partial T}{\partial r}\right) N\; dV = -4\pi \left(\frac{\partial T}{\partial r}\right)_P h_P$$

$$-2\int\limits_{r>R} \frac{h}{r}\frac{\partial T}{\partial r}\frac{\partial N}{\partial r}dV - \frac{2}{R}\int\limits_{r=R} h\frac{\partial T}{\partial r}N\; dS$$

$$-\int\limits_{r=R} h\frac{\partial^2 T}{\partial r^2}N\; dS + \int\limits_{r=R} h\frac{\partial T}{\partial r}\frac{\partial N}{\partial r}dS. \qquad (57)$$

Now, substituting both the results into Eq. (55), we arrive at

$$\left(K^{(1)}T\right)_P = \left(\frac{\partial T}{\partial r}\right)_P h_P + \frac{1}{4\pi}\int\limits_{r=R} h\frac{\partial^2 T}{\partial r^2}N\; dS \qquad (58)$$

and subsequently at

$$F_P + \left(K^{(1)}T\right)_P = \left(\frac{\partial T}{\partial r}\right)_P h_P + \frac{1}{4\pi}\int\limits_{r=R} \delta g\, N\; dS$$

$$-\frac{1}{4\pi}\int\limits_{r=R} h\frac{\partial \delta g}{\partial r}N\; dS. \qquad (59)$$

Finally, going back to our iteration process, we obtain

$$\left(T_n^{(1)}\right)_P = \left(\frac{\partial T_{n-1}^{(1)}}{\partial r}\right)_P h_P + \frac{1}{4\pi}\int\limits_{r=R} \left[\delta g - h\frac{\partial (\delta g)_{n-1}^{(1)}}{\partial r}\right] N\; dS$$

$$(60)$$

with

$$(\delta g)_{n-1}^{(1)} = -\frac{\partial T_{n-1}^{(1)}}{\partial r}. \qquad (61)$$

7   Final Comments

The discussion in this paper gave us a possibility to gain a deeper insight into the problems associated with the use of the method of successive approximations for the solution of the simple gravimetric boundary value problem. The results achieved represent rather an initial step, but in essence also a springboard for further studies. They will be continued. For instance a stimulus comes from the topography dependent coefficients A_i. We immediately see that the linear theory in the last section is rather weak for larger slopes. In particular the coefficient A_2 can be very often much stronger affected by the term $(|\mathbf{grad}_1 h|/r)^2$ than by the simple linear term h/r. Therefore, a higher order theory will be investigated. Our intention also is to substitute the sphere by an oblate ellipsoid of revolution and to interpret the scheme of our reasoning for a transformation of coordinates that will represent a one-to-one correspondence between the outer space of the Earth and the exterior of the ellipsoid. This will bring our

studies closer to reality and in particular to the general form of the linear gravimetric boundary value problem.

References

Borre K (ed) (2006) Mathematical foundations of geodesy, selected papers of Torben Krarup. Springer, Heidelberg

Gilbarg D, Trudinger NS (1983) Elliptic partial differential equations of second order. Springer, Heidelberg

Hofmann-Wellenhof B, Moritz H (2005) Physical geodesy. Springer, New York

Holota P (1985) A new approach to iteration solutions in solving geodetic boundary value problems for real topography. In: Proceedings of the 5th international symposium on geodynamics and physics of the Earth, GDR, Magdeburg, 23–29 September 1984, Part II. Veroff. d. Zentr. Inst. f. Phys. d. Erde, Nr. 81, Teil II, pp 4–15

Holota P (1986) Boundary value problems in physical geodesy: present state, boundary perturbation and the Green-Stokes representation. In: Proceedings of the 1st Hotine-Marussi symposium on mathematical geodesy, Rome, 3–5 June 1985, vol 2. Politecnico di Milano, pp 529–558

Holota P (1989) Laplacian versus topography in the solution of the Molodensky problem by means of successive approximations. In: Kejlso E, Poder K, Tscherning CC (eds) Festschrift to Torben Krarup. Geodaetisk Inst., Meddelelse No. 58, Kobenhavn, pp 213–227

Holota P (1992a) On the iteration solution of the geodetic boundary-value problem and some model refinements. Contribution to geodetic theory and methodology. XXth General Assembly of the IUGG, IAG-Sect. IV, Vienna, 1991. Politecnico di Milano, 1991, pp 31–60; also in: Travaux de l'Association Internationale de Geodesie, Tome 29, Paris, pp 260–289

Holota P (1992b) Integral representation of the disturbing potential: effects involved, iteration technique and its convergence. In: Holota P, Vermeer M (eds) Proceedings of the first continental workshop on the geoid in Europe, Prague, 11–14 May 1992. Research Institute of Geodesy, Topography and Cartography, Prague, in co-operation with IAG-subcommission for the geoid in Europe, Prague, pp 402–419

Holota P (1997) Coerciveness of the linear gravimetric boundary value problem and geometrical interpretation. J Geodesy 71, pp 640–651

Holota P (2003) Green's function and external masses in the solution of geodetic boundary-value problems. In: Tziavos IN (ed) Gravity and geoid, 3rd meeting of the International Gravity and Geoid Commission, Thessaloniki, Greece, 26–30 August 2002. Ziti Editions, Thessaloniki, pp 108–113

Holota P (2004) Some topics related to the solution of boundary-value problems in geodesy. In: Sansò F (ed) V Hotine-Marussi symposium on mathematical geodesy, Matera, Italy, 17–21 June 2002. International Association of Geodesy Symposia, 127. Springer, Heidelberg, pp 189–200

Kufner A, John O, Fučík S (1977) Function space. Academia, Prague

Lyusternik LA, Sobolev VI (1965) Foundations of functional analysis. Nauka Publishers, Moscow (in Russian)

Moritz H (1980) Advanced physical geodesy. Herbert Wichmann Verlag, Karlsruhe and Abacus Press, Tunbridge, Wells Kent

Nečas J (1967) Les methods directes en théorie des équations elliptiques. Academia, Prague

Sokolnikoff IS (1971) Tensor analysis. Theory and applications to geometry and mechanics of continua. Nauka Publishers, Moscow (in Russian)

A New Argentinean Gravimetric Geoid Model: GEOIDEAR

D.A. Piñón, K. Zhang, S. Wu, and S.R. Cimbaro

Abstract

A new Argentinean gravimetric geoid model named GEOIDEAR was developed using the remove-compute-restore technique and incorporating the GOCO05S satellite-only global geopotential model (GGM) together with 560,656 land and marine gravity measurements. Terrain corrections were calculated for all gravity observations using a combination of the SRTM_v4.1 and SRTM30_Plus_v10 digital elevation models. For the regions that lacked of gravity observations, the DTU13 gravity model was utilised. The residual gravity anomalies were gridded using the tensioned spline algorithm. The resultant gravity anomaly grid was applied in the Stokes' integral using the spherical multi-band FFT approach and the deterministic kernel modification proposed by Wong and Gore. The accuracy of GEOIDEAR was assessed by comparing it with GPS-levelling derived geoid undulations at 1904 locations and the EGM2008 GGM. Results show that the new Argentinean geoid model has an accuracy of less than 10 cm.

Keywords

Argentina • Geoid • GPS-levelling • Gravity

1   Introduction

Two precise Argentinean geoid models have been published so far: GAR (Corchete and Pacino 2007) and ARG05 (Tocho et al. 2007). The first one was determined using the remove-compute-restore (RCR) technique (Schwarz et al. 1990) and was based on the global geopotential model (GGM) EIGEN-GL04C (Förste et al. 2008). The gravity anomalies used in

D.A. Piñón (✉)
The SPACE Research Centre, Royal Melbourne Institute of Technology (RMIT) University, Melbourne, VIC, Australia

Instituto Geográfico Nacional, Buenos Aires, Argentina
e-mail: dpinon@ign.gob.ar

K. Zhang • S. Wu
The SPACE Research Centre, Royal Melbourne Institute of Technology (RMIT) University, Melbourne, VIC, Australia

S.R. Cimbaro
Instituto Geográfico Nacional, Buenos Aires, Argentina

GAR's computation were reduced to the geoid by means of the Helmert's second method of condensation (Heiskanen and Moritz 1967) and using the digital elevation models (DEMs) SRTM (Slater et al. 2006), over the land, and ETOPO2 (U.S. Department of Commerce 2006), over the oceans. The Stokes' integral in convolution form was solved applying the 1D fast Fourier transformation (FFT) technique (Haagmans et al. 1993). Finally, GAR was evaluated using 393 co-located GPS and levelling benchmarks distributed in 8 of the 23 Argentinean provinces. According to the authors, the standard deviation of the differences between the geoid heights derived from GAR and those derived from the GPS-levelling benchmarks was 21 cm.

The ARG05 geoid model was also determined using the RCR technique on the Stokes-Helmet approach. However, it was based on the EGM96 (Lemoine et al. 1998) GGM. The downward continuation was achieved using the GTOPO30 (U.S. Geological Survey 1996) DEM. ARG05 was evaluated using 539 GPS-levelling benchmarks distributed in 9 of the 23 Argentinean provinces and, according to the authors,

the standard deviation of the differences between the geoid heights derived from ARG05 and those derived from the GPS-levelling benchmarks was 32 cm.

Since the development of GAR and ARG05, new and improved datasets became available. Regarding the GGMs, in 2009 the GOCE gravity space mission (Drinkwater et al. 2003) was launched, and therefore, a new generation of GGMs, which precisely describe the long- to medium-wavelength part of the Earth's gravity field, began to be freely distributed through the International Centre for Global Earth Models (ICGEM) website. With respect to the GPS-levelling observations, two significant improvements to the vertical component of the Argentinean GPS and spirit-levelling measurements were recently achieved: first, the geodetic reference frame POSGAR 2007 (Cimbaro et al. 2009), based on the international terrestrial reference frame ITRF 2005 (Altamimi et al. 2007) at 2006.6 epoch, was determined by the Instituto Geográfico Nacional (IGN) in 2009. Secondly, a least-squares adjustment of the spirit-levelling network in terms of geopotential numbers was performed by the IGN in 2014, and afterwards, Mader (1954) orthometric heights were determined, with a mean standard deviation of 0.058 m, for all the levelling benchmarks. Finally, in relation to the gravity observations, a new gravimetric absolute network called RAGA was established in 2014 and several gravity campaigns performed by the IGN before RAGA were reprocessed using the new absolute gravity values. Moreover, new land and marine gravity measurements collected during the last decade by many public and private agencies and universities became available.

After considering the accuracies of the aforementioned two Argentinean geoid models (i.e. GAR and ARG05) and the new available datasets (i.e. GNSS-levelling and gravity measurements, MDTs and GGMs), the IGN, together with the SPACE Research Centre of RMIT University, determined that a new precise geoid model fitted to the official vertical datum and geocentric reference frame was urgently required. This paper describes the methodology, techniques and datasets utilized for determining the new Argentinean gravimetric geoid model GEOIDEAR.

2   Computation Procedure

2.1   Helmert's Second Condensation Method

In order to obtain a geoid model using Stokes' formula there must be no masses above the surface of the geoid. Therefore, observed gravity anomalies should be given at the boundary surface (i.e. the geoid), and the topographic masses need to be removed and condensed in a thin mass layer onto the geoid (Heiskanen and Moritz 1967). In this research, the first requirement was met by applying the first-order free-air reduction (Δg_{FA}), together with the atmospheric correction, given by Hinze et al. (2005), to the observed gravity points. The land and salt water densities were considered 2.67 g cm^{-1} and 1.03 g cm^{-1} respectively. Finally, all the observed gravity and normal gravity values were referred to the IGSN71 gravity system (Morelli et al. 1972) and GRS80 reference ellipsoid (Moritz 1980, 2000) respectively.

The second requirement was satisfied by conducting the Helmert's second condensation method. The direct topographical effect of this method (i.e. the difference between the gravitational attraction of the actual topography and the one that has been condensed onto the geoid) was determined by applying the planar approach of the well-known Bouguer plate reduction (Heiskanen and Moritz 1967) and the linear approximation of the classical terrain correction (Moritz 1968) to the gravity anomalies. Then, the resultant gravity anomalies, usually called refined Bouguer anomalies, are given by

$$\Delta g_{RB} = \Delta g_{FA} - 2\pi G\rho H + C_T \qquad (1)$$

where G is the Newtonian gravitational constant, ρ is the density of the topographic masses, and C_T is the terrain correction determined up to a distance of 166.7 km from each gravity location using the 3″ resolution SRTM_v4.1 (Jarvis et al. 2008) and the 30″ resolution SRTM30_Plus v10 (Becker et al. 2009) DEMs in the TC software (Forsberg 1984), which applies the rectangular prism integration method (Nagy 1966).

2.2   RCR Technique

The RCR technique is a well-known method for gravimetric geoid determination used in the Stokes-Helmert approach. It implies a spectral decomposition of the Earth's gravity field into three parts: the long-wavelength contribution from the GGM, the medium-wavelength signal from regional gravity observations and the short-wavelength part of the gravity spectrum from the topography (Zhang 1997). Therefore, geoid heights can be expressed as (Forsberg 1993)

$$N = N_{RES} + N_{IND} + N_{GGM} \qquad (2)$$

where N_{RES} is the contribution from the observed gravity anomalies reduced using a GGM, N_{IND} is the indirect effect

caused by a variation in the Earth's gravity potential from condensing the topographic masses onto the geoid, and N_{GGM} is the geoidal undulation derived from the spherical harmonic expansion of the GGM and it is given by (Heiskanen and Moritz 1967).

$$N_{GGM} = \frac{GM}{\gamma a} \sum_{n=2}^{\infty} \left(\frac{a}{n}\right)^n \sum_{m=0}^{n} \left(C_{nm} \cos m\lambda + S_{nm} \sin m\lambda\right) P_{nm}(\cos\varphi) \tag{3}$$

where GM is the geocentric gravitational constant, a is the Earth radius, n and m are the degree and order of the spherical harmonic expansion respectively, C_{nm} and S_{nm} are the fully normalised spherical harmonics coefficients, and $P_{nm}(\cos\varphi)$ is the fully normalized associated Legendre polynomials.

2.2.1 Removing Step and Gridding of the Residual Gravity Anomalies

The first step of the RCR technique is the removal of the low-frequency part of the Earth's gravity field from Δg_{RB}. The residual gravity anomalies can be obtained from

$$\Delta g_{RES} = \Delta g_{RB} - \Delta g_{GGM} \tag{4}$$

where Δg_{GGM} is the gravity anomaly derived from the GGM and described by Heiskanen and Moritz (1967).

In this study, the GOCO05S satellite-only GGM (Mayer-Guerr 2015) was applied complete to degree and order 280 using the GEOCOL17 software (Tscherning 1985) for determining Δg_{GGM} at every gravity observation location.

Moreover, since the FFT technique was used to calculate the Stokes' integral, a regular grid generated from the discrete Δg_{RES} values was required. Due to the fact that there were many areas that lacked of land and marine gravity measurements, the world gravimetric model DTU13 (Andersen et al. 2013) was used to fill-in all the gravity voids before performing the gridding procedure. The fill-in procedure was achieved by: (1) determining a mask area using 25-km-radius circles centred on each of the land and marine gravity measurements, (2) inverting the mask area, (3) selecting those DTU13 grid nodes that overlap the inverted mask area, and (4) determining Δg_{RES} for the selected DTU13 fill-in gravity points. Then, the tensioned spline algorithm, introduced by Smith and Wessel (1990), with the recommended tension parameter $T = 0.25$ was applied to determine a 1′ gravity anomaly grid (Δg_{RES}^{grid}) using the observed and selected DTU13 gravity anomalies.

Finally, the residual Faye gravity anomaly grid, required as the input for Stokes' integral, was "reconstructed" by adding the Bouguer plate reduction to the grid nodes of Δg_{RES}^{grid} (Featherstone and Kirby 2000)

$$\Delta g_{RESFaye}^{grid} = \Delta g_{RES}^{grid} + 2\pi G\rho H^{grid} \tag{5}$$

where the height H was derived from the DEM.

The use of Faye gravity anomalies causes a change in the gravity potential due to the shifting of the topographic masses. Therefore, the so-called co-geoid is computed when using Faye anomalies. In order to determine the geoid, the indirect effect has to be determined and added to the computed co-geoid. This procedure is described in the next section.

2.2.2 Computing Step: Stokes' Integral

Stokes' integral is applied to determine geoid undulations from Δg quantities and it is given by (Heiskanen and Moritz 1967)

$$N(\varphi, \lambda) = \frac{R}{4\pi\rho} \iint_{\sigma} \Delta g S(\psi) \, d\sigma \tag{6}$$

where R is the mean radius of the Earth, $S(\psi)$ is the so-called Stokes' kernel and σ is the integration domain defined by a spherical cap of angular radius ψ_0.

In this study, Eq. (6) was calculated using the multi-band spherical FFT approximation technique (Sideris and Forsberg 1991) implemented in the SPFOUR software. The following central-latitude bands were selected for the computation: $-20.00°$, $-29.25°$, $-38.50°$, $-47.75°$ and $-57.00°$. Moreover, the Wong and Gore (1969) modification to Stokes' kernel, which removes the low-degree Legendre polynomials that distort the long-wavelength signal of the geoid when integrating over a spherical cap, was adopted. The low harmonics were completely removed up to degree 120 and then linearly tapered to degree 130.

2.2.3 Restoring Step

The restore step of the RCR technique is achieved by adding the N_{GGM} and N_{IND} terms to the Stokes' integral result (i.e. N_{RES}). In this study, N_{GGM} was determined by Eq. (3) using the GEOCOL17 software together with GOCO05S GGM complete to degree and order 280.

Regarding N_{IND}, it can be split into the primary indirect effect (PITE) and the secondary indirect topographical effect (SITE). In this paper, the SITE was neglected due to the fact that the correction is less than 1 mm (Vaníček et al. 1999).

The PITE was calculated using the planar approximation introduced by Wichiencharoen (1982).

3 Gravity Data and Pre-processing

About 700,000 land and marine gravity observations that covered the area of interest (i.e. from latitude 20–57°S and from longitude 52–76°W) were collected from many public agencies and universities, including IGN; Instituto de Física de Rosario, Instituto de Geociencias Básicas, Aplicadas y Ambientales de la Universidad de Buenos Aires; Laboratorio de Geofísica Aplicada y Ambiental de la Universidad Nacional de Tucumán; Departamento de Física de la Universidad Nacional del Sur; Technische Universität Berlin; U.S. National Geospatial-Intelligence Agency; Bureau Gravimétrique International; Instituto Brasileiro de Geografia e Estatística; U.S. National Oceanic and Atmospheric Administration; Japan Agency for Marine-Earth Science and Technology; Marine Geoscience Data System; Rolling Deck to Repository; and British Antarctic Survey.

These observations, which are referred to the IGSN71 gravity system, were collected during the last 70 years using different types of methods and gravimeters, and therefore, the accuracy in most cases is uncertain. For this reason, the dataset was validated using three methods: (1) shipborne gravity observations were compared with oceanic gravity grids derived from satellite altimetry (independent of the ship-track gravity surveys), (2) observed gravity anomalies were compared with those derived from a satellite-only GGMs (Featherstone 2009), and (3) the least-squares collocation (LSC) method was used to detect gross errors in the gravity spatially-correlated database (Tscherning 1991).

The first method was applied using the Sandwell et al. (2014) 23.1-version altimeter-derived gravity anomaly grid. Table 1 shows the statistics of the differences between the retained marine gravity anomalies and the Sandwell's model.

The large differences appreciated in Table 1 mainly correspond to points in coastal areas, where the satellite altimetry data is not reliable.

The second method was achieved using the GOCO05S GGM complete to degree and order 280. The differences between the GGM and the observed gravity anomalies

Table 1 Statistics of the differences between the shipborne gravity anomalies and Sandwell's 23.1 version gravity model from 489,653 measurements [Unit: (mgal)]

Min	Max	Mean	STD
−121.8	116.1	5.2	18.0

Table 2 Statistics of the differences between the observed gravity anomalies and the GOCO05S GGM from 560,656 measurements [Unit: (mgal)]

Min	Max	Mean	STD
−268.9	240.5	−10.6	33.3

were plotted on a map using level contours, where the existence of any deep holes or steep spikes indicated the existence of suspicious observations that were removed. Table 2 shows the statistics of the differences between the retained observed gravity anomalies and the GOCO05S GGM.

The third method was applied using the EGM2008 GGM complete to degree and order 2159 and a gravity estimated error variance equal to 1 and 5 mgal for land and marine observations respectively.

A total of 560,656 gravity points were left after the quality check (Fig. 1) that were used to determine the required reduced gravity anomaly grid.

4 GEOIDEAR Validating and Fitting

The accuracy of GEOIDEAR was assessed using 1904 co-located GPS-levelling benchmarks (Fig. 2), whose ellipsoidal and orthometric heights were referred to the POSGAR 2007 geodetic reference frame and the 2014 Argentinean vertical datum respectively. GEOIDEAR was also fitted to these points by determining a trend surface using the four-parameter Helmert model (Iliffe et al. 2003)

$$N_{GPS-levelling} - N_{GEOAR} = a_1 \cos\varphi \cos\lambda + a_2 \cos\varphi \sin\lambda + a_3 \sin\varphi + a_4 + \varepsilon \quad (7)$$

where ε is the residual estimated by LSC. The covariance function was determined using the second-order Gauss-Markov model, in which an apriori error of 5 cm and a correlation length of 25 km were assumed.

Moreover, EGM2008-derived (Pavlis et al. 2008, 2012) geoid undulations were also computed for the 1904 locations and compared to GPS-levelling derived undulations. Table 3 shows the statistics of the differences between the GPS-levelling geoid undulations and those derived from GEOIDEAR and EGM2008 (complete to degree and order 2159).

Given that the published ARG05 and GAR Argentinean geoid models accuracies were defined using 539 and 393 points respectively, they were not comparable with the GEOIDEAR. Therefore, the geoid undulations derived from the 1904 co-located GPS-levelling benchmarks were used to determine the new accuracies of the ARG05 and GAR. Table 4 shows the differences between the GPS-levelling
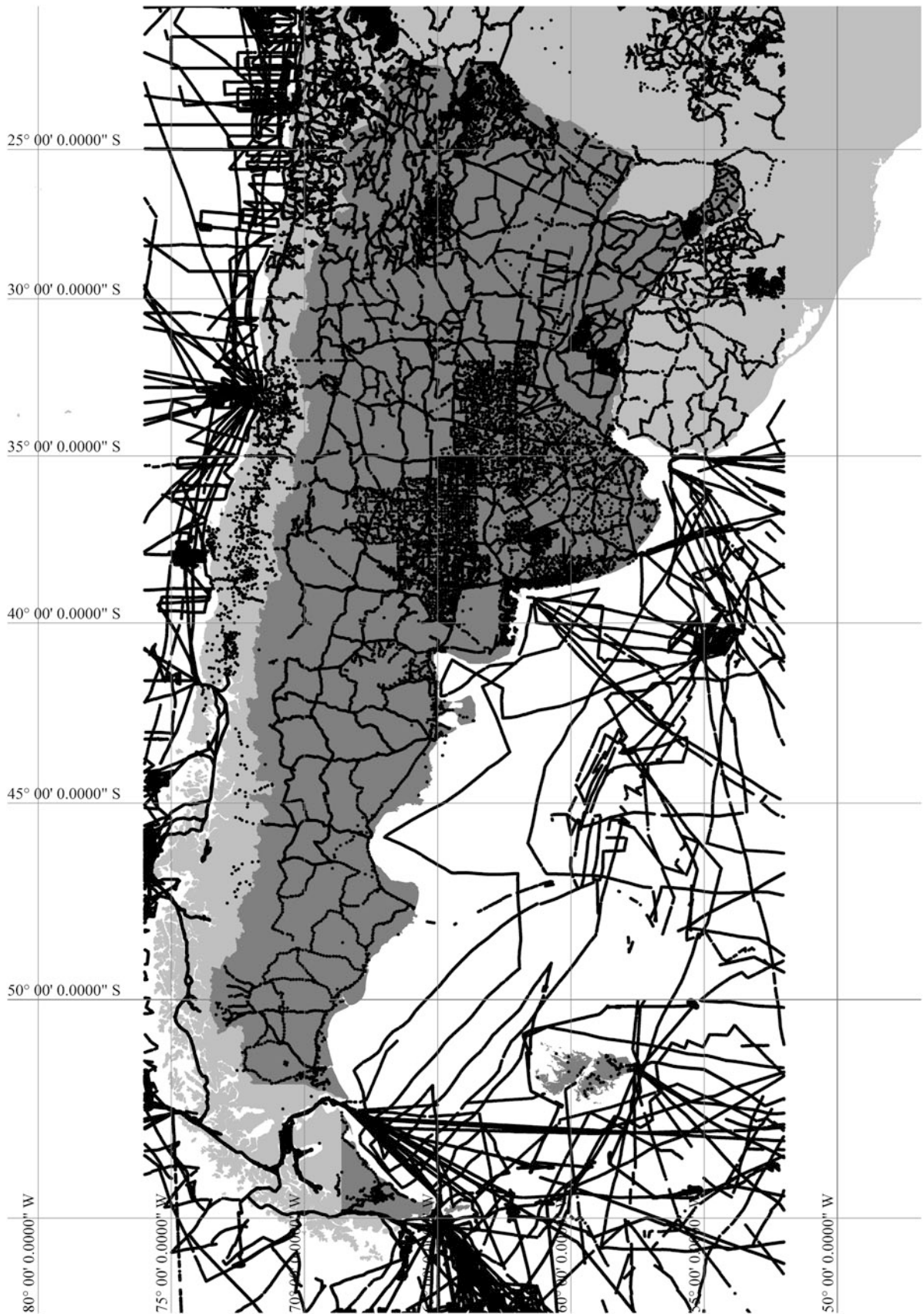
Fig. 1 Land and marine gravity observations
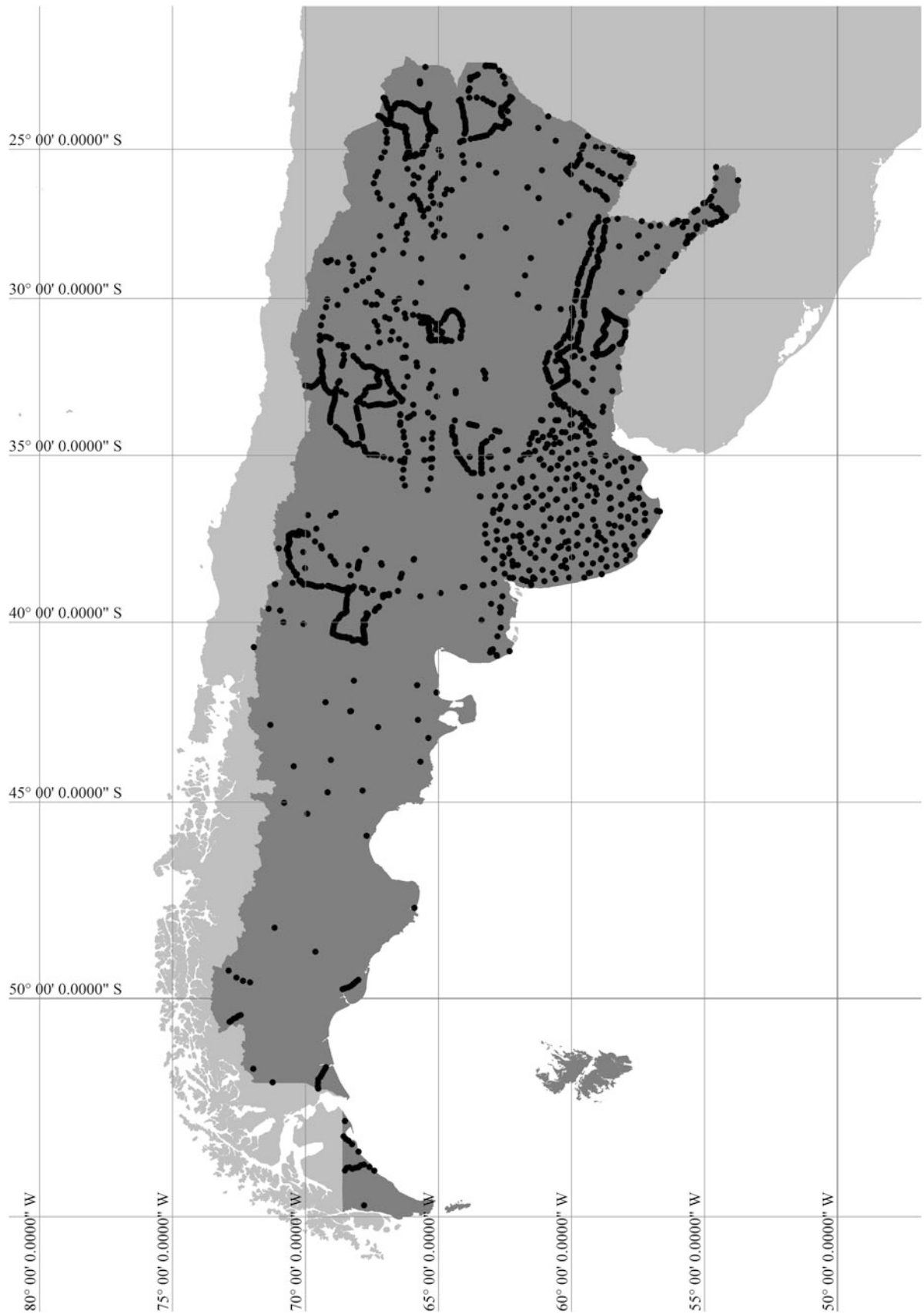
Fig. 2 GPS-levelling measurements

Table 3 Statistics for the differences between the GPS-levelling and GEOIDEAR derived geoid undulations [Unit: (m)]

Model	Min	Max	Mean	STD
EGM2008	−0.98	1.67	0.62	0.31
GEOIDEAR (not fitted)	−0.91	1.86	0.69	0.27
GEOIDEAR (fitted)	−0.31	0.29	0.00	0.04

Table 4 Statistics for the differences between the GPS-levelling and the previous Argentinean geoids (i.e. ARG05 and GAR) [Unit: (m)]

Model	Min	Max	Mean	STD
ARG05	−0.04	5.32	1.92	0.59
GAR	−2.13	1.75	−0.09	0.29

geoid undulations and those derived from ARG05 and GAR.

Finally, the relative accuracy of the fitted GEOIDEAR model was determined for baselines within 500 km using the 1904 GPS-levelling benchmarks. Results show that 91% of the relative differences are less than ±0.1 m and 98% of the differences are under ±0.2 m. Figure 3 shows the relative differences for those baselines within 500 km (i.e.

351,582 baselines), which indicates that the results are not correlated with the location, and therefore, the relative precision of the new fitted geoid model can be considered homogenous.

The results show that GEOIDEAR (Fig. 4) outperforms EGM2008, GAR and ARG05 over Argentina. This is a consequence of the improved GGM's long-wavelength accuracy, the DEM's resolution reduction and corrections (e.g. voids elimination), and the use of the enhanced and recent dataset available (i.e. gravity, spirit-levelling and GPS measurements). GEOIDEAR's (fitted) STD shows an improvement of 83% with respect to GAR and 92% with respect to ARG05.

5 Conclusions

A new $1' \times 1'$ Argentinean gravimetric geoid model called GEOIDEAR was determined. The results showed that the STD of the GEOIDEAR is 4 cm. However, due to the ellipsoidal and orthometric heights accuracies used to fit the geoid (i.e. 5–10 cm), the propagated GPS-levelling derived geoid
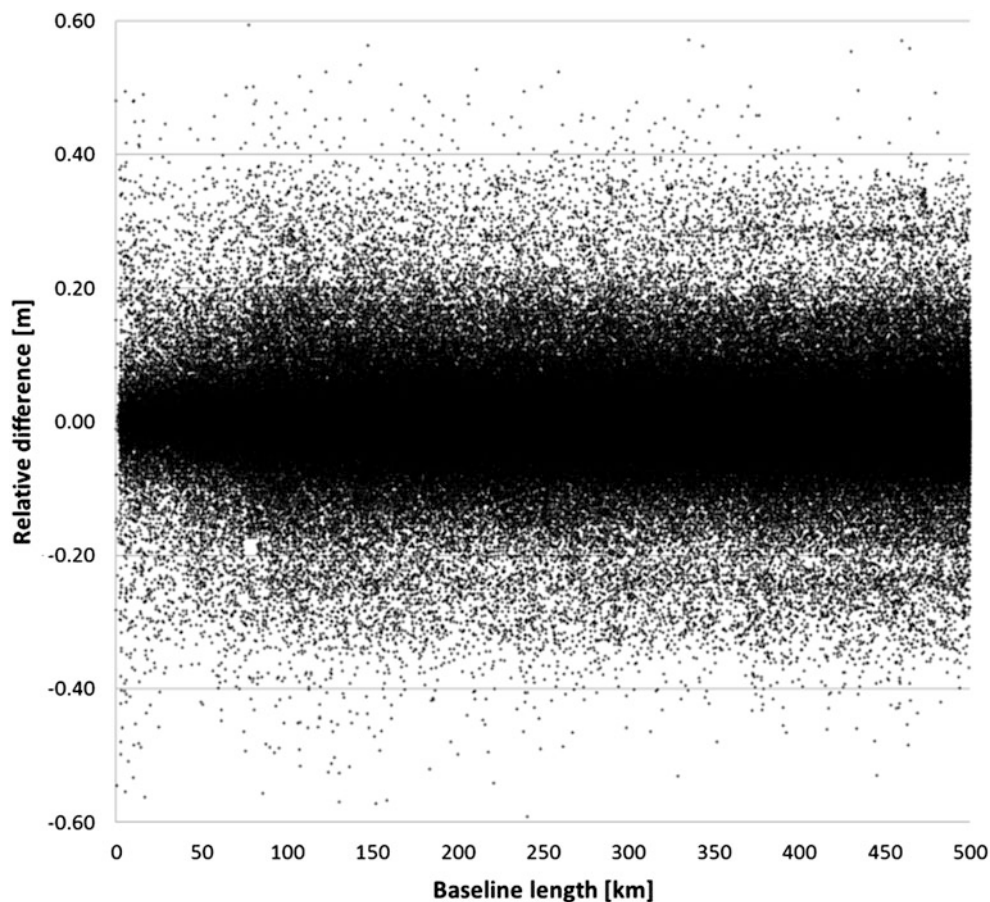
Fig. 3 Relative differences between GEOIDEAR and the co-located GPS-levelling points
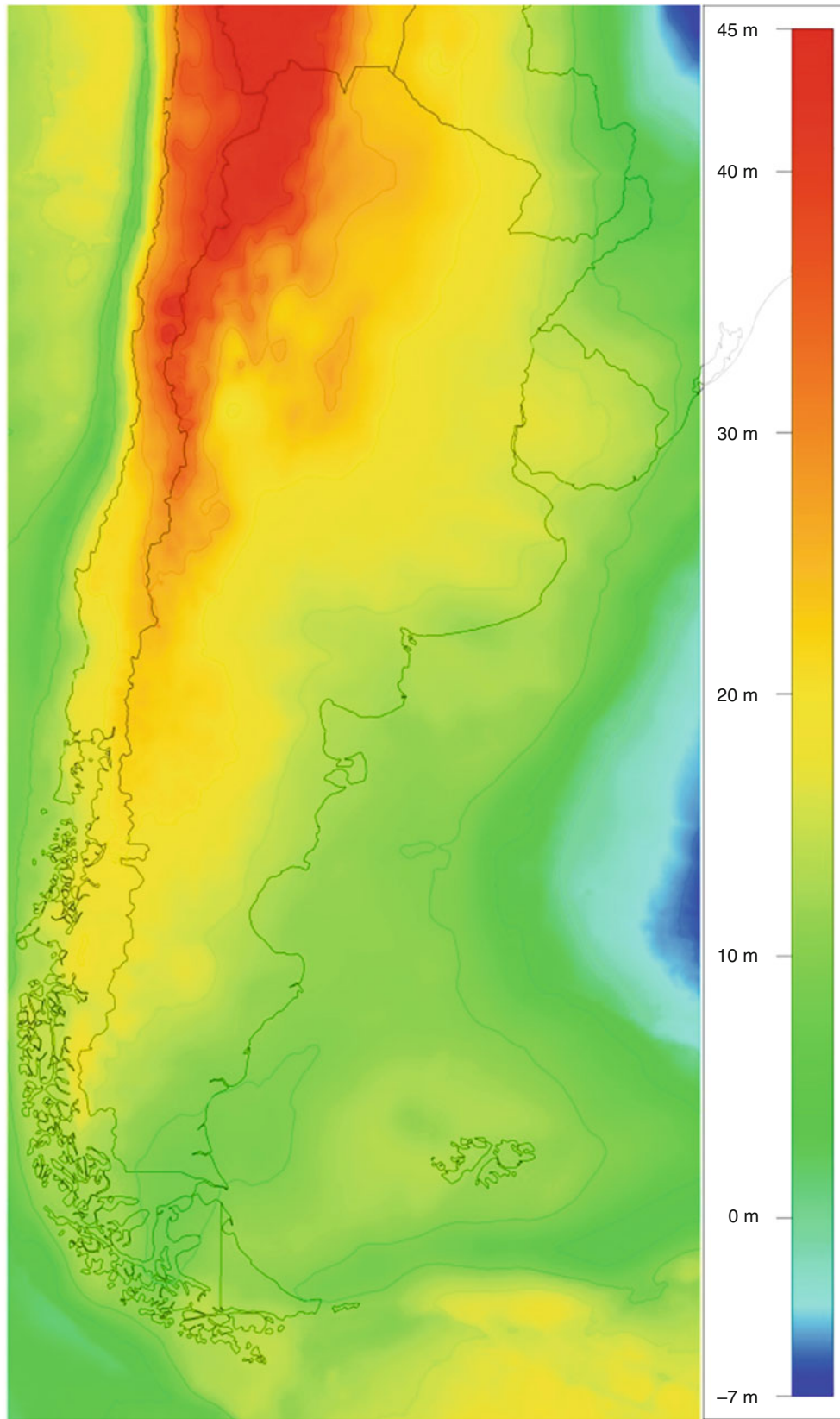
Fig. 4 GEOIDEAR geoid model

undulations accuracy is considered 7–14 cm, and therefore, the fitted GEOIDEAR's accuracy is expected to be 10 cm.

The use of GOCE data together with the latest released DTU's gravity field model, SRTM's products and IGN's co-located GPS-levelling benchmarks significantly improved the accuracy of the Argentinean geoid model. However, there are still many gravity voids that should be covered with land or airborne gravimetry in order to develop an improved geoid model.

References

Altamimi Z, Collilieux X, Legrand J, Garayt B, Boucher C (2007) ITRF2005: a new release of the international terrestrial reference frame based on time series of station positions and earth orientation parameters. J Geophys Res Solid Earth (1978–2012), 112

Andersen OB, Knudsen P, Kenyon SC, Factor JK, Holmes S (2013) The DTU13 global marine gravity field. Ocean surface topography science team meeting 2013. Boulder, USA

Becker JJ, Sandwell DT, Smith WHF, Braud J, Binder B, Depner J, Fabre D, Factor JK, Ingalls S, Kim SH (2009) Global bathymetry and elevation data at 30 arc seconds resolution: SRTM30_PLUS. Mar Geod 32:355–371

Cimbaro SR, Lauŕ́iA EA, Piñón DA (2009) Adopción del nuevo marco de referencia geodésico nacional. Instituto Geográfico Militar, Buenos Aires

Corchete V, Pacino MC (2007) The first high-resolution gravimetric geoid for Argentina: GAR. Phys Earth Planet Inter 161:177–183

Drinkwater MR, Floberghagen R, Haagmans R, Muzi D, Popescu A (2003) GOCE: ESA's first earth explorer Core mission. Earth gravity field from space—From sensors to earth sciences Springer

Featherstone WE (2009) Only use ship-track gravity data with caution: a case-study around Australia. Aust J Earth Sci 56:195–199

Featherstone WE, Kirby JF (2000) The reduction of aliasing in gravity anomalies and geoid heights using digital terrain data. Geophys J Int 141:204–212

Forsberg R (1984) A study of terrain reductions, density anomalies and geophysical inversion methods in gravity field modelling. The Ohio State University, Columbus

Forsberg R (1993) Modelling the fine-structure of the geoid: methods, data requirements and some results. Surv Geophys 14:403–418

Förste C, Schmidt R, Stubenvoll R, Flechtner F, Meyer U, König R, Neumayer H, Biancale R, Lemoine J-M, Bruinsma S, Loyer S, Barthelmes F, Esselborn S (2008) The GeoForschungsZentrum Potsdam/groupe de Recherche de Gèodésie spatiale satellite-only and combined gravity field models: EIGEN-GL04S1 and EIGEN-GL04C. J Geod 82:331–346

Haagmans R, De Min E, Van Gelderen M (1993) Fast evaluation of convolution integrals on the sphere using 1D FFT, and a comparison with existing methods for Stokes' integral. Manuscr Geodaet 18:227–227

Heiskanen WA, Moritz H (1967) Physical geodesy. W.H. Freeman, San Francisco

Hinze WJ, Aiken C, Brozena J, Coakley B, Dater D, Flanagan G, Forsberg R, Hildenbrand T, Keller GR, Kellogg J (2005) New standards for reducing gravity data: the north american gravity database. Geophysics 70:J25–J32

Iliffe JC, Ziebart M, Cross PA, Forsberg R, Strykowski G, Tscherning CC (2003) OSGM02: a new model for converting GPS-derived heights to local height datums in great britain and Ireland. Surv Rev 37:276–293

Jarvis A, Reuter HI, Nelson A, Guevara E (2008) Hole-filled SRTM for the globe version 4. available from the CGIAR-CSI SRTM 90m Database (http://srtm. csi. cgiar. org)

Lemoine FG, Kenyon SC, Factor JK, Trimmer RG, Pavlis NK, Chinn DS, Cox CM, Klosko SM, Luthcke SB, Torrence MH (1998) The development of the joint NASA GSFC and the National Imagery and Mapping Agency (NIMA) geopotential model EGM 96. NASA, Greenbelt

Mader K (1954) Die orthometrische Schwerekorrektion des Prazisions-Nivellements in den Hohen Tuaern. Osterreichischer Verein fur Vermessungswesen, Wien, p 1

Mayer-Guerr T (2015) The combined satellite gravity field model GOCO05s. EGU General Assembly, Vienna

Morelli C, Gantar C, Mcconnell RK, Szabo B, Uotila U (1972) The international gravity standardization net 1971 (IGSN 71). DTIC Document

Moritz H (1968) On the use of the terrain correction in solving Molodensky's problem. The Ohio State University, Columbus

Moritz H (1980) Geodetic reference system 1980. J Geod 54:395–405

Moritz H (2000) Geodetic reference system 1980. J Geod 74:128–133

Nagy D (1966) The gravitational attraction of a right rectangular prism. Geophysics 31:362–371

Pavlis NK, Holmes SA, Kenyon SC, Factor JK (2008) An earth gravitational model to degree 2160: EGM 2008. EGU General Assembly, 13–18

Pavlis NK, Holmes SA, Kenyon SC, Factor JK (2012) The development and evaluation of the earth gravitational model 2008 (EGM 2008). J Geophys Res Solid Earth 117

Sandwell DT, Muller RD, Smith WH, Garcia E, Francis R (2014) New global marine gravity model from CryoSat-2 and Jason-1 reveals buried tectonic structure. Science 346:65–67

Schwarz KP, Sideris MG, Forsberg R (1990) The use of FFT techniques in physical geodesy. Geophys J Int 100:485–514

Sideris MG, Forsberg R (1991) Testing the spherical FFT formula for the geoid over large regions. AGU spring meeting. Maryland, Baltimore

Slater JA, Garvey G, Johnston C, Haase J, Heady B, Kroenung G, Little J (2006) The SRTM data "finishing" process and products. Photogramm Eng Remote Sens 72:237–247

Smith WHF, Wessel P (1990) Gridding with continuous curvature splines in tension. Geophysics 55:293–305

Tocho C, Font G, Sideris MG (2007) A new high-precision gravimetric geoid model for Argentina. In: Tregoning P, Rizos C (eds) Dynamic planet: monitoring and understanding a dynamic planet with geodetic and oceanographic tools IAG Symposium Cairns, Australia 22–26 August, 2005. Springer, Berlin Heidelberg

Tscherning CC (1985) GEOCOL-A FORTRAN-program for gravity field approximation by collocation. Technical Note, Geodaetisk Institut, 3

Tscherning CC (1991) The use of optimal estimation for gross-error detection in databases of spatially correlated data. Bull Inform 68:79–89

U.S. Department Of Commerce, National Oceanic and Atmospheric Administration, National Geophysical Data Center (2006) 2-minute Gridded Global Relief Data (ETOPO2v2) [Online]. Available: http://www.ngdc.noaa.gov/mgg/fliers/06mgg01.html

U.S. Geological Survey (1996) Global 30 arc-second elevation (GTOPO30). USGS Earth Resources Observation and Science (EROS) Center, Sioux Falls

Vaníček P, Huang J, Novák P, Pagiatakis S, Véronneau M, Martinec Z, Featherstone WE (1999) Determination of the boundary values for the Stokes–Helmert problem. J Geod 73:180–192

Wichiencharoen C (1982) The indirect effects on the computation of geoid undulations. The Ohio State University, Columbus

Wong L, Gore R (1969) Accuracy of geoid heights from modified Stokes kernels. Geophys J Int 18:81–91

Zhang K (1997) An evaluation of FFT geoid determination techniques and their application to height determination using GPS in Australia. Doctor of Philosophy, Curtin University of Technology

Exploitation of Marine Gravity Measurements of the Mediterranean in the Validation of Global Gravity Field Models

M.F. Lequentrec-Lalancette, C. Salaűn, S. Bonvalot, D. Rouxel, and S. Bruinsma

Abstract

Over the oceans, data from altimetry are currently the only input data for the latest global geoid models such as EGM08 or EIGEN6C. Over the Mediterranean sea, satellite altimetry does not give good results for gravity models. In particular because of the high ocean variability and in the vicinity of the coast in some areas. A marine gravity data compilation and screening was conducted as part of an international project GEOMED2 for calculating the geoid of the Mediterranean sea. In this paper, marine gravity data and their processing are described. The shipborne gravity data are validated and an estimation of the error is done. Then the cleaned data are used to validate the Global Geoid models (GGm).

Keywords

BGI • GOCE • Mediterranean • Shipborne gravity

1   Introduction

Global geoid models are computed from gravimetric satellite missions for the low and medium resolution. Since GRACE and GOCE satellite missions, the global gravity models (GGm) with satellite only data provide spatial resolution up to degree 300 (wavelength around 134 km). Over the oceans, the GGm are complemented by satellite altimetry derived gravity data (Bruinsma et al. 2014, Főrste et al. 2014, Pavlis et al. 2012). For local geoids airborne and shipborne data are used for the marine areas. Some examples can be taken from Featherstone et al. (2001); Featherstone (2003), Denker et al. (2005), Hunegnaw et al. (2009), Olesen et al. (2002)—this list is not exhaustive. Shipborne data complements

successfully the gravity signal in the small wavelengths. The drawback of this data is related to the gravimeters technology and the principles of gravity survey. Gravity data may include non-corrected drift, false tying due to an old gravity system or to wrong terrestrial station data or navigation defaults for the oldest survey (Wessel and Watts 1988; Denker and Roland 2003). The challenge is then to process and validate these in situ gravity data recorded only from marine surveys for 40–50 years and showing the improvement of the technology i.e. different degree of data quality over this period. The oldest shipborne gravity data in the Mediterranean Sea dates from the mid twentieth century. In our data set these are represented by the so called -Morelli dataset. The other datasets are marine gravity surveys extracted from national and international databases. In this study, we present first, the works done to clean and to validate marine gravity data, to ensure an appropriate quality for geoid estimation and for GGm validation. Secondly comparison with global models and its interpretation will conclude the paper. Section 2 presents the data, the cleaning and validating processes are described in Sect. 3. Comparisons with GGm and derived altimetry models are done in Sect. 4. Finally the discussion focuses on the quality estimation of shipborne data and its use in the satellite data validation.

M.F. Lequentrec-Lalancette (✉) • C. Salaűn • D. Rouxel
Shom/GRGS, 13 rue du Chatellier, 29200 Brest, France
e-mail: marie-francoise.lalancette@shom.fr

S. Bonvalot
BGI/GRGS - GET (CNES, CNRS, IRD, UPS), 14 av. Ed. Belin, 31400 Toulouse, France

S. Bruinsma
CNES - Space Geodesy, 18 avenue E. Belin, 31401 Toulouse

2   The Data

The data has been processed taking individually the Morelli dataset and each shipborne gravity surveys. The Morelli data files are supplied by the BGI (Bureau Gravimétrique International). Informations about the quality can be founded in the papers from Allan and Morelli (1971) and Allan et al. (1962). The surveys have been done between 1961 and 1972 when navigation was of poor quality. The use of LoranC positioning system with fixed landmarks, in parts of the Gulf of Lyon, Tyrrhenian Sea and Balearic Sea, improved the accuracy of gravity point positioning up to better than 0.5 miles. The navigation accuracy is directly correlated with the Eotvős correction on the gravity data and have a great impact on the final gravity results. The gravimeters used in the surveys were first generation sea gravimeters: the Lacoste-Romberg freely suspended and the Graf-Askania mounted on a gyro-stabilized platform. At that time, after validation processes, the marine gravity data quality estimated by the differences on crossing points showed for 50% of the cross over points, values lower than 2 mgal with loranC navigation and lower than 4 mgal with radar navigation. The other datasets are 152 marine gravity surveys extracted from four databases: the NOAA Geophysical Data Center (NGDC, 28 surveys), the BGI (Drewes et al. 2012) (21 surveys) and the IFREMER (French Institute for Marine research) and SHOM data center (103 surveys).

3   Data Processing and Validation

The marine data have been validated and qualified taking into account the usual rules applied for the SHOM processes (Lequentrec-Lalancette 1992) and the internal and external Cross Over Errors (COE). The reader can refer to several authors for the cleaning and validating criteria in addition to the citations in introduction, there are—Wessel and Watts (1988)—Denker and Roland (2003). In this study, the processing tools are parts of a SHOM dedicated software called CTGeoS and written for Linux OS. The validation process needs as input, data ranking along tracks (lines of data point measurements) inducing a high constraint on formatting data work. Internal and external COE have been computed at different steps of processing: first to estimate wrong profiles, or surveys and secondly to validate each survey and the global set. The differences at cross over points are not signed. Internal COE computed from the crossing tracks points inside a survey are a good way to quantify the error. First it provides information on the intrinsic quality of each survey. Secondly, it allows to weight the influence of each survey depending on its quality in the final dataset. The external COE are computed between two or more surveys and allows

the validation of surveys without internal cross over points but crossing another datasets. These two characteristic values have been computed following Hunegnaw et al. (2009). For each survey i, COE is quantified by the standard deviation of the residuals at the n crossing points:

$$\sigma_i = \sqrt{\frac{1}{2n} \sum_1^n (\Delta g_{i1} - \Delta g_{i2})^2} \qquad (1)$$

The global quality of the whole data set by the standard deviation of the weighted residuals between two surveys i and j at m COE is described below Eq. (2).

$$\sigma_{i,j} = \sqrt{\frac{\sum_{l=1}^m \frac{(\Delta g_{il} - \Delta g_{jl})^2}{\sigma_i^2 - \sigma_j^2}}{\sum_{l=1}^m (\frac{1}{\sigma_i^2} + \frac{1}{\sigma_j^2})}} \qquad (2)$$

Except for the Morelli dataset, the analyzed gravity surveys were of two types: a transit track type cutting the whole zone between two distant campaigns or a pack of localized profiles (Fig. 2). Some of them, have been ranked. Data were edited one survey and one profile at a time in order to detect and remove outliers. It has been performed in several successive steps and the unwanted points have been removed following five fixed criteria.

– An insufficient density of the data along the profile, set at 1 point/1500 m at least. The density of the data depends of the area and of the age of the survey. Thus, most of the profiles concerned by this removal criterion were often a part 1960s and 1970s surveys. It has to be noted that this removal criteria were not applied on the Morelli dataset because of its large sampling (see below).
– The observation of a profile showing at least two COE value widely higher than the general trend of the internal COE for the whole survey. The concerned profiles have been considered as isolated and incoherent with the whole survey.
– A general or local wrong trend along a profile, as an important dispersion, an important noise or acquisition issues that wouldn't be filtered during the processing.
– Numerical jumps in the gravity anomaly values that were not correlated with the physics and inconsistent with close or crossing profiles.
– removing of some two-way profiles

The Morelli Dataset These data have been extracted from the BGI database with no formal information and contain 122461 observations. They have been transformed from Potsdam reference to IGSN71 according to a previous unpublished study by Moysan (2010). As it can be noted in the Fig. 1, the gravity data are in line along navigation tracks. The content of the data files from the BGI database
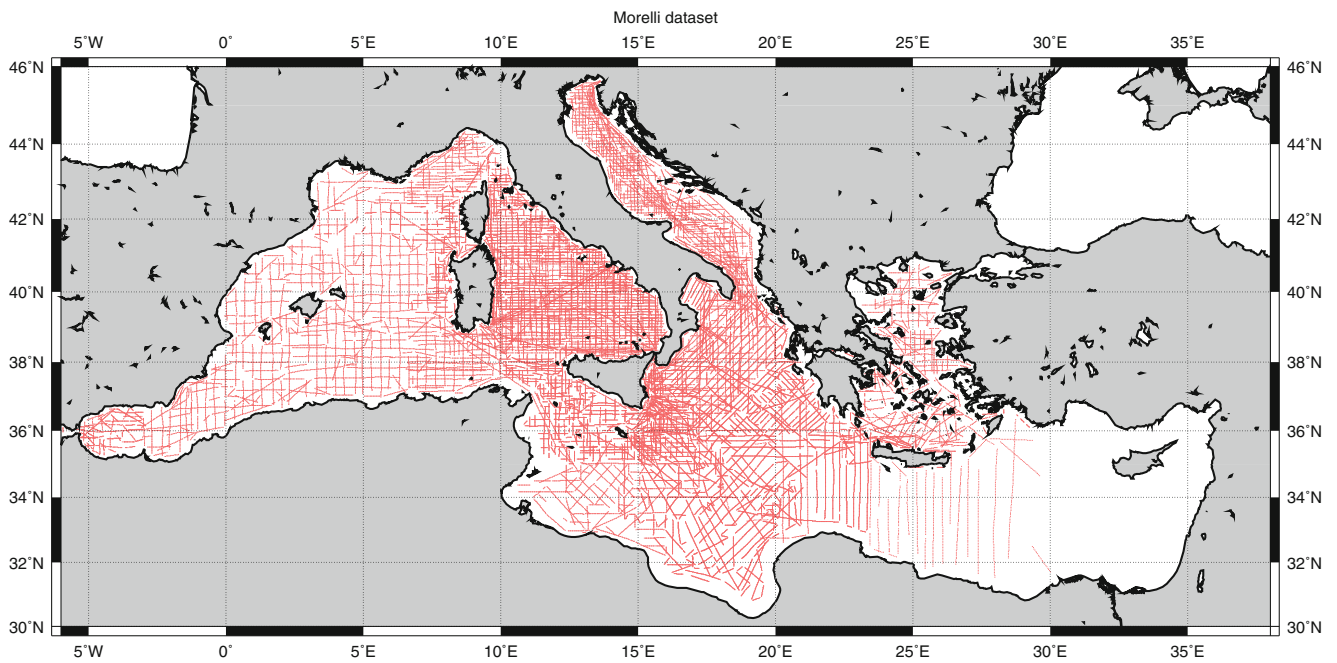
Fig. 1 Morelli dataset
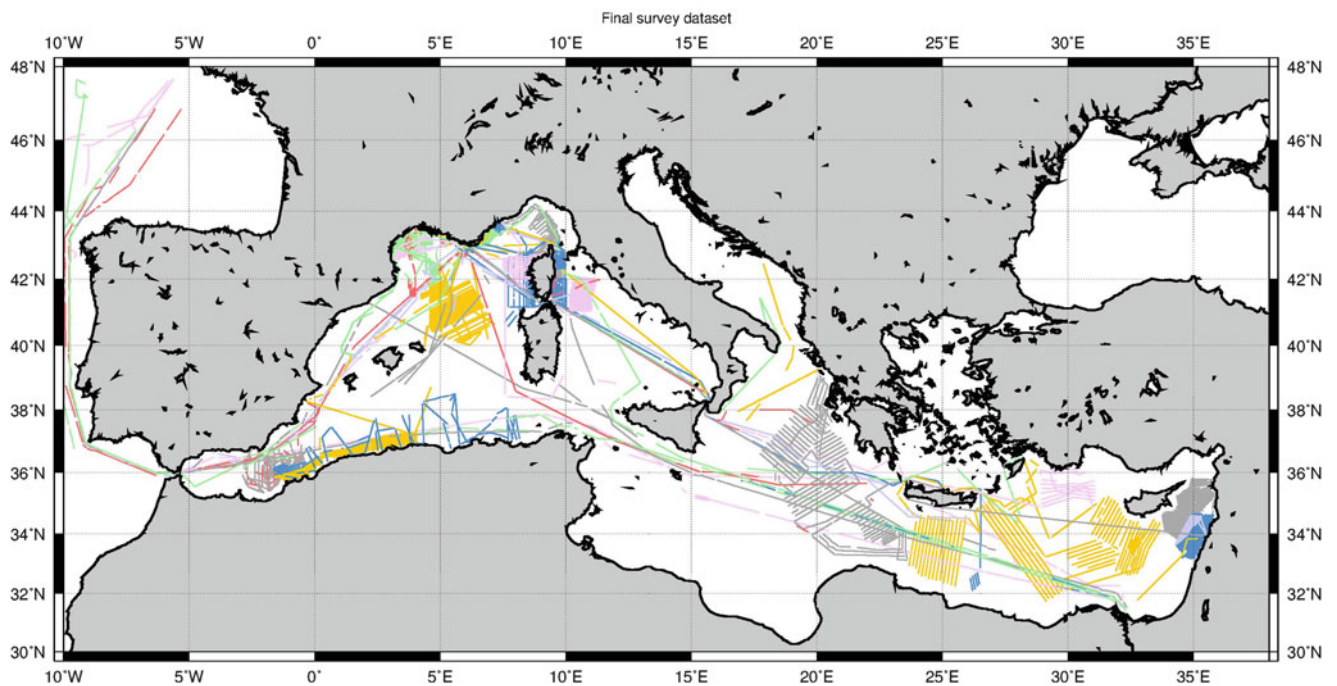
Fig. 2 Survey dataset

is gravity points ordered by increased latitude and longitude. So the original ordering along the lines with a time recorded has been lost and as Denker and Roland (2003), we need to rank the files before using the validation and processing numerical tools. During this step, the editing of each profile also allowed a preliminary detection and removal of wrong records. The gravity records during gyrations have to be eliminated because of too much gravity perturbations. Finally, the dataset showed 2396 tracks (100,173 observations—Fig. 1) with various spatial sampling. On the Adriatic and Tyrrhenian seas, it can be up to one point per 0.8 km and in areas as the North of Lybia, the sampling decreases to one point per 4 km (Fig. 1).

Table 1 Survey COE statistics in mgal

Source	Number	sd	min/max
External COE	8211	2.02	$+/-13.65$

Table 2 Total dataset COE statistics in mgal

Source	Number	sd	min/max
Total dataset COE	23,818	3.6	$+/-26.4$

The Survey Dataset The validation process was applied on all the surveys and 58 campaigns (2,726,521 pts) have been kept to the end. The final quality has been estimated by internal COE. The internal COE have showed good quality surveys with small values between 0.12 mgal and 3.1 mgal with a mean of 1.5 mgal. But 42 surveys didn't have any internal crossing points. They were qualified thanks to external crossing points with reference dataset of very good quality surveys in the same area. The standard deviation of the differences at the external crossing points was recorded as an error estimation of each of those 42 surveys and showed a value of 2.02 mgal for 8211 crossing points (Table 1).

For the total (Morelli + Surveys) dataset COE, we compute a standard deviation value of 3.6 mgal which is a good quality (Table 2). No systematic errors along track remained in it. The quality of the IGSN71 station network and of the calibration (Torge 1989) can have implied systematic errors at long wavelength. The results on the survey dataset, the Morelli dataset and the total dataset show small values and then small residual systematic errors. The persisting errors are located on high free air anomaly variations and on few points of a track. Here is a necessary compromise between the spatial coverage of the data and their quality. The choice in this study has been to keep the whole track even if few points were wrong and to assign error on them. It allows users to integrate the data error in their modeling tool for free air anomaly or geoid estimation (e.g. collocation). The aim of this study is to construct a reference data set, we don't want to apply any mathematic modeling tools to level the data that could be done by a lot of methods.

4 Validation of Global Models

We have computed the differences of the dataset with GGms models and gravity derived altimetry models (cf. Tables 3 and 4). Except for satellite only gravity field Go-cons-gcf-2-dir-r5 named DIR5 there after (Bruinsma et al. 2014), these models have most the same contribution on the oceans. The values show better results with the altimetric derived models than with the spherical harmonic models EIGEN6C4 (Főrste et al. 2014) and EGM08 (Pavlis et al. 2012). The smallest value has been obtained with the V23.1 model

Table 3 Differences with altimetry derived gravity models in mgal

Source	Mean	sd	min	max
Survey dataset/DTU13	-1.78	4.89	-52.08	46.85
Survey dataset/V23.1	-0.68	3.78	-44.75	38.04
Morelli dataset/DTU13	4.25	5	-57.84	79.96
Morelli dataset/V23.1	4.6	4.77	-55.85	81.14
Total data/DTU13	-1.57	4.96	-57.84	79.96
Total data/V23.1	-0.48	3.95	-55.85	81.14

Table 4 Differences with GGms in mgal

Source	Mean	sd	min	max
Survey dataset/EIGEN6C4	-1.59	5.71	-53.24	48.94
Morelli dataset/EIGEN6C4	4.07	5.71	-51.6	76.8
Total dataset/EIGEN6C4	-1.39	5.8	-53.24	76.8
Survey dataset/EGM08	-1.77	6.01	-57.31	54.64
Morelli dataset/EGM08	4.27	5.98	-55.72	75.34
Total dataset/EGM08	-1.55	6.11	-57.31	75.34
Survey dataset/DIR5	-8.68	26.4	-144.06	157.06
Morelli dataset/DIR5	-0.63	22.71	-119.54	137.25
Total dataset/DIR5	-8.35	26.37	-144.06	157.06

Table 5 Differences with filtered V23.1 in mgal

Source	Mean	sd	min	max
Survey dataset/filtered V23.1	-5.93	22.34	-122.99	137.63
Morelli dataset/filtered V23.1	1.89	19.67	-120.27	128.26
Total dataset/filtered V23.1	-5.65	23	-122.99	137.63

(Sandwell and Smith 1997) with a standard deviation of 3.78 mgal. For the DTU13 model (Andersen et al. 2010), the value is 4.83 mgal. As noticed by Hunegnaw et al. (2009), a good altimetric model must show errors at most of 2 mgal due to hydrodynamic topography at basins scales. In the Mediterranean sea, the oceanic variability can be high and not well corrected in the Aviso products and rms on gravity models can rise from 3 mgal to 5 mgal. This was confirmed by the geographic distribution of the differences showing high value in the area where hydrodynamic features arise (liguro-provencal current, alboran gyres) or near the coast.

The largest values for the DIR5 model is mainly due to the omission error of GOCE data (expansion of the model up to degree and order 300 equivalent to wavelength of 134 km). The differences between the Morelli dataset and DIR5 are smaller than for the survey dataset. This is a good example of the aliasing effect of the sampling. In fact, Morelli data have a large spatial coverage but a low sampling along tracks. To confirm that, the differences between the dataset and a filtered V23.1 version, have been done. The result is in this case, similar to that of DIR5 (cf Table 5.). The greatest differences between DIR5 and the total dataset is located on small topographic or hydrodynamic features.

5 Conclusions

In this study we present a new shipborne dataset in the Mediterranean Sea. The validation process has been described. The main work has been the editing steps. For shipborne data, the initial ranking has to be kept for integrating modern processing software. The Morelli data set even if old, being under sampled and of average quality has to be kept due to its very good spatial coverage. The final quality of the data can be estimated at 3.6 mgal. For each survey, we have computed an error from the internal or external COE. The data set will be available soon from the BGI website. The data set will be available soon from the BGI website (doi:10.18168/BGI). Thanks to the dataset, global models and altimetry derived models have been validated. The results highlight the interest of marine gravity dataset for the geophysical and oceanographic studies.

References

Allan TD, Morelli C (1971) A geophysical study of the Mediterranean sea. Nato Subcommittee on oceanographic Research, Technical reports n 55, 141 pp

Allan TD, Dehlinger P, Gantar C, Morelli C, Pisani M, Harrison JC (1962) Comparison of Graf-Askania and Lacoste-Romberg surface-ship gravity meters. J Geophys Res 67:5157–5162

Andersen OB, Knudsen P, Berry P (2010) The DNSC08GRA global marine gravity field from double retracked satellite altimetry. J Geod 84:3. doi:10.1007/s00190-009-0355-9

Bruinsma SL, Foerste C, Abrikosov O, Marty JC, Mulet S, Rio MH, Bonvalot S (2014) ESA's satellite-only gravity field model via the direct approach based on all GOCE data. Geophys Res Lett 40:3607–3612

Denker H, Roland R (2003) Compilation and evaluation of a consistent marine gravity data set surrounding Europe. Poster IUGG, Sapporo, June 30–July 11

Denker H, Barriot JP, Barzaghi R, Forsberg R, Ihde J, Kenyeres A, Marti U, Tziavos IN (2005) Status of the European gravity and geoid project EGGP. In: Jekeli C, Bastos L, Fernandes J (eds) Gravity, geoid and space missions. Springer, Berlin, pp 218–223

Drewes H, Hornik H, Adam J, Rozsa S (eds) (2012) The international gravimetric bureau. In: The Geodesist's handbook. International Association of Geodesy. J Geodesy 86(10). doi:10.1007/s00190-012-0584-1

Featherstone WE (2003) Comparison of different satellite altimeter-derived gravity anomaly grids with ship-borne gravity data around Australia. In: Tziavos IN (ed) Gravity and geoid-3rd meeting of the international gravity and geoid commission, Thessaloniki, 26–30 Aug 2002, pp 326–331

Featherstone WE, Kirby JF, Kearsley AHW, Gilliland JR, Johnston GM, Steed J, Forsberg R, Sideris MG (2001) The AUSGeoid98 geoid model of Australia: data treatment, computations and comparisons with GPS-levelling data. J Geodesy 75:313–330

Főrste C, Bruinsma SL, Abrikosov O, Lemoine J-M, Schaller T, Gtze H-J, Ebbing J, Marty JC, Flechtner F, Balmino G, Biancale R (2014) EIGEN-6C4 the latest combined global gravity field model including GOCE data up to degree and order 2190 of GFZ Potsdam and GRGS Toulouse, presented at the 5th GOCE User Workshop, Paris, 25–28ăNovă2014

Hunegnaw A, Hipkin RG, Edwards J (2009) A method of error adjustment for marine gravity with application to Mean Dynamic Topography in the northern North Atlantic. J Geod 83:161–174

Lequentrec-Lalancette M-F (1992) Tutorial BGI. http://www.bgi.fr

Moysan Y. (2010) Traitement et validation gravimetrique en Mediterranee. Shom report, 30pp. http://www.shom.fr/

Olesen AV, Tziavos IN, Forsberg R (2002) New airborne gravity data around Crete - First results from the CAATER campaign. In: Proceedings of the 3rd meeting of the international gravity and geoid commission, GG2002, Thessaloniki, Aug 26–30

Pavlis NK, Holmes SA, Kenyon SC, Factor JK (2012) The development and evaluation of the Earth gravitational model 2008 (EGM2008). J Geophys Res 117:B04406. doi:10.1029/2011JB008916

Sandwell DT, Smith WHF (1997) Marine gravity anomaly from Geosat and ERS1 satellite altimetry. J Geophys Res102(B5):10039–10054

Torge W (1989) Gravimetry. Walter de Gruyter, Berlin/New York, 254 pp

Wessel P, Watts AB (1988) On the accuracy of marine gravity measurements. J Geophys Res 93(B1):393–413

Traceability of the Hannover FG5X-220 to the SI Units

Manuel Schilling and Ludger Timmen

Abstract

The absolute measurement of *g* is currently realized through the laser interferometric measurement of a free falling retro-reflector. The Micro-g LaCoste FG5X is a free-fall gravimeter with a laser interferometer in Mach-Zehnder configuration which uses simultaneous time and distance measurements to calculate the absolute value of *g*. Because the instrument itself contains the necessary working standards for precise time and length measurements, it is considered independent of external references. The timing is kept with a 10 MHz rubidium oscillator with a stability of 5×10^{-10}. The length unit is realized by the laser interferometer. The frequency calibrated and iodine stabilized helium-neon laser has a wavelength of 633 nm and an accuracy of 2.5×10^{-11}.

In 2012 the FG5-220 of the Institut für Erdmessung (IfE) was upgraded to the FG5X-220. The upgrade included a new dropping chamber with a longer free fall and new electronics including a new rubidium oscillator. The metrological traceability to measurement units of the Système International d'unités (SI unit) is ensured by two complementary and successive approaches: the comparison of frequencies with standards of higher order and the comparison of the measured *g* to a reference measured by absolute gravimeters defined as primary standards within the SI. A number of experiments to test the rubidium oscillator were performed. The oscillator showed a linear drift of 0.2×10^{-3} Hz per month ($= 0.3 \, \mathrm{nm \, s^{-2}}$ per month) in the first 18 months of use. A jump in the frequency of 0.01 Hz ($= 20 \, \mathrm{nm \, s^{-2}}$) was revealed recently and the drift rate changed to -0.4×10^{-3} Hz/month.

Since the upgrade of the absolute gravimeter the instrument participated in several international comparisons, which showed no significant measuring offset between the instrument prior and after the upgrade.

Keywords

Absolute gravimetry • Frequency standard • Gravimeter comparison • SI units

1 Introduction

Absolute gravimetry allows monitoring of secular gravity variations over time spans of several years to decades. Post-glacial land-uplift in northern Europe is just one example of slow changes which have been measured by the Hannover absolute gravimetry group (Gitlein et al. 2008; Timmen et al. 2011). In the center of the Fennoscandian land uplift area gravity decreases with approximately $20 \, \mathrm{nm \, s^{-2}}$/year. The determination of this rate and even smaller ones further away from the central area, requires annual measurements for at least 5–10 years with current generation absolute gravimeters. These instruments reach a long-term stability of $20 \, \mathrm{nm \, s^{-2}}$ or even better in the occupied laboratories.

M. Schilling (✉) • L. Timmen
Institut für Erdmessung, Leibniz Universität Hannover, Schneiderberg 50, 30167 Hannover, Germany
e-mail: schilling@ife.uni-hannover.de

For most applications in geodynamics the observation of temporal gravity variations are important and a constant measuring offset to the true value of g can be accepted. For the reproducibility of the instruments measurement a stable offset to the true value of g over several years is a necessity. Otherwise, an unknown change of the offset might be interpreted as a geophysical signal. A rigorous control of the absolute accuracy with respect to a true gravity value at the moment of an absolute gravity measurement is not possible. The real g-value with a superior accuracy is not known, and a standard absolute gravimeter which is superior to the state-of-the-art FG5 meters does not exist. Therefore, international key comparisons are organized periodically with absolute gravimeters as primary standards maintained by national metrology institutes or designated institutes. These key gravimeters define official reference values within the traceability chain of SI for all sites occupied by the key instruments and are provided to the other participating gravity meters, see e.g. Francis et al. (2015). In addition, two or more gravimeters may be combined within a geodynamics project, and the offsets between the instruments are controlled by episodic comparisons during the project live time outside of the official traceability chain (Timmen et al. 2015).

The most commonly used absolute gravimeters are the Micro-g LaCoste FG5 and the latest development, the FG5X (Niebauer et al. 1995, 2013). Micro-g LaCoste offers an upgrade from the FG5 to the FG5X, in which major parts of the instrument are replaced.

The Hannover FG5-220 was upgraded in 2012 which leads to two questions: (1) How well can absolute gravimeter measurements be traced back to the SI units for comparability? and (2) How does the FG5-220 upgrade affect the comparability of measurements performed prior and after the aforementioned upgrade?

2 The Absolute Gravimeters FG5-220 and FG5X-220

After 10 years of reliable deployment without hardware updates the FG5-220 was upgraded to the FG5X-220 (cf. Fig. 1) in 2012. The upgrade included a new dropping chamber. The drag-free cart is now mounted centrically between opposing sides of the lifting mechanism, and counterweights are added, accelerating in the opposite direction of the test mass to minimize vibrations and reduce recoil effects. The free-fall time was extended by 50 ms corresponding to a change of length from 20 cm to 31 cm. The elongated dropping distance resulted in a change of the instrumental reference height[1] from approximately 120 cm to 125 cm. The

---

[1]This is the reference height above floor level in which the vertical gravity gradient does not affect the derived g-result.

Fig. 1 FG5X-220 at the Institute for Geophysics, Clausthal University of Technology, Germany

number of interferometer fringes used for the calculation of g doubled from 600 to more than 1200. This corresponds to every 1,000th acquired fringe for the FG5-220 and every 800th acquired fringe for the FG5X-220. These numbers vary between different FG5(X) currently employed. The complete electronics were replaced in addition to the new dropping chamber. This includes the rubidium oscillator, discriminator circuit for fringe detection, and superspring controller. The superspring itself and the laser system were not replaced. Due to the different hardware components the self attraction correction changed from $-15 \, \text{nm s}^{-2}$ to $-12 \, \text{nm s}^{-2}$ (Niebauer et al. 2013).

3 Traceability of the FG5X-220

The traceability of absolute gravimeter measurements to SI units has most recently been described by the Working Group on Gravimetry (CCM-WGG) of the Consultative Committee for Mass and Related Quantities (Marti et al. 2015). In general, the traceability can be established by (a) the independent calibration of the integrated working standards, and (b) by comparison of the instrument with a reference

instrument (primary standard) or station (measured with a primary standard). These two approaches are not mutually exclusive and should be combined. Absolute gravimeters like the FG5(X) incorporate two frequency units. First, a 10 MHz rubidium oscillator provides the timing. Secondly, the frequencies of an iodine stabilized helium-neon laser are calibrated and are defining the corresponding wavelengths. Those are used for scaling the interference measurements within the laser displacement interferometer. The latter realizes the length unit of the gravimeter (Vitushkin 2011, 2015). Additional external references are not needed. But even proper calibration of these working standards does not ensure correct measurements of g. It should be mentioned that the calibration of frequencies is usually not performed on drop level timescales of a few tenths of a second, but with averaging over durations of minutes to hours (Vitushkin 2015). The comparison with a reference, on the other hand, is a test of the whole instrument. This includes a proper calibration of the absolute gravimeters barometer and the setup of the interferometer with the fringe acquisition components. The latter is necessary because the diffraction correction is beam waist dependent (Robertsson 2007) and measured g varies with fringe signal amplitude and distortion (Křen et al. 2015). These effects combined can reach some tens of nm s^{-2}. Additionally, the instrumental setting itself is to some degree (10 nm s^{-2} to 20 nm s^{-2}) influenced by the operator, e.g. due to imprecise verticalisation of the instrument.

3.1 Standards of Time and Length

3.1.1 Rubidium Oscillator

The 10 MHz rubidium oscillator of the FG5 is originally described by Niebauer et al. (1995).[2] The relative uncertainty of the frequency is given with 3.4×10^{-10} and a linear drift of 4×10^{-11}/month which translates to 0.4×10^{-3} Hz/month. The effect of a difference between the nominal and actual frequency of $\Delta f = 5 \times 10^{-3}$ Hz corresponds to a systematic change in gravity of 10 nm s^{-2}. If 0.4×10^{-3} Hz/month is the upper limit of the drift, an annual calibration of the rubidium oscillator would be sufficient to keep the influence of the accumulated drift below 10 nm s^{-2}.

The FG5X-220 electronics includes a new rubidium oscillator requiring a new characterisation. A GPS receiver is also incorporated in the FG5X electronics, allowing a GPS disciplined operation of the FG5X rubidium. However, this feature is not used, because most stations do not offer the possibility to connect to a GPS antenna outdoors. During
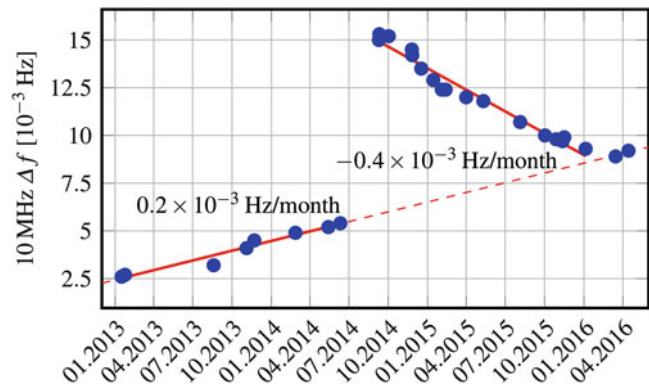
Fig. 2 Frequency comparison of FG5X-220 rubidium oscillator with reference oscillators. The jump in frequency in July 2014 might be caused by a helium event and would result in an error of 20 nm s^{-2}, if not corrected

measurements at geodetic observatories or metrology institutes the FG5X rubidium oscillator is compared to the local frequency standards of higher order accuracy (1×10^{-14} or even better). In Hannover and during longer campaigns a GPS stabilized rubidium clock (GRP[3]) is compared with the FG5X rubidium oscillator. With GPS stabilisation the GRP accuracy is given with 2×10^{-12}. Without GPS assistance the accuracy is 1.5×10^{-11} $\left(5 \times 10^{-11}\right)$ after a day (month) of free run. During a comparison with a 10 MHz signal provided by the local hydrogen maser at the Onsala Space Observatory (OSO, Sweden) the frequency of the GRP oscillator without GPS assistance deviated by 0.3×10^{-3} Hz from 10 MHz.

The FG5X-220 rubidium oscillator is usually compared with the GRP oscillator prior to measurement campaigns. The comparison of the FG5X-220 rubidium oscillator at institutions offering a 10 MHz reference allows the indirect comparison of the GRP oscillator with the FG5X rubidium as traveling standard. The results of all frequency comparisons are shown in Fig. 2. During the first 18 months of deployment the rubidium oscillator showed a linear drift of 0.2×10^{-3} Hz/month. After a stay at the Black Forrest Observatory in Schiltach (BFO, Germany) for the calibration of the local superconducting gravimeter (SG) a jump in the FG5X-220 rubidium oscillator of 10×10^{-3} Hz was discovered using the GRP oscillator and confirmed during a visit at a metrology institute. This is equal to a change in measured g of 20 nm s^{-2}. The most likely cause is an intrusion of atmospheric helium into the rubidium cell (Riehle 2004; van Westrum et al. 2014), as the underground laboratory in Schiltach is not ventilated and helium can accumulate in the tunnel leading to the superconducting gravimeter. The FG5X-220 was installed at BFO for approximately 48 hours. Similar effects have been reported, e.g., by Mäkinen et al.

---

[2]The FG5-220 featured a Datum LPRO rubidium oscillator and the FG5X-220 a Microsemi (formerly Symmetricon) SA.22c rubidium oscillator. Both oscillators are comparable in stability and drift to the original Efratom FRK-L.

[3]Meinberg GPS-receiver Rubidium Portable (GRP) frequency reference.

(2015). In theory this effect can be avoided by not measuring in the vicinity a superconducting gravimeter, which bear the risk of a higher helium concentration in the air. This is, however, an unlikely scenario as SGs depend on FG5 measurements for calibration and drift determination. It should also be noted that the FG5X-220 measured alongside several SGs, e.g., for almost two weeks of continuous operation at OSO in February 2015, without an effect on the rubidium oscillator. The more likely course of action is to limit the time of exposure to potentially higher helium concentrations (e.g. after helium refill or coldhead change of the SG) of the affected FG5X and to monitor the rubidium frequency directly prior and after a co-location with a SG. After the detection of the frequency jump the FG5X rubidium oscillator was compared more often to a reference to determine the development of the effect. The resulting drift was -0.4×10^{-3} Hz/month, although an exponential function is a better fit. Both van Westrum et al. (2014) and Mäkinen et al. (2015) observed, that keeping the rubidium oscillator turned on supports a quicker reversal to the original driftrate. The FG5X-220 is only powered on during measurements, thus elongating the time for reversal. It is still under investigation if the driftrate reverts to 0.2×10^{-3} Hz/month. The last two comparisons shown in Fig. 2, conducted by the Mexican national metrology laboratory (CENAM, Querétaro) and after air transport back to Hannover, align with the projected drift of the first 18 months of operation.

3.1.2 Laser

The WEO Model 100 laser in the FG5 and FG5X is an iodine stabilized helium-neon laser with a wavelength of 633 nm, a frequency reproducibility of 5 kHz and a relative frequency stability of 2×10^{-13} (Chartier et al. 1993). This implementation is a realization of the definition of the SI meter by the Comité International des Poids et Mesures (Quinn 2003). The length unit itself is established by the interferometric measurement. The wavelengths of laser light resulting from the peaks of iodine spectroscopy are determined by the manufacturer and are, up to now, not directly compared to a reference. For the Hannover FG5(X)-220,[4] Winters Electro-Optics, Inc., specifies a frequency accuracy of 2.5×10^{-11} for the WEO Model 100 laser (S/N 193). A significant change of frequency would be uncovered during comparisons with other absolute gravimeters. The other aforementioned effects related to the laser interferometer are accounted for by careful setup and adjustment (e.g. beam waist diameter, fringe signal amplitude) of the instrument.

3.2 Comparison of the Instrument with a Reference in *g*

The *g*-result of absolute gravimeter measurements depends not only on the calibration of working standards but also on the setup and measurement protocol followed by the operators. It is possible to judge the performance of the whole instrument and ensure its traceability to the SI unit by comparison with a reference. However, there is no absolute gravimeter of higher order accuracy available for the FG5(X). The reference is, as described in Marti et al. (2015), provided either by a group of absolute gravimeters during a key comparison (KC) or at a reference station monitored by an independently calibrated and validated absolute gravimeter and possibly a continuously recording SG.

3.2.1 Comparison of Absolute Gravimeters

Gravimeter comparisons in Europe are currently organized every two years, alternating between International and European Comparisons of Absolute Gravimeters (ICAG and ECAG or CCM.G-K*x* and EURAMET.M.G-K*x* according to the CIPM MRA[5]). ICAGs were held directly at the Bureau International des Poids et Mesures (BIPM) until 2009. Since 2013 the ICAG is held in the Walferdange Underground Laboratory for Geodynamics, which also hosts the ECAG. At these comparisons, with more than 20 attending absolute gravimeters, the instruments measure simultaneously during several setups. The attendees from national metrology institutes (NMI) and designated institutes (DI) participate in the KC. The key comparison reference value (KCRV) including its uncertainty of each measurement position is calculated from these measurements. All other attending gravimeters, including the FG5(X)-220, participate in the pilot study (PS). Their measurements, or more specifically the measured differences on the different positions, enter the adjustment of the KCRV as constraints. The result of the comparison is the degree of equivalence (DoE, Cox 2002) and the compatibility index E_n (Steele and Douglas 2006) for each absolute gravimeter measurement. The DoE is essentially the average difference between the measured gravity x_i and the KCRV $x_{i,KCRV}$ of position i over n setups of the respective gravimeter:

$$DoE = \frac{\sum_{i=1}^{n} x_i - x_{i,KCRV}}{n} \qquad (1)$$

The compatibility index E_n is the ratio of the difference between measured gravity and KCRV, and the expanded

---

[4]FG5(X)-220 refers to the original FG5-220 and the upgraded version.

[5]Comité International des Poids et Mesures Mutual Recognition Arrangement, a framework ensuring the comparability of national metrology services.
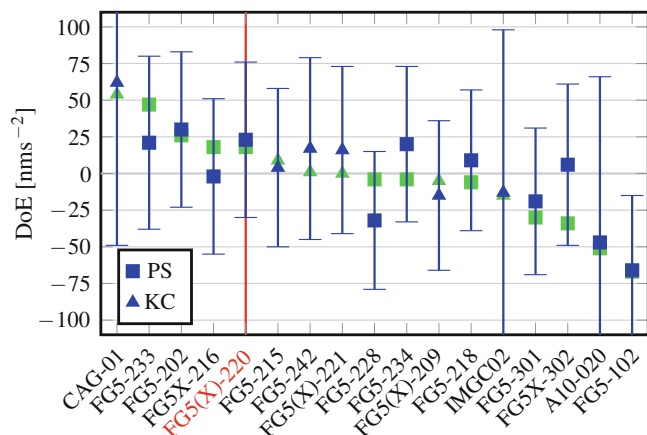
Fig. 3 Result of common instruments of ECAG-2011 and ICAG-2013 in Walferdange (Luxembourg) sorted by degree of equivalence of ECAG-2011 (Francis et al. 2013, 2015). *Error bars* represent the RMS of the expanded uncertainties of three setups of the AG in ICAG-2013. Instruments identified as FG5(X) were upgraded between ECAG-2011 and ICAG-2013

Fig. 4 Regional and international comparisons of the FG5(X)-220 with uncertainties according to the respective final report (standard deviations of expanded uncertainties of multiple setups). RICAG are organized by the German Federal Agency for Cartography and Geodesy (BKG) in Wettzell with six participating AGs. The FG5(X)-220 results of RICAG are deviations from the mean of the participants. Because the RICAG results are not published yet, no error bars are depicted here

uncertainty u (k=95%) of this difference:

$$E_n = \frac{x_i - x_{i,KCRV}}{\sqrt{u^2(x_i) + u^2(x_{i,KCRV})}} \qquad (2)$$

A ratio larger than 1 indicates that the measured gravity value x_i and the KCRV for the same position are not compatible. Only a single measurement out of more than 70, performed by all participants during the last comparison, was not compatible with the final KCRV (Francis et al. 2015).

Comparisons are linked by common NMI/DI participants. For the full description of the levels and interconnections of absolute gravimeter comparisons and CIPM terminology, we refer to Marti et al. (2015).

Figure 3 shows the resulting DoE of the instruments which participated in both the ECAG-2011 (green) and ICAG-2013 (blue). The FG5-220 (highlighted in red) was upgraded to the FG5X-220 between these comparisons. Instruments participating in only one of these comparisons are omitted in Fig. 3 and the complete results can be found in Francis et al. (2013, 2015). The zero-level is determined by KC instruments only. The difference in DoE between the FG5-220 and FG5X-220 is 5 nm s^{-2} only and not significant. For some instruments the change in DoE is above 20 nm s^{-2}, which is the level of stated uncertainty (reproducibility) for FG5 instruments. A more extensive collection of four international comparisons is described in Francis et al. (2013). The results of key comparisons are also listed in the key comparison database[6] starting in 2009.

Figure 4 shows the results of all comparisons of absolute gravimeters the FG5(X)-220 participated in (Francis et al. 2005, 2010; Jiang et al. 2012; Francis et al. 2013, 2015). The listed results of RICAG are from comparisons carried out at the Geodetic Observatory Wettzell by the Federal Agency for Cartography and Geodesy (BKG, Germany). The number of participants in this regional comparison is relatively small and the plotted results for the FG5(X)-220 are the deviation of the mean from all six instruments. RICAG2013 was held in January and ICAG2013 in November of the same year. The result from ECAG2003 is most likely caused by a hardware fault which was discovered after the comparison. Generally, the DoE of the FG5(X)-220 shows only a small variation from 17 nm s^{-2} to 25 nm s^{-2} since 2007, documenting a stable level of measurements. Moreover, since the upgrade of the instrument, the level has not changed.

3.2.2 Reference Station

In addition to a comparison with a number of other absolute gravimeters (primary standards), a reference g can also be provided at a station, which is measured by a gravimeter that participated in a KC, and which is carefully monitored by a SG. As suggested by the CCM-WGG (Marti et al. 2015), this only applies to locations monitored by NMIs and DIs, e.g. the respective home laboratory at a NMI/DI. IfE is not a NMI/DI but has a long history of gravimetric measurements at several stations which are used mainly for quality control between KCs. Clausthal is located in the Harz mountains close to Hannover and measurements started in 1986 with the JILAg-3 gravimeter.

---

[6]http://kcdb.bipm.org.
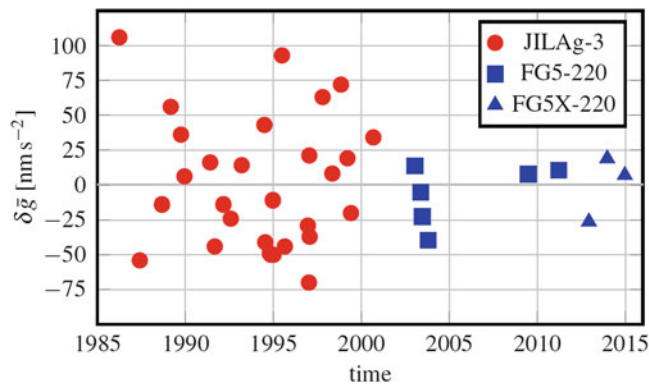
Fig. 5 Measurements of IfE AGs at TU Clausthal since 1986. Results shown refer to a height of 1.05 m, the mean height between JILAg and FG5X reference height. A bias of 90 nm s^{-2} was removed from JILAg-3 results (Timmen 2010)

Figure 5 shows the time series of all observations performed at the Institute for Geophysics, Clausthal University of Technology (Germany), with the Hannover gravimeters. The scatter of the JILAg-3 is also a result of its lower instrumental accuracy of about 50 nm s^{-2} (Torge 1991) compared to the FG5(X). The decline in the four observed g-values in 2003 should be connected to the very dry season in central Europe. The Geodetic Observatory Wettzell reported a decrease of 150 nm s^{-2} in the same period of time (Creutzfeldt et al. 2012). No significant trend has been found in this time series of 30 years length. It should be noted, that a systematic bias of 90 nm s^{-2} has been removed from all JILAg-3 measurements (Timmen 2010). A similar bias was reported by the Austrian group for their JILAg gravimeter (Ruess and Ullrich 2011). The Clausthal series does not reveal a systematic change in the measuring level between FG5-220 and FG5X-220. These episodic measurements serve as a validation for the correct functioning of the gravimeter showing its measuring strength and precision over a period of some days. Larger gravity variations occur during extreme weather conditions and seasonal hydrological variations. Clausthal is not a reference station in the scope of Marti et al. (2015).

The Hannover group has performed measurements at the Onsala Space Observatory since 2003. Onsala is located on the border of the Fennoscandian land-uplift area with only a small trend in uplift and the results have been published in Timmen et al. (2015). Here, the secular land-uplift trend serves also as a validating signal to prove the stability of the absolute gravimeter. Due to a large number of g-determinations, seasonal and short periodic variations as well as instrumental errors are averaged out to a certain extend, which helps to reveal a long-periodic trend after some years. The observational trend is compared with rates predicted by geophysical modeling. A measurement in February of 2015,

which is not part of that publication, agrees within 10 nm s^{-2} to the predicted trend.

The laboratory in Hannover itself is not well suited to characterize the long-term stability of the gravimeter due to hydrological effects and extensive construction work in close vicinity.

4 Summary

All modern absolute gravimeters hold incorporated working standards of length and time thus making measurements independent of external references. One method to establish the traceability to the SI units is by comparing these standards to those of higher order. Regular comparisons of the FG5X-220 rubidium oscillator showed a linear drift of 0.2×10^{-3} Hz/month for the first 18 months of operation. A jump of 0.01 Hz in the frequency, equal to an offset of 20 nm s^{-2}, and the subsequent change of the drift rate to -0.4×10^{-3} Hz/month underlines the necessity for a regular validation of the rubidium oscillator. An adaptation of the measurement regime at superconducting gravimeter sites is needed for affected FG5(X) instruments with rubidium oscillators which are sensitive to helium gas concentrations in the air.

The second complementary method, which is also obligatory, is the regular comparison of the absolute gravimeter with references, either at key comparisons with other gravimeters (primary standards) or at reference stations. The participation at several international comparisons since 2007 with the FG5-220 and the upgraded FG5X-220 shows a non-significant variation of the respective DoE of less than 10 nm s^{-2} and no offset since the upgrade in 2012. In addition to the international comparisons, the time series at the stations Clausthal and Onsala, reoccupied episodically as required or annually, do also not indicate any change in the gravimeter measuring level after the upgrade of FG5-220 to FG5X-220 in 2012.

References

Chartier JM, Labot J, Sasagawa G, Niebauer TM, Hollander W (1993) A portable iodine stabilized He-Ne laser and its use in an absolute gravimeter. IEEE Trans Instrum Meas 42(2):420–422. doi:10.1109/19.278595

Cox MG (2002) The evaluation of key comparison data. Metrologia 39(6):589–595. doi:10.1088/0026-1394/39/6/10

Creutzfeldt B, Ferré T, Troch P, Merz B, Wziontek H, Güntner A (2012) Total water storage dynamics in response to climate variability and extremes: inference from long-term terrestrial gravity measurement. J Geophys Res 117:D08112. doi:10.1029/2011jd016472

Francis O, van Dam T, Amalvict M, Andrade de Sousa M, Bilker M, Billson R, D'Agostino G, Desogus S, Falk R, Germak A, Gitlein O, Jonhson D, Klopping F, Kostelecký J, Luck B, Mäkinen J, McLaughlin D, Nunez E, Origlia C, Pálinkáš V, Richard P, Rodriguez E, Ruess D, Schmerge D, Thies S, Timmen L, Van Camp M, van Westrum D, Wilmes H (2005) Results of the international comparison of absolute gravimeters in Walferdange (Luxembourg) of November 2003. In: Mertikas S (ed) International Association of Geodesy Symposia, vol 129, pp 272–275. Springer, Berlin/Heidelberg. doi:10.1007/3-540-26932-0_47

Francis O, van Dam T, Germak A, Amalvict M, Bayer R, Bilker-Koivula M, Calvo M, D'Agostino GC, Dell'Acqua T, Engfeldt A, Faccia R, Falk R, Gitlein O, Gjevestad J, Hinderer J, Jones D, Kostelecký J, Le Moigne N, Luck B, Mäkinen J, Mclaughlin D, Olszak T, Olsson PA, Pachuta A, Pálinkáš V, Pettersen B, Pujol R, Prutkin I, Quagliotti D, Reudink R, Rothleitner C, Ruess D, Shen C, Smith V, Svitlov S, Timmen L, Ulrich C, Van Camp M, Walo J, Wang L, Wilmes H, Xing L (2010) Results of the European comparison of absolute gravimeters in Walferdange (Luxembourg) of November 2007. In: International Association of Geodesy Symposia, vol 137, pp 31–35. Springer, Berlin/Heidelberg. doi:10.1007/978-3-642-10634-7_5

Francis O, Baumann H, Volarik T, Rothleitner C, Klein G, Seil M, Dando N, Tracey R, Ullrich C, Castelein S, Hua H, Kang W, Chongyang S, Songbo X, Hongbo T, Zhengyuan L, Pálinkáš V, Kostelecký J, Mäkinen J, Näränen J, Merlet S, Farah T, Guerlin C, Pereira Dos Santos F, Le Moigne N, Champollion C, Deville S, Timmen L, Falk R, Wilmes H, Iacovone D, Baccaro F, Germak A, Biolcati E, Krynski J, Sekowski M, Olszak T, Pachuta A, Ågren J, Engfeldt A, Reudink R, Inacio P, McLaughlin D, Shannon G, Eckl M, Wilkins T, van Westrum D, Billson R (2013) The European comparison of absolute gravimeters 2011 (ECAG-2011) in Walferdange, Luxembourg: results and recommendations. Metrologia 50(3):257–268. doi:10.1088/0026-1394/50/3/257

Francis O, Baumann H, Ullrich C, Castelein S, Van Camp M, Andrade de Sousa M, Melhorato RL, Li C, Xu J, Su D, Wu S, Hu H, Wu K, Li G, Li Z, Hsieh WC, Pálinkáš V, Kostelecký J, Mäkinen J, Näränen J, Merlet S, Pereira Dos Santos F, Gillot P, Hinderer J, Bernard JD, Le Moigne N, Fores B, Gitlein O, Schilling M, Falk R, Wilmes H, Germak A, Biolcati E, Origlia C, Iacovone D, Baccaro F, Mizushima S, De Plaen R, Klein G, Seil M, Radinovic R, Sekowski M, Dykowski P, Choi IM, Kim MS, Borreguero A, Sainz-Maza S, Calvo M, Engfeldt A, Ågren J, Reudink R, Eckl M, van Westrum D, Billson R, Ellis B (2015) CCM.G-K2 key comparison. Metrologia 52(1A):07009. doi:10.1088/0026-1394/52/1a/07009

Gitlein O, Timmen L, Müller J, Denker H, Mäkinen J, Bilker-Koivula M, Pettersen BR, Lysaker DI, Gjevestad JGO, Breili K, Wilmes H, Falk R, Reinhold A, Hoppe W, Scherneck HG, Engen B, Omang OCD, Engfeldt A, Lilje M, Ågren J, Lidberg M, Strykowski G, Forsberg R (2008) Observing absolute gravity acceleration in the Fennoscandian land uplift area. In: Peshekhonov VG (ed) Terrestrial Gravimetry: Static and Mobile Measurements (TG-SMM2007) – 20.-23.8.2007, pp 175–180. State Research Center of Russia Elektropribor, St. Petersburg

Jiang Z, Pálinkáš V, Arias FE, Liard J, Merlet S, Wilmes H, Vitushkin L, Robertsson L, Tisserand L, Pereira Dos Santos F, Bodart Q, Falk R, Baumann H, Mizushima S, Mäkinen J, Bilker-Koivula M, Lee C, Choi IM, Karaboce B, Ji W, Wu Q, Ruess D, Ullrich C, Kostelecký J, Schmerge D, Eckl M, Timmen L, Le Moigne N, Bayer R, Olszak T, Ågren J, Del Negro C, Greco F, Diament M, Deroussi S, Bonvalot S, Krynski J, Sekowski M, Hu H, Wang LJ, Svitlov S,

Germak A, Francis O, Becker M, Inglis D, Robinson I (2012) The 8th international comparison of absolute gravimeters 2009: the first key comparison (CCM.G-K1) in the field of absolute gravimetry. Metrologia 49(6):666–684. doi:10.1088/0026-1394/49/6/666

Křen P, Pálinkáš V, Mašika P (2015) On the effect of distortion and dispersion in fringe signal of the FG5 absolute gravimeters. Metrologia 53(1):27–40. doi:10.1088/0026-1394/53/1/27

Mäkinen J, Virtanen H, Bilker-Koivula M, Ruotsalainen H, Näränen J, Raja-Halli A (2015) The effect of helium emissions by a superconducting gravimeter on the rubidium frequency standards of absolute gravimeters. In: International Association of Geodesy Symposia. doi:10.1007/1345_2015_205

Marti U, Richard P, Germak A, Vitushkin L, Pálinkáš V, Wilmes H (2015) CCM - IAG strategy for metrology in absolute gravimetry - Role of CCM and IAG. Available online. http://www.bipm.org/wg/AllowedDocuments.jsp?wg=CCM-WGG. Retrieved 10 Oct 2015

Niebauer TM, Sasagawa GS, Faller JE, Hilt R, Klopping F (1995) A new generation of absolute gravimeters. Metrologia 32(3):159–180. doi:10.1088/0026-1394/32/3/004

Niebauer TM, Billson R, Schiel A, van Westrum D, Klopping F (2013) The self-attraction correction for the FG5X absolute gravity meter. Metrologia 50(1):1–8. doi:10.1088/0026-1394/50/1/1

Quinn T (2003) Practical realization of the definition of the metre, including recommended radiations of other optical frequency standards (2001). Metrologia 40(2):103–133. doi:10.1088/0026-1394/40/2/316

Riehle F (2004) Frequency standards. Wiley, Weinheim. doi:10.1002/3527605991

Robertsson L (2007) On the diffraction correction in absolute gravimetry. Metrologia 44(1):35–39. doi:10.1088/0026-1394/44/1/005

Ruess D, Ullrich C (2011) 20 years of international comparison of absolute gravimeters (ICAG) at the Bureau International des Poids et Mesures (BIPM) in Paris with participation of the BEV. Vermessung Geoinf 99(2):154–161

Steele AG, Douglas RJ (2006) Extending E_n for measurement science. Metrologia 43(4):S235–S243. doi:10.1088/0026-1394/43/4/s10

Timmen L (2010) Absolute and relative gravimetry. In: Xu G (ed) Sciences of Geodesy - I: Advances and Future Directions, Chap 1, pp 1–48. Springer, Berlin/Heidelberg. doi:10.1007/978-3-642-11741-1_1

Timmen L, Gitlein O, Klemann V, Wolf D (2011) Observing gravity change in the Fennoscandian uplift area with the Hanover absolute gravimeter. Pure Appl Geophys 169(8):1331–1342. doi:10.1007/s00024-011-0397-9

Timmen L, Engfeldt A, Scherneck HG (2015) Observed secular gravity trend at Onsala station with the FG5 gravimeter from Hannover. J Geodetic Sci 5(1):18–25. doi:10.1515/jogs-2015-0001

Torge W (1991) The present state of absolute gravimetry. In: Poitevin C (ed) Proceedings of the workshop: non tidal gravity changes – intercomparison between absolute and superconducting gravimeters, vol 3, pp 9–22. Centre Européen de Géodynamique et de Séismologie, Walferdange (Luxemburg), September 5th–9th 1990

van Westrum D, Bianchi T, Billson R, Ellis B, Niebauer TM, Rohner H (2014) The effect of helium contamination on rubidium clock references in absolute gravity meters. In: Peshekhonov VG (ed) IAG Symposium on Terrestrial Gravimetry: Static and Mobile Measurements (TG-SMM2013) – 17.-20.9.2013, pp 125–130. State Research Center of Russia Elektropribor, St. Petersburg

Vitushkin L (2011) Measurement standards in gravimetry. Gyroscopy Navig 2(3):184–191. doi:10.1134/s2075108711030126

Vitushkin L (2015) Absolute ballistic gravimeters. Gyroscopy Navig 6(4):254–259. doi:10.1134/s207510871504015x

Evaluation of Robert Sterneck's Historical Gravity Pendulum Measurements in the Czech Territory

Alena Pešková, Martin Lederer, and Otakar Nesvadba

Abstract

Robert Daublebsky von Sterneck, bohemian aristocrat, astronomer, geophysicist and geodesist, devoted part of his live to pendulum gravity measurements.

More than one hundred Sterneck's pendulum gravity observations were performed between 1889 and 1895 on the Czech territory (i.e Bohemia, Moravia and Czech Silesia). Until present, thorough evaluation of the accuracy of these measurements was not accomplished. On the basis of original Sterneck's field books the station locations were investigated and their true positions identified. For this purpose, all available original handwritten notes were translated and often even puzzled out. The observed values have been compared with the actual knowledge of the Earth's gravity field.

Keywords

Gravity reference system • Pendulum gravity observation • Robert Daublebsky von Sterneck

1   Introduction

Robert Daublebsky von Sterneck (∗ 1839, † 1910) was prominent bohemian aristocrat, astronomer, geophysicist and geodesist (Fig. 1). As a military officer, Sterneck worked in the k.u.k. Militärgeographische Institut (MGI) of Austro-Hungarian Empire in Vienna, where he was involved in astronomical observations, triangulation, levelling, etc. The scientifically most important part of Sterneck's fruitful life was dedicated to gravity and time pendulum measurements. He pioneered the pendulum coincidence method, where on the pendulum instrument of his own construction (Fig. 1)

he developed the 'coincidence device' for an accurate measurement of pendulum swing periods.

Robert Sterneck and his collaborators measured several hundred pendulum stations over Europe and Asia within the period 1881–1898. More than one hundred of the stations were located at the present-day Czech Republic territory. Until now, no comprehensive evaluation of these Sterneck's measurements has been done. The actual detailed knowledge of the gravity field over the Czech Republic give us an opportunity to interpret these historical measurements in terms of their quality.

1.1   Sterneck's Approach to Pendulum Time Observations

The connection between gravity g and pendulum swing period S is based on the well known formula $S = \pi \sqrt{l/g}$ (simple pendulum of a length l). For two gravity stations then stand $g_2 = g_1 (S_1/S_2)^2$. It becomes clear that the determination of the pendulum swing time is crucial. For this purpose Sterneck developed the coincidence method, based on an

A. Pešková
Czech Technical University, Thákurova 7, 160 00 Praha 6, Czech Republic
e-mail: peskova.alena@seznam.cz

M. Lederer (✉) • O. Nesvadba
Land Survey Office, Pod sídlištěm 9, 182 11 Praha 8, Czech Republic
e-mail: ledererm@seznam.cz
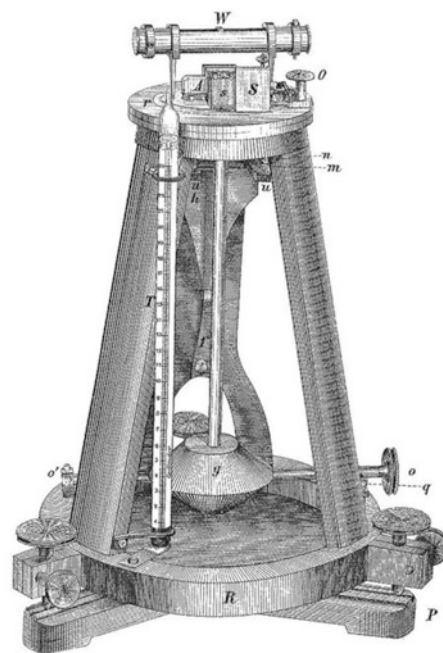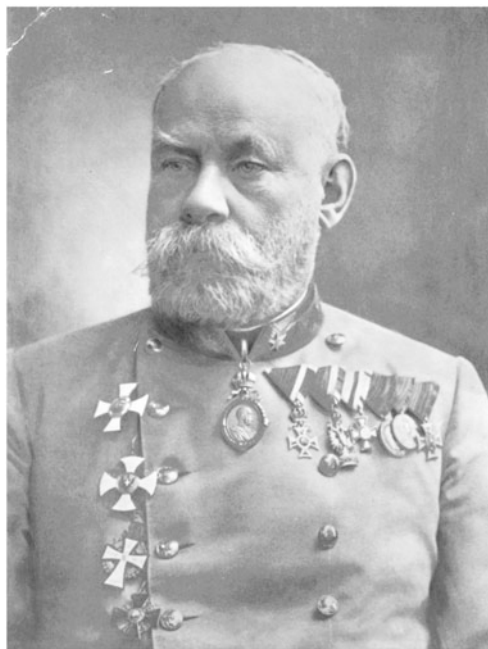
identification of the coalesce events of the pendulum swings with the given frequency reference. Observed length c of a single coincidence interval than gives $S = \frac{c}{2c \pm 1}$ (in the case of a half second pendulum and 1 Hz frequency reference).

Sterneck considered all known environmental corrections and effects, like reduction to zero amplitude, temperature correction, air-drag correction or a correction from a reference clock drift. A calculation of the pendulum period S, that takes all the corrections into account, is illustrated with the original field book. From the fieldbook in Fig. 2 we can identify:

- coincidence interval $c = \frac{1}{60}(34{:}32.68) \doteq 34.545\,s$ obtained from ten observations of 60 coincidences time span,
- observed pendulum period $s = \frac{c}{2c-1} \doteq 0.5073433\,s$,
- reduction to zero amplitude $\alpha = -s\frac{A^2}{16} \doteq -0.4\,\mu s$, where $A = 13.28'$ is the pendulum mean amplitude,
- temperature correction $\tau = -4.84T \doteq -93.3\,\mu s$, where $T = 19.39°C$ is the environment mean temperature,
- air-drag correction $\delta = -54.1D \doteq -48.9\,\mu s$, where $D = \frac{B}{760(1+0.004T)} \doteq 0.904$, while $B = 740.3\,mmHg$ is the observed atmospheric pressure,
- clock drift correction $u = 123.5\,\mu s$ and transformation of the pendulum period from sidereal to mean solar time $\Sigma\delta t = 1386.5\,\mu s$.

The period $S = s + \alpha + \tau + \delta + u + \Sigma\delta t \doteq 0.5087131\,s$ can be identified on the bottom of the page (Fig. 2) as the result of one pendulum observation at the station. Usually, there were three or four different pendulums used at the station, where each pendulum observation was repeated at least twice. Therefore, the station full survey consists of at least six pendulum measurements.

2 Pendulum Station Identification

The catalogue of the station geodetic coordinates φ, λ and Adria sea-level heights H were provided directly in Sterneck (1893) and Šimon (1962). Nevertheless, these coordinates and heights were too inaccurate for a correct identification of the actual stations locations, and thus inapplicable in the subsequent gravity interpolation. Therefore, we decided to reconstruct all the stations locations with the aid of the original field books, Sterneck et al. (1889). Handwritten text notes and station descriptions, if available (like in the case of Fig. 2), were deciphered, translated and used in a station georeferencing process, according to Pešková (2015).

In the following we divide the stations, as you can see in the Fig. 3, to two groups:

- **Group A** represents measurements from the period 1889–1891, the stations were situated mostly at hilltops predominantly in Bohemia.
- The stations from **Group B**, were measured in the years 1894 and 1895 and were located mostly at urban districts of Moravia and Silesia.

Gravity stations from Group A were observed just as a supplement to astronomical observations. Therefore, their positions are known to a sufficient accuracy from the astronomic and trigonometric records. The coordinates were transformed to ETRS (European Terrestrial Reference System) and displayed over the current aerial orthophoto WMS (Web Map Service), Land Survey Office (2015), to check the position. On the contrary, localisation of the Group B stations was oftentimes difficult, since archive maps and other resources

Fig. 2 An original handwritten field book, pendulum No. VII observed in Osoblaha (Hotzenplotz) station at 07/17/1895 9:15 a.m

had to be studied to piece informations together. Besides, during our research we realised, that the original station heights are often inaccurate in magnitude of several meters or more. It turned out, we have to verify and correct the original stations height information with the aid of a terrain model. Recent airborne LiDAR (Light Detection And Ranging) data, Land Survey Office (2015), have been used for this purpose.

2.1 An Example of the Localisation Process

The pendulum station No. 425 *Osoblaha* (Hotzenplotz in German) from Group B was chosen to demonstrate the overall process.

We can translate the original description (Fig. 2) "*in Hotzenplotz (Obergasse Nr. 136 in einem ebenerdigen Zimmer)* 60^X *West von der Kirche, gleich hoch*" as "in Osoblaha (Obergasse alley No. 136 in a ground floor room) 60 steps west from the church, equal height".

From the *indicative scheme* (Fig. 4–top) available on `geoportal.cuzk.cz`, Land Survey Office (2015), we can identify Obergasse No. 136 house and the respective cadastral index No. 68. Consequently, using the information from an original cadastral mapping made with graphical intersection in 1836 (Fig. 4–bottom) we get the parcel No. 68 position and thus the relative location of the pendulum station.

In order to georeference the station, we have to find a transformation of the cadastral map local coordinates to the present geodetic reference system. Unfortunately, almost the

whole Osoblaha town was destroyed during WWII, so there are no identical point to reference. Luckily, the remains of few buildings and a church visible on georeferenced panchromatic orthophoto taken in 1954 (Fig. 5–top) allow us to bridge the gap and establish the transformation of the old cadastral map with respect to ETRS (Fig. 5–bottom). We can conclude, that the ETRS/GRS80 position of the pendulum station was $\varphi = 50.274138°$, $\lambda = 17.713650°$, while $\epsilon\varphi = \pm 5$ m, $\epsilon\lambda = \pm 6$ m limit the position uncertainty at 95 % confidence level. The station was located ca 75 m far from the church (its main west entrance) in azimuth of ca 290°, which agrees well with the original description.

As the pendulum station was located on the ground level and the local terrain has not changed significantly since that time, we can use a terrain information from recent airborne LiDAR mapping and estimate the original station altitude. Based on Land Survey Office (2015) data, for the ETRS/GRS80 position of the station given above we obtain $h = 281.9$ m, thus the Adria sea-level height of the station would be $H = 240.3$ m of uncertainty $\epsilon H = \pm 1$ m. It seems to be, the original Sterneck's station height $H = 238$ m was just a rough estimate, taken from the military map 1 : 75 000, cf. *Special map Zo. 4, Co. XVII* noted in Fig. 2, where the value 238 m is stated as a mean height of the town. The actual terrain height at the church location (i.e. former main west entrance location) is $h = 281.5$ m, i.e. almost the same as the terrain height in the location of the pendulum station, that agrees with Sterneck's description.

Fig. 4 Cadastral indicative scheme (*top*) and the so-called imperial imprint of the cadastral map 1 : 2 880 (*bottom*) of Osoblaha town centre

3 Gravity Determination

Since we know the accurate positions of the stations, it would be feasible to visit them and measure the respective gravity values, like for example on the Osoblaha station location shown in Fig. 6. Nevertheless, since we want to estimate not only the point gravity value but also its uncertainty with respect to uncertainty of the station location, we decided to derive the corresponding gravity quantities from the Czech gravimetric database by means of the geostatistical interpolation. According to Nesvadba and Holota (2016), for the surface gravity g we can write

$$g = \delta g_B + \gamma_{EGM} + 0.112 \left(h - N_{EGM} - H_{DTM} \right) + \delta g_T$$

where the gravity topocorrection δg_T is computed for a constant mass density $\rho = 2670 \, \text{kg/m}^3$ with the aid of

the mentioned LiDAR terrain data (Fig. 7–top). *Bouguer disturbances* $\delta g_B = g - \gamma_{EGM} - 0.112(h - N_{EGM} - H_{DTM}) - \delta g_T$ are calculated for observed gravity g at given points (Fig. 7–bottom). By means of EGM2008 geopotential related to DTM06 surface H_{DTM} over EGM2008 geoid N_{EGM}, Pavlis et al. (2012), we removed long-period terms from the gravity signal. Finally, δg_B quantity for the position of pendulum station is interpolated with the ordinary kriging, where damped periodic covariance function model of δg_B is considered, Nesvadba and Holota (2016) and Cressie (1993).

3.1 Sterneck's Gravity System Level

The reference point for all Sterneck's pendulum measurements was situated on a pillar in a cellar room of the MGI building in Vienna. The knowledge of the Sterneck's gravity reference is fundamental for the gravity level of all his

relative pendulum measurements. First we can start with the reference value $g_{MGI}^{(<1891)} = 980\,851$ mGal given in Sterneck (1890). Nevertheless, this value was not evidently fixed. Later, in 1891, Sterneck reconsidered the reference to $g_{MGI}^{ref} = 980\,876$ mGal, as confirmed in Sterneck (1891, 1893).

Nowadays we can estimate the true gravity reference value as $g_{MGI}^{abs} = 980\,845 \pm 0.5$ mGal (uncertainty at 95 % confidence level). Therefore, the Sterneck's reference g_{MGI}^{ref} was biased by $\Delta g_{MGI} = 31$ mGal, which is applicable to all his pendulum measurements, since the measurements carried out before 1891 have been already transformed to g_{MGI}^{ref} in Sterneck (1893).

4   Results

As the result we get $\Delta g_i = g_i^{Sterneck} - g_i$, i.e. the differences between Sterneck's gravity values $g_i^{Sterneck}$ and the 'true' gravity g_i estimated at all the pendulum stations. Few observations from both the groups has been excluded as outliers, according to Pešková (2015). An average Δg_i for Group A and Group B is 12.6 mGal and 34.3 mGal, respectively. The sample standard deviation of Δg_i for Group A and Group B is ± 10.4 mGal and ± 10.5 mGal, respectively. The result indicates on the difference of about -18.4 mGal and 3.3 mGal with respect to the gravity level determined by Sterneck, see Fig. 8. The distribution of differences (after the offsets subtraction) is shown in the Fig. 9.

To look more into the detail of measurements carried out in 1895 we can divide Group B into two subgroups, **Group B1** observed by J. Hässler with tombac alloy pendulums No. 65, 66, 67 and **Group B2** observed by F. Filz von Ritterdank with brazen pendulums No. VII, VIII, IX, see Fig. 10.

For both the groups a linear trend of about 0.11 mGal/day, though not fully supported statistically, is visible in Fig. 10. It can be explained as a long term drift of the pendulums, i.e. the progressive change of the pendulum length, which has been considered and partly corrected in Group B1 observations by Sterneck et al. (1889).

Fig. 5 Osoblaha panchromatic orthophoto 1954 (*top*) and 2013 orthophoto and cadastral map composition (*bottom*)

Fig. 6 Street view of Osoblaha pendulum station location before 1925 (*left*, zanikleobce.cz) and present (*right*, Google.com 2012); *red-shaded area* estimates the house No. 136 location

Fig. 7 δg_T (*top*, in mGal units) computed from the terrain data and δg_B (*bottom*, in mGal units) for the Osoblaha pendulum station (*red star* 1895) gives $g = 981037.5$ mGal. The uncertainty of δg_B, δg_T together with the station location uncertainty is projected to interval -1.2 mGal, $+1.1$ mGal of 95 % confidence. *Black crosses* represent the positions and years of available gravimetric observations
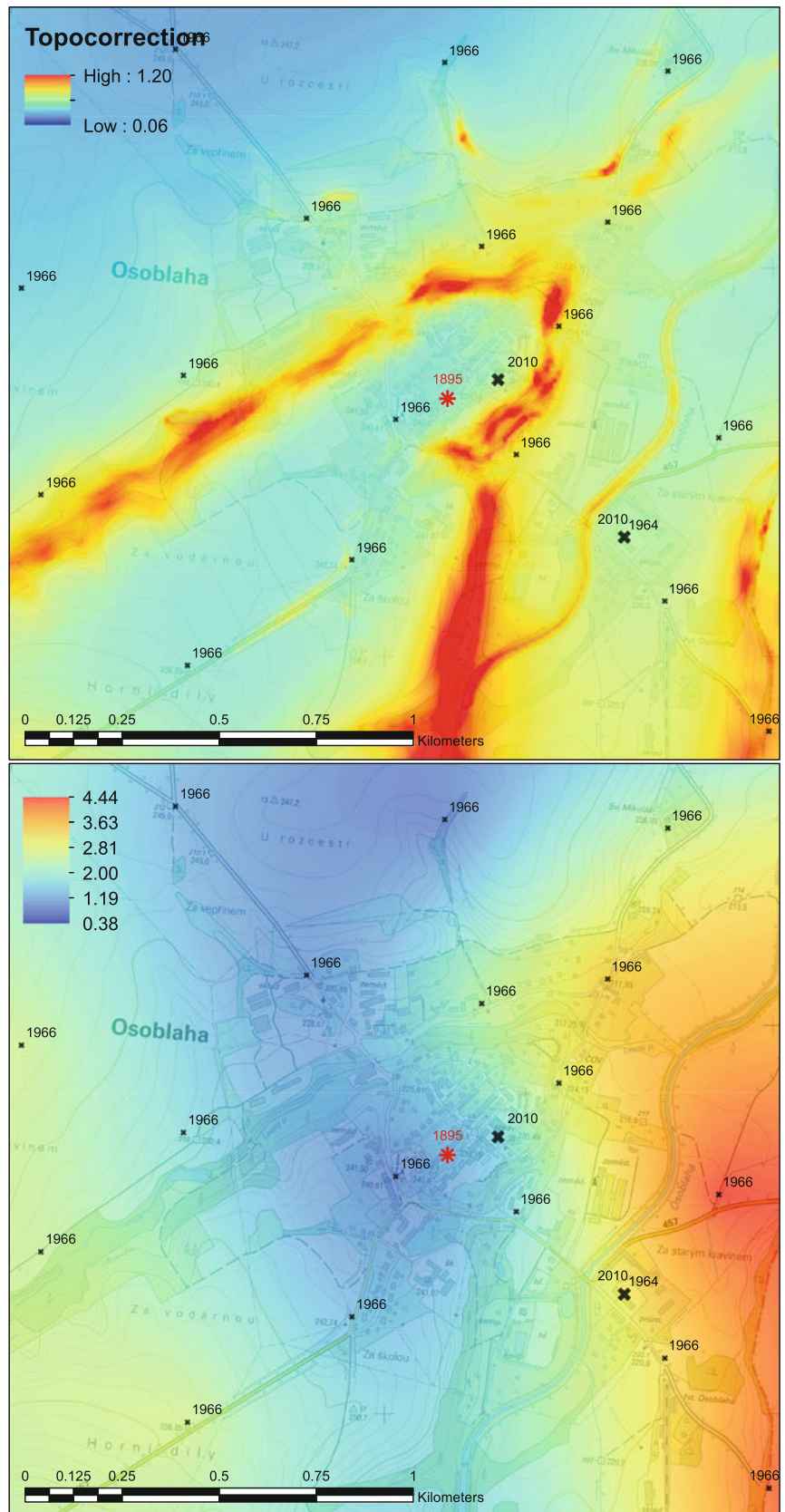
Fig. 8 Differences
$\Delta g_i = g_i^{Sterneck} - g_i$ of Group
A (*blue dots*) and Group B (*red dots*). The *circles* represent
excluded pendulum stations
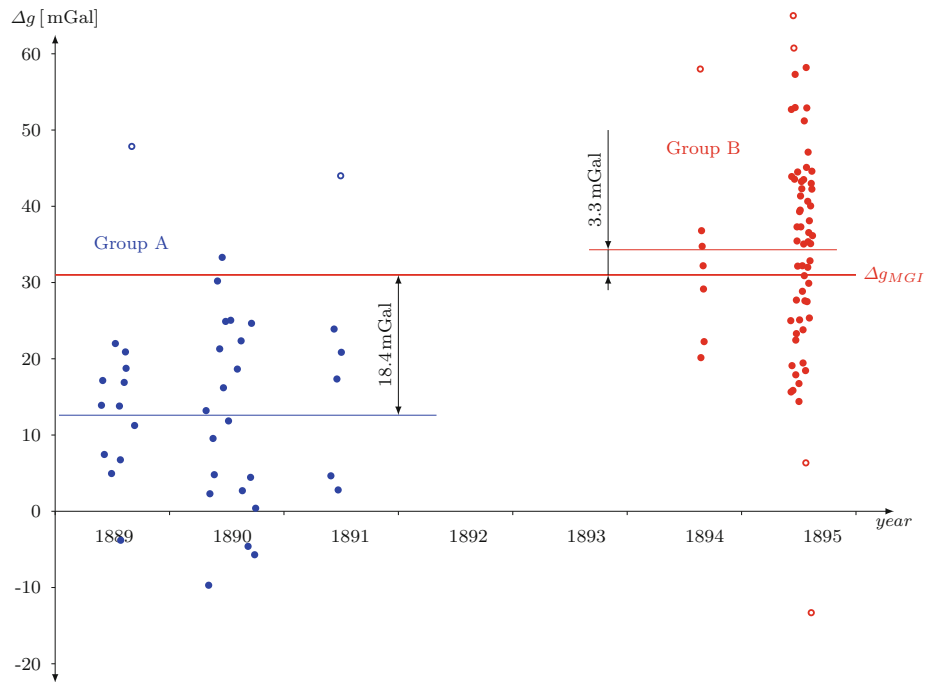
Fig. 9 Histogram of differences
$\Delta g_i = g_i^{Sterneck} - g_i$, after the
offset removal
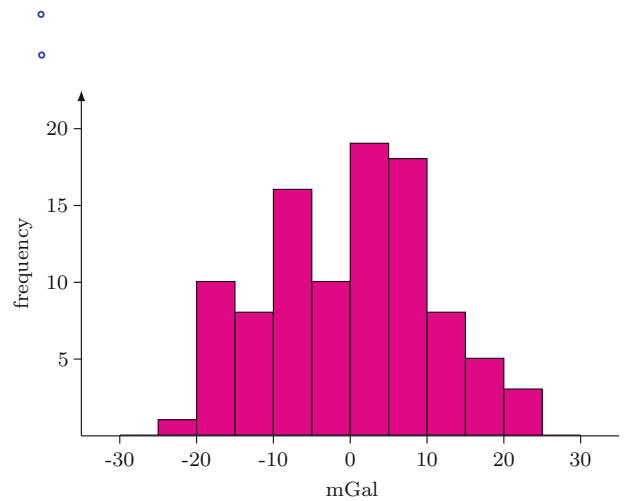
Fig. 10 A posteriori gravity
difference $\Delta g_i = g_i^{Sterneck} - g_i$
of two observation series of the
summer 1895. The error bars
represent total uncertainties of
the g_i estimates (at 95 %
confidence level). Linear trend of
both the series is shown with the
straight line; the first and the last
measurement of the series in
Vienna MGI are highlighted

5 Conclusions

We have compared original Sterneck's pendulum gravity measurements at 106 stations with the actual most accurate gravity knowledge. Distinguishing two groups of the stations, we found gravity offsets $\Delta g_A = 12.6$ mGal and $\Delta g_B = 34.3$ mGal. The offset Δg_B is very close to Sterneck's gravity reference bias $\Delta g_{MGI} = 31$ mGal that might convince, the later pendulum observations of Group B accounts for lower uncorrected systematical effects. The difference of the mean gravity between the groups might have been sourced in:

- brand new pendulums and upgrades of the instrument after 1891, including revised models of environmental corrections,
- well established surveying technique after 1892 in contrast to 1889–1891 period,
- time reference changes and subsequent corrections or transformations:
  - in 1889–1891 marine chronometers Fisher and Nardin (mean solar time) were used and the clock drift was estimated by local astronomical observations,
  - on the contrary in 1895 astronomical clocks Tiede (sidereal time) were used, drift corrected with a temporarily established time service (via the telegraph).

The linear trend of about 0.11 mGal/day found in two data sets of 1895 is probably caused by pendulum reduced length change.

Finally, after the outliers removal, we can estimate a precision of the Sterneck's pendulum measurements on the Czech territory by standard deviation ca **10.5** mGal. Considering also the gravity offsets, an estimate of the overall Sterneck's accuracy is around ±20 mGal.

5.1 Closing Remark

It is interesting to see that the gravity offset/bias variability was always very delicious. As the Sterneck's measurements 120 years ago show biases about 10–20 mGal, 20 years old gravity measurements contain biases on 10 μGal level, see Pálinkáš et al. (2013).

References

Cressie NAC (1993) Statistics for spatial data, revised edn. Wiley, New York

Land Survey Office (2015) Geoportal ČÚZK. URL http://geoportal.cuzk.cz

Nesvadba O, Holota P (2016) Detailed quasigeoid for the Czech Republic: gravimetric solution. Stud Geophys Geod (in publication)

Pavlis NK, Holmes SA, Kenyon SC, Factor JK (2012) The development and evaluation of the Earth gravitational model 2008 (EGM2008). J Geophys Res Solid Earth 117:(B04406)

Pešková A (2015) Accuracy assesments of pendulum gravity measurements of R. Sterneck. Master's thesis, Czech Technical University, Prague (in Czech)

Pálinkáš V, Lederer M, Kostelecký J Jr, Šimek J, Mojzeš M, Ferianc D, Csapó G (2013) Analysis of the repeated absolute gravity measurements in the Czech Republic, Slovakia and Hungary from the period 1991–2010 considering instrumental and hydrological effects. J Geod 87(1):29–42

Šimon Z (1962) Pendulum measurements done in 1956–1962 period. Research Note, Geodetický a topografický ústav, Prague (in Czech)

Sterneck R (1890) Bestimmung der Intensität der Schwerekraft in Böhmen, vol Volume X. Mitheilungen des k. u. k Militär-Geographischen Insitutes, Wien (in German)

Sterneck R (1891) Die Schwerekraft in den Alpen, und Bestimmung ihres Wertes für Wien, vol Volume XI. Mitheilungen des k. u. k Militär-Geographischen Insitutes, Wien (in German)

Sterneck R (1893) Relative Schwerebestimmungen, vol Volume XIII. Mitheilungen des k. u. k Militär-Geographischen Insitutes, Wien (in German)

Sterneck R, Křifka O, Simony O, Filz F, Hässler J (1889) Relative gravity pendulum measurement. Field Books, 1889,1890, 1891,1894,1895

Part III

Detection and Modelling of Gravity Field Variations

Ground-Satellite Comparisons of Time Variable Gravity: Results, Issues and On-Going Projects for the Null Test in Arid Regions

J. Hinderer, J.-P. Boy, R. Hamidi, A. Abtout, E. Issawy, A. Radwan, K. Zharan, and M. Hamoudi

Abstract

This paper is devoted to the problem of the ground-satellite comparison of time-variable gravity. We first review the different methods used to validate satellite gravity observations (ground truth experiment) and point out possible issues. We first show results obtained in Europe where a moderate amplitude hydrological signal exists using both satellite (GRACE) and surface gravity measurements from the GGP (Global Geodynamics Project) network of superconducting gravimeters. We show also the nice agreement between ground and GRACE observations in Djougou (West Africa) where hydrological changes due to monsoon are important. We finally present on-going projects for the so-called 'null test' which is related to observations in a region with no (or very small) hydrological contribution to gravity. First results for the Sahara (Algeria) are reported and future missions in Egypt and Saudi Arabia briefly introduced.

Keywords

Africa • Ground truth • Hydrology • Satellite gravity • Surface gravity

1 Introduction

The need for calibration/validation (CAL/VAL) was pointed out very early by Watkins et al. (2001) even before the launch in 2002 of the GRACE (Gravity Recovery And Climate Experiment) mission. The GRACE mission has led to numerous papers with a special focus on continental hydrology and glaciology – for a review see e.g. Ramillien et al. (2008). As for any new type of measurement in metrology, it is necessary to test the quality of the data with respect to independent data. Most of the time the satellite data are often compared to predictions of global models for the atmosphere, oceans and continental water, whereas they are supposed to be used as constraints to improve these models. Therefore several studies proposed to collect a set of new, independent and high quality ground data to test the quality of the satellite observations and to investigate how information from space and ground gravity can be combined and optimally used to assess and improve the quality of global models.

Before reviewing the different approaches that have been used in the ground-satellite combined studies, one has first to recall that a true calibration of GRACE solutions is indeed not possible since the satellite gravity changes are inferred from a complex inversion scheme based on the precise orbitography of the satellite using mostly distance changes K-Band Range Rates (KBRR) between the two GRACE satellites. It is hence better to speak of intercomparison of different data sets.

J. Hinderer (✉) • J.-P. Boy
IPGS/EOST, University of Strasbourg/CNRS, Strasbourg, France
e-mail: Jacques.Hinderer@unistra.fr

R. Hamidi
INCT, Service de Gravimétrie, Algiers, Algeria

A. Abtout
Département de Géophysique, CRAAG, Algiers, Algeria

E. Issawy • A. Radwan • K. Zharan
Geodynamics Department, NRIAG, Cairo, Egypt

M. Hamoudi
Université des Sciences et de la Technologie Houari Boumediene,
Laboratoire de Géophysique, Algiers, Algeria

The next section reviews different validation methods that have been proposed so far. We concentrate then on the gravity method where surface gravity measurements are compared to satellite observations. We consider different cases of amplitude of hydrological signal in Europe (moderate), West Africa (large) and arid regions (negligible) in the Sahara (Algeria), Egypt and Saudi Arabia.

2   A Review of Validation Methods

In this section we will review different methodologies that have been used in the comparison between satellite gravity data and ground measurements. Most of these studies are never direct gravity-gravity comparisons but rather rely on the concept of equivalent (to gravity) water mass changes. Among existing studies which are numerous, we can cite in a non exhaustive way the following comparison/validation methods:

- The use of dense networks of in situ borehole records of water levels to extract the water storage changes (WSC) (e.g. Swenson et al. 2006 in Illinois; Shamsudduha et al. 2012 in Bengal Basin); this method is difficult because of the poorly known separation between water table effects (including specific yield uncertainty), soil humidity and surface water;
- The use of various global models for the hydrosphere and cryosphere to compute the satellite gravity changes; this method is not very satisfactory from the conceptual point of view since GRACE satellites were launched in 2002 to improve existing models;
- The use of a man-made 'controlled' experiment like the water impoundment of the Three-Gorges Reservoir in China (with detailed monitoring of water level and ground geodesy) (Boy and Chao 2002; Wang et al. 2011): this method is also difficult because of small spatial extension (typically a 40 km^3 volume and 1,000 km^2 area) and unknown underground contribution;
- The use of Ocean Bottom Pressure (OBP) sensors like in tropical northwest Atlantic in the case of the project MOVE (Meridional Overturning Variability Experiment) (Kanzow et al. 2005), linked to Kuroshio Current in Western Pacific Ocean (Park et al. 2008) or in the Crozet-Kerguelen region (Rietbroek et al. 2006): this method is difficult because of limited number of sensors available in a specific region but led to interesting results;
- The use of GPS observations of ground motion like in the study of hydrology-driven vertical deformation (Davis et al. 2004 in the Amazon basin; van Dam et al. 2007 in Europe; King et al. 2006; Tregoning et al. 2009): this method is indirect (comparing vertical displacement to gravity) but one advantage is that displacement and satellite gravity have similar spatial sensitivity to surface loading; however some GPS stations can also face local effects, especially in coastal regions or on islands. Degree-1 terms or geocenter motions (present in GPS but not in GRACE data) have to be added to GRACE in order to compute surface displacements. Different methodologies have been proposed: using series of geocenter motions from SLR for example, or the Swenson et al. (2008) combination technique. However all these estimates are not perfect and may further complicate this approach;
- The direct gravity-gravity comparison using ground based gravity data (Crossley and Hinderer 2002, 2005; Crossley et al. 2003, 2012; Neumeyer et al. 2008; Abe et al. 2012; Weise et al. 2012) in specific zones of interest where several superconducting gravimeters (SG) and absolute gravimeters (AG) stations are available together with collocated GPS measurements for the vertical displacement correction: this will be our approach here.

3   Ground Truth Using Gravity Data

The method comparing surface gravity measurements to satellite observations is an independent method which is more straightforward in terms of physical quantity (gravity) but is still an indirect comparison since space gravity is derived from orbitography as mentioned before. This method can be applied observing the seasonal hydrological signal of continental size present in many regions (Ramillien et al. 2008). The resolution of GRACE is on the order of a few hundreds of km which means that continental water storage can be retrieved e.g. for major river basins (with surface typically larger than 200,000 km^2). We can introduce three specific cases based on the amplitude of the hydrological signal: small amplitude in arid zones that will correspond to the null test presented later, moderate amplitude like in Europe and large amplitude in the monsoonal zone.

There are numerous studies comparing satellite data to ground SG observations either concerning isolated stations (Neumeyer et al. 2006, 2008; Hinderer et al. 2006; Weise et al. 2009, 2012; Abe et al. 2012) for GRACE or using an EOF (Empirical Orthogonal Function) decomposition of the SG stations in Europe (Crossley et al. 2004, 2009, 2012, 2014; Crossley and Hinderer 2005; Abe et al. 2012; Weise et al. 2012).

A first issue in the ground-orbit comparison is due to the fact that the gravimeter is moving with the Earth's surface while the satellite is moving differently. This means that the surface gravity is changed by the vertical motion on the contrary to the satellite. This leads to different transfer functions between satellite and surface gravity for any surface hydrological loading source and this difference has to be taken into account. It is more important for low harmonic

Fig. 1 First principal component of the EOF decomposition of the gravity changes from GRACE-GRGS solutions (in *brown*) and surface gravity from the European GGP SG network (in *black*) for the 2002–2008 time interval. The sampling rate is 10 days. The two horizontal *red lines* indicate the times where GRACE and GGP are in agreement or not. The level of agreement is 79% when all stations (seven) are kept (reprinted from Fig. 5 in Crossley et al. 2012)
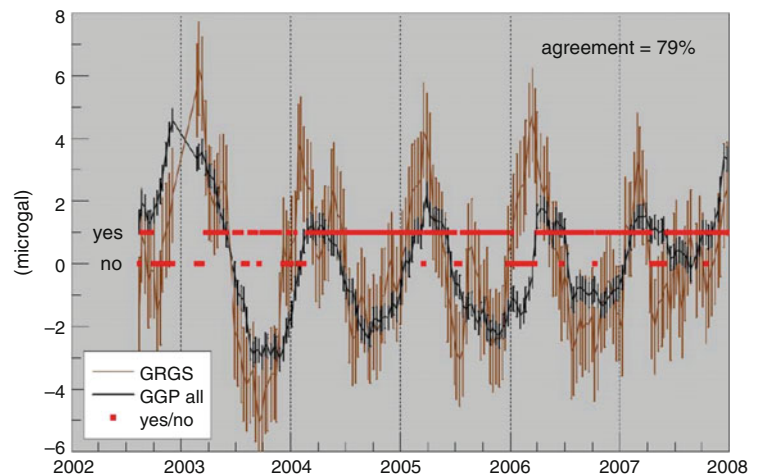
degrees and tends to cancel out for high degrees of the loading source (Hinderer et al. 2007).

A second issue deals with the role played by local hydrology. Several studies investigated this point and it is of course very important to distinguish underground stations where the water layer is above the gravimeter from surface stations where it is below. A clear proof can be found for instance in the Strasbourg SG data which show a gravity decrease when rain occurs that is typical of an underground station (Longuevergne et al. 2009). More insight on the scale problem (local versus global) we are facing in hydrology can also be found in Crossley et al. (2012, 2014) and Van Camp et al. (2014).

3.1 Moderate Amplitude Hydrology: The Case of Europe

An example of a ground gravity validation of GRACE for moderate amplitude hydrology signal in Europe is given in Crossley et al. (2012, 2014). In this study the European network of GGP was used with the following seven SG stations: Bad Homburg (BH), Moxa (MO) and Wettzell (WE) in Germany, Membach (MB) in Belgium, Strasbourg (ST) in France, Medicina (ME) in Italy and Vienna (VI) in Austria (see Fig. 1 in Crossley et al. 2012 for their location). GRACE level-2 products and surface gravity were corrected for tides, atmospheric pressure and polar motion; surface gravity samples initially at 1 min were decimated to 10 day samples like the GRACE-GRGS RL01 solutions (Lemoine et al. 2007). An EOF (Empirical orthogonal function) analysis was done on the period 2002–2008 to infer the time (principal components) and space (eigenvectors) main characteristics of the ground and satellite gravity fields.

Assuming errors of 1.5 μGal for the GRACE-GRGS solutions and 1 μGal for GGP, we derived a quantitative agreement for the first principal component of satellite (GRACE-

GRGS) and ground (GGP) gravity data from the proportion of overlapping data with respect to the whole data. The agreement (see Fig. 1) was found to be quite large, 79% using the seven stations mentioned above (GGP all) and even 90% when keeping only the three surface stations (WE, ME, BH) and excluding the four other ones that are partly or totally underground (ST, MO, MB, VI).

3.2 Large Amplitude Hydrology: The Case of West Africa

As can be seen in Fig. 2, West Africa exhibits a very strong hydrology signal originating from the monsoon with heavy rains during a short period (in late summer). This leads to a seasonal increase in water storage changes (WSC) in the range of 10–25 cm of water equivalent thickness depending on the type of GRACE solutions (GRGS or CSR for instance) (Boy et al. 2012). We used the RL05 of the GRACE official products, i.e. GFZ and UT-CSR with a Gaussian filter of 350 km, the RL03 of the GRGS solution (all with monthly temporal resolution) (Bruinsma et al. 2010) and the global 1-degree mascon solution from NASA/GSFC (Luthcke et al. 2013). As the GRGS solution is regularized and constrained, it does not require any filtering, as stated in Lemoine et al. (2007). Such seasonal changes are also present in continental scale hydrology models like GLDAS/Noah (Rodell et al. 2004) or MERRA/Land (Reichle et al. 2011) for instance. Figure 2 also shows the long term trend (in cm/year) of the GRACE solutions and hydrology models. The color scale means that blue corresponds to an increase in water content.

The concept of water equivalent thickness i.e. water mass changes per surface area (with 1 mm of water corresponding to 1 kg m^{-2}) is classical in the GRACE studies devoted to hydrology where the formula relating the Stokes coefficients of the gravitational potential to surface mass density can be found e.g. in Wahr et al. (1998). In this formula appears a
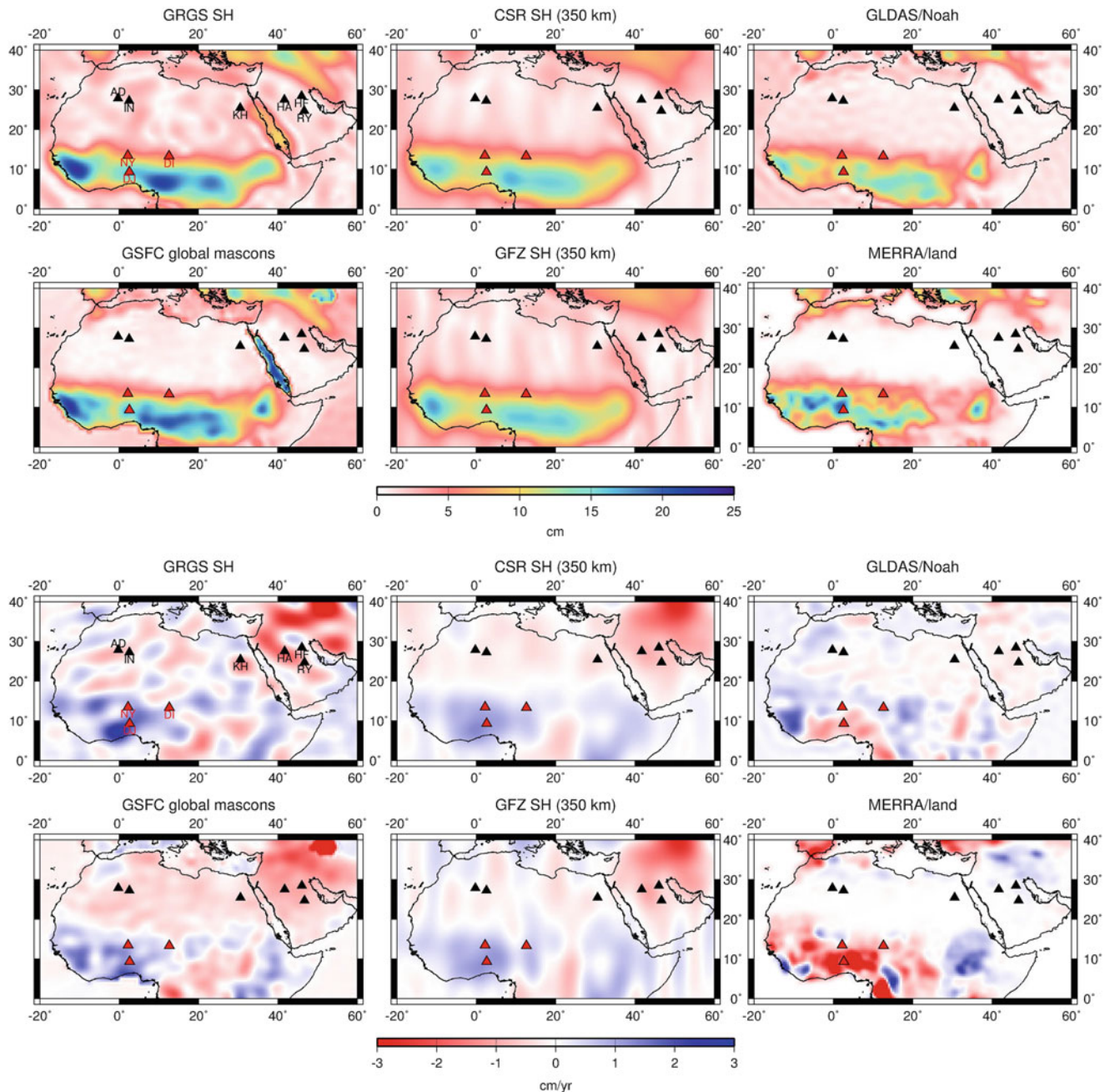
Fig. 2 Hydrology changes in Africa derived from different GRACE solutions (spherical harmonic approach for GRGS, CSR and GFZ, global mascon approach for GSFC) and predicted by GLDAS/Noah model and MERRA/Land. The *top part* depicts the mean annual contribution in cm of water equivalent to gravity, the *bottom part* the trend in cm/year. Locations where AG values are available are indicated by *black triangles* in the arid part [Adrar (AD), In-Salah (IN), Kharga (KH), HA (Hail), RY (Ryad) and HF (Hafar)] and *red triangles* in West Africa [Niamey (NY), Diffa (DI) and Djougou (DJ)]

factor $1 + k'_n$, where k'_n is the elastic load Love number of degree n (in a spherical harmonic decomposition). Following the numerical values computed for k'_n in Table 1 of Wahr et al. (1998), it is easy to see that k'_n is <0.1 for n > 5 and tends to 0 for large n, meaning that elasticity is negligible with respect to the total loading effect (gravitational + elasticity) except for continental size loads (n < 5). This is why

one can convert WSC to gravity changes by using the factor 42 μGal/m which is the classical Bouguer effect of an infinite plate of water density without topography (De Linage et al. 2007).

The ground-orbit comparison in West Africa was one of the targets of the GHYRAF project (Hinderer et al. 2012) where absolute gravity measurements were done with a
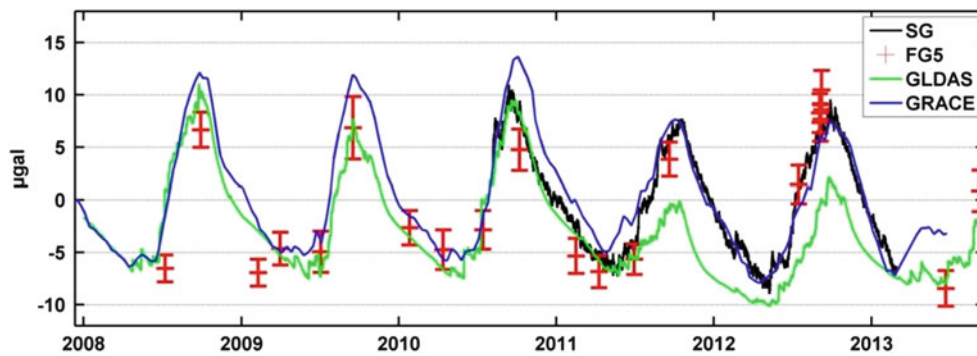
Fig. 3 Gravity changes in Djougou (West Africa) for the 2008–2013 period observed by GRACE (in *blue*), ground gravity from a SG (in *black*) and AG (in *red*) and predicted by GLDAS hydrology model (in *green*)

FG5 AG on two sites in the Sahelian zone (Niamey and Diffa in Niger) and one site in Djougou (Benin) in the monsoonal zone. Several studies related to this region are available in hydrogravimetry (Pfeffer et al. 2011; Genthon et al. 2015; Hector et al. 2013, 2014). We have also set up in Djougou a permanent SG in 2010 in order to follow more precisely the WSC only observed episodically with AG measurements. Figure 3 shows the gravity temporal changes of about 15 μGal amplitude as seen by the SG, AG, GRACE and GLDAS hydrology model although there was only one AG measurement during the humid season in the first years. The 15 μGal amplitude of the seasonal signal is much larger than the 3–4 μGal amplitude observed in the European comparison previously described.

It is interesting to note the relatively close agreement between the surface measurements (SG/AG) and GRACE. On the contrary, more discrepancies exist with the GLDAS hydrology model, especially in summer 2011. As discussed by Hector et al. (2014), the summer 2011 discrepancy has no clear explanation till now. Possible causes could be due to the SG itself (change in drift, wrong corrections of offsets), the impact of a change in vertical displacement (not taken into account) or indeed a problem in the GLDAS modeling.

3.3 Small Amplitude Hydrology: Null Test Experiments in Algeria, Egypt and Saudi Arabia

As can be seen on Fig. 2, Africa and Saudi Arabia arid regions are obvious locations for attempting the null test experiment: comparing on a specific region without rain (or very low rain) ground and satellite data.

This is what we performed in the Sahara desert in South Algeria. We re-measured in 2012 the Adrar and In-Salah sites that were already measured in 2001 when the gravity network of Algeria was upgraded with absolute base stations under the coordination of INCT (Institut National de Cartographie

et de Topographie) in Algiers. We have hence the opportunity to compare gravity changes on a 11 year time span. The results for Adrar are given in Fig. 4 for GRACE using a fully-iterated global 1-degree mascon approach (Luthcke et al. 2013; Loomis and Luthcke 2014) and for our AG measurements. The WSC from Fig. 2 have been converted into surface gravity changes directly comparable to ground observations. The linear drift of −0.27 μGal/year which corresponds to a trend of −6.4 mm/year in WSC is clearly larger than the one predicted for the GLDAS/Noah model which is close to zero but it is still smaller than the value of −0.64 ± 0.19 μGal/year inferred from a standard least-squares fitting of a straight line taking into account the error bars on the two absolute gravity values. Since the 2001 measurement was done in April and the 2012 one in October i.e. with a 6 month shift, there is a seasonal contribution to the measured absolute gravity change but of limited extent according to Fig. 2. This would also lead to reduce the trend in ground gravity and hence make it closer to the GRACE trend.

This is an indication that water depletion in Adrar region is most probably of anthropogenic origin mostly caused by irrigation; very little information is available but Adrar is known to have a strong agricultural development (mainly for export) and irrigation uses the old water circulation system based on 'foggaras' (underground water conduits) (Remini et al. 2010). In the Middle East and North Africa, the water shortage is essentially due to water demand rather than to the climate changes (Droogers et al. 2012). Similar groundwater depletion has been observed elsewhere in the Middle East (Joodaki et al. 2014; Voss et al. 2013; Longuevergne et al. 2012) and in Africa (Ramillien et al. 2014).

If we take into account both Adrar and In-Salah AG changes, the drift is −3.1 ± 3.9 μGal/year close to what GRACE sees but our ground trend is not significant because of its large error. Of course our ground measurements only rely on two AG campaigns in an 11 year interval; moreover two different FG5 models have been used and it is known from the regular intercomparison campaigns (e.g. Jiang et al.

Fig. 4 Gravity changes in Adrar (Sahara, Algeria) as seen by GRACE observations using the global degree-1 mascon approach, predictions from GLDAS/Noah hydrology model and 2 FG5 AG ground measurements
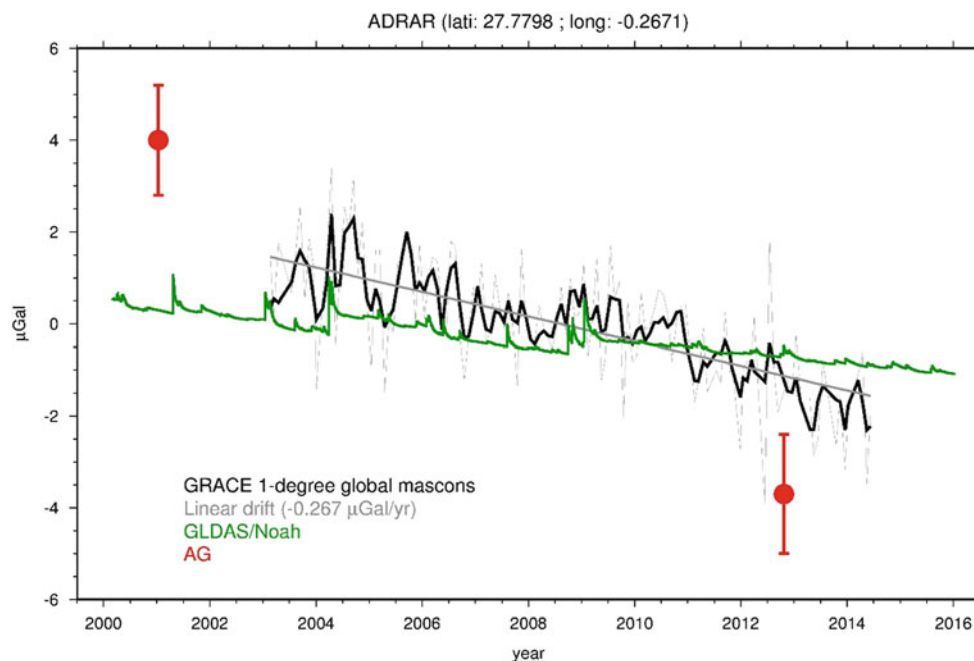
2011) that several µGal discrepancy among different instruments are classical. We clearly need further measurements in the future to have a more precise trend from ground observations. Security reasons have unfortunately postponed such repetitions in South Algeria and we plan to move to two other regions for our null test experiment, namely Egypt and Saudi Arabia.

In Egypt we plan to repeat the absolute gravity measurement in El Kharga, which was done with FG5 AG by NIMA (National Imagery and Mapping Agency now called National Geospatial-Intelligence Agency) in 1997 in the frame of the renewal of the national gravity network of Egypt (Dawod and Alnaggar 2000). An existing cooperation project with NRIAG (National Research Institute for Astronomy and Geophysics) aims to extend the initial absolute base network and to repeat these stations.

In Saudi Arabia, we have identified three locations in the Arabic desert namely Ryad, Hail and Hafar where A10 AG measurements have been performed recently in the renewal of the Saudi Arabian gravity network (Al-Shahrani et al. 2015) under the supervision of GCS (General Commission for Survey) in Ryad.

Like previously in Algeria, GRACE global mascon solutions in the Egyptian and Arabic deserts (Fig. 2) show more water depletion than in the GLDAS/Noah model suggesting additional ground measurements to verify this point.

4   Conclusion

In this paper we first reviewed different methods that have been used to validate satellite gravity measurements. We focused then on the ground validation of satellite gravimetry with surface gravity, which is possible using the hydrological signal of large spatial scale. Even if local effects present on some stations (especially the underground ones) cannot be avoided, the best method is to use EOF decomposition on SG network data in order to extract coherent signals. In this way, the EOF results for ground and satellite gravity will show an agreement depending on the number of underground stations that is however smaller than using only surface stations (or underground stations properly corrected for local hydrology). Following this method a nice quantitative agreement was found in Europe where a moderate amplitude of seasonal hydrology signal exists as well as in West Africa exhibiting a large monsoonal signal. We have also presented on-going experiments for the null test (lack of hydrological signal) in South Algeria. In particular it seems that ground and satellite gravity observations in Adrar (Sahara) suggest more depletion in water storage than predicted in the GLDAS hydrological model and this is most probably caused by intensive irrigation. We finally mention several locations in Egypt and Saudi Arabia where a similar ground-satellite

comparison would be worth to achieve in the future since first AG measurements do exist, the quality of them will have to be checked. Finally, we intend to apply this methodology for validating the forthcoming mission GRACE Follow-On.

References

Abe M et al (2012) A comparison of GRACE-derived temporal gravity variations with observations of six European superconducting gravimeters. Geophys J Int 191:545–556

Al-Shahrani S et al (2015) Introduction to gravity calibration baseline between Jeddah and Taif in Saudi Arabia. In: Conference paper presented at IUGG General Assembly, Prague

Boy J-P, Chao BF (2002) Time-variable gravity signal during the water impoundment of China's Three-Gorges Reservoir. Geophys Res Lett 29(24):2200. doi:10.1029/2002GL016457

Boy J-P, Hinderer J, de Linage C (2012) Retrieval of large scale hydrological signal in Africa from GRACE time-variable gravity fields. Pure Appl Geophys 169(8):1373–1390. doi:10.1007/s00024-011-0416-x

Bruinsma S, Lemoine J-M, Biancale R et al (2010) CNES/GRGS 10-day gravity field models (release 02) and their evaluation. Adv Space Res 45(4):587–601. doi:10.1016/j.asr.2009.10.012

Crossley D, Hinderer J (2002) GGP ground truth for satellite gravity missions. Bull Inf Marées Terr 136:10735–10742

Crossley D, Hinderer J (2005) Using SG arrays for hydrology in comparison with GRACE satellite data, with extension to seismic and volcanic hazards. Korean J Remote Sens 21(1):31–49

Crossley D, Hinderer J, Llubes M, Florsch N (2003) The potential of ground gravity measurements to validate GRACE data. Adv Geosci 1:1–7

Crossley D, Hinderer J, Boy J-P (2004) Regional gravity variations in Europe from superconducting gravimeters. J Geodyn 38:325–342

Crossley D et al (2009) Validation of GRACE data using GGP stations from Europe and Asia. Bull Inf Mar Terr 145:11741–11750

Crossley D et al (2012) A comparison of the gravity field over Central Europe from superconducting gravimeters, GRACE and global hydrological models, using EOF analysis. Geophys J Int 189:877–897. doi:10.1111/j.1365-246X.2012.05404.x

Crossley D et al (2014) Comment on: 'The quest for a consistent signal in ground and GRACE gravity time series', by Michel Van Camp et al. Geophys J Int 199(3):1811–1817

Davis J et al (2004) Climate-driven deformation of the solid earth from GRACE and GPS. Geophys Res Lett 31:L24605. doi:10.1029/2004GL021435

Dawod G, Alnaggar D (2000) Quality control measures for the Egyptian National Gravity Standardization Network (ENGSN97). In: Proceedings of the second international conference on civil engineering, Helwan University, Cairo, 1–3 April, pp 578–587

De Linage C, Hinderer J, Rogister Y (2007) A search for the ratio between gravity variation and vertical displacement due to a surface load. Geophys J Int 171:986–994

Droogers P et al (2012) Water resources trends in Middle East and North Africa towards 2050. Hydrol Earth Syst Sci 16:3101–3114. doi:10.5194/hess-16-3101-2012

Genthon P, Hector B, Luxereau A, Hinderer J (2015) Groundwater recharge by Sahelian rivers-consequences for agricultural development: example from the lower Komadugu Yobe River (Eastern Niger, Lake Chad Basin). Environ Earth Sci 74(2):1291–1302

Hector B et al (2013) Gravity effect of water storage changes in a weathered hard-rock aquifer in West Africa: results from joint absolute gravity, hydrological monitoring and geophysical prospection. Geophys J Int 194(2):737–750. doi:10.1093/gji/ggt146

Hector B et al (2014) Hydro-gravimetry in West-Africa: first results from the Djougou (Benin) superconducting gravimeter. J Geodyn 80:34–49. doi:10.1016/j.jog.2014.04.003

Hinderer J et al (2006) Seasonal changes in the European gravity field from GRACE: a comparison with superconducting gravimeters and hydrology model predictions. J Geodyn 41:59–68

Hinderer J, Crossley D, Warburton R (2007) Superconducting gravimetry. In: Herring T, Schubert G (eds) Treatise on geophysics, vol 3: Geodesy. Elsevier, Amsterdam, pp 65–122

Hinderer J et al (2012) Land water storage changes from ground and space geodesy: first results from the GHYRAF (Gravity and hydrology in Africa) experiment. Pure Appl Geophys 169(8):1391–1410. doi:10.1007/s00024-011-0417-9

Jiang Z et al (2011) Final report on the Seventh International comparison of absolute gravimeters (ICAG 2005). Metrologia 48:246–260

Joodaki G, Wahr J, Swenson S (2014) Estimating the human contribution to groundwater depletion in the Middle East, from GRACE data, land surface models, and well observations. Water Resour Res 50:2679–2692. doi:10.1002/2013WR014633

Kanzow T et al (2005) Seasonal variation of ocean bottom pressure derived from gravity recovery and climate experiment (GRACE): local validation and global patterns. J Geophys Res 110:C09001. doi:10.1029/2004JC002772

King M et al (2006) Choice of optimal averaging radii for temporal GRACE gravity solutions, a comparison with GPS and satellite altimetry. Geophys J Int 166:1–11

Lemoine J-M et al (2007) Temporal gravity field models inferred from GRACE data. Adv Space Res 39:1620–1629. doi:10.1016/j.asr.2007.03.062

Longuevergne L et al (2009) Local and global hydrological contributions to gravity variations observed in Strasbourg. J Geodyn 48(3–5):189–194

Longuevergne L et al (2012) GRACE water storage estimates for the Middle East and other regions with significant reservoir and lake storage. Hydrol Earth Syst Sci 17:4817–4830. doi:10.5194/hess-17-4817-2013. www.hydrol-earth-syst-sci.net/17/4817/2013/

Loomis BD, Luthcke, SB (2014) Optimized signal denoising and adaptive estimation of seasonal timing and mass balance from simulated GRACE-like regional mass variations. Adv Adap Data Anal 6(1). doi:10.1142/S1793536914500034

Luthcke SB et al (2013) Antarctica, Greenland and Gulf of Alaska land-ice evolution from an iterated GRACE global mascon solution. J Glaciol 59(216):613–631

Neumeyer J et al (2006) Combination of temporal gravity variations resulting from superconducting gravimeter (SG) recordings, GRACE satellite observations and global hydrology models. J Geod 79(10–11):573–585. doi:10.1007/s00190-005-0014-8

Neumeyer J et al (2008) Analysis of gravity field variations derived from superconducting gravimeter recordings, the GRACE satellite and hydrological models at selected European sites. Earth Planets Space 60:505–518

Park J-H et al (2008) A comparison of in situ bottom pressure array measurements with GRACE estimates in the Kuroshio extension. Geophys Res Lett 35:L17601. doi:10.1029/2008GL034778

Pfeffer J et al (2011) Hydrological contribution to time – variable gravity: influence of the West African Monsoon in Southwest Niger. Geophys J Int 184(2):661–672

Ramillien G, Famiglietti J, Wahr J (2008) Detection of continental hydrology and glaciology signals from GRACE: a review. Surv Geophys 29(4):361–374. doi:10.1007/s10712-008-9048-9

Ramillien G, Frappart F, Seoane L (2014) Application of the regional water mass variations from GRACE satellite Gravimetry to large-scale water management in Africa. Remote Sens 2014(6):7379–7405. doi:10.3390/rs6087379

Reichle RH et al (2011) Assessment and enhancement of MERRA land surface hydrology estimates. J Clim 24:6322–6338

Remini B, Achour B, Kechad R (2010) Foggara en Algérie: un patrimoine hydraulique mondial. J Water Sci 23(2):105–117

Rietbroek R et al (2006) Comparison of in situ bottom pressure data with GRACE gravimetry in the Crozet-Kerguelen region. Geophys Res Lett 33:L21601. doi:10.1029/2006GL027452

Rodell M et al (2004) The global land data assimilation system. Bull Am Meteorol Soc 85(3):381–394

Shamsudduha M, Taylor RG, Longuevergne L (2012) Monitoring groundwater storage changes in the highly seasonal humid tropics: validation of GRACE measurements in the Bengal Basin. Water Resour Res 48:W02508. doi:10.1029/2011WR010993

Swenson S et al (2006) A comparison of terrestrial water storage variations from GRACE with in situ measurements from Illinois. Geophys Res Lett 33:L16401. doi:10.1029/2006GL026962

Swenson S, Chambers D, Wahr J (2008) Estimating geocenter variations from a combination of GRACE and ocean model output. J Geophys Res 113:B08410. doi:10.1029/2007JB005338

Tregoning P et al (2009) Glacial isostatic adjustment and nonstationary signals observed by GRACE. J Geophys Res 114:B06406. doi:10.1029/2008JB006161

Van Camp M et al (2014) The quest for a consistent signal in ground and GRACE gravity time series. Geophys J Int 199(3):1811–1817

van Dam T, Wahr J, Lavallée D (2007) A comparison of annual vertical crustal displacements from GPS and gravity recovery and climate experiment (GRACE) over Europe. J Geophys Res 112:B03404. doi:10.1029/2006JB004335

Voss KA et al (2013) Groundwater depletion in the Middle East from GRACE with implications for transboundary water management in the Tigris-Euphrates-Western Iran region. Water Resour Res 49. doi:10.1002/wrcr.20078

Wahr J, Molenaar M, Bryan F (1998) Time-variability of the earths gravity field: hydrological and oceanic effects and their possible detection using GRACE. J Geophys Res 103:30205–30230

Wang X, et al (2011) Gravity recovery and climate experiment (GRACE) detection of water storage changes in the three Gorges reservoir of China and comparison with in situ measurements. Water Resour Res 47:W12502. doi:10.1029/2011WR010534

Watkins M et al (2001) Time and space validation of the new gravity missions, EOS, AGU, 82 (47), Fall Meet. Suppl

Weise A et al (2009) Terrestrial gravity observations with superconducting gravimeters for validation of satellite-derived (GRACE) gravity variations. J Geodyn 48(3–5):325–330

Weise A et al (2012) Tackling mass redistribution phenomena by time-dependent GRACE and terrestrial gravity observations. J Geodyn 59–60:82–91

Impact of Groundtrack Pattern of Double Pair Missions on the Gravity Recovery Quality: Lessons from the ESA SC4MGV Project

S. Iran Pour, M. Weigelt, T. Reubelt, and N. Sneeuw

Abstract

The launch of the GRACE mission brought a broad interest within the geophysical community in monitoring temporal gravity field variations. Due to the limited lifetime of GRACE, several studies have been conducted for the search of optimal GRACE follow-on and future satellite gravity missions. These studies mainly discuss the use of alternative formations like Pendulum, Cartwheel and LISA as well as the double inline pair missions with different orbits as a possible substitute of the current GRACE mission. The double satellite pair configuration in a so-called Bender constellation, however, is currently in the focus of research into time-variable gravity field recovery by future satellite missions, where the primary objective is to achieve higher temporal and spatial resolutions.

When looking for optimal double inline missions, one important aspect is the impact of the groundtrack pattern of such missions on the quality of gravity recovery. The investigation of pattern distribution impact on the recovery quality may lead to a better understanding of orbital parameter optimization. This study, in particular, investigates the influence of relative differences between the ascending nodes (longitude) in a double pair mission. The research aims to show how the variations in ascending node difference change the quality of gravity solutions to the large extent. We also show the impact of the time-variable gravity field itself on the error level of the gravity solutions, i.e. how the quality of the gravity field changes simply by changing the signal being sampled, but holding the sampling constant.

S. Iran Pour (✉) • N. Sneeuw
Institute of Geodesy, University of Stuttgart, Geschwister-Scholl-Str. 24D, 70174 Stuttgart, Germany
e-mail: iranpour.siavash@gmail.com

M. Weigelt
German Federal Agency for Cartography and Geodesy (BKG), Frankfurt am Main, Germany

T. Reubelt
Landesamt für Geoinformation und Landentwicklung Baden-Württemberg, Büchsenstrasse 54, 70174 Stuttgart, Germany

1 Introduction

Several previous studies like Sharifi et al. (2007), Bender et al. (2008), Wiese et al. (2009), Elsaka (2010), Wiese et al. (2011), Ellmer (2011), Elsaka et al. (2012), Iran Pour et al. (2013), Reubelt et al. (2014), Elsaka et al. (2014) and NGGM-D (2014) investigated the performance of satellite gravity missions of the next generations, where alternative (advanced) formations like Pendulum, Cartwheel, LISA as well as dual mission scenarios (two pairs of inline formation) have been considered. Additionally, the ESA project "Assessment of a Next Generation Mission

for Monitoring the Variations of Earth's Gravity" (SD-RP-AI-0668) was conducted for investigation of science requirements, performance criteria and design of future satellite gravity missions, where two advanced formations and a Bender configuration consisting of two pairs of collinear satellites with one polar pair and one moderately inclined pair, were briefly discussed (Anselmi et al. 2011). In some of these studies such as Wiese et al. (2011), Ellmer (2011) and Iran Pour et al. (2013), a range of parameter choices for such dual satellite missions for full repeat period and sub-Nyquist solutions has been suggested.

In most of the studies above, the individual constellation scenarios were chosen through the (rough) assessment of sampling behaviour of the missions. However, the works by Wiese et al. (2011); Ellmer (2011) and Iran Pour et al. (2013) have particularly discussed and considered some performance criteria for their optimal dual mission scenario search strategies. Furthermore, the geopotential recovery from short repeat cycle orbits and sub-Nyquist gravity recovery by GRACE and future missions have been discussed by Wagner et al. (2006), Weigelt et al. (2012) and Iran Pour et al. (2013).

It should be mentioned that the use of alternative formations such as Pendulum or Cartwheel is currently not of the community interest, since several technical studies like NGGM-D (2014) show the technical implementation of such formations is still very challenging. Therefore, the current researches now focus on the orbit optimization of the dual pair inline missions. On the other hand, the search space of the orbital parameters of the double pair missions to be optimized is vast and the isolated influence by individual parameters on the quality of the gravity products is difficult to be seen. That is specially the case when the satellite orbits have different drift rates of node and hence the gravity recovery quality changes with time. For the single near-polar pair mission, one can associate the time and space evolution of the groundtrack pattern with the gravity product quality much easier (Iran Pour et al. 2013). But, in case of double pair mission with different inclination angles of the two pairs, the task is not very straightforward. This study, then, aims to investigate the impact of that time-variable change of the groundtrack patterns on the quality of gravity solutions. We will show how the change of longitude of ascending node difference of the two pairs in a double pair mission affects the results. We also show the influence of the time-variable gravity field itself on the error level of the gravity products. At the end, some suggestions for orbital parameters optimization are discussed.

2 Geophysical Input Models and Gravity Recovery Simulation

The dominant mass variations of hydrology, ice and solid Earth of the Earth system are modeled for the simulation

Table 1 Model definition for hydrology, ice, solid Earth (Gruber et al. 2011), ocean tide model error as difference of two tide models EOT08a (Savchenko and Bosch 2008) and GOT4.7 (Ray 2008) and AO error (ESA-SC4MGV 2015)

	Model
Hydrology	PCR-GLOBWB driven with
	ECMWF meteorological data
Ice	ECMWF operational analysis
Solid Earth	DEOS Delft University of Technology
Ocean tide error	EOT08a – GOT4.7
Atmosphere-ocean error	IAPG (TU Munich)

environment. This paper makes use of the time-variable gravity field models generated within the ESA-project "Monitoring and Modeling Individual Sources of Mass Distribution and Transport in the Earth System by Means of Satellites" (ESA-contract 20403, van Dam et al. 2008) refined within the ESA-project "Assessment of a Next Generation Gravity Mission for Monitoring the Variations of Earth's Gravity Field" (ESA-contract No. 22643/09/NL/AF, Anselmi et al. 2011 and Gruber et al. 2011). These models are provided as spherical harmonic coefficients up to degree and order 180 at 6 h intervals. The time-span applied in our study is between January and December 1996. The ocean tide error is assumed as the difference between two ocean tide models (Table 1), where it is considered as an important source for aliasing of the high frequency signals to the low frequency signals (Visser et al. 2010). Furthermore, the atmosphere-ocean error (AO error) product from IAPG (TU Munich) is employed for the forward modeling, where the error model is defined as two atmosphere models difference (ECMWF – NCEP) plus 10% of the ocean signal of the model OMCT. Finally, all geophysical models are smoothed by Gaussian filter of radius $40,000/2L_{\max}$ [km] to avoid ringing effects (Gibbs phenomenon) caused by truncation error. For the gravity recovery simulation, we use a nominal circular orbit simulation package of so-called Reduced-Scale Tool, RST (previously called Quick-look Tool, QLT) where the satellite orbits are considered as nominal (only influenced by J_2 effect), i.e. the semi-major axis, inclination angle and eccentricity of the satellites are not time-variable parameters (Iran Pour et al. 2013). In fact, the RST simulation software for time-variable gravity field analysis from ll-SST missions (low-low satellite-to-satellite tracking), as a closed loop tool, makes use of the observation equation for range acceleration:

$$\ddot{\rho} - \frac{1}{\rho(t)}\left((\Delta\dot{\mathbf{r}}_{12})^2 - \dot{\rho}^2(t)\right) = \mathbf{e}_{12} \cdot (\nabla V(\mathbf{r}_2(t)) - \nabla V(\mathbf{r}_1(t)))$$

(1)

where ρ is range, $\dot{\rho}$ is range rate, $\ddot{\rho}$ is range acceleration, $\Delta\dot{\mathbf{r}}_{12}$ is the relative velocity vector, and $\mathbf{e}_{12}$ is the unit vector of the inter-satellite distance of one pair. The gradients of

the potential V at the satellites' positions for the epoch t are given by $\nabla V(\mathbf{r}_1(t))$ and $\nabla V(\mathbf{r}_2(t))$.

The right side of the equation is calculated at the nominal positions of the satellites for the time interval of interest. The time-variable potential of the Earth at the positions of the satellites is calculated by the provided time-variable gravity field models at those epochs. The calculated values for the right side of the equation are afterwards set to the left side as the observables at those epochs. Then, the gravitational potential, in terms of spherical harmonics coefficients, is estimated through the system of equations for that time interval. Although the assumption of keeping the satellites in a perfect nominal orbit is not realistic, the tool provides a quick comparison of gravity recoveries of different formations, which can later be studied in more details by full-scale recovery tools. An evaluation of the RST is made with the ll-SST acceleration approach applied to orbits from real orbit integration by Iran Pour et al. (2013). Despite the differences between both methods, Iran Pour et al. (2013) showed a good agreement between the results of the two approaches for gravity recoveries.

3 Drifting Orbits of Satellite Pairs

As we expect, the groundtrack pattern distribution of double pair mission changes with time. Obviously, the main reason for this variation is the different gap evolution of the repeat orbits of the two pairs. One important factor for the groundtrack pattern variation is simply the change of the difference of the longitude of the ascending nodes between the satellite pairs ($\Delta\Omega$) as well as the mean anomaly between the pairs (ΔM), where the parameters Ω and M of each satellite pair change within the time, as follows:

$$\dot{\Omega} = \frac{1}{na^2\sqrt{1-e^2}\sin I}\frac{\partial T}{\partial I} \tag{2a}$$

$$\dot{M} = n - \frac{1-e^2}{na^2 e}\frac{\partial T}{\partial e} - \frac{2}{na}\frac{\partial T}{\partial a} \tag{2b}$$

with a, e and I for respectively the semi-major axis, eccentricity (here sets to zero for the circular orbits) and inclination angle, $n = \sqrt{\frac{GM}{a^3}}$ as the mean motion of the satellite and T as the disturbing potential field.

Therefore, from the relative variations of the parameters Ω and M of the two pairs, the time evolution of groundtrack pattern of the dual pair mission scenarios is expected to be more complicated than the single pair cases.

Equation (2) expresses that a difference in drift rate of the node between the two pairs cannot be avoided, as the pairs have different inclination in Bender-type formation. However, we can avoid a difference in drift rate of mean

Table 2 A selected double pair mission scenario

Scenario	β/α (rev./day)	Inclination (deg.)	Altitude (km)	Sub-cycle (day)	ρ (km)
Dual pair	172/11	92	361.9	3	100
	460/29	115	342.5	7	

The baseline constellation of ESA-SC4MGV project (ESA-SC4MGV 2015)

anomaly, specifically if the two pairs are placed at the same altitude.

4 Results

4.1 Impact of the Groundtrack Pattern Variations on Quality of the Gravity Solutions

In order to see the impact of $\Delta\Omega$ and ΔM on the recovery quality, we analyse the solutions of a selected double pair mission scenario (constellation scenario of Table 2) where only the relative Keplerian parameters $\Delta\Omega$ and ΔM change. As mentioned before, the gravity recovery of the scenario is simulated by "Reduced-Scale Tool" (RST) in which the satellites are orbiting the Earth in nominal orbits (only influenced by J_2 effect). Here, we make use of "hydrology + ice + solid Earth" (HIS) geophysical signals as well as AO-error and ocean tide model error for the forwarding models of our simulation tool. Figure 1 illustrates the effect for three different solutions (maximum spherical harmonics (SH) degree and order 40, 100 and 130), where the influence of changes in $\Delta\Omega$ on the solutions quality can be clearly seen. It is also observed that the impact of ΔM is not significant. Please note that by the term "error" we mean the difference between gravity recovery (by satellites) and mean of the input models. The figure also shows that the minimum of the errors happens at $\Delta\Omega$ around 80 and 240 degrees. This feature was also seen in the other tests by running the gravity solutions of several other satellite scenarios. At the time, the reason for this behavior is not well understood by the authors, therefore more works will be planned for addressing the issue in the future.

The pure impact of groundtrack pattern evolution on the gravity recovery quality can be also seen from another view angle: Fig. 2 illustrates the recovery error of HIS signals in terms of geoid height RMS of one year time-series of 10-day solutions of the aforementioned scenario in which the HIS input signals within every 10 days are intentionally taken constant (i.e. no variation for the 10-day input signals within one year). That means only the groundtrack pattern of every 10-day solution is different from the other solutions, and not the input signals themselves. However, as it is seen in the
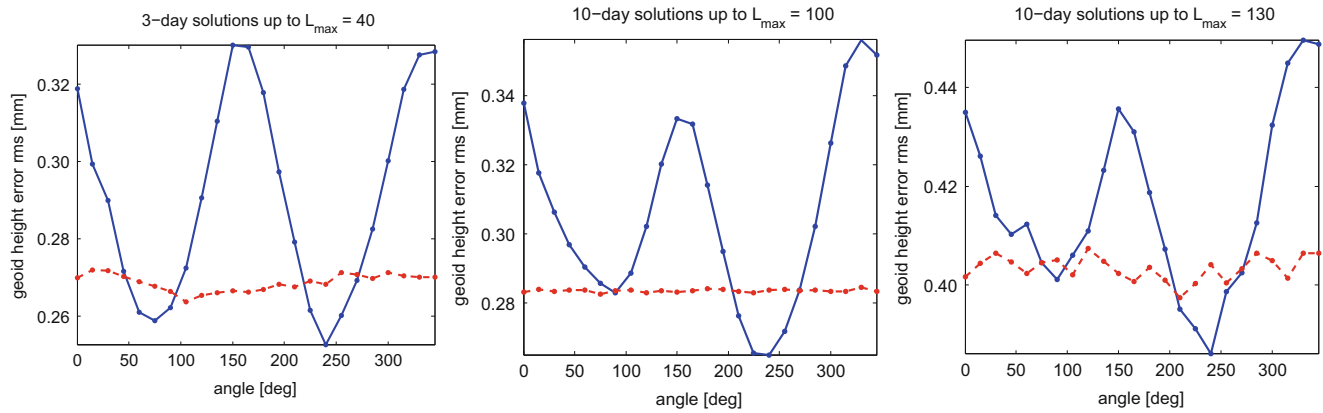
Fig. 1 Quality change of the gravity solutions within the changes in $\Delta\Omega$ (*blue line*) and ΔM (*red line*)
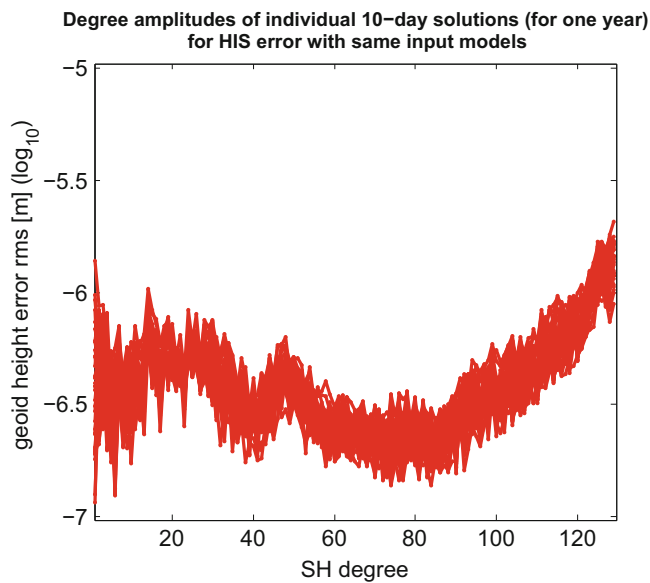
Fig. 2 Pure effect of the groundtrack pattern on the gravity solutions: recovery error spread of 1-year time-series of 10-day solutions of the Table 2 scenario with the same input HIS signals (solutions up to SH degree and order 130)

Fig. 3 Pure effect of the time-variable gravity field on the gravity solutions: recovery error spread of 1-year time-series of 10-day solutions of the Table 2 scenario with the same groundtrack pattern within all the solutions (solutions up to SH degree and order 130)

figure, we have still a spread of error curves (the red band) which means that the quality of the solutions varies by the pure effect of the groundtrack pattern evolution.

4.2 Impact of Gravity Field Variations on Quality of the Gravity Solutions

It would be of our interest to also investigate the pure effect of time-variable gravity field when the groundtrack pattern does not change within the gravity solutions. For this reason, we run our RST with changing gravity field of the HIS signals where within each 10-day solution, the Keplerian parameters for our nominal orbit simulation tool remain the same. The

pure influence of time-variable gravity field is then illustrated in the Fig. 3 where an error curves spread (red band) in terms of geoid height RMS is still observed. That means by keeping the groundtrack fixed, we still have variations in quality of gravity recovery.

5 Summary and Discussion

This paper presented the impact of groundtrack pattern evolution and time-variable gravity field on the quality or error level of the gravity solutions. In case of the groundtrack impact, it is expected that the evolution of spatial-temporal sampling affects the quality of the gravity products. The

sampling pattern of each satellite pair of a double pair mission with different repeat periods evolves differently in time domain. Therefore, one should expect that within a specific time-interval gravity solution, e.g. 10-day solution, the groundtrack pattern changes. Another reason for this variation is that the difference of the longitude of ascending nodes of the two pairs ($\Delta\Omega$) changes within the time. That means the two orbits have different drifting rates, and hence different sampling pattern within each time window is expected. This fact makes the task of orbital parameters optimization challenging. In particular, that is the case for some of the optimal orbit search strategies such as genetic algorithm where we usually do the optimization for a single gravity solution and do not consider the time evolution of the solutions (time-series of gravity products) in our optimization procedure. On the other hand, this fact that the orbits of the single satellite pairs of a double pair mission have different drifting rates, opens new possibilities for orbit design in which one looks for specific spatial shift of the groundtrack pattern within the time intervals. In this case, by tuning the orbital parameters such as inclination angle of the satellite pairs and thus the orbital drifts, a desirable spatial sampling pattern shift can be achieved. This task was very well addressed in Wiese et al. (2011). Obviously for the future works and deeper insight into the subject, further investigations should be directed in this way.

References

Anselmi A, Visser PNAM, van Dam T, Sneeuw N, Gruber T, Altès B, Christophe B, Cossu F, Ditmar PG, Murböck M, Parisch M, Renard M, Reubelt T, Sechi G, Texieira da Encarnação JG (2011) Assessment of a next generation gravity mission to monitor the variations of Earth's gravity field, ESA-contract No. 22643/09/NL/AF, Executive Summary, Thales Alenia Space report SD-RP-AI-0721

Bender PL, Wiese DN, Nerem RS (2008) A possible dual-GRACE mission with 90 degree and 63 degree inclination orbits. In: Proceedings of the third international symposium on formation flying, missions and technologies, pp 1–6. ESA/ESTEC, Noordwijk

Ellmer M (2011) Optimization of the orbit parameters of future gravity missions using genetic algorithms. MSc thesis, University of Stuttgart. http://elib.uni-stuttgart.de/opus/volltexte/2012/7122/pdf/Ellmer.pdf

Elsaka B (2010) Simulated satellite formation flights for detecting temporal variations of the Earth's gravity field. PhD thesis, University of Bonn. http://hss.ulb.unibonn.de/2010/2151/2151.htm

Elsaka B, Kusche J, Ilk KH (2012) Recovery of the Earth's gravity field from formation-flying satellites: temporal aliasing issues. Adv Space Res 50(11). doi:10.1016/j.asr.2012.07.016

Elsaka B, Raimondo J-C, Brieden Ph, Reubelt T, Kusche J, Flechtner F, Iran Pour S, Sneeuw N, Müller J (2014) Comparing seven candidate mission configurations for temporal gravity field retrieval through full-scale numerical simulation. J Geodesy 88(2):31–43. doi:10.1007/s00190-013-0665-9

ESA-SC4MGV Study Team with contributions by Iran Pour S, Reubelt T, Sneeuw N, Daras I, Murböck M, Gruber T, Pail R, Weigelt M, van Dam T, Visser P, Texieira da Encarnação J, van den IJssel J, Tonetti S, Cornara S, Cesare S (2015) Assessment of satellite constellations for monitoring the variations in Earth's gravity field. ESA-SC4MGV project, Final Report

Gruber T, Bamber JL, Bierkens MFP, Dobslaw H, Murböck M, Thomas M, van Beek LPH, van Dam T, Vermeersen LLA, Visser PNAM (2011) Simulation of the time-variable gravity field by means of coupled geophysical models. Earth Syst Sci Data 3:19–35. doi:10.5194/essd-3-19-2011

Iran Pour S., Reubelt T, Sneeuw N (2013) Quality assessment of sub-Nyquist recovery from future gravity satellite missions. Adv Space Res 52(5). doi:10.1016/j.asr.2013.05.026

NGGM-D Study Team with contributions by Baldesarra M, Brieden P, Danzmann K, Daras I, Doll B, Feili D, Flechtner F, Flury J, Gruber T, Heinzel G, Iran Pour S, Kusche J, Langemann M, Löcher A, Müller J, Müller V, Murböck M, Naeimi M, Pail R, Raimondo J-C, Reiche J, Reubelt T, Sheard B, Sneeuw N (2014) e2motion - Earth system mass transport mission - concept for a next generation gravity field mission. Final Report of Project "Satellite Gravimetry of the Next Generation (DLR NGGM-D)", Munich 2014. ISBN 978-3-7696-8597-8

Savcenko R, Bosch W (2008) EOT08a – empirical ocean tide model from multi-mission satellite altimetry. Report No. 81, Deutsches Geodätisches Forschungsinstitut (DGFI), München

Sharifi M, Sneeuw N, Keller W (2007) Gravity recovery capability of four generic satellite formations. In: Kilicoglu A, Forsberg R (eds) Gravity field of the Earth, general command of mapping. ISSN 1300-5790. Special issue 18, pp 211–216

Ray R (2008) GOT4.7 (2008) (Private communication), extension of Ray R, A global ocean tide model from Topex/Poseidon altimetry. GOT99.2 NASA Tech Memo 209478, Sept. 1999

Reubelt T, Sneeuw N, Iran Pour S, Hirth M, Fichter W, Müller J, Brieden Ph, Flechtner F, Raimondo J-C, Kusche J, Elsaka B, Gruber T, Pail R, Murböck M, Doll B, Sand R, Wang X, Klein V, Lezius M, Danzmann K, Heinzel G, Sheard B, Rasel E, Gilowski M, Schubert C, Schäfer W, Rathke A, Dittus H, Pelivan I (2014) Future gravity field satellite missions. In: Flechtner F, Sneeuw N, Schuh W-D (eds) Observation of the system Earth from space - CHAMP, GRACE, GOCE and future missions. GEOTECHNOLOGIEN Science Report No. 20, Series "Advanced Technologies in Earth Sciences". Springer, Berlin. ISBN 978-3-642-32134-4

van Dam T, Visser P, Sneeuw N, Losch M, Gruber T, Bamber J, Bierkens M, King M, Smit M (2008) Monitoring and modelling individual sources of mass distribution and transport in the Earth system by means of satellites. ESA-contract 20403, Final Report

Visser PNAM, Sneeuw N, Reubelt T, Losch M, van Dam T (2010) Space-borne gravimetric satellite constellations and ocean tides: aliasing effects. Geophys J Int 181:789–805

Wagner C, McAdoo D, Klokočník J, Kostelecký J (2006) Degradation of geopotential recovery from short repeat-cycle orbits: application to GRACE monthly fields. J Geodesy 80(2):94–103. doi:10.1007/s00190-006-0036-x

Weigelt M, Sneeuw N, Schrama EJO, Visser PNAM (2012) An improved sampling rule for mapping geopotential functions of a planet from a near polar orbit. J Geodesy. doi:10.1007/s00190-012-0585-0

Wiese DN, Folkner WM, Nerem RS (2009) Alternative mission architectures for a gravity recovery satellite mission. J Geodesy 83:569–581. doi:10.1007/s00190-008-0274-1

Wiese DN, Nerem RS, Lemoine FG (2011) Design considerations for a dedicated gravity recovery satellite mission consisting of two pairs of satellites. J Geodesy 86:81–98. doi:10.1007/s00190-011-0493-8

A Posteriori De-aliasing of Ocean Tide Error in Future Double-Pair Satellite Gravity Missions

W. Liu, N. Sneeuw, S. Iran Pour, M.J. Tourian and T. Reubelt

Abstract

Ocean tides cause notable aliasing errors in the gravity field from single pair space-borne gravimetry missions like GRACE. Several studies into future gravity missions have shown that constellations with two or more GRACE-like tandems lead to a significant reduction of aliasing error from all kinds of high-frequency signal sources. Despite such reduction, tidal aliasing will remain an error source. We here investigate the efficiency of tidal error de-aliasing in the post-processing mode for such future double-pair missions. To that purpose, we analyze how a certain satellite mission samples each tidal constituent. Given the repeat orbit patterns and the observation time span, we examine and model the alias periods and amplitudes constituent by constituent based on data-driven analysis. Results show that a double-pair formation has indeed better de-aliasing properties than a single-pair formation in terms of distribution and amplitude of ocean tide aliasing error. After least-squares (LS) spectral estimation of the tidal aliases at the derived alias periods, the aliasing error is reduced significantly.

Keywords

De-aliasing • Future mission • Ocean tides • Satellite gravity

1 Introduction

Over the past few years GRACE has played an irreplaceable role in observing mass changes. Due to under-sampling from satellite orbit, high-frequency ocean tidal signal will alias into the all wavelengths of the gravity signal with probably different magnitudes. Likewise, errors in ocean tide models, used for de-aliasing in the gravity field retrieval, will directly alias into the recovered gravity field. When laser ranging is applied in a future low-low satellite-to-satellite tracking (SST) mission, the ocean tide aliasing errors are expected to be two orders of magnitude larger than the gravity recovery error caused by laser range observation noise (Flechtner et al.

2016). Thus, reducing ocean tide aliasing errors is of great importance. Several researches have focused on the analysis and explanation of the ocean tide aliasing error (Han et al. 2004; Seo et al. 2008a,b; Chen et al. 2009; Visser et al. 2010).

In case of repeat orbits, the spectrum of the tidal aliasing periods is known and the tide errors can be corrected from the recovered gravity field in a post-processing mode. However, the correction process is limited by the fact that (1) some tidal alias periods are close to periods of signals of interest and thus difficult to be separated, and (2) some alias periods may be longer than the observation time span. Beyond these limitations, we here investigate the efficiency of tidal error de-aliasing in the post-processing mode for future double-pair missions. In particular, we analyze how a double-tandem mission samples the six main tidal constituents M_2, N_2, S_2, O_1, P_1 and Q_1, as opposed to a single pair. Assuming a repeat orbit pattern, we examine and model the aliasing periods and their amplitudes for each constituent.

W. Liu (✉) • N. Sneeuw • S. Iran Pour • M.J. Tourian • T. Reubelt
Institute of Geodesy, University of Stuttgart, Geschwister-Scholl-Str. 24D, 70174 Stuttgart, Germany
e-mail: wei.liu@gis.uni-stuttgart.de

This paper is organized as follows: data and scenarios applied in the simulation are described in Sect. 2. Section 3 briefly outlines the methodology for alias period computation and tidal error de-aliasing. In Sect. 4, alias periods of six ocean tide constituents are determined for each scenario, based on which de-aliasing is performed and results are analyzed. Finally, we summarize this study and draw the conclusions in Sect. 5.

2 Simulation Setup

Gravity field recovery simulations were conducted with quick-look simulation software in a closed-loop. This software assumes a nominal repeat orbit for satellites flying in low-low satellite-to-satellite tracking formation. Residuals of potential difference at simulated orbits for two satellites are calculated as follows:

$$dV_{1,2}(t) = \delta V_1(t) - \delta V_2(t), \quad (1)$$

where δV_1 and δV_2 are perturbed gravity potential at the positions of two tracking satellites $(r_i, \theta_i, \lambda_i)(i = 1, 2)$, and t is the sampling epoch. The perturbed gravity potential is calculated from the time-variable gravity field models, ocean tide models in this case, at each epoch. Afterwards, spherical harmonic coefficients are estimated by taking the $dV_{1,2}$ as observations. Despite the embedded simplification, the quick-look tool provides realistic error levels. An evaluation of the simulation software was made with the ll-SST acceleration approach applied to orbits from real orbit integration by Iran Pour et al. (2013) and it showed a good agreement between the results of the two approaches for gravity recoveries.

In order to investigate how an individual tidal constituent is observed by single-pair and double-pair missions, GRACE-type and Bender formations are simulated. The so-called Bender scenario is a promising future formation with two pairs of tandem satellites, which might have several advantages over a single-pair formation (Wiese et al. 2012):

– increasing time resolution and spatial resolution within the same time span,
– reducing striping behavior.

The simulated missions are inline, circular and in repeat orbit mode, i.e. the ground-track pattern of the orbit repeats every β revolutions and α nodal days. The following orbit parameters are chosen according to a scenario selection by the ESA project "Assessment of Satellite Constellations for Monitoring the Variations in Earth's Gravity (SC4MGV)" (ESA-SC4MGV 2015), cf. Table 1. These parameters were

Table 1 Main orbit parameters

	β / α	I	Altitude [km]
Polar pair	172/11	92°	362
Inclined pair	460/29	115°	342

selected using a genetic algorithm with a cost function of minimum global geoid height RMS. For more details please refer to ESA-SC4MGV (2015).

In GRACE practice, ocean tide de-aliasing is conducted during the main processing stage of gravity field recovery with ocean tide models. Because of the under-sampling of ocean tides by satellites and the limited accuracy of de-aliasing ocean tide model, errors are left in the recovered gravity field. This study aims to deal with these errors. Here we assume the difference of two ocean tide models, EOT08a (Savcenko and Bosch 2008) and GOT4.7 (Ray 1999), as a realistic tidal model error, that will become aliased in the recovered gravity fields:

$$\delta C_{lm} = C_{lm}^{\text{EOT08a}} - C_{lm}^{\text{GOT4.7}}$$
$$\delta S_{lm} = S_{lm}^{\text{EOT08a}} - S_{lm}^{\text{GOT4.7}}, \quad (2)$$

in which C_{lm} and S_{lm} are the normalized spherical harmonic (SH) of degree l and order m. As EOT08a and GOT4.7 tide models assimilated much of same data from Altimetry satellites, the errors may be underestimated.

We feed the simulation only with one single ocean tide constituent at a time and no other time-variable gravity signals are included, so the dominant aliasing spectrum can be identified for each tidal constituent. In this case, the recovered gravity field only contains the ocean tide information, showing its characteristics in two aspects: (1) single-pair vs. double-pair, (2) before de-aliasing vs. after de-aliasing. We want to remind readers that in our research, de-aliasing means removing the aliasing errors caused by ocean tide model errors via post-processing. The simulation setup is summarized in Table 2. The six constituents in Table 2 together with K_1 and K_2 account for the major eight constituents for ocean tides which have relative large magnitudes comparing with the other constituents. The alias periods of K_1 and K_2 are far larger than the length of time series in our simulations and, thus, the K_1- and K_2-aliases cannot be de-aliased. So K_1 and K_2 are not further considered in this research.

3 Methodology

As the periods of the ocean tidal constituents are known, the aliasing period T_a of single-pair satellites with repeat orbits

Table 2 Simulation setup in both scenarios

Scenario	Formation type	Input	Tide component	Recovery period	Mission duration
Single pair	Polar pair	Only ocean tide error : EOTO8a $-$ GOT4.7	M_2, N_2, S_2 O_1, P_1, Q_1	11 days	352 days
Double pair	Polar + inclined pair				
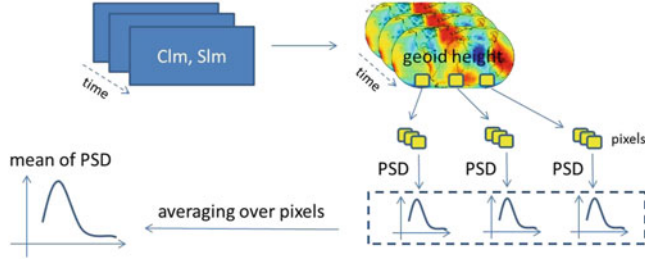
Fig. 1 Flow chart of computing mean of PSD in geoid height

can be calculated a prior by formula (Parke et al. 1987; Han et al. 2004):

$$\frac{1}{T_a} = \text{abs}\left[\text{mod}\left(\frac{1}{T} + \frac{1}{T_N}, \frac{2}{T_N}\right) - \frac{1}{T_N}\right], \qquad (3)$$

in which T is the signal period, and T_N is the Nyquist period which is two times the sampling period. In the following text we refer to this formula as *classic formula* (CF).

Nevertheless, the applicability of the classic formula needs to be investigated further for a double-tandem gravity mission, consisting of two different repeat orbits. Therefore, we develop a method which acquires the alias periods based on the recovered gravity field time series by computing the mean power spectral density (PSD) in terms of geoid height. Figure 1 shows the main idea of obtaining the mean PSD: (1) acquiring gravity field time series with a certain time resolution (here, e.g., 11-day solutions), expressing the solutions in geoid height with specific spatial resolution (e.g. $1° \times 1°$), (2) forming time series expressed in geoid height for each pixel, (3) computing the PSD for each time series, (4) averaging them over certain area, and (5) deriving the mean PSD in terms of geoid height.

The retrieval procedure provides time series of 11-day spherical harmonic coefficients $C_{lm}(t)$, $S_{lm}(t)$. These are the time series before de-aliasing. Our aims are (1) to see the sampling difference between single pair and double pair formation in magnitudes and patterns, and (2) to de-alias those errors with alias periods of tidal constituents.

We apply least-squares (LS) harmonic analysis on these time series at the known alias periods T_a^n to estimate amplitudes of ocean tide constituent $A_{c,lm}^n$, $B_{c,lm}^n$, $A_{s,lm}^n$, $B_{s,lm}^n$ for each constituent. The difference between this paper and Visser et al. (2010) is that we do the constituent-wise analysis

and N is the number of alias periods for each constituent, typically 1 or 2. The observation equations:

$$C_{lm}(t) = \sum_{n=1}^{N}[A_{c,lm}^n \cos \frac{2\pi}{T_a^n}t + B_{c,lm}^n \sin \frac{2\pi}{T_a^n}t]$$

$$S_{lm}(t) = \sum_{n=1}^{N}[A_{s,lm}^n \cos \frac{2\pi}{T_a^n}t + B_{s,lm}^n \sin \frac{2\pi}{T_a^n}t], \qquad (4)$$

where t is the time in the middle of each 11-day recovery, connect the observed (and aliased) SH coefficient time series to the unknown parameters $A_{c,lm}^n$, $B_{c,lm}^n$, $A_{s,lm}^n$, $B_{s,lm}^n$. After estimating the unknown parameters, the corresponding spherical harmonic representation of the tide aliasing errors $\hat{C}_{lm}^{\text{alias}}(t)$, $\hat{S}_{lm}^{\text{alias}}(t)$ can be computed. Finally, de-aliasing now means to subtract the estimated $\hat{C}_{lm}^{\text{alias}}(t)$, $\hat{S}_{lm}^{\text{alias}}(t)$ from the original $C_{lm}(t)$, $S_{lm}(t)$ to provide the coefficients after de-aliasing $\hat{C}_{lm}^{\text{dealiased}}(t)$, $\hat{S}_{lm}^{\text{dealiased}}(t)$:

$$\hat{C}_{lm}^{\text{dealiased}}(t) = C_{lm}(t) - \hat{C}_{lm}^{\text{alias}}(t)$$

$$\hat{S}_{lm}^{\text{dealiased}}(t) = S_{lm}(t) - \hat{S}_{lm}^{\text{alias}}(t). \qquad (5)$$

Here we summarize the notation of spherical harmonic coefficients in this paper:

– $\delta C_{lm}, \delta S_{lm}$, errors in ocean tide models, input signals for simulation, as indicated by Eq. (2),
– $C_{lm}(t), S_{lm}(t)$, recovered gravity field corresponding to the input signals, containing aliasing errors,
– $\hat{C}_{lm}^{\text{alias}}(t), \hat{S}_{lm}^{\text{alias}}(t)$, estimated aliasing errors, alias correction in Figs. 5 and 6,
– $\hat{C}_{lm}^{\text{dealiased}}(t), \hat{S}_{lm}^{\text{dealiased}}(t)$, after de-aliasing.

4 Ocean Tide De-aliasing

4.1 Determining Aliasing Periods

According to Sect. 3, we compute the alias periods of six constituents for each scenario. To calculate the mean PSD, zero-padding is used to fine tune the alias periods because the 352-day simulation duration gives only a limited spectral resolution. This might bias the estimated alias periods. To be on the safe side, we check whether different areas have different alias periods, taking M_2 as an example, see Fig. 2a,
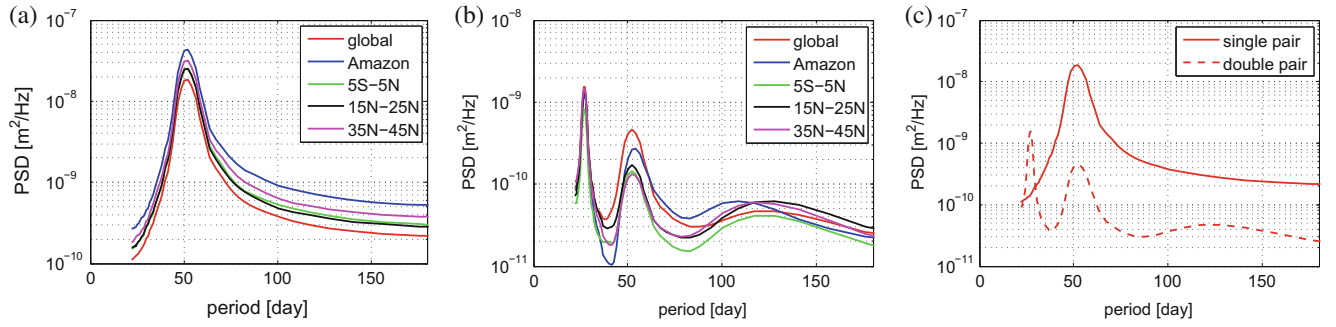
Fig. 2 Mean of PSD in terms of geoid height, taking M_2 constituent as an example: (**a**) different areas for single-pair formation; (**b**) different areas for double-pair formation; (**c**) global mean of PSD in terms of geoid height for both scenarios

Table 3 Periods, alias periods in days for simulated scenario

Tide	T	T_a (by CF) Single pair	T_a (by mean PSD) Single pair	Double pair
M_2	0.5175	55.7	52.1	27.1, 52.1
N_2	0.5274	54.5	58.7	22.0, 58.7
S_2	0.5000	182.6	176	70.4, 176
O_1	1.0758	55.7	54.1	37.1, 54.1
P_1	1.0027	182.6	176	156.4, 176
Q_1	1.1195	54.5	56.3	27.1, 56.3

b. From these figures we can see that for both scenarios, the PSD patterns in terms of geoid height are similar between different areas: same frequency with slightly different total energy.

Figure 2c shows the de-aliasing potential of a double-pair formation which is indicated by the difference in total energy. For all the figures in Fig. 2, the curves start from the Nyquist period of 22 days on the horizontal axis, because the smallest repeat period of both scenarios is 11 days (Parke et al. 1987). Table 3 shows the periods and alias periods for each tidal constituent. Note that we aim to remove the aliasing errors rather than improve the ocean tide model, so when two constituents map onto the same alias period it will not cause problem. Differences between alias periods computed by CF and by the mean PSD are due to: (1) limited simulation mission duration of 352 days, which can not represent the alias periods of S_2 and P_1 precisely, and (2) coarse spectral resolution in combination with a sensitivity of the alias period towards the sampling period. Figure 3 demonstrates the sensitivity of estimated aliasing period of M_2 to sampling period, using CF (Eq. (3)). The red cross corresponds to the alias period of M_2 under simulated single pair scenario.

4.2 De-aliasing

Global Analysis As indicated in Sect. 2, the retrieved gravity fields represent the remaining ocean tide errors after sam-
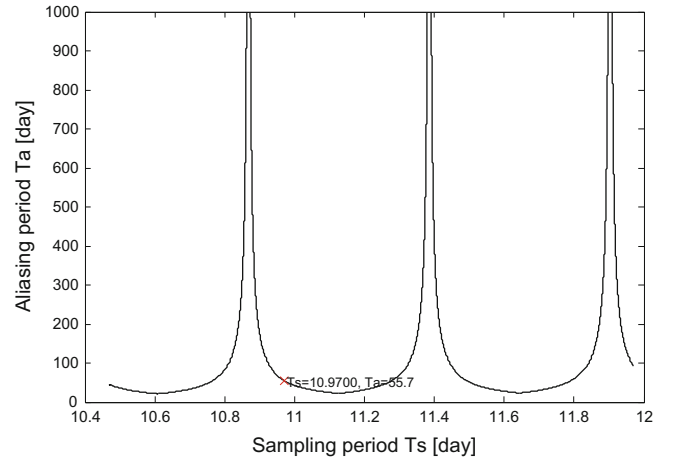
Fig. 3 Sensitivity of alias period towards sampling period variation

pling by satellites. We now express this residual ocean tide aliasing signal in terms of geoid height, for each of the six constituents individually and for both scenarios (Fig. 4). In order to facilitate comparison among results from the single pair and the double pair, both before and after de-aliasing, the color bar is unified into the same range. The pattern of S_2 is not due to the Sun-synchronous orbits, but because the magnitude of S_2-aliasing for most areas is almost one order of magnitude higher than the absolute maximum value of the color bar range. One representative epoch is chosen to show the distribution and amplitude of the ocean tide errors. Note that the distribution and magnitude for an individual constituent under the same scenario will vary from epoch to epoch. Figure 4 shows that the ocean tide errors produce the typical stripes as seen for GRACE for the single pair formation. In comparison, the ocean tide errors of the double-pair scenario show a more homogeneous distribution for all constituents. Moreover, the amplitude of each constituent sampled by the double-pair is smaller than that of the single-pair scenario.

Comparing the ocean tide errors after de-aliasing with those before de-aliasing (Fig. 4), we see a significant reduc-
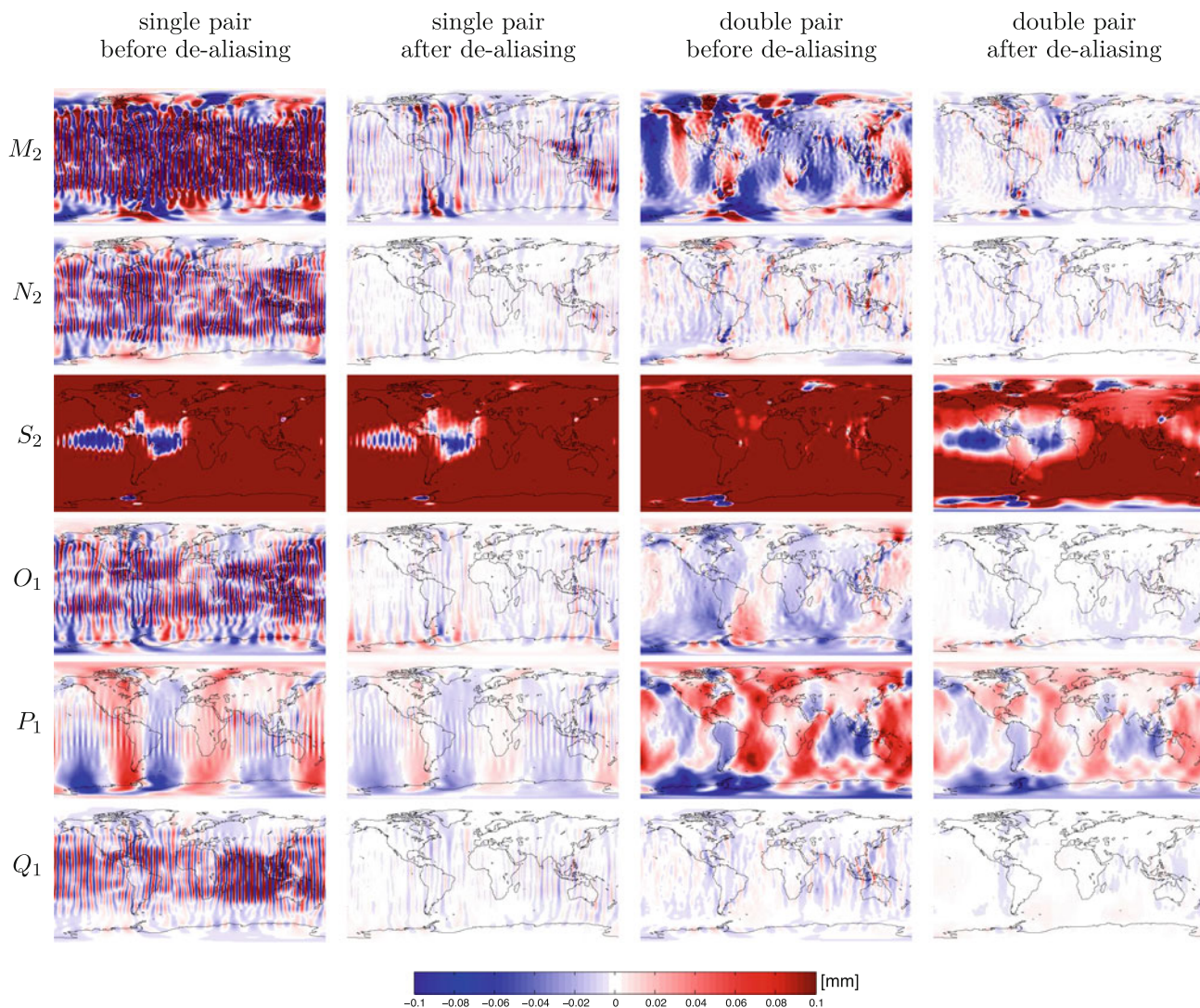
Fig. 4 Comparison of single pair before and after de-alasing with double pair before and after de-aliasing in terms of geoid height

tion for both formations. Nevertheless, some residual aliasing signal remains, because the time series in reality cannot be modeled fully by the sum of sinusoidal functions with a finite number of frequencies.

Spherical Harmonic Coefficients We examine the spectral change due to the LS estimation de-aliasing procedure as well. Specifically, the magnitudes of the coefficients before and after de-aliasing are presented, see Fig. 5. We arbitrarily choose coefficient $C_{22,3}$ of the M_2 simulation for example. Figure 5 demonstrates a very good performance of LS spectral estimation at the PSD-derived alias periods for modeling and reducing ocean tide aliasing errors.

Degree RMS Degree RMS of tidal residual signals in terms of geoid height is considered in three cases: before de-aliasing, after de-aliasing and the reduced magnitude in

Fig. 6. The same conclusion as from the previous analysis of spherical harmonic coefficients can be drawn. Another point one might notice is that the geoid height RMS of single-pair and double-pair mission have different patterns and magnitude levels over the SH degree span from 2 to 60 in this study: (1) the difference in terms of magnitude between two scenarios are small below SH degree 20, while the variation among different epochs for double-pair scenario are larger than that of single-pair scenario, (2) for degrees above 20, the geoid height RMS is decreasing for double pair but growing for single pair, and the highest difference is more than one order of magnitude around SH degree 50, and (3) from SH degree 40 on, the RMS level of double-pair scenario before de-aliasing is even lower than that of single-pair scenario after de-aliasing. Overall, double-pair formation is superior to single-pair formation in terms of reducing the aliasing error level, especially for high SH degrees.
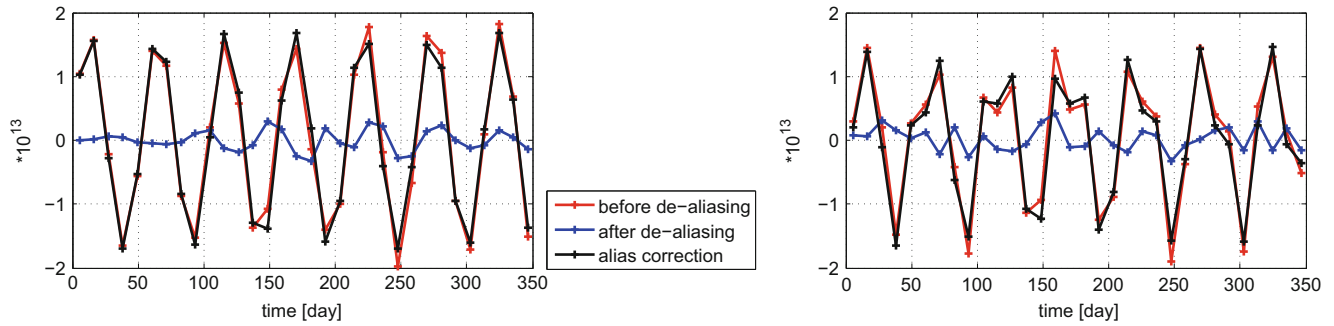
Fig. 5 Spherical harmonic coefficient before de-aliasing $C_{22,3}$, after de-aliasing $\hat{C}_{22,3}^{\text{dealiased}}$ and the alias correction $\hat{C}_{22,3}^{\text{alias}}$: single-pair scenario (*left*), double-pair scenario (*right*), M_2 constituent as input
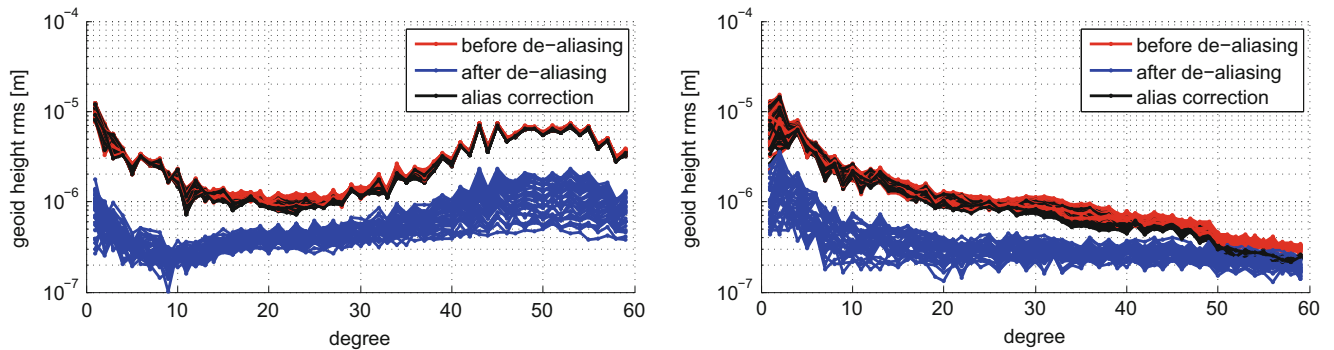
Fig. 6 Degree RMS of residual tidal aliasing signal in terms of geoid height before de-aliasing, after de-aliasing and the alias correction: single-pair scenario (*left*), double-pair scenario (*right*), each line corresponds to a single 11-day gravity solution. M_2 constituent as input

5   Conclusions and Outlook

We simulate the ocean tide error with the difference of two current ocean tide models for six constituents M_2, N_2, S_2, O_1, P_1 and Q_1 with single-pair and double-pair mission scenarios. The results demonstrate that:

– a double-pair has de-aliasing capability in comparison to single-pair formation in two respects, the total error energy of each constituent and the spatial distribution and amplitude of ocean tide error,
– the remaining ocean tide errors can be successfully reduced further with LS spectral estimation, but not fully eliminated,
– the average-PSD approach for determining the alias periods is successful, although it is limited by the spectral resolution of the simulated time series,
– the method allows to determine the alias periods for double-pair missions.

Nevertheless, a more realistic simulation of combined constituents is expected for the next step. As we aim to remove the ocean tide aliasing errors rather than improve the ocean tide models, similar alias periods from different constituents can be estimated simultaneously. When dealing with the real data, this de-aliasing procedure should be avoided at the

alias period the same as or even close to period of signal of interest. Moreover, the relationship between sampling (repeat period) and averaging (resolution of the solution) needs to be investigated in the future.

References

Chen J, Wilson C, Seo KW (2009) S2 tide aliasing in GRACE time-variable gravity solutions. J Geod 83(7):679–687. doi:10.1007/s00190-008-0282-1

ESA-SC4MGV (2015) Study team with contributions by Iran Pour, S, Reubelt, T., and Sneeuw, N., Daras, I., Murböck, M., Gruber, T., Pail, R., Weigelt, M., van Dam, T., Visser, P., Texieirada Encarnacao, J., van den IJssel, J., Tonetti, S., Cornara, S., and Cesare, S., Assessment of satellite constellations for monitoring the variations in Earth's gravity field. ESA-SC4MGV project, Final Report

Flechtner F, Neumayer KH, Dahle C, Dobslaw H, Fagiolini E, Raimondo JC, Gntner A (2016) What can be expected from the GRACE-FO laser ranging interferometer for Earth science applications? Surv Geophys 1–18. doi:10.1007/s10712-015-9338-y

Han SC, Jekeli C, Shum CK (2004) Time-variable aliasing effects of ocean tides, atmosphere, and continental water mass on monthly mean GRACE gravity field. J Geophys Res 109(B4):B04,403. doi:10.1029/2003JB002501

Iran Pour S, Reubelt T, Sneeuw N (2013) Quality assessment of sub-Nyquist recovery from future gravity satellite missions. Adv Space Res 52(5):916–929. doi:10.1016/j.asr.2013.05.026

Parke ME, Stewart RH, Farless DL, Cartwright DE (1987) On the choice of orbits for an altimetric satellite to study ocean circulation and tides. J Geophys Res 92(C11):11,693–11,707. doi:10.1029/JC092iC11p11693

Ray RD (1999) A global ocean tide model from TOPEX/POSEIDON altimetry: GOT99.2. NASA Tech Memo 209478, pp 1–58

Savcenko R, Bosch W (2008) Eot08a-a new global ocean tide model derived by empirical analysis of multi-mission altimetry data. Geophys Res Abstr 10, EGU2008-A 7470

Seo KW, Wilson CR, Chen J, Waliser DE (2008a) GRACE's spatial aliasing error. Geophys J Int 172(1):41–48. doi:10.1111/j.1365-246X.2007.03611.x

Seo KW, Wilson CR, Han SC, Waliser DE (2008b) Gravity recovery and climate experiment (GRACE) alias error from ocean tides. J Geophys Res 113(B3):B03,405. doi:10.1029/2006JB004747

Visser PNAM, Sneeuw N, Reubelt T, Losch M, Van Dam T (2010) Space-borne gravimetric satellite constellations and ocean tides: aliasing effects. Geophys J Int 181(2):789–805. doi:10.1111/j.1365-246X.2010.04557.x

Wiese D, Nerem R, Lemoine F (2012) Design considerations for a dedicated gravity recovery satellite mission consisting of two pairs of satellites. J Geodesy 86(2):81–98. doi:10.1007/s00190-011-0493-8

A Method of Airborne Gravimetry by Combining Strapdown Inertial and New Satellite Observations via Dynamic Networks

J. Skaloud, I. Colomina, M.E. Parés, M. Blázquez, J. Silva, and M. Chersich

Abstract

We revisit the concept of scalar gravity anomaly determination by an airborne strapdown INS–GNSS system. We built on the previously investigated concepts (mainly within 1995–2005 period) while trying to decrease the error spectrum of the system caused by accelerometer biases at lower frequencies and GNSS-position/velocity noise at shorter wavelengths. We propose to determine the random long-term accelerometer bias through combination of $-$GRACE $+$ GOCE data that provide an unbiased field with 80 km resolution while the decrease in velocity noise is expected by precise-point-positioning (PPP) method that merges satellite-phase observations from GPS and Galileo. In the absence of Galileo constellation we focus our practical demonstration on the gravity-anomaly determination via INS/GNSS data filtering. We present first the modeling of an extended Kalman filter/smoother that determines the gravity anomaly together with the trajectory, which is a preferred method over the cascade determination (i.e. separate estimation of trajectory and specific forces, GNSS acceleration and low-pass filtering of the merged signal). Second, we show how to incorporate the same modeling within the concept of dynamic networks. This approach allows imposing cross-over conditions on the state of gravity anomaly at trajectory intersections while estimating the sensor and trajectory errors at the same time. This is indeed rigorous formulation of the problem that is expected to surpass the conditioning via cross-over adjustment that in previous investigations followed the filtering-smoothing. Despite the remaining challenges of the method of dynamic network caused by large number of parameters (i.e. $>10^6$), we present first assessment of such implementation that was obtained within European FP7 GAL project.

Keywords

Airborne gravimetry • Dynamic networks • Gravity anomalies • INS/GNSS integration

J. Skaloud (✉)
Geodetic Engineering Laboratory (TOPO), EPFL, Station 18, CH-1015 Lausanne, Switzerland
e-mail: jan.skaloud@epfl.ch

I. Colomina • M. Blázquez
GeoNumerics, Av. de Carl Friedrich Gauss 11, E-08860 Castelldefels, Spain

M.E. Parés
CTTC, Av. de Carl Friedrich Gauss 7, E-08860 Castelldefels, Spain

J. Silva
DEIMOS Engenharia, Av. Dom João II-2 41, 1998-023 Lisboa, Portugal

M. Chersich
ESRI Italia c/o EUCENTRE, Via Ferrata 1, 27100 Pavia, Italy

1   Introduction

Despite the improved resolution of global gravity field thanks to low orbiting satellites, kinematic airborne gravity (KAG) surveys remain a fundamental source of information for the determination of precise and high-resolution gravity field, especially in areas with no or limited ground infrastructure.

Although some innovatory systems were proposed and tested, e.g. Brown et al. (2002), modern airborne scalar gravimetry is mainly conducted using either gravimeters on a Schuler-tuned stabilized platform, or with (mainly strapdown) Inertial Navigation System (INS). The former concept was successfully deployed already in nineties for scalar airborne gravity surveys in Greenland, Antarctica and Switzerland where resolution of at least 10 km wavelength were reported with an accuracy of 3–5 mGal, e.g. Brozena et al. (1996), Forsberg et al. (2002), Jones and Johnson (1995), Klingele et al. (1997), and Timmen et al. (1999). The main source of error in these cases was insufficient platform stabilization. This can be somewhat mitigated with complex design on dedicated instrumentation as shown by Ferguson and Hammada (2002), who reports accuracies of 1 mGal for a half wavelength as low as 2 km.

The concept of using integration of strapdown inertial navigation systems (SINS) with satellite navigation for kinematic gravity determination is somewhat simple to materialize due to the absence of physical stabilising platform. The method has been formulated almost 30 years ago by Schwarz (1987) while good airborne results with non-stabilized platform were reported in the second part of the nineties, e.g. Wei and Schwarz (1998) and Glennie and Schwarz (1999). The results in KAG through non-stabilized INS/GNSS during this period consistently demonstrated a precision level of 11, 3.5, 2.5 and 2 mGal at 3, 6, 9 and 12 km wavelengths, respectively, corresponding to 30 s, 60 s, 90 s smoothing intervals. A more recent experiments (Gerlach et al. 2010) following the same methodology (and software setup) but with newer instrumentation reports similar precision over a relatively small (20×20 km) region, i.e. ≈ 3 mGal for 1/80 s low-pass filter cut-off freq. that due to lower speed of the aircraft corresponds to 2 km spatial resolution. The same reference also reports that kinematic acceleration derived from PPP after long-period of convergence is similar to that of differential carrier processing. The accuracies of ≈ 3 mGals with similar technology are also reported for large-field campaign by Li (2011), however, for considerably longer smoothing window of 240 s.

A number of past investigations in this domain concluded that the quality of gravity recovery by this method is limited by the process of separation of the gravitational and kinematic acceleration due to GPS and INS-instrumental errors (Wei and Schwarz 1994). Due to the different noise characteristics of these two instruments, it is GPS-derived accelerations may limit the short term/wavelength accuracy while non-compensated inertial errors are likely to influence long-term (i.e. longer wavelength) resolution as stated in Li et al. (1994) or Schwarz and Li (1995). The reality is, however, more complex as additional factors as imperfections in sensor synchronization as well as the remaining influence of INS initialization and/or attitude affect the observation process. The ideas on mitigating the error sources gave rise to different processing approaches to strapdown inertial vector/scalar gravimetry (SIVG/SISG), but without affecting significantly the conclusion on precision or accuracy limits.

1.1   Motivation

The situation evolved slowly but steadily since the nineties to a point that enhancement is possible thanks to the combination of new available technologies, observations and data processing approaches. First, the exploitation of multi-constellation and new satellite signals, especially those of GPS and Galileo is a prerequisite to improve short-term resolution. Second, since GOCE gradiometry resolves globally the gravity field with an accuracy of 1–2 mGal at 100 km wavelength (Migliaccio et al. 2009) it spectrally overlaps with SISG. Such overlap provides redundancy, which can serve for consistent calibration of the airborne gravimetric system to a global gravity reference frame. Finally, additional enhancement become possible due to the development of new processing approach (Termens and Colomina 2006) that unifies several adjustment steps into one.

Such "revised" approach to SISG was pursuit during a 2-year project supported by the European Global Navigation Satellite Systems Agency (GSA 2011), and can be summarized to the following challenges:

- To develop a procedure for enhancing the positioning/acceleration accuracy enabled by GNSS multi-constellation with particular attention to the introduction of the Galileo system (i.e. improve short-term spectral resolution).
- To develop a procedure for integrating GOCE into kinematic airborne gravimetry for gravity fields and geoid determination (i.e. improve long-term spectral resolution and enhance redundancy).
- To implement a one step procedure that optimally integrates strapdown INS/GNSS for gravity determination.

1.2   Paper Outline

The remaining content of the paper is organized as follows. After introducing the available data sets and reference collected during the project we study the possible accuracy

Fig. 1 Flight during GAL project over Pyrenees with trajectory crossing
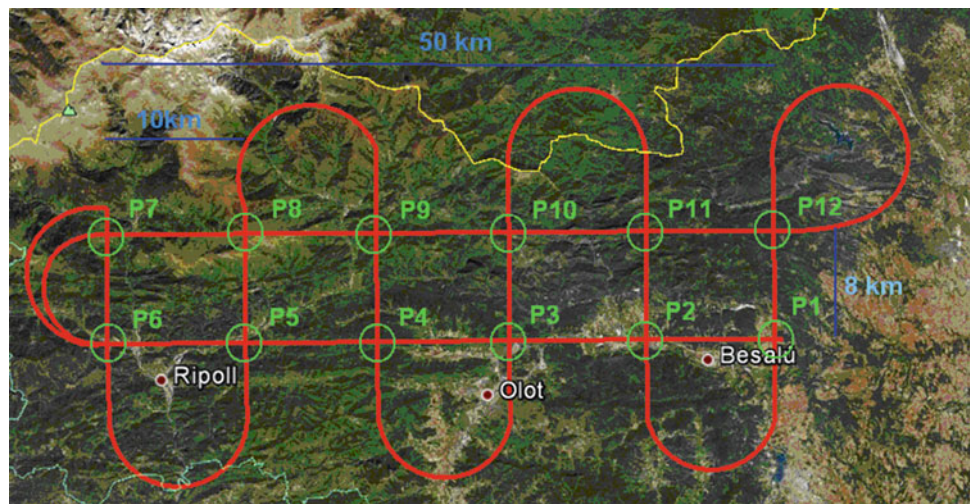
improvement due to Galileo. Second, we briefly explain the concept of integrating GOCE data into strapdown inertial scalar gravimetry, while leaving the details to simultaneous publication (Sampietro et al. 2015). Then we describe the modelling of the system parameters (including gravity anomaly) and their estimation by two – theoretically equivalent – formulations: state-space approach and dynamic networks. After we present a comparison with discussion on data smoothing ability of the proposed method. We conclude with processing recommendations based on build experience during the GAL project.

2 The Benefit of Multi-GNSS

2.1 Available GNSS Data

Two gravimetric flights were performed in the Pyrenees (Fig. 1) and Lleida regions (in the Northeast of Spain) in February 2013 for a total amount of 3:30 and 4:30 h data respectively. Flying altitude was about 2,400 and 900 m respectively. The GNSS data on board were taken from state-of-the-art receivers (namely Novatel OEMV-3 and Javad TRE-G3T) at 10 Hz sampling rate. The inertial data were issued from two navigation-grade strapdown inertial systems using fibro-optic gyro technology (FJI from IMAR and Airins from XBLUE) sampling at 400 Hz and 200 Hz respectively, characteristics of which are summarized in Table 1.

Since we use "loosely coupled" integration of GNSS-derived position and velocities with SINS observation we can study the possible accuracy improvement due to dual GPS-Galileo constellation as an improvement in epoch-by-epoch position/velocity GNSS determination, i.e. without INS. Given the limited number of Galileo satellites in orbit and the limited number of GPS satellites with modernized signals the potential benefit of dual constellation

Table 1 Characteristics of employed inertial sensors

	FJI-gyro	XB-gyro
Drift at ambient t (°/h)	0.003	0.003
Drift over t-range (°/h)	0.010	0.010
Random walk (°/$\sqrt{h}$)	0.001	0.001
Scale factor (ppm)	10	30
	FJI-acc	XB-acc
Bias stability at ambient t (μg)	<20	20
Bias stability over t-range (μg)	80	100
Long-term stability (μg/year)	150	500
Noise (μg/$\sqrt{Hz}$)	8	15
Scale factor at ambient t (ppm)	10	40

with modernized signals was studied via an emulation scenario. We have employed the GRANADA GNSS simulator developed by DEIMOS Engenharia to emulate GPS L1, L2, L5 and Galileo E1, E5a, E5b observables along the real trajectories (Diez et al. 2006). The synthetic measurements were taking into account many effects as orbital errors, thermal noise, receiver clock error, cycle-slips and outliers, multipath and tracking loop aiding error. The "reality" of emulation was first verified with respect to the residuals of the real observations (i.e. GPS L1, L2) on all available satellites.

2.2 GNSS Data Processing

The data processing strategy was driven by two main considerations or requirements: the possibility to use the system in regions not covered by local elements (permanent GNSS stations) and a careful approach to phase measurements combination in order to avoid cross noise contamination. For the purpose of local element infrastructure independence, a dedicated precise point positioning (PPP) software has been developed, being the starting processing chain of the GAL

system. The core of the PPP software is a batch least-squares estimator mixing weighted undifferenced GPS and Galileo observables and using the best ancillary products available such as precise ephemerides, 1 Hz precise satellite clocks and proper models for accounting for code biases, atmospheric delays, wind-up effect, etc. Linear combinations of carrier phase measurements, like the ionospheric free ones or those related to relative positioning, like double differences, as opposed to absolute positioning, like undifferenced PPP, have not been used to avoid the larger noise of combined or differenced measurements. The estimator is based on a sparse matrix technique (Sarjakoski 1984) in order to optimize the memory usage and to process several hours of data at 1 Hz with a reasonable computation time.

2.3 Assessment

The main objective of this assessment was the accuracy estimation of the displacements of the airplane between consecutive epochs that takes into account both two frequency (actual) and three frequency (emulated) GPS + Galileo data. The evaluation was based on the following strategy:

- Assessing the precision in trajectory reconstruction by processing:
  (a) *Two* frequency *actual* GPS data;
  (b) *Two* frequency *emulated* GPS data considering "pseudo-realistic" conditions in terms of signal errors and thermal noise;
  (c) *Three* frequency *emulated* GPS and Galileo data, data with "pseudo-realistic" conditions in terms signal errors and thermal noise;
- Computing so-called *Simulator likelihood factor* evaluated as the ratio of precision of results obtained in (b) and (a). Such scale factor represent the *trueness* of the simulated observables with respect to actual observables in terms of precision (the closer to one, the more realistic are the simulated data);
- Estimating the expected precision of the GNSS multi-constellation by scaling results of (c) by the previously mentioned *Simulator likelihood factor*.

The outcome of testing is resumed in Table 2 in terms of positioning precision. The reason for using precision and not accuracy is that a small bias in position has negligible impact on the determination of kinematic acceleration in earth-fixed

frame (and thus gravity) as long as is kept below 1 m. On the other hand, it is the precision (from epoch to epoch) that is more influential with respect to kinematic acceleration (Schwarz and Li 1995). The difference between the precision obtained with real data (estimated from residuals) and their emulated counterpart can be mainly explained by the absence of atmospheric influences on signal propagation in the emulated scenario and possibly by larger bandwidth (and thus also the noise-level) of the tracking loops in the employed receivers. Therefore, the ratio between real/emulated precision with GPS dual frequency data was used to scale up the emulated scenario with GPS + Galileo triple frequency observations. This value is presented in the right column of Table 2 as "Expected GPS+Galileo" precision and is about 1.6 cm, which is indeed a very good perspective.

3 Integration of Global Gravity Reference

The integration between GOCE gravity field, ground gravity observations and the kinematic airborne gravity data to produce an optimal grid of geoid undulation or free air gravity anomaly is indeed a complex task. In the GAL project, a particular remove-restore technique was used. It is based on an adaptation of the space-wise approach (Reguzzoni and Tselfes 2009) to airborne gravimetry. The original idea consists in applying the procedures used in Gilardoni et al. (2013) of least-squares collocation to merge local geoids with the aid of satellite-only gravity models and that of Gilardoni et al. (2014) in using GOCE to straighten and sew European local geoids, in order to merge gravity anomalies with satellite data Fukushima (2012). The prototype algorithm has been improved to build a fully operative software. The first item of this improved product, GTE, i.e. the one related to the terrain correction, has just been published (Sampietro et al. 2016) while the core of the processing (i.e. the remove-restore procedure) will be the subject of a forecoming publication.

The methodology presented herein is applied for two different purposes, namely:

- for enhancing gravity modelling input to strapdown navigation equations
- for calibrating residual systematic sensor errors (e.g. accelerometer) gravity anomaly δg (mainly due to residual accelerometer offsets)

Table 2 Precision of GNSS positioning along trajectory

	Real GPS L(1,2)	Emulated GPS L(1,2)	Emulated GPS + Galileo L(1,2,3)E(1,5a,5b)	Expected GPS + Galileo L(1,2,3)E(1,5a,5b)
Precision (cm)	5.4	0.6	0.16	1.6
Simulator likelihood factor	0.1 (10%)			
Improvement factor	0.7 (70%)			

Although in case of dynamic networks, these two purposes meet in a common estimation step, in case of state-space plus cross-over estimation they correspond to these two distinct stages of data adjustments. Hence, for the purpose of SISG input that senses the difference between the kinematic acceleration and the gravity, i.e. the specific force in body frame f^b, we are concerned with the former purpose. The gravity term used in the first-order differential equation for velocity v determination (1) is modified as $g_0 = \gamma + \Delta g$ to include not only normal gravity $\gamma = f(\varphi, \lambda)$ but also the high resolution part $\Delta g = f(\varphi, \lambda)$ from global gravity models based on GOCE with adaptation to aircraft position (φ, λ). Expressing this relation in ECEF reference frame reads:

$$\dot{v}^e = R_b^e f^b - 2\omega_{ie}^e \times v^e + g_0^e \qquad (1)$$

where R_b^e is the rotational matrix from body frame to ECEF frame, and ω_{ie}^e is the Earth-rotation vector, which in product with the velocity represents the Coriolis term.

More specifically, the global gravity model used (called GECO) and partially developed within the GAL project, is a combination between the GOCE and EGM2008 global models (Gilardoni et al. 2016) and has been used up to degree 1420 corresponding to a wavelength of about 12 km.

4 State-Space Formulation

The previously mentioned best results achieved by non-stabilized INS/GNSS were obtained directly by differencing the GPS and INS sensed accelerations, albeit the latter were corrected first for systematic effects of IMU specific-force sensors via INS/GPS integration. On the other hand, the GPS acceleration were obtained by numerical differentiators operating either on observations (phase, phase-rate) or estimated quantities (position/velocity) (Bruton et al. 1999). This so called *traditional approach* is somewhat similar to conventional airborne gravity on stabilized platform where no stochastic gravity model is necessary, with the difference of using the signal from all three accelerometers and expressing them in navigation frame.

4.1 Dynamic Model

An alternative way of determining the gravity anomaly components is with the Kalman filter based approach: first, to integrate the navigation equations associated with an INS, and second, to model the INS errors and gravity anomalies as stochastic processes. GNSS positions and/or velocities are used as updates in a Kalman filter estimation of the errors, including the gravity anomalies. The optimal smoothing follows the filtering step and is usually implemented either as

fixed interval smoother, or via Rauch-Trung-Striebel (RTS) algorithm (Gelb 1988) leading to same level of confidence of the estimated parameters. This approach has been successfully tested even with tactical-grade IMU (Bastos et al. 2000), while Tome (2002) reported his equivalence in performance with the previously mentioned *traditional approach* promoted by researchers from The University of Calgary in nineties (Wei and Schwarz 1998; Glennie and Schwarz 1999). The modified strapdown navigation equation in ECEF (e-)frame for position, velocity and attitude thus reads:

$$\begin{pmatrix} \dot{r}^e \\ \dot{v}^e \\ \dot{q}_b^e \end{pmatrix} = \begin{pmatrix} v^e \\ R_b^e f^b + \delta f^b - 2\omega_{ie}^e \times v^e + g_0^e + \delta g^e \\ \frac{1}{2} q_b^e \otimes \left[\omega_{ib}^b + \delta\omega_{ib}^b - \omega_{ie}^b \right]_q \end{pmatrix} \qquad (2)$$

where the first relation concerning position is trivial, second is comparable to Eq. (1) and the third containing the quaternion representation of the attitude (q_b^e) with condition $\|q_b^e\|_2 = 1$, gyro-sensed rotation vector (ω_{ib}^b) and earth-rotation vector (ω_{ie}^b) in the body frame. The symbol ($\otimes$) represents the quaternion multiplication and $[\cdot]_q$ the 3D vector in a quaternion form (i.e. with real part = 0). The terms preceded by δ are those estimated via Kalman-filtering smoothing. These are related to systematic time-correlated errors of accelerometers (δf^b) and possibly also gyroscopes ($\delta\omega_{ib}^b$) as well as the anomalous gravity (δg^e). Those values are principally zero prior the estimation process starts. Once the initial conditions are known (i.e. by GNSS-fix for position, zero velocity, and static alignment for attitude), the differential equation is resolved based on observed IMU data of f^b and ω_{ib}^b through numerical integration. For the discussion in Sect. 5 it is important to state that (a) numerical methods for ordinary differential equations are used despite the fact that the nature of the forcing input is stochastic; (b) first-order approximation by Euler-method is not sufficient and therefore higher-order methods are employed (e.g. Runge-Kutta or predictor-corrector methods).

4.2 Estimation Model

The estimation is based on the state-space modelling and extended Kalman filtering (EKF) and smoothing. In a general formulation this model takes a form: $\delta\dot{x} = F\delta x + Gw$, where δx is the *error* state vector, w is the white noise and F, G are the dynamic and shaping matrices, respectively. Considering the left side of (2) as navigation states, its linearization defines the first part of the estimation model. The second part is related to time evolution of the sensor errors and gravity anomaly. Considering a particular case in which the time-correlated part of sensors errors and gravity are modelled as first-order Gauß-Markov processes with inverse correlation

times β_x, and strength w_x, an example of a complete error state-space model reads:

$$\begin{pmatrix} \delta\dot{r}^e \\ \delta\dot{v}^e \\ \delta\dot{\varepsilon}^e \\ \delta\dot{\omega}^b \\ \delta\dot{f}^b \\ \delta\dot{g}^e \end{pmatrix} = \begin{pmatrix} \delta v^e \\ -f^e \times \varepsilon^e - \omega_{ie}^e \times \delta v^e + R_b^e \delta f^b + \delta g^e \\ -\omega_{ie}^e \times \delta\varepsilon^e + R_b^e \delta\omega_{ib}^b \\ -\beta_\omega \delta\omega^b + w_\omega \\ -\beta_f \delta f^b + w_f \\ -\beta_g \delta g^e + w_g \end{pmatrix}$$

$$(3)$$

where $\delta\varepsilon$ are small angular errors and the terms with numerically insignificant contributions were left apart. Note that although the gravity anomaly vector depends on position, due to the characteristics of an airborne gravimetric campaign (where data is acquired uninterruptedly) it can be assumed that gravity anomaly is also a time-dependent or dynamic model. For this reason the choice on inverse correlation time of gravity anomaly β_g can be adapted in a relation to aircraft speed.

The filtering/smoothing is based on external measurements, which are in principal GNSS-derived quantities. This so called *static* observation model is in case of GNSS position r_s^e derived for an antenna separated from IMU by a known-vector a_s:

$$\delta r^e + v_r = r^e + R_b^e a_s^b - r_s^e \qquad (4)$$

It should be stressed that it is important to determine the lever-arm vector a_s^b separately with cm-level precision and in body frame. For the sake of parameter separation (e.g. δf^b from δg^e) it is recommended to formulate static observation equation with gravity control point (g_c) on the airport:

$$\delta g^e + v_g = g_c^e - g_0^e \qquad (5)$$

Such observations can be used prior to take-off and after landing.

4.3 Limitations

The state-space approach is sometimes referred to as the *navigation* approach due to its optimality for real-time estimation. This real-time focus has however some disadvantages and limitations. For instance, it can consider only one dynamic model. Also, while allowing relating state parameters in time, conditioning them in space is more difficult. Moreover, while in terms of gravity anomalies determination, the state-space approach is relatively precise it is potentially inaccurate under operational conditions. Indeed, the analysis of the covariances of the smoothed trajectory reveals a precision of 15 mGal for the estimated gravity disturbances and of 10 mGal for the accelerometer biases. Considering

the frequency of the inertial measurements (400 Hz), the typical flying speeds (60–80 m/s) and dumping the estimated accelerometer errors into the gravity estimates, we end up with precision estimates within the 0.5 mGal at wavelengths of 1 km or longer. On the other side, in spite of using surveyed gravity values at the airport, their propagation to the rest of the gravity mission can be "interrupted" by GNSS reception events. Thus, in our case, in one of the GAL flights, an airport localization radar interference resulted in loss of lock of the GNSS receiver and, ultimately, on bad calibration of the accelerometer biases: up to 30 mGal root mean square (RMS) errors were observed after comparison with upward continued ground reference gravity. For these type of problems, the determination of unbiased gravity anomalies requires an additional step. Such *cross-over* adjustment minimizes (in least-square sense) the residual biases(s) and trend(s) by employing reference gravity values as well as conditions on anomaly correspondences at crossings (Glennie and Schwarz 1999). However, as this second estimation step acts on non-linearly transformed observations (i.e. f, ω) and their corrections (i.e. δf, $\delta\omega$) the formulation of the problem is sub-optimal.

5   Dynamic Network Formulation

We strive to replace the previously described two-step adjustment strategy with single *geodetic* strategy that allows simultaneous IMU calibration, optimal trajectory estimation as well as optimal gravity anomaly recovery. We will call this method *dynamic networks* for the reason that it allows rigorous formulation of the problem in terms of time and space modelling. In kinematic geodesy, this approach is frequently employed in orbit determination (Seeber 1993). It was also used in early works of precise carrier-phase positioning (Friess 1990). Its practical application to inertial data processing is, however, in its beginning, despite the fact that it was suggested already 10 years ago by Colomina and Blazquez (2004) for sensor orientation and by Termens and Colomina (2006) for KAG. Its potential benefits for mobile laser scanning were demonstrated within a simulation scenario by Rouzaud and Skaloud (2011).

5.1 General Formulation

A time dependent or dynamic network is a network such that some of its parameters are time dependent (stochastic processes). To solve a time dependent network is to perform an optimal estimation of its parameters (e.g. in the sense of least-squares). In the classical network adjustment theory, the network is completely defined by observations (random variables l and their corrections v), parameters or unknowns

(random variables x) and their relationship, set of *static* observations equations:

$$f_s\,(l_s + v_s, x) = 0 \qquad (6)$$

and dynamic observation equations; in our case stochastic differential equations:

$$f_d\,(l_d(t) + v_d(t), x(t), \dot{x}(t)) = 0 \qquad (7)$$

The differential equations governing inertial navigation can be approximated by difference equation. The resulting relation then resembles condition equations in the classical network approach:

$$f_d\,(l_d(t) + v_d(t), x(t), \varXi_i x(t)) = 0 \qquad (8)$$

with $\varXi_i$ denoting a differentiation filter of order i that is applied to the chain of states x. For example, Eq. (9) returns the numerical derivative using the first order central difference, i.e. a windowed filter of width 3, with coefficients as in (10).

$$\dot{x}_{d_i} = \varXi_i x_d = \frac{(x_{d+1} - x_{d-1})}{2} \qquad (9)$$

$$\varXi_i = \begin{bmatrix} 0 \cdots 0 -\frac{1}{2} \ 0 \ \frac{1}{2} \ 0 \cdots 0 \end{bmatrix} \qquad (10)$$

It is interesting to note that the outcome of such *differencing* operations is not explicitly defined in the case the states are influence by a certain level of noise. Nevertheless, as will be shown later, a good numerical approximation is practically feasible even with the first order divided difference (Newton's difference quotient) since the evolution of states in KAG is rather smooth (in the absence of vibrations).

5.2 Dynamic Model

To create the [dynamic] model in the sense of a geodetic network we take the differential observation Eq. (2) governing strapdown navigation and express them as observation equations after approximating the parameter derivatives as in Eq. (8). This leads to a Gauß-Helmert formulation of the network adjustment. If an explicit formula on the observations (i.e. Gauß-Markov formulation) of the strapdown navigation model is required, the following equation can be used:

$$\begin{pmatrix} 0 \\ f^b \\ [\omega_{ib}^b]_q \end{pmatrix} = \begin{pmatrix} v^e - \varXi_i r^e \\ [R_b^e]_q^T \left(2\omega_{ie}^e \times v^e - g_0^e - \delta g^e \right) \\ + \varXi_i v^e - \delta f^b \\ [\omega_{ie}^b - \delta\omega_{ib}^b]_q + 2q_e^b \otimes \varXi q_b^e \end{pmatrix} \qquad (11)$$

where $\left[R_b^e\right]_q$ denotes quaternion rotation operator (matrix) for the estimated quaternion q_b^e. Although we followed a Gauß-Helmert formulation, the above formula is provided and further discussed for the sake of clarity and completeness.

The first row of Eq. (11) can be seen as *pseudo - observation* which value is zero (or, alternatively, as a condition in the Gauß-Helmert formulation). In practice these observations come with an uncertainty that should not be too small to avoid numerical instability. Such pseudo- observations (or conditions in the Gauß-Helmert formulation) are used also for the second part of the dynamic model related to sensor errors and that of gravity anomaly:

$$\begin{pmatrix} 0 \\ 0 \\ 0 \end{pmatrix} = \begin{pmatrix} \beta_\omega \delta\omega_{ib}^b - \varXi_i \delta\omega_{ib}^b \\ \beta_f \delta f^b - \varXi_i \delta f^b \\ \beta_f \delta g^e - \varXi_i \delta g^e \end{pmatrix} \qquad (12)$$

It is worth noting that in the Gauß-Markov formulation such *pseudo-observations* are necessary, otherwise the dynamic network (11) + (12) would be undetermined. At the same time their appropriate weighting allows absorbing the approximation due to numerical derivatives. There is obviously no redundancy as we have $10 + 6$ parameters in 16 relations. As the quaternions are not independent we need an additional observation to avoid deficiency. This can be formulated either as a condition between parameters or as an additional *static* observation equation as presented in the following section.

5.3 Static Models

First *static* observation model is related to the quaternion dependency and can be expressed also by a *pseudo-observation*:

$$0 = \sqrt{q_0^2 + q_1^2 + q_2^2 + q_3^2} - 1 \qquad (13)$$

which value is also zero.

Second *static* observation is related to GNSS position fix [Eq. (4)]. A similar relation can be introduced for GNSS-derived velocity vector. These observations create certain (albeit small) redundancy in the network.

Additional static observations are related to gravity. These are either absolute [Eq. (5)] or relative gravity observations. However, one of the main interest in formulating SISG using the framework of a dynamic network is the possibility to constrain some states by static conditions either in time and/or space. These constrains can be applied on states separately as in the case at trajectory

crossing:

$$\delta g^e \left(t_i\right) = \Omega \left(\Delta h_{i,j}\right) \delta g^e \left(t_j\right) \qquad (14)$$

where gravity anomalies at the same horizontal positions at time t_i and t_j are the same, once accounting for their (practically small) separations in height $\Delta h_{i,j}$ through $\Omega()$, i.e. $\Omega(\Delta h_{i,j}) = 1$ if $h_i \approx h_j$.

5.4 Advantages

The dynamic network formulation of the navigation-/SISG problem is basically a Gauß-Helmert solution in a least-squares filter. It has several advantages over the iterated Extended Kalman Filter (EKF): it supports multiple redundant dynamic models in a centralized filter architecture; it supports implicit non-linear static models (Gauß-Helmert approach); it performs a non-linear numerically-stable generic least-squares estimation without resorting to the efficient but less flexible gain matrix approach of the classical Kalman filter.

5.5 Estimation

The state-space estimation is, however, useful and even necessary as a first approximation for parameter estimation. Most observation equations in the system [Eqs. (11)–(14)] are either in a linear form or in a form that is simple to linearise (i.e. combined function derivative is necessary only for the quaternion condition [Eq. (13)]). It should be mentioned that as long as cross-over conditions [Eq. (14)] are absent the system can be solved in recursive least-square manner, which performance shall be equivalent to that of the smoother. This will be subject of following investigations.

6 Comparison

6.1 Test Data

The original GAL testing plan called for a three-step phased test plan with static terrestrial, kinematic terrestrial and kinematic airborne acquisition campaigns. INS/GNSS static terrestrial measurements were conducted for the purpose of acquisition system testing and static calibration of the IMUs by comparison to traditional gravimeter measurements (LaCoste & Romberg G921) and by IMU self-calibration through rotation sequences. Kinematic terrestrial measurements were conducted in Switzerland and the national Swiss gravimetric data base was used to extract a gravity reference data set. This kinematic terrestrial campaign was conducted at the end of the project and was not processed. Airborne gravimetric campaigns, two flights, were conducted in the Lleida and Girona/Pyrenees (Fig. 1) in Catalonia, Spain, as described in Sect. 2.1. Due to last minute administrative and technical problems with flying permits, the flight had to be conducted with a replacement aircraft (Cessna Skymaster) for which the prepared instrument mount with dampeners was inadequate. This resulted in unforeseen vibrational motion of high amplitude, which frequency was higher than the IMU sampling frequency. In turn, this spoiled (by aliasing) the inertial signals so the inertial observations were not exploitable for the recovery of gravity anomaly. Synthetic inertial measurements and gravity signal were then generated along the trajectory with an inertial measurement software simulator (Parés et al. 2015) that emulated the error properties of the used IMUs, and with realistic gravity computed from global models and local terrain elevations (Sampietro et al. 2015), respectively.

6.2 Test Results and Gravity Recovery

The static tests confirmed the specifications of the IMU manufacturers in the run-to-run biases between 20 and 60 μg – within the specifications – and absolute (constant) biases around 50 μg.

Recovery of gravity with the state-space approach – i.e., of gravity differences with respect to the gravity model used in the INS mechanization equations – is illustrated in Fig. 2 and was achieved at the 4 mGal level precision and 15 mGal accuracy. Since the focus of this article is on the dynamic network method, we will not discuss further this method and the reader is referred to the work of Bastos et al. (2000). Figure 3 depicts the estimated precision of the estimated gravity differences with respect to the gravity model.

Recovery of gravity with the dynamic network approach was restricted to short time periods because of software capacity limitations and because the main goal was to gain insight in the performance of the method for gravity recovery. For this purpose periods between 1 and 10 min of data were selected and the feasibility of the method was analyzed. Two conclusions could be drawn: the use of tie-gravity anomaly points in the cross-overs worked as expected in a sense that the resulting gravity anomalies were the same – non significantly different – and that a correct gravity was recovered under the assumption that gravity ground control points were available and that there is enough maneuvering in between observation flying lines to de-correlate the IMU
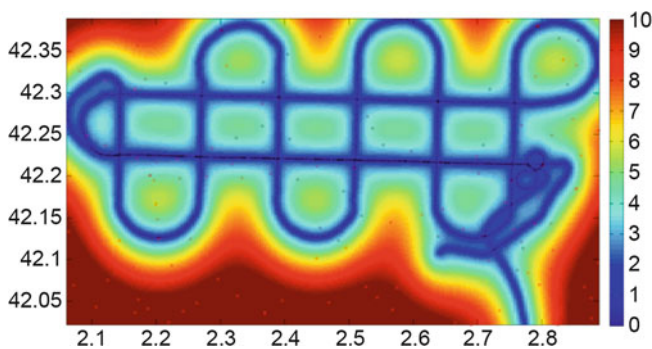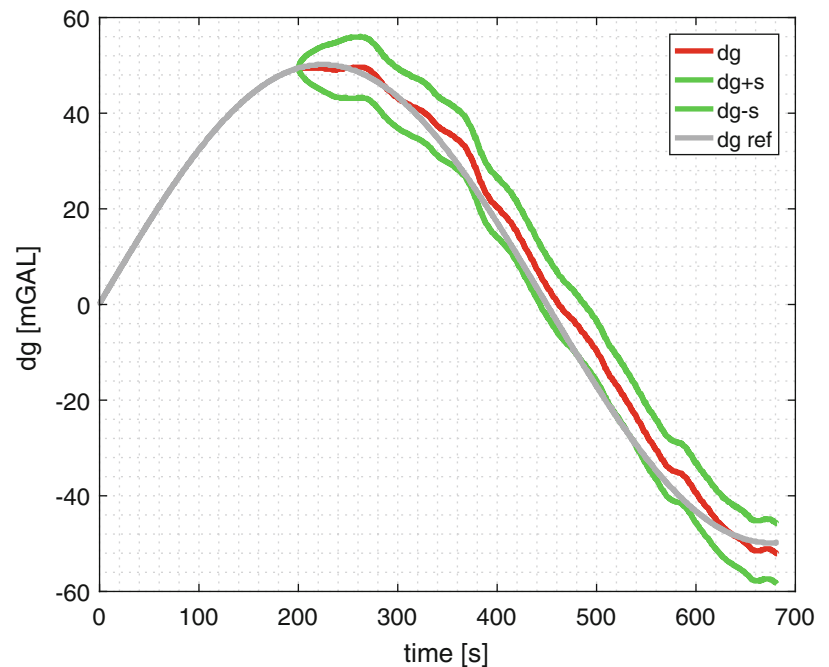
Fig. 3 Predicted standard deviations of the recovered free gravity anomaly (δg) along the flight path with the scale of color-coding in mGal

biases from the gravity corrections to the model. Figure 4 depicts the gravity correction states for a 7 min period were the IMU unknown calibration states were assumed to be constant, thus mimicking the situation of an appropriate trajectory geometry – i.e., with calibration maneuvers – for a longer time period. The estimated standard deviation of the recovered gravity is 2 mGal at each epoch and the empirical accuracy is 4 mGal.

6.3 State-Space vs. Dynamic Network

A thorough comparative analysis of the advantages and disadvantages of the state-space and the dynamic network methods against each other is not possible at this point in time. However, the partial results presented seem to confirm

the theoretical expectations: while the state-space approach is faster, the dynamic network approach is more accurate. Although IMU redundancy was implemented within the GAL project, the final quality of the measurements did not allow to investigate this aspect. Yet, we note that the network approach can manage instrument redundancy in a natural and elegant way. From a software development and operation point of view, dynamic networks tend to reduce the complexity of production lines as there are less software components/modules to integrate. Last but not least, the dynamic network approach generates results that can be interpreted with the theory, the tools and the intuition of geodesy and geodesists.

6.4 Requirement on Further Smoothing

The previous investigations in KAG have revealed considerable level of noise in the gravity anomalies (Wei and Schwarz 1998). As the predominant noise content is usually of higher frequency than the signal of interest, a low pass filter is highly suitable to remove this noise. For this purpose, a filter has been designed employing *equiripple* method with the following characteristics:

- negligible amplitude distortion of the signal in the pass band,
- relatively steep transition between pass- and stop bands,
- zero-phase distortion of the signal.

The correct functionality of filter was tested with respect to previously reported methodology (Glennie 1999). There the decision on the choice of cut-off frequency depended on

Fig. 4 Reference and recovered
gravity anomaly
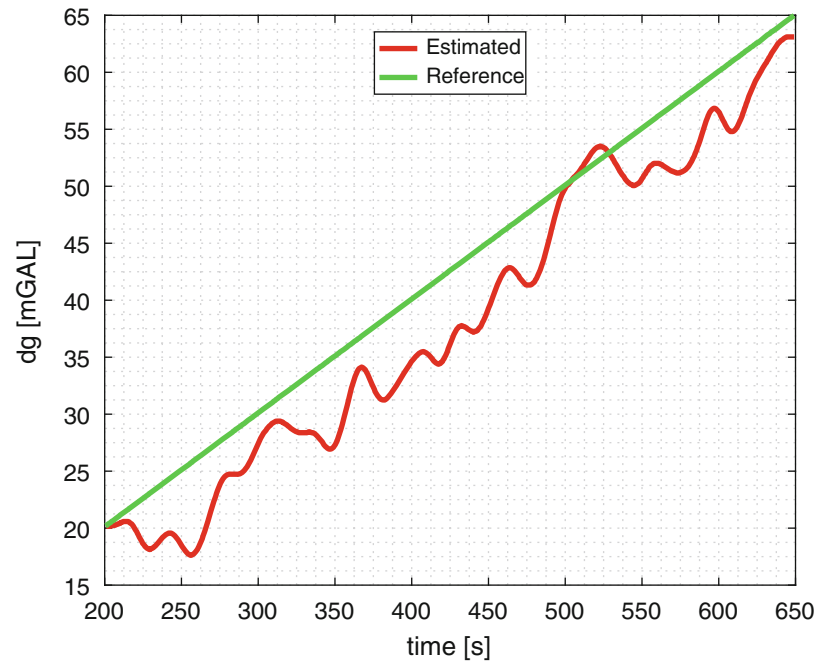
Fig. 5 The difference between
unfiltered and low-passed filtered
gravity anomalies (both estimated
by the presented approach) with
cut-off frequency of 1/30 Hz
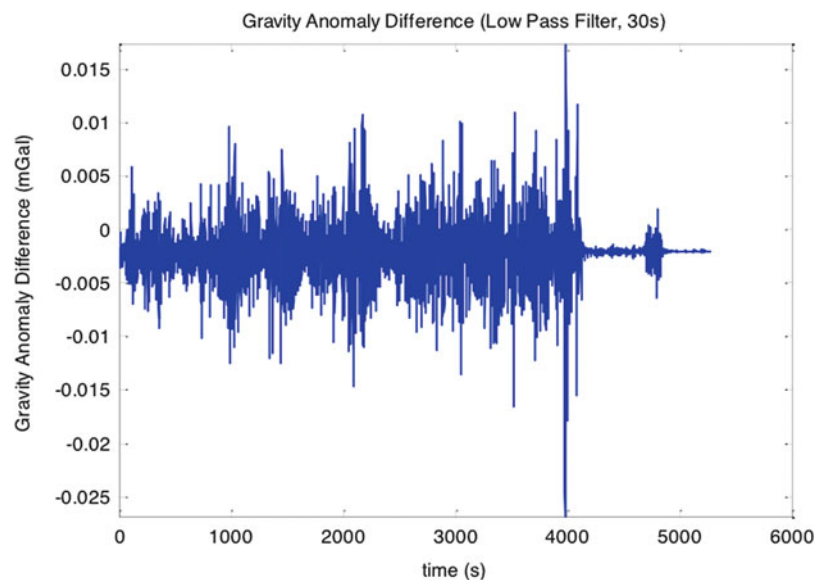
several factors such as the terrain roughness, the speed of the
aircraft or the resolution versus accuracy requirements of the
final estimate.

The experience with data processed by the proposed
methodology is quite different. Here the Kalman fil-
ter/smoother (or dynamic networks) dampened the high
frequency content to such a level that further smoothing
of gravity anomalies is no longer necessary. This situation
is depicted in Fig. 5. It shows the effect of further low-
pass filtering on the KAG-determined gravity anomalies.
As can be seen from this figure, the difference between
unfiltered and filtered gravity anomalies is less than
0.02 mGal, which is negligible. That empirically verified

the theoretical assumption that for a correctly designed state-
space estimator or dynamic network no further smoothing of
gravity anomalies is necessary.

7 Conclusions and Recommendations

The aerial gravimetric part of the GAL project has been
described and put in the context of the historical development
of KAG and its particular realization by the method of
GNSS/INS integration with strapdown inertial measurement
units. The progress in motion sensing technology and estima-
tion methods has been discussed and, to a certain extend also

investigated considering the lack of actual Galileo signals. For this purpose, realistic emulations were performed for Galileo measurements along actual flights in Northeastern Spain. GPS and simulated Galileo data were processed to obtain an insight on the advantages of multi-constellation GNSS configurations – focused on the GPS/Galileo combination – under the PPP processing approach in order to avoid the noisier differential approach. Also for the same purpose, short time periods of inertial and GNSS measurements were processed with the implemented dynamic network method and compared to the more traditional state-space method – i.e., using an extended Kalman filtering and smoothing technique. In spite of the lack of actual data and of the challenge of processing inertial measurements, the various partial project results recommend: (a) the use of multi-constellation GNSS receiver with range and phase measurements of at least GPS and Galileo; (b) the use of the PPP post-processing technique and (c) the further development and use of the dynamic network adjustment technique for a single-step, consistent estimation of scalar gravity anomalies (or disturbances with respect to a global gravity model).

References

Bastos L, Tome P, Cunha T, Cunha S (2000) Gravity anomalies from airborne measurements - experiments using a low cost IMU device. In: The International Association of Geodesy Symposia Serie, Banff, vol 123

Brown J, Niebauer TM, Klopping FJ (2002) Towards a dynamic absolute gravity system. In: Sideris M (ed) International Association of Geodesy Symposia, vol 123. Springer, New York, pp 223–225

Brozena J, Peters M, Salman R (1996) Arctic airborne gravity measurement program. In: IAG symposia GRAGEOMAR, gravity, geoid and marine geodesy, vol 117, pp 131–138

Bruton A, Glennie C, Schwarz K (1999) Differentiation for high precision GPS velocity and acceleration determination. GPS Solutions 2(4):7–22

Colomina I, Blazquez M (2004) A unified approach to static and dynamic modeling in photogrammetry and remote sensing. Int Arch Photogramm Remote Sensing Spat Inf Sci 35-B1:178–183

Diez J, Fernández A, D'Angelo P, Caramagno A (2006) GRANADA: a low-cost commercial simulator for GNSS receivers design and evaluation. In: Proceedings of the NAVITEC 2006, Noordjwik, p 8

Ferguson S, Hammada Y (2002) Experiences with AIRGrav: results from a new airborne gravimeter. In: Sideris M (ed) International Association of Geodesy Symposia, vol 123. Springer, New York, pp 211–222

Forsberg R, Olesen A, Keller K (2002) Airborne gravity survey of the north greenland continental shelf. In: Sideris M (ed) International Association of Geodesy Symposia, vol 123. Springer, New York, pp 225–240

Friess P (1990) Kinematische positionsbestimmung fur die aerotriangulation mit dem navstar global positioning system. Ph.D. thesis, TU Munchen

Fukushima T (2012) Numerical computation of spherical harmonics of arbitrary degree and order by extending exponent of floating point numbers. J Geod 86:271–285

Gelb A (1988) Applied optimal estimation. The MIT Press, Cambridge

Gerlach C, Dorobantu R, Ackermann C, Kjorsvik NS, Boedecker G (2010) Preliminary results of a GPS/INS airborne gravimetry experiment over the german alps. In: Mertikas SP (ed) International Association of Geodesy Symposia, vol 135. Springer, New York, pp 3–9

Gilardoni M, Reguzzoni M, Sampietro D (2013) A least-squares collocation procedure to merge local geoids with the aid of satellite-only gravity models: the Italian/Swiss geoids case study. Boll Geofis Teor Appl 54(4):303–319

Gilardoni M, Reguzzoni M, Sampietro D (2014) Using GOCE to straighten and sew European local geoids: preliminary study and first results. In: Marti U (ed) Gravity, geoid and height systems. International Association of Geodesy Symposia, vol 141. Springer, New York, pp 229–234

Gilardoni M, Reguzzoni M, Sampietro D (2016) GECO: a global gravity model by locally combining GOCE data and EGM2008. Stud Geophys Geod 60:228–247

Glennie C (1999) Analysis of airborne gravity by SINS/DGPS. INS, gravity, University of Calgary

Glennie C, Schwarz K (1999) A comparison and analysis of airborne gravimetry results from two strapdown inertial/DGPS systems. J Geod 73(6):311–321

Global Navigation Satellite Systems Agency (2011) GAL: Galileo for gravity. GSA research project FP7-287193

Jones P, Johnson AC (1995) Airborne gravity survey in southern palmer land, antartica. In: IAG symposia G4, IUGG XXI general assembly, Boulder, pp 117–124

Klingele E, Cocard M, Kahle H, Halliday M (1997) Kinematic GPS as a source for airborne gravity reduction: the airborne gravity survey of Switzerland. J Geophys Res 102(B4):7705–7715

Li X (2011) Strapdown INS/DGPS airborne gravimetry tests in the Gulf of Mexico. J Geod 85:597–605

Li Y, Schwarz K, Wei M (1994) The spectral window for airborne gravity and geoid determination. In: International symposium on kinematic systems in geodesy, geomatics and navigation (KIS 1994), pp 445–456

Migliaccio F, Reguzzoni M, Sanso F, Tselfes N (2009) An error model for the GOCE space-wise solution by Monte Carlo methods. In: Sideris M (ed) International Association of Geodesy Symposia, vol 133. Springer, New York, pp 337–344

Parés M, Navarro J, Colomina I (2015) On the generation of realistic simulated inertial measurements. In: Proceedings of the DGON 2015 inertial sensors and systems (ISS), Karlsruhe

Reguzzoni M, Tselfes N (2009) Optimal multi-step collocation: application to the space-wise approach for GOCE data analysis. J Geod 83(1):13–29

Rouzaud D, Skaloud J (2011) Rigorous integration of inertial navigation with optical sensors by dynamic networks. J Inst Navig 58(2):141–152

Sampietro D, Mansi AH, Amodio A, Sanso F (2015) Gravity anomalies and geoid undulation from strapdown airborne gravimetry: outcomes

from the gal project. In: IAG symposia G2, IUGG general assembly 26, Prague

Sampietro D, Capponi M, Triglione D, Mansi A, Marchetti P, Sansò F (2016) GTE: a new software for gravitational terrain effect computation: theory and performances. Pure Appl Geophys 1–19. doi:10. 1007/s00024-016-1265-4

Sarjakoski T (1984) On sparse matrix techniques for computing weight coefficient matrices. ISPRS Int Arch Photogramm Remote Sens XXV-A3:932–944

Schwarz K (1987) Approaches to kinematic geodesy. In: Geodetic theory and methodology. Department of Geomatics Engineering, The University of Calgary

Schwarz K, Li Y (1995) What can airborne gravimetry contribute to geoid determination? In: IAG Symposia G4, IUGG XXI general assembly, Boulder, pp 143–152

Seeber G (1993) Satellite geodesy. Walter de Gruyter, Berlin

Termens A, Colomina I (2006) Network approach versus state-space approach for strapdown inertial kinematic gravimetry. In: International Association of Geodesy Symposia, vol 131. Springer, New York, pp 107–112

Timmen L, Bastos L, Forsberg R, Gidskehaug A, Meyer U (1999) Airborne gravity surveying for oceanography, geology and geodesy - the experiences from AGMASCO. In: IAG General Assembly, Birmingham. International Association of Geodesy Symposia, vol 121, pp 118–123

Tome P (2002) Integration of inertial and satellite navigation systems for aircraft attitude determination. Ph.D. thesis, Department of Applied Mathematics, University of Porto

Wei M, Schwarz K (1994) An error analysis of airborne vector gravimetry. In: International symposium on kinematic systems in geodesy, geomatics and navigation (KIS 1994)

Wei M, Schwarz K (1998) Flight test results from a strapdown airborne gravity system. J Geod 72:323–332

Hybrid Gravimetry as a Tool to Monitor Surface and Underground Mass Changes

J. Hinderer, B. Hector, A. Mémin, and M. Calvo

Abstract

This paper is devoted to an overview of the use of hybrid gravimetry in Earth and Environmental Sciences. We first recall the concept of hybrid gravimetry which relies on the simultaneous use of different types of gravimeters either superconducting, absolute or relative spring gravimeters. This combination of instruments provides a complete tool for time-lapse gravimetry: while superconducting gravimeters and/or absolute gravimeters are used to obtain temporal gravity changes at one or several base stations, relative gravity surveys provide spatial differences with respect to these base stations, and allow to cover a much wider area than base stations only. Hybrid gravimetry therefore provides time-lapse gravity changes at a survey scale. We present here an overview of different published applications in hydrology, glaciology, volcanology and geothermics in order to point out that hybrid gravimetry is a powerful tool to monitor spatially and temporarily surface and underground mass changes.

1 Introduction

The term Hybrid Gravimetry (HG) was first introduced by Okubo et al. (2002) in a study dedicated to the gravity monitoring of a Japanese volcano (Mt Fuji) where the design for a gravity network included a transportable absolute gravimeter (AG) acting as reference for relative measurements (RG) done with spring meters. Later on Sugihara and Ishido (2008) introduced the concept of Super Hybrid Gravimetry (SHG) for geothermal reservoir monitoring by adding a new generation of superconducting gravimeter (SG) to the hybrid system (AG + RG). A last example of Hybrid Gravimetry can be found on Micro-g LaCoste Web site (http://www.microglacoste.com) as an announcement for HybridGravity™ Survey by adding A10 AG measurements to Scintrex CG-5 RG measurements. Earlier work also used the concept of hybrid gravimetry, although without naming it (e.g. Pool et al. 2000; Crossley and Hinderer 2005).

In this paper, we will first review the concept of Hybrid Gravimetry and will try to show the interest or even the necessity to combine different types of gravimeters in many research fields. To illustrate this we later give some examples of published applications in close connection to Earth and Environmental Sciences. We begin with hydrology and consider the case of a small catchment in West Africa. We then move to glaciology in Svalbard where hybrid gravimetry

J. Hinderer (✉) • M. Calvo
Institut de Physique du Globe de Strasbourg, UMR 7516 CNRS, University of Strasbourg, Strasbourg, France
e-mail: jacques.hinderer@unistra.fr

B. Hector
LTHE, UMR 5564, CNES/IRD/UJF-Grenoble 1/CNRS/G-INP, 38041, Grenoble, France

A. Mémin
CNRS, OCA, IRD, Géoazur, Université Côte d'Azur, 250 rue Albert Einstein, Sophia Antipolis, 06560, Valbonne, France

M. Calvo
Observatorio Geofísico Central, Instituto Geográfico Nacional, Madrid, Spain

Fig. 1 The concept of hybrid gravimetry to investigate an underground reservoir with the combination of superconducting gravimeter (SG), absolute gravimeter AG and relative spring meter RG (adapted from Sugihara et al. 2013)
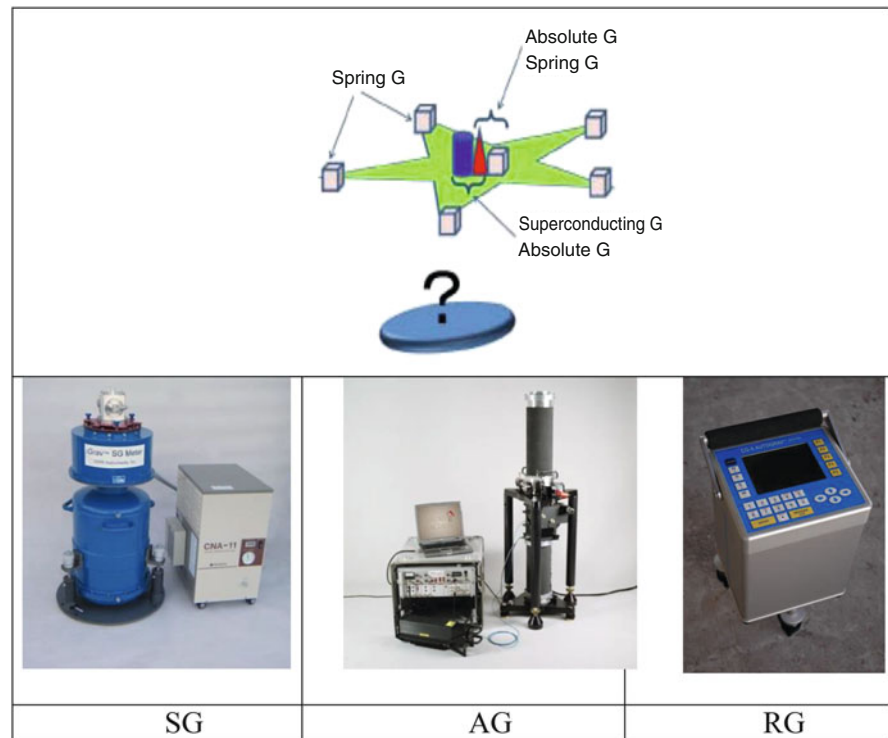
helps in assessing geodetic consequences of Present-day Ice Melting (PDIM). We finally end this section by presenting studies in volcanology and geothermics.

2 Hybrid Gravimetry

Several studies have introduced the concept of hybrid gravimetry (Okubo et al. 2002; Sugihara and Ishido 2008; Hector et al. 2015) that is the ideal combination of different types of gravimeters (see Fig. 1):

- a permanent gravimeter which allows a precise continuous monitoring of the time-varying gravity at a reference station located on the investigated site; this is usually done with a superconducting gravimeter (SG) rather than a spring meter because of its very small instrumental drift and better precision;
- a ballistic absolute gravimeter (AG) that allows to control the long term gravity changes by repeated parallel recording over short periods of time with the SG, as well as to check the calibration stability of the SG;
- a spring relative gravimeter (RG) to repeat observations on a micro-gravimetric network around reference stations by successive loops in order to gain more insight into the space-time changes in the investigated region.

The concept of hybrid gravimetry (HG) is illustrated on Fig. 1 where a combination of SG, AG, and RG observations at the Earth's surface aims to characterize the time

evolution of any redistribution of mass (density, geometry, location) whatever its origin (glaciology, hydrology, geothermal reservoir, CO_2 sequestration). The diversity of user requirements and of gravimetric observation techniques has become obvious in many fields (e.g. Boedecker 2002). Of course a number of geophysical effects have to be corrected first (Earth and ocean tides, air pressure, polar motion) before investigating the body of interest.

In general there are two main approaches in time-lapse gravity studies.

The first observational strategy is to use a continuous monitoring with a SG. The advantage of such a permanent station is a strong time resolution (typically 1 s) and high precision (better than 0.1 μGal) (Hinderer et al. 2007). The disadvantage is that no spatial coverage is achieved and the small remaining instrumental drift of the SG requires regular AG measurements.

The second observational strategy is to use gravity networks with a RG (Naujoks et al. 2010). The main advantage is a better spatial coverage and the control of the (large) instrumental drift of the RG by loop repetition but there is still a large disadvantage which is the need for a reference point where the gravity changes are known. Moreover network gravity studies are expensive in manpower and time for obtaining a large number of measurements and processing the data.

Hybrid gravimetry is in fact a way to combine both strategies to optimize gravity measurements and processing. We can separate the following approaches:

Fig. 2 Gravity changes in Djougou (West Africa) for the 2008–2013 period from the GRACE mascon solution (in *blue*), ground gravity from a SG (in *black*) and AG (in *red*) and predicted by GLDAS hydrology model (in *green*)
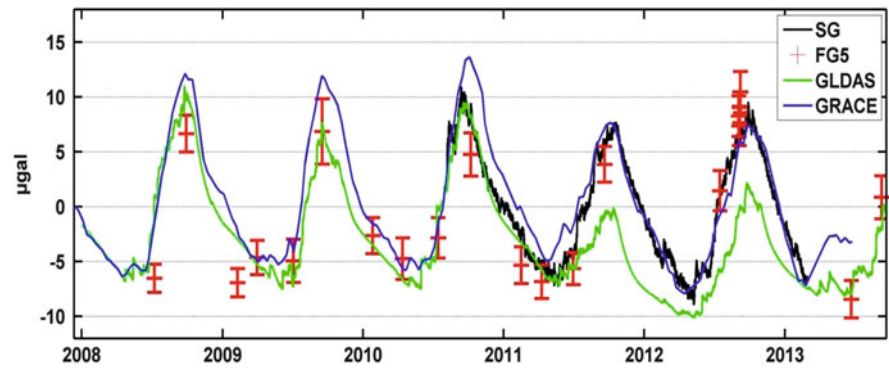
– To tie local measurements (RG) on a network (only relative with respect to? local base station) to a known reference (AG) leads to absolute changes in space
– To tie continuous local measurements (SG) to a reference (AG) leads to absolute changes in time
– The ideal solution is combining the two previous approaches which leads to the knowledge of absolute changes in both space and time.

3   Examples of Hybrid Gravimetry Studies

3.1   Hydrology

Underground water storage changes (WSC) are fundamental unknowns of the water cycle which are still challenging to derive from classical point measurements (i.e. moisture probes, water table depths . . .). Hydrogravimetry has become very important in linking spatially-integrated WSC to surface gravity changes using SG, AG and RG measurements or specific combinations of the three (Davis et al. 2008; Hare et al. 2008; Jacob et al. 2008, 2010; Longuevergne et al. 2009; Creutzfeldt et al. 2010; Naujoks et al. 2010; Pfeffer et al. 2011; Hector et al. 2015).

We focus here on the study of a small (16 ha) subcatchment of the Ara river in West Africa near Djougou (Benin). This catchment belongs to the Upper-Ouémé catchment in northern Benin with a humid Sudanian-type climate. This catchment is studied since several years by hydrologists in the frame of the AMMA-CATCH observatory (Lebel et al. 2009; Séguis et al. 2011). A dense monitoring network dedicated to water redistribution process studies has been set up since 2003, including neutron probe (NP) measurements. A NP allows to derive moisture contents (hence WSC) from neutron counts in a 0.15 m radius around a borehole at each measurement depth. Gravity observations were added to the previously existing hydro-meteorological sensors for air pressure, soil humidity, and aquifer levels in the GHYRAF (Gravity and Hydrology in Africa)

project since 2008 (Hinderer et al. 2012). In the beginning we mainly relied on episodic AG measurements 4 times a year (Hector et al. 2013). Later on, in 2010 we installed a permanent SG on this catchment a few meters besides the AG pillar (Hinderer et al. 2013; Hector et al. 2014).

We also established in 2011 a gravity network with RG measurements (Hector et al. 2015). The repetition of this network of 13 stations was typically once a month in the dry season and once a week in the rainy period i.e. in summer. The uncertainty we achieve on this network where the RG is hand-carried on small distance loops is excellent (<2.5 μGal). In this hybrid gravity experiment, we hence have available a continuous series of the SG complemented with regular AG measurements, and a dense RG repetition network. Figure 2 shows the gravity temporal changes as seen by the continuous SG data with episodic AG measurements (Hector et al. 2013, 2014), as well as GRACE satellites data and GLDAS (Rodell et al. 2004) global hydrology model prediction. The GRACE data shown here are obtained from the mascon (mass concentration) solution (Luthcke et al. 2013). AG measurements helped in validating the removal of the instrumental drift (modeled as an initial exponential followed by a linear part). It is interesting to note the close agreement between the surface measurements (SG/AG) and GRACE. On the contrary, more discrepancies exist with the hydrology model, especially in summer 2011.

The large set of available data (70 surveys between July 2011 and September 2013) allowed us to perform an EOF (Empirical Orthogonal Function, a well suited method for the extraction of coherent time and space patterns in the data) decomposition of the gravity field and water content from the neutron probe data.

A recent gravimetry study performed using the EOF method is illustrated in Crossley et al. (2012). Figure 3 shows the results of this EOF decomposition on a time span covering 2 contrasted years (Hector et al. 2015) with, respectively, the EOFs of the first mode for gravity changes and NP-derived WSCs. For both datasets, the first mode explains much of the variance in the data (79% for gravity changes, and 90% for WSCs) meaning that the signal can be

Fig. 3 EOF results for gravity
and NP data in Djougou (West
Africa): (**a**) Mode I EOF for
hybrid gravity data. (**b**) Mode I
EOF for NP data. (**c**) Cumulated
variance explained for each EOF
mode for each dataset. (**d**)
Expansion coefficients of mode I
for hybrid gravity data and NP
data and daily precipitation (from
Hector et al. 2015)
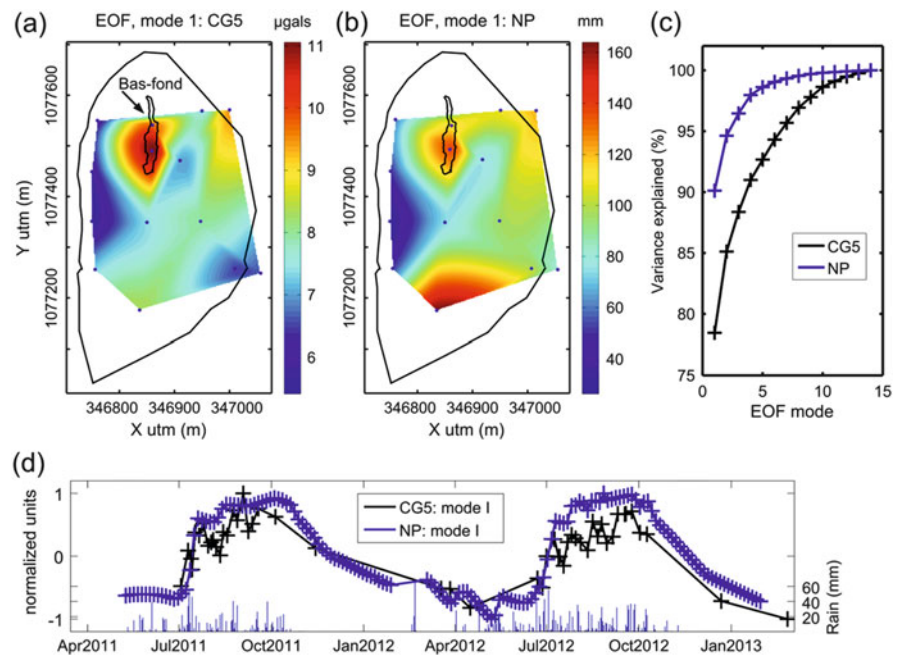
reconstructed up to 79% for gravity and up to 90% for WSCs.
The temporal aspect of mode 1 for all datasets shows that
it is the seasonal signal that dominates the variance. EOFs
therefore represent the spatial distribution of variations in
this seasonal behavior.

WSCs from NP data show similar space-time patterns
than gravity changes despite different footprints (about
100 m radius for gravity observation and about 0.15 m
radius for NP data). In the study of Hector et al. (2015),
these patterns could be related to the catchment lithology,
explaining the similar results from both datasets with
different footprints, and streamflow generation processes
were derived from these observations. It is important to
note that, without the inclusion of the seasonal changes,
brought by the SG monitoring of the reference station and
which contribute highly to the signal variance, the EOF
decomposition of the RG data alone fails because of signal
to noise problems. In this case, the variance is governed by
higher frequency components (i.e. days to weeks) which
often fall within the data error bars. There is much less space
and time coherence of the variance when using RG data only.
It is clearly the hybrid gravimetry approach that enables us to
extract the coherent spatio-temporal variation of the gravity
field.

3.2 Ice Melting

Our second example of interest for hybrid gravimetry deals
with glaciology such as in Svalbard (Norway) in the Arctic.
Svalbard is known to be one location where PDIM occurs
in addition to past ice melting. Besides, there is a geode-

tic reference station, in Ny-Alesund, coupling gravity and
positioning measurements. The goal there is to relate surface
gravity variations and crustal vertical motion to ice melting
from glaciers (Mémin et al. 2009) either originating from
today deglaciation (PDIM), caused by global warming, or
from past (Pleistocene) deglaciation (Mémin et al. 2011,
2012, 2014). This goal was achieved by combining the
hybrid gravimetry approach with positioning measurements.

The station of Ny-Alesund benefits both from precise
positioning with the help of various independent techniques
(VLBI, GPS, DORIS), tide gauge observations and gravity
measurements thanks to a permanent SG since 2000 and
regular (once a year or once every 2 years) AG measurements
(Fig. 4). When considered alone the AG values (in blue) lead
to a trend of -1.23 ± 0.51 µGal/year which is quite uncer-
tain (error of about 42%). But if one takes into account the
seasonal variability as observed by the SG and corrects the
AG values (the hybrid approach), the gravity trend becomes
-1.39 ± 0.11 µGal/year (Mémin et al. 2014). This value is
larger than before but, more important, the scattering of the
corrected values around the linear trend is greatly reduced
which leads to a trend uncertainty reduced by a factor close
to 5 (corresponding to an error of about 7%).

Several studies focused on explaining simultaneously the
gravity changes and the vertical land motion due to the defor-
mation induced by the past and present-day ice-mass changes
and observed in Ny-Alesund (e.g. Omang and Kierulf 2011;
Mémin et al. 2011). In that regard, they usually consider
several melting histories. Thanks to the gravity rate estimated
using the hybrid gravimetry strategy, Mémin et al. (2014)
were able to refine the modeling and explain both gravity
and vertical displacement changes in Ny-Alesund. They

Fig. 4 Gravity variations measured at the Ny-Alesund geodetic observatory by a superconducting gravimeter (*grey line*) and an absolute gravimeter (*blue squares*). The *black line* shows the SG measurements after filtering out the high frequencies using a moving average over 1 month. The *red squares* show the absolute gravity measurements corrected for a seasonal signal estimated from the SG measurements. The *blue* and *red lines* are the linear trends estimated using the AG and the corrected AG measurements, respectively
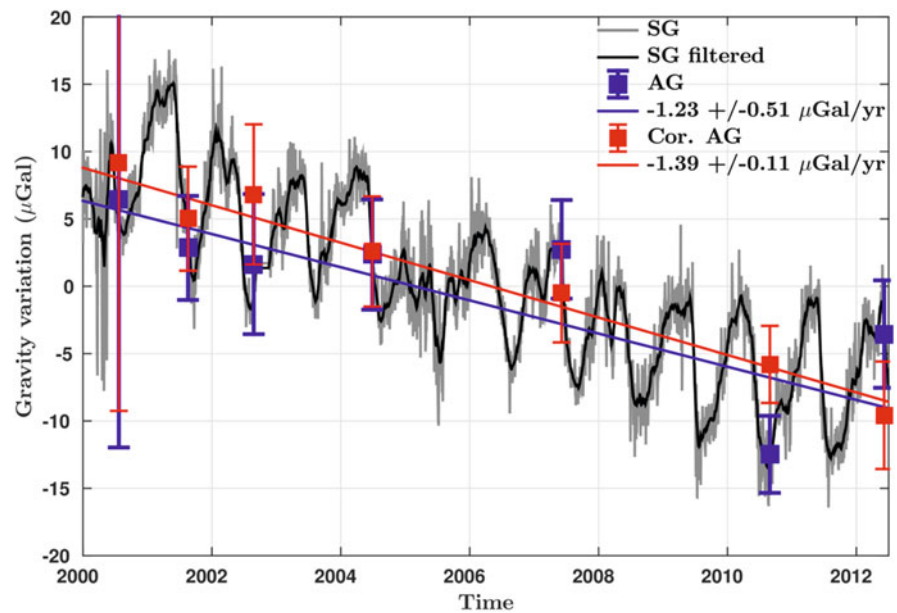
added contributions to the deformation that were previously neglected. These contributions involve a new component to the melting history, known as the little Ice Age, and the sea level change due to present-day ice-mass change.

3.3 Volcanology

In volcanology the goal using geodetic and gravity observations is the modeling of volcano dynamics and associated eruptions. A nice example was given by Furuya et al. (2003) on Miyakejima volcano in Japan where the combination of AG and RG measurements together with GPS and tilt observations helped the authors to correct the gravity data for the effect of collapsed topography during an eruption and to propose a speculative scenario for the temporal evolution of the volcanic activity. For more references in volcano-gravimetry we refer the reader to Crossley et al. (2013).

New results were obtained from hybrid gravimetry on other volcanoes using mostly AG and RG measurements (Carbone and Greco 2007; Hautmann et al. 2010; Battaglia et al. 2008) that allow to determine absolute changes in the local network which were unknown in previous studies based only on RG observations (e.g. Jousset et al. 2000). An example of hybrid gravimetry approach can be found on Etna volcano in Italy. Figure 5 shows the network established on this volcanoe combining RG and AG measurements (Greco et al. 2012). More recently SG continuous monitoring was added to RG and AG and promising results are expected (Carbone and Greco 2015).

3.4 Geothermics

The final field where hybrid gravimetry is promising is related to geothermal activity (Nishijima et al. 2000; Oka et al. 2012; Sofyan et al. 2011; Sugihara and Ishido 2008; Takemura et al. 2000; Schultz et al. 2012) which has clearly become important as a possible alternative energy resource for the future. Many experiments have started and more references can be found in Hinderer et al. (2015). The goal of these studies is the modeling of the geothermal fluid circulation and mass transport which is often occurring at large depths (several hundreds or even thousands of meters); it is hence much more difficult to detect than surface or sub-surface mass changes like in glaciology or hydrology. A nice example of hybrid gravimetry applied to geothermics can be found in Oka et al. (2012) on the Takigami geothermal field in Japan producing 25 MW power. A study involving AG and RG (together with GPS) could identify the spatial distribution of gravity on this geothermal site just after the start of the power generation and the modeling leads to an estimate of 12 Mt of water extraction per year. Another example of using hybrid gravimetry to optimize time-lapse monitoring data can be found in Sofyan et al. (2015). Figure 6 (left) shows the network of the Kamojang geothermal field in Indonesia where both AG and RG measurements are regularly repeated. Figure 6 (right) shows the time evolution of the AG benchmarks indicating that at several locations gravity decreased between 2010 and 2011 while it was more constant in the period 2009–2010. This is important because gravity monitoring with RG alone assume

Fig. 5 The hybrid gravity
network of Etna volcano (Italy)
showing the RG and AG
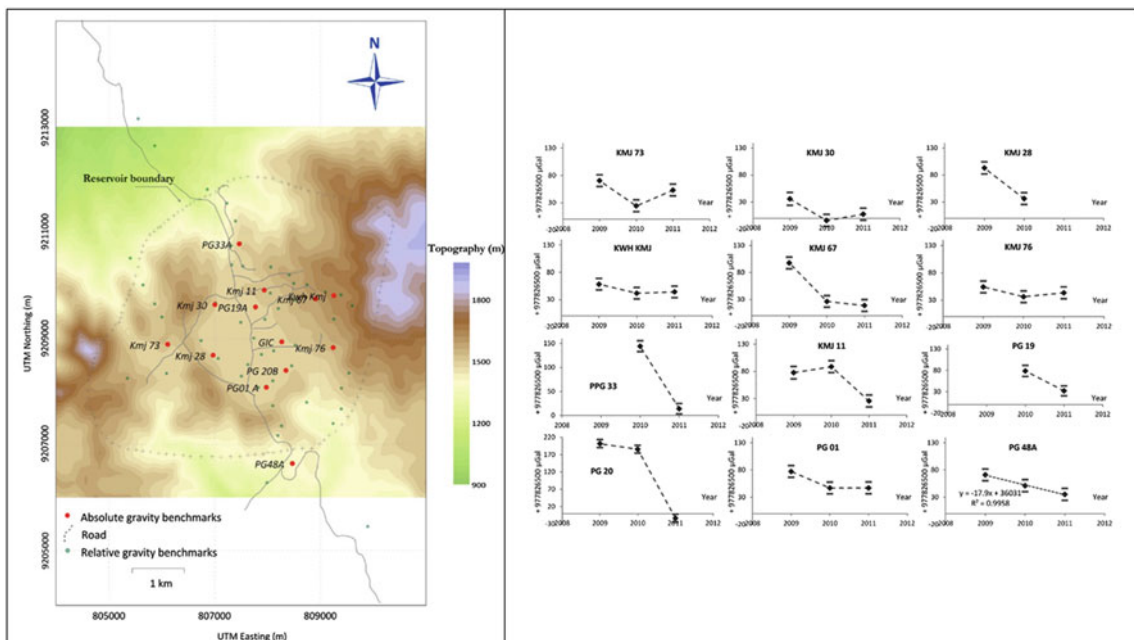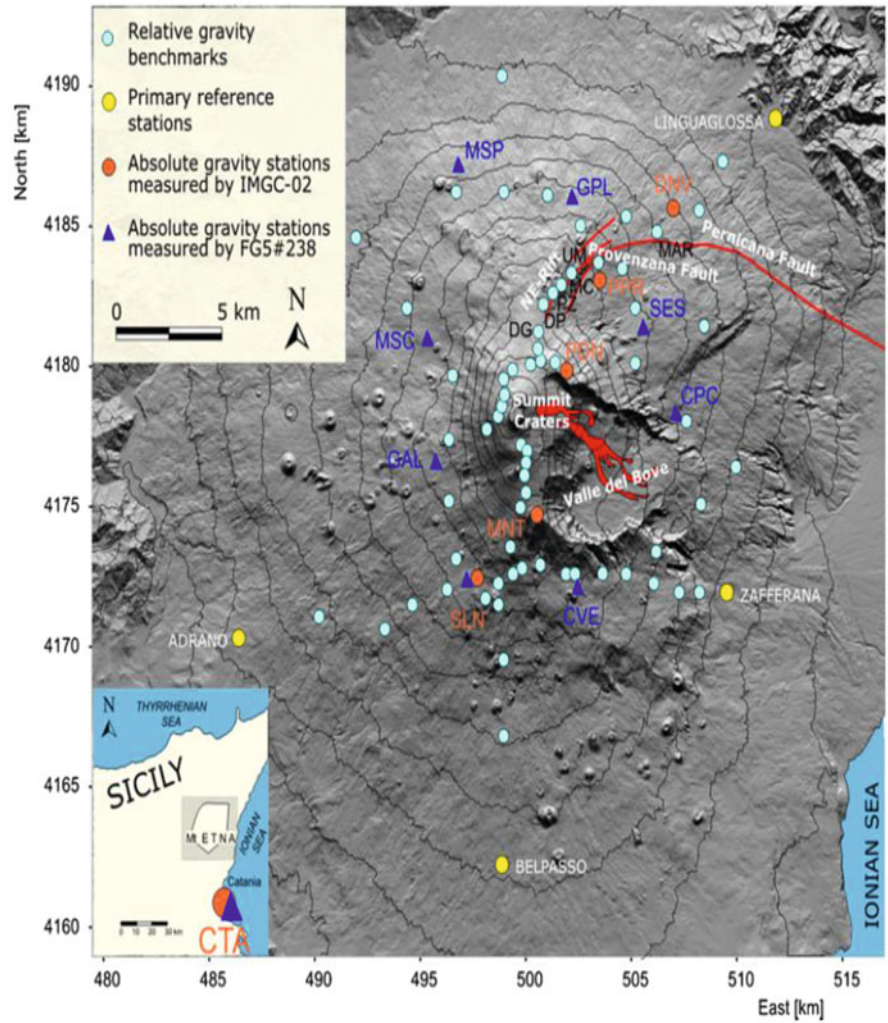benchmarks (from Greco et al.
2012)

Fig. 6 The hybrid gravity network of the Kamojang geothermal field (Indonesia) showing the location of the RG and AG benchmarks (*left*) and the time changes of gravity at these absolute benchmarks (*right*) (from Sofyan et al. 2015)

that the reference station is constant. This assumption is not true if there is for instance a regional effect and AG measurements are then the best way to correct the gravity changes at the reference station.

4 Conclusion

The combination of several types of gravimeters (AG, SG, RG) involved in the hybrid gravimetry approach leads to valuable information on any surface or underground mass redistribution in time and space. Hybrid gravimetry associated with geodesy (GNSS, InSAR, VLBI) allows more insight into the physical processes since mass transport effects in gravity can be isolated from geometrical effects linked to the vertical motion of the ground. We have shown one example of application in hydrology in West Africa where hybrid gravimetry led to characterize the space-time behavior of water storage changes in a catchment of small size. Another example came from ice melting in Svalbard in the Arctic where combining continuous SG measurements to episodic AG observations led to infer a more precise gravity trend over a decade which helped in modeling the contribution of past and present-day ice melting. We also reviewed applications of hybrid gravimetry in volcanology and geothermic. More applications are expected in various fields in Earth and Environmental Sciences.

References

Battaglia M et al (2008) 4D volcano gravimetry. Geophysics 73:WA3–WA18. doi:10.1190/1.2977792

Boedecker G (2002) World gravity standards – present status and future challenges. Metrologia 39:429–433

Carbone D, Greco F (2007) Review of microgravity observations at Mt. Etna: a powerful tool to monitor and study active volcanoes. Pure Appl Geophys 164:769–790

Carbone D, Greco F (2015) The iGrav superconducting gravimeter as a tool to monitor and study active volcanoes. Preliminary results from Mt. Etna (Italy). Geophysical Research Abstracts, vol 17, EGU2015-11138, 2015

Creutzfeldt B et al (2010) Measuring the effect of local water storage changes on in situ gravity observations: case study of the Geodetic Observatory Wettzell, Germany. Water Resour Res 46:W08531. doi:10.1029/2009WR008359

Crossley D, Hinderer J (2005) Using SG arrays for hydrology in comparison with GRACE satellite data, with extension to seismic and volcanic hazards. Kor J Remote Sens 21(1):31–49

Crossley D, Hinderer J, Riccardi U (2013) The measurement of surface gravity. Rep Prog Phys 76. doi:10.1088/0034-4885/76/4/046101

Crossley D, de Linage C, Hinderer J, Boy J-P, Famiglietti J (2012) A comparison of the gravity field over Central Europe from superconducting gravimeters, GRACE and global hydrological models,

using EOF analysis. Geophys J Int 189:877–897. doi:10.1111/j.1365-246X.2012.05404.x

Davis K, Li Y, Batzle M (2008) Time-lapse gravity monitoring: a systematic 4D approach with application to aquifer storage and recovery. Geophysics 73. doi:10.1190/1.2987376

Furuya M et al (2003) Spatiotemporal gravity changes at Miyakejima volcano, Japan: caldera collapse, explosive eruptions and magma movement. J Geophys Res 108:2219

Greco F et al (2012) Combining relative and absolute gravity measurements to enhance volcano monitoring. Bull Volcanol 74:1745–1756. doi:10.1007/s00445-012-0630-0

Hare JL, Ferguson JF, Brady JL (2008) The 4D microgravity method for waterflood surveillance: Part IV – Modeling and interpretation of early epoch 4D gravity surveys at Prudhoe Bay, Alaska. Geophysics 73:WA173–WA180. doi:10.1190/1.2991120

Hautmann S et al (2010) Mass variations in response to magmatic stress changes at Soufriere Hills Volcano, Montserrat (WI): insights from 4-D gravity data. Earth Planet Sci Lett 290:83–89. doi:10.1016/j.epsl.2009.12.004

Hector B et al (2013) Gravity effect of water storage changes in a weathered hard-rock aquifer in West Africa: results from joint absolute gravity, hydrological monitoring and geophysical prospection. Geophys J Int. doi:10.1093/gji/ggt146

Hector B et al (2014) Hydro-gravimetry in West-Africa: first results from the Djougou (Benin) superconducting gravimeter. J Geodyn 80:34–49. doi:10.1016/j.jog.2014.04.003

Hector B et al (2015) Hybrid gravimetry and water storage changes in a headwater basement catchment of Sudanian West-Africa. Water Resour Res. doi:10.1002/2014WR015773

Hinderer J, Crossley D, Warburton R (2007) Superconducting gravimetry. In: Herring T, Schubert G (eds) Treatise on geophysics 3 (Geodesy). Elsevier, Amsterdam, pp. 65–122

Hinderer J et al (2012) Land water storage changes from ground and space geodesy: first results from the GHYRAF (Gravity and Hydrology in Africa) experiment. Pageoph 169(8):1391–1410. doi:10.1007/s00024-011-0417-9

Hinderer J et al (2013) Preliminary results from the superconducting gravimeter OSG-60 installed in West Africa (Djougou, Benin). In: Rizos C, Willis P (eds) Earth on the edge: science for a sustainable planet. Proceedings of the IAG General Assembly, Melbourne, Australia, June 28 - July 2, 2011. International Association of Geodesy Symposia, vol 139. Springer, Berlin, pp 413–420

Hinderer J et al (2015) Monitoring of a geothermal reservoir by hybrid gravimetry; feasibility study applied to the Soultz-sous-Forêts and Rittershoffen sites in the Rhine graben. Geotherm Energy 3:16. doi:10.1186/s40517-015-0035-3

Jacob T et al (2008) Absolute gravity monitoring of water storage variation in a karst aquifer on the larzac plateau (Southern France). J Hydrol 359(12):105–117. doi:10.1016/j.jhydrol.2008.06.020

Jacob T et al (2010) Time-lapse microgravity surveys reveal water storage heterogeneity of a karst aquifer. J Geophys Res 115:B06402. doi:10.1029/2009JB006616

Jousset P et al (2000) Temporal gravity at Merapi during the 1993–1995 crisis: an insight into the dynamical behaviour of volcanoes. J Volcanol Geotherm Res 100:289–320. doi:10.1016/S0377-0273(00)00141-4

Lebel T et al (2009) AMMA-CATCH studies in the Sahelian region of West-Africa: an overview. J Hydrol 375(1–2):3–13. doi:10.1016/j.jhydrol.2009.03.020

Longuevergne L et al (2009) Local and global hydrological contributions to gravity variations observed in Strasbourg. J Geodyn 48(3–5):189–194

Luthcke SB, Sabaka TJ, Loomis BD, Arendt AA, McCarthy JJ, Camp J (2013) Antarctica, Greenland and gulf of Alaska land-ice evolution from an iterated GRACE global mascon solution. J Glaciol 59(216):613–631. doi:10.3189/2013JoG12J147

Mémin A et al (2009) Ground deformation and gravity variations modelled from present-day ice thinning in the vicinity of glaciers. J Geodyn 48:195–203

Mémin A et al (2011) Secular gravity variations at Svalbard (Norway) from ground observations and GRACE satellite data. Geophys J Int 184(3):1119–1130. doi:10.1111/j.1365-246X.2010.04922.x

Mémin A, Hinderer J, Rogister Y (2012) Separation of the geodetic consequences of past and present ice-mass change: influence of topography with application to Svalbard (Norway). Pure Appl Geophys 169(8):1357–1372. doi:10.1007/s00024-011-0399-7

Mémin A et al (2014) Decadal geodetic variations in Ny-Alesund (Svalbard): role of past and present ice-mass changes. Geophys J Int 198(1):285–297. doi:10.1093/gji/ggu134

Naujoks M et al (2010) Evaluating local hydrological modelling by temporal gravity observations and a gravimetric three-dimensional model. Geophys J Int 182:233–249. doi:10.1111/j.1365-246X.2010.04615.x

Nishijima J et al (2000) Gravity monitoring of geothermal reservoirs in the Takigami Geothermal Field, Central Kyushu, Japan – gravity changes caused by production and reinjection of geothermal fluids. J Geotherm Res Soc Japan 22(2000):117–130

Oka D et al (2012) Evaluation of geothermal reservoir mass change from the gravity change at the Takigami geothermal area, Oita prefecture, Japan. In: Proceedings of the thirty-seventh workshop on geothermal reservoir engineering, Stanford University, Stanford, 30 Jan–1 Feb 2012, SGP-TR-194

Okubo S et al (2002) Grand design for the hybrid gravity network around the Mt. Fuji volcano. In: International symposium on geodesy in Kanazawa abstract, pp 39–40

Omang OCD, Kierulf HP (2011) Past and present-day ice mass variation on Svalbard revealed by superconducting gravimeter and GPS measurements. Geophys Res Lett 38:L22304. doi:10.1029/2011GL049266

Pfeffer J et al (2011) Hydrological contribution to time – variable gravity: influence of the West African monsoon in Southwest Niger. Geophys J Int 184(2):661–672

Pool DR, Winster D, Cole KC (2000) Land-subsidence and ground-water storage monitoring in the Tucson active management area, Arizona. USGS – U.S. Geological Survey. http://pubs.er.usgs.gov/publication/fs08400

Rodell M et al (2004) The Global land data assimilation system. Bull Am Meteorol Soc 85(3):381–394

Schultz A et al (2012) Newberry Volcano-novel use of 4D monitoring techniques to improve reservoir longevity and productivity in enhanced geothermal systems. In: 21st EM induction workshop, Darwin, Extended Abstract, 4 pp

Séguis L et al (2011) Origins of streamflow in a crystalline basement catchment in a sub-humid Sudanian zone: the Donga basin (Benin, West Africa). Inter-annual variability of water budget. J Hydrol 402(1–2):1–13. doi:10.1016/j.jhydrol.2011.01.054

Sofyan Y et al (2011) Mass variation in outcome to high production activity in Kamojang geothermal field, Indonesia: a reservoir monitoring with relative and absolute gravimetry. Earth Planets Space 63(11):1157–1167

Sofyan Y et al (2015) Hybrid gravimetry for optimization of time-lapse monitoring data: a case study in Kamojang geothermal field. In: Proceedings of the World Geothermal Congress 2015, Melbourne, 19–25 Apr 2015

Sugihara M, Ishido T (2008) Geothermal reservoir monitoring with a combination of absolute and relative gravimetry. Geophysics 73(6):WA37–WA47

Sugihara M, Nawa K, Nishi Y, Ishido T, Soma N (2013) Continuous gravity monitoring for CO2 geo-sequestration. Energy Procedia 37:4302–4309. doi:10.1016/j.egypro.2013.06.333

Takemura T et al (2000) Gravity monitoring in Yanaizu-Nishiyama geothermal field, Japan. In: Proceedings of the World Geothermal Congress 2000, Kyushu–Tohoku, 28 May–10 June 2000, pp 2937–2941

Tidal Spectroscopy from a Long Record of Superconducting Gravimeters in Strasbourg (France)

Marta Calvo, Séverine Rosat, and Jacques Hinderer

Abstract

We present a comparison in the various tidal bands, between two different spectral analyses of long gravimetric time series. The first one is performed using a long gravity series recorded by superconducting gravimeters at J9 Observatory (Strasbourg) and the second one uses a theoretical series of the same length, almost 28 years, computed for the same location according to the Hartmann and Wenzel tidal potential development.

Long term gravity records are of great interest when performing spectral analysis. The length of the data series allows us to retrieve small amplitude waves in the major tidal groups (e.g. tides generated by the third-degree potential, as for example $3MO_1$ in the diurnal, $3MO_2$ in the semi-diurnal, and MN_3 in the ter-diurnal frequency band, with amplitudes respectively of 2.29, 5.97 and 1.44 nm/s^2), to separate waves close in frequency, as the waves NO_1 and NO_{1X} which need more than 18 year data length to be separated and finally to detect very low-frequency signals such as the monthly, semiannual or annual waves. Several examples for each of these cases are shown in our series.

1 Introduction

We analyze 28 year series of data of hourly tide readings by superconducting gravimeters (SG) at J9 Observatory near Strasbourg (France) are analyzed. We expect to benefit from this unprecedented length by achieving high spectral resolution in the tidal bands. Thus, we will attempt to detect very small amplitude signals in order to separate contributions of near-frequency waves and also to detect low-frequency signals that cannot be observed in gravity set of shorter length.

In addition to the length of the series, the quality of the data and the temporal stability of the noise are also very important. This is why long records collected with SGs are preferred over long spring gravimeter records, even when the former are slightly shorter, mainly because of their long-term stability, lower noise level and very small instrumental drift.

The spectral amplitudes of the Strasbourg SG time series are compared with the amplitude spectrum of a theoretical series of the same length computed for the same location. This theoretical series is used in order to verify whether some of the peaks observed in the SG spectrum, are really tidal waves. Especially in the case of weak amplitude waves this theoretical series helps to confirm that observed peaks do not come from any instrumental or environmental noise.

M. Calvo (✉) • S. Rosat • J. Hinderer
Institut de Physique du Globe de Strasbourg, IPGS – UMR 7516, CNRS/Université de Strasbourg (EOST), 5 rue René Descartes, 67084 Strasbourg Cedex, France

M. Calvo
Observatorio Geofísico Central, Instituto Geográfico Nacional (IGN), c/Alfonso XII 3, 28014 Madrid, Spain
e-mail: mcalvo@fomento.es

2 Instrumentation and Data

Several types of absolute and relative gravimeters have been recording at J9 Observatory since the 1970s. This Gravimetric Observatory has a long history of recording solid Earth tides (Calvo et al. 2014b). In this study we only use data from the SGs installed there. The first SG was installed in 1987. It was a TT70 model (TT70-T005) (Hinderer et al. 1998), which was recording for almost 10 years. In 1996 it was replaced by a more compact model, the SG-C026. This new gravimeter is still recording up to date and will be replaced by a new model, even more compact, in the near future. Both gravimeters have been installed not only in the same observatory, but also on the same pillar, and there were only few days between the removal of the old instrument and the installation of the new one. So we can consider these two independent series and merge them, obtaining the longest available series ever recorded by SGs at the same observatory to date, almost 28 years. We have used a total of 10,180 days to perform this study, from August 1997 to June 2015. We have pre-processed and corrected each series independently before merging them, using for each one its own calibration factor and phase delay (both have been calibrated through parallel absolute gravity measurements, using absolute measurements from a JILAg-5 for the T005 (Hinderer et al. 1998) and from the FG5#206 for the C026 (Amalvict et al. 2002). The phase lag for the C026 was determined experimentally in 1999 (Van Camp et al. 2000), while that of T005 was determined from the phase differences of the eight major diurnal and semidiurnal waves between tidal analyses of the C026 and T005), and we have filled the gap between the removal of the old gravimeter and the installation of the new one (11 days) using a local tidal model, obtained from a tidal analysis at the station.

Theoretical series were computed with PREDICT (Wenzel 1996) for the same period (from August 1987 to June 2015) using the Hartmann and Wenzel (1995) tidal potential development and the Dehant, Defraigne and Wahr (DDW) non-hydrostatic Earth model (Dehant et al. 1999).

3 Spectral Analysis of a Long Gravity Series

Once both observed and theoretical 28 year data series have been prepared, a spectral analysis is performed for each one applying a Hanning window. In principle, using the Rayleigh criterion we know that two tidal frequencies can be separated on an interval of n equally spaced observations if their angular speeds differ at least by $360°/n$, where L is the data length (L = number of samples n times the sampling rate Δt). It is equivalent to request that their respective frequency separation Δf is given by $1/\Delta f \leq L$, hence the smallest detectable frequency is $f_0 = 1/L$. This means that the highest frequency resolution we can reach to separate two neighboring waves is inversely proportional to the length of the data set. We also know that the lowest frequency in the spectrum is also the inverse of the data length. In our case, we have more than 10,000 days of data, so it will lead us to obtain a frequency resolution of 10^{-4} cpd in the various tidal bands. So we tried to take advantage of this length to: search for very small amplitude signal, separate contributions of near frequency waves, and also detect very long frequency signals.

3.1 Small Amplitude Tidal Signals

First we investigate some of the very weak tidal signals present in our observed gravity data series. By comparing with the spectral amplitudes of the theoretical series, we can check that some signals that could be confused with noise actually correspond to tidal waves. The lower noise level of the SG series compared to the spring gravimeter allows us to detect some low-amplitude tidal waves that now are not hidden by the instrumental noise (Calvo et al. 2014a). Ducarme (2011) was able to determinate M_1, $3MK_2$, $3MO_2$ and M_3 with a precision of 0.1%, using long series from 17 SGs. In our case, several examples for the diurnal tidal band are given in Fig. 1, where we can clearly detect low-amplitude waves such as TAU_1 (theoretical amplitude for DDW non-hydrostatic Earth model = 4.01 nm/s²), $2NO_1$ (1.98 nm/s²) and even smaller peaks such as for example those waves indicated in blue, which correspond to the wave 4573 and wave 4597 in the potential catalogue of Hartmann and Wenzel (1995) or 432 and 434 in the catalogue of Tamura (Tamura 1987); these waves have amplitudes lower than 1 nm/s².

These small waves have been also detected in a tidal analysis performed using ETERNA 3.4 software (Wenzel 1996) leading to the values of the tidal parameters (amplitude and phase) for $2NO_1$ and TAU_1 indicated in Fig. 1.

Similar examples in the semi-diurnal tidal band are shown in Fig. 2, where we can detect waves GAM_2 (0.98 nm/s²), BET_2 (0.99 nm/s²), ALF_2 (1.13 nm/s²) and DEL_2 (0.38 nm/s²).

Just to emphasize how weak these signals are, we remind that the theoretical amplitudes for the largest waves in each band, diurnal and semi-diurnal, at this location are 308 nm/s² for O_1 and 328 nm/s² for M_2, exceeding by two orders of magnitude our small detected signals.
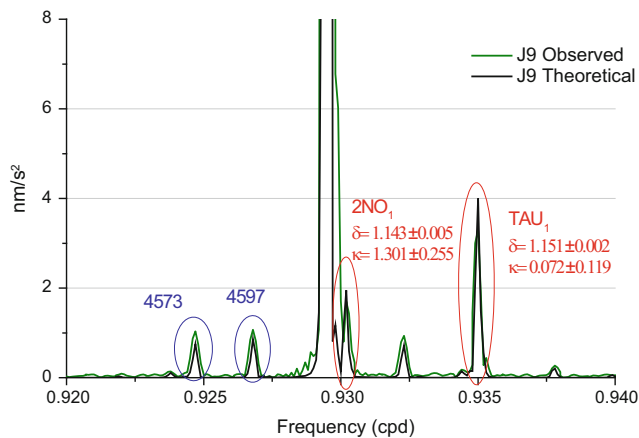
Fig. 1 Spectral amplitude in the diurnal frequency band of the observed 28 year series (T005 & C026), and of the theoretical series in *black*. *Blue numbers* correspond to the number wave in the potential catalogue of Hartmann and Wenzel (1995); frequency units: cycle-per-day (cpd)

Fig. 2 Spectral amplitude in the semidiurnal frequency band of the observed 28 year series (T005 & C026) and of the theoretical series in *black*. Frequency units: cycle-per-day (cpd)
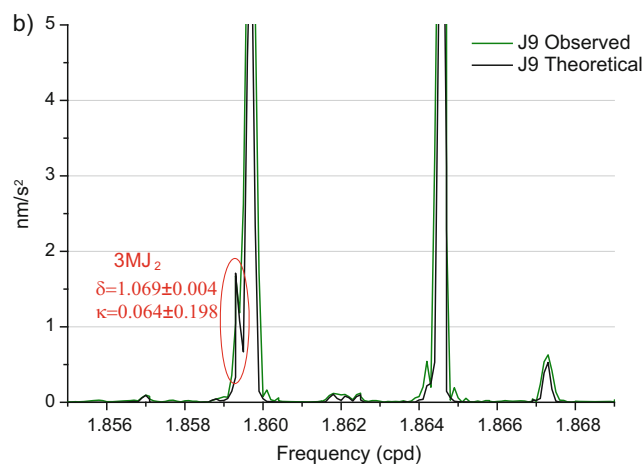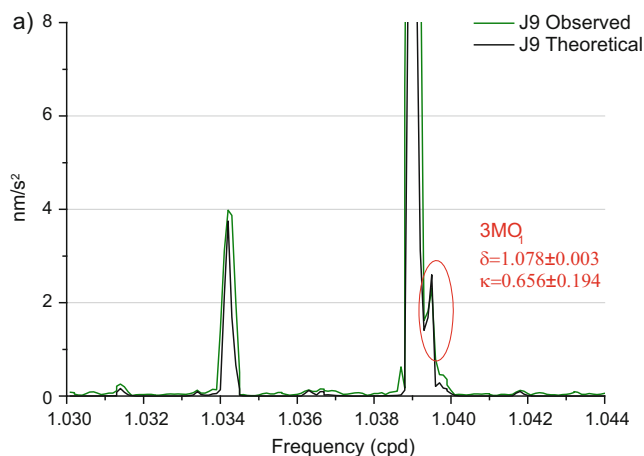
Fig. 3 Spectral amplitude of the observed 28 year series (T005 & C026) in *green*, and of the theoretical series in *black*, (**a**) in the diurnal frequency band, (**b**) in the semidiurnal frequency band

Fig. 4 Spectral amplitude of the observed 28 year series (T005 & C026) in *green*, and of the theoretical series in *black* in the quart diurnal frequency band

3.1.1 Tides Generated by the Third-Degree Potential

Another example of weak amplitude tidal wave detection is the case of waves generated by the third-degree potential. One example in the diurnal ($3MO_1$, 2.59 nm/s^2) and another one in the semi-diurnal ($3MJ_2$, 1.65 nm/s^2) frequency bands are shown in Fig. 3a, b.

Several other examples of tides generated by the third-degree potential have been observed in our total series, as for example waves M_1, $3MO_1$ in the diurnal frequency band, waves $3MKx$, $3MK_2$, MOx, $3MO_2$ and $3KM_2$ in the semi-diurnal frequency band and waves MN_3, M_3, M_3x, ML_3 and MK_3 in the ter-diurnal frequency band. In addition, two waves generated by the fourth-degree potential in the quart-diurnal tidal bands (N_4 and M_4) which have an amplitude

even smaller (0.018 and 0.052 nm/s^2 respectively) have also been detected (Fig. 4).

Spectral Analysis
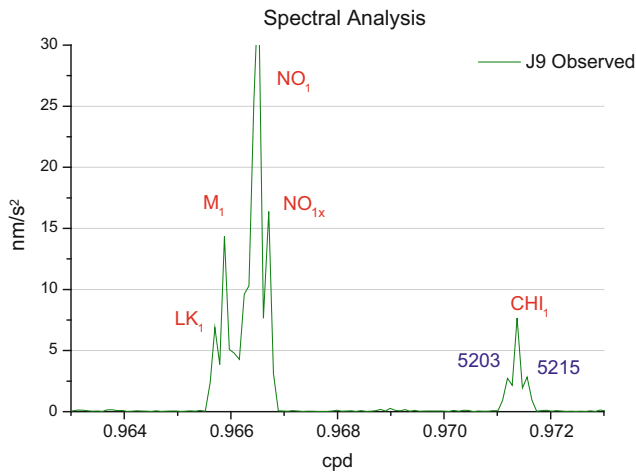
Fig. 5 Spectral amplitude of the observed 28 year series (T005 & C026) at Strasbourg J9 Observatory in the diurnal frequency band. Several close waves are indicated. *Blue numbers* correspond to the number wave in the potential catalogue of Hartmann and Wenzel (1995)

Table 1 List of the tidal waves shown in Fig. 5

Wave	Frequency cpd	Years (Rayleigh criterion)
LK_1	0.96583	
M_1	0.96614	8.85
NO_1	0.96644	8.85
NO_{1X}	0.96659	18.63
5203	0.97116	0.60
CHI_1	0.97130	19.01
5215	0.97145	18.25

For each one, its frequency is indicated in cpd, as well as the minimum length in years necessary to separate two consecutives waves, estimated by the Rayleigh criterion as a function of their frequencies

3.2 Close Frequency Waves

The length of the data series allows us also to separate narrowly spaced spectral lines at a resolution of 10^{-4} cpd in our case. In Fig. 5 some examples of waves very close in the tidal spectrum that have been detected are shown. The number of years needed to separate these waves estimated by the Rayleigh criterion as a function of their frequency, is indicated in Table 1.

3.3 Low-Frequency Signals

Another advantage of the long length of the J9 SG record is the possibility of studying long period signals such as the long period tides. The much lower instrumental drift of SGs with respect to mechanical spring meters has enabled more precise studies on long period tides (Mf, Mm, Ssa, Sa) (Sato et al. 1997; Hinderer et al. 1998; Ducarme et al. 2004; Boy

et al. 2006). However, the presence of a small long term drift leads still to spectral noise which increases with decreasing frequency (colored noise) as it is clearly shown in Fig. 2 of Van Camp et al. (2005). This means that the detection of signals is more and more difficult when the frequency of the signal decreases, even if the data set is in principle long enough to allow the spectral detection, at least in the noise free case.

In our case, due to the significantly lower instrumental drift of the C026 with respect to the T005, we have subtracted the modeled drift of each SG independently before merging the series. Drifts are modeled (exponential for the entirely T005 series and small initial exponential followed by a small linear term for the C026) using the residual gravity data computed by subtracting from each series the body tides and the ocean tidal loading, correcting for local pressure effects using a standard barometric admittance of -3 nms^{-2}/hPa and subtracting the polar motion contribution from IERS data (http://www.iers.org/).

Comparing the spectral analyses for the observed and theoretical signals (Fig. 6) we see that some of the long period waves are properly detected as for example the annual, semiannual, monthly, etc. Despite the length (about 28 years) of our observed series, we are still not able to retrieve the so called Draconic tidal waves of 9.3 and 18.6 year period, due to precession of the plane of the lunar orbit and its repetition because of the two nodes of the lunar orbit plane. These two waves, which are lunar nodal tidal waves, are of special interest for investigating the rheological behavior of the solid Earth at such periods, and are extremely difficult to identify in gravity (the lunar nodal tide amplitude represents only
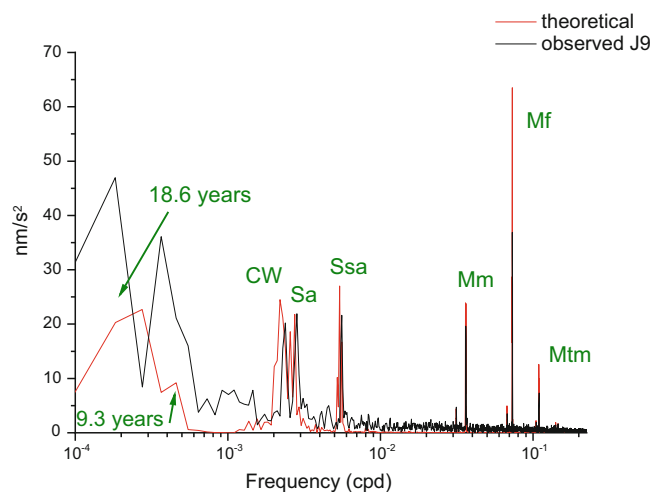
Fig. 6 Spectral amplitude of the observed 28 year series (T005 & C026) at Strasbourg J9 Observatory in *black*, and of the theoretical series in *red*. Figure modified from Calvo et al. (2014a). *CW* Chandler Wobble, *Sa* annual, *Ssa* semi-annual, *Mm* monthly, *Mf* fortnightly and *Mtm* ter-monthly tides
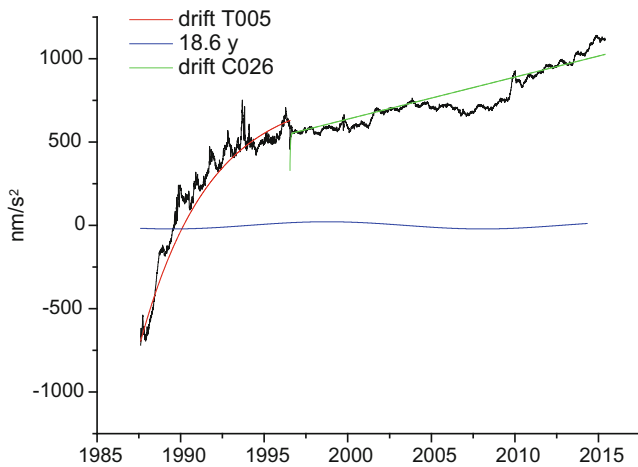
Fig. 7 Superposition of the gravity residuals (in *black*) at J9 Observatory, the modeled instrumental drift (T005 in *red*, C026 in *green*) and the theoretical 18.6 year wave at the same location (*blue*)

about 5% of the amplitude of the daily diurnal tide from the Moon) (Doodson and Warburg 1941). Our spectral peaks are obviously biased by the large noise still present in the SG data in the low-frequency band.

One of the main problems to detect these long period waves is the presence of the long term drift and of the nontidal gravity changes due to natural phenomena (such as polar motion or seasonal hydrological effects) in the data. In Fig. 7, the amplitude of the instrumental drift of the SGs at J9 is compared with the theoretical amplitude of the 18.6 year period signal computed for the same location using PREDICT. It is evident that this signal is hidden by the drift. In the case of the tidal wave of 9.3 year period, it is even more complicated to try to detect it, because its theoretical amplitude is almost 300 times smaller than the theoretical amplitude of the 18.6 year tide.

Moreover we currently have only 28 years that is to say 1.5 cycle of the 18.6-year tide which is clearly not optimal to avoid spectral leakage.

4 Conclusion

This study shows some examples of the benefits coming from very long gravity records when performing a spectral analysis. We have used the gravity data recorded at J9 Observatory by two different SGs (T005 & C026), resulting after merging, in the longest available series ever recorded by SG at the same site to date, almost 28 years. We have computed a theoretical series of the same length for the same location. Spectral analyses have been performed for both series giving a high resolution spectrum in the tidal bands. We compared their spectral amplitudes in various frequency ranges, from the quar-diurnal to the 18.6-year tidal band.

Clear examples of small amplitude tides in the diurnal and semi-diurnal frequency bands are pointed out, as for example several waves generated by the third-degree potential and even two waves generated by the fourth-degree potential in the quar-diurnal tidal bands. It is evident that the ability of SGs to reliably measure effects at the nanogal (0.01 nm/s^2) level has opened up many interesting scientific possibilities. Other results obtained thanks to the considerable length of the series, is the possibility to separate near frequency waves, due to the fact that the frequency resolution is the inverse of the data length.

To conclude, the long period part of the gravity spectrum is discussed. As it is well known, SGs have a very small instrumental drift and a long-term stability. These are the main reasons why studies of long period tides are particularly suited to SG data. In our case some of the long period waves are properly detected. However, at even longer periods, there are lunar nodal tidal waves at 9.3 and 18.6 year period which are extremely difficult to identify in gravity, and which escape detection despite the length of our series, because of the mismodeled long-term drift and unmodeled hydrological signal. Additional years of tidal records, as well as improvements in drift modeling are needed.

References

Amalvict M, Hinderer J, Gegout P, Rosat S, Crossley D (2002) On the use of AG data to calibrate SG instruments in the GGP network: example of Strasbourg - J9. Bull Inform Marees Terr 135:10621–10626

Boy JP, Llubes M, Ray R, Hinderer J, Florsch N (2006) Validation of long-periodoceanic tidal models with superconducting gravimeters. J Geodyn 41:112–118

Calvo M, Hinderer J, Rosat S, Legros H, Boy J-P, Ducarme B, Zürn W (2014a) Time stability of spring and superconducting gravimeters through the analysis of very long gravity records. J Geodyn 80:20–33

Calvo M, Rosat S, Hinderer J, Legros H, Boy J-P, Riccardi U (2014b) Study of the time stability of tides using a long term (1973–2011) gravity record at Strasbourg, France. In: Rizos C, Willis P (eds) Earth on the edge: science for a sustainable planet, vol 139. Springer, Berlin, pp 377–381. doi:10.1007/978-3-64237222-3_50

Dehant V, Defraigne P, Wahr J (1999) Tides for a convective earth. J Geophys Res 104(B1):1035–1058

Doodson AT, Warburg HD (1941) Admiralty manual of tides. H.M. Stationary Office, London

Ducarme B (2011) Determination of the main Lunar waves generated by the third degree tidal potential and validity of the corresponding body tides models. J Geod. doi:10.1007/s00190-011-0492-9

Ducarme B, Venedikov AP, Arnoso J (2004) Determination of the long period tidalwaves in the GGP superconducting gravity data. J Geophys Res 38(3–5):307–324

Hartmann T, Wenzel H-G (1995) The HW95 tidal potential catalogue. Geophys Res Lett 22(24):3553–3556

Hinderer J, Boy JO, Legros H (1998) A 3000 day registration of the superconducting gravimeter GWR T005 in Strasbourg (France) In: Ducarme B, Pâquet P (eds) Proceedings 13th international symposium on earth tides, Brussels, pp 617–624

Sato T, Ooe M, Nawa K, Shibuya K, Tamura Y, Kaminuma K (1997) Long-period tides observed with a superconducting gravimeter at Syowa Station, Antarctica, and their implication to global ocean tide modeling. Phys Earth Planet Inter 103(1–2):39–53

Tamura Y (1987) A harmonic development of the tide-generating potential. Bull Inform Marees Terr 99:6813–6855

Van Camp M, Wenzel H-G, Schott P, Vauterin P, Francis O (2000) Accurate transfer function determination for superconducting gravimeters. Geophys Res Lett 27(1):37–40

Van Camp M, Williams SD, Francis O (2005) Uncertainly of absolute gravity measurements. J Geophys Res Solid Earth 110(B5). doi:10.1029/2004JB003497

Wenzel H-G (1996) The nanogal software: earth tide data processing package ETERNA 3.30. Bull Inform Marees Terr 124:9425–9439

Investigations of a Suspected Jump in Swedish Repeated Absolute Gravity Time Series

Per-Anders Olsson, Andreas Engfeldt, and Jonas Ågren

Abstract

Since 2006 the gravity change at 17 points in Sweden has been observed with Lantmäteriet's absolute gravimeter FG5-233. The main purpose of the observations is to study the postglacial rebound in Fennoscandia. In 2010, a suspected jump of a few μGal can be seen in the gravity time series that significantly affects the estimated gravity rate of changes. It is shown that if the jump is not considered, then the absolute value of the gravity rate of change is systematically underestimated compared to the land uplift model NKG2014LU_test. In this paper two different ways to estimate and apply corrections of the jump are demonstrated. The first is to estimate the jump from the observations themselves within a least squares adjustment, while the second is to assume the instrument bias obtained in international comparisons of absolute gravimeters. The best agreement between land uplift model and estimated rates of change of gravity is achieved by correcting the data with the official biases reported from the international comparisons.

Keywords

Absolute gravity • Fennoscandia • FG5 • GIA

1   Introduction

The first ambitious effort to observe and study the temporal gravity change induced by postglacial rebound, or glacial isostatic adjustment (GIA), in Fennoscandia, was the establishment of the Fennoscandian land uplift gravity lines. Along four east–west oriented lines, passing through the Fennoscandian land uplift area, repeated relative gravity observations were carried out between 1967 and 2003 (Mäkinen et al. 1986; Mäkinen et al. 2005). Since 2003, the relative gravity observations have been fully replaced by modern absolute gravity (AG) observations.

The first repeated absolute gravity observations in Fennoscandia were carried out from 1988 (to 2003) by the Finnish Geodetic Institute (FGI) using a JILAg instrument. In 1993 and 1995, the National Oceanic and Atmospheric Administration (NOAA) and Bundesamt für Kartographie und Geodäsie (BKG) observed a number of points in Fennoscandia with FG5 type of gravimeter (Niebauer et al. 1995). During 2003–2008, comprehensive campaigning was carried out with FG5-220 by the Institute für Erdmessung (IfE) (Gitlein (2009) and Timmen et al. 2012). During that time, also FGI, Norwegian University of Life Sciences (UMB) and Lantmäteriet (Swedish mapping, cadastral and land registration authority) started repeated AG measurements with their respective FG5 gravimeters.

The main, long term goal with the ambitious absolute gravity campaigning in Fennoscandia is to obtain reliable estimates of the GIA-induced gravity rate of changes, to be used to improve the postglacial land uplift models. In Sweden the rates are expected to vary between 0 and ∼20 nm s^{-2} yr^{-1}. The goal is to get estimated rates with a standard uncertainty as low as ∼1 nm s^{-2} yr^{-1}, or even better; cf.

P.-A. Olsson (✉) • A. Engfeldt • J. Ågren
Lantmäteriet (Swedish Mapping, Cadastral and Land Registration Authority), SE-801 82 Gävle, Sweden
e-mail: per-anders.olsson@lm.se

for instance the discussions in Olsson (2013) and Van Camp et al. (2005, 2011).

The absolute gravity campaigns in Fennoscandia have been coordinated by the Nordic Geodetic Commission (NKG). Some results are presented by Pettersen (2011). Gitlein (2009) gives a detailed description of the IfE campaigns 2003–2008, but apart from that not much have been published concerning the Fennoscandian absolute gravity campaigns during the last decade.

The NKG working group on Geodynamics now has the intention to publish a compilation of all the repeated absolute gravity observations in Fennoscandia. As a first step, each participating country will process, analyse and publish all own observations. In this paper, we share some first experiences from the work with the Swedish data, with special emphasis on a suspected large jump (change of the instrumental bias) that was discovered in the time series in 2010.

With Swedish data, here we mean repeated observations with the FG5-233, until 2014-12-31, on Swedish points only.

2   The Gravity Observations

The FG5-233 absolute gravimeter was purchased by Lantmäteriet in 2006. Since then, it has mainly been used for repeated absolute gravity observations in the Fennoscandian land uplift area. To a lesser extent, it has also been used for the establishment of national gravity systems, in e.g. Serbia (2007), Macedonia (2010) and Bosnia Hercegovina (2013). The instrument participated in International/European Comparisons of Absolute Gravimeters (ICAG/ECAG) 2007 (Francis et al. 2010), 2009 (Jiang et al. 2012), 2011 (Francis et al. 2013), 2013 (Francis et al. 2015) and has annually taken part in various regional and local comparisons with other absolute gravimeters.

The Swedish absolute gravity network consists of 17 AG-points allocated on 13 sites; see Fig. 1. The absolute gravity site Mårtsbo hosts two points and Onsala four. All points, except Gävle and Borås, consist of concrete pillars mounted on solid bedrock co-located with permanent reference stations for GNSS. In Gävle and Borås, the points are located on a concrete floor. At some sites the gravity points are co-located with tide gauges, and the Onsala site also operates a superconducting gravimeter since 2009.

During the period 2006–2014, 120 absolute gravity observations were performed with the FG5-233 on the Swedish points (Table 1). The relatively high number of observations at Martsbo_AA is due to the fact that this site was chosen as the experimental one in terms of the capability of AG measurements to determine gravity rate of changes. Gavle, with 41 measurements, is the home station of the instrument, located in the same building as Lantmäteriet. It is customarily
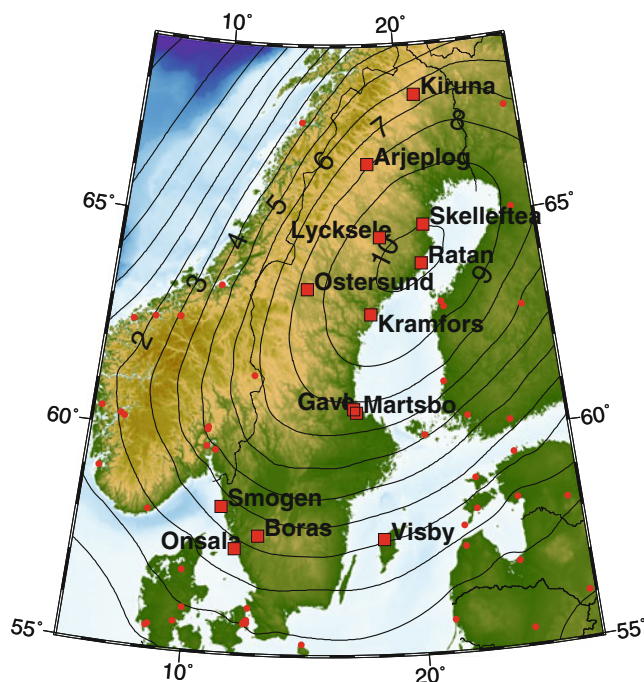
Fig. 1 Absolute gravity sites in Sweden (*red squares*) and surrounding countries (*red circles*). *Black lines* and *numbers* show the absolute land uplift according to the NKG2014LU_test_abs model [mm yr^{-1}]

Table 1 Distribution of absolute gravity observations with FG5-233 on the Swedish points

Point	No. of obs	Timespan	First	Last
Arjeplog	4	6.1	070810	130913
Boras	2	1.1	130420	140607
Gavle	41	7.3	070120	140522
Kiruna	3	5.0	070813	120815
Kramfors	4	6.0	070927	130916
Lycksele	5	4.9	070924	120811
Martsbo_AA	19	7.3	061209	140319
Martsbo_AB	5	6.1	070528	130625
Onsala_AA	5	4.9	090703	140601
Onsala_AC	2	4.9	090705	140529
Onsala_AN	2	2.6	100921	130501
Onsala_AS	6	6.1	070321	130503
Ostersund	4	4.0	070822	110904
Ratan	5	5.0	070819	120808
Skelleftea	4	5.0	070816	120818
Smogen	5	4.7	081011	130609

used for checking the instrument before and after the gravity campaigns and by this way it contributes to the monitoring of the stability of the FG5-233.

With one observation we here mean

- the mean value of two consecutive setup measurements, where the first setup is made with the instrument oriented

towards the north and the second to the south (or vice versa) in order to minimize the risk of Coriolis effects caused by horizontal movements of the test mass during the drop,

- 24 h per setup,
- 1 set per hour,
- 50 drops per set,
- standard corrections for atmospheric effects (using single admittance factor of -0.3 μGal/hPa), polar motion-, tidal- and ocean tide loading effects computed with the g-software version 9.12.04.23

3 Different Ways to Consider a Jump in the Time Series

Absolute gravimeters have to be regularly maintained due to e.g. wear and tear of mechanical parts. It can happen that the bias of a gravimeter is changing during the maintenance, e.g. due to rotation of the corner cube (Rothleitner and Francis 2010) or due to changes in electronics (Křen et al. 2016). As can be seen from Fig. 2a there is a suspected change of the FG5-233 instrumental bias in 2010 (when the instrument returned from a service at Micro-g Lacoste). In order to investigate if the jump is significant and if/how it will affect the results, the rate of change of gravity $\dot{g}$ is estimated using three different approaches and the results are compared to a reference land uplift model. The reference model and the three different approaches are described below and the results are presented in Figs. 2 and 3 and Table 3 and discussed in the next section. Only points with a time span larger than 2 years and with more than 2 observations are considered

(a) Original data without jump correction

In this approach, the gravity rate of change $\dot{g}$ and gravity value g^0 in the reference epoch with $T = 0$ are estimated for each point i using least-squares adjustment with the observation equation,

$$g_{ij}^{obs} = \dot{g}_i T_j + g_i^0 + \varepsilon_{ij}$$

where g_{ij}^{obs} is one gravity observation at point i and epoch T_j. All observations are assumed to have equal a priori standard uncertainties, using a unit weight matrix. Estimated rates and standard deviations from the adjustment are presented in Table 3. If all the individual point adjustments are merged to one large adjustment, the common a posteriori standard deviation for the observations is estimated to

$$\hat{\sigma}_0 = 24 \; \left[\text{nm s}^{-2}\right].$$
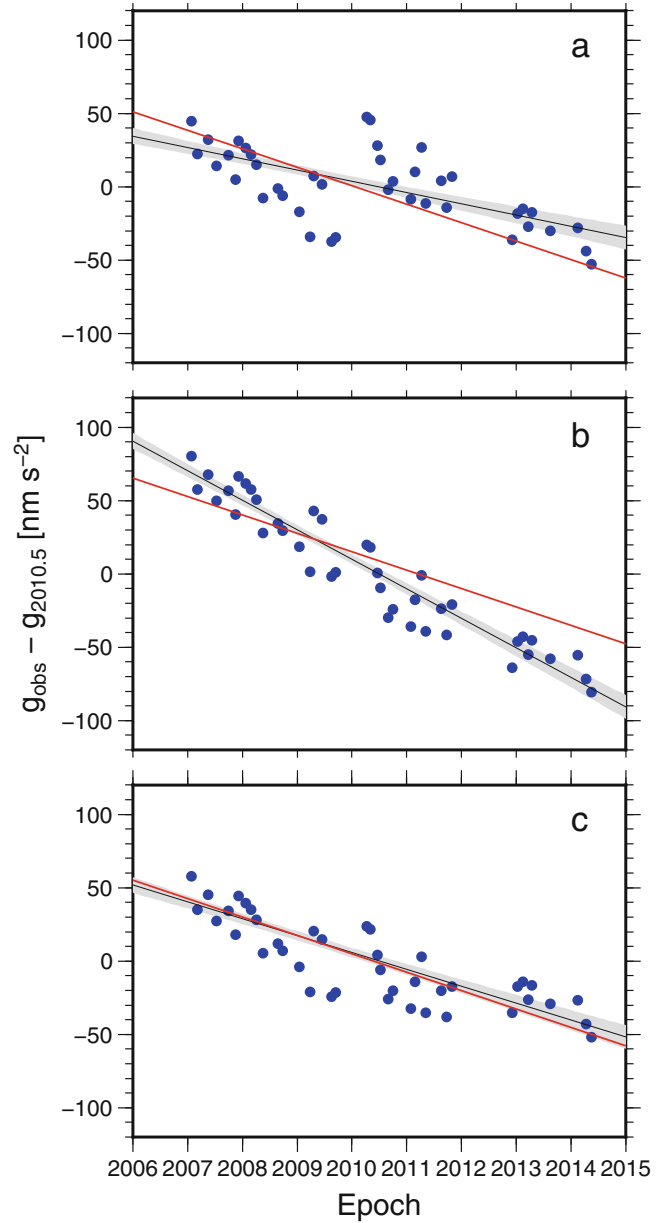
Fig. 2 Observations and estimated trends at the Gavle point based on (**a**) original data without correction for the jump, (**b**) data corrected for a 63.2 nm s^{-2} offset after epoch 2010.2 and (**c**) offsets according to ICAG/ECAG 2007, 2009, 2011 and 2013. *Blue dots* represent the gravity observations and the *black line* an estimated linear regression trend. The *red line* is the land uplift in Gävle from the land uplift model NKG2014LU_test_abs multiplied with -1.63 nm s^{-2} mm^{-1} (from Olsson et al. (2015))

(b) Jump determined in a common least squares adjustment

In a common least squares adjustment similar to (a) above an unknown jump Δ is introduced at the epoch 2010.2 (the time when the instrument came back
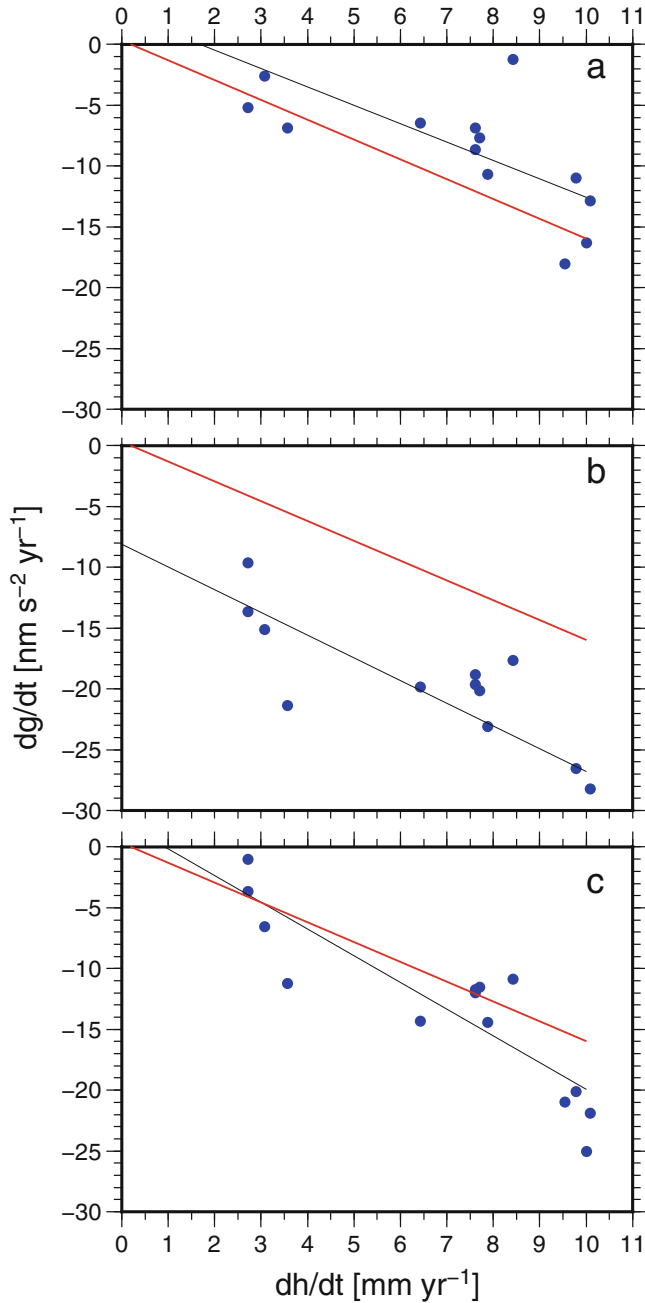
Fig. 3 Estimated rates of change of gravity for the Swedish points (*blue dots*) plotted against the corresponding land uplift value from the land uplift model NKG2014LU_test_abs. The *black line* is a linear regression line and the *red line* represents a theoretical linear relation between $\dot{g}$ and $\dot{h}$ (Olsson et al. 2015). (**a**), (**b**) and (**c**) corresponds to the same data sets as in Fig. 2

from service) according to

$$g_{ij}^{obs} = \begin{cases} \dot{g}_i T_j + g_i^0 + \varepsilon_{ij} + \Delta & T > 2010.2 \\ \dot{g}_i T_j + g_i^0 + \varepsilon_{ij} & T < 2010.2 \end{cases}$$

Table 2 Compilation of results from international comparisons and of epochs for FG5-233 services. Degree of Equivalence (DoE) corresponds to the bias of FG5-233 with respect to the comparison reference value and its standard uncertainty

Event	Epoch	DoE	Reference
ECAG 2007	2007.9	10 ± 9	(Francis et al. 2010)
Service	2008.6		
ICAG 2009	2009.8	10 ± 14	(Jiang et al. 2012)
Service	2010.2		
ECAG 2011	2011.9	47 ± 17	(Francis et al. 2013)
Service	2012.8		
ICAG 2013	2013.9	22 ± 17	(Francis et al. 2015)
Service	2015.2		

The offset is estimated to $\hat{\Delta} = 63.2$ nm s^{-2} with the standard deviation $\hat{\sigma}_\Delta = 14.3$ nm s^{-2}. Estimated rates and their standard deviations are presented in Table 3. The a posteriori standard deviation from the adjustment for the observations now decreases to

$$\hat{\sigma}_0 = 17 \left[\text{nm s}^{-2} \right].$$

(c) Offsets given by international comparisons

An unprejudiced way to introduce corrections for offsets, independent of the data, is to use the results from comparisons with other absolute gravimeters. As already mentioned, FG5-233 has participated in four International/European Comparisons of Absolute Gravimeters (ICAG/ECAG) and a large number of regional and local comparisons. In Table 2, the ICAG/ECAGs and the epochs for service at Micro-g LaCoste are listed together with the Degree of Equivalence (DoE) that represents the bias of AG at the comparison. The results (c) in Table 3 have been achieved in the same way as in (a) but with the data first corrected for the offsets (or DoEs) in Table 2. A certain offset correction is applied for the time between the two adjacent services. Using this approach, the a posteriori standard uncertainty of unit weight for the observations is estimated to

$$\hat{\sigma}_0 = 18 \left[\text{nm s}^{-2} \right].$$

This is a little bit larger than for the (b) approach but, as will be shown below, the estimated rates of change of gravity fits better with the reference land uplift model.

Table 3 Rate of change of gravity $\dot{g}$ estimated in four different ways. "model" $= \dot{h}$ from land uplift model NKG2014LU_test_abs multiplied with -1.63 [nm s^{-2} mm^{-1}]; Subscript a, b and c refers to the different approaches described in the text. Diff$_x = \dot{g}_x - \dot{g}_{model}$. All numbers in nm s^{-2} yr^{-1}

Point	$\dot{g}_{model}$	$\dot{g}_a$	Diff$_a$	$\dot{g}_b$	Diff$_b$	$\dot{g}_c$	Diff$_c$
Arjeplog	-12.9	-10.7 ± 9.4	2.2	-23.2 ± 4.6	-10.3	-14.4 ± 5.6	-1.5
Gavle_LMV	-12.6	-7.4 ± 1.0	5.2	-19.8 ± 0.9	-7.2	-10.8 ± 0.6	1.7
Kiruna	-10.4	-6.6 ± 15.5	3.8	-19.9 ± 7.3	-9.5	-14.4 ± 9.3	-3.9
Kramfors	-15.5	-18.0 ± 9.5	-2.5	-30.0 ± 4.6	-14.5	-20.8 ± 5.7	-5.3
Lycksele	-16.0	-11.1 ± 13.3	4.9	-26.6 ± 6.5	-10.6	-20.2 ± 8.0	-4.2
Martsbo_AA	-12.4	-5.7 ± 2.1	6.7	-18.1 ± 1.4	-5.8	-10.5 ± 1.3	1.9
Martsbo_AB	-12.4	-8.7 ± 7.7	3.7	-19.7 ± 3.7	-7.3	-12.1 ± 4.6	0.3
Onsala_AA	-4.4	-4.5 ± 12.2	-0.1	-13.6 ± 5.5	-9.2	-3.6 ± 7.3	0.8
Onsala_AS	-4.4	2.8 ± 9.5	7.2	-9.9 ± 4.6	-5.5	-1.2 ± 5.7	3.2
Ostersund	-13.7	-1.4 ± 22.5	12.3	-17.7 ± 10.6	-4.1	-10.9 ± 3.4	2.7
Ratan	-16.5	-12.6 ± 13.6	3.8	-28.1 ± 6.6	-11.6	-21.7 ± 8.2	-5.2
Skelleftea	-16.3	-16.3 ± 12.8	-0.0	-31.2 ± 6.3	-14.9	-25.1 ± 7.7	-8.8
Smogen	-5.9	-6.9 ± 12.7	-1.0	-21.4 ± 6.2	-15.5	-11.2 ± 7.6	-5.3
Visby	-5.1	-2.5 ± 9.3	2.6	-15.0 ± 4.5	-10.0	-6.3 ± 5.6	-1.3
		Mean	3.5		-9.7		-1.8
		Stddev	3.8		3.6		3.7
		Weighted mean	4.5		-8.4		-0.1

Reference Land Uplift Model

Next, the estimated gravity change rates in (a), (b) and (c) are compared with a reference postglacial land uplift model. For this purpose, the empirical land uplift model NKG2014LU_test_abs model was preferred together with a theoretical linear relation between the absolute land uplift and the rate of change of gravity. NKG2014LU_test_abs is a preliminary, updated version of NKG2005LU_abs. They are both based on the principles described by Vestøl (2006) and Ågren and Svensson (2007), but the new version is updated with more observations, most notably extended GNSS time series. From the model's absolute land uplift rates, $\dot{h}$ [mm yr^{-1}], the gravity rate of change is computed using the theoretical linear relation,

$$\dot{g} = -1.63\dot{h} + 0.3 \ \left[\text{nm s}^{-2}\text{yr}^{-1}\right].$$

Olsson et al. (2015) show by GIA-modelling (normal mode approach) that this relation is valid in Fennoscandia, assuming a 1D spherical earth with Maxwell rheology. The reason for choosing an empirical model with this linear factor is that it presently agrees best with all the available observations (of different types).

4 Discussion of the Results

In Fig. 2, the observations and the estimated rate of change of gravity at the Gavle point are plotted for the approaches (a), (b) and (c) above. All points show similar patterns (cf. Fig. 3), but due to the large number of observations in Gavle, the pattern is most explicit there. It can be seen that without correcting for any jump in the data set (a), the absolute value of the gravity rate of change, $\dot{g}$, is underestimated compared to the reference model. If the jump is estimated from the data (b), the absolute value of $\dot{g}$ is overestimated. If offsets from the international comparisons are applied (c), then the estimated rates correspond closely to the reference model.

This is confirmed in Table 3 by the weighted mean of the differences between the reference model and the various approaches (a–c), where the weighting is made with the number of observations. In this case, the estimated absolute rates for the (a) approach are at average 4.5 nm s^{-2} smaller (less negative) compared to the reference model, with the (b) approach 8.4 nm s^{-2} larger and with the (c) approach only 0.1 nm s^{-2} larger.

The scatter of the observations around the trend lines probably contains a contribution from local hydrological

effects (Pálinkáš et al. 2013) since the observations have not been corrected for that.

In Fig. 3, the estimated rates for all points are plotted as a function of the corresponding land uplift value from the NKG2014LU_test_abs model. Compared to the theoretical relation of Olsson et al. (2015) between $\dot{g}$ and $\dot{h}$ (red line) it is clear that in the absolute value of $\dot{g}$ is systematically underestimated in (a) and systematically overestimated in (b). In (c), the slope of the regression line differs from the theoretical one. This is probably due to the fact that the four points with the largest land uplift values (to the right in the graph) happen to have relatively few observations after 2013.0 (in total only one) which means that the estimated rates for three of these points will not be affected by the result from ICAG 2013, therefore the offset in 2010 will have larger impact on these rates and they will be larger (more negative).

In the (c) approach, the data were corrected with the DoE before the adjustment. This means that the introduced offsets are independent of the data set under consideration, which is the reason behind this choice. Other alternative uses of the results from the comparisons are (1) to correct for the DoE only if it is significant (in our case only ECAG 2011) or (2) to include the DoEs as pseudo-observations, with their (a priori) standard uncertainties, in the adjustment. In both cases the results will be closer to those in the (b) approach.

Except for Gavle and Martsbo_AA, each point has less than 7 observations, normally 4–5. With that few observations it is very hard to distinguish a potential instrumental jump from e.g. the normal observational scatter or from local environmental effects such as local hydrology or 3D atmospheric loading. The relatively dense data series in Gavle and Martsbo_AA are therefore crucial for detection and evaluation of potential offsets.

5   Summary and Conclusions

Based on data from 8 years of repeated observations with the absolute gravimeter FG5-233 on 17 Swedish points, a suspected jump in the data set and its impact on estimated rates have been investigated. We have shown that if and how the suspected jump is treated is very crucial for interpretation of the results. The best agreement with a reference model (empirical land uplift model and theoretical relation between land uplift and gravity change) is achieved by applying the official results from international comparisons of absolute gravimeters.

Based on this work we recognize the importance of regular comparisons with other instruments, as well as to have (at least) one dense data series which makes it possible monitor the behaviour of the instrument.

It should be pointed out that the purpose of this paper is to investigate a suspected instrumental jump and that the results are based on data from only the FG5-233 instrument. Work is in progress with common official publications of observations and rates for all the Fennoscandian absolute gravity points together. These will include more observations, made by other organisations, also on the Swedish points and the estimated rates will differ from those published in this paper. We have also used only one reference model. When the official rates are published, based on longer time series and therefore more reliable, they will be used to evaluate other empirical as well as geophysical (GIA) models.

References

Ågren J, Svensson R (2007) Postglacial land uplift model and system definition for the new Swedish height system RH 2000. LMV-Rapport 2007:4, Lantmäteriet, the Swedish mapping, cadastral and land registration authority

Francis O et al (2010) Results of the European comparison of absolute gravimeters in Walferdange (Luxembourg) of November 2007. In: Mertikas SP (ed) Gravity, geoid and earth observation, International Association of Geodesy Symposia 135. Springer, Berlin/Heidelberg. doi:10.1007/978-3-642-10634-7_5

Francis O et al (2013) The European Comparison of Absolute Gravimeters 2011 (ECAG-2011) in Walferdange, Luxembourg: results and recommendations. Metrologia 50:257–268. doi:10.1088/0026-1394/50/3/257

Francis O et al (2015) Final report: international comparison of absolute gravimeters, CCM.G-K2 key comparison. Metrologia 52(1A):07009

Gitlein O (2009) Absolutgravimetrische Bestimmung der Fennoskandischen Landhebung mit dem FG5-220. Dissertation, Leibniz Universität

Jiang Z et al (2012) The 8th International Comparison of Absolute Gravimeters 2009: the first Key Comparison (CCM.G-K1) in the field of absolute gravimetry. Metrologia 49:666–684. doi:10.1088/0026-1394/49/6/666

Křen P, Pálinkáš V, Mašika P (2016) On the effect of distortion and dispersion in fringe signal of the FG5 absolute gravimeters. Metrologia 53

Mäkinen J, Ekman M, Midtsundstad Å, Remmer O (1986) The Fennoscandian land uplift gravity lines 1966–1984. Report of the Finnish Geodetic Institute 85:4, Finnish Geodetic Institute

Mäkinen J, Engfeldt A, Harsson BG, Ruotsalainen H, Strykowski G, Oja T (2005) The Fennoscandian land uplift gravity lines 1966–2004. In: Jekeli C, Bastos L, Fernandes J (eds) Gravity, geoid and space missions. International Association of Geodesy Symposia, vol 129. Springer, Berlin/Heidelberg, pp 328–332

Niebauer TM, Sasagawa GS, Faller JE, Hilt R, Klopping F (1995) A new generation of absolute gravimeters. Metrologia 32:159–180

Olsson PA (2013) On modelling of postglacial gravity change. Dissertation, Chalmers University of Technology

Olsson PA, Milne G, Scherneck HG, Ågren J (2015) The relation between gravity rate of change and vertical displacement in previously glaciated areas. J Geodyn 83:76–84

Pálinkáš V, Lederer M, Kostelecký J, Šimek J, Mojzeš M, Ferianc D, Csapó G (2013) Analysis of the repeated absolute gravity measurements in the Czech Republic, Slovakia and Hungary from the period 1991–2010 considering instrumental and hydrological effects. J Geodesy 87:29–42

Pettersen BR (2011) The postglacial rebound signal of Fennoscandia observed by absolute gravimetry GPS and tide gauges. Int J Geophys. doi:10.1155/2011/957329

Rothleitner C, Francis O (2010) On the influence of the rotation of a corner cube reflector in absolute gravimetri. Metrologia 47. doi:10.1088/0026-1394/47/5/007

Timmen L, Gitlein O, Kleman V, Wolf D (2012) Observing gravity change in the Fennoscandian uplift area with the Hanover absolute gravimeter. Pure Appl Geophys 169:1331–1342

Van Camp M, Williams SDP, Francis O (2005) Uncertainty of absolute gravity measurements. J Geophys Res 110, B05406. doi:10.1029/2004JB003497

Van Camp M, de Viron O, Scherneck H-G, Hinzen K-G, Williams S, Lecocq T, Quinif Y, Camelbeeck T (2011) Repeated absolute gravity measurements for monitoring slow intraplate vertical deformation in Western Europe. J Geophys Res 116. doi:10.1029/2010JB008174

Vestøl O (2006) Determination of postglacial land uplift in Fennoscandia from levelling, tide-gauges and continuous GPS stations using least squares collocation. J Geodesy 80:248–258

Detailed Analysis of Diurnal Tides and Associated Space Nutation in the Search of the Free Inner Core Nutation Resonance

Séverine Rosat, Marta Calvo, and Sébastien Lambert

Abstract

We propose a comparison of the tidal analysis results obtained from the continuous records of time-varying surface gravity collected by a worldwide network of Superconducting Gravimeters with the analysis results of space nutation observed by the international Very Long Baseline Interferometry (VLBI) network. The length of the surface gravity time series (20 years for the longest) enables now to look for additional diurnal tides that were previously not analyzed. In parallel, we now possess 35 years of VLBI data permitting to look for additional nutation terms. We focus our analysis on the diurnal prograde frequency band in the search for a possible resonance effect linked to the Free Inner Core Nutation. This Earth's normal mode has never been clearly observed. Its direct deformation effect at the Earth's surface is theoretically predicted to be too small to be detected. However, the tidal forcing at a frequency close to its eigenfrequency could enhance some tidal or nutation amplitude resulting in the characterization of this mode through its resonance effect.

Keywords

Diurnal tides • Free inner core nutation • Nutation • Superconducting gravimeters • VLBI

1   Introduction

A rotating elliptical Earth's model possesses four rotational normal modes: the Free Core Nutation (FCN), the Chandler Wobble (CW), the Free Inner Core Nutation (FICN) and the Inner Core Wobble (ICW). While the first two have already been well-studied, the two other modes, related to the presence of the inner core (IC), have never been directly observed. In this paper, we will focus on the FICN, which is very similar to the FCN in terms of feedback mechanism and tidal effect.

The existence of the FICN is related to the presence of a slightly tilted and oblate solid IC in the fluid outer core (Mathews et al. 1991a, b; de Vries and Wahr 1991; Herring et al. 1991). The misalignment of the rotation and geometric figure axes of the IC with respect to the figure axis of the mantle induces fluid pressure acting on the elliptical inner core boundary (ICB). Gravitational forces on the tilted inner core also contribute to the internal torque (Dumberry 2009). The FICN has a nearly diurnal retrograde motion in a terrestrial reference frame but a prograde motion in space (positive period), while the FCN has a retrograde motion in space (negative period).

Theoretically, the transfer function of the Earth to the tidal forcing predicts a resonance effect when a tidal wave has a frequency close to the frequency of the free mode. While this resonance effect for the FCN has been clearly observed

S. Rosat (✉) • M. Calvo
Institut de Physique du Globe de Strasbourg, IPGS – UMR 7516, CNRS/Université de Strasbourg (EOST), 5 rue René Descartes, 67084 Strasbourg Cedex, France
e-mail: Severine.Rosat@unistra.fr

M. Calvo
Observatorio Geofísico Central, Instituto Geográfico Nacional (IGN), c/Alfonso XII 3, 28014 Madrid, Spain

S. Lambert
SYRTE, Observatoire de Paris, PSL Research University, CNRS, Sorbonne Universités, UPMC Univ. Paris 06, LNE, 75014 Paris, France

Table 1 Theoretically predicted and observationally adjusted periods of the FICN in a celestial reference frame

	T_{FICN} (in sidereal days)	Models
Theory		
Mathews et al. (1991b)	475.5	PREM
	512.2	1066A
de Vries and Wahr (1991)	471.0	PREM
Dehant et al. (1993)	485.7	PREM
Mathews et al. (1995)	455.8	M-PREM
Greff-Lefftz et al. (2000)	75	PREM + quasi-fluid IC
	485	PREM + quasi-elastic IC
	Some thousands	PREM + large magnetic field at ICB
Rogister (2001)	388.4–473.9	PREM
Mathews (2001)	939.0	Modified PREM
Rogister and Valette (2009)	432.7	PREM
	513.6	1066A
	200–1,000	Coupling with core modes
Observations		
Mathews et al. (2002)	930–1,140	"Best-fit" theory of VLBI nutation (MHB – IERS Convention)
Koot et al. (2008)	875–1,100	VLBI nutation
Koot et al. (2010)	870–975	VLBI nutation

and analyzed using either space Very Long Baseline Interferometry (VLBI) nutation (e.g. Lambert and Dehant 2007) or geophysical (gravity, strain, tilt, borehole water level . . .) surface observations (see for instance Blum et al. 1973; Neuberg and Zürn 1986; Zaske et al. 2000; Ducarme et al. 2007; a review table in Rosat et al. 2009; Amoruso et al. 2012) or both (Defraigne et al. 1994, 1995; Rosat and Lambert 2009), no resonance effect associated with the FICN has been clearly observed yet. There are several reasons for the non-observability of the FICN resonance; the most obvious ones are the strength of the resonance that is predicted to be about 1% weaker than for the FCN (de Vries and Wahr 1991) and the strong attenuation of this mode with a quality factor less than 500 (Koot et al. 2010).

Past works also predict a very weak surface amplitude of a few tens of micro-arcseconds (where 1 μ as ∼ 0.03 mm of equatorial shift at the Earth surface) corresponding to a gravity perturbation of ∼0.1 nGal (where 1 nGal = 10^{-2} nm/s^2), well below the precision of Superconducting Gravimeters (SGs) and VLBI time series. For an elastic Earth model, a resonance appears at the FICN frequency close to S_1 (e.g. Dehant et al. 1993; Legros et al. 1993).

The values of the deep Earth's parameters involved in the expression of the FICN period are in fact poorly constraints. They are the flattening of the inner core, the densities of the inner core and outer core, the deformation of the ICB due to the fluid dynamic pressure acting on it (Dehant et al. 1997) and some compliances related to the visco-magnetic couplings at the core boundaries (Mathews et al. 2002). The rheological behavior of the inner core seems to play also a critical role in its rotation, particularly the viscosity of the

inner core and the frictional constant at the ICB (Greff-Lefftz et al. 2000) resulting in predicted periods much different (cf. Table 1).

More recently, Rogister and Valette (2009) showed a strong coupling of the FICN with gravito-inertial core modes involving also a rigid nutation of the mantle. So the inner core nutation and the nutation of the mantle become coupled and the period of the FICN is clearly unconstrained, with possible values ranging from 200 to 1,000 sidereal days.

Using VLBI nutation observations, Mathews et al. (2002) then Koot et al. (2008, 2010) have inverted a semi-analytic model of the Earth's response to the gravitational forcing and indirectly suggested a period of the FICN close to 1,000 sidereal days (1.0017 cycle per solar day in the rotating frame). However these estimations are mostly constrained by the 18.6-year nutation since no resonance has been observed in the prograde nutations (Greff-Lefftz et al. 2002). The values of the IERS Convention 2010 are based on these VLBI best-fit estimates of Earth's parameters by Mathews et al. (2002) and referred as the MHB model. When considering such anelastic model the resonance is not visible anymore because of the damping of the mode. This later parameter depends on the dissipation processes at ICB which are encompassed within the quality factor Q of the mode. Mathews et al. (2002) obtained a Q-value of 677 and Koot et al. (2010) proposed a smaller value between 430 and 500. Besides the period, the quality factor of the FICN is also very poorly constrained.

Since we have long gravimetric time series, we will perform a frequency search for small diurnal tidal constituents that can now be separated from nearby larger constituents in

Table 2 Superconducting gravimeter time series used in the search for the FICN resonance effect

Acronym	Location	Time periods	Duration (days)	Possible enhancement of 553
BE	Brussels, Belgium	1982–2000	6,722	Yes
BFO	Black Forest Observatory,Germany	2009–2015	1,425.33	No
BH	Bad-Homburg, Germany	2001–2015	5,128.1	Yes
CA	Cantley, Canada	1989–2013	7,353.7	Yes
CB	Canberra, Australia	1997–2013	6,028.3	Yes
KA	Kamioka, Japan	2004–2013	3,203.8	Yes
MB	Membach, Belgium	1995–2014	6,767.3	Yes
MC	Medicina, Italy	1998–2015	5,415.4	No
ME	Metsahovi, Finland	1994–2015	7,363.6	No
MO	Moxa, Germany	2000–2013	5,110.4	Yes
PE	Pecny, Czech Republic	2007–2015	2,921.3	No
ST	Strasbourg, France	1996–2014	6,720.2	Yes
SU	Sutherland, South Africa	2000–2014	4,833.4	Yes
VI	Vienna, Austria	1997–2006	3,470.3	No
WE	Wettzell, Germany	1996–2015	6,448.7	Yes

order to try to detect any possible resonance effect associated with the FICN. As given the wide range of possibilities for the FICN frequency, a search for its resonance effect will require a systematic scan of the whole diurnal spectrum between P_1 and K_1 waves, with a great care concerning the vicinity of the gravitational and thermal S_1 wave.

2 Tidal Analysis of SG Records

The data for the different SGs used in this study (Table 2) were obtained from the GGP database (http://isdc.gfz-potsdam.de/) (Crossley et al. 1999), where are available raw gravity, pressure data and all the necessary information such as the calibration factor and the time delay specific for each gravimeter. All these records have been preprocessed and corrected independently from the spikes, steps (sudden offsets) and gaps (missing samples) contained in the raw gravity series, which are mainly due to instrumental problems, human intervention, and also from true geophysical signals such as earthquakes. They have then been low-pass filtered before decimation to hourly samples. We have used the tidal analysis software ETERNA3.4 (Wenzel 1996) applied with the HW95 tidal potential (Hartmann and Wenzel 1995) in order to estimate the gravimetric amplitude factors. ETERNA analysis is performed on tidal groups. The number of tidal waves that can be determined and the precision obtained in our tidal analyses depend on the record data length (the frequency resolution is the inverse of the data length) and on the noise characteristics of the instrument used.

Relying on the frequency interval estimated in previous studies (cf. Table 1) we expand the range from 430 to 1,400

Table 3 Frequencies in cycle per day of the diurnal tidal waves of the Tamura's tidal potential catalogue (Tamura 1987) between S_1 and K_1 waves and their associated nutation periods

Frequency (cpd)	Tidal wave name	Nutation period (sidereal days)	Wavegroup name
1.000000	S_1	365.27	S_1
1.000147	551	386.01	
1.001825	552	1,095.31	553
1.001972	553	1,305.82	
1.002281	*554*	*2,190.9*	K_{1x-}
1.002428	*555*	*3,232.1*	
1.002443	556	3,400.5	
1.002575	*557*	*6,163.3*	
1.002591	K_{1x-}	6,796.6	
1.002738	K_1	Precession	K_1

The last column corresponds to the tidal groups used for the ETERNA tidal analysis. The waves deriving from the degree-3 potential are written in italic

sidereal days (corresponding to a range between P_1 and K_1) to focus the search of a possible resonance effect in diurnal tidal amplitudes. Several tests, modifying the frequency limits of the wave groups on the period range $[S_1, K_{1x-}]$ are done to try to separate small waves in the diurnal tidal band. K_{1x-} is a lunar nodal wave of K_1 (precession) corresponding to a modulation of 18.6 year sidereal period. We have tried several group configurations by including simultaneously or separately some small amplitude tidal waves of the Tamura's tidal potential catalogue (Tamura 1987) given in Table 3. For instance we have tested a solution with four groups $(S_1 + 551, 552 + 553, 554 + 555 + 556 + 557, K_{1x-})$, giving similar results as the final grouping we used (last column of Table 3), that is to say $(S_1 + 551, 552 + 553,$
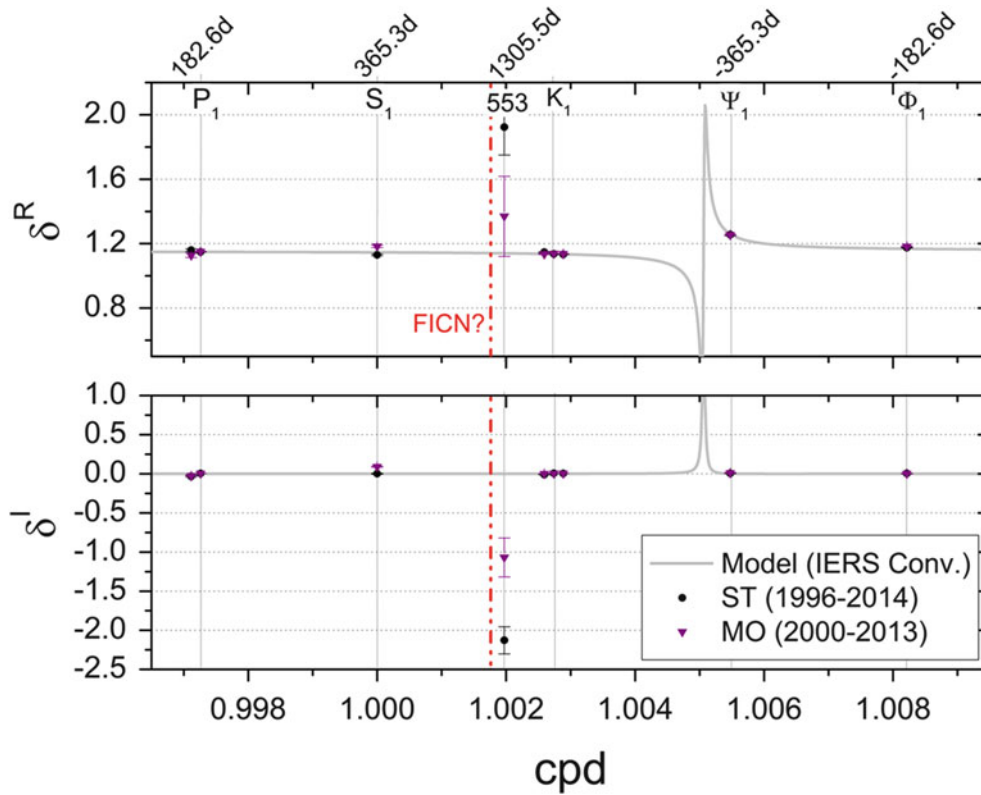
Fig. 1 Real and imaginary parts of the gravimetric factors obtained by an ETERNA 3.4 tidal analysis of the SG record in Strasbourg and in Moxa. Only the results between P_1 and Φ_1 frequency bands are shown. The resonance curve associated with the IERS Conventions 2010 is superimposed in *gray line*. The period for the FICN resonance proposed in MHB is indicated as a *vertical dashed–dotted line*. In *vertical gray lines*, we have indicated the frequency (in cycle per solar day) in a terrestrial reference frame of the diurnal tides as well as their respective nutations (in sidereal days) in a celestial reference frame

$554 + 555 + 556 + 557 + K_{1x-}$). Please note that the waves 554, 555 and 557 are deriving from the third degree tidal potential and should not be in the same group as 553. One possible resonance is finally found near 1.0019 cpd, i.e. near the tidal constituent number 553 (Fig. 1) for several SG sites. Note that we have employed the grouping and naming from Tamura's catalogue and not the numbering of HW95 catalogue, even if the tidal analysis was performed using HW95 catalogue, since the later contains 12,935 tidal waves and is then more precise.

A summary of the possible enhancement of the 553 tidal constituent for the SG sites considered here is given in Table 2.

If such observation corresponds to a resonance associated with the FICN, it would correspond to a period for the FICN around 1,300 sidereal days that is slightly larger than the VLBI nutation estimates.

Since the diurnal tides of spherical harmonic degree 2 are associated with the forced space nutation, we can do a similar search in the celestial pole offsets and check for a possible similar enhancement of some nutation terms.

3 VLBI Nutation Analysis

A few years ago we had investigated the time-frequency spectrum of VLBI nutation series in order to search for the forced free motion associated with the FICN (Lambert et al. 2012). The FICN was not detected but we had pointed out only some unexplained structures at seasonal and interannual time scales that could be artifacts associated with the analysis method, including the strategy adopted for estimating the troposphere delay and gradients and the radio source coordinates.

Here we are looking for a possible resonance effect due to the presence of the inner core. For that, we use 35 years of VLBI celestial pole offsets to MHB produced by the Observatory of Paris (opa2015a) in the framework of the International VLBI Service for Geodesy and Astrometry (IVS; Schuh and Behrend 2012). In a first step, the forced-free motion of time-variable amplitude associated with the free core nutation was removed by fitting a retrograde circular term of period −430.21 sidereal days over a sliding
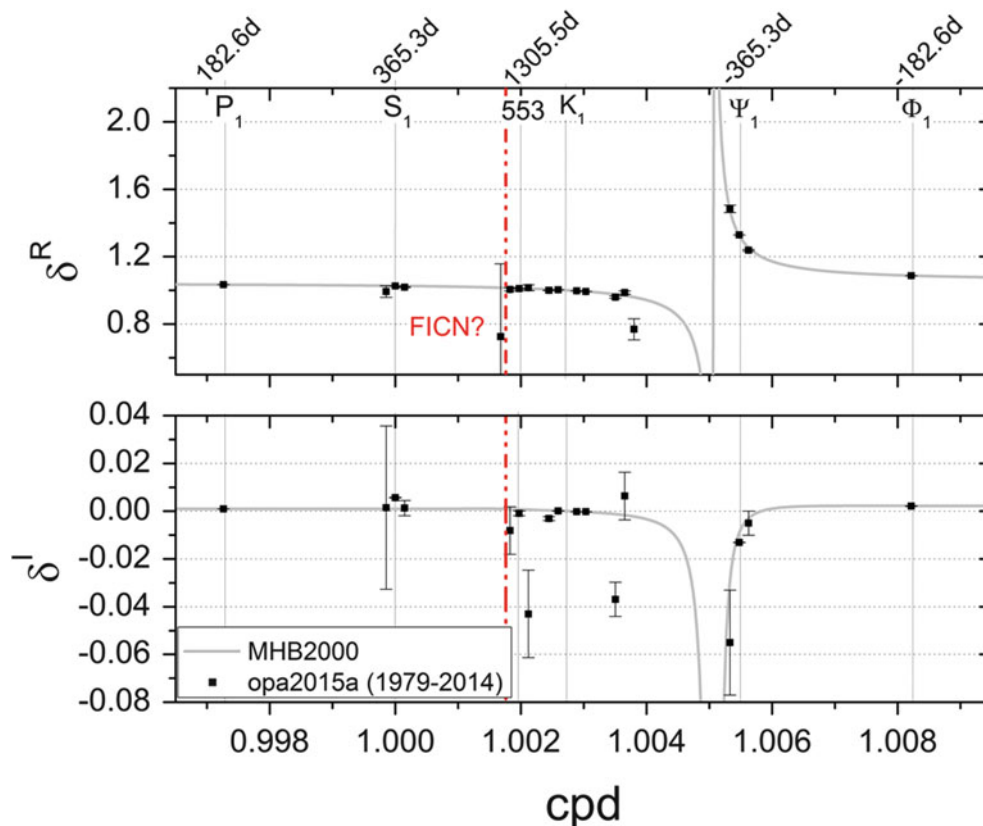
Fig. 2 Real and imaginary parts of the ratio between observed and rigid nutations obtained by least-squares fit of the opa2015a celestial offset series. Only the results between P_1 and Φ_1 frequency bands are shown. The resonance curve associated with the IERS Conventions 2010 is superimposed in *gray line*. The period for the FICN resonance proposed in MHB is indicated as a *vertical dashed–dotted line*. In *vertical gray lines*, we have indicated the frequency (in cycle per solar day) in a terrestrial reference frame of the diurnal tides as well as their respective nutations (in sidereal days) in a celestial reference frame

window. The period was arbitrarily fixed to the MHB value. The sliding window aimed at accounting for the variable amplitude: we took a length of 6.7 years in order to ensure that the estimate is not correlated with the amplitude of the retrograde annual nutation. We displaced the window by steps of one year. We checked that taking other displacement steps has no significant impact on the final results of this study. The obtained FCN amplitudes are comparable to those raised by other filtering techniques based on least-squares (e.g., Herring et al. 2002; Vondrák et al. 2005; Lambert 2006; Krásná et al. 2013), wavelets (Malkin 2014) or Panteleev filter (Zotov and Bizouard 2015). In a second step, we analyze the amplitudes and phases of 48 nutation terms. The 48 frequencies correspond to those of prominent nutations. We included the 42 nutation terms used by Mathews et al. (2002) in the MHB work. An additional six frequencies were identified by frequency analysis of the residuals. They correspond to less prominent nutations which are, however, in the FCN or FICN frequency band. Corrections to MHB nutation series that amount to a few tens of microarcseconds for the prominent terms were fitted with an accuracy of a few microarcseconds.

As for the gravimetric tides, at each tidal frequency, we compute the transfer function as the ratio between the full observed nutation amplitude (i.e., MHB amplitude plus the adjusted correction) to the corresponding REN 2000 (Souchay et al. 1999) amplitude. The obtained nutation ratios are plotted in Fig. 2. The nutation associated with the tidal constituent number 553 identified in the previous section is the prograde nutation with period 1,305.5 sidereal days. We do not see any offset for this term with respect to the theory for a rigid Earth.

Since the moment of inertia of the inner core is about 1,400 times smaller than the one of the whole Earth, the expected effect in nutation is very small. The gravity effect may hence be larger because of additional deformational effects. Besides, we have analyzed one product of celestial pole time series, but it has recently been shown that the amplitudes of nutation terms can be significantly different between the operational series released by the different VLBI analysis centers. Differences can amount to several microarcseconds. Among the possible causes of such variability, the way of processing VLBI data (Gattano et al. 2015) and the choice of the reference radio sources (Lambert 2014) have

been identified. More consistent treatment of VLBI data is necessary before looking for smaller nutational terms.

4 Results and Interpretations

We have found a possible enhancement of the tidal wave number 553 in Tamura's tidal potential catalogue (corresponding to the prograde 1,305.5-sidereal day nutation) observed in the SG records at nine sites for which the length of records is larger than 10 years (BE (18.4 years), CA (20 years), CB (16.5 years), BH (14 years), MO (14 years), MB (18.5 years), SU (13.2 years), ST (18.4 years) and WE (17.6 years)). It was not observed at sites with shorter time-series (BFO (6 years), PE (8 years), VI (9 years)) neither at MC and ME which have noisier data. If this enhancement of the tidal constituent 553 is true and if it is associated with the resonance effect of the FICN then the FICN period would be shortly larger than the MHB value (around 1,300 sidereal days instead of 1,027 sidereal days) and the dissipation processes responsible for its damping much smaller than predicted in MHB.

In the associated prograde nutation terms, we have not identified any perturbation of the 1,305.5 sidereal day term which corresponds to the tidal constituent 553. However, because of the weak moment of inertia of the inner core, the effect of the FICN could be much smaller in nutation than in gravity.

Even if all these results are promising, the theoretical prediction of the FICN period is not sufficiently accurate to unambiguously link those perturbations with the FICN resonance. Hence, it seems to be necessary to improve the theoretical estimates of the FICN period to make its search in the observational data more efficient. Further analyses with additional and longer time-series are also required to have a chance to clearly detect the resonance effect of the FICN on the tidal gravimetric records, particularly to analyze additional diurnal tidal constituents that could be affected by the presence of the FICN.

References

Amoruso A, Botta V, Crescentini L (2012) Free core resonance parameters from strain data: sensitivity analysis and results from the Gran Sasso (Italy) extensometers. Geophys J Int 189:923–936

Blum PA, Hatzfeld D, Wittlinger G (1973) Résultats expérimentaux sur la fréquence de résonance due à l'effet dynamique du noyau liquide. C R Acad Sci Paris, 277, Ser B:241–244

Crossley D, Hinderer J, Casula G, Francis O, Hsu H-T, Imanishi Y, Meurers B, Neumeyer J, Richter B, Shibuya K, Sato T, van Dam T (1999) Network of superconducting gravimeters benefits a number of disciplines. Eos Trans AGU 80(11):121–126

de Vries D, Wahr JM (1991) The effects of the solid inner core and nonhydrostatic structure on the Earth's forced nutations and Earth tides. J Geophys Res B96:8275–8293

Defraigne P, Dehant V, Hinderer J (1994) Stacking gravity tide measurements and nutation observations in order to determine the complex eigenfrequency of the nearly diurnal free wobble. J Geophys Res 99(B5):9203–9213

Defraigne P, Dehant V, Hinderer J (1995) Correction to 'stacking gravity tide measurements and nutation observations in order to determine the complex eigenfrequency of the nearly diurnal free wobble'. J Geophys Res 100(B2):2041–2042

Dehant V, Hinderer J, Legros H, Lefftz M (1993) Analytical approach to the computation of the earth, the outer core and the inner core rotational motions. Phys Earth Planet Inter 76:259–282

Dehant V, Feissel M, Defraigne P, Roosbeek F, Souchay J (1997) Could the energy near the FCN and the FICN be explained by luni-solar or atmospheric forcing? Geophys J Int 130:535–546

Ducarme B, Sun H-P, Xu J-Q (2007) Determination of the free core nutation period from tidal gravity observations of the GGP superconducting gravimeter network. J Geod 81:179–187

Dumberry M (2009) Influence of elastic deformations on the inner core wobble. Geophys J Int 178:57–64

Gattano C, Lambert S, Bizouard C (2015) Comparison of VLBI nutation series, to be published in Proceedings of 22th European VLBI Group for Geodesy and Astrometry (EVGA) Working Meeting

Greff-Lefftz M, Legros H, Dehant V (2000) Influence of the inner core viscosity on the rotational eigenmodes of the Earth. Phys Earth Planet Inter 122:187–204

Greff-Lefftz M, Dehant V, Legros H (2002) Effects of inner core viscosity on gravity changes and spatial nutations induced by luni-solar tides. Phys Earth Planet Inter 129:31–41

Hartmann T, Wenzel H-G (1995) The HW95 tidal potential catalogue. Geophys Res Lett 22(24):3553–3556

Herring TA, Buffett BA, Mathews PM, Shapiro II (1991) Forced nutations of the Earth: influence of inner core dynamics, 3. Very long interferometry analysis. J Geophys Res 91:4755–4765

Herring TA, Mathews PM, Buffett BA (2002) Modeling of nutation-precession: very long baseline interferometry results. J Geophys Res 107.doi:10.1029/2001JB000165

IERS Conventions (2010) In: Petit G, Luzum B (eds) (IERS Technical Note 36). Verlag des Bundesamts für Kartographie und Geodäsie, Frankfurt am Main, p 179. ISBN 3-89888-989-6

Koot L, Rivoldini A, de Viron O, Dehant V (2008) Estimation of Earth interior parameters from a Bayesian inversion of very long baseline interferometry nutation time series. J Geophys Res 113, B08414. doi:10.1029/2007JB005409

Koot L, Dumberry M, Rivoldini A, de Viron O, Dehant V (2010) Constraints on the coupling at the core-mantle and inner core boundaries inferred from nutation observations. Geophys J Int 182:1279–1294

Krásná H, Böhm J, Schuh H (2013) Free core nutation observed by VLBI. Astron Astrophys 555:29

Lambert S (2006) Atmospheric excitation of the Earth's free core nutation (research note). Astron Astrophys 457:717–720

Lambert S (2014) Comparison of VLBI radio source catalogs. Astron Astrophys 570:108

Lambert SB, Dehant V (2007) The Earth's core parameters as seen by the VLBI. Astron Astrophys 469:777–781

Lambert S, Rosat S, Cui X, Rogister Y, Bizouard C (2012) A search for the free inner core nutation in VLBI data. In: IVS 2012 General Meeting Proceedings, pp 370–374

Legros H, Hinderer J, Lefftz M, Dehant V (1993) The influence of the solid inner core on gravity changes and spatial nutations induced by luni-solar tides and surface loading. Phys Earth Planet Inter 76:283–315

Malkin Z (2014) On the accuracy of the theory of precession and nutation, Astron. Reports, 58, No. 6, pp 415–425

Mathews PM (2001) Love numbers and gravimetric factor for diurnal tides. Proceedings of 14th international symposium Earth tides. J Geod Soc Jpn 47(1):231–236

Mathews PM, Buffett BA, Herring TA, Shapiro II (1991a) Forced nutations on the Earth: influence of inner core dynamics, 1. Theory. J Geophys Res 96:8219–8242

Mathews PM, Buffett BA, Herring TA, Shapiro II (1991b) Forced nutations of the Earth: influence of inner core dynamics: 2. Numerical results and comparisons. J Geophys Res 96:8243–8257

Mathews PM, Buffet BA, Shapiro II (1995) Love numbers for diurnal tides: relation to wobble admittances and resonance expansions. J Geophys Res 100(B7):9935–9948

Mathews PM, Herring TA, Buffett BA (2002) Modeling of nutation-precession: new nutation series for nonrigid Earth and insights into the Earth's interior. J Geophys. Res 107 (B4):ETG3-1-3-30

Neuberg J, Zürn W (1986) Investigation of the nearly diurnal resonance using gravity, tilt and strain data simultaneously. In: Vieira R (ed) Proceedings of 10th international symposium earth tides. Cons. Sup. Inv. Cient., Madrid, pp 305–311

Rogister Y (2001) On the diurnal and nearly diurnal free modes of the Earth. Geophys J Int 144:459–470

Rogister Y, Valette B (2009) Influence of liquid core dynamics on rotational modes. Geophys J Int 176(2):368–388

Rosat S, Lambert SB (2009) Free core nutation resonance parameters from VLBI and superconducting gravimeter data. Astron Astrophys 503:287–291

Rosat S, Florsch N, Hinderer J, Llubes M (2009) Estimation of the free core nutation parameters from SG data: sensitivity study and comparative analysis using linearized Least-Squares and Bayesian methods. J Geodyn 48:331–339

Schuh H, Behrend D (2012) VLBI: a fascinating technique for geodesy and astrometry. J Geodyn 61:68–80. doi:10.1016/j.jog.2012.07.007

Souchay J, Loysel B, Kinoshita H, Folgueira M (1999) Corrections and new developments in rigid earth nutation theory: III. Final tables "REN-2000" including crossed-nutation and spin-orbit coupling effects. Astron Astrophys Suppl Ser 135:111–131

Tamura Y (1987) A harmonic development of the tide generating potential. Bull Inf Mar Terr 99:6813–6855

Vondrák J, Weber R, Ron C (2005) Free core nutation: direct observations and resonance effects. Astron Astrophys 444:297–303

Wenzel H-G (1996) The nanogal software: Earth tide data processing package ETERNA 3.30. Bull Inf Mar Terr 124:9425–9439

Zaske J, Zürn W, Wilhelm H (2000) NDFW analysis of borehole water level data from the hot-dry-rock test site Soultz-Sous-Forêts. Bull Inf Mar Terr 132:10,241–10,270

Zotov L, Bizouard C (2015) Regional atmospheric influence on the Chandler wobble. Adv Sp Res 55(5):1300–1306

Chandler Wobble and Frequency Dependency of the Ratio Between Gravity Variation and Vertical Displacement for a Simple Earth Model with Maxwell or Burgers Rheologies

Yann Ziegler, Yves Rogister, Jacques Hinderer, and Séverine Rosat

Abstract

To study the Earth global deformation at periods ranging from a few hours to a few thousand years, we consider a homogeneous compressible Earth model with either a Maxwell or a Burgers rheology. First, we compute, for the harmonic degree $\ell = 2$, the ratio between the gravity variation and the vertical surface displacement due to surface loading as a function of the forcing period. In the elastic domain, up to the relaxation time of the rheological model, which is 226 years, the ratio is almost constant and equal to $-0.26\,\mu$Gal/mm. In the viscoelastic domain, above 10,000 years, the ratio tends to $-0.08\,\mu$Gal/mm. In between, the transition is smooth. Second, we compute the period T_{CW} and quality factor Q_{anel} of the Chandler wobble as a function of the rheological parameters of a Burgers model. The influence of both the steady-state and transient viscosities on T_{CW} is significant only for viscosity values smaller than what can usually be found in the literature for the mantle viscosities and Q_{anel} is more sensitive than T_{CW} to the transient viscosity.

1   Introduction

From the propagation of seismic waves to large-scale convection, through Glacial Isostatic Adjustment (GIA), the geophysical processes occurring in the Earth's mantle are extremely diverse. Their modelling relies on linear constitutive equations between stress and strain that describe the rheological behaviour of the Earth's materials. To explain the observations of mantle deformation over a broad range of timescales, different constitutive equations must be assumed at different timescales. In the seismic band, between 1 s and 1 h, the mantle exhibits an elastic behaviour with a slight anelastic dissipation. At timescales of several thousands of years, it viscoelastically deforms, while it convects as a viscous fluid over millions of years. The stress-strain relation that makes a model agree with the observations is generally not unique. In that case, the simplest constitutive equation is used. In the gap between the seismic band and the GIA timescale, specific deformations and observational data are sparse. Postseismic deformation, periodic solid Earth tides, polar motions driven by seasonal motions in the ocean and atmosphere and the Chandler wobble (CW) belong to this small set of deformations. Therefore, the rheology of the mantle is not clearly understood and the rheological parameters are not well known in that window of timescales. Although the Burgers model can describe at once elastic deformations, transient deformations and viscous flows, its use to account for the mantle rheology is subject to many questions (Ranalli 1995).

   The Earth response to the melting of glaciers contains both an instantaneous elastic rebound and a long-term

Y. Ziegler (✉) • J. Hinderer • S. Rosat
IPGS/EOST, Université de Strasbourg/CNRS, 5 rue René Descartes, 67000 Strasbourg, France
e-mail: yann.ziegler@unistra.fr

Y. Rogister
EOST, Université de Strasbourg, 5 rue René Descartes, 67000 Strasbourg, France

viscoelastic rebound. So, the present-day ice melting (PDIM) is accompanied by an elastic response and the Pleistocene deglaciation has been followed by an isostatic adjustment that involves the rise of deep mantle materials. It is common to separate these two components at a fixed location subject to both phenomena by estimating the ratio $\Delta g/\Delta u$ between the gravity variation Δg and the vertical displacement Δu (de Linage et al. 2007; Mémin et al. 2011, 2012). Its value ranges from $-0.26\,\mu$Gal/mm (de Linage et al. 2007) for the elastic deformation, and, including the direct Newtonian attraction of the load, to $-0.15\,\mu$Gal/mm for the viscoelastic deformation (Wahr et al. 1995). In between, it is poorly known.

A clue on the rheological properties of the mantle at the yearly timescale can be searched for in the attenuation of the CW, which is a rotational eigenmode with a period approximately 435 days (Chandler 1891; Munk and MacDonald 1960; Smith and Dahlen 1981). Except if the CW interacts with the spectrum of the liquid outer core, in which case it would be accompanied by oscillations in the core, its eigendisplacement is largely dominant in the mantle (Register and Valette 2009). The CW attenuation is quantified by the quality factor Q_{CW} whose observational estimates are shown in Fig. 1 for previous studies (Ooe 1978; Wilson and Vicente 1980; Lenhardt and Groten 1985; Furuya and Chao 1996; Kuehne et al. 1996; Vicente and Wilson 1997; Nastula and Gross 2015). Because the contribution from various possible physical mechanisms to the excitation of the free CW is not exactly known, although pressure variations at the bottom of the oceans might be dominant (Gross 2000), the determination of Q_{CW} is a complicated task that results in wide ranges of values. The length of the analyzed polar motion time series is also critical in evaluating the period and quality factor of the CW (Gross 2007). Although the quality factor encompasses various dissipative processes, its
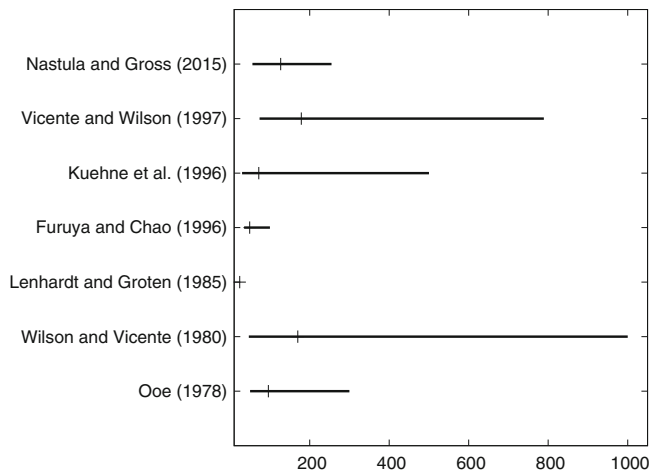
accurate estimate would help in better understanding mantle dissipation. There is, however, no accurate model of mantle anelasticity at the CW frequency (Gross 2007).

In this paper, we consider a homogeneous rotating Earth model with either a Maxwell or a Burgers rheology. We study the influence of the rheology on $\Delta g/\Delta u$ at different timescales and on the CW. The paper is organized as follows. In Sect. 2, we describe the modelling of the dynamics of the Earth model, which is based on the local equations of conservation of linear momentum. We introduce the rheological models and the correspondence principle, which allows for the definition of complex rheological parameters. In Sect. 3, we introduce the load Love numbers and compute $\Delta g/\Delta u$ as a function of the period of the surface loading that deforms a model with either a Maxwell or a Burgers rheology. Section 4 is devoted to the computation of the period and quality factor of the CW of a model with a Burgers rheology. We conclude in Sect. 5.

2 Modelling of Earth Dynamics and Rheological Models

We use the linear momentum approach developed by Smith (1974) and improved by Schastok (1997), Register (2001, 2003) and Huang and Liao (2003) to model the dynamics of a rotating, elliptical, self-gravitating Earth model. In this approach, the displacement field of a rotational mode is described by a series of spheroidal displacements $\boldsymbol{\sigma}$ and toroidal displacements $\boldsymbol{\tau}$ according to the following rule:

$$\mathbf{s} = \sum_{\ell=1,3,5,\dots}^{\infty} (\boldsymbol{\tau}_\ell^m + \boldsymbol{\sigma}_{\ell+1}^m) \qquad (1)$$

where ℓ is the harmonic degree and $m = \pm 1$, the harmonic order. For the Chandler wobble, $m = -1$.

To solve numerically the equations of motion, the series (1) must be truncated after a finite number of terms. For the homogeneous solid Earth models we will consider in the next two sections, we may safely assume that a two-term truncature is accurate enough (Hough 1896). This leaves us with a set of ordinary differential equations of the eighth order over radius. Longer coupling chains are however required to describe the rotational modes of Earth models that include a liquid outer core and a solid inner core (Crossley and Rochester 2014; Register and Valette 2009; Rochester et al. 2014). Rotation and ellipticity are necessary for the CW to exist, but they will be consistently neglected for the loading computation in Sect. 3.

Linear viscoelasticity or anelasticity can be included in the strain-stress relationship by invoking the correspondence principle (Lee 1955), which states that in the Laplace domain

Fig. 1 Observational estimates of the CW quality factor Q_{CW} with their uncertainties

the linear viscoelastic and anelastic constitutive equations take the same form as an isotropic linearly elastic constitutive equation, the Lamé elastic parameters being simply replaced by complex parameters whose imaginary parts contain the anelastic or viscous parameters.

If we denote by T_{ij} a Cartesian component (i and $j = 1$, 2 or 3) of the stress tensor, e_{ij} a Cartesian component of the strain tensor, δ_{ij} the Kronecker symbol, λ_0 and μ_0 the first and second Lamé parameters, respectively, and η_0 the viscosity, the Maxwell constitutive stress-strain relation writes (Peltier et al. 1981)

$$\frac{d}{dt}T_{ij} + \frac{\mu_0}{\eta_0}(T_{ij} - \frac{1}{3}\delta_{ij}\sum_{k=1}^{3}T_{kk})$$
$$= 2\mu_0\frac{d}{dt}e_{ij} + \lambda_0\delta_{ij}\sum_{k=1}^{3}\frac{d}{dt}e_{kk} \quad (2)$$

The Maxwell model can be thought of as a spring in series with a dashpot. The Laplace transform of Eq. (2) is

$$T'_{ij} = \lambda_M\delta_{ij}\sum_{k=1}^{3}e'_{kk} + 2\mu_M e'_{ij} \quad (3)$$

where the prime denotes the Laplace transform, $s = i\omega$ is the Laplace variable, ω is the complex frequency,

$$\lambda_M(s) = \frac{s\lambda_0 + \frac{\mu_0}{\eta_0}(\lambda_0 + 2\mu_0/3)}{s + \frac{\mu_0}{\eta_0}} \quad (4)$$

$$\mu_M(s) = \mu_0 s\tau_M(1 + s\tau_M)^{-1} \quad (5)$$

and

$$\tau_M = \frac{\eta_0}{\mu_0}. \quad (6)$$

Equation (3) looks like an isotropic linearly elastic constitutive relation. This is the correspondence principle.

The Burgers constitutive stress-strain relation is (Peltier et al. 1981)

$$\frac{d^2}{dt^2}T_{ij} + \left(\frac{\mu_1 + \mu_2}{\eta_2} + \frac{\mu_1}{\eta_1}\right)\left(\frac{d}{dt}T_{ij} - \frac{1}{3}\delta_{ij}\sum_{k=1}^{3}\frac{d}{dt}T_{kk}\right)$$
$$+ \frac{\mu_1\mu_2}{\eta_1\eta_2}\left(T_{ij} - \frac{1}{3}\delta_{ij}\sum_{k=1}^{3}T_{kk}\right)$$
$$= 2\mu_1\frac{d^2}{dt^2}e_{ij} + \lambda_1\delta_{ij}\sum_{k=1}^{3}\frac{d^2}{dt^2}e_{kk}$$
$$+ \frac{2\mu_1\mu_2}{\eta_2}\left(\frac{d}{dt}e_{ij} - \frac{1}{3}\delta_{ij}\sum_{k=1}^{3}\frac{d}{dt}e_{kk}\right) \quad (7)$$

Table 1 Rheological parameters of a homogeneous Earth model

Rheology	Parameter	Value	
B and M	λ_0	3.5×10^{11}	Pa
B and M	μ_0 (M) or μ_1 (B)	1.4×10^{11}	Pa
B	μ_2	1.4×10^{11}	Pa
B and M	η_0 (M) or η_1 (B)	10^{21}	Pa s
B	η_2	5×10^{19}	Pa s

The parameters λ_0, μ_0, μ_1 and μ_2 are mean values of the first and second Lamé parameters of the PREM model (Dziewonski and Anderson 1981). The value for viscosity η_1 has been adopted by Peltier et al. (1981), Wahr et al. (1995) or Nakada and Karato (2012). In the rheology column, B and M stand for Burgers and Maxwell, respectively

The spring-and-dashpot analogy for the Burgers model is a spring and a dashpot in parallel, both in series with a Maxwell element. The spring and the dashpot in parallel made up a Kelvin element. Equation (7) therefore involves two viscosities η_1 and η_2 and two rigidities μ_1 and μ_2. Subscript 1 (respectively 2) refers to the rigidity and viscosity of the Maxwell (resp. Kelvin) element. As mentioned in Sect. 1, the Burgers model can describe at once elastic deformations, transient deformations and viscous flows. The Maxwell model, however, can only describe elastic deformations and viscous flows. The Laplace transform of Eq. (7) provides an equation of the same form as Eq. (3) where λ_M and μ_M have to be replaced, respectively, by λ_B and μ_B defined by

$$\lambda_B(s) = \lambda_1 + \frac{2}{3}[\mu_1 - \mu_B(s)], \quad (8)$$

where

$$\mu_B(s) = \mu_1 s\,(s + \mu_2/\eta_2)$$
$$\left[s^2 + \left(\frac{\mu_1 + \mu_2}{\eta_2} + \frac{\mu_1}{\eta_1}\right)s + \frac{\mu_1\mu_2}{\eta_1\eta_2}\right]^{-1}. \quad (9)$$

The numerical values for the elastic and viscous parameters of a homogeneous model of density $\rho_0 = 5515\,\text{kg/m}^3$ are given in Table 1 for both the Maxwell and Burgers rheologies.

3 $\Delta g/\Delta u$ Due to Surface Loading

In this section, we consider the Maxwell and Burgers rheologies and numerically compute the load Love numbers and $\Delta g/\Delta u$ for forcing periods ranging from 0.1 year up to 10 Myr. At periods longer than a few hours, no resonance is to be expected with the seismic spectrum of the model. We neglect the rotation and elliptical shape of the Earth, which have a small influence, of order 1/300, on the deformation. Therefore, the toroidal and spheroidal displacements decou-

ple and the equations of motion do not explicitly depend on m. The loading potential, however, possibly depends on m. The frequency of the forced motion being known, we only have to compute the displacement scalars and the Eulerian variation $\phi_{1\ell}$ of the gravity potential. We denote the loading potential of harmonic degree ℓ by

$$\chi_\ell = \frac{3g_0}{2\ell+1} \frac{\Sigma_\ell}{\rho_0} \quad (10)$$

where ρ_0 and g_0 are the density and the gravity, respectively, at the Earth surface and Σ_ℓ is the degree-ℓ component of the surface mass density of the loading. The load Love numbers h'_ℓ and k'_ℓ and the load Shida number l'_ℓ are then given by Munk and MacDonald (1960)

$$h'_\ell = g_0 \frac{U_\ell}{\chi_\ell}, k'_\ell = \frac{\phi_{1\ell}}{\chi_\ell} - 1 \text{ and } l'_\ell = g_0 \frac{V_\ell}{\chi_\ell} \quad (11)$$

where U_ℓ and V_ℓ are the degree-ℓ components of the spheroidal displacement scalars, U_ℓ being the radial displacement.

Outside the load, the ratio between the gravity variation measured by a gravimeter moving with the ground and the vertical displacement of the ground is (de Linage et al. 2007)

$$\frac{\Delta g}{\Delta u} = -\frac{2g_0}{a} \left(1 - \frac{1}{4h'_\ell} - \frac{\ell+1}{2} \frac{k'_\ell}{h'_\ell} \right), \quad (12)$$

where a is the Earth radius. The ratio given by Eq. (12) obviously depends on ℓ. Above or below the load, the ratio $\Delta g/\Delta u$ is slightly different from Eq. (12) (de Linage et al. 2007). To avoid the unnecessary complication of having to consider two different ratios at a single location, we will only consider locations outside the load.

To compute the Love numbers, we solve the system of ordinary differential equations over radius obtained by separating the equations of motion, which are partial differential equations, in polar spherical coordinates using spherical harmonics. We can either run solvers that handle complex numbers or double the order, equal to 6, of the system of the real elastic ordinary differential equations. We have opted for the second alternative.

The amplitude and phase of $\Delta g/\Delta u$ are plotted for $\ell = 2$ in Fig. 2.

For a given harmonic degree, the relaxation time differs from the Maxwell time (Legros et al. 2006), the latter being given by Eq. (6) and close to 200 years for the rheological parameters given in Table 1. The change from the elastic to the viscous regime occurs at the forcing period of 3000 years, which is the value at which the phase reaches its maximum. For shorter periods, the deformation is elastic and the amplitude of $\Delta g/\Delta u$ is equal to $-0.26\,\mu$Gal/mm. It increases to
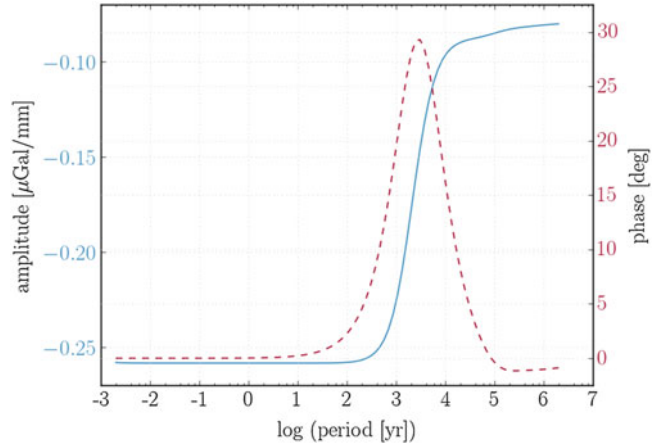
Fig. 2 $\Delta g/\Delta u$ amplitude (*blue line*) and phase (*red dashed line*) for harmonic degree $\ell = 2$ as a function of the forcing period for the Maxwell rheology
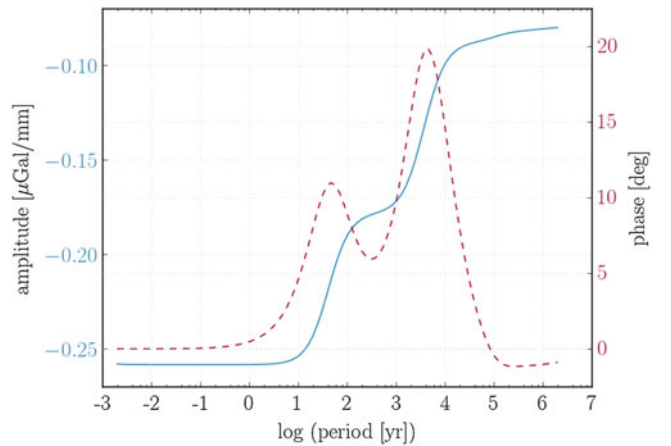
Fig. 3 Same as Fig. 2 for the Burgers rheology

$-0.08\,\mu$Gal/mm in the viscous regime, at longer periods. The phase characterizes the phase delay between the gravity perturbation and the radial displacement. Figure 2 shows that it tends to zero at both high and low periods, which means that anelastic influence on the phase delay is more significant in the vicinity of the viscoelastic domain, between the elastic and viscous regimes.

Similar trends at the lowest and largest periods are observed for the Burgers rheology (Fig. 3) with the exception of an additional smaller relaxation time at intermediate periods, due to the Kelvin element. Another difference is the absolute maximum value of the phase which is smaller, close to 20°, whereas the elastic and viscous limits remain the same.

We therefore obtain a continuous transition between the short-term elastic regime and the long-term fluid regime. As expected, the rheological models and their parameters, in particular the viscosity of the mantle, are decisive in

the timescales at which this change occurs but, for a given harmonic degree, do not affect the size of the viscoelastic domain. For $\ell = 2$, whatever the viscosity, the width of the viscoelastic domain always covers two or three orders of magnitude—roughly between 100 and 10,000 years for the Maxwell rheology and between 10 and 10,000 years for the Burgers rheology.

4 Chandler Wobble Attenuation

In this section, we compute the complex eigenfrequency ω_{CW} of the CW of a homogeneous model with the Burgers rheology. The quality factor Q_{anel} of the mode is directly related to the imaginary part of ω_{CW} by

$$\omega_{CW} = (\omega_0 + \delta\omega)\left(1 + i\frac{1}{2Q_{anel}}\right), \quad (13)$$

where ω_0 is the CW frequency of the elastic homogeneous model which has the same density and elastic parameters as our homogeneous dissipative model, and $\delta\omega$ is the variation due to the mantle anelasticity. For the Earth, mantle anelasticity is only one dissipation mechanism among others. But for our simple model, it is the only dissipation mechanism. So we denote the quality factor due to mantle anelasticity by Q_{anel} to distinguish it from the total quality factor Q_{CW}. After the CW has been excited and in the absence of any subsequent excitation, its amplitude $A(t)$ exponentially decays with an attenuation rate α given by

$$\alpha = \frac{\omega_0}{2Q_{anel}} \quad (14)$$

such that

$$A(t) = A_0 e^{-\alpha t}. \quad (15)$$

We only consider the Burgers rheology because the Maxwell rheology is most probably not suited to represent the rheological behaviour of the Earth at the yearly timescale.

In Figs. 4 and 5, we plot $T_{CW} = 2\pi/(\omega_0 + \delta\omega)$ and Q_{anel} as a function of the steady-state and transient viscosities η_1 and η_2, respectively. First, we allow η_1 to vary between 10^{17} and 10^{25} Pa s while η_2 is kept fixed and equal to 5×10^{19} Pa s. Next, we allow η_2 to vary between 10^{15} and 10^{22} Pa s while η_1 is kept fixed and equal to 10^{21} Pa s. λ_0 is given in Table 1 and we first assume that μ_1 and μ_2 are equal and take the value of Table 1. The CW period $2\pi/\omega_0$ of the corresponding elastic model is 291.9 days, which is the elastic limit reached by T_{CW} when the viscosities become large.

η_1 has only a small influence on T_{CW} when it is smaller than 5×10^{18} Pa s, which is unlikely if the mantle rheology has to be modeled by a Burgers' law. On the contrary, the influence of η_1 on Q_{anel} is significant, in particular when
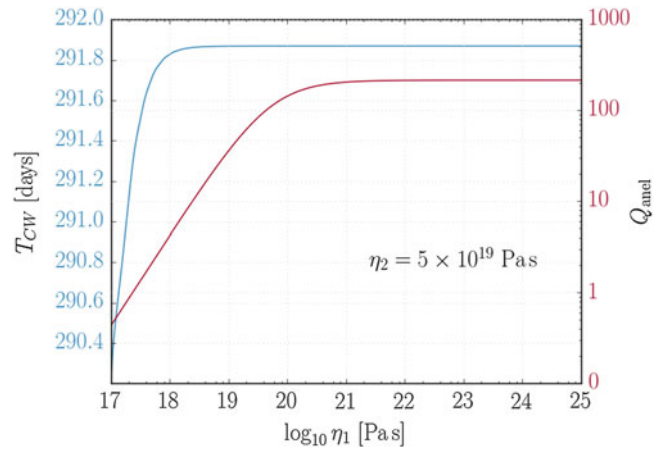
Fig. 4 Period T_{CW} (*blue*) and quality factor Q_{anel} (*red*) as a function of steady-state viscosity η_1 for $\mu_1 = \mu_2$
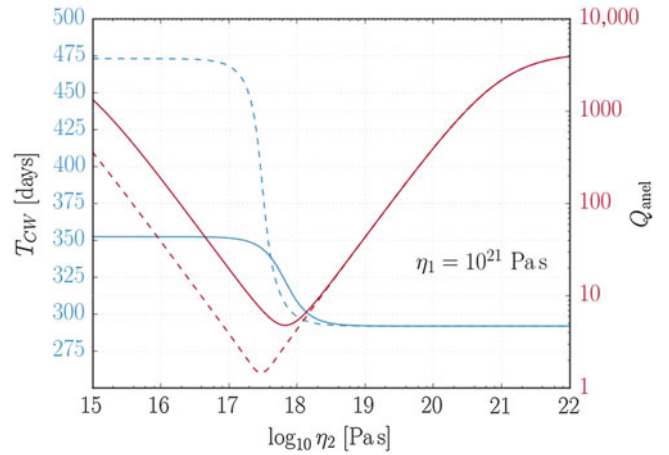
Fig. 5 Period T_{CW} (*blue*) and quality factor Q_{anel} (*red*) as a function of transient viscosity η_2 for $\mu_1 = \mu_2$ (*solid lines*) and $\mu_1 = 3\mu_2$ (*dashed lines*)

η_1 is smaller than 5×10^{20} Pa s. Above this value, Q_{anel} is almost constant and equal to 200, which corresponds to a relaxation time of 320 years. For the lower Q_{CW} value of 56 provided by Nastula and Gross (2015), η_1 should be greater than 2×10^{19} Pa s, which is consistent with viscosity estimates from GIA studies (Paulson et al. 2007). The upper Q_{CW} value of 255 obtained by Nastula and Gross (2015) is, however, never reached by our modeled Q_{anel} for a fixed $\eta_2 = 5\times10^{19}$ Pa s.

η_2 has a much stronger influence than η_1 has on both T_{CW} and Q_{anel}. T_{CW}, which is almost constant and equal to 352 days when η_2 is smaller than 10^{17} Pa s, decreases to 291.9 days for η_2 larger than 5×10^{18} Pa s. The shape of the plot of Q_{anel} as a function of η_2 is reminiscent of Fig. 4 of Yuen and Peltier (1982), who computed the quality factors for seismic normal modes of a homogeneous Earth model whose rheology was that of a standard linear solid. Q_{anel}

reaches a minimum value of 5 when $\eta_2 = 7\times10^{17}$ Pa s. That minimum would of course not be plausible for a realistic Earth model.

Let us now consider that $\mu_1 \neq \mu_2$. According to Sabadini (1985), Trubienko et al. (2013), or Lefftz et al. (1994), μ_2 might be three to ten times smaller than μ_1. We take $\mu_1 = 3\mu_2$ and recompute T_{CW} and Q_{anel} as a function of η_1 or η_2 (Fig. 5). Their pattern look the same as when $\mu_1 = \mu_2$ but, for η_2 smaller than 3×10^{18} Pa s, T_{CW} and Q_{anel} are, respectively, larger and smaller than in the case $\mu_1 = \mu_2$. η_2 being smaller than 3×10^{18} Pa s in the mantle is, however, not likely.

Of course, for a conclusive result be obtained about the mantle viscosity, a more realistic Earth model should be taken into account.

5 Conclusion

The rheological behaviour of the Earth is known to be almost elastic, with small energy dissipation, in the seismic frequency band and viscoelastic at the GIA timescale. Our intent has been to explore the sensitivity of Earth's global deformation to the rheological properties of the mantle at intermediate timescales. For homogeneous compressible Earth models, we have investigated, on the one hand, the dependence of the Chandler wobble period and quality factor on the elastic and viscous parameters of a Burgers rheological model and, on the other hand, the ratio between the gravity variation and the vertical surface displacement as a function of the timescale of a surface loading for the Maxwell and Burgers rheologies.

With regard to $\Delta g/\Delta u$, we showed that its amplitude tends toward two distinct values at low and high forcing periods, the long-period viscous limit being smaller in absolute value than the short-period elastic limit. For the Maxwell rheology, the phase reaches a maximum of 30° for the $\ell = 2$ relaxation time, which is also the transition time for the amplitude, and is close to zero otherwise. For the Burgers rheology, the phase shows an absolute maximum of 20° for the $\ell = 2$ relaxation time and a smaller relative maximum at the relaxation time of the Kelvin element.

The viscosities have an almost negligible influence on the CW period when they are of the same order of magnitude as the values found in the literature for the mantle viscosities. The same conclusion holds for the rigidity μ_2, whose influence is only significant when η_2 is smaller than 3×10^{18} Pa s, which is much smaller than estimates of the viscosities of the mantle modelled as a Burgers body. The quality factor depends more strongly on η_2 than the period does and the influence of η_1 is non-negligible only for values of η_1 smaller than 10^{21} Pa s.

Considering a realistic stratified Earth model is the obvious next step that should be done.

References

Chandler SC (1891) On the variation of latitude. Astron J 249:65–70

Crossley DJ, Rochester MG (2014) A new description of Earth's wobble modes using Clairaut coordinates 2: results and inferences on the core mode spectrum. Geophys J Int 198(3):1890–1905

Dziewonski AM, Anderson DL (1981) Preliminary reference Earth model. Phys Earth Planet Inter 25:297–356

Furuya M, Chao BF (1996) Estimation of period and Q of the Chandler wobble. Geophys J Int 127:693–702

Gross RS (2000) The excitation of the Chandler wobble. Geophys Res Lett 27:2329–2332

Gross RS (2007) Earth rotation variations – long period. In: Herring T, Schubert G (ed) Treatise on geophysics, vol 3. Elsevier, Amsterdam, pp 239–294

Hough SS (1896) The rotation of an elastic spheroid. Philos Trans R Soc Lond A 189b:319–344

Huang CL, Liao XH (2003) Comment on 'Representation of the elastic-gravitational excitation of a spherical Earth model by generalized spherical harmonics' by Phinney & Burridge. Geophys J Int 155(2):669–678

Kuehne J, Wilson CR, Johnson S (1996) Estimates of the Chandler wobble frequency and Q. J Geophys Res 101(B6):13573–13579

Lee EH (1955) Stress analysis in viscoelastic materials. Q Appl Math 3(13):183–190

Lefftz M, Sabadini R, Legros H (1994) Mantle rheology, viscomagnetic coupling at the core-mantle boundary and differential rotation of the core induced by Pleistocene deglaciation. Geophys J Int 117:1–18

Legros H, Greff M, Tokieda T (2006) Physics inside the Earth: deformation and rotation. In: Dynamic of extended celestial bodies and rings. Springer, Berlin

Lenhardt H, Groten E (1985) Chandler wobble parameters from BIH and ILS data. Manuscr Geodaet 10(4):296–305

de Linage C, Hinderer J, Rogister Y (2007) A search for the ratio between gravity variation and vertical displacement due to a surface load. Geophys J Int 171:986–994

Mémin A, Rogister Y, Hinderer J, Omang OC, Luck B (2011) Secular gravity variation at Svalbard (Norway) from ground observations and GRACE satellite data. Geophys J Int 184:1119–1130

Mémin A, Rogister Y, Hinderer J (2012) Separation of the geodetic consequences of past and present ice-melting: influence of topography with application to Svalbard (Norway). Pure Appl Geophys 169(8):1357–1372

Munk WH, MacDonald GJF (1960) The rotation of the Earth: a geophysical discussion. Cambridge University Press, Cambridge

Nakada M, Karato SI (2012) Low viscosity of the bottom of the Earth's mantle inferred from the analysis of Chandler wobble and tidal deformation. Phys Earth Planet Inter 192–193:68–80

Nastula J, Gross R (2015) Chandler wobble parameters from SLR and GRACE. J Geophys Res Solid Earth 120(6):4474–4483

Ooe M (1978) An optimal complex AR.MA model of the Chandler wobble. Geophys J R Astron Soc 53:445–451

Paulson A, Zhong S, Wahr J (2007) Limitations on the inversion for mantle viscosity from postglacial rebound. Geophys J Int 168:1195–1209

Peltier W, Wu P, Yuen A (1981) The viscosities of the Earth's mantle. In: Anelasticity in the Earth. American Geophysical Union, Washington, DC, pp 59–77

Ranalli G (1995) Rheology of the Earth, 2 edn. Chapman and Hall, London

Rochester MG, Crossley DJ, Zhang YL (2014) A new description of Earth's wobble modes using Clairaut coordinates: 1. Theory. Geophys J Int 198(3):1848–1877

Rogister Y (2001) On the diurnal and nearly diurnal free modes of the Earth. Geophys J Int 144(2):459–470

Rogister Y (2003) Splitting of seismic-free oscillations and of the Slichter triplet using the normal mode theory of a rotating, ellipsoidal earth. Phys Earth Planet Inter 140(1–3):169–182 (2003)

Rogister Y, Valette B (2009) Influence of liquid core dynamics on rotational modes. Geophys J Int 176(2):368–388 (2009)

Sabadini R (1985) The effects of transient rheology on the interpretation of lower mantle viscosity. Geophys Res Lett 12(6):362–364

Schastok J (1997) A new nutation series for a more realistic model earth. Geophys J Int 130(1):137–150 (1997)

Smith ML (1974) The scalar equations of infinitesimal elastic-gravitational motion for a rotating, slightly elliptical Earth. Geophys J Int 37(3):491–526 (1974)

Smith ML, Dahlen FA (1981) The period and Q of the Chandler wobble. Geophys J R Astron Soc 64:223–281

Trubienko O, Fleitout L, Garaud JD, Vigny C (2013) Interpretation of interseismic deformations and the seismic cycle associated with large subduction earthquakes. Tectonophysics 589:126–141

Vicente RO, Wilson CR (1997) On the variability of the Chandler frequency. J Geophys Res 102(B9):20439

Wahr JM, DaZhong H, Trupin A (1995) Predictions of vertical uplift caused by changing polar ice volumes on a viscoelastic earth. Geophys Res Lett 22:977–980

Wilson CR, Vicente RO (1980) An analysis of the homogeneous ILS polar motion series. Geophys J R Astron Soc 62:605–616

Yuen DA, Peltier W (1982) Normal modes of the viscoelastic earth. Geophys J R Astron Soc 69:495–526

Detection of the Atmospheric S_1 Tide in VLBI Polar Motion Time Series

Anastasiia Girdiuk, Michael Schindelegger, Matthias Madzak, and Johannes Böhm

Abstract

The contribution of the diurnal atmospheric S_1 tide to Earth's wobble is assessed by tidally analyzing hourly polar motion (PM) estimates from approximately 25 years of geodetic Very Long Baseline Interferometry (VLBI) observations. Special emphasis is placed on the dependency of S_1 estimates on various settings in the a priori delay model and on the method of time series analysis in post-processing. The considered VLBI solutions differ with regard to the inclusion/exclusion of weak network geometries and the choice of a priori geophysical corrections such as thermal antenna deformation. Prograde PM coefficients $A^+ + iB^+$ of S_1 are on the level of $9 + i10\,\mu$as (microarcseconds) for all solutions and none of the changes in the processing strategies perturbs this estimate beyond the twofold S_1 standard deviation ($\sim 2.6\,\mu$as). An independent validation of the deduced harmonics against excitation estimates from atmosphere-ocean models shows that space geodetic and geophysical accounts of the S_1 effect in PM are still inconsistent by about $10\,\mu$as.

Keywords

Atmospheric tides • High-frequency Earth rotation • Single session time series approach • VLBI

1 Introduction

Cyclic heating of air masses with a Sun-locked period of 24 h generates the diurnal atmospheric S_1 tide, which in turn forces significant oceanic variability at the very same frequency through pressure gradients at the sea surface (Ray and Egbert 2004). This coupled global phenomenon excites small but measurable perturbations of Earth Rotation Parameters (ERP), for instance, Polar Motion (PM) is affected at a level of $10\,\mu$as (microarcseconds) (Brzeziński 2011). The reliable determination of these small-magnitude signals from long-term space geodetic observations poses a challenge, and published S_1 estimates in PM vary to some extent; see Schinde-

legger (2014) for a compilation of some recent S_1 solutions. Moreover, geophysical excitation values from atmosphere-ocean circulation models (Brzeziński et al. 2004; Brzeziński 2011) have, thus far, shown no agreement with any geodetic ERP estimate. As a result, conventional high-frequency Earth rotation models usually lack appropriate a priori accounts of the atmosphere-induced S_1 effect in PM. In this study, we focus mostly on the geodetic part of the problem and derive a range of S_1 estimates from geodetic Very Long Baseline Interferometry (VLBI) observations using different processing strategies and various settings in the geophysical part of the delay model. This should lead to a better understanding of the reliability of S_1 tidal terms and their dependency on individual components in the VLBI analysis. Our work follows the path of previous assessments of high-frequency Earth rotation variations (Artz et al. 2011; Böhm et al. 2012a; Gipson 1996) but unlike the global solutions pursued by these authors, we derive the tidal coefficients from a single session time series approach (TSA). The principal difference

A. Girdiuk (✉) • M. Schindelegger • M. Madzak • J. Böhm
Department of Geodesy and Geoinformation, TU Wien,
Gußhausstraße 27-29, 1040 Vienna, Austria
e-mail: anastasiia.girdiuk@geo.tuwien.ac.at

between the two approaches is: a global solution accumulates normal equations of all participating sessions and introduces the parameters of interest as unknowns before the main inversion; in the single session approach the hourly ERP values (at maximum 25 points) are estimated separately for each session before an a posteriori fit of tidal terms to the ERP time series is carried out. While a global solution is arguably more rigorous, the estimation on a time series basis allows us to study some of the impact factors on the tidal ERP variations *after* completing the computationally costly VLBI analysis. Specifically, one can improve the quality of the time series by freely excluding sessions and scans with an imperfect network geometry that appear to be the source of frequent outliers and systematic ERP behavior. In upcoming studies, the cleaned compilation of sessions will be adopted for refined global solutions. Here, three slightly different methods of single session TSA are applied in order to assess the robustness of the obtained S_1 coefficients. Given the numerous time gaps and undetected small systematics in the PM time series, some variability in the estimates of a minor tide such as S_1 can be expected. Moreover, the influence of omitting the diurnal cycle in other components of the VLBI analysis is assessed. In particular, we feed the standard mapping function model and the thermal antenna deformation routine with temperature values from different geophysical models.

2 The Single Session Time Series Approach

Hourly PM time series were derived by inverting each VLBI session separately with the widely used VieVS package (Vienna VLBI Software, Böhm et al. 2012b). Observational data come from routine 24-h VLBI sessions from 1989.10 to 2014.01 and include the operational R1 and R4 sessions as well as experimental sessions such as CORE-1, RD1, RDV, RD0, continuous VLBI campaigns, and other experiments (Behrend 2013). All sessions were analyzed in two steps: in the first run, we computed daily celestial pole offsets (CPO) by using a priori models as recommended by the IERS Conventions (Petit and Luzum 2010): libration, high-frequency ocean tidal effects, and daily Earth orientation parameter values from the C04 08 series, with precession and nutation initially set to the IAU 2000/2006 model (Mathews et al. 2002; Capitaine et al. 2003). In the second run, the CPO values from the first run were fixed to allow for an unambiguous estimation of hourly ERP and additional parameters. For both processing steps, we employed the following settings and reductions:

- TRF (Terrestial Reference Frame) fixed to VieTRF13 (Krásná et al. 2014) and CRF (Celestial Reference Frame) fixed to ICRF2 (Fey et al. 2015);

- Solid Earth tides from the IERS Conventions;
- Ocean pole tide model by Desai (2002);
- Conventional mean pole as made available by the IERS Earth Orientation Centre;
- Ocean tide loading: FES2004 (Lyard et al. 2006);
- Tidal and non-tidal atmospheric loading (Wijaya et al. 2013);
- Vienna Mapping Function: VMF1 (Böhm et al. 2006);
- Thermal deformation model for geodetic VLBI antennas (Nothnagel 2009);
- Internal outlier test for baseline observations as provided by VieVS.

The parameters given below were estimated as offsets at integer hours (or minutes) of UTC, to which we customarily refer to as "continuous piece-wise linear offsets" (CPWLO); cf. Schuh and Böhm (2013). Relative constraints on the differences between successive offsets are specified where appropriate.

- Quadratic clock polynomial plus CPWLO functions with clock values every 1 h and constraints of 1.3 cm/h;
- Zenith wet delays as CPWLO every 30 min and constraints of 1.5 cm/30 min;
- Tropospheric gradients as CPWLO every 6 h and constraints of 0.05 cm/6 h;
- Earth Orientation Parameters as CPWLO once per day (at 0 UTC) with tight constraints of 1 μas/day and 1 μs/day (microseconds) in the first run;
- ERP as CPWLO per hour with loose constraints of 60 mas/h (milliarcseconds) in the second run.

High-frequency ERP time series obtained in that manner still include some deficiencies and segments of non-harmonic behavior that may affect fitted S_1 terms substantially. As a restriction, outlier trimming for PM residuals relative to the a priori model was applied, using thresholds of 3 mas on the PM estimates and 1 mas on the formal uncertainties. This processing steps removed ∼15% of the time series and resulted in somewhat cleaner ERP records, which are labeled as "original time series" hereinafter.

2.1 Time Series Analysis

The original ERP time series contain both the S_1 effect as well as large variations due to gravitationally forced ocean tides. We imposed a standard harmonic model of diurnal and semidiurnal oscillations on them with

$$x_p = \sum_{j=1}^{n} \left[(-A_j^+ - A_j^-) \cos\alpha_j(t_i) + (B_j^+ - B_j^-) \sin\alpha_j(t_i) \right],$$

$$y_p = \sum_{j=1}^{n} \left[(B_j^+ + B_j^-) \cos\alpha_j(t_{i,j}) + (A_j^+ - A_j^-) \sin\alpha_j(t_i) \right],$$

$$(1)$$

where $x_p = x_p(t_i)$, $y_p = y_p(t_i)$ denote pole coordinates at discrete integer hours t_i. $\{A_j^+, B_j^+\}$ are prograde PM coefficients for n tidal terms, $\{A_j^-, B_j^-\}$ are the corresponding retrograde coefficients, and $\alpha_j(t_i)$ signifies the angular (fundamental) arguments as given by Simon et al. (1994). The stochastic model associated with Eq. (1) utilizes the standard deviations of the hourly PM estimates, but covariances between the parameters of the individual sessions were not taken into account. We acknowledge that such a stochastic setup is not complete and that a global solution would allow for a more realistic consideration of variances, covariances, and the effect of weak network geometries. Notwithstanding these differences between our TSA and the global solution, tidal S_1 estimates from both approaches have been shown to agree well within their formal uncertainties (Böhm 2012).

In the first (and standard) method to retrieve S_1, eight major tidal terms, some minor terms, zero tides where no excitation signals are expected, and S_1 were estimated together by means of a least squares adjustment (LSA) of the original time series. The prograde and retrograde coefficients of PM, which are the parameters of interest, were extracted from the fitted sine- and cosine-amplitudes through appropriate linear combinations as indicated in Eq. (1). Numerical results obtained thereof are presented in Table 1 and agree with estimates from our reference studies (Artz et al. 2011; Böhm et al. 2012a) within about 5% for the larger-magnitude constituents. Associated standard deviations (σ) were found to barely vary across the set of coefficients $\{A^+, B^+, A^-, B^-\}$ for each tide and are therefore tabulated as tide-specific averages. The suggested 3σ level is $4\,\mu$as throughout and consistent with the largest zero tides that serve as separate measurements for the solution noise level. All retrograde diurnal PM coefficients fall below this threshold, suggesting that the signal content in this frequency band has been correctly attributed to nutation and our post-processing does not produce questionable signals in the retrograde band. For S_1, both tidal components ($\sim 9\,\mu$as) are significantly above the noise level, yet these estimates might still be affected by some systematic errors, e.g., due to various problems at individual stations or an uneven distribution of observations over the course of a 24-h session and the entire time span. In an attempt to mitigate these influences and explore the variability of our S_1 results, we test other time series analysis strategies below.

In the second method, the tidal terms of Table 1 – excluding S_1 – were fitted to the original ERP time series by means of LSA similar to the first approach. Harmonic coefficients deduced at this step did not deviate by more than $1\,\mu$as from those listed in Table 1. A "reconstructed" time series was then built from the estimated amplitudes according to Eq. (1). Thus, the residuals $\Delta\Theta(t_i)$ between the original and reconstructed time series at epoch t_i include the S_1 signal and also inherit the noise and possible systematic

Table 1 Tidal terms estimated in this work

Tide	Period (solar days)	A^+ (μas)	B^+ (μas)	A^- (μas)	B^- (μas)	σ (μas)
$2Q_1'$	1.16712	−3.0	−4.5	1.3	−0.1	1.2
Q_1'	1.11969	−7.4	−0.0	−0.4	−1.3	1.3
Q_1	1.11951	−27.5	5.5	−2.0	−0.9	1.3
O_1'	1.07597	−22.8	10.7	−0.9	−0.6	1.3
O_1	1.07580	−128.0	56.5	0.2	3.8	1.3
M_1	1.03471	6.8	−3.6	−0.1	−0.7	1.2
P_1	1.00274	−47.2	27.9	−3.4	1.6	1.3
S_1	$1 - 10^{-8}$	8.6	9.8	−1.0	−0.5	1.3
K_1	0.99726	157.5	−93.8	1.1	−2.3	1.3
K_1'	0.99712	19.1	−14.0	−1.9	1.6	1.3
ψ_1	0.99455	−1.1	−0.4	−0.1	2.1	1.3
J_1	0.96243	8.3	−5.2	1.1	3.1	1.2
	0.92916	0.1	−0.1	−0.0	1.9	1.2
N_2	0.52743	10.0	−14.3	−1.3	41.8	1.2
	0.51882	1.4	0.4	−0.4	0.8	1.2
M_2'	0.51756	−3.1	6.4	4.9	−8.9	1.3
M_2	0.51752	32.1	−71.8	−19.2	257.8	1.3
T_2	0.50068	−1.0	−2.8	−4.9	4.8	1.3
S_2	0.50000	−4.6	−29.4	−73.1	109.9	1.3
R_2	0.49931	0.3	2.0	−0.3	1.1	1.3
K_2''	0.49867	−1.6	−0.1	4.7	1.4	1.3
K_2	0.49863	3.1	−12.7	−17.7	23.5	1.3
K_2'	0.49859	1.8	2.8	−6.8	11.4	1.3
Zero	1.15170	−3.5	−1.9	1.9	1.8	1.2
Zero	1.12670	2.2	0.6	0.3	−0.8	1.2
Zero	1.03210	3.0	−1.1	−0.8	1.4	1.2
Zero	0.54750	2.2	−0.8	−0.4	−0.6	1.2
Zero	0.52830	1.8	0.5	−1.4	1.7	1.2
Zero	0.48250	0.2	−0.1	1.1	−0.5	1.2

The last six tides are zero tides and have been included to assess the time series noise level. The last column lists average, tide-specific standard deviations that are representative of the formal errors of the individual coefficients $\{A^+, B^+, A^-, B^-\}$ to within 0.1 μas

effects from the original time series. We used these residuals to estimate the S_1 tide only, adopting the stochastic model from the first method. Standard deviations of the PM polar motion coefficients at S_1 are thus similar to the values shown in Table 1 ($\sigma \sim 1.2\,\mu$as).

In the third method, we make use of the fact that the residual time series are sampled at hourly intervals (with gaps) and that the S_1 tide has a period equal to 24 h. Hence, the hourly PM values can be mapped to the S_1 cycle by stacking them to a mean day composite of exactly 24 points $\{\Theta_k\}_{k=0^h}^{23^h}$ for each of the two PM components labeled as Θ. The stacking by aid of a weighted average for each integer hour k with corresponding time stamps t_l (a subset of t_i) is expressed as

$$\{\Theta_k\}_{k=0^h}^{23^h} = \sum_{l=1}^{N_k} \Delta\Theta(t_l) p_l \Big/ \sum_{l=1}^{N_k} p_l, \quad p_l = \frac{1}{\sigma^2(\Delta\Theta(t_l))}. \quad (2)$$
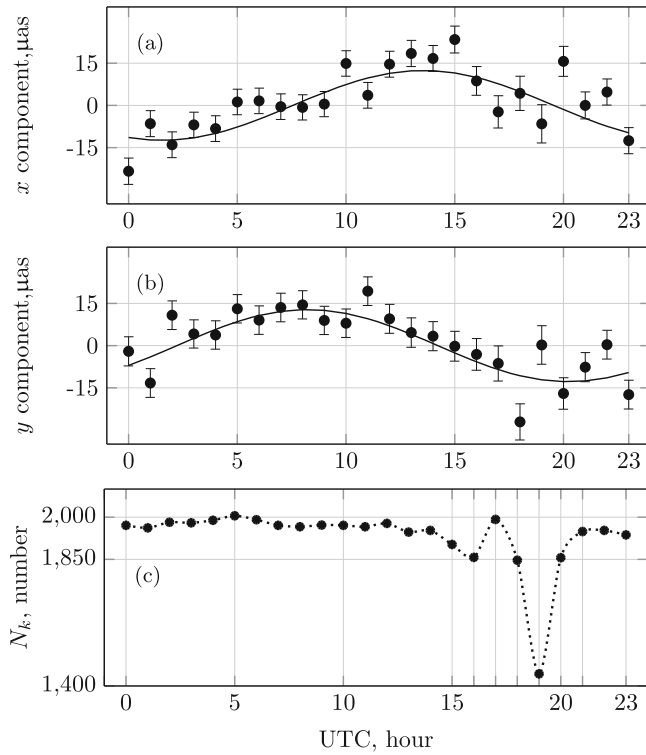
Fig. 1 The stacked time series of x_p (**a**) and y_p (**b**) with standard deviations from error propagation based on σ values of the original time series. Panel (**c**) shows the number of observations N_k per hour

Fig. 2 Estimates of S_1 in PM for the complete and the reduced data set derived from the first (#1), second (#2), and third (#3) TSA method and for the reduced data set with varying geophysical models

Here, $\sigma(\Delta\Theta(t_l))$ represents the formal errors at epochs t_l in the original time series and N_k denotes the total count of PM residuals $\Delta\Theta(t_l)$ used in the averaging at each hour. As an example, the stacked x- and y-components of PM are shown in Fig. 1 together with the observation count for each stacking epoch. A decrease in the number of ERP residuals at around 19 UTC is apparent, presumably due to a loss of observations when some of the stations take a break from regular sessions to participate in 1-h intensive sessions from 18 UTC to 19 UTC (Behrend 2013). Finally, in this third TSA approach, diurnal harmonics, a 24-h trend, and a mean value were adjusted to the stacked composites, yielding formal S_1 errors that were somewhat larger than for the first two TSA solutions ($\sigma \sim 1.8\,\mu$as). The obtained sinusoids with hourly sampling were then repeated to simulate S_1 series of several years duration, allowing us to apply the standard LSA using fundamental arguments.

Estimates of S_1 PM variations from the three analysis strategies are displayed in Fig. 2 and exhibit a particularly close agreement for the first and the second method of TSA. The stacking approach results in a reduction of A^+ from $8.6\,\mu$as (in the standard approach) to $7.0\,\mu$as – a change that is only in slight excess of the onefold standard deviation of any solution. Test calculations have shown that this small reduction arises from the inclusion of a 24-h trend

component in the fit of the stacked x_p and y_p components which has no correspondence in the other TSA solutions. Such a trend over the duration of each session might have a physical explanation or not; here, we leave it as an attribute of our third method to illustrate the dependence of S_1 estimates on small details in the post-processing. More general, it is not possible to identify one approach being "better" or more feasible than the others. We rather prefer to retain estimates from all three methods below to illustrate the spread of the obtained solutions.

2.2 Processing Strategies

Outliers and non-harmonic segments in the ERP time series have been already mentioned in Sect. 2. In this regard particular attention has to be paid to the data selection. Two strategies – analyzing all available hourly ERP and analyzing a reduced data set selected on the basis of the network geometry (Dermanis and Mueller 1978) – were considered. Both the network volume computed from tetrahedrons in the fashion of Malkin (2009) as well as the east-west and the north-south orientation of baselines were employed as selection criteria and calculated a posteriori in hourly time slots.

Different subjectively chosen thresholds were applied on this network measures to subset the ERP series into a higher-quality dataset. The overall feasibility of our selection criteria is verified by the fact that the outlier trimming described earlier becomes unnecessary. Yet, the network geometry restriction removes up to 50% of the original time series, so in upcoming research the data set should be expanded with new VLBI sessions.

Figure 2 presents the comparison between the complete and the reduced data set in terms of S_1 estimates of prograde polar motion for all three TSA methods. In general, the estimates agree reasonably well, with the largest deviation of approximately $1.6\,\mu$as again occurring for the tidal terms from the third method (stacking approach). Additionally, the S_1 estimates from the reduced data set differ slightly from the complete one, however within the 2σ level. The formal uncertainties are found to be higher for the reduced data set due to the decrease in the number of PM observations. A final conclusion cannot be drawn as to which data set is the more accurate one. Thus, as suggested above, we keep estimates from both variants for the remainder of the paper.

As a second experiment, the VLBI analysis outlined in Sect. 2.1 was repeated based on the reduced input dataset but with changed geophysical model settings. First, VMF1 was replaced with GPT2 (Global Pressure and Temperature, version 2, Lagler et al. 2013) and, in a second run, the temperature values T were also taken from GPT2 instead of in situ values as provided within the NGS files. Since GPT2 is not equipped with a diurnal cycle, we virtually neglect the S_1 effect in the tropospheric delay model and in the thermal antenna deformation correction. One might expect some repercussions from these omissions on the estimated tidal terms in the diurnal band. However, as shown in Fig. 2, both the replacement of the mapping function and the temperature by climatological values from GPT2 has little effect on the S_1 signal in PM.

2.3 Comparison with Geophysical Excitation

We round out this study by a comparison of the VLBI-observed S_1 effect with PM excitation estimates from three coupled atmosphere-ocean models in Table 2. The tested atmospheric assimilation systems include MERRA (Modern-Era Retrospective Analysis for Research and Applications, Rienecker et al. 2011), CFSR (Climate Forecast System Reanalysis, Saha et al. 2010), and the ECMWF (European Centre for Medium-Range Weather Forecasts) operational model (EC OP); see Schindelegger et al. (2016) for a detailed description of these datasets. For each model, a long-term average (2004–2013) of the diurnal air pressure variation at the sea surface was used to force a barotropic time-stepping

Table 2 Estimates of prograde diurnal polar motion (S_1) from geophysical modeling and VLBI analysis

	A^+, μas	B^+, μas
MERRA (2004–2013)	**1.2**	**1.7**
Atmosphere + Ocean	$-0.0 + 1.2$	$-0.6 + 2.3$
CFSR (2004–2010)	**0.9**	**2.6**
Atmosphere + Ocean	$-0.2 + (-0.6)$	$1.1 + 3.2$
EC OP (2004–2013)	**6.1**	**0.1**
Atmosphere + Ocean	$5.7 + (-3.6)$	$0.4 + 3.7$
Brzeziński et al. (2012)	**−0.9**	**1.9**
Atmosphere + Ocean	$-0.9 + (-1.8)$	$-1.1 + 3.0$
VLBI		
This study[a, b]	8.6 ± 1.3	9.8 ± 1.3
This study[a, c]	7.8 ± 2.6	8.7 ± 2.6
Artz et al. (2011)	8.8	10.4
Böhm et al. (2012a,b)	11.3	11.4
Gipson (personal communication, 2015)	0.1	9.0

[a]The effect of the gravitational S_1 tide in the oceans is $1.0\,\mu$as (A^+) and $-0.7\,\mu$as (B^+) and has been reduced from all VLBI-based tidal estimates

[b]First method of TSA, complete data set

[c]Third method of TSA, reduced data set

model and derive respective solutions for the oceanic S_1 tide (Schindelegger et al. 2016). Values of atmospheric and oceanic angular momentum (AAM and OAM) are readily accessible through standard formulae and were converted to PM excitation by the proper transfer ratios at the prograde S_1 frequency (Schindelegger 2014); see also Brzeziński et al. (2004) and references therein for more background information. The fitted functional S_1 model, with phases referred to fundamental arguments, is purely harmonic, as the modeling efforts of Schindelegger et al. (2016) are limited to climatological mean values.

The oceanic S_1 tide influences PM through robust equatorial OAM mass and motion terms of about $\sim 2.0 \times 10^{23}\,\text{kg}\,\text{m}^2\,\text{s}^{-1}$ in amplitude. Accordingly, related oceanic excitation estimates in Table 2 agree reasonably well among each other. Inter-model discrepancies are larger for the atmospheric component, likely because mass and motion terms are subject to a distinct cancellation and the total atmospheric effect ($\leq 0.5 \times 10^{23}\,\text{kg}\,\text{m}^2\,\text{s}^{-1}$ in terms of AAM) is thus not well determined. In fact, at the frequencies of atmospheric tides, Earth-atmosphere interaction torques appear to be more robust excitation measures than angular momentum (Lott et al. 2008; Schindelegger 2014). We have therefore validated all our AAM estimates with the corresponding torques on the atmosphere by means of the AAM budget equation; see Schindelegger (2014) for the analytical expressions. In essence, the AAM budget relationship is well fulfilled for MERRA and CFSR but violated by EC OP, giving

rise to suspiciously large excitation values of almost 6 μas. Results from MERRA and CFSR are evidently more credible and suggest that the atmospheric contribution to diurnal PM variations is at the level of 1 μas; cf. also the comparably small PM estimates of Brzeziński et al. (2012) which are also included in Table 2. In any case, S_1 tidal terms from VLBI deviate from the combined atmosphere-ocean signal in PM by about 10 μas. This discrepancy is documented in previous studies and requires further investigation.

A validation of the VLBI-derived S_1 harmonics against the estimates of other authors (Artz et al. 2011; Böhm et al. 2012a; Gipson 1996) complements the comparisons in Table 2. Our tidal analysis results agree particularly well with the global solution of Artz et al. (2011) but somewhat larger PM coefficients (10–12 μas) have been obtained by Böhm et al. (2012a) within a global solution using a modified VieVS version. Estimates provided by J. Gipson (personal communication, 2015) reveal a large discrepancy of >7 μas for the A^+ component, possibly due to different reduction strategies in the delay model. In particular, earlier ERP models of this author were estimated together with diurnal station motions for some strong VLBI sites. This analysis option has been previously suggested to force changes of the S_1 terms in ERP models; see Artz et al. (2011) for further discussion.

3 Conclusion

Diurnal and semidiurnal tidal terms were fitted to high-frequency PM time series derived from 25 years of VLBI observations. We particularly focused on the small Sun-synchronous S_1 variations, which were determined using three different methods of time series analysis, two standard least-squares fits and one stacking approach. We do find a reasonable agreement between the three methods within 2σ (corresponding to approximately 2.5 μas). Yet, the disparities between geodetic S_1 estimates and geophysical model results are at the level of 10 μas which is beyond the 3σ level of any VLBI solution presented here.

In further investigations and in order to reduce the unexplained discrepancies compared to atmospheric and oceanic excitation estimates, we will examine diurnal loading effects and the possible influence of unmodelled diurnal station motions on the S_1 tidal ERP terms. Furthermore, newer VLBI data and improved atmospheric reanalyses could allow us to revise the picture of S_1 in polar motion.

References

Artz T, Tesmer S, Nothnagel A (2011) Assessment of periodic sub-diurnal Earth rotation variations at tidal frequencies through transformation of VLBI normal equation systems. J Geod 85:565–584

Behrend D (2013) Coordinating center report. In: Baver KD, Behrend D, Armstrong K (eds) International VLBI Service for Geodesy and Astrometry 2012 Annual Report, NASA/TP-2013-217511, pp 55–57

Böhm S (2012) Tidal excitation of Earth rotation observed by VLBI and GNSS. Geowissenschaftliche Mitteilungen, Heft 90. Vienna University of Technology, Vienna, 167 pp

Böhm J, Werl B, Schuh H (2006) Troposphere mapping functions for GPS and very long baseline interferometry from European Centre for Medium-Range Weather Forecasts operational analysis data. J Geophys Res 111:B02406. doi:10.1029/2005JB003629

Böhm S, Brzeziński A, Schuh H (2012a) Complex demodulation in VLBI estimation of high frequency Earth rotation components. J Geodyn 62:56–68

Böhm J, Böhm S, Nilsson T, Pany A, Plank L, Spicakova H, Teke K, Schuh H (2012b) The New Vienna VLBI Software VieVS. In: Kenyon S, Pacino MC, Marti U (eds) Geodesy for Planet Earth. Springer Berlin Heidelberg, pp 1007–1011

Brzeziński A (2011) Diurnal excitation of Earth rotation estimated from recent geophysical models. In: Capitaine N (ed) Proc Journées 2010 Systèmes de Référence Spatio-temporels, Observatoire de Paris, pp 131–136

Brzeziński A, Ponte R, Ali A (2004) Nontidal oceanic excitation of nutation and diurnal/semidiurnal polar motion revisited. J Geophys Res 109:B11407. doi:10.1029/2004JB003054

Brzeziński A, Dobslaw H, Thomas M, Ślusarczyk Ł (2012) Subdiurnal atmospheric and oceanic excitation of Earth rotation estimated from 3-hourly AAM and OAM data. Geophysical research abstracts 14, EGU2012-10530, EGU General Assembly 2012, Vienna, 22–27 April

Capitaine N, Wallace P, Chapront J (2003) Expressions for IAU 2000 precession quantities. Astron Astrophys 412:567–586

Dermanis A, Mueller I (1978) Earth rotation and network geometry optimization for very long baseline interferometers. Bull Geod 52:131–158

Desai S (2002) Observing the pole tide with satellite altimetry. J Geophys Res Oceans 107:3186. doi:10.1029/2001JC001224

Fey A et al (2015) The Second Realization of the International Celestial Reference Frame by Very Long Baseline Interferometry. Astron J 150:58. doi:10.1088/0004-6256/150/2/58

Gipson J (1996) Very long baseline interferometry determination of neglected tidal terms in high-frequency Earth orientation variation. J Geophys Res 101:28051–28064

Krásná H, Böhm J, Plank L, Nilsson T, Schuh H (2014) Atmospheric Effects on VLBI-Derived Terrestrial and Celestial Reference Frames. In: Rizos C, Willis P (eds) Earth on the Edge: Science for a Sustainable Planet. International Association of Geodesy Symposia. Springer Berlin Heidelberg, pp 203–208

Lagler K, Schindelegger M, Böhm J, Krásná H, Nilsson T (2013) GPT2: Empirical slant delay model for radio space geodetic techniques. Geophys Res Lett 40:1069–1073

Lott F, de Viron O, Viterbo P, Vial F (2008) Axial atmospheric angular momentum budget at diurnal and subdiurnal periodicities. J Atmos Sci 65:156–171

Lyard F, Lefevre F, Letellier T, Francis O (2006) Modelling the global ocean tides: modern insights from FES2004. J Ocean Dyn 56:394–415

Malkin Z (2009) On comparison of the Earth orientation parameters obtained from different VLBI networks and observing programs. J Geod 83:547–556

Mathews P, Herring T, Buffett B (2002) Modeling of nutation and precession: new nutation series for nonrigid Earth and insights into the Earth's interior. J Geophys Res 107:B42068

Nothnagel A (2009) Conventions on thermal expansion modelling of radio telescopes for geodetic and astrometric VLBI. J Geod 83:787–792

Petit G, Luzum B (eds) (2010) IERS conventions (2010). Verlag des Bundesamts für Kartographie und Geodäsie, Frankfurt am Main, Germany, 179 pp

Ray R, Egbert G (2004) The global S$_1$ Tide. J Phys Oceanogr 34:1922–1935

Rienecker M, Suarez M, Gelaro R et al (2011) MERRA: NASA's Modern-Era Retrospective Analysis for Research and applications. J Clim 24:3624–3648. doi:10.1175/JCLI-D-11-00015.1

Saha S, Moorthi S, Pan HL et al (2010) The NCEP Climate Forecast System Reanalysis. Bull Am Meteorol Soc 91:1015–1057

Schindelegger M (2014) Atmosphere-induced short period variations of Earth rotation. Geowissenschaftliche Mitteilungen, Heft 96. Vienna University of Technology, Vienna, 152 pp

Schindelegger M, Einšpigel D, Salstein D, Böhm J (2016) The global S$_1$ tide in Earth's nutation. Surv Geophys 37:643–680

Schuh H, Böhm J (2013) Very Long Baselines Interferometry for Geodesy and Astronomy. In: Xu G (ed) Sciences of Geodesy–II: Innovations and Future Developments. Springer Berlin Heidelberg, pp 339–376

Simon J, Bretagnon P, Chapront J, Chapront-Touze M, Francou G, Laskar J (1994) Numerical expressions for precession formulae and mean elements for the Moon and the planets. Astron Astrophys 282:663–683

Wijaya D, Böhm J, Karbon M, Krasna H, and Schuh H (2013) Atmospheric Pressure Loading. In: Böhm J, Schuh H (eds) Atmospheric Effects in Space Geodesy. Springer Berlin Heidelberg, pp 137–157

Free Core Nutation Parameters
from Hydrostatic Long-Base Tiltmeter Records
in Sainte Croix aux Mines (France)

U. Riccardi, J-P. Boy, J. Hinderer, S. Rosat, and F. Boudin

Abstract

The resonance associated with the Free Core Nutation (FCN) has been widely studied in Very Long Base Interferometry (VLBI) network measurements and in superconducting gravity records, but few experiments have been done with tiltmeters. In this study we use records collected with a pair of about 100 m long hydrostatic silica tiltmeters, orthogonally installed in an abandoned silver mine at Sainte Croix aux Mines (Alsace, in North-Eastern France). Main difficulties in retrieving FCN parameters from tidal analysis arise from the weak amplitude of PSI1 tidal wave (the closest in frequency to the FCN), as well as from the inaccuracy of the available ocean loading correction. Moreover because of the closeness in frequency of the single constituents of the diurnal tidal band, long (>1 year) records are needed for resolving K1, PSI1 and PHI1 waves. Hence we analyze a 10-year dataset of tilt records, which has preliminarily required a critical review and a relevant editing for making records suitable for tidal analysis and subsequent inversion of the tidal parameters. A Bayesian inversion is used for a preliminary retrieval of the FCN parameters.

1 Introduction

Because of the presence of an elliptic fluid core rotating around an axis, which is slightly inclined with respect to the axis of rotation of the mantle, the Earth exhibits a rotational eigenmode called free core nutation (FCN). In an inertial space-fixed reference frame, the resonant period (T) of the FCN is close to 430 sidereal days, while in a terrestrial rotating frame it is nearly diurnal. The FCN parameters (T, quality factor-Q and resonance strength) contribute to constraining some deep Earth's properties (e.g. dynamic ellipticity of the core, dissipation through electro-magnetic coupling at the core-mantle boundary, etc.). The FCN can also be observed by the resonance effects on the forced nutations of the Earth's figure axis detectable in VLBI observations, or in the diurnal tidal waves, retrieved from whatever geophysical recording sensor (e.g. gravimeters, tiltmeters, strainmeters, etc). These phenomena have been widely studied by means of VLBI network measurements (e.g. Herring et al. 1986; Koot et al. 2008; Rosat and Lambert 2009), superconducting gravity records (e.g. Florsch and Hinderer 2000; Ducarme et al. 2007; Rosat et al. 2009) and by strainmeter records (Sato 1991; Amoruso et al. 2012), but only few experiments have been done with tiltmeters.

U. Riccardi (✉)
Dipartimento di Scienze della Terra, dell'Ambiente e delle Risorse (DiSTAR) Università "Federico II" di Napoli, Largo S. Marcellino 10, 80138 Naples, Italy
e-mail: umbricca@unina.it

J.-P. Boy • J. Hinderer • S. Rosat
Institut de Physique du Globe de Strasbourg, IPGS – UMR 7516, CNRS et Université de Strasbourg (EOST), 5 rue René Descartes, 67084 Strasbourg Cedex, France

F. Boudin
Ecole Normale Supérieure – 24 Rue Lhomond 75231, Paris CEDEX 5, France

Here we present the preliminary results of a Bayesian inversion applied on the γ-factors (see below) retrieved from a tidal analysis carried out on about 10 years of records collected with two long-base hydrostatic tiltmeters.

The main difficulties in retrieving FCN parameters from tidal analysis arise from the closeness in frequency of the single constituents of the diurnal tidal band (P1, K1, PSI1, PHI1), requiring very long time series for a suitable spectral resolution, and from the weak amplitude of PSI1 wave (the closest in frequency to the FCN).

The Earth deforms under the tidal stress so that the response of the Earth can be found by integration of the normal mode equations to yield a surface displacement and surface gravity potential. The formalism to describe mathematically the tidal transfer functions for a Spherically symmetric, Non-Rotating, perfectly Elastic and Isotropic Earth model (SNREI) was predicted by Love (1911) and Shida (1912) using a set of dimensionless numbers, now called the Love (h, k) and Shida (l) numbers. In modern and more realistic Earth models, the effects due to rotation, ellipticity, inelasticity and anisotropy are accounted for (Crossley et al. 2013). Here we just remind the elementary definition of the well-known tidal factors for gravity ($\delta = 1 + h - 3/2\,k$) and tilt ($\gamma = 1 + k - h$) as a linear combination of such dimensionless numbers. A nominal pair of values for amplitude and phase for the degree $n = 2$ of the tidal potential is taken as [$\delta_{ref} = 1.16$, $k = 0°$]; [$\gamma_{ref} = 0.7$, $\varphi = 0°$].

The FCN resonance model as seen by tiltmetry can be expressed through the following conceptual equation for the observed gamma factor (γ_{obs}):

$$\gamma_{obs}(\sigma) = \gamma_{ref} + \frac{a}{\sigma - \sigma_{nd}} + loadings + \varepsilon$$
$$+ \text{"}strain - tilt \text{ coupling"} \qquad (1)$$

All the quantities expressed in the Eq. (1) are complex, so that both real and imaginary parts have to be computed; γ_{ref} is the reference gamma factor, namely without resonance, assumed as a linear combination of the Love numbers (h_0, k_0): $\gamma_{ref} = 1 + k_0 - h_0 \approx 0.7$; σ and σ_{nd} are the tidal frequency and the near-diurnal tidal frequency respectively; a is the resonance strength, corresponding to the response of the whole Earth to the FCN, the transfer function relating to the geometric shape of the Earth and the rheological properties of the mantle (Rosat et al. 2009); for tilt, $a < 0$, leading to $\gamma_{obs} < \gamma_{ref}$ for $\sigma > \sigma_{nd}$. Moreover, for the tiltmetric observations the resonance strength (a) cannot be written analytically in a simple form because of the well-known strain-tilt coupling effect (Neuberg and Zürn 1986). The term "strain-tilt coupling" or "cavity effect" is a clue concept introduced by King and Bilham (1973) and Harrison (1976) into Earth tide studies to explain the large scattering frequently observed in measurements of tidal tilts. This effect clearly seen by

Neuberg and Zürn (1986) in tilt and strain observations is due to the presence of a free surface (e.g. tunnel or cavity where tidal instruments are housed) inducing coupling of strain tides into tilts. Such inhomogeneity in an elastic volume will produce local deformations, able to modify the tidal strains and tilts for an Earth with only radial variations; also an irregular free surface, like topography, will have similar effects.

Equation (1) also indicates that for a reliable retrieving of γ-factors loadings (mainly oceanic and atmospheric) and the different error sources (statistical, calibration and model errors) have to be accounted for.

The FCN resonance in tilt data as in gravity can be represented by a damped harmonic oscillator model to be inverted in order to determine the FCN period (T), quality factor (Q) and the transfer function of the mantle (the resonance strength, a). This is a classical "non-linear" inverse problem whose solution is achievable through two approaches: (1) a Levenberg-Marquardt optimization method for non-linear least-squares inversion; (2) a Bayesian inversion. The first approach requires that the parameters to be retrieved follow a Gaussian distribution. Florsch and Hinderer (2000) have demonstrated the inadequacy of using such a least-squares method, because the statistical distribution of Q is definitely not Gaussian. Therefore, the Bayesian method is the most suitable one to perform the inversion of this non-linear problem (Florsch and Hinderer 2000; Rosat et al. 2009).

The Bayesian inversion consists in propagating the information provided by the measurements through an assumed physical model (probabilistically known) to the parameters and to include the a priori knowledge of the model parameters (Tarantola and Valette 1982). Since the information provided by the data is of probabilistic nature the inverse problem solution is the probability density function (pdf) of the parameters. The general probability distribution laws for the parameter vector (ϑ) can be written as follows:

$$p(\vartheta) = p\left(x, \sigma_{nd}^R, a^R, a^I\right)$$
$$= k \exp\left\{ -\frac{1}{2} \sum_j \left[\left(\frac{\text{Re}\left(\gamma_j^{th}\right) - \text{Re}\left(\gamma_j\right)}{\Delta \text{Re}\left(\gamma_j\right)} \right)^2 \right.\right.$$
$$\left.\left. + \left(\frac{\text{Im}\left(\gamma_j^{th}\right) - \text{Im}\left(\gamma_j\right)}{\Delta \text{Im}\left(\gamma_j\right)} \right)^2 \right] \right\} \qquad (2)$$

where (x, σ_{nd}^R, a^R, a^I) are the parameters to be inverted, $x = log\,Q$; the superscript R and I indicate the real (Re) and imaginary part (Im), respectively, of the complex values; k is a normalization factor in order that the integral of this equation is unity; the superscript th stands for theoretical; terms $\Delta(\gamma)$ represent the error (standard deviation) on the

computed γ-factors from tidal analyses. The law for one or two parameters (the marginal pdfs) is computed by integration of the probability function over selected parameters. For instance, the joint pdf on a 2D parameter space (x and a^R) is obtained by integrating with respect to σ^R_{nd} (Eq. 2):

$$p_{x,a^R}\left(x, a^R\right) = \int p\left(x, \sigma^R_{nd}, a^R\right) d\sigma^R_{nd} \qquad (3)$$

A further integration of the pdf (Eq. 3) lead to the marginal probability law for each of the parameters.

2   Site, Instruments and Dataset

Two 100 m long-base hydrostatic tiltmeters (LBHT) were installed in Sainte-Croix-aux-Mines (Vosges Mountains, North-Eastern France) (SCX) in two orthogonal branches of an ancient silver mine, in a gneissic context. Installation was carried out in two subsequent steps: the first LBHT, having a N37E azimuth, was installed in December 2004, followed later on in November 2005, by a second tiltmeter, with N120E azimuth. The LBHTs are composed of two pyrex end vessels and the ground tilt is detected by means of two silica linear variable displacement transducers (LVDTs); further details on this installation as well as on technical features of the instruments can be found in Boudin et al. (2008). The 160 m high rock overburden ensures the environment is very stable (annual temperature variation of about 10^{-1} °C). A well-known fracture system intersects the hill quasi-orthogonal to the N37E instrument (Longuevergne et al. 2009).

The data set used in this study consists of height level changes of the distilled water in the two vessels (or pots) for each LBHT as well as the calibrated signal, namely tilt variations, expressed in angle units. The data set (Fig. 1) spans about 10 years from December 2004 to July 2014, but different troubles or failures affected the two instruments over time, so that the effectively available tilt records amount only to 2102 and 1807 days for N37E and N120E instruments respectively. Large gaps affect the time series collected in 2008–2012 with both tiltmeters because of a misfunctioning of one of the two vessels, so that any tilt signal can be retrieved during that period (Fig. 1).

3   Data Analysis

Raw data, sampled at different rates (15 s or 30 s) over different epochs, are preliminarily low-pass filtered in order to avoid aliasing, then decimated to 60 s (1 min) and prepared for a pre-processing aimed at detecting instrumental disturbances. A massive pre-processing based on the classical slew
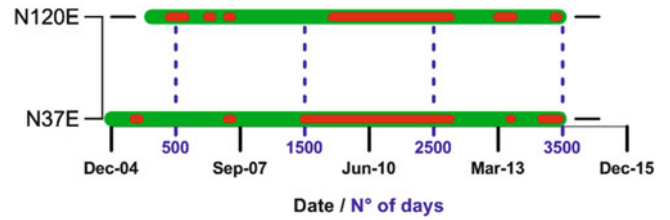

Fig. 1 Chronological table of the datasets: time intervals with data suitable for tidal analyses (*green bars*); time intervals characterized by instrumental troubles or failures (*red bars*)

rate (Crossley et al. 1993) and "residue-restore" approaches is applied with the help of TSoft software (Van Camp and Vauterin 2005) on the dataset to reduce artefacts (spikes, earthquakes, gaps and steps) in the records. The 2004–2008 data sub-set has also required being linearly re-interpolated in order to account for a large drift detected in the clock of the data acquisition system.

As the main interest of this study is an accurate harmonic analysis in the diurnal tidal band, the tilt records are low-pass filtered by means of a FFT filter having 0.1 cycles-per-day (cpd) as cut-off frequency and 0.01 cpd as bandwidth. Indeed, a long-term trend has been modelled by means of a low-pass filtering then it has been subtracted from the records, so that the resulting signal is equivalent to high-pass filtered ones (Fig. 2). As a consequence of the filtering, the long-term temporal trend, mainly due to the strain induced by the interactions between hydrology and the fracture system, is reduced (Fig. 2c, d). Unfiltered and filtered tilt records are presented in Fig. 2. The low-pass filtered dataset is then decimated to 3,600 s (1 h) through a low-pass filtering to avoid aliasing and prepared for a 2-channel tidal analyses by assembling tilt and air-pressure records both collected at SCX station; the tidal analysis are performed with ETERNA 3.4 (Wenzel 1996). The tidal wave grouping is selected with the aim of attaining the best resolution in the diurnal band, hence, besides the main semi-diurnal waves, we use only the 9 main diurnal tidal groups (Q1, O1, M1, P1, K1, Psi1, PHI1, J1 and OO1)+S1.

Before proceeding with the inversion of the tidal factors (γ) we need to correct for the ocean tide loading effect (OTL). We compute the OTL effect for all of the main tidal constituents according to FES99 model (Lefèvre et al. 2002). γ-factors and phases corrected for OTL are shown in the Figs. 3 and 4 and the values are listed in Table 1; a comparison with respect to some modern OTL models, CSR4 (an update of Eanes 1994) FES99 (Lefèvre et al. 2002), FES2004 (Lyard et al. 2006) and NAO99 (Matsumoto et al. 2000), for the main tidal constituents, is plotted too. Actually the small oceanic tides as PSI1 and PHI1, are customarily not directly computed, but only O1, Q1, K1 and P1 are actually computed and assimilated using altimetry and eventually tide gauges. All the other minor diurnal constituents are
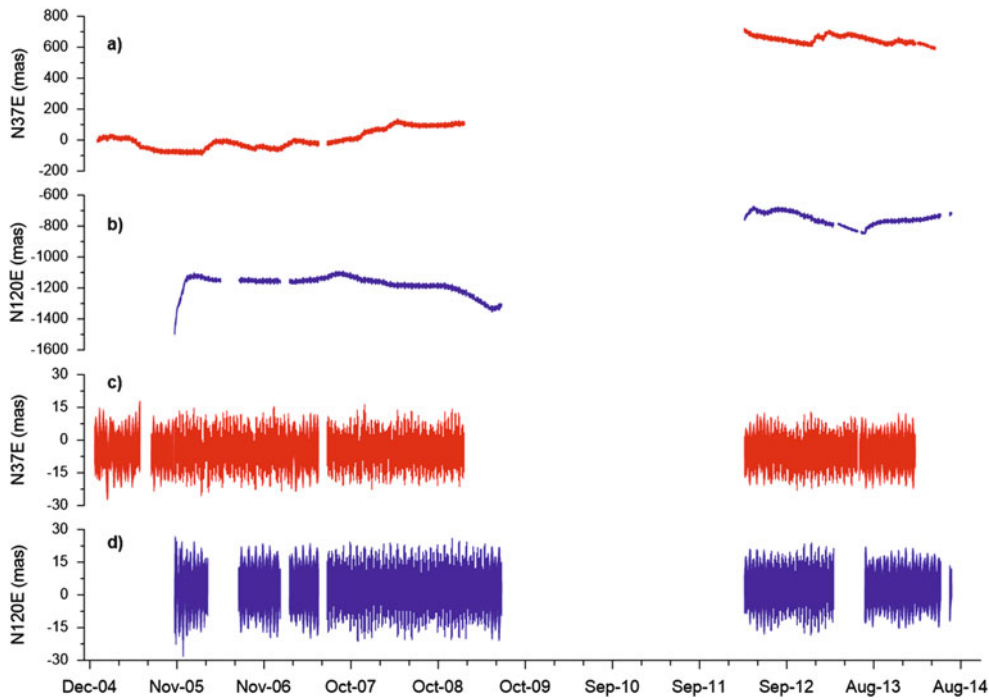
Fig. 2 Tiltmeter signal collected at Sainte Croix aux Mines over the recorded period (December 2004–July 2014) measured in direction N37E (**a**) and N120E (**b**); low-pass filtered signals (**c**, **d**); units are milliarcsecond (mas)
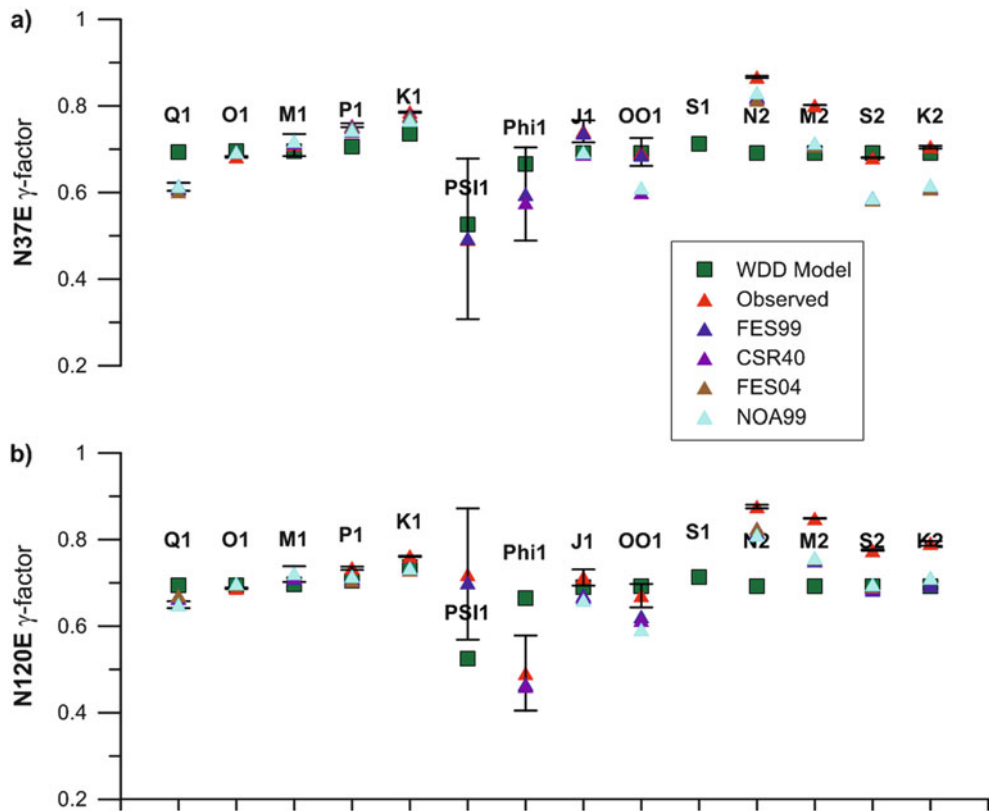
Fig. 3 γ-factors corrected for OTL by means of different models: FES99 (all waves), FES04, NOA99, CSR4 (only main tidal constituents); γ for WDD oceanless Earth model (Dehant et al. 1999) is plotted as a reference for both tiltmeters N37E (**a**) and N120E (**b**)

Fig. 4 Phases of the main tidal waves corrected for OTL by means of different models same as in Fig. 3

estimated assuming that the ocean response to tidal forces is quite smooth with the frequency (true except in some very enclosed basins) by interpolation within the frequency bands (the so called "admittance" method). Furthermore, from work with gravity tides, it is known that the influence of the 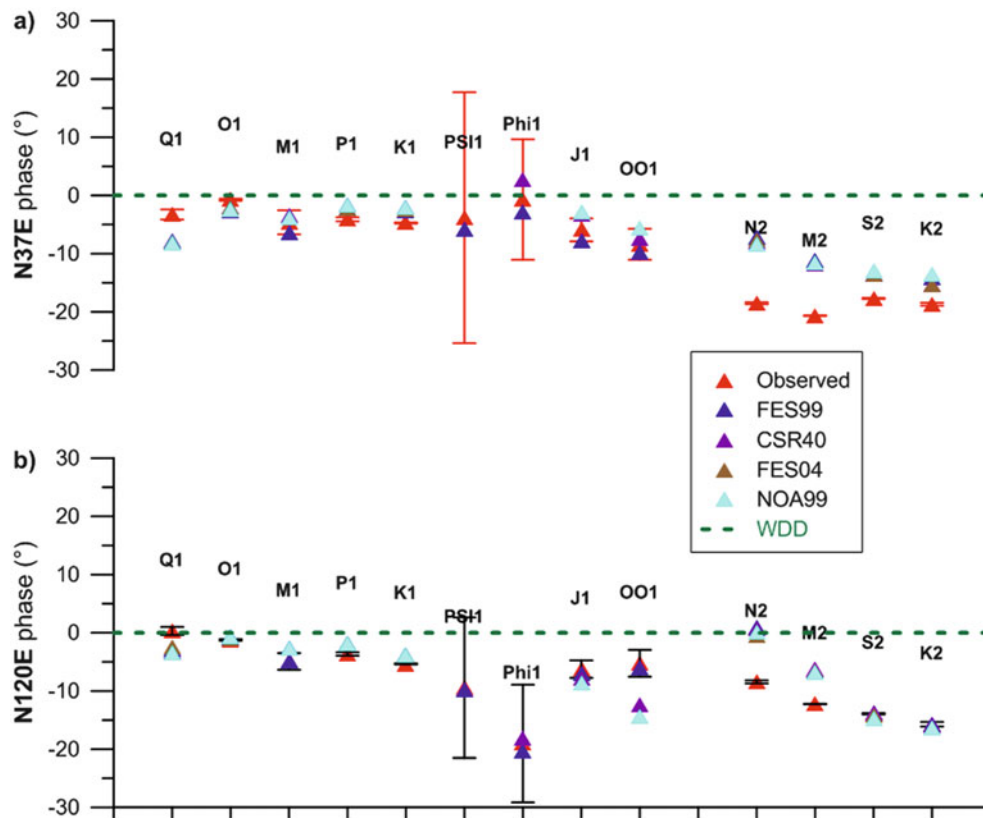different methods to estimate the ocean loading for the minor tides does not have a large influence on the NDFW parameters.

Resonance effects due to the FCN on the luni-solar tidal forcing of the Earth at diurnal periods are quite evident in the results of the corrected tidal analyses for the N37E tiltmeter (Fig. 3a), a clear minimum can be envisaged at the PSI1 wave, the closest in frequency to the FCN. This is not the case for the N120E tiltmeter, here the minimum amplitude of the γ-factor is at PHI1 frequency (Fig. 3b), just nearby the resonance frequency of FCN. In both cases the amplitude and phase of the small *PSI1* and *PHI1* tidal constituents estimated from the ETERNA analysis are affected by a large statistical error (standard deviation) (Figs. 3 and 4).

4   Results

Despite the poor quality of the outcome from the tidal analyses, a Bayesian inversion is tried following the procedure described in Rosat et al. (2009) and Florsch and Hinderer

(2000); the inversion procedure is separately applied on the records collected with both tiltmeters.

In the inversion procedure we apply minimum constrains on the a-priori model. The results are obtained by inverting the 9 diurnal waves (O1, M1, P1, K1, Q1, PSI1, PHI1, J1, OO1) and using as reference γ-factor (Eqs. 1 and 2) the mean value of the theoretical inelastic amplitude factors (O1 and OO1). The 2D plots (Fig. 5) are the joint (*logQ, T, a^R, a^I*) pdfs. The sub-plots are, for instance, results from integration over a^R and a^I (Fig. 5-top-left). The second plot (Fig. 6) shows the marginal laws (probability laws) obtained by integrating over the remaining parameters, for instance, in Fig. 6 (top left) we integrate over T, a^R and a^I (Eq. 3); the values on Y-axis are far from unity because they are not normalized. Several bumps (in the marginal laws) or patches appear in the 2D pdfs due to the difficulty in constraining the FCN parameters. A period around 240 days (far from the expected 430 days) turns out, but surprisingly the obtained Q value (*Q > 20,000*) is realistic (Rosat et al. 2009). The 2D pdfs show some correlation (tilted-shape) between a^I (imaginary part of the resonance strength) and T, but we do not have any explanation for this. Indeed, the imaginary parts of the tidal factors are poorly determined, especially for the small amplitude waves; furthermore, as demonstrated by Sato et al. (2004) they could be very sensitive to the ocean loading correction error; so that both a poor statistical quality

Table 1 Comparison between theoretical *(γ_WDD)*, observed *(γ_Obs, φ)* and corrected for OTL FES99 *(γ_cor, Alfa)* **γ**-factors and phases; theoretical values are computed according to an oceanless Earth model (Dehant et al. 1999)

Wave	γ_WDD	γ_Obs	γ_std	φ (°)	φ_std (°)	γ_cor	Alfa (°)
N37E							
Q1	0.69397	0.61328	0.00926	−3.28	0.865	0.60864	−7.76939
O1	0.69438	0.68238	0.00191	−0.75	0.16	0.69431	−2.59369
M1	0.69557	0.70974	0.02537	−4.62	2.048	0.71753	−6.43857
P1	0.70538	0.75558	0.00448	−4.10	0.339	0.75178	−2.31918
K1	0.73620	0.78568	0.00141	−4.73	0.103	0.77709	−2.73796
PSI1	0.52581	0.49304	0.18548	−3.83	21.556	0.49417	−5.90905
Phi1	0.66470	0.59648	0.10777	−0.70	10.353	0.59617	−2.85087
J1	0.69038	0.74116	0.0254	−5.92	1.964	0.73849	−7.86062
OO1	0.69181	0.69371	0.03224	−8.40	2.663	0.68616	−9.89355
S1	0.71221	1.46590	0.27618	77.75	10.798	1.76257	62.92553
N2	0.69110	0.86711	0.00243	−18.51	0.161	0.82335	−7.17347
M2	0.69110	0.80210	0.00046	−20.66	0.033	0.70712	−11.18046
S2	0.69110	0.68060	0.00098	−17.70	0.083	0.58596	−13.67001
K2	0.69110	0.70490	0.00311	−18.69	0.253	0.60773	−14.09941
N120E							
Q1	0.69397	0.64965	0.00784	0.31	0.692	0.66542	−2.78587
O1	0.69438	0.68750	0.00158	−1.22	0.131	0.69626	−0.95940
M1	0.69557	0.72021	0.01814	−4.92	1.44	0.71147	−4.91779
P1	0.70538	0.73371	0.00362	−3.65	0.283	0.70705	−1.96696
K1	0.73620	0.76119	0.00116	−5.35	0.088	0.72916	−3.90531
PSI1	0.52581	0.72045	0.15171	−9.43	12.068	0.69965	−9.79538
Phi1	0.66470	0.49158	0.08671	−19.03	10.109	0.46605	−20.32817
J1	0.69038	0.71230	0.01865	−6.25	1.5	0.67010	−6.95254
OO1	0.69181	0.67044	0.02701	−5.25	2.309	0.62294	−6.10349
S1	0.71221	4.76308	0.22473	−168.78	2.703	4.33896	−169.9375
N2	0.69110	0.87627	0.00404	−8.45	0.264	0.81738	0.92209
M2	0.69110	0.84899	0.00077	−12.25	0.052	0.75177	−6.34383
S2	0.69110	0.77556	0.00166	−13.90	0.122	0.68321	−13.78602
K2	0.69110	0.79119	0.00537	−15.71	0.389	0.69417	−15.79531

of the γ-factors and an unsatisfactory OTL modelling could be an explanation for this.

The 2D pdfs for the N120E tiltmeters show some tilted-shaped trends or correlation (Fig. 7), for instance between the resonance strength amplitudes a^R (real part) and T, and a^I (imaginary part) and $x = log(Q)$, as well as a strong correlation between a^R and a^I. Also in this case a period (T) around 130 days, far from the expected 430 days, and a realistic Q value is obtained (Fig. 8).

5 Conclusions

Notwithstanding the poor statistical quality of the results coming from the tidal analyses, a very preliminary Bayesian inversion of the γ-factors has been tried.

The N120E tiltmeter does not provide satisfactory parameters, but more promising results come from the N37E

instrument. Looking at the joint pdfs (Fig. 5), forcing a^I to values closer to 0 we could force the inversion towards T values larger than 400 days.

Here we can comment on the possible sources of error preventing more precise assessment of tidal parameters (γ and phase) from tiltmetric records with respect to other geophysical observations, like gravity records. A first main general concern refers to some unavoidable local effects, like strain-tilt coupling that could be important (Neuberg and Zürn 1986) and at the same time such effect could be strongly specific and site-dependent resulting in being different on the two tiltmeters. We know (Harrison 1976) that "regional" tidal stress field acting on local inhomogeneites can produce additional coherent signal on tilt-strainmeters. Actually the N37E sensor is orthogonal to a well known fracture affecting the long-term tilt change, with very minor effect on the N120E direction, quasi-parallel to the fracture (Longuevergne et al. 2009). A second but not less important limit of tiltmeter
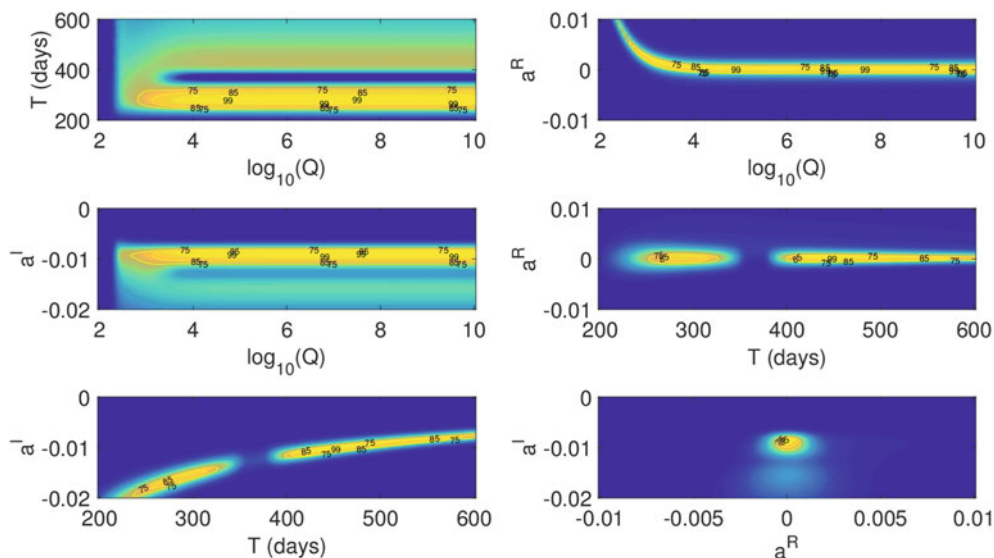
Fig. 5 Joint 2D pdfs for the FCN parameters (a^R, a^I, T and $x = LogQ$) estimated from N37E tiltmetric records using the Bayesian method
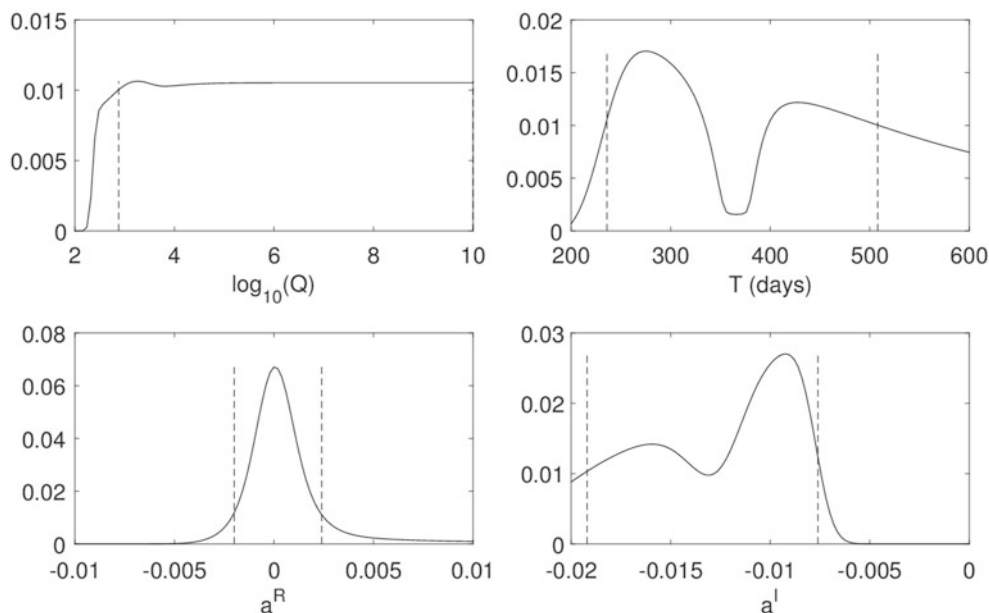

Fig. 6 Probability law (marginal pdfs) for each FCN parameter from Bayesian inversion of γ-factors from N37E tiltmeter (non-normalized values); the *vertical dashed lines* correspond to the 90% C.I. (Confidence Intervals)

records relies on the calibration accuracy of the sensors amounting to 3–4% for both tiltmeters (Boudin et al. 2008), which is one order of magnitude higher than the accuracy (<0.3%) achievable in the calibration of superconducting gravity sensors (Amalvict et al. 2001; Riccardi et al. 2012). Indeed, the comparison of calibration uncertainties in the tilt data with the ones in data from superconducting gravimeters has to take into account that the geophysical contribution (including the NDFW resonance) to the total signal in tidal gravity is about 16%, while in tidal tilt it is larger than 30%, so these numbers should be accordingly weighted.

However even if calibration errors does not really perturb the resonance effect, they lead to larger discrepancies in the tidal factors corrected for OTL with respect to the theoretical ones. However we are confident that some future improvements are possible through more focused analyses. For instance, it is well known that tiltmetric records are sensitive to the horizontal gradient of the atmospheric loading, and this effect could be accounted for by using models for the atmospheric correction, instead of the classical admittance method, only based on the local pressure. Moreover some benefits could come from a better monitoring of the time variability of the
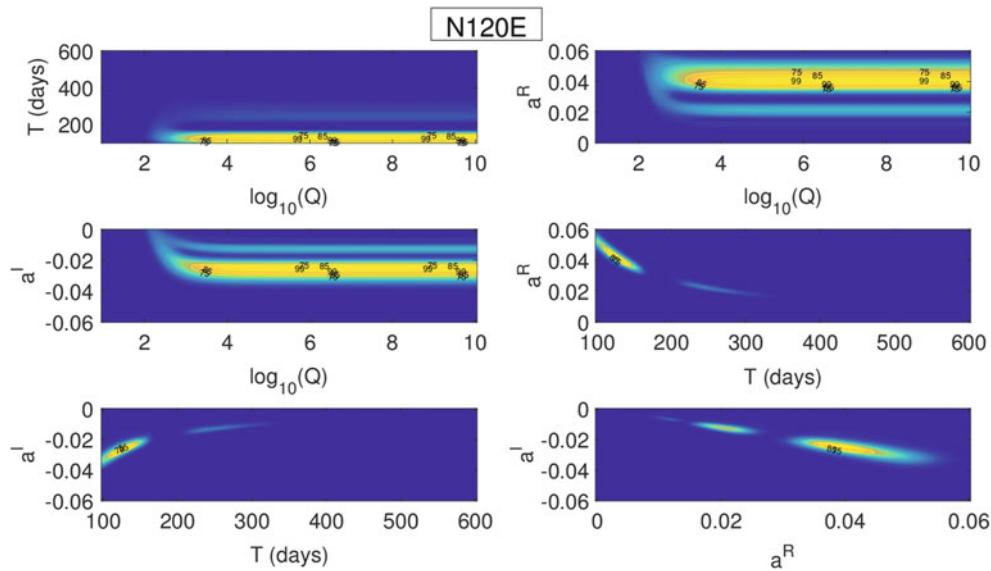
Fig. 7 Joint 2D pdfs for the FCN parameters (a^R, a^I, T and $x = LogQ$) estimated from N120E tiltmetric records using the Bayesian method
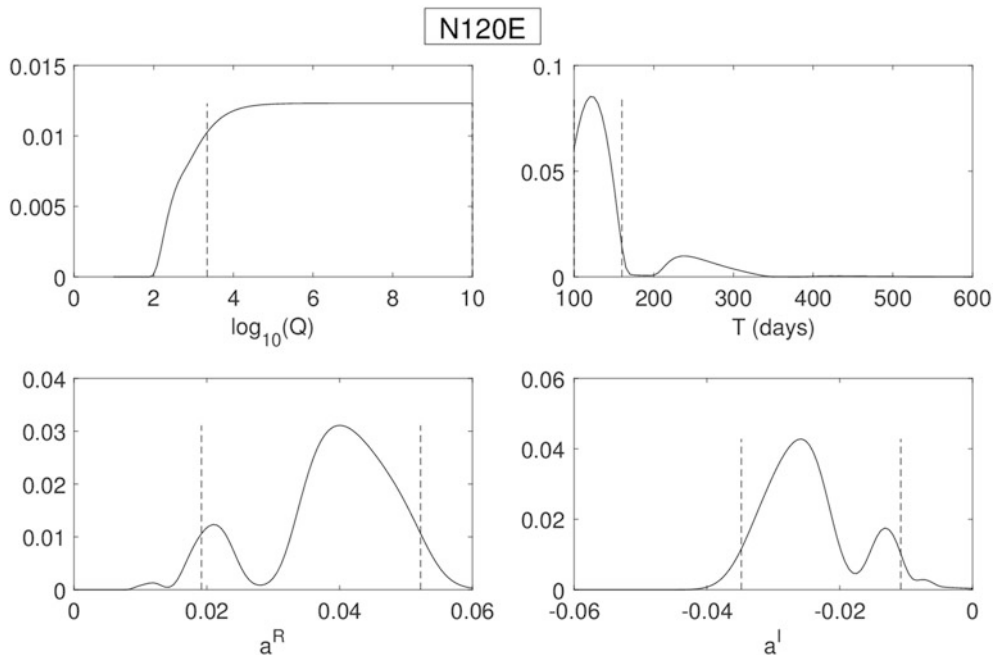

Fig. 8 Probability law (marginal pdfs) for each FCN parameter from Bayesian inversion of γ-factors from N120E tiltmeter (non-normalized values); the *vertical dashed lines* correspond to the 90% C.I. (Confidence Intervals)

instrumental sensitivity, through a sequential tidal analysis in order to suppress problematic records from the timeseries. Last but not least, a stacking with more tilt data from different stations could improve the statistical robustness of the retrieval of FCN parameters.

References

Amalvict M, Hinderer J, Boy J-P, Gegout P (2001) A three year comparison between a superconducting gravimeter (GWR C026) and an absolute gravimeter (FG5#206) in Strasbourg (France). J Geod Soc Jpn 47:334–340

Amoruso A, Botta V, Crescentini L (2012) Free core resonance parameters from strain data: sensitivity analysis and results from the Gran Sasso (Italy) extensometers. Geophys J Int 189:923–936

Boudin F, Bernard P, Longuevergne L, Florsch N, Larmat C, Courteille C, Blum P-A, Vincent T, Kammentaler M (2008) A silica long base tiltmeter with high stability and resolution. Rev Sci Instrum 79:034502. doi:10.1063/12829989

Crossley DJ, Hinderer J, Jensen O, Xu H (1993) A slew rate detection criterion applied to SG data processing. Bull d'Inf Mar Terr 117:8675–8704

Crossley D, Hinderer J, Riccardi U (2013) The measurement of surface gravity. Rep Prog Phys 76:046101. doi:10.1088/0034-4885/76/4/046101

Dehant V, Defraigne P, Wahr JM (1999) Tides for a convective Earth. J Geophys Res 104(B1):1035–1058

Ducarme B, Sun H-P, Xu J-Q (2007) Determination of the free core nutation period from tidal gravity observations of the GGP superconducting gravimeter network. J Geodesy 81:179–187. doi:10.1007/s00190-006-0098-9

Eanes RJ (1994) Diurnal and semidiurnal tides from TOPEX/POSEIDON altimetry. Eos Trans AGU 75(16):108

Florsch N, Hinderer J (2000) Bayesian estimation of the free core nutation parameters from the analysis of precise tidal gravity data. Phys Earth Planet Inter 117(1):21–35

Harrison JC (1976) Cavity and topographic effects in tilt and strain measurements. J Geoph Res l81(2):319–328

Herring TA, Gwinn CR, Shapiro II (1986) Geodesy by radiointerferometry: studies of the forced nutations of the earth 1 data analysis. J Geophys Res 91(b5):4745–4754

King GCP, Bilham R (1973) Tidal tilt measurement in Europe. Nature 243:74–75

Koot L, Rivoldini A, de Viron O, Dehant V (2008) Estimation of earth interior parameters from a Bayesian inversion of very long baseline interferometry nutation time series. J Geophys Res 113:B08414. doi:10.1029/2007JB005409

Lefèvre F, Lyard FH, Le Provost C, Schrama E (2002) FES99: a tide finite element solution assimilating tide gauge and altimetric information. J Atmos Oceanic Tech 19(9):1345–1356

Longuevergne L, Boy J-P, Florsch N, Viville D, Ferhat G, Ulrich P, Luck B, Hinderer J (2009) Local and global hydrological contributions to gravity variations observed in Strasbourg. J Geodyn 48:189–194

Lyard L, Lefèvre L, Letellier T, Francis O (2006) Modelling the global ocean tides: insights from FES2004. Ocean Dyn 56:394–415

Matsumoto K, Takanezawa T, Ooe M (2000) Ocean tide models developed by assimilating TOPEX/POSEIDON altimeter data into hydrodynamical model: a global model and a regional model around Japan. J Oceanogr 56:567–581

Neuberg J, Zürn W (1986) Investigation of the nearly diurnal resonance using gravity, tilt and strain data simultaneously. In: Proceedings of the 10th international symposium on earth tides, Madrid, pp 305–312

Riccardi U, Rosat S, Hinderer J (2012) On the accuracy of the calibration of superconducting gravimeters using absolute and spring sensors: a critical comparison. Pure Appl Geophys 169:1343–1356. doi:10.1007/s00024-011-0398-8

Rosat S, Lambert SB (2009) Free core nutation resonance parameters from VLBI and superconducting gravimeter data. Astron Astrophys 503:287–291. doi:10.1051/0004-6361/200811489

Rosat S, Florsch N, Hinderer J, Llubes M (2009) Estimation of the free core nutation parameters from SG data: sensitivity study and comparative analysis using linearized Least-Squares and Bayesian methods. J Geodyn 48:331–339. doi:10.1016/jjog200909027

Sato T (1991) Fluid core resonance measured by quartz tube extensometers at Esashi earth tide station. In: Kakkuri J (ed) Proceedings of the 11th international symposium on earth tides. Schweizerbart, Stuttgart, pp 573–582

Sato T, Tamura Y, Matsumoto K, Imanishi Y, McQueen H (2004) Parameters of the fluid core resonance inferred from superconducting gravimeter data. J Geodyn 38:375–389

Tarantola A, Valette B (1982) Inverse problems-quest for information. J Geophys 50:159–170

Van Camp M, Vauterin P (2005) Tsoft: graphical and interactive software for the analysis of time series and Earth tides. Comput Geosci 31(5):631–640. doi:10.1016/jcageo200411015

Wenzel H-G (1996) The nanogal software: earth tide data processing package ETERNA 330. Bull Inf Mar Terr 124:9425–9439

Numerical Issues in Space-Geodetic Data Analysis and Their Impact on Earth Orientation Parameters

Thomas Artz, Sebastian Halsig, Andreas Iddink, and Axel Nothnagel

Abstract

Space-Geodetic techniques are used to provide fundamental scientific products like the terrestrial and celestial reference frame or the Earth orientation parameters (EOPs). These parameters are typically determined in a least squares adjustment of redundant observations. Within this process, numerical issues materializing in the condition of the equation system as well as in insufficient stability of the solution play an important role. While bad condition numbers are an indicator of numerical problems having no connection to the solution strategy i.e., the algorithms used for solving the equation system, numerical stability refers to the algorithms which are used. This paper focuses on the impact of numerical conditioning on EOPs.

Exemplarily for other space-geodetic techniques, we analyze the data analysis of Very Long Baseline Interferometry (VLBI) observations. For VLBI, the equation system of the least squares adjustment is apparently ill-conditioned. Thus, errors of the observations would be amplified during the adjustment process. However, we show that the conditioning is not that bad as it highly depends on the parametrization and we present options to improve the conditioning in VLBI data analysis. We present methods to reveal the relationship between numerical characteristics of the involved matrices and the EOPs.

Keywords

Condition • Earth orientation • Numerical stability • VLBI

1 Introduction

The observations of space-geodetic techniques are used to determine fundamental products for a wide scientific area. In particular, these products are especially the terrestrial and celestial reference frames (TRF/CRF) as well as the link between these frames: the Earth orientation parameters (EOPs). But for observations in the radio frequency domain also the time and phase delays of the observed signals due to atmospheric refraction are used, e.g., by weather forecasting services.

Typically, a huge amount of observations of one single technique is used to determine a specific set of geophysical parameters and some nuisance parameters like, e.g., clock offsets or range biases. This is done by defining linearized observation equations which represent the functional dependences between the observations and the parameters. As these equation systems are overdetermined, i.e., more observations than parameters are present, the parameters are typically estimated in a least squares adjustment by minimizing the squared residual functions. These parameters are then combined to the final products. To determine, e.g., a TRF with consistent EOPs, the normal equations of several techniques can be stacked, weighted, and solved to derive a combined product (e.g., Seitz et al. 2012).

T. Artz (✉) • S. Halsig • A. Iddink • A. Nothnagel
Institute of Geodesy and Geoinformation, University of Bonn, Nußallee 17, 53115 Bonn, Germany
e-mail: artz@igg.uni-bonn.de; halsig@igg.uni-bonn.de; iddink@igg.uni-bonn.de; nothnagel@igg.uni-bonn.de

For the combination, the relative weighting is a crucial point. To judge the precision and the reliability of the individual solutions, the covariance matrices of the parameters and residuals are analyzed. However, the matrices might be corrupted by numerical issues, as computers can calculate only with a limited number of digits. For instance, the Very Long Baseline Interferometry (VLBI) results are corrupted if the precision of the calculation is changed from double to single precision. This, however, depends on the set-up as several algebraically equivalent approaches might lead to different results. The reason is that (1) the problem to be solved is ill-conditioned, and (2) the algorithms which are used provide different levels of numerical stability.

Within this paper we focus on VLBI exemplarily for other space-geodetic techniques. Here, we aim at describing the effects of conditioning in VLBI data analysis and its dependence on the solution set-up. Furthermore, we show how to optimize conditioning and present the implications of set-up changes with a focus on EOPs. We do not investigate the stability of the EOPs, which is described by, e.g., Artz et al. (2007).

2   Adjustment Principles and Numerical Issues

To derive parameters from the observations, typically a least squares adjustment is performed. There is a multitude of approaches for a least squares adjustment. Here, we focus on the linearized Gauss-Markov-Modell (e.g., Koch 1999) and its numerical characteristics.

2.1   Least Squares Adjustment

When a VLBI session is analyzed, the observations are used to estimate a set of parameters starting with the known functional relationship

$$\mathbf{b} = \varphi(\mathbf{x}) \tag{1}$$

with the parameter vector $\mathbf{x}$ and the vector of the observations $\mathbf{b}$. This leads to the linearized equation system

$$\mathbf{A}\mathbf{x} = \mathbf{b} \tag{2}$$

with the functional, design or Jacobian matrix $\mathbf{A}$ containing the partial derivatives of the observation equations w.r.t. the parameters. As there are typically more observations than parameters, there are various solutions for Eq. (2). As none is exact, the equation system is extended by the post-fit residuals $\mathbf{r}$

$$\mathbf{A}\mathbf{x} = \mathbf{b} + \mathbf{r}. \tag{3}$$

Thus, we try to find the optimal solution in the sense of a least squares adjustment, where the gradient of the squared residual function Φ vanishes

$$\nabla\Phi = 0, \qquad \Phi = \|\mathbf{r}\|_2^2 = \|\mathbf{A}\mathbf{x} - \mathbf{b}\|_2^2 \tag{4}$$

here $\|\cdot\|_2$ represents the L_2-norm.

2.2   Numerical Issues

When numerical issues of the least squares adjustment are discussed, two distinct aspects have to be investigated. On the one hand, the numerical stability of the algorithm is important. On the other hand, the conditioning of the equation system has to be analyzed. In this way, one is able to optimize the problem to be solved and to choose an adequate algorithm.

2.2.1   Numerical Stability

To solve the equation system, several approaches can be used. These approaches are algebraically equivalent, but, from a numerical point of view, they might lead to different results as the calculation is only performed with a finite number of digits. If a numerically unstable algorithm is used, the errors of the input data might be amplified in an uncontrolled way at an unknown point (Demmel 1997). This would then lead to totally corrupted results. Here, we briefly present three approaches to solve the least squares adjustment.

Equation (4) directly leads to the normal equation approach

$$\mathbf{0} = \mathbf{A}^T (\mathbf{A}\mathbf{x} - \mathbf{b}) = \mathbf{A}^T\mathbf{A}\mathbf{x} - \mathbf{A}^T\mathbf{b}$$
$$\Rightarrow \mathbf{A}^T\mathbf{A}\mathbf{x} = \mathbf{A}^T\mathbf{b} \quad \Leftrightarrow \quad \mathbf{N}\mathbf{x} = \mathbf{n}, \tag{5}$$

where $\mathbf{N}$ is the normal matrix and $\mathbf{n}$ the normal vector. The normal equations might be solved by a Cholesky decomposition of the normal matrix and subsequent forward and backward substitution. This is the computationally fastest approach, but, from a numerical point of view, it is relatively unstable (Demmel 1997). However, the normal equation approach is typically used in VLBI data analysis.

Equivalently, a QR-decomposition

$$\mathbf{A} = \mathbf{Q}\mathbf{R} \tag{6}$$

or a singular value decomposition (SVD)

$$\mathbf{A} = \mathbf{U}\mathbf{S}\mathbf{V}^T \tag{7}$$

of the Jacobian matrix could be used to derive the solution

$$\mathbf{x}_{QR} = \mathbf{R}^{-T}\mathbf{Q}^T\mathbf{b}, \tag{8}$$

$$\mathbf{x}_{SVD} = \mathbf{V}\mathbf{S}^{-1}\mathbf{U}^T\mathbf{b} = \sum_{i=1}^{n} \frac{\mathbf{u}_i^T\mathbf{b}}{s_i}\mathbf{v}_i. \tag{9}$$

In the above equations, $\mathbf{R}$ represents an upper tri-angular matrix and $\mathbf{Q}$ is an orthonormal basis of the column space of the Jacobian matrix. Equivalently, $\mathbf{U}$ and $\mathbf{V}$ are matrices with the left and the right singular vectors, and $\mathbf{S}$ is a diagonal matrix containing the singular values ($\mathbf{S} = diag(s_i)$). Thus, its inverse is simply made up of the reciprocal singular values.

Algebraically, these three approaches should lead to identical results. However, while the normal equation approach is the fastest, its numerical stability is relatively poor in comparison to the approaches via QR-decomposition or SVD (Demmel 1997). However, first tests showed no significant impact on the results of a VLBI adjustment.

So far, these explanations assumed equal precision and, thus, equal weight of all observations. To achieve a relative weighting of the observations, a weight matrix $\mathbf{W}$, which depends on the stochastical properties of the observations (expressed by their variance-covariance matrix $\boldsymbol{\Sigma}_{bb}$), has to be applied

$$\mathbf{W} = \boldsymbol{\Sigma}_{bb}^{-1}, \tag{10}$$

$$\mathbf{A}^T\mathbf{W}\mathbf{A}\mathbf{x} = \mathbf{A}^T\mathbf{W}\mathbf{b}. \tag{11}$$

To use algorithms different to the normal equation approach, a de-correlation has to be performed via Cholesky decomposition of the weight matrix into a lower triangular matrix $\mathbf{L}$

$$\mathbf{W} = \mathbf{L}^T\mathbf{L}, \tag{12}$$

$$\widetilde{\mathbf{A}} = \mathbf{L}\mathbf{A}. \tag{13}$$

Subsequently, the matrix $\widetilde{\mathbf{A}}$ can replace $\mathbf{A}$ and then the weight matrix is the identity matrix.

2.2.2 Condition of a Solution

The condition of a solution and can be expressed by the dimensionless condition number of the Jacobian matrix which is derived by dividing the largest by the smallest singular value

$$\kappa(\widetilde{\mathbf{A}}) = \frac{s_{max}}{s_{min}}. \tag{14}$$

A large condition number indicates that the problem to be solved is ill-conditioned and that errors of the observations are magnified during the adjustment procedure. The optimal condition number is one, indicating that the problem is
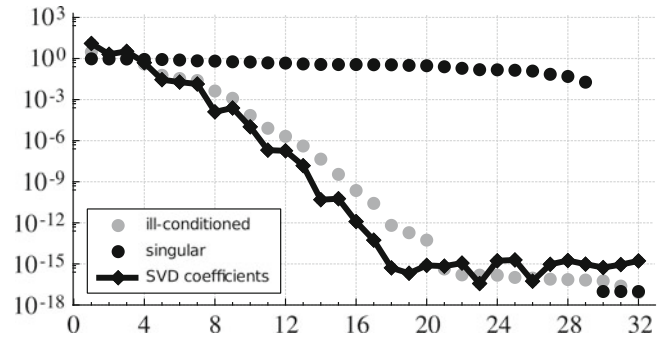

Fig. 1 Singular values for (a) a singular (*black circles*) and (b) an ill-conditioned problem (*gray circles*) together with SVD coefficients (diamonds connected by *lines*; identical for both set-ups)

well-conditioned, and a small perturbation of the input data leads to small variations of the results. Contrary, in an ill-conditioned case, even a small perturbation of the input data might lead to large errors of the output (Meyer 2000). In turn, the results of the adjustment might not be optimal due to an insufficient solution set-up. However, these effects are not represented by the covariance matrix of the parameters. Thus, the results might be not as precise as indicated by the standard deviations.

First of all, one has to distinguish between singularities and bad condition numbers. As depicted in Fig. 1, a bad condition might result from various situations. In the singularity case (a), the majority of the singular values are on the same level, and others are on a different, significantly lower level. This jump in the spectrum of the singular values indicates a singularity due to non-estimatable parameters. In the other case (b), constantly but significantly decreasing singular values indicate an ill-conditioned problem. In this case, it can also be noted that the discrete Picard condition is only fulfilled for the first parameters (corresponding to large singular values) which represent the unperturbed right-hand side.

Furthermore, not all errors are magnified in the same way. Equation (9) reveals, that especially the observational errors in direction of the small singular values are magnified the most as the SVD coefficients $|\mathbf{u}_i^T\mathbf{b}|$ are divided by these small singular values. Thus, a regularization can be applied. where filter factors f_i are used to dampen the small singular values

$$\mathbf{x}_{filtered} = \sum_{i=1}^{n} f_i \frac{\mathbf{u}_i^T\mathbf{b}}{s_i}\mathbf{v}_i. \tag{15}$$

2.3 Tikhonov-Regularization and the L-Curve Criterion

A very common method to deal with ill-conditioning is the Tikhonov-Regularization (Tikhonov and Arsenin 1977) for

which various methods exist to determine the necessary filter factors. These are, e.g., the L-curve (Hansen 1999) criterion or the generalized cross-validation (GCV, Golub et al. 1979). These methods were also applied to various ill-conditioned geodetic problems as, e.g., coordinate transformations (Ge and Wu 2012), determination of geophysical parameters from Global Positioning System observations (Jin and Zhang 2014), or gravity field estimations (Kusche and Klees 2002 or Save et al. 2012).

For the Tikhonov-Regularization, the residual squared sum is minimized with an additional constraint of the solution

$$\min_x \left\{ \|\mathbf{Ax} - \mathbf{b}\|_2^2 + \lambda^2 \|\mathbf{x}\|_2^2 \right\} \qquad (16)$$

$$\Rightarrow f_i = \frac{s_i^2}{\lambda_i^2 + s_i^2}. \qquad (17)$$

The corresponding regularization parameter λ can be derived, e.g., from the so-called L-curve, which is a log-log plot of the size of the regularized solution versus the size of the corresponding residual norm for all valid regularization parameters. Thus, it is a tradeoff between smoothing parameters, i.e., minimal norm, and minimizing the residuals. To obtain this curve, 200 solutions have been performed where the minimal and the maximal λ are choosen according to the singular values

$$\lambda_{min} = \max[s_{min}, \epsilon \cdot s_{max}]$$
$$\lambda_{max} = s_{max} \qquad (18)$$

with a tiny value ϵ which is sixteen times the next positive representable value after zero. The optimal regularization is the one in the lower left corner of the L-shape as this represents minimal smoothing of the parameters and minimal residual norm. In this point, the L-curve has the maximum curvature, thus, it can be easily determined (Hansen 1999).

We use the L-curve to demonstrate the characteristics of various solutions as it clearly visualizes the effects of the solutions norm as well as the residual norm depending on different regularization parameters. Although it has been shown, that the GCV principle often leads to more reliable results (Kusche and Klees 2002), we focus on the L-curve as it is more robust (Hansen 1999). L-curves for a typical VLBI solution with the software package Calc/Solve (Ma et al. 1990) are shown in Fig. 2.

3 Condition in VLBI Data Analysis

Looking at an example, the condition of a Jacobian matrix within the VLBI data analysis with Calc/Solve is bad, e.g.,
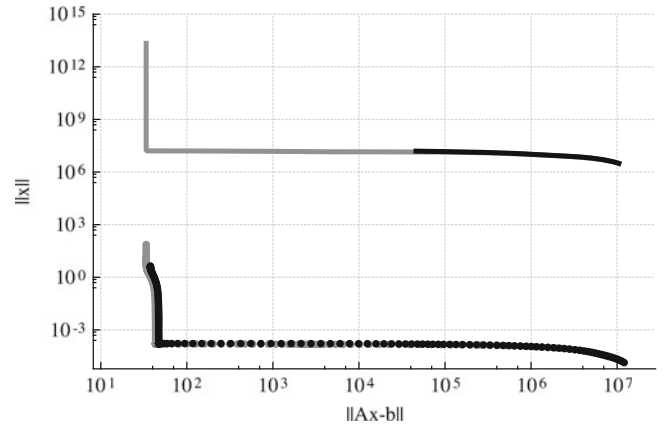

Fig. 2 L-curve for unconstrained (*gray circles*), and constrained (*black circles*) solutions as well as preconditioned unconstrained (*gray line*), and constrained (*black line*) solutions all with traditional units

$\kappa(\widetilde{\mathbf{A}}) \approx 10^{16}$ for the first session of the continuous VLBI campaign 2002 (CONT02). CONT02 provides high quality VLBI observations with a relatively small number of observations (3500) which improves the illustration of the effects. The results presented here are not depending on the number of observations, and thus, would be similar for the most recent CONT campaign in 2014 with more than 20,000 observations. The reason is that for the individual VLBI observations highly control each other.

For the solution, the estimated parameters are clocks (second degree polynomials plus 1 h continuous piece-wise linear functions, CPWLF), zenith wet delays (ZWDs with 1 h CPWLF), tropospheric gradients in North-South and East-West direction (24 h CPWLF) as well as the EOPs. For the EOPs, X-/Y-polar motion and universal time minus atomic time (UT1-TAI) are estimated as offset and drift, while nutation parameters are set up as constant daily offsets. However, this solution constellation is ill-posed and leads to singularities. Estimating the clock polynomials together with the CPWLF leads to huge correlations and, thus, to unresolvable parameters. Artz et al. (2015) have shown, that adding standard prior information in form of constraint equations improves the condition to $\kappa(\widetilde{\mathbf{A}}) \approx 6 \times 10^{11}$. Here we force two subsequent CPWLF parameters to be equal with standard deviations of $\sigma_{cl} = 10^{-14}$ s/s for clocks, $\sigma_{ZWD} = 40$ ps/h for ZWDs, and $\sigma_{grad} = 2$ mm/d for tropospheric gradients. The corresponding L-curves for the unconstrained and the constrained case are depicted in Fig. 2 with circles. The constraints (black circles) do not eliminate the L-shape of the curve. Only for the fairly small regularization parameters, a slight reduction of the parameter norm can be seen at the very first part of the L-curve. Obviously, the constraints lead to a slight smoothing, but do not eliminate the need of a regularization. The reason is a persistent bad condition to be seen also in the singular values (not shown here) which is

Table 1 Modified solution set-up implementing the old and new units (Artz et al. 2015)

Parameter	Set-up	Old units	New units
Clocks	Polynomial (deg i)	s^i/d^i	$\mu s^i/d^i$
	Hourly CPWLF	s	μs
ZWDs	Hourly CPWLF	s	μs
trop. grad.	Daily CPWLF	mm	m
X-/Y-pole	Offset + rate	rad, rad/d	μrad, μrad/d
UT1-TAI	Offset + rate	ms, ms/d	μrad, μrad/d
Nutation	Offset	rad, rad/d	μrad

primarily forced by the set-up of the tropospheric gradients as well as UT1-TAI (see Artz et al. 2015).

Contrary, a preconditioning might be applied which is actually done in Calc/Solve for the inversion of the normal matrix. This preconditioning scales the main diagonal elements of the normal matrix to ones

$$\mathbf{F} = diag\left(\left(diag\left(\widetilde{\mathbf{A}}^T\widetilde{\mathbf{A}}\right)\right)^{-\frac{1}{2}}\right), \tag{19}$$

$$\hat{\mathbf{A}} = \widetilde{\mathbf{A}}\mathbf{F}. \tag{20}$$

It has to be noted that this procedure leads to parameters with arbitrary units, thus, the solution norm appears to be different in Fig. 2. As a consequence, the have to be scaled back to the original units after the solution. Applying the preconditioning leads to a condition of $\kappa(\hat{\mathbf{A}}) \approx 200$ for the first session of CONT02. The L-curve for this preconditioned solution (cf. lines in Fig. 2) indicate a singularity which is eliminated by applying the constraints. Thus, the least squares solution without any filtering is the optimal one and the ill-conditioned one which appears in the original constrained case is only due to an inadequacy of the parameter units. Furthermore, it can be seen that the constraints are slightly too tight as the black line in Fig. 2 is not starting directly in the lower corner of the gray line (unconstrained case). Thus, slightly too much smoothing might be applied in this case by the standard constraints. This situation can be changed in a simplified way by directly multiplying the weights of the constraints by 10^7.

As the procedure of preconditioning is equivalent to changing the units of the estimated parameters to some meaningless units, one might modify the units in a reasonable and meaningful way (cf. Table 1). These are μrad and μrad/d for all components of the EOPs which leads to a condition of $\kappa(\widetilde{\mathbf{A}}) \approx 480$ for the first CONT02 session. The condition numbers are still far from one, indicating the need for a complete new parametrization of the clocks as the largest as well as the smallest singular values can be assigned to these parameters.
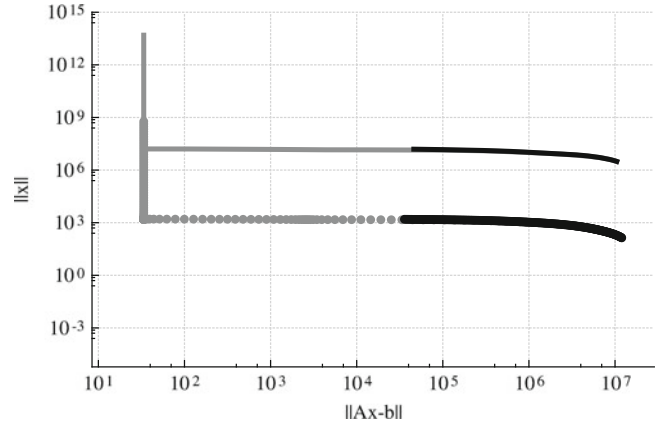

Fig. 3 L-curve for unconstrained (*gray circles*), and constrained (*black circles*) solutions as well as preconditioned unconstrained (*gray line*), and constrained (*black line*) solutions all with optimized units

Table 2 Standard deviations from a time series of 10,000 Monte Carlo simulation runs

	Old units	New units
UT1-TAI [μs]	0.5	0.6
X-pole [μas]	13	13
Y-pole [μas]	9	7
X-nutation [μas]	8	8
Y-nutation [μas]	9	9

The L-curves for the modified set-up are depicted in Fig. 3. The solutions with preconditioning are identical to the old set-up. Contrary, the solutions without preconditioning act in the same way representing the improvements due to the new units. Unfortunately, the necessary scaling factors are not only depending on the entries of the Jacobian matrix **A**, but also on the standard deviations of the observations, as the weight matrix **W** is incorporated into the Jacobian matrix when performing the full de-correlation (cf. Eq. (13)).

4 Impact on EOPs

To investigate the effects of the optimized conditioning, two CONT02 solutions have been performed: one with the original units and one with the new units. In neither case a preconditioning has been applied. However, the large condition numbers when using the old units have no impact on the EOP estimates. The differences for all EOPs between the two solutions are almost zero. For instance, the standard deviation of the UT1-TAI differences between both solutions is only 3×10^{-8} μs. The same holds for the formal errors. Obviously and surprisingly, condition numbers around $\kappa(\widetilde{\mathbf{A}}) \approx 10^{11}$ can be handled by the typical solution algorithms. This is not
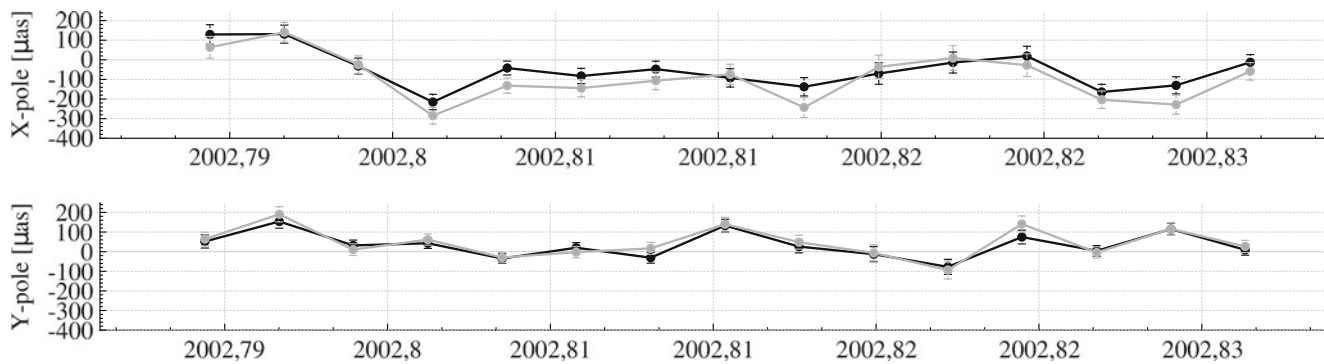
Fig. 4 CONT02 polar motion estimates with default weighting of the constraints (*black*) and weights deflated by 10^7 (*gray*)

only the case for EOPs with a daily resolution. Estimating polar motion and UT1 with 60 min CPWLF, increases the condition numbers by a factor of two for either unit set-up. Furthermore, the parameters do not change significantly (not shown here).

Additionally, to represent different input errors for the solutions, a Monte Carlo simulation with 10,000 runs has been performed. For this purpose, white noise with standard deviations of 10 ps have been added to the observations. Again, solutions with original units and optimized ones have been performed. The results are almost identical (cf. Table 2), indicating that the large condition numbers in VLBI data analysis have no impact on the EOP estimates. The reasons are unclear and have to be investigated in more depth in future.

Considering the potentially too strong constraining of the parameters as indicated by the L-curves in Fig. 3, a solution has been performed where the constraints have been deflated by a factor of 10^7. The corresponding polar motion time series are shown in Fig. 4. As the differences between the two solutions, are within the formal errors, the constraining of the nuisance parameters has no significant impact on the EOPs.

5   Conclusions and Outlook

We have demonstrated, that VLBI data analysis appears to be ill-conditioned. Furthermore, we have shown options to separate singularities from bad condition numbers and have performed a simple scaling of the parameters to improve the condition of the Jacobian matrix.

Although condition is improved by about ten orders of magnitude, no effects on the estimated EOPs can be seen. This has been evaluated by raw differences as well as by Monte Carlo simulations. Thus, the condition number appears to be not a crucial point in VLBI. The reasons are unclear and will be investigated in future.

Nevertheless, optimizing the parameter units leads to a better insight into the adjustment. In this way, it could be shown that the typical constraining of the solution leads to a smoothing of the parameters. This is based on the interpretation of the so called L-curve for the Tikhonov regularization which is not possible with the old unit set-up. Changing the constraints in a simplified way, leads to small changes of the EOPs. For future investigations, this methodology can be adopted to evaluate an optimized constraining.

Finally, we can conclude that the conditioning of VLBI data analysis is not as bad as expected, but also not optimal. Further optimization can, however, be only achieved with a significant modification of the clock set-up. Nevertheless, the EOPs seem to be not affected by the bad conditioning of the equation system.

References

Artz T, Böckmann S, Nothnagel A, Tesmer V (2007) ERP time series with daily and sub-daily resolution determined from CONT05. In: Boehm J, Pany A, Schuh H (eds) Proceedings of the 18th EVGA working meeting, pp 69–74. Schriftenreihe der Studienrichtung Vermessung und Geoinformation, TU Wien, Heft Nr. 79

Artz T, Halsig S, Iddink A, Nothnagel (2015) Numerical issues of VLBI data analysis. In: Haas R, Colomer F (eds) Proceedings of the 22th EVGA working meeting, Ponta Delgada, pp 181–184. ISBN 978-989-20-6191-7

Demmel JW (1997) Applied numerical linear algebra. SIAM, Philadelphia

Ge X, Wu J (2012) A new regularized solution to ill-posed problem in coordinate transformation. Int J Geosci 3:14–20 (2012). doi:10.1007/BF01933214

Golub GH, Heath M, Wahba G (1979) Generalised cross-validation as a method for choosing a good ridge parameter. Technometrics 21(2):215–223. doi:10.2307/1268518

Hansen PC (1999) The L-curve and its use in the numerical treatment of inverse problems. IMM, Department of Mathematical Modelling, Technical University of Denmark

Jin S, Zhang X (2002) A Tikhonov regularization method to estimate Earth's oblateness variations from global GPS observations. J Geodyn 79:23–29 (2002). doi:10.1016/j.jog.2014.04.011

Koch KR (1999) Parameter estimation and hypothesis testing in linear models, vol 2, upd. and enl. ed. Springer, Berlin/Heidelberg/New York/Barcelona/Hong Kong/London/Milan/Paris/Singapore/Tokyo

Kusche J, Klees R (2002) Regularization of gravity field estimation from satellite gravity gradients. J Geod 76(6):359–368. doi:10.1007/s00190-002-0257-6

Ma C, Sauber JM, Clark TA, Ryan JW, Bell LJ, Gordon D, Himwich WE (1990) Measurement of horizontal motions in Alaska using very long baseline interferometry. J Geophys Res 95(B13):21991–22011. doi:10.1029/JB095iB13p21991

Meyer CD (2000) Matrix analysis and applied linear algebra. SIAM, Philadelphia

Save H, Bettadpur S, Tapley BD (2012) Reducing errors in the GRACE gravity solutions using regularization. J Geod 86(9):695–711. doi:10.1007/s00190-012-0548-5

Seitz M, Angermann D, Bloßfeld M, Drewes H, Gerstl M (2012) The 2008 DGFI realization of the ITRS: DTRF2008. J Geod 86(12):1097–1123. doi:10.1007/s00190-012-0567-2

Tikhonov A, Arsenin VY (1977) Solutions of ill-posed problems. Wiley, New York

A Non-tidal Atmospheric Loading Model: On Its Quality and Impacts on Orbit Determination and C20 from SLR

Rolf König, Elisa Fagiolini, Jean-Claude Raimondo, and Margarita Vei

Abstract

Based on European Centre for Medium-Range Weather Forecasts (ECMWF) ERA-Interim data we model displacements of global station coordinates due to non-tidal atmospheric loading based on Farrel's theory. We compare these displacements to publicly available external displacements. We apply our displacements to Satellite Laser Ranging (SLR) data processing over a recent 6 years period of the LAGEOS, LARES, AJISAI, STARLETTE and STELLA geodetic satellites. We assess the impact of the loading model on the orbital fits of these missions. Indeed a tiny improvement shows up. We also quantify the impact of the non-tidal loading model on the large scale figure of the Earth expressed in terms of weekly C(2,0) harmonics. It turns out that here no effect is visible.

1 Introduction

Variations of atmospheric pressure cause distortions of the Earth surface which result in changes in the positions of stations, a phenomenon called atmospheric loading in analogy to ocean loading being triggered by oceanic mass variations. Whereas the application of ocean loading became standard in the International Earth Rotation and reference systems Service (IERS) Conventions 2010 (Petit and Luzum 2010), atmospheric loading is not taken into account for the generation of modern geodetic products as the International Terrestrial Reference Frame (ITRF), e.g. the newest ones being the ITRF2008 (Altamimi et al. 2011) and the recently released ITRF2014.

With the increasing level of precision in the modern space-geodetic techniques during the last 20 years, the effect of the atmospheric surface pressure loading on the Earth crust cannot be neglected anymore for precise scientific studies. Several authors have already investigated this effect for instance in relation with the Very Long Baseline Interferometry (VLBI) observations (Petrov and Boy 2004) or in relation with Global Positioning System (GPS) observations (Tregoning and vanDam 2005). Petrov and Boy (2004) have identified the source of errors in the computation of atmospheric pressure loading displacements and they have found that the major contributions to the error budget is coming from the uncertainties in the surface pressure field and in the ocean response to the atmospheric pressure load.

In order to derive station displacements introduced by atmospheric pressure variations, we adopt Farrel's theory (Farrel 1972). For the load Love numbers we use h_l, l_l, and k_l as provided by Gegout (1998, Private communication) (see also Gegout et al. 2010). The Earth model used is the Preliminary Earth Model (PREM) from Dziewonski and Anderson (1981). Then we derive 6-hourly station displacements from 6-hourly surface pressure data taken from the European Centre for Medium-Range Weather Forecasts (ECMWF) ERA-Interim data (ECMWF 2015). The atmospheric surface pressure data ("PSFC") do have a resolution according to a

R. König (✉) • E. Fagiolini • J.-C. Raimondo • M. Vei
GFZ German Research Centre for Geosciences, Potsdam, Germany
e-mail: koenigr@gfz-potsdam.de

reduced Gaussian grid N160, i.e. 320 latitudes with variable number of longitudes, 18 at the poles and up to 640 near the equator (see https://software.ecmwf.int/wiki/display/EMOS/N160). We use the 6-hourly ECMWF ERA-Interim data with the S1 and S2 atmospheric tides not removed, the Inverse Barometer (IB) assumption and mass conservation not enforced. The surface pressure variations are computed about a 2-year mean, namely the years 2001 and 2002 (this is to be consistent with the GRACE AOD1B data). The resolution of the land-sea mask is $0.5° \times 0.5°$.

In contrast to ocean loading where the displacements are related to the tides given by some model, here the displacements are of short-term nature and not connected to any tide (of course the diurnal and semi-diurnal constituents are clearly visible in the data). The displacements are therefore called non-tidal atmospheric loading (NTAL). The ECMWF operational data are the basis for atmospheric and oceanic de-aliasing (AOD) products within the GRACE project (Flechtner and Dobslaw 2013). The ERA-Interim data have been adopted for the generation of long-term AOD products back to 1976 and applied to LAGEOS data processing (Flechtner et al. 2008). The ERA-Interim data are advantageous as there are no jumps in the data series as opposed to the case of operational data. The station displacements are evaluated for all ITRF2008 DOMES stations and packed into yearly files (where also January of the following year is added in order to avoid the need to change files when processing data at the end of the year). The files are available at ftp://gfzop.gfz-potsdam.de/nt-atml.

In Chap. 2 we compare our displacements to the publicly available International Mass Loading Service (IMLS) displacements (Petrov 2015). In Chap. 3 we use our displacements in a recent 6-years period of Satellite Laser Ranging (SLR) data evaluation with all major geodetic satellites. We examine whether the orbital fits benefit from the use of NTAL. In a second trial we derive weekly C(2,0)-harmonics (the dynamic flattening of the Earth) either by considering NTAL or not.

2   Comparison to an External Model

We compare our displacements to the IMLS displacements publicly available (Petrov 2015). The IMLS displacements are derived based on NASA Modern Era Retrospective-Analysis for Research and Application (MERRA, Reichle et al. 2011) data, so to say the US counterpart of the ERA-Interim data. A major difference to our approach is that diurnal and semi-diurnal frequencies are removed from the IMLS displacements. Because the IMLS displacements are based on an approach mostly different to ours, the differences yield an assessment of the accuracies of the displacements.
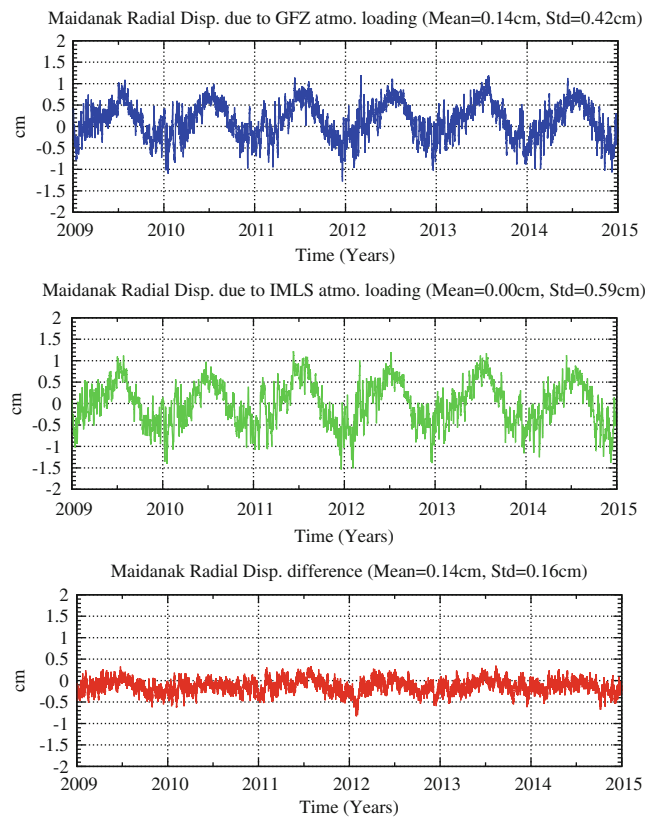

Fig. 1 Comparison for station Maidanak

For the graphical comparison we choose three explicit SLR stations: Maidanak, Potsdam, and Yarragadee. The first one, Maidanak, is located in the middle of Asia, so it is likely that atmospheric pressure variations do have a large impact in the vertical component of the station position. The second one, Potsdam, lies in Europe but not that far from the coast as Maidanak. So the impact of NTAL should be smaller. The third station, Yarragadee, is located in Australia about 50 km from the coast, so again one can expect some noticeable signal however with opposite sign compared to Maidanak and Potsdam as the weather is that of the Southern hemisphere.

Figures 1, 2, and 3 display the vertical components of our model, the IMLS model, and the differences between the two models for stations Maidanak, Potsdam, and Yarragadee respectively. A significant yearly signal turns out for Maidanak and Yarragadee as expected with a maximum peak-to-peak variation of 2 cm for Maidanak. The differences between the two models vary at the level of 1.4–2.0 mm for the stations shown. It looks as if some annual or semi-annual signal shows up in the differences with a few mm peak-to-peak variation. The reason could come from differences of the input data ERA-Interim or MERRA. Luckily no bias between the models can be observed.
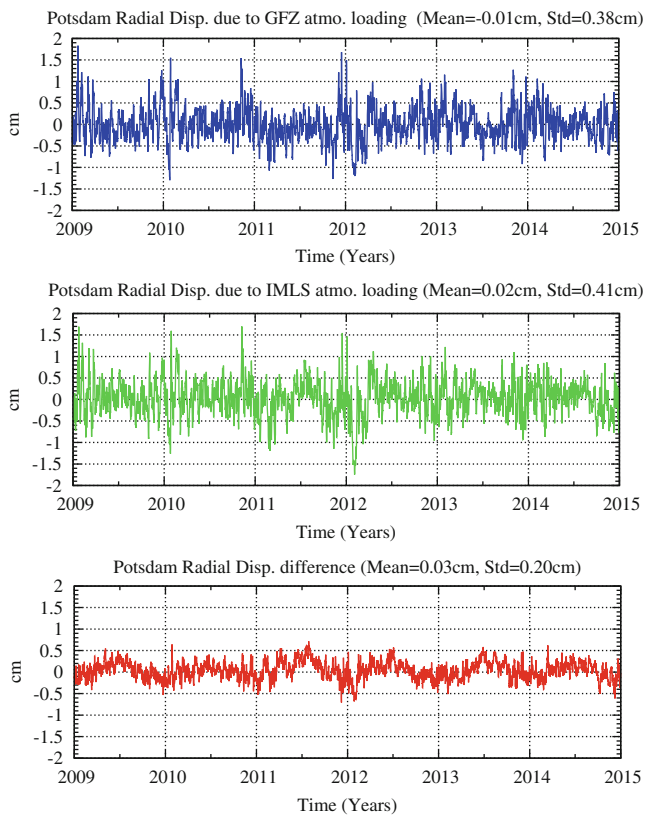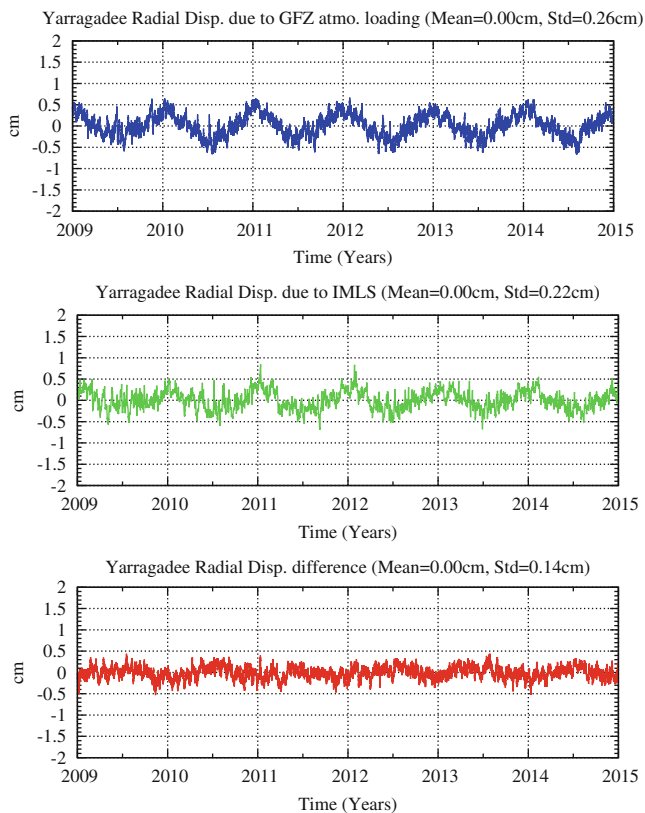
Potsdam Radial Disp. due to GFZ atmo. loading (Mean=-0.01cm, Std=0.38cm)

Potsdam Radial Disp. due to IMLS atmo. loading (Mean=0.02cm, Std=0.41cm)

Potsdam Radial Disp. difference (Mean=0.03cm, Std=0.20cm)

Fig. 2 Comparison for station Potsdam

Yarragadee Radial Disp. due to GFZ atmo. loading (Mean=0.00cm, Std=0.26cm)

Yarragadee Radial Disp. due to IMLS (Mean=0.00cm, Std=0.22cm)

Yarragadee Radial Disp. difference (Mean=0.00cm, Std=0.14cm)

Fig. 3 Comparison for station Yarragadee

Yarragadee Radial Disp. due to GFZ atmo. loading

Yarragadee Radial Disp. due to IMLS atmo. loading
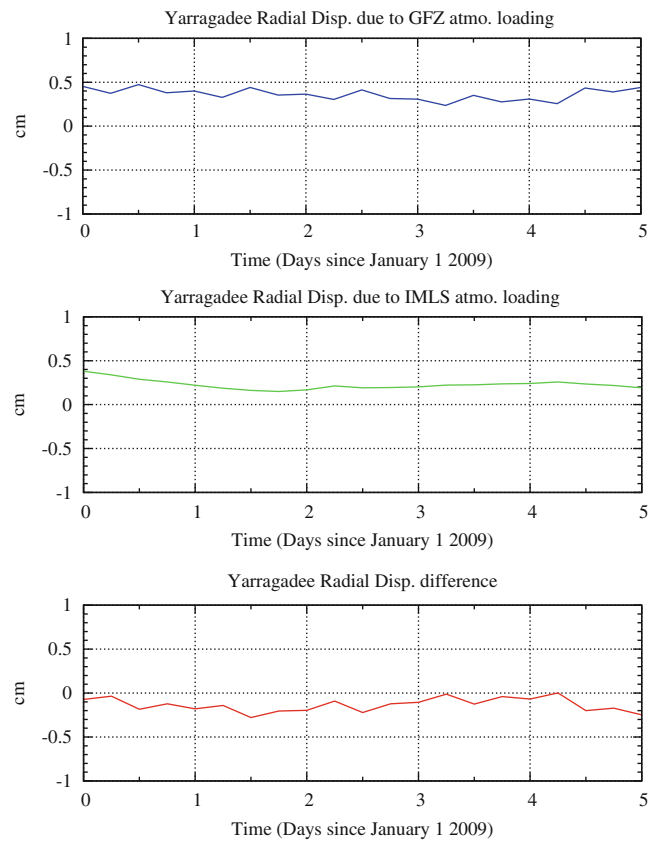
Yarragadee Radial Disp. difference

Fig. 4 Comparison of 5 days for station Yarragadee

One major difference between the models shows up when zooming into the series as done in Fig. 4 for station Yarragadee over 5 days. The differences feature a zig-zag curve which is due to the removal of the diurnal and semi-diurnal frequencies in case of the IMLS displacements.

The comparison between our model and the IMLS model in the radial component is done for all the 33 stations used in the following analysis of SLR data over 6 years. The global statistics for 289,212 differences arrive at 0.2 mm in mean and 1.7 mm in standard deviation confirming the graphical results found above. In summary our displacements behave well in comparison to IMLS displacements with no bias and differences in the mm range which is about one tenth of the signal variability.

3   Application to SLR Data Processing

In order to assess the impact of NTAL on SLR data processing we took the orbital analyses of all major geodetic satellites over a 6 years period in 2009–2014. The suite of geodetic satellites consists of LAGEOS-1 and -2, LARES, AJISAI, STARLETTE, and STELLA. The orbit characteristics in terms of altitude and inclination and the satellite

Table 1 Features of the geodetic satellites

Satellite	Altitude (km)	Inclination (deg)	A/M (m²/kg)
LAGEOS-1	5900	110	0.0007
LAGEOS-2	5800	53	0.0007
LARES	1500	70	0.0003
AJISAI	1500	50	0.0053
STARLETTE	900	50	0.0010
STELLA	800	97	0.0009

Table 2 Orbital fits summary

Sat.	RMS (cm) −AOD −NTAL	+NTAL	+AOD −NTAL	+NTAL	No. res.
L1&2	1.0172	1.0131	0.9969	0.9928	848,670
LAR	1.2153	1.2126	1.0895	1.0868	248,091
AJI	1.5340	1.5321	1.4549	1.4539	862,615
STA	1.3846	1.3828	1.2606	1.2595	486,055
STE	1.6052	1.6044	1.5301	1.5298	238,070

characteristics in terms of area-to-mass ratios are compiled in Table 1. The area-to-mass ratio is a typical number that determines the dependence of the satellite on non-conservative forces such as atmospheric drag, solar radiation pressure and albedo pressure, the smaller the number the less nuisance forces to be handled in Precise Orbit Determination (POD). In this respect LARES behaves best, AJISAI worst.

For POD we use the EPOS-OC software suite (see Zhu et al. 2004). EPOS-OC determines orbits and parameters in a dynamic approach by differential orbit improvement to minimize the residuals of the observations in the least squares sense. For background modeling the IERS Conventions 2010 are mostly followed. However for the gravity field model the EIGEN-6C (Förste et al. 2011) is adopted and for a priori station coordinates the SLRF2008 (http://ilrs.gsfc.nasa.gov/science/awg/-SLRF2008.html) is used. All satellites are processed in 7-day arcs. In all arcs the initial orbital elements are solved for. Also all station coordinates and the Earth Orientation Parameters (EOPs) at daily intervals are solved for. These parameters get an a priori sigma of 1 m to care for the datum defect (this approach is standard for the operational products of the analysis centers of the International Laser Ranging Service (ILRS, Pearlman et al. 2002). In order to reduce remaining errors of background models driving the dynamical model in POD also once per revolution (1cpr) empirical accelerations in transversal and normal direction are introduced, for the LAGEOS and LARES satellites two times per arc, for the others four times per arc.

Orbit quality is assessed in terms of Root Mean Square (RMS) values of the observation residuals that are the differences of the SLR range observations to the restituted orbit (therefore also called orbital fit). All orbital fits for all arcs show RMS values of around 1 cm. LARES was launched in 2012 lately, so this satellite exceptionally covers not the full analysis period. The analysis of STELLA shows some problems as the RMS is increasing slightly with time. The reason for this is not known. The additional estimation of a scaling parameter of solar radiation pressure does not help. Also solar tides mismodeling cannot be blamed because the model is used as

given in the IERS Conventions 2010 at an accuracy beyond need.

Our aim is to see the effect of the loading displacements of our model on the orbital fits. As the variations of atmospheric density lead also to considerable changes of the geopotential, likewise the gravitational variations by adopting the GRACE Atmosphere and Ocean Dealiasing level 1B (AOD1B) products (Flechtner and Dobslaw 2013) are taken into account. By comparing the results of case "without AOD, without NTAL" to case "without AOD, with NTAL" and case "with AOD, without NTAL" to case "with AOD, with NTAL" i.e. repeating processing with the displacements being considered or not, the pure impact of NTAL can be assessed.

An overall summary of the orbital fits is given in Table 2. The improvement in the orbital fits becomes clear when looking at the differences arc-wise in terms of RMS values. Figure 5 shows the RMS values for NTAL being considered or not and their differences for the LAGEOS satellites. Indeed the differences stay significantly in the positive region (RMS without NTAL minus RMS with NTAL, i.e. RMS without NTAL is larger). This behaviour can be observed for all satellites, Table 3 compiles the values. So in general, the consideration of NTAL improves the orbits by 0.004 cm in the case of LAGEOS and somewhat less for the other satellites. These values are admittedly small but a systematic improvement is indicated. The errors in the loading displacements should be small relative to the size of the displacements themselves. So the adoption of the loading corrections can be recommended despite of their errors.

In an other issue the LAGEOS arcs are taken to determine the C(2,0)-terms of the gravity field at weekly intervals with NTAL being considered or not with the objective to check whether our loading model has any effect on the C(2,0) estimates. In order to not spoil the geophysical signal, here the 1cpr empirical accelerations in normal direction are not solved for. Again the cases are distinguished where the gravitational variations of the atmosphere, i.e. AOD, have been considered or not. Figure 6 displays the C(2,0) estimates from the weekly LAGEOS arcs when AOD has not been

Fig. 5 Differences of orbital fits (*upper curve*) and orbital fits for both runs (*lower curve*)
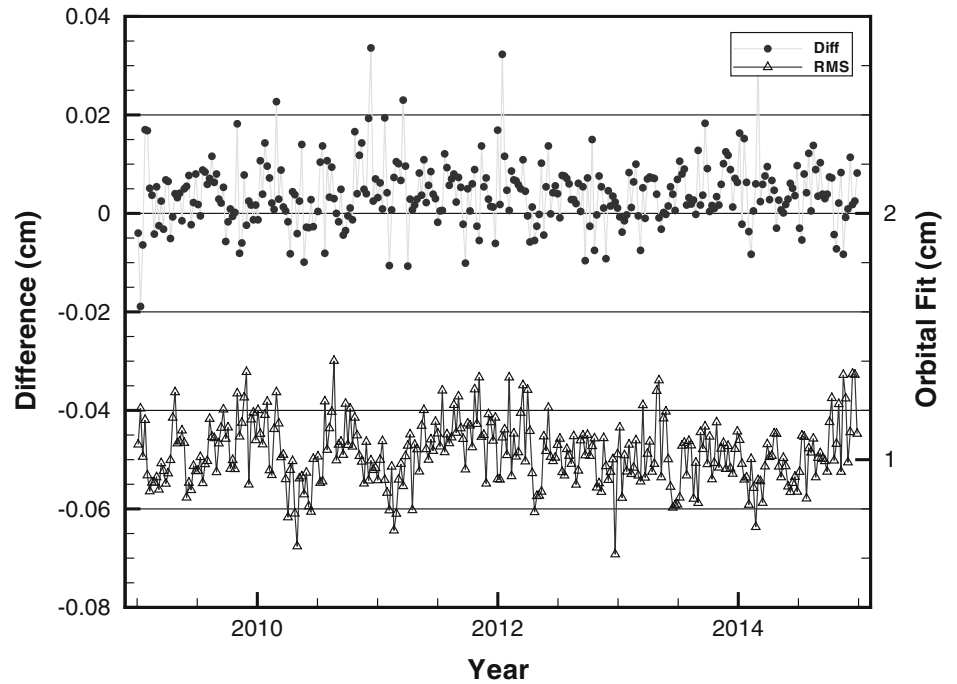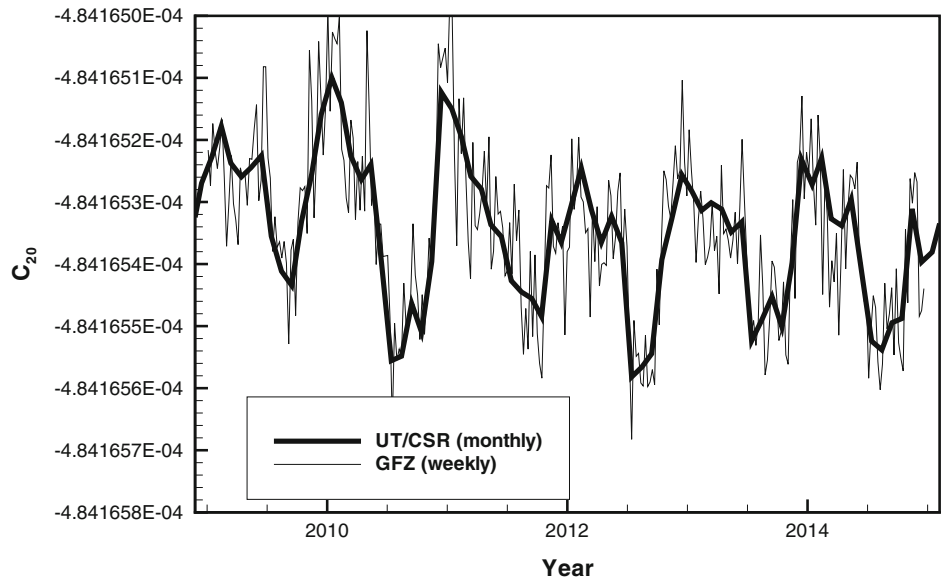

Table 3 Improvement of orbital fits by atmospheric loading model

Satellite	RMS (cm)	
	−AOD	+AOD
LAGEOS-1 & -2	0.0040 ± 0.0004	0.0041 ± 0.0004
LARES	0.0026 ± 0.0004	0.0027 ± 0.0004
AJISAI	0.0019 ± 0.0003	0.0010 ± 0.0005
STARLETTE	0.0018 ± 0.0009	0.0011 ± 0.0003
STELLA	0.0008 ± 0.0007	0.0004 ± 0.0005

Fig. 6 The C(2,0) weekly estimates versus the UT/CSR monthly RL-05 series

considered versus the monthly series generated by the Center for Space Research at the University of Texas (UT/CSR) based on SLR observations from the LAGEOS-1 and -2, AJISAI, STARLETTE, and STELLA satellites (Cheng et al. 2013). The differences in the weekly C(2,0) estimates when adopting NTAL or not can not be distinguished at the scale of Fig. 6. In numbers the differences are in mean $0.0017 * 10^{-11} \pm 0.0056 * 10^{-11}$.

When the gravitational effect, i.e. AOD, is considered the amplitude of the seasonal signal of the C(2,0) series is substantially reduced (Flechtner et al. 2008). Then the differences of the weekly C(2,0) estimates when applying NTAL or not are in mean $0.0016 * 10^{-11} \pm 0.0056 * 10^{-11}$. This means that the differences are statistically zero when NTAL is used or not (in both cases, AOD adopted or not) and that there is no effect by using the NTAL displacements on the C(2,0) estimates.

4 Summary

GFZ provides station displacements due to atmospheric pressure loading based on ECMWF ERA-Interim surface pressure data compatible with GRACE AOD1B data. The displacements agree with IMLS at the 1.7 mm level in radial direction which gives some assessment of accuracy of these corrections. The displacements are used to examine SLR data to 6 satellites for 6 years in 2009–2014. There is a small systematic improvement of the orbital fits by 0.004 cm maximum. There is no impact on the C(2,0) series in the LAGEOS only solution.

References

Altamimi Z, Collilieux X, Metivier L (2011) ITRF 2008: an improved solution of the international terrestrial reference frame. J Geod 85(8):457–473

Cheng MK, Tapley BD, Ries JC (2013) Deceleration in the Earth's oblateness. J Geophys Res 118(2):740–747

Dziewonski AH, Anderson DL (1981) Preliminary reference Earth model. Phys Earth Planet Inter 25:297–356

ECMWF (2015) European centre for medium-range weather forecasts, data archive services web site. http://www.ecmwf.int/products/-data/archive/index.html. Accessed 30 Oct 2015

Farrel W E (1972) Deformation of the Earth by surface loads. Rev Geophys 10(3):761–797

Flechtner F, Dobslaw (2013) AOD1B product description document for product release 05. GRACE Document GRACE 327–750 (GR-GFZ-AOD-0001). http://isdc.gfz-potsdam.de/-index.php?name=UpDownload&req=getit&lid=619. Accessed 30 Oct 2015

Flechtner F, Thomas M, König R (2008) A long-term model for non-tidal atmospheric and oceanic mass redistributions and its implications on LAGEOS-derived solutions of Earth's oblateness. Scientific Technical report STR08/12, GFZ German Research Centre for Geosciences, Potsdam. ISSN 1610-0956

Förste C, Bruinsma S, Shako R, Marty J-C, Flechtner F, Abrikosov O, Dahle C, Lemoine J-M, Neumayer H, Biancale R, Franz Barthelmes F, König R, Balmino G (2011) EIGEN-6 a new combined global gravity field model including GOCE data from the collaboration of GFZ-Potsdam and GRGS-Toulouse. Geophysical Res Abstr 13, EGU2011-3242-2, 2011, EGU General Assembly 2011. http://icgem.gfz-potsdam.de/ICGEM/documents/Foerste-et-al-EGU_2011-01.pdf. Accessed 30 Oct 2015

Gegout P, Böhm J, Wijaya D (2010) Practical numerical computation of love numbers and applications. http://ggosatm.hg.tuwien.ac.at/LOADING/-COSTES0701/04_2010_COST_Vienna_Gegout.pdf. Accessed 15 June 2016

IERS (2015) International Earth rotation and reference systems service web site. http://www.iers.org. Accessed 30 Oct 2015

Pearlman MR, Degnan JJ, Bosworth JM (2002) The international laser ranging service. Adv Space Res 30(2):135–143

Petit G, Luzum B, IERS Conventions (2010). Bundesamts für Kartographie und Geodäsie, Frankfurt am Main. http://www.iers.org/TN36. Accessed 16 Sept 2013

Petrov L (2015) The international mass loading service. http://arxiv.org/abs/1503.00191

Petrov L, Boy J-P (2004) Study of the atmospheric pressure loading signal in very long baseline Interferometry observations. J Geophys Res 109:B03405. doi:10.1029/2003JB002500

Reichle RH, Koster RD, De Lannoy GJM, Forman BA, Liu Q, Mahanama SPP, Toure A (2011) Assessment and enhancement of MERRA land surface hydrology estimates. J Clim 24:6322–6338

Tregoning P, vanDam T (2005) Atmospheric pressure loading corrections applied to GPS data at the observation level. Geophys Res Lett 32:L22310

Zhu S, Reigber C, König R (2004) Integrated adjustment of CHAMP, GRACE and GPS data. J Geod 78(1–2):103–108

Effects of Meteorological Input Data on the VLBI Station Coordinates, Network Scale, and EOP

Robert Heinkelmann, Kyriakos Balidakis, Apurva Phogat, Cuixian Lu, Julian A. Mora-Diaz, Tobias Nilsson, and Harald Schuh

Abstract

The requirement for the quantification of sea level rise and other global change phenomena are precise and stable reference frames. To accord with these science driven requirements, GGOS, the Global Geodetic Observing System, aims for reference frame accuracy of 1 mm, stability of 0.1 mm/year, and Earth Orientation Parameters accuracy of $\sim$30 μas. At this level of precision a variety of otherwise neglected effects has to be taken into account. In our article we investigate whether the use of meteorological data for the analysis of space geodetic techniques could be one of these effects that need to be considered. The article moves forward in finding an optimized meteorological data set in order to provide results at the required accuracy level. At the Very Long Baseline Interferometry (VLBI) stations of the International VLBI Service for Geodesy and Astrometry meteorological data are observed and are customarily applied for analyses. Observed data can contain outliers and inhomogeneities that have to be appropriately accounted for. We test the two blind models GPT and GPT2 as a replacement for locally observed data. We find that both cause small seasonal signals in the celestial pole offsets with an amplitude of $\sim$15 μas. We also assess whether the mean values as obtained by extrapolation of surface or near-surface data of ERA-Interim reanalysis product or of the World Meteorological Organization can be used as reference values for homogenization of the observed meteorological data. In particular at sites where the model surface height and the height of the space geodetic reference point differ significantly, very large differences were found. Hence, we cannot recommend shifting the mean value of the observed data to the mean values derived by hypsometrically adjusted surface data.

R. Heinkelmann (✉) • C. Lu • J. Mora-Diaz • T. Nilsson
GFZ German Research Centre for Geosciences, Potsdam, Germany
e-mail: heinkelmann@gfz-potsdam.de

K. Balidakis • A. Phogat
Institute of Geodesy and Geoinformation Science, Technische
Universität Berlin, Berlin, Germany

H. Schuh
GFZ German Research Centre for Geosciences, Potsdam, Germany
Institute of Geodesy and Geoinformation Science, Technische
Universität Berlin, Berlin, Germany

1   Introduction

Atmospheric effects in space geodesy (Böhm and Schuh 2013) are one of the largest systematic and random error source on space geodetic techniques at radio wavelengths, such as GNSS (Global Navigation Satellite System) and VLBI (Very Long Baseline Interferometry). Several models applied in the analyses of space geodetic techniques at radio wavelengths require meteorological input data (MD): (i) atmospheric (tidal and non-tidal) pressure loading (APL), (ii) ray tracing or mapping functions and a priori gradients, (iii) zenith hydrostatic delays, and—in case of VLBI—antenna thermal deformations. As APL (Petrov and Boy 2004) is a geographically extensive effect ($\sim$1000 km), its calculation customarily involves pressure anomalies that are provided by pressure fields at the epoch of evaluation and by a reference pressure field. The assimilation of local air pressure data in these fields allows to account for high frequency pressure variations. For ray tracing (Nafisi et al. 2012) as well as for mapping functions (e.g. VMF1) (Böhm et al. 2006) and a priori gradients that are based on ray tracing (Böhm et al. 2012), 3D refractivity fields and a ray trace algorithm are necessary. The aforementioned models require MD from numerical weather models (NWM) customarily provided by weather agencies, such as the European Centre for Medium-Range Weather Forecasts (ECMWF[1]). For the calculation of zenith hydrostatic delays (ZHD) (Davis et al. 1985; Saastamoinen 1972) and antenna thermal deformations (Nothnagel 2008), locally observed MD are required. The accuracy of ZHD is directly proportional to the accuracy of local air pressure measurements. For thermal deformation modelling, the temperature anomaly, i.e. the difference between the local temperature and a reference temperature, the undeformed antenna dimensions refer to, has to be known (Böhm et al. 2008). Our investigations here are limited to the models that apply locally observed MD and we do not alternate reference temperatures.

Here, we compare various MD in terms of statistics such as bias, rms, and empirical correlation coefficients (Sect. 2) and test their impact on the VLBI-derived station coordinates, network scale, and EOP by investigating parameter differences between VLBI solutions derived by alternating either air pressure or temperature (Sect. 4). At the IVS (International VLBI Service for Geodesy and Astrometry; Nothnagel et al. 2015) VLBI stations MD have been recorded whenever geodetic or astrometric VLBI observations were carried out with only a very few exceptions (Heinkelmann et al. 2007, 2011). This dataset is very valuable because it allows to assess the quality of derived MD directly at the stations. The motivation is to quantify what effects on geodetic results can be expected through the application of MD, locally measured or taken from models.

2   Meteorological Data Sets and On-Site Comparisons

Our investigations include (i) the two blind models GPT (Global Pressure and Temperature model) (Böhm et al. 2007) and GPT2 (Lagler et al. 2013), (ii) in-situ observed values provided by the IVS, and (iii) in-situ observed values (as for (ii)) but homogenized and shifted to the mean level derived by extrapolation of ERA-Interim (Dee et al. 2011) of ECMWF or of World Meteorological Organization (WMO[2]) data.

So-called blind models can be applied for analyses without restrictions, since they are available for any geographical location and time and do not require input of additional data. This reliability makes them valuable backup data sets applied in several GNSS and VLBI analysis software packages. In order not to introduce artifacts in case of missing data, the models have to match the observed values as close as possible, particularly not introducing systematics. GPT and GPT2 are derived from monthly mean profiles of ERA-40 (GPT) or ERA-Interim (GPT2) re-analysis products of ECMWF through pressure level interpolation and thus, they cannot contain signals with periods shorter than 1 month. Both models represent the data by mean values and seasonal signals, annual (GPT) and annual and semi-annual terms (GPT2), respectively. They cannot capture inter-annual variations and thus, it can be expected that the differences between the observed and the blind modeled data still contain residual seasonal signals. For the temperature, the seasonal signals are usually pronounced (large correlation coefficients in Table 1) but the amplitude may vary considerably on the inter-annual scale. Atmospheric pressure variations are dominated by synoptic weather patterns, highs and lows, spanning frequencies of a few days to a few weeks. Since this sequence appears irregularly, it cannot be modeled by a small number of Fourier series coefficients. The seasonal signals of the pressure are much smaller and do not sufficiently describe the observed data (low correlation coefficients in Table 1). Input for GPT are the years 1999–2002 and 2001–2010 for GPT2. It can be seen at some stations that this choice results in rather large differences of the pressure approximation, e.g. at Zelenchukskaya, Russia (Fig. 1). At the same site a phase shift can be found as well. While GPT2 estimates phases together with amplitudes, GPT fixes the phases for the seasonal variations to January 28.

As the logging interval of the meteorological sensors is only a few minutes, the observed data provide the highest

---

[1]http://www.ecmwf.int/.

[2]https://www.wmo.int/.

Table 1 Comparison between observed and empirical (GPT/GPT2) values of pressure (hPa) and temperature (°C) in terms of shift (difference of the median values), rms in brackets and empirical correlation coefficients ("corr.")

Pressure				
Station	GPT		GPT2	
IVS name	Shift	Corr.	Shift	Corr.
ALGOPARK	−3.4(8.3)	−0.04	−3.5(8.2)	0.18
BADARY	−0.4(6.6)	0.49	0.1(6.2)	0.56
GILCREEK	−3.5(11)	0.11	−0.3(11)	0.32
HARTRAO	−1.9(3.1)	0.55	−0.8(3.0)	0.60
HOBART12	1.2(9.7)	−0.06	1.2(9.5)	0.20
HOBART26	−4.1(9.9)	−0.06	−4.5(9.7)	0.18
KATH12M	−1.3(2.4)	0.78	−0.4(2.4)	0.79
KOKEE	−4.8(2.2)	−0.22	0.8(2.1)	0.30
MATERA	−1.7(6.5)	−0.04	−2.2(6.0)	0.20
MEDICINA	1.8(7.3)	0.16	0.4(7.2)	0.22
NYALES20	−5.9(12)	0.20	−1.0(11)	0.31
ONSALA60	−0.7(11)	0.06	−0.8(11)	0.16
SESHAN25	−3.1(5.7)	0.81	−0.5(4.8)	0.85
SVETLOE	−4.5(12)	0.03	−4.5(12)	0.03
TIGOCONC	−0.2(4.0)	0.38	0.4(3.7)	0.40
TSUKUB32	−3.1(6.7)	0.33	−1.8(6.7)	0.35
WESTFORD	−1.6(7.9)	0.01	−1.5(7.8)	0.17
WETTZELL	−1.7(7.6)	−0.08	−2.1(7.5)	0.11
YARRA12M	−0.2(4.2)	0.61	−0.7(3.9)	0.64
YEBES40M	−2.0(6.3)	−0.10	−0.7(5.7)	0.22
ZELENCHK	−3.8(7.5)	−0.07	−2.5(6.6)	0.22
Mean	−2.0(6.9)	0.17	−1.2(6.6)	0.33

Temperature				
Station	GPT		GPT2	
IVS name	Shift	Corr.	Shift	Corr.
ALGOPARK	−0.8(7.1)	0.85	2.0(6.8)	0.85
BADARY	1.6(7.6)	0.85	2.0(6.7)	0.89
GILCREEK	−3.6(8.5)	0.81	−2.1(7.0)	0.85
HARTRAO	−0.3(6.5)	0.51	3.2(5.8)	0.59
HOBART12	0.6(4.3)	0.58	−0.4(4.2)	0.58
HOBART26	1.5(4.3)	0.62	0.5(4.1)	0.62
KATH12M	−0.5(6.1)	0.35	0.8(5.5)	0.54
KOKEE	1.0(3.3)	0.35	−2.4(3.3)	0.34
MATERA	0.9(4.6)	0.83	0.8(4.6)	0.83
MEDICINA	−1.3(4.9)	0.86	0.3(4.9)	0.87
NYALES20	−1.7(5.2)	0.74	−3.8(4.9)	0.78
ONSALA60	−0.6(4.2)	0.84	−1.2(4.0)	0.84
SESHAN25	−0.4(4.7)	0.89	−1.9(4.8)	0.88
SVETLOE	1.5(6.0)	0.86	0.5(5.3)	0.86
TIGOCONC	1.0(3.8)	0.61	1.5(3.8)	0.61
TSUKUB32	−0.9(4.3)	0.88	0.0(4.6)	0.86
WESTFORD	−1.9(6.4)	0.82	−0.5(6.3)	0.82
WETTZELL	−1.2(5.0)	0.81	0.3(4.8)	0.82
YARRA12M	−0.1(6.1)	0.69	0.5(5.8)	0.69
YEBES40M	−0.7(5.3)	0.83	−1.0(5.3)	0.83
ZELENCHK	−2.8(5.8)	0.80	−1.2(4.8)	0.81
Mean	−0.4(5.4)	0.73	0.0(5.1)	0.75

Stations with small numbers of observations are omitted. The last row labeled "mean" gives the mean value of the shifts and correlation coefficients and the squared mean of the rms of the respective column
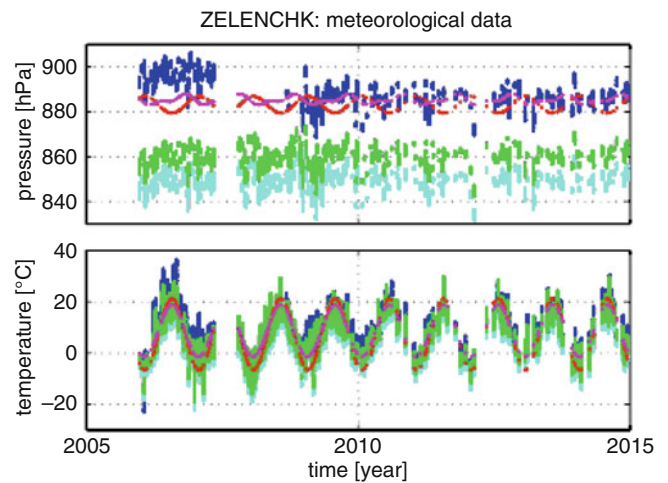

Fig. 1 Pressure and temperature at Zelenchukskaya, Russia, recorded during the IVS VLBI sessions between 2006.0 and 2015.0. Observed meteorological data (*blue*), homogenized observed data shifted to the level of extrapolated WMO data (*cyan*), homogenized observed data shifted to the level of extrapolated ERA-Interim (*green*), GPT (*red*) and GPT2 (*magenta*)

temporal resolution in comparison to any other MD and are thus preferred for application in the VLBI analysis. The observed data, however, usually include unflagged outliers and missed values have to be replaced in a way that does not impose shifts or other systematic effects. On long time scales the observed MD are prone to inhomogenities, such as sudden jumps, trends, or drifts of the running mean value. Such artifacts have to be appropriately accounted for (Heinkelmann et al. 2005) through a process called homogenization. During homogenization a choice has to be made regarding the mean value of the homogenized data set. This choice is usually made involving meta data such as information about sensor problems, relocation or calibration events. If such information is unavailable, external information may help in order to identify the absolute reference value. For most meteorological sensors operated at IVS sites no calibrations were performed after the installation suggesting that the early registrations, the ones obtained right after the installation, probably are the most accurate. In our example (Fig. 1), however, the comparison with GPT and GPT2 indicates that the later level might be more reliable because it is closer to the empirical models. In this study we test two different approaches for providing the absolute mean value (i) by GPT, GPT2, based on interpolation between adjacent pressure level fields and (ii) by extrapolation from surface (or near-surface) data (ERA-Interim, WMO).

The ERA-Interim and WMO data were not applied directly in the analysis. They only served for homogenization to define the absolute mean value of the observed data. The WMO mean values were obtained averaging all available WMO sites in the immediate vicinity (standard search criteria were $d_{3D} < 50$ km and $d_H < 500$ m). WMO data are

given daily, while ECMWF analysis fields are available at six-hourly intervals. To achieve the three-hourly resolution applied by us, forecasts were interposed on ERA-Interim. Horizontally, the ECMWF data were bilinearly interpolated. ERA-Interim and WMO mean values were then derived by vertical extrapolation from (near) surface values applying the hypsometric adjustment equation, e.g. Heinkelmann et al. (2005). The two data sets are widely available and the application of hypsometric adjustment of surface values is common practice in weather- or climate-related sciences.

An example of the various MD involved in this study is presented in Fig. 1, where the upper plot shows the pressure and the lower plot the temperature at Zelenchukskaya. At most of the other network stations (Table 1) the data sets show comparable characteristics. At Zelenchukskaya, however, a significant jump of the observed pressure data can be additionally found following a registration break between about mid 2007 and mid 2008. Looking at Table 1, GPT and GPT2 pressures perform very similar w.r.t. the observed pressure and show only very small or no significant shifts. At a few stations, however, the GPT pressure shows unusual large shifts w.r.t. the observed values and GPT2, e.g. −4.8 hPa at Kokee Park, Hawaii, USA. These shifts are most likely due to the coarser horizontal resolution of GPT (spherical harmonics expansion up to degree and order 9, ∼2222 km at the equator) in comparison to GPT2 (5° grid ∼557 km).

Absolute mean values derived by extrapolation from surface data can show significant shifts w.r.t. the observed data and w.r.t. GPT/GPT2 that may become very large, if the equation has to overcome large height differences, e.g. ∼1150 m at Kokee Park (Table 2). Besides Kokee, a very large shift of about −69 hPa between surface-derived and observed pressure appears at Badary, Russia (about −619 m height difference). Badary site is located in a plane surrounded by mountains. The horizontal resolution of ERA-Interim (1° grid ∼111 km) is probably too coarse so that the surface height of Badary station in ERA-Interim is based on an average value including the adjacent mountains. At several sites large shifts can be found with respect to the pressure derived from WMO. For example at Yebes, Spain, we found a difference of −37.4 hPa compared to the observed pressure (∼296 m height difference) and about the same difference with respect to ERA-Interim (∼56 m height difference to the pressure sensor at the VLBI site). For WMO data sometimes no station could be found in the immediate vicinity, here for Kokee Park. In this case, the standard horizontal and vertical distances for pair matching had to be increased and consequently the correlation got significantly reduced. In comparison to the pressure, the temperature shows very small or no shifts (Table 2) with only a very few exceptions, e.g. Kokee Park. ERA-Interim temperature derived from 2 m-temperature by extrapolation results in a remarkable shift of the mean value of the temperature of 8.3°C at Kokee

Table 2 Comparison of originally observed and homogenized absolute mean values based on ERA-Interim or WMO; pressure in hPa ("pres."), temperature in °C ("temp.") and height difference in m. *average of the vertical distances of the sites within 50 km Sign convention is ERA-Interim/WMO derived minus observed mean values

Station	ERA-Interim			WMO		
IVS name	Pres.	Temp.	d_H	Pres.	Temp.	d_H^*
ALGOPARK	−12.8	0.4	−109.3	−33.0	−0.2	−137.5
BADARY	−69.0	−4.0	−619.2	−69.3	−4.3	−114.2
GILCREEK	−10.7	−1.3	−72.8	−16.3	1.4	−26.6
HARTRAO	2.5	1.9	43.8	−30.0	−0.0	13.3
HOBART12	−23.0	−2.0	−221.8	−22.3	−1.0	−0.4
HOBART26	−23.4	−1.3	−197.7	−20.0	−0.3	4.2
KATH12M	−10.3	−0.3	−33.9	−17.5	−1.0	7.8
KOKEE	123.8	8.3	1151.8	105.3	−2.0	1154.2
MATERA	28.7	1.5	360.4	−11.1	−0.2	1.1
MEDICINA	−18.8	−1.7	−161.1	−8.1	−1.7	−4.3
NYALES20	−21.3	−1.7	−95.9	−26.1	0.7	43.6
ONSALA60	−3.7	−0.2	11.5	−7.2	−1.5	−3.3
SESHAN25	−0.0	−1.0	23.2	−10.9	−0.3	13.9
SVETLOE	0.7	0.6	54.1	−9.7	0.6	0.1
TIGOCONC	−3.5	1.1	5.0	13.4	0.6	143.3
TSUKUB32	−12.3	−0.5	−57.8	−6.0	2.3	6.3
WESTFORD	−4.5	−0.2	−66.9	−5.3	−0.0	9.6
WETTZELL	12.8	−0.2	177.4	15.4	0.3	41.6
YARRA12M	6.1	1.5	31.2	−17.8	−0.3	0.5
YEBES40M	0.9	−0.3	56.0	−37.4	0.2	296.1
ZELENCHK	−27.2	−2.5	−48.0	−37.9	−5.3	−173.2

Park. Since the station is situated on a high altitude plateau, a temperature shift can be expected if derived from ERA-Interim (Gao et al. 2012).

3 VLBI Analysis

Our approach is a diagnostic one: we determine parameter time series obtained from VLBI solutions using the GFZ version of the Vienna VLBI software (Nilsson et al. 2015). In each solution, we alternate one of the MD, pressure or temperature, while keeping all other a priori data and reductions and corrections in the a priori delay model fixed. The test solutions are compared against the reference solution by computing the difference between estimated parameters. The reference solution is the solution where locally observed pressure and temperature as provided by IVS are applied. We used the current standard Rapid Turnaround Sessions (IVS-R1 and IVS-R4) starting in 2002 until the end of 2014; a total number of 1325 sessions during 13 years. The solution fully adheres to IERS Conventions 2010 (Petit and Luzum 2010) concerning analysis models. The fact that constant or slowly varying pressure partly compensates for atmospheric pressure loading (Steigenberger et al. 2009) does not play a role for our investigations. The estimated parameters are

defined as follows:

- station coordinates (with no-net translation (NNT) and no-net rotation (NNR) constraints imposed on a priori coordinates of those stable sites included in ITRF2008 (Altamimi 2011) that were unaffected by major Earthquakes),
- full set of unconstrained EOP (with a priori values taken from USNO finals,[3])
- radio source coordinates (with NNR on the coordinates of radio sources of ICRF2 (Fey et al. 2015) of categories defining or other),
- clock parameters (one or more sets of coefficients of a 2nd order polynomial and coefficients of a piece-wise linear function with 1 h resolution describing clock synchronization, trend, and drift w.r.t. a reference clock),
- zenith delays (a piece-wise linear function with 30 min resolution describing zenith delays due to non-hydrostatic atmospheric effects at every station), and
- horizontal gradients (piece-wise linear functions separated in north-south and east-west directions with 6 h resolution at every station).

4 Results

4.1 Station Coordinates

Figure 2 show the MD and the corresponding station coordinate differences of GPT vs. the ones obtained by the in-situ observed MD. At Hobart, Australia, the GPT pressure shows almost no variation, while the observed pressure varies considerably. Accordingly, the height component but also the horizontal components differ significantly. The moving median reaches absolute values of up to ∼2 mm. Applying GPT temperature results in small seasonal waves in the time series of coordinates at Badary with amplitudes of ∼1.5–2 mm being largest in the height component. Here, the GPT temperature shows maxima during boreal summer with peaks of ∼20°C while the observed summer temperature maxima are at ∼25°C–30°C. In addition to the large temperature differences, the antenna at Badary has quite large dimensions that enhance the effects of thermal expansion.

Pressure and temperature effects through GPT2 are comparable to GPT at most of the sites. The above mentioned break of the running mean value of the observed pressure at Zelenchukskaya (Fig. 1) causes a systematic shift of the height of ∼1 mm in comparison to the coordinate after the break (Fig. 3). The GPT2 temperature at Hartebeesthoek, South Africa, matches the observed summer temperature better than the winter temperature resulting in an asymmetric
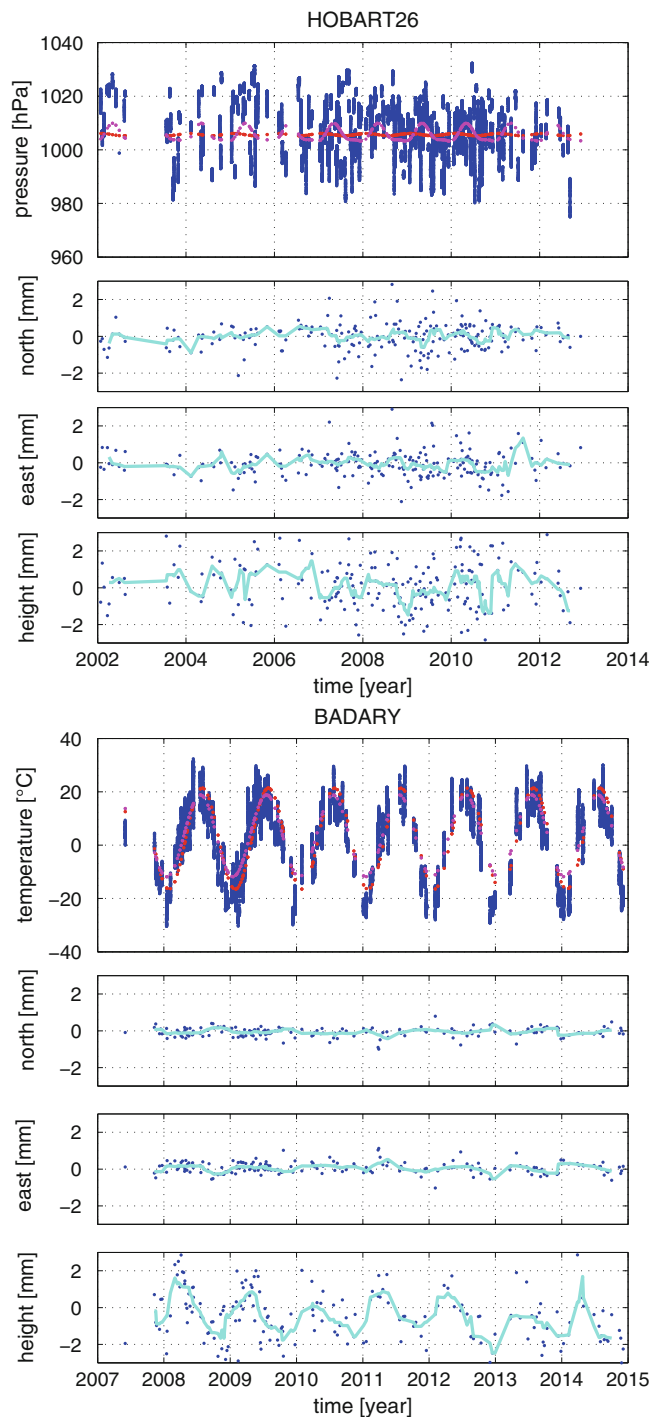

Fig. 2 GPT: pressure at Hobart (26 m) and temperature at Badary during the IVS VLBI observations between 2002 and the end of 2014. Badary joined IVS operations by the end of 2007. The observed meteorological data are shown in *blue* and the two empirical models: GPT in *red* and GPT2 in *magenta*. The plots below the meteorological data show the station coordinate differences in *blue*, north, east, and height as well as a 90 day moving median in *cyan*

correction of the antenna deformation that is evident by the small shift in the height component of ∼0.5–1 mm.

[3]http://www.usno.navy.mil/USNO/earth-orientation/eo-products.
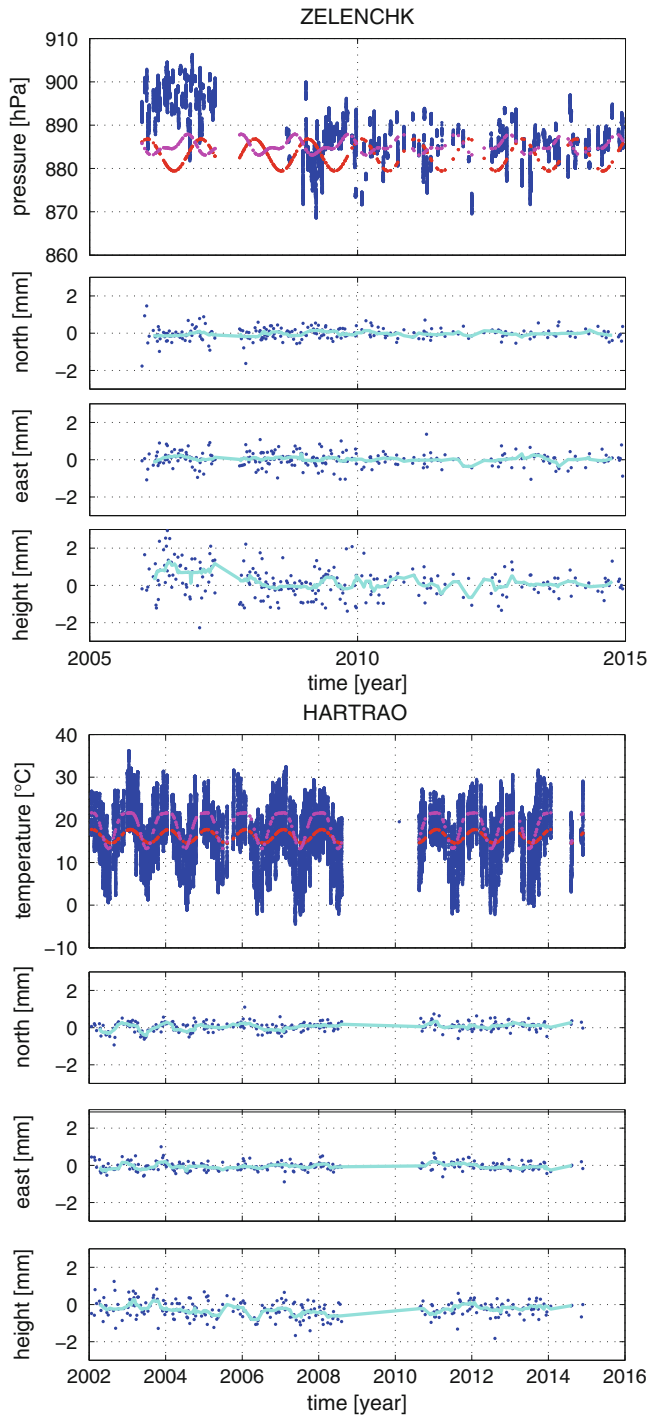
Fig. 3 GPT2: pressure at Zelenchukskaya and temperature at Hartebeesthoek during the IVS VLBI observations between 2002 and the end of 2014. Zelenchukskaya joined IVS operations in 2006. The observed meteorological data are shown in *blue* and the two empirical models: GPT in *red* and GPT2 in *magenta*. The plots below the meteorological data show the station coordinate differences in *blue*, north, east, and height as well as a 90 day moving median in *cyan*
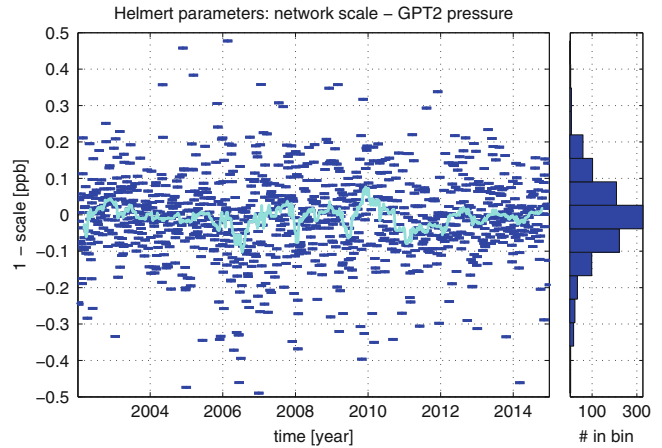
Fig. 4 GPT2: network scale parameter differences during the IVS VLBI observations between 2002 and the end of 2014 in *blue* and a 90 day moving median in *cyan*. The corresponding bar diagram inset on the right suggest Gaussian distribution

4.2   Network Scale

With network scale we denote the scale parameter of a seven-parameter similarity transformation (Helmert transformation). A scale difference of 0.16 ppb (parts per billion) equals ~1 mm at the Earth surface. Figure 4 depicts the scale effects when applying GPT2 vs. the observed pressure. Since the larger pressure and temperature shifts occur at some of the stations only, the effect on the network scale can only be found in the sessions that include the significantly affected stations. As a consequence, the global effect is not obvious. In both cases, pressure and temperature (not shown here), we found no clear systematic effects but large scatter at about ± 0.2 ppb. The results are very similar for GPT (not shown here). When the pressure refers to WMO mean values large scale differences occurred caused by the aforementioned shifts (Table 2).

4.3   Earth Orientation Parameters

As demonstrated in the previous sections, the choice of MD used in the analysis may affect the station coordinates and the network scale parameter of the resulting terrestrial frame. Thus, it is not surprising that the EOP slightly change as well. Since the terrestrial frame is altered one might expect effects mainly on Earth Rotation Parameters (ERP; x_{pole}, y_{pole}, and $dUT1$). Figure 5 shows the differences in Celestial Pole Offsets (CPO) when applying GPT2 instead of the observed
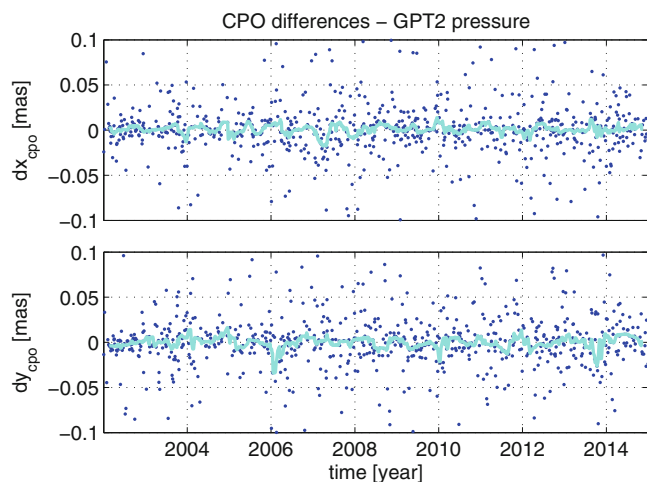
Fig. 5 CPO differences when applying GPT2 pressure instead of the observed pressure. Upper plot x_{CPO}; lower plot y_{CPO}

pressure where a small but systematic annual signal appears in the CPO differences with an amplitude of $\sim 15\mu$ as. Given the frequency relationship between the terrestrial and the celestial frame, a strictly diurnal wave (S1) in the terrestrial frame corresponds to the prograde part of any annual CPO oscillation (Richter et al. 2010). The annual signal in Fig. 5 is probably the manifestation of an uncorrected S1 effect in the ZHD component due to the usage of GPT2, which comes without a diurnal cycle. A similar effect can be found for GPT (not shown here).

5 Summary, Discussion and Conclusions

In previous works Heinkelmann et al. (2008, 2009) we assessed effects when applying the Berg model (Berg 1948) and GPT that are sometimes used in GNSS analyses instead of observed MD. We quantified the effects on Helmert parameters (translation, rotation, and network scale) between TRFs obtained by VLBI applying different MD as input. The differences between our previous work and this work are: the MD derived from the weather model ERA-40 of ECMWF were obtained by interpolation between pressure levels, whereas with our current approach we test hypsometrically adjusted surface data sets derived from ERA-Interim of ECMWF and from WMO, respectively. In addition, in our current study we include a more modern blind model, GPT2, and we extend our investigations to effects on the Earth Orientation Parameters (EOP).

The pressure enters the reduced observations on the observation level but effects are partly compensated by estimated zenith wet delays. If the zenith wet delays are of interest, this

effect can not be ignored in most cases. Because of small differences between hydrostatic and wet mapping functions and because of the different temporal resolutions (the estimated delays are usually obtained for time intervals between 30 min and 2 h that cover a large number of observations) not the entire effect is compensated. In some cases a part of the erroneous pressure propagates into geodetic parameters, e.g. at Zelenchukskaya, where it becomes obvious because of the pressure break (Fig. 3). Besides the pressure error, the size of the effect on station coordinates depends on the ratio of the mapping functions at the specific site and epoch. Apart from that, the temperature errors directly propagate into estimated parameters because antenna thermal deformations are considered on the observation level as a correction without estimation of further parameters. Besides the temperature errors, the size of this correction mainly depends on the antenna dimensions. Thermal antenna deformation is customarily not considered in routine GNSS analyses. Since the height of the GNSS antenna pillar is much smaller, temperature variations do probably play a minor role for GNSS. The effects induced by pressure, however, should be equal or very similar for GNSS because the same models are used for VLBI and GNSS data reduction.

ERA is a global model with finite resolution. It is not designed to sufficiently represent surface parameters, in particular in complex terrain. Due to this fact, ERA surface pressure cannot serve as a reference for providing the absolute pressure mean value. The WMO stations are geographically well distributed and available for free what motivates their application. The WMO surface data, however, contain a significant amount of missing registrations and errors, such as wrong names of sites, which cannot be detected easily due to the partial absence of meta data. GPT2 clearly outperforms GPT. However, both are incapable of providing inter-annual variations and both models do not cover diurnal cycles. The lacking diurnal cycles referring to TRF can manifest theirselves as annual variations referring to CRF. With VLBI it is possible to determine the effect. If observations are unevenly distributed during the day or if sub-daily parameters are estimated, further problems might occur. This needs to be investigated. For the pressure besides diurnal pressure waves, the one- to two-weekly variations that customarily dominate the total variations are not represented through GPT or GPT2. This is the main reason for the large scatter between the observed and the GPT-/GPT2-based pressure.

Various groups apply hypsometrically adjusted surface data sets for derivation of zenith wet delays from GNSS. At some sites, in particular where the height of the surface model of ERA-Interim or the height of the WMO station and the height of the space geodetic instrument differ significantly, e.g. at Kokee Park, very large pressure shifts were found. GPT and GPT2 as derived from interpolation

between data given at surrounding pressure levels of global weather models do not suffer from these shifts as much as the extrapolated surface data do. Thus, the conclusion can be made that the surface height is sometimes not representative and that the extrapolation over large height differences can introduce substantial uncertainty. The exact causes of the shifts need to be identified and it needs to be investigated whether the differences vary with time. Extrapolating surface or near-surface data to the height of the reference point of the space geodetic instrument can not be considered an accurate method to realize an absolute mean value for pressure in general. This finding is in agreement with literature, e.g. Tregoning and Herring (2006).

In this empirical analysis we have shown that the choice of MD (pressure and temperature) can have significant effects on the geodetic results determined by VLBI: station positions, network scale of TRF, and EOP. Therefore, our results obtained for VLBI contradict the findings of Ray et al. (2005), who claimed that using meteorological surface data in comparison to a global seasonal model shows no significant effects on GNSS-derived station coordinates. This requires further investigations.

References

Altamimi Z, Collilieux X, Métivier L (2011) ITRF2008: an improved solution of the international terrestrial reference frame. J Geod 85:457–473

Berg H (1948) Allgemeine Meteorologie. Dümmler, Bonn

Böhm J, Werl B, Schuh H (2006) Troposphere mapping functions for GPS and very long baseline interferometry from European Centre for Medium-Range Weather Forecasts operational analysis data. J Geophys Res 111:B02406

Böhm J, Heinkelmann R, Schuh H (2007) Short note: a global model of pressure and temperature for geodetic applications. J Geod 81:679–683

Böhm J, Heinkelmann R, Schuh H, Nothnagel A (2008) Validation of mean temperature values as provided by GPT, IVS memorandum 2008-003v02. ftp://ivscc.gsfc.nasa.gov/pub/memos/ivs-2008-003v02.pdf

Böhm J, Urquhart L, Steigenberger P et al (2012) A priori gradients in the analysis of space geodetic observations. IAG Symposium, vol. 138, pp 105–109

Böhm J, Schuh H (eds) (2013) Atmospheric effects in space geodesy. Springer Atmospheric Sciences. Springer/Dordrecht, Heidelberg/New York/London

Davis JL, Herring TA, Shapiro II et al (1985) Geodesy by radio interferometry: effects of atmospheric modeling errors on estimates of baseline length. Radio Sci 20(6):1593–1607

Dee DP, Uppala SM, Simmons AJ et al (2011) The ERA-interim reanalysis: configuration and performance of the data assimilation system. Q J R Meteorol Soc 137:553–597

Fey AL, Gordon D, Jacobs CS et al (2015) The second realization of the international celestial reference frame by very long baseline interferometry. Astron J 150:58

Gao L, Bernhardt M, Schulz K (2012) Elevation correction of ERA-Interim temperature data in complex terrain. Hydrol Earth Syst Sci 16:4661–4673

Heinkelmann R, Böhm J, Schuh H (2005) Homogenization of surface pressure recordings and its impact on long-term series of VLBI tropospheric parameters. In: Vennebusch M, Nothnagel A (eds) Proceedings of the 17th working meeting on European VLBI for geodesy and astrometry, pp 74–78

Heinkelmann R, Böhm J, Schuh H et al (2007) Combination of long time-series of troposphere zenith delays observed by VLBI. J Geod 81:483–501

Heinkelmann R, Böhm J, Schuh H (2008) Effects of surface pressure and temperature on the VLBI reference frames. In: Finkelstein A, Behrend D (eds) IVS 2008 general meeting proceedings, pp 188–192

Heinkelmann R, Böhm J, Schuh H, Tesmer V (2009) The effect of meteorological input data on the VLBI reference frames. IAG Symposium, vol. 134, pp 245–251

Heinkelmann R, Böhm J, Bolotin S et al (2011) VLBI-derived troposphere parameters during CONT08. J Geod 85:377–393

Lagler K, Schindelegger M, Böhm J et al (2013) GPT2: empirical slant delay model for radio space geodetic techniques. Geophys Res Let 40:1069–1073

Nafisi V, Madzak M, Böhm J et al (2012) Ray-traced tropospheric delays in VLBI analysis. Radio Sci 47:RS2020

Nilsson T, Soja B, Karbon M, Heinkelmann R, Schuh H (2015) Application of Kalman filtering in VLBI data analysis. Earth, Planets Space 67:136–144

Nothnagel A (2008) Conventions on thermal expansion modelling of radio telescopes for geodetic and astrometric VLBI. J Geod 83:787–792

Nothnagel A et al (2015) The IVS data input to ITRF2014. International VLBI Service for Geodesy and Astrometry. GFZ Data Services. http://doi.org/10.5880/GFZ.1.1.2015.002

Petit G, Luzum B (eds) (2010) IERS conventions (2010). IERS Technical Note 36. Verlag des Bundesamts für Kartographie und Geodäsie, Frankfurt am Main

Petrov L, Boy J-P (2004) Study of the atmospheric pressure loading signal in very long baseline interferometry observations. J Geophys Res 109:B03405

Ray J, Morrison M, Hilla S et al (2005) Geodetic sensitivity to surface meteorological data: 24-h and 6-h observing sessions. GPS Sol 9:12–20

Richter B, Engels J, Grafarend E (2010) Transformation of amplitudes and frequencies of precession and nutation of the earth's rotation vector to amplitudes and frequencies of diurnal polar motion. J Geod 84:1–18

Saastamoinen J (1972) Atmospheric correction for the troposphere and stratosphere in radio ranging of satellites. In: Henriksen SW, Mancini A, Chovitz BH (eds) The use of artificial satellites for geodesy. Geophysical Monograph Series. vol 15. American Geophysical Union (AGU), pp 247–251

Steigenberger P, Böhm J, Tesmer V (2009) Comparison of GMF/GPT with VMF1/ECMWF and implications for atmospheric loading. J Geod 83:943–951

Tregoning P, Herring TA (2006) Impact of a priori zenith hydrostatic delay errors on GPS estimates of station heights and zenith total delays. Geophys Res Let 33:L23303

History of Monitoring Earth Orientation, and Re-analyses of Old Data

Jan Vondrák

Abstract

The history of monitoring Earth orientation goes back to the end of nineteenth century, when polar motion was discovered. Description of international efforts in organizing coordinated observations to determine Earth's orientation is presented. The services, such as International Latitude Service (ILS), Bureau International de l'Heure (BIH), International Polar Motion Service (IPMS) and, finally, International Earth Rotation and Reference Systems Service (IERS), are described, as well as the observational techniques used by them. Each improvement of the techniques and their accuracies led to new discoveries and corresponding improvements of the theory of Earth's rotation. From the very beginning of these efforts, classical astrometric observations were used for almost one century. Later on, as more precise modern data obtained by space geodesy appeared, new and more accurate theories of precession-nutation became necessary. Finally, to explain the differences between the observations and theory, more and more data from other sources (mainly of geophysical origin) became necessary to be considered. These data and their effects are also shortly commented. Here we concentrate on optical astrometry that dominated throughout the twentieth century; namely we present some important re-analyses of these observations. Special attention is devoted to the re-analyses done in 1998–2012 at the Astronomical Institute, Czech Academy of Sciences. Data covering 1899.7–1992.0 were used to derive Earth orientation parameters and to improve star positions and proper motions in the Hipparcos celestial reference frame.

1   Introduction

Earth rotation in a wider sense is a total orientation of the body, defined by Earth Orientation Parameters (precession-nutation, polar motion, proper rotation – see Fig. 1), affected by:

- External torques (by the Moon, Sun, planets);
- Geophysical influences (internal composition of the Earth, transfer of mass at core-mantle boundary, geomagnetic core-mantle coupling, oceans, hydrosphere, atmosphere...).

Earth rotation has a fundamental importance in astronomy, especially for transformation between celestial and terrestrial reference systems, but also in other applications:

- geodesy, such as positioning and navigation on the Earth;
- space navigation;
- geophysics etc...

J. Vondrák (✉)

Astronomical Institute, Boční II, 141 00 Prague 4, Czech Republic
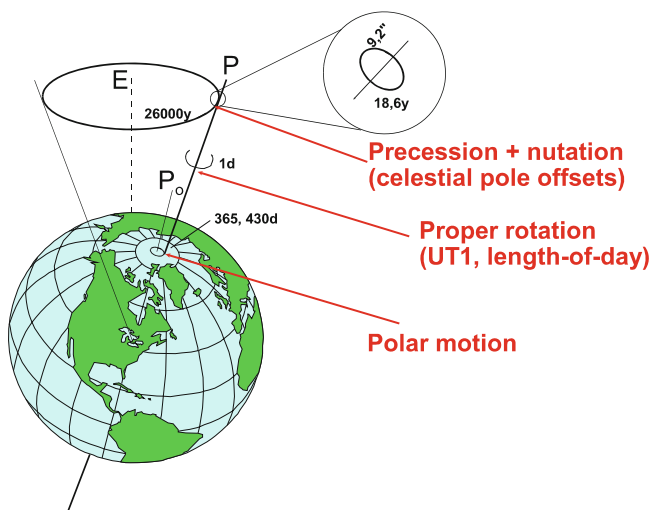e-mail: vondrak@ig.cas.cz

Fig. 1 Earth orientation parameters

Historically, the following phenomena, closely tied with the Earth's orientation, were discovered step by step:

Precession is the secular part of a more general precession-nutation motion. Since it is relatively fast (about 50″ per year), it was known already to Hipparcos (second century BC), from the observed differences of ecliptical longitudes of the stars at different epochs. As the observation techniques became more and more precise, the model of precession was improved. During the twentieth and twenty-first centuries, three models were used:

- Newcomb (1898),
- Lieske et al. (1977),
- Capitaine et al. (2003).

Polar motion was theoretically predicted as free oscillation by Leonhard Euler in 1765, with a period equal to 305 days. It was observationally first detected (from the observed changes of astronomical latitude) by Karl Friedrich Küstner in Berlin (1884–1985), and shortly afterwards confirmed by Ladislaus (László) Weinek in Prague (1889–1892). Two main components (with periods 425 and 365 days) were later determined by Seth Carlo Chandler (1891), and the difference between predicted (305 days) and observed (425 days) free oscillation periods was explained by Simon Newcomb in 1902 by non-rigidity of the Earth. Since 1899 polar motion started to be regularly monitored by different services. A concise history of its monitoring is given by Dick (2000) and other papers of the same Proceedings.

Nutation, the periodic part of precession-nutation motion, was first observed by James Bradley (1728) and theoretically explained by Leonhard Euler (1748). Its main term has amplitude of about 9″ and period 18.6a. Since then systematic improvement of the nutation theory took place,

using more and more sophisticated models of the Earth:

- Peters (1842),
- Oppolzer (1882),
- Newcomb (1898),
- Woolard (1953),
- Wahr (1981), and
- Mathews et al. (2002).

All theories before 1980 were based on rigid Earth model, the last ones (Wahr 1981; Mathews et al. 2002) refer to non-rigid Earth, considering visco-elastic mantle, fluid outer core, and some more components. All nutation theories are based on the constant of precession and main nutation term, determined from the observations.

Changes of speed of rotation – secular deceleration of Moon's motion was observed by Edmond Halley (1695), and later studied by Pierre Simon de Laplace (eighteenth century). Moon's influence on deceleration of Earth rotation was implied by George Darwin (end of nineteenth century), and secular and decadal variations were studied by Simon Newcomb (1882), Willem de Sitter (1927) and Harold Spencer Jones (1939). Seasonal (annual, semi-annual) variations were detected in the first half of the twentieth century, after quartz clocks were invented and used to compare their independent time with Universal Time, based on the rotation of the Earth. After the first findings obtained by Pavel and Uhink (1935), who mentioned that 'the observed variability that shows up in two quartz clocks is rather likely because of the variable rotation of the Earth', it was Stoyko (1936) who detected these variations.

2 Services Monitoring Earth Orientation

International Latitude Service (ILS) was established by the IAG to monitor polar motion, and was active since 1899. It consisted of the seven stations located at latitude 39°08′ (Mizusawa, Tschardjui, Kitab, Carloforte, Gaithersburg, Cincinnati, Ukiah). All stations were equipped with the same type of visual zenith telescope (see Fig. 2), used the same method of observation (Horrebow-Talcott) and observing program; the same star catalog was used to reduce the observations. More detailed history of ILS is described, e.g. by Dick (2000) or Yokoyama et al. (2000).

Bureau International de l'Heure (BIH) began its operation in 1912, but was formally established by the IAU in 1919. Its task was to unify and maintain Universal Time (UT), later on it started monitoring also polar motion. To this end, BIH used astrometric observations with various instruments,
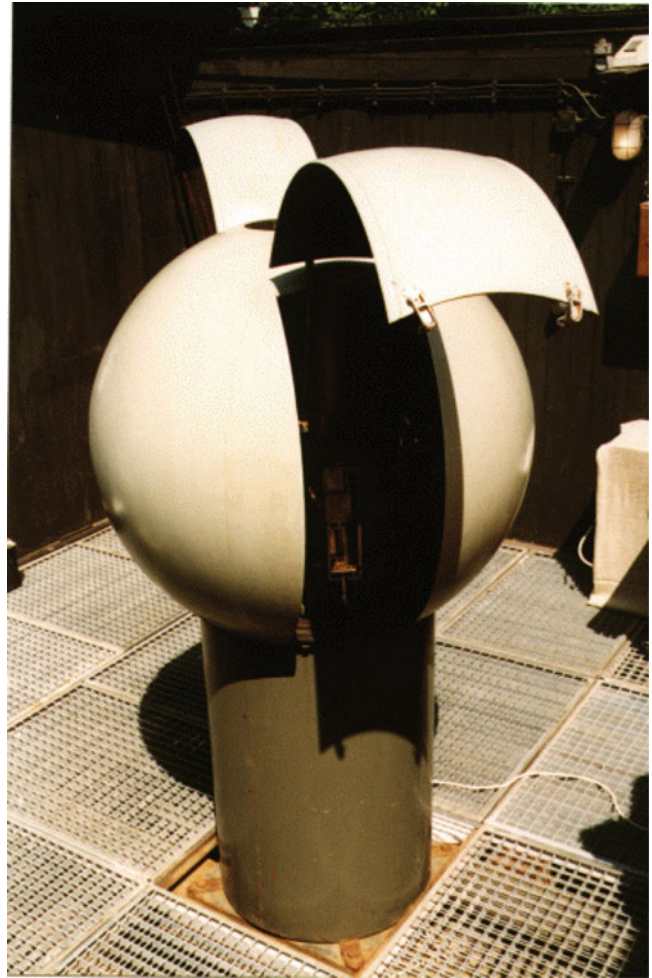
Fig. 2 Visual zenith-telescope

Fig. 3 Photographic Zenith Tube Zeiss

radio time signals were coordinated to be as close to UT as possible. More details on its history are described by Guinot (2000).

International Polar Motion Service (IPMS) was set up by the IAU and IUGG to replace ILS since 1962. IPMS used astrometric observations with different types of instruments at tens of observatories. In addition to monitoring polar motion, IPMS also measured Universal Time. Yokoyama et al. (2000) describe the history of IPMS in detail.

In addition to classical visual zenith-telescopes used by ILS, the latter two services used instruments such as, e.g., Photographic Zenith Tubes (Fig. 3) to measure both latitude and Universal Time, Transit instruments, both visual (Fig. 4) and photoelectric, to measure Universal Time, Danjon astrolabes (Fig. 5), photoelectric astrolabes (Fig. 6), or circumzenithals (Fig. 7) to measure both

latitude and Universal Time by the method of equal altitudes.

Since 1969, Doppler observations of Navy navigation satellites were also used to determine polar motion (Dahlgren Polar Monitoring Service) and integrated in the BIH and IPMS solutions.

A sort of revolutionary change took place in 1987, when International Earth Rotation Service (IERS) was set up by IAU and IUGG to replace all preceding services to monitor Earth orientation, and maintain celestial and terrestrial reference frames. In 2003 the IERS was renamed to International Earth Rotation and Reference Systems Service, but its acronym has been retained. Space geodesy techniques, such as Satellite and Lunar Laser Ranging (SLR, LLR), Very Long Baseline Interferometry (VLBI), Global Navigation Satellite Systems (GNSS), and Doppler Orbitography and Radiopositioning Integrated by Satellite

Fig. 4 Transit instrument Zeiss

(DORIS) replaced optical astrometry used so far. These techniques are now located at hundreds of sites all over the world. Unlike the preceding astrometric techniques, they are much more accurate. Completely different approach is used, both in underlying reference frames (both terrestrial and celestial) and wavelengths that are used for observation:

- For optical astrometry, terrestrial reference frame was realized by the directions of local verticals of observing sites, and celestial frame by positions and proper motions of observed stars. Observations were made in optical wavelength.
- For space geodesy techniques, terrestrial reference frame is realized by geocentric rectangular coordinates of observation sites (for satellite methods) and by directions of baselines connecting the sites (for VLBI). Celestial frame is, in principle, defined and realized by adopted positions of extragalactic radio sources (for VLBI). For satellite methods (SLR, LLR, GNSS, DORIS) its realization is accomplished by orbits of the observed objects around the Earth, whose elements must be determined together with Earth orientation parameters. Observations are made only partly in optical wavelengths (laser

Fig. 5 Danjon astrolabe

Fig. 6 Chinese photoelectric astrolabe

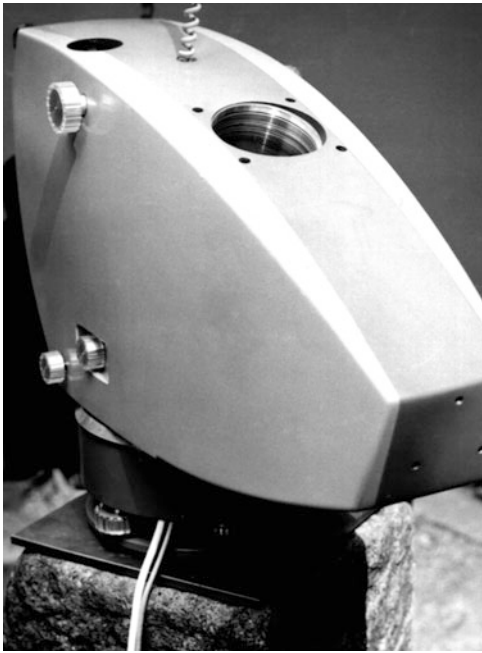ranging), mostly in radio wavelengths (VLBI, GNSS, DORIS).

Fig. 7 Circumzenithal VÚGTK

3 Role of External Torques and Geophysical Effects in Earth Orientation

From the theory of Earth rotation it follows that external torques (Moon, Sun and planets) affect:

- dominantly precession/nutation;
- about a half of changes in speed of rotation (through tidal deformation);
- only marginally polar motion.

On the other hand, geophysical influences (motion of the atmosphere, oceans, hydrosphere, geomagnetic torque between mantle and core...) affect:

- dominantly polar motion;
- about a half of changes in speed of rotation (mainly zonal winds);
- only marginally precession/nutation.

As the accuracy of observing techniques is improving, new theories are required to explain differences between theory and observations. Thus the geophysical effects are more and more important; to study these effects in detail, the IERS established IERS Global Geophysical Fluids Center, consisting of special bureaus for

- atmosphere,
- oceans,
- hydrology,

responsible for gathering relevant data and publishing corresponding excitations.

4 Re-analyses of Old Astrometric Observations

As the astrometric observations of time and latitude become more and more numerous, attempts to use them for solutions independent of those published by existing services appeared. Here we mention only some of them.

Fedorov et al. (1972) used observations of latitude variations made at 75 observatories, referred to groups of stars, and obtained polar motion in interval 1890.0–1969.0 with 0.05 year step. All observations were referred to original star catalogs, used by different observatories.

Yumi and Yokoyama (1980) re-analyzed observations made at all seven ILS stations to obtain polar motion in interval 1899.9–1979.0 with 0.05 year step. Average values of latitude from groups of stars were used, based on Melchior-Dejaiffe star catalog (Melchior and Dejaiffe 1969).

Several re-analyses of observations made by optical astrometry were worked out by Vondrák et al. (1998–2012) at the Astronomical Institute, Czech Academy of Sciences. Individual solutions, that were step by step improved, are denoted as OA97 (Vondrák et al. 1998), OA99 (Vondrák and Ron 2000), OA03 (Ron and Vondrák 2004), OA04 (Vondrák and Ron 2005), OA07 (Vondrák et al. 2008), OA09 (Vondrák et al. 2010), and OA10 (Vondrák et al. 2012), where OA stands for Optical Astrometry and the two digits denote the year of the solution. Only observations at selected best observatories were used to derive polar motion, celestial pole offsets, Universal time, and some rheological parameters of the Earth. The aim was to use star by star observations, referred to Hipparcos Catalogue (ESA 1997), as an optical realization of the International Celestial Reference Frame (ICRF).

Whole project was first proposed by Martine Feissel, then the President of IAU Commission 19 Rotation of the Earth. Working Group on Earth Rotation in Hipparcos Reference Frame was set up by the IAU in 1988 to accomplish this task, under the chair of the present author. A theoretical study (Vondrák et al. 1992) was worked out, estimating the expected accuracy of the prepared solution.

First we selected the best observatories monitoring Earth rotation since 1899, according to:

1. length of observational series;
2. stability of the results;
3. quality of observations.

Since 1991 we started collecting star by star observations from the selected observatories. The observations were

1. re-calculated with a unique system of astronomical constants and standards, based on MERIT standards (Melbourne et al. 1983) (later on, IERS Conventions Petit and Luzum 2010);

2. corrected for plate motions (NUVEL-1A model),
3. corrected for site- and/or instrument-specific corrections (due to instrumental constants, deformations of the local almucantar, oceanic tide loading effects, …), and
4. referred to the same star catalog (Hipparcos at the beginning, Earth Orientation Catalogs later on).

The Earth Orientation Catalogs (EOC) are the star catalogs based on combination of Hipparcos, Tycho-2, ARIHIP, and some other catalogs with the observations made in the programs of monitoring Earth orientation. The aim was to improve the proper motions of stars that are often not very reliable in Hipparcos Catalog, and later to add orbital motions of double or multiple stars. Thus these catalogs are 'tailored' to be used namely to reduce the observations of Earth orientation. There are four versions of the EOC:

1. EOC-1, constructed from only meridian observations, described by Ron and Vondrák (2004). It contains positions, parallaxes and proper motions of 3784 stars.
2. EOC-2, described in Vondrák and Ron (2005). Observations by all 47 instruments, covering the interval 1899.7–2003.0, were used to improve the positions and proper motions of 4418 stars.
3. EOC-3, containing positions and proper motions of 4418 stars, with periodic motions of 585 stars (Vondrák and Štefka 2007).
4. EOC-4, worked out by Vondrák and Štefka (2010) as a further improvement of EOC-3. It contains the same 4418 stars, but periodic motions of 599 stars are included.

The collected and re-reduced observations were used to obtain:

1. Polar motion in 5-day intervals (1899.7–1992.0);
2. Universal Time in 5-day intervals, since the introduction of Atomic Time (1956.0–1992.0);
3. Celestial pole offsets (1899.7–1992.0):
   - in 5-day intervals, referred to IAU1976 precession and IAU1980 nutation, in the first group of solutions (OA97, OA99);
   - quadratic representation, referred to IAU2006 precession and IAU2000 nutation, in the second group of solutions (OA03–OA10);
4. Rheological parameter $\Lambda = 1 + k - l$ (combination of Love and Shida numbers, applied to account for solid Earth tidal variations of the local vertical) for each instrument;
5. Local seasonal deviations and drifts in latitude/longitude of each instrument.

Typically, about 30,000 unknown parameters were estimated by least-squares method from almost five million observation equations. Appropriate criteria were applied to detect and to exclude the outliers; about 1–2% of observations were rejected from the final solution.
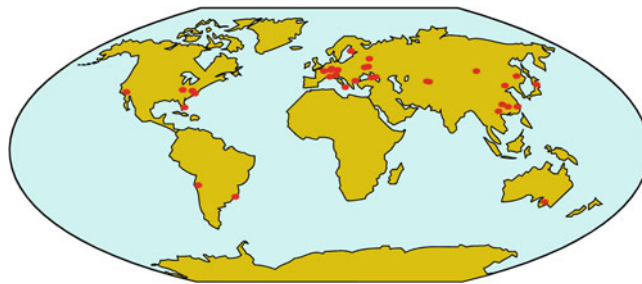

Fig. 8 Geographic distribution of participating observatories

Table 1 Solutions of EOP by optical astrometry

Name	Observatories/ instruments	Observations in millions	Catalog
OA97	31/45	4.32	HIP
OA99	33/47	4.45	HIP+corr.
OA03[a]	27/33	3.26	EOC-1
OA04	33/47	4.54	EOC-2
OA07	33/47	4.54	EOC-3
OA09	33/47	4.53	EOC-4
OA10[b]	33/47	4.51	EOC-4

[a]OA03 is based only on observations made in local meridian
[b]OA10 is linked to ITRS via IERS solution C04

Forty-seven different instruments located at 33 observatories participated with their observations in the project, their geographic distribution being depicted in Fig. 8. The observations were made by 10 photographic zenith tubes, 7 photoelectric transit instruments, 16 visual zenith-telescopes, 5 Danjon astrolabes, 6 photoelectric astrolabes, and 3 circumzenithals.

Overview of all above mentioned solutions OA is given in Table 1. For each solution, the number of observatories and instruments, approximate number of individual observations and the star catalogs that were used, are reported. Much lower number of observatories/instruments and observations of the solution OA03 is caused by the fact that only the observations made in local meridian are used (catalog EOC-1 does not contain the stars observed by the method of equal altitudes).

5 Results

Only the results of our most recent solution OA10 are shown here. The solution was constructed from 4,505,442 optical astrometry observations of individual stars, and it was linked to the ICRF via the star catalog EOC-4. Its linking to the International Terrestrial Reference Frame (ITRF) was assured from comparing it with the IERS solution C04. Only the interval 1978.0–1992.0, primarily
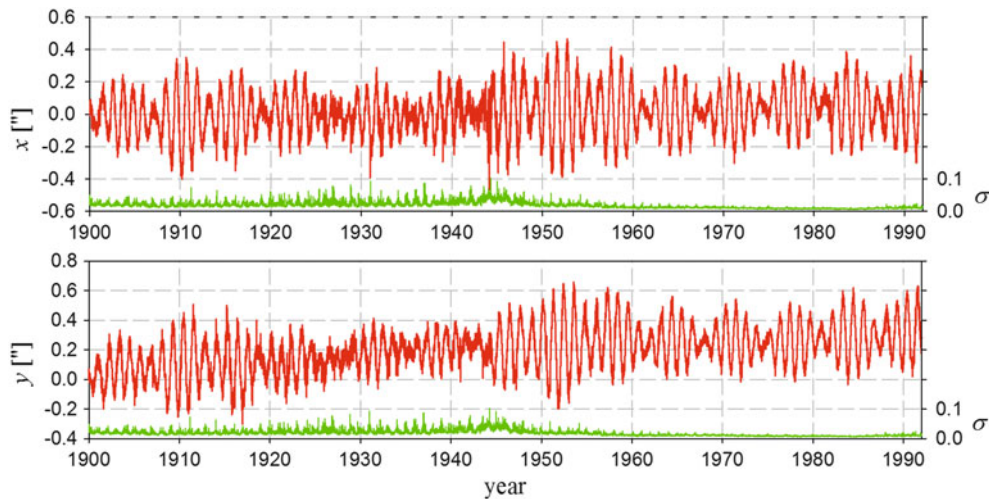
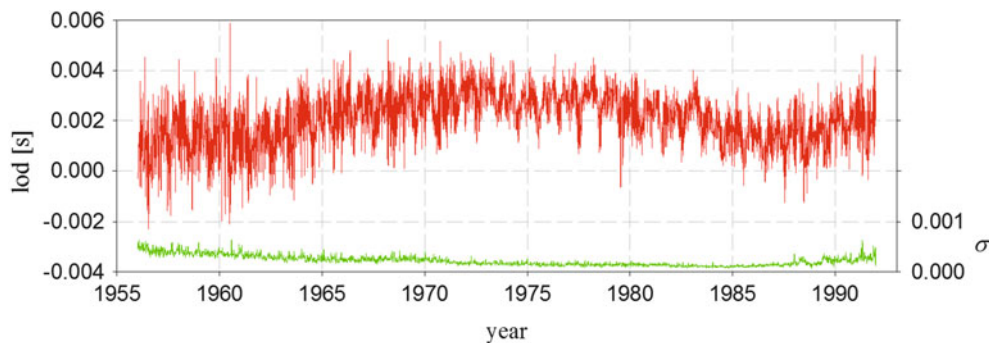**Fig. 9** Polar motion from optical astrometry

Fig. 10 Length-of-day from optical astrometry

based on modern space techniques and common to both solutions, was used to estimate a bias, linear drift and annual and semi-annual deviations. The link was estimated to be established with uncertainty of about 1–2 mas in bias, 0.09 mas/a in rotation around X, Y axes and 0.9 mas/a around Z axis.

Polar motion of the solution (its coordinates x, y) is graphically displayed in Fig. 9. Lower part of each graph depicts the uncertainties of each 5-day value shown in its upper part, in two times larger scale. The figure clearly demonstrates the secular trend towards Greenland. Periodic variations, whose amplitudes change due to interference between Chandler and annual terms, are also evident. The accuracy was worse during World War II, when European stations stopped working, and also towards the end of the interval, when new techniques became available.

Figure 10 shows the length-of-day changes, computed from Universal Time of the solution as negatively taken time derivative of UT1-TAI. Again, the uncertainties of each 5-day point are depicted in the lower part of the graph. Decadal

variations, slow secular increase, and also shorter-periodic variations (mostly due to the tides and atmospheric zonal winds) are clearly visible. The negative trend in accuracy towards the end of the interval is even more significant than in case of polar motion.

We also obtained, as a by-product of the solution, rheological parameter $\Lambda = 1 + k - l$, a combination of Love and Shida numbers, defined, e.g., by Melchior (1978). It expresses the reaction of non-rigid solid Earth to tidal forces exerted by the Moon and the Sun, causing small variations of the local verticals, with dominant semi-diurnal and diurnal periods. We derived the values of Λ for each instrument, from daily and sub-daily variations of the observed quantities. In Fig. 11 we display these values and their error bars for each observatory. The results are arranged by increasing geographic longitudes of the observatories, so that we can see any systematic differences among continents. Theoretical value of Λ is around 1.2, and our results seem to be consistent with this value. The values do not seem to be systematically different for different continents.
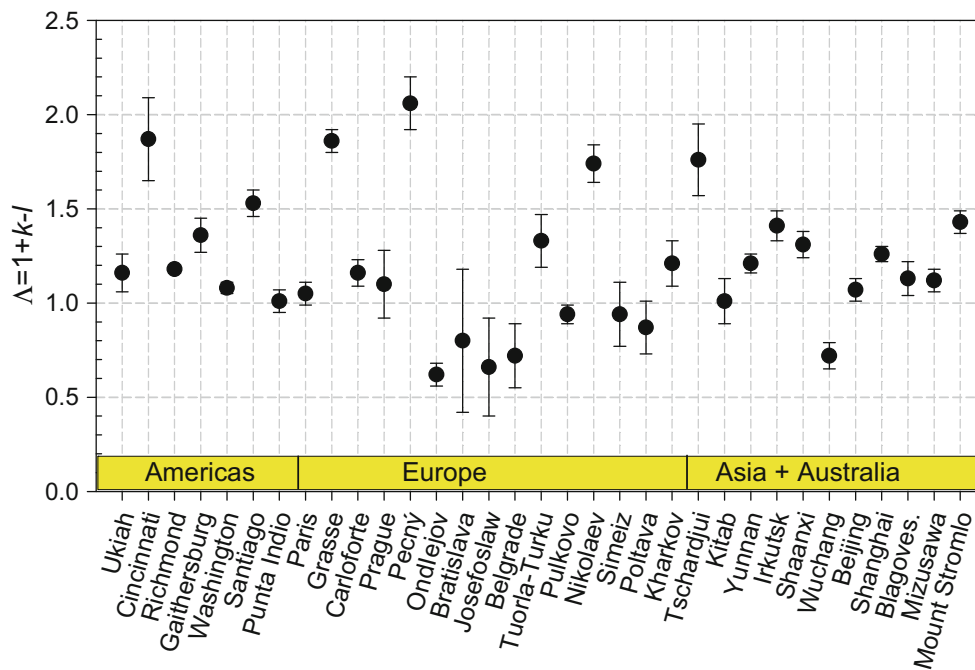
Fig. 11 Rheological parameter Λ of individual observatories

6 Conclusions

The paper describes the services monitoring Earth orientation since the end of the nineteenth century, and concentrates on the re-analyses of optical astrometry observations. In the most recent re-analysis of historical astrometric observations of Earth orientation, covering the interval 1899.7–1992.0, almost five million observations of individual stars, observed by 47 instruments located at 33 observatories were collected. They were re-reduced with the most recent astronomical constants/standards and referred to a unique celestial system, based on Hipparcos Catalog. From these observations, Earth orientation parameters plus additional local parameters were obtained. All input data and the respective solutions are archived at the Astronomical Institute of the Czech Academy of Sciences, and available on demand for further studies.

References

Capitaine N, Wallace PT, Chapront J (2003) Expressions for IAU 2000 precession quantities. Astron Astrophys 412. Doi: 10.1051/0004-6361:20031539

Dick SJ (2000) Polar motion: a historical overview on the occasion of the centennial of the International Latitude Service. In: Dick S, McCarthy DD, Luzum B (eds) Polar motion: historical and scientific problems. Proceedings of the IAU colloquium No. 178. ASP conference series, pp 3–26

ESA (1997) The Hipparcos and Tycho catalogues, ESA SP-1200

Fedorov EP, Korsuń AA, Mayor SP, Panchenko NI, Tarady VK, Yatskiv YaS (1972) Dvizhenie polyusa Zemli 1890.0–1969.0. Naukova Dumka, Kiev

Guinot B (2000) History of the Bureau International de l'Heure. In: Dick S, McCarthy DD, Luzum B (eds) Polar motion: historical and scientific problems. Proceedings of the IAU colloquium No. 178. ASP conference Series, pp 175–184

Lieske JH, Lederle T, Fricke W, Morando B (1977) Expression for the precession quantities based upon the IAU (1976) system of astronomical constants. Astron Astrophys 58:1–16

Mathews PM, Herring TA, Buffet BA (2002) Modeling of nutation and precession: new nutation series for nonrigid Earth and insights into the Earth's interior. J Geophys Res 107:B4. Doi:10.1029/2001JB000390

Melbourne W, Anderle R, Feissel M, King R, McCarthy D et al (1983) Project MERIT standards, USNO Circ. 167

Melchior P (1978) The tides of the planet Earth. Pergamon Press, Oxford

Melchior P, Dejaiffe R (1969) Calcul des déclinaisons et mouvement propres des étoiles du Service International des Latitudes à partir des catalogues méridiens. Ann Obs R Belgique 10:63–339

Newcomb S (1898) Tables of the Sun. Astronomical papers prepared for the use of the American ephemeris and nautical almanac, vol 6. U.S. Government Printing Office, Washington, DC, pp 1–169

Pavel F, Uhink W (1935) Die Quarzuhren des geodätischen Institutes in Potsdam. Astron Nachr 257:365–390

Petit G, Luzum B (eds) (2010) IERS conventions (2010). IERS Technical Note 36

Ron C, Vondrák J (2004) Earth orientation parameters in 1899–1992 based on the new Earth orientation catalogue. In: Finkelstein A, Capitaine N (eds) Journées 2003 systèmes de référence spatio-temporels, IAA St. Petersburg and Observatoire de Paris, pp 144–149

Stoyko N (1936) Sur l'irrégularité de la rotation de la Terre. C R Acad Sci 203:29

Vondrák J, Ron C (2000) Survey of observational techniques and Hipparcos reanalysis. In: Dick S, McCarthy DD, Luzum B (eds)

Polar motion: historical and scientific problems. Proceedings of the IAU colloquium No. 178. ASP Conference Series, pp 206–213

Vondrák J, Ron C (2005) Solution of Earth orientation parameters in the frame of new Earth orientation catalogue. Kinematika i fizika nebesnykh tel, Suppl Ser No. 5, pp 305–310

Vondrák J, Štefka V (2007) Combined astrometric catalogue EOC-3: an improved reference frame for long-term Earth rotation studies. Astron Astrophys 463:783–788

Vondrák J, Štefka V (2010) The Earth orientation catalog 4: an optical reference frame for monitoring Earth's orientation in the 20th century. Astron Astrophys 509:A3. Doi:10.1051/0004-6361/200912472

Vondrák J, Feissel M, Essaïfi, N (1992) Expected accuracy of the 1900–1990 Earth orientation parameters in the Hipparcos reference frame. Astron Astrophys 262:329–340

Vondrák J, Pešek I, Ron C, Čepek A (1998) Earth orientation parameters 1899.7–1992.0 in the ICRS based on the HIPPARCOS reference frame. Publication of the Astronomical Institute of the Academy of Sciences of the Czech Republic, No. 87, pp 1–56

Vondrák J, Ron C, Štefka V (2008) Solution of Earth orientation parameters in 20th century based on optical astrometry and new catalog EOC-3. In: Jin WJ, Platais I, Perryman MAC (eds) Proceedings of the IAU symposium. 248. A Giant step: from milli- to micro-arcsecond astrometry, pp 89–92

Vondrák J, Ron C, Štefka V (2010) Earth orientation parameters based on EOC-4 astrometric catalog. Acta Geodyn Geomater 7:245–251

Vondrák J, Ron C, Štefka V, Chapanov Ya (2012) New solution of Earth orientation parameters 1900–1992 from optical astrometry, and its linking to ICRF and ITRF. In: Tsvetkov MK, Dimitrijević MS, Tsvetkova K, Kounchev O, Mijajlović Zh (eds) Proceedings of the VII Bulgarian-Serbian astronomical conference, Publ. Astron. Soc 'Rudjer Bošković', pp 63–74

Wahr JM (1981) The forced nutations of an elliptical, rotating, elastic and oceanless Earth. Geophys J R Astron Soc 64:705–727

Yokoyama K, Manabe S, Sakai S (2000) History of the international polar motion service/international latitude service. In: Dick S, McCarthy DD, Luzum B (eds) Polar motion: historical and scientific problems. Proceedings of the IAU colloquium No. 178. ASP conference series, pp 147–162

Yumi S, Yokoyama K (1980) Results of the international latitude service in a homogeneous system 1899.9–1979.0. Central Bureau IPMS, Mizusawa

Advances in GNSS Technologies, Data Processing, and Applications

Multi-GNSS PPP-RTK: Mixed-Receiver Network and User Scenarios

P.J.G. Teunissen, A. Khodabandeh, and B. Zhang

Abstract

In this contribution, we present full-rank observation equations of the network and user receivers, of mixed types, through an application of $\mathcal{S}$-system theory. We discuss the important roles played by the inter system biases (ISBs), and we show how the three-component structure of PPP-RTK is affected by the inclusion of the ISBs as extra parameters in the model.

1 Introduction

In recent years, we are witnessing rapid development in the satellite-based navigation and positioning, along with launching new global and regional satellite systems. This means that many more satellites will be visible to the GNSS users, tracking data on many more frequencies than the current GPS dual-frequency setup, thereby expecting considerable improvement in the performance of the positioning and non-positioning GNSS applications (Simsky et al. 2008; de Bakker et al. 2012; Teunissen et al. 2014; He et al. 2014; Odolinski et al. 2015; Nadarajah et al. 2015).

The stated improvement may not be realized however, would one not properly integrate the multi-system, multi-frequency data. Indeed, recent contributions have revealed the existence of non-zero inter system biases – experienced

P.J.G. Teunissen (✉)
GNSS Research Centre, Department of Spatial Sciences, Curtin University of Technology, Perth, WA, Australia

Department of Geoscience and Remote Sensing, Delft University of Technology, Delft, The Netherlands
e-mail: p.teunissen@curtin.edu.au

A. Khodabandeh • B. Zhang
GNSS Research Centre, Department of Spatial Sciences, Curtin University of Technology, Perth, WA, Australia

by receivers of different types – that, if ignored, result in a catastrophic failure of integer ambiguity resolution (IAR), thus deteriorating the corresponding ambiguity-resolved solutions (Odijk and Teunissen 2013a; Paziewski and Wielgosz 2014; Nadarajah et al. 2014; Torre and Caporali 2015). The availability of the new multi-system, multi-frequency data does therefore require proper functional models so as to enable one to correctly integrate such data, thus correctly linking the data to the estimable parameters of interest.

The present contribution is intended to provide such proper functional models through a careful application of $\mathcal{S}$-system theory (Baarda 1973; Teunissen 1985). The formulations are presented within the context of IAR-enabled precise point positioning, namely, PPP-RTK (Wubbena et al. 2005; Mervart et al. 2008; Teunissen et al. 2010). With the current single-system, dual-frequency PPP-RTK setup, the network-derived satellite orbit and clock corrections are further extended by the satellite phase bias corrections to recover the integerness of the user ambiguities, making single-receiver IAR feasible, see e.g., (Laurichesse and Mercier 2007; Collins 2008; Ge et al. 2008). Single-receiver IAR would then reduce the positioning convergence time as compared to that of the standard precise point positioning (Teunissen and Khodabandeh 2015).

In this contribution we show, with the multi-system, multi-frequency PPP-RTK setup, that additional estimable network-derived corrections are needed, in order to recover

the integerness of the *entire* set of the single-receiver user's estimable ambiguities. A way to convey such additional corrections is also presented.

2 Single-System PPP-RTK

As our point of departure, we first briefly review the mechanism of single-system PPP-RTK. We will then be in a position to make a comparative analysis and identify all the subtle differences that are driven by the inclusion of additional systems.

The three components of PPP-RTK, together with their interactions, are visualized in Fig. 1 and discussed below.

2.1 Network-Component

The functionality of the network-component is to collect and process the GNSS observations. The outcomes of a least-squares network adjustment would then serve as the products well-suited to both the positioning and non-positioning users.

Consider the network receiver r ($r = 1, \ldots, n$) tracking satellite s ($s = 1, \ldots, m$) on frequency j ($j = 1, \ldots, f$). The corresponding observation equations read (Teunissen and Kleusberg 1998)

$$
\begin{aligned}
\Delta\phi_{r,j}^s &= \Delta\rho_r^s + dt_r - dt^s - \mu_j \iota_r^s + \lambda_j(z_{r,j}^s + \delta_{r,j} - \delta_{\cdot,j}^s) \\
\Delta p_{r,j}^s &= \Delta\rho_r^s + dt_r - dt^s + \mu_j \iota_r^s + d_{r,j} - d_{\cdot,j}^s
\end{aligned}
\tag{1}
$$

where $\Delta\phi_{r,j}^s$ and $\Delta p_{r,j}^s$ denote the 'observed minus computed' phase and code observations, respectively. Here and in the following, the precise orbital corrections are assumed included in $\Delta\phi_{r,j}^s$ and $\Delta p_{r,j}^s$. The increment of the geometric range, lumped with that of the zenith tropospheric

Fig. 1 Three components of PPP-RTK: (1) Network-component, (2) Correction-component and (3) User-component

delay (ZTD), is denoted by $\Delta\rho_r^s$. This increment can be further parametrized by the position and ZTD increment Δx_r through $\Delta\rho_r^s = g^{sT}\Delta x_r$, with g^s containing the receiver-satellite direction vector and the tropospheric mapping function. The common receiver and satellite clock parameters are, respectively, denoted as dt_r and dt^s that are accompanied by the frequency-dependent code receiver and satellite biases $d_{r,j}$ and $d_{\cdot,j}^s$. Ambiguities, in units of cycles, are composed of the integer part $z_{r,j}^s$ and the receiver/satellite non-integer parts $\delta_{r,j}$ and $\delta_{\cdot,j}^s$, respectively. They show themselves through the wavelengths λ_j. The (first-order) slant ionospheric delay is denoted by ι_r^s that is experienced on the first frequency. Thus we have the scalars $\mu_j = (\lambda_j^2/\lambda_1^2)$ linking the ionospheric delays to the observations. Apart from $z_{r,j}^s$, $\delta_{r,j}$ and $\delta_{\cdot,j}^s$, the rest of the quantities are all expressed in units of range.

The network's system of observation equations, as formulated in (1), is *not* yet in the form to enable one to perform the network adjustment. This is due to the fact that the information content in the observations (1) is not sufficient to determine the network's 'absolute' parameters. Only estimable combinations of the absolute parameters, the network observations are able to solve for. As shown in Teunissen and Khodabandeh (2015), a careful application of $\mathcal{S}$-system theory removes the underlying rank-deficiency of the model, thereby linking the observations to the stated estimable combinations. Through such rank-deficiency removal, a *minimum* set of parameters, the $\mathcal{S}$-basis, is chosen to make the system of equations (1) full-rank. A detailed explanation of the full-rank GNSS observation equations using the $\mathcal{S}$-system theory is presented in Odijk et al. (2015).

Given a choice of $\mathcal{S}$-basis parameters, a full-rank version of the network model (1) can be shown to be given as

$$
\begin{aligned}
\Delta\phi_{r,j}^s &= \Delta\tilde{\rho}_r^s + d\tilde{t}_r - d\tilde{t}^s - \mu_j\tilde{\iota}_r^s + \lambda_j(\tilde{z}_{r,j}^s + \tilde{\delta}_{r,j} - \tilde{\delta}_{\cdot,j}^s) \\
\Delta p_{r,j}^s &= \Delta\tilde{\rho}_r^s + d\tilde{t}_r - d\tilde{t}^s + \mu_j\tilde{\iota}_r^s + \tilde{d}_{r,j} - \tilde{d}_{\cdot,j}^s
\end{aligned}
\tag{2}
$$

with $\Delta\tilde{\rho}_r^s = g^{sT}\Delta\tilde{x}_r$. Compare the full-rank model (2) with (1). Both look identical in structure. The absolute parameters are just replaced by the corresponding estimable combinations, highlighted by the ˜-symbol. For instance, the role of the absolute slant ionospheric delay ι_r^s is now taken by its estimable counterpart $\tilde{\iota}_r^s$. Despite their resemblance however, they differ in their interpretations, i.e. $\tilde{\iota}_r^s \neq \iota_r^s$. The estimable ionospheric delay $\tilde{\iota}_r^s$ is structured by the absolute ionospheric delay ι_r^s and the geometry-free (GF) combinations of the code biases, i.e. $d_{r,GF}$ and $d_{\cdot,GF}^s$ (cf. Table 1). We recall that these geometry-free combinations are nothing else, but scaled versions of the 'differential code biases' (Schaer 1999).

Table 1 presents the interpretation of the estimable parameters involved in the network model (2), together with
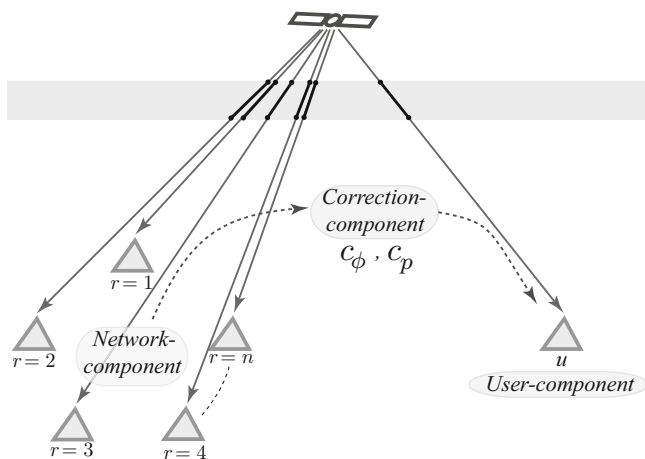
the chosen $\mathcal{S}$-basis. As shown for instance, the estimable receiver and satellite clocks are, respectively, biased by the ionosphere-free (IF) combinations of the code biases, i.e. $d_{r,IF}$ and $d^s_{,IF}$, whereas the estimable ambiguities are the double-differenced (DD) integer-valued ambiguities.

2.2 Correction-Component

Not *all* of the network's parameters, given in Table 1, are of interest to the PPP-RTK users, of course. Apart from the orbital corrections, the PPP-RTK users need to be provided with the satellite clock, phase/code bias and (sometimes) the ionospheric corrections. Here we consider the case where no ionospheric correction is provided to the user. With this in mind, the PPP-RTK corrections here are referred to as the estimable satellite clocks $d\tilde{t}^s$, phase biases $\tilde{\delta}^s_{,j}$ and, in the multi-frequency scenario ($f > 2$), the code biases $\tilde{d}^s_{,j}$. One can therefore structure the following combined corrections,

$$c^s_{\phi,j} = d\tilde{t}^s + \lambda_j \tilde{\delta}^s_{,j}$$
$$c^s_{p,j} = \begin{cases} d\tilde{t}^s & j = 1,2 \\ d\tilde{t}^s + \tilde{d}^s_{,j} & j > 2 \end{cases} \quad (3)$$

in which $c^s_{\phi,j}$ and $c^s_{p,j}$ are the combined corrections to be added to the user phase and code data, respectively.

As pointed out in the previous section, the estimable corrections do *not* represent the 'absolute' parameters, but instead *act* as such. Their interpretation changes, would the choice of the network's $\mathcal{S}$-basis change. With the aid of the interpretation given in Table 1, the combined corrections (3) can be characterized through the following *fivefold*

expressions

$$\begin{bmatrix} c^s_{\phi,j} \\ c^s_{p,j} \end{bmatrix} = \mathbf{I} - \mathbb{II}_1 - \mathbb{III}_1 - \mathbb{IV}_1 - \mathbb{V}_{[1,2]} \quad (4)$$

Each of these five terms has its own insightful functionality (cf. Table 2). The first term $\mathbf{I}$ contains the 'absolute' parameters dt^s, $\delta^s_{,j}$ and $d^s_{,j}$. Its functionality is considered to be the most primary one, since it does what it is supposed to do, namely to remove the satellite clocks, phase and code biases from the user observation equations.

The second term $\mathbb{II}_1$ contains the increment of the geo-metric/tropospheric range of the reference network receiver, i.e. $\Delta\rho^s_1$. Its functionality is therefore to establish a *positional* link between the user and the reference network receiver $r = 1$. That the first receiver is taken as the reference network is due to the choice of $\mathcal{S}$-basis by the network-component. Would one lump the geometric/tropospheric range of the second network receiver (i.e. $\Delta\rho^s_2$) with the satellite clocks, the interpretation of $\mathbb{II}_1$ would then change to

$$\mathbb{II}_1 \mapsto \mathbb{II}_2 = \begin{bmatrix} \Delta\rho^s_2 \\ \Delta\rho^s_2 \end{bmatrix}, \quad (5)$$

which then establishes a positional link between the user and the reference network receiver $r = 2$. One can also consider a more general case, when the satellite clocks are lumped with an *average* of the geometric/tropospheric ranges over all the network stations, say $\Delta\rho^s_{\bar{r}} = (1/n)\sum_{r=1}^n \Delta\rho^s_r$. Given such $\mathcal{S}$-basis, the interpretation of $\mathbb{II}_1$ changes to

$$\mathbb{II}_1 \mapsto \mathbb{II}_{\bar{r}} = \frac{1}{n}\sum_{r=1}^n \mathbb{II}_r, \quad (6)$$

Table 1 Estimable parameters formed by the chosen $\mathcal{S}$-basis of the single-system network model

Positions/ZTDs	$\Delta\tilde{x}_r = x_{1r}; \; r \neq 1$
Ionospheric delays	$\tilde{\iota}^s_r = \iota^s_r + d_{r,GF} - d^s_{,GF}$
Receiver clocks	$d\tilde{t}_r = dt_{1r} + d_{1r,IF}; \; r \neq 1$
Satellite clocks	$d\tilde{t}^s = (dt^s + d^s_{,IF}) - (dt_1 + d_{1,IF}) - g^{sT}\Delta x_1$
Ambiguities	$\tilde{z}^s_{r,j} = z^s_{1r,j} - z^1_{1r,j}; \; r \neq 1, s \neq 1,$
Rec. phase biases	$\tilde{\delta}_{r,j} = \delta_{1r,j} + \frac{1}{\lambda_j}(\mu_j d_{1r,GF} - d_{1r,IF}) + z^1_{1r,j}; \; r \neq 1$
Sat. phase biases	$\tilde{\delta}^s_{,j} = \delta^s_{,j} + \frac{1}{\lambda_j}(\mu_j[d^s_{,GF} - d_{1,GF}] - [d^s_{,IF} - d_{1,IF}]) - \delta_{1,j} - z^s_{1,j}$
Rec. code biases	$\tilde{d}_{r,j} = d_{1r,j} - (d_{1r,IF} + \mu_j d_{1r,GF}); \; r \neq 1, j > 2$
Sat. code biases	$\tilde{d}^s_{,j} = [d^s_{,j} - (d^s_{,IF} + \mu_j d^s_{,GF})] - [d_{1,j} - (d_{1,IF} + \mu_j d_{1,GF})]; \; j > 2$
$\mathcal{S}$-basis parameters	$\Delta x_1, \; dt_1, \; d_{1,j}, \; \delta_{1,j}, \; z^1_{1,j}, \; z^1_{r,j}, \; d_{r \neq 1, j=1,2}, \; d^s_{,j=1,2}$

$$(.)_{,IF} = \frac{1}{\mu_2-\mu_1}\{\mu_2(.)_{,1} - \mu_1(.)_{,2}\}; \quad (.)_{,GF} = \frac{1}{\mu_2-\mu_1}\{(.)_{,2} - (.)_{,1}\}$$

Table 2 The fivefold expression of the single-system PPP-RTK corrections, given the $\mathcal{S}$-basis in Table 1

	I		$\mathbb{II}_1$		$\mathbb{III}_1$		$\mathbb{IV}_1$		$\mathbb{V}_{[1,2]}$
$\begin{bmatrix} c^s_{\phi,j} \\ c^s_{p,j} \end{bmatrix} =$	$\begin{bmatrix} dt^s + \lambda_j \delta^s_{,j} \\ dt^s + d^s_{,j} \end{bmatrix}$	$-$	$\begin{bmatrix} \Delta\rho^s_1 \\ \Delta\rho^s_1 \end{bmatrix}$	$-$	$\begin{bmatrix} \lambda_j z^s_{1,j} \\ 0 \end{bmatrix}$	$-$	$\begin{bmatrix} \Delta dt_1 + \lambda_j \Delta\delta_{1,j} \\ \Delta dt_1 + \Delta d_{1,j} \end{bmatrix}$	$-$	$\begin{bmatrix} -\mu_j \\ +\mu_j \end{bmatrix} d^s_{,GF}$
	Absolute-term		Positional-link		Ambiguity-link		Receiver-specific link		Ionosphere-specific link

$$\Delta dt_1 = dt_1 + d_{1,IF}; \quad \Delta\delta_{1,j} = \delta_{1,j} + \frac{1}{\lambda_j}(\mu_j d_{1,GF} - d_{1,IF}); \quad \Delta d_{1,j} = d_{1,j} - (\mu_j d_{1,GF} + d_{1,IF})$$

making a positional link between the user and the average of the network receivers, i.e. $\bar{r}$.

The third term III_1 contains the integer ambiguities of the reference network receiver $r = 1$, i.e. $z_{1,j}^s$. Thus it establishes an *ambiguity* link between the user and the reference network receiver $r = 1$. Similar to the second term, one can change its dependency on the first receiver to another by changing the network's $\mathcal{S}$-basis.

The fourth term IV_1 contains the receiver-dependent parameters of the reference network receiver $r = 1$. Its functionality is to make the user receiver-dependent parameters estimable with respect to those of the reference receiver $r = 1$. Similar to the second and third terms II_1 and III_1, the interpretation of IV_1 can change, for instance, to IV_2 or $\mathrm{IV}_{\bar{r}}$, would the network's $\mathcal{S}$-basis change.

We finally consider the functionality of the last term $\mathrm{V}_{[1,2]}$. It contains the geometry-free components of the satellite code biases on the first two frequencies ($j = 1, 2$), i.e. $d_{,GF}^s$. As it is accompanied by the coefficients $[-\mu_j, \mu_j]^T$, it gets fully absorbed by the user ionospheric parameters. Due to its dependency on the network's $\mathcal{S}$-basis, the interpretation of $\mathrm{V}_{[1,2]}$ can change. One can form $d_{,GF}^s$ based on the first and *third* frequencies instead of the first and second frequencies (cf. Table 1). With such newly-defined geometry-free combinations, the last term $\mathrm{V}_{[1,2]}$ switches to $\mathrm{V}_{[1,3]}$, making a different estimable ionospheric parameter for the user.

2.3 User-Component

Replacing the subscript r by the user index u in (1), the single-receiver user observation equations follow as

$$
\begin{aligned}
\Delta\phi_{u,j}^s &= \Delta\rho_u^s + dt_u - dt^s - \mu_j \iota_u^s + \lambda_j (z_{u,j}^s + \delta_{u,j} - \delta_{,j}^s) \\
\Delta p_{u,j}^s &= \Delta\rho_u^s + dt_u - dt^s + \mu_j \iota_u^s + d_{u,j} - d_{,j}^s
\end{aligned}
\tag{7}
$$

The above user system of observation equations is not solvable for an integer ambiguity resolved position. Applying the network-derived corrections (3), the user observation equations (7) can, however, be corrected as

$$
\begin{aligned}
\Delta\phi_{u,j}^s + c_{\phi,j}^s &= \Delta\tilde{\rho}_u^s + d\tilde{t}_u - \mu_j \tilde{\iota}_u^s + \lambda_j (\tilde{z}_{u,j}^s + \tilde{\delta}_{u,j}) \\
\Delta p_{u,j}^s + c_{p,j}^s &= \Delta\tilde{\rho}_u^s + d\tilde{t}_u + \mu_j \tilde{\iota}_u^s + \tilde{d}_{u,j}
\end{aligned}
\tag{8}
$$

with $\Delta\tilde{\rho}_u^s = g^{sT} \Delta\tilde{x}_u$. The above user corrected observation equations are now solvable, but only for the estimable parameters (with the $\tilde{}$-symbol) driven by the fivefold functionality of the corrections (4). Their interpretation follows from the user version of those in Table 1, i.e. with r replaced by u. We recall the *integer-recovery* role of the ambiguity link

III_1 in (4), making the integer-recovered user ambiguities the straightforward DD ambiguities, that is

$$
\tilde{z}_{u,j}^s = z_{1u,j}^{1s} \in \mathbb{Z}, \quad s \neq 1
\tag{9}
$$

3 Multi-System PPP-RTK

In the previous section, the three components of single-system PPP-RTK were discussed. In this section, we extend the concept to q satellite systems $\star = \mathrm{G, J, \ldots, E}$. As one needs to discriminate between the satellites of different systems, our earlier satellite index 's' becomes obsolete. Instead, we make use of the satellite index $s_\star$ ($s_\star = 1_\star, \ldots, m_\star$) for the system $\star$. Although each system can broadcast signals on different frequency bands, in this study we restrict ourselves to those frequency bands that are in common with these q systems. With this in mind, our earlier frequency index 'j' now stands for the jth *overlapping* frequency of the systems. This restriction does, of course, not affect the generality of our discussion as one can apply the rank-deficiency removal to the multi-system models, of different frequencies, along similar lines as that of the single-system models.

3.1 Inter System Biases

In the multi-system case, the receiver bias delays are experienced in a *different* way from system to system, see e.g. (Hegarty et al. 2004; Montenbruck et al. 2011; Odijk and Teunissen 2013a). Under this assumption, the observation equations of the receiver r, tracking the system $\star \neq \mathrm{G}$, follow as

$$
\begin{aligned}
\Delta\phi_{r,j}^{s_\star} &= \Delta\rho_r^{s_\star} + dt_r - dt^{s_\star} - \mu_j \iota_r^{s_\star} + \lambda_j [z_{r,j}^{s_\star} + \delta_{r,j} - \delta_{,j}^{s_\star} + \delta_{r,j}^{G\star}] \\
\Delta p_{r,j}^{s_\star} &= \Delta\rho_r^{s_\star} + dt_r - dt^{s_\star} + \mu_j \iota_r^{s_\star} + d_{r,j} - d_{,j}^{s_\star} + d_{r,j}^{G\star}
\end{aligned}
\tag{10}
$$

Compare the above equations with their single-system counterparts (1). The additional parameters $\delta_{r,j}^{G\star}$ and $d_{r,j}^{G\star}$ are, respectively, referred to as the phase and code inter system biases (ISBs). They capture the difference between the receiver biases of two systems G and $\star \neq \mathrm{G}$. They are therefore, by definition, *absent* in the observation equations of the first system $\star = \mathrm{G}$. Note also that the data in (10) are registered in the 'time-system' of G, i.e. only one receiver clock dt_r is taken for all the systems. This is allowed as the difference between the time-systems of G and $\star \neq \mathrm{G}$ is fully absorbed by the satellite clocks $dt^{s_\star}$ ($s_\star = 1_\star, \ldots, m_\star$).

3.2 Network-Component Affected by the ISBs

Inclusion of the additional unknowns $\delta_{r,j}^{G\star}$ and $d_{r,j}^{G\star}$ leads to extra rank-deficiencies in the network model (10). This means that the interpretation of some of the earlier estimable parameters, given in Table 1, would change. Indeed, after the rank-deficiency removal, a full-rank form of the network model can be shown to read

$$
\begin{aligned}
\Delta\phi_{r,j}^{s_\star} &= \Delta\tilde{\rho}_r^{s_\star} + d\tilde{t}_r - d\tilde{t}^{s_\star} - \mu_j\tilde{\tilde{\iota}}_r^{s_\star} + \lambda_j[\tilde{\tilde{z}}_{r,j}^{s_\star} + \tilde{\delta}_{r,j} - \tilde{\tilde{\delta}}_{\cdot,j}^{s_\star} + \tilde{\delta}_{r,j}^{G\star}] \\
\Delta p_{r,j}^{s_\star} &= \Delta\tilde{\rho}_r^{s_\star} + d\tilde{t}_r - d\tilde{t}^{s_\star} + \mu_j\tilde{\iota}_r^{s_\star} + \tilde{d}_{r,j} - \tilde{d}_{\cdot,j}^{s_\star} + \tilde{d}_{r,j}^{G\star}
\end{aligned}
\tag{11}
$$

The two times fn number of absolute ISBs $\delta_{r,j}^{G\star}$ and $d_{r,j}^{G\star}$ are now, respectively, replaced by $f(n-1)$ number of *estimable* phase ISBs $\tilde{\delta}_{r,j}^{G\star}$ and $(f-1)(n-1)$ number of *estimable* code ISBs $\tilde{d}_{r,j}^{G\star}$ (per system $\star \neq G$). The ISBs also change the interpretation of the estimable parameters corresponding to the systems $\star \neq G$. They are highlighted by the $\tilde{\tilde{\cdot}}$-symbol rather than the $\tilde{\cdot}$-symbol. Their interpretations are given in Eqs. (12) and (17), but with the subscript r replaced by u.

3.3 Correction-Component Affected by the ISBs

As the ISB-affected network-derived estimable parameters, our earlier estimable satellite clocks $d\tilde{t}^{s_\star}$, phase biases $\tilde{\delta}_{\cdot,j}^{s_\star}$ and code biases $\tilde{d}_{\cdot,j}^{s_\star}$, of systems $\star \neq G$, are modified to

$$
\begin{aligned}
d\tilde{t}^{s_\star} &\mapsto d\tilde{\tilde{t}}^{s_\star} = d\tilde{t}^{s_\star} - d_{1,IF}^{G\star} \\
\tilde{\delta}_{\cdot,j}^{s_\star} &\mapsto \tilde{\tilde{\delta}}_{\cdot,j}^{s_\star} = \tilde{\delta}_{\cdot,j}^{s_\star} - \frac{1}{\lambda_j}(\mu_j d_{1,GF}^{G\star} - d_{1,IF}^{G\star}) - \delta_{1,j}^{G\star} \\
\tilde{d}_{\cdot,j}^{s_\star} &\mapsto \tilde{\tilde{d}}_{\cdot,j}^{s_\star} = \tilde{d}_{\cdot,j}^{s_\star} + (\mu_j d_{1,GF}^{G\star} + d_{1,IF}^{G\star}) - d_{1,j}^{G\star}; \ j > 2
\end{aligned}
\tag{12}
$$

These changes in the above PPP-RTK corrections are important, as they in turn change the estimability of the user parameters. To see this, we revisit the combined corrections (3), where the satellite index 's' is replaced by '$s_\star$'. With the link given in (12), our earlier fivefold expression (4) admits the extra term

$$
\text{VI}_1^{G\star} = \begin{bmatrix} \lambda_j \Delta\delta_{1,j}^{G\star} \\ \Delta d_{1,j}^{G\star} \end{bmatrix}
\tag{13}
$$

as follows

$$
\begin{bmatrix} c_{\phi,j}^{s_\star} \\ c_{p,j}^{s_\star} \end{bmatrix} = \text{I} - \text{II}_1 - \text{III}_1 - \text{IV}_1 - \text{V}_{[1,2]} - \text{VI}_1^{G\star}
\tag{14}
$$

where

$$
\begin{aligned}
\Delta\delta_{1,j}^{G\star} &= \delta_{1,j}^{G\star} + \frac{\mu_j}{\lambda_j}d_{1,GF}^{G\star} \\
\Delta d_{1,j}^{G\star} &= d_{1,j}^{G\star} - \mu_j d_{1,GF}^{G\star}
\end{aligned}
\tag{15}
$$

The additional term $\text{VI}_1^{G\star}$ contains the ISB parameters of the network reference receiver $r = 1$. It is absent in the first system G, and present in the systems $\star \neq G$. Its functionality is to make the user ISB parameters estimable with respect to those of the reference receiver $r = 1$. The dependency on $r = 1$ stems from the fact that the ISBs of the first network receiver, i.e. $\delta_{1,j}^{G\star}$ and $d_{1,j}^{G\star}$, are chosen as the network's $\mathcal{S}$-basis.

3.4 User-Component Affected by the ISBs

Applying the network-derived corrections (14), the multi-system user corrected observation equations follow as

$$
\begin{aligned}
\Delta\phi_{u,j}^{s_\star} + c_{\phi,j}^{s_\star} &= \Delta\tilde{\rho}_u^{s_\star} + d\tilde{t}_u - \mu_j\tilde{\tilde{\iota}}_u^{s_\star} + \lambda_j[\tilde{\tilde{z}}_{u,j}^{s_\star} + \tilde{\delta}_{u,j} + \tilde{\delta}_{u,j}^{G\star}] \\
\Delta p_{u,j}^{s_\star} + c_{p,j}^{s_\star} &= \Delta\tilde{\rho}_u^{s_\star} + d\tilde{t}_u + \mu_j\tilde{\iota}_u^{s_\star} + \tilde{d}_{u,j} + \tilde{d}_{u,j}^{G\star}
\end{aligned}
\tag{16}
$$

The above model is now solvable as it is linked to the network's $\mathcal{S}$-system. While the interpretation of the receiver specific parameters is the same as that of (8), the interpretation of the ionospheric delays and ambiguities changes, respectively, to

$$
\begin{aligned}
\tilde{\tilde{\iota}}_u^{s_\star} &= \tilde{\iota}_u^{s_\star} + d_{u,GF}^{G\star}, \\
\tilde{\tilde{z}}_{u,j}^{s_\star} &= \tilde{z}_{u,j}^{s_\star} - \tilde{z}_{u,j}^{1_\star} \in \mathbb{Z}; \quad s_\star \neq 1_\star
\end{aligned}
\tag{17}
$$

According to the user corrected model (16), the f number of *non-integer* phase ISBs $\tilde{\delta}_{u,j}^{G\star}$ take the role of the *integer* estimable ambiguities of the first satellite of each system $\star \neq G$, i.e. $\tilde{z}_{u,j}^{1_\star}$. Now the question is whether it is possible to bring back $\tilde{z}_{u,j}^{1_\star}$, thereby *maximizing* the number of integer estimable ambiguities. This would then result in an increase in the user model's redundancy. To address this question, recall that non-zero ISBs pop up, when the types of the network and user receivers are different. In case the type (i.e., make, type, firmware) of the user receiver u would be the *same* as that of a network receiver, say receiver q, their estimable code ISBs and the fractional part of their estimable phase ISBs are identical (Odijk and Teunissen 2013b). Such possibility can therefore be taken advantage of, would the network-component provide, next to the PPP-RTK corrections, a '*look-up*' table of its ISB solutions $\tilde{\delta}_{r,j}^{G\star}$ and $\tilde{d}_{r,j}^{G\star}$ for $r = 1, \ldots, n$. The user can then search the table
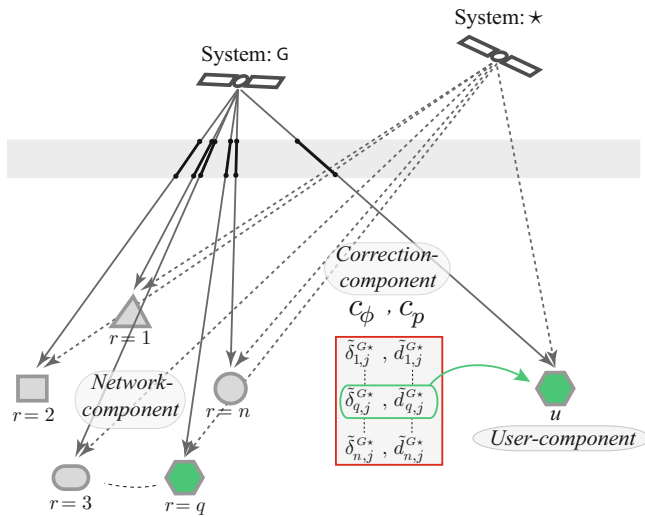
Fig. 2 Three components of multi-system PPP-RTK supported by the ISB look-up table (in *red*). Given a network of mixed-receiver types, the user '*u*' has the possibility of finding the network-derived ISBs of the network receiver of the *same* type, say $r = q$ (in *green*)

for a network receiver of the same type (i.e. receiver $r = q$) and pick up the corresponding ISBs $\tilde{\delta}_{q,j}^{\text{G}\star}$ and $\tilde{d}_{q,j}^{\text{G}\star}$ (see Fig. 2). Such a user *ISB-corrected* model reads therefore

$$
\begin{aligned}
\Delta\phi_{u,j}^{s_\star} + c_{\phi,j}^{s_\star} - \lambda_j \tilde{\delta}_{q,j}^{\text{G}\star} = \\
\Delta\tilde{\rho}_u^{s_\star} + d\tilde{t}_u - \mu_j \tilde{t}_u^{s_\star} + \lambda_j[\tilde{z}_{u,j}^{s_\star} + \tilde{\delta}_{u,j}] \\
\Delta p_{u,j}^{s_\star} + c_{p,j}^{s_\star} - \tilde{d}_{q,j}^{\text{G}\star} = \\
\Delta\tilde{\rho}_u^{s_\star} + d\tilde{t}_u + \mu_j \tilde{t}_u^{s_\star} + \tilde{d}_{u,j}
\end{aligned}
\tag{18}
$$

Compare the above model (18) with (16). The $(f - 1)$ number of code ISBs $\tilde{d}_{u,j}^{\text{G}\star}$ are corrected. Thus the model is strengthened as the model's redundancy increases by $(f - 1)$ per system $\star \neq \text{G}$. Note also that the f number of integer ambiguities $\tilde{z}_{u,j}^{1\star}$ are now recovered. Thus after integer ambiguity resolution, the redundancy even increases further by f per system $\star \neq \text{G}$.

Also compare the user ISB-corrected model (18) with its single-system counterpart (8). Both are identical in structure. Therefore, the ISB-corrected model acts as if a single-system setup is considered, with a difference, that the number of visible satellites can then be much larger than that of the single-system setup.

4   Concluding Remarks

As the network observation equations are not capable of determining the absolute parameters, the $\mathcal{S}$-system theory must be applied to remove the rank-deficiencies underlying the model, thereby identifying the interpretation of the

PPP-RTK corrections. Next to their most primary functionality, the corrections were shown to establish important links between the network and the users (cf. Table 2). In case of multi-system PPP-RTK, additional ISB parameters enter, affecting all the three components of PPP-RTK. The corrections are further biased by the ISBs (cf. (12)) and the estimability of the user ionospheric and ambiguity parameters would also change (cf. (17)). In this contribution, we proposed the network-derived ISB look-up table. Integrated with such additional information, the PPP-RTK corrections can then recover the integerness of the *entire* set of the single-receiver user's estimable ambiguities (cf. Fig. 2).

References

Baarda W (1973) S-transformations and Criterion Matrices. Technical Report, Netherlands Geodetic Commission, Publications on Geodesy, New Series, vol. 5(1), Delft

Collins P (2008) Isolating and estimating undifferenced GPS integer ambiguities. In: Proceedings of the ION NTM, pp 720–732

de Bakker PF, Tiberius CC, van der Marel H, van Bree RJ (2012) Short and zero baseline analysis of GPS L1 C/A, L5Q, GIOVE E1B, and E5aQ signals. GPS Solutions 16(1):53–64

Ge M, Gendt G, Rothacher M, Shi C, Liu J (2008) Resolution of GPS carrier-phase ambiguities in precise point positioning (PPP) with daily observations. J Geod 82(7):389–399

He H, Li J, Yang Y, Xu J, Guo H, Wang A (2014) Performance assessment of single-and dual-frequency BeiDou/GPS single-epoch kinematic positioning. GPS Solutions 18(3):393–403

Hegarty C, Powers E, Fonville B (2004) Accounting for timing biases between GPS, modernized GPS, and Galileo signals. In: Proceedings of 36th annual precise time and time interval (PTTI) meeting, Washington, DC, 7–9 Dec, pp 307–317

Laurichesse D, Mercier F (2007) Integer ambiguity resolution on undifferenced GPS phase measurements and its application to PPP. In: Proceedings of the 20th international technical meeting of the satellite division of the institute of navigation (ION GNSS 2007), pp 839–848

Mervart L, Lukes Z, Rocken C, Iwabuchi T (2008) Precise point positioning with ambiguity resolution in real-time. In: Proceedings of ION GNSS, pp 397–405

Montenbruck O, Hauschild A, Hessels U (2011) Characterization of GPS/GIOVE sensor stations in the CONGO network. GPS solutions 15(3):193–205

Nadarajah N, Teunissen PJG, Sleewaegen JM, Montenbruck O (2014) The mixed-receiver Beidou inter-satellite-type bias and its impact on RTK positioning. GPS Solutions, 1–12. Published Online

Nadarajah N, Khodabandeh A, Teunissen PJG (2015) Assessing the IRNSS L5-signal in combination with GPS, Galileo, and QZSS L5/E5a-signals for positioning and navigation. GPS Solutions, 1–9. Published Online

Odijk D, Teunissen PJG (2013a) Characterization of between-receiver GPS-Galileo inter-system biases and their effect on mixed ambiguity resolution. GPS Solutions 17(4):521–533

Odijk D, Teunissen PJG (2013b) Estimation of differential inter-system biases between the overlapping frequencies of GPS, Galileo, BeiDou and QZSS. In: Proceedings of the 4th international colloquium scientific and fundamental aspects of the Galileo programme, Prague, Czech Republic

Odijk D, Zhang B, Khodabandeh A, Odolinski R, Teunissen PJG (2015) On the estimability of parameters in undifferenced, uncombined GNSS network and PPP-RTK user models by means of S-system theory. J Geod 90(1):15–44

Odolinski R, Teunissen PJG, Odijk D (2015) Combined BDS, Galileo, QZSS and GPS single-frequency RTK. GPS Solutions 19(1):151–163

Paziewski J, Wielgosz P (2014) Assessment of GPS+Galileo and multi-frequency Galileo single-epoch precise positioning with network corrections. GPS Solutions 18(4):571–579

Schaer S (1999) Mapping and predicting the Earth's ionosphere using the global positioning system. Ph.D. Thesis, University of Bern, Bern, Switzerland

Simsky A, Mertens D, Sleewaegen JM, De Wilde W, Hollreiser M, Crisci M (2008)Multipath and tracking performance of Galileo ranging signals transmitted by GIOVE-B. In: Proceedings of ION GNSS, pp 1525–1536

Teunissen PJG (1985) Generalized inverses, adjustment, the datum problem and S-transformations. In: Grafarend EW, Sanso F (eds) Optimization and design of geodetic networks, Springer, Berlin

Teunissen PJG, Khodabandeh A (2015) Review and principles of PPP-RTK methods. J Geod 89(3):217–240

Teunissen PJG, Kleusberg A (1998) GPS for geodesy, 2nd edn. Springer, Berlin

Teunissen PJG, Odijk D, Zhang B (2010) PPP-RTK: results of CORS network-based PPP with integer ambiguity resolution. J Aeronaut Astronaut Aviat 42(4):223–229

Teunissen PJG, Odolinski R, Odijk D (2014) Instantaneous BeiDou+ GPS RTK positioning with high cut-off elevation angles. J Geod 88(4):335–350

Torre AD, Caporali A (2015) An analysis of intersystem biases for multi-GNSS positioning. GPS Solutions 19(2):297–307

Wubbena G, Schmitz M, Bagg A (2005) PPP-RTK: precise point positioning using state-space representation in RTK networks. In: Proceedings of ION GNSS, pp 13–16

A New Method for Real-Time PPP Correction Updates

Yang Gao, Wentao Zhang, and Yihe Li

Abstract

Real-time Precise Point Positioning (PPP) is expected to find more and more applications with various precise satellite orbit and clock products becoming more easily and reliably available. A crucial aspect for current real-time PPP system is the transmission of precise satellite orbit and clock correction data to the PPP users at a high update rate, typically 1–2 min for orbit corrections and 1–10 s for clock corrections. Such a high update rate is a challenge to many applications since it requires continuous data links for PPP users to timely receive the correction data. Therefore, latency and loss of the correction data incurred by the data links are major concerns in addition to communication cost. This paper describes a new correction update method with potential to address the concerns, which transmits initial parameters for orbit and clock to the users which can be at a much lower update rate. The preliminary numerical results have been provided with encouraging performance.

Keywords

Orbit and clock corrections • Orbit and clock initial parameters • PPP • Real-time

1 Introduction

Precise point positioning (PPP) is a method that performs precise position determination using a single GNSS receiver (Gao 2006). A crucial aspect in PPP is the use of precise satellite orbit and clock correction data to substantially reduce the errors in GNSS satellite orbits and clocks. With increased availability of real-time precise satellite orbit and clock correction data, real-time PPP are being performed by more and more researchers and product manufacturers who can develop the user processing algorithms and software (Bisnath and Gao 2009). In the past, real-time precise orbit and clock corrections were available only from few commercial suppliers with significant subscription fees, which were once a limiting factor for developing real-time PPP applications (Gao and Chen 2005). The development of the Networked Transport of RTCM via Internet Protocol (NTRIP) has made the correction transmission with much lower cost than the satellite-based transmission, with great potential to be widely adopted in applications (Weber et al. 2005). Real-time PPP is therefore expected to find more and more applications and become a mainstream approach for real-time precise positioning in the future.

The system architecture to implement a real-time PPP system typically consists of three major components, namely the server system, the communication system and the user system. The server system is responsible for the generation of real-time precise satellite orbit and clock correction data using GNSS observations from a network of globally distributed GNSS reference stations. The communication system is responsible for the transmission of the correction data to PPP users using either Internet connection or communication satellites. The user system is responsible to apply the correction data to mitigate the satellite orbit and clock errors and conduct precise position determination using PPP techniques. Current real-time PPP systems however have some concerns for practical applications since the satellite

Y. Gao (✉) • W. Zhang • Y. Li
University of Calgary, Calgary, AB, Canada
e-mail: ygao@ucalgary.ca

orbit and clock correction data generated at the server system are in essence the differences of precise orbit/clock with respect to the broadcast orbit/clock and therefore they must be transmitted to PPP users at a high update rate (typically 1–2 min for orbit corrections and 1–10 s for clock corrections) to ensure sufficient accuracy. Such a high update rate is a challenge to applications since it requires PPP users to maintain continuous wireless connections in order to timely receive the correction data. This makes the performance of current systems sensitive to the latency of the orbit and clock corrections and susceptible to connectivity restrictions. In real-time applications, the correction data from communication satellites could be blocked or attenuated by buildings or trees in urban canopy and loss of correction data could also occur due to poor wireless network connections (Li and Gao 2013). Loss of corrections has been reported as an issue by real-time PPP system developers. Leandro et al. (2011) pointed out that communication satellite signals are typically susceptible to frequent message packet losses depending on the user environment, such as when a receiver is operating under canopy. Further the correction data might also not be completely available during certain masking conditions. In Mozo et al. (2012), a significant effort has been made to provide robustness of the real-time PPP system solution against communication losses of different durations. A situation that can affect in-the-field real-time PPP is the temporarily loss of wireless connections with the server, for example when operating far from urban areas or main routes. The loss of correction data in turn will also reduce the availability of the PPP system due to performance degradation and re-convergence of the PPP solutions. Further, the requirement for PPP users to receive the correction data at a high update rate will result in increased communication cost and higher power consumption in the devices. This may limit the adoption of precise positioning technologies to many applications such as precise positioning with mobile devices. It is therefore important to carefully consider the bandwidth, latency and data transfer cost for correction data transmission in the development of a real-time PPP system in addition to other parameters (Bisnath and Gao 2009; Mozo et al. 2012).

In Gao et al. (2015), a new orbit and clock augmentation method has been proposed which can be applied to allow real-time PPP to work with very low update rate augmentation data. The low update rate augmentation data are initial parameters which contain the position, velocity and Solar Radiation Pressure (SRP) parameters (Herring et al. 2010; Choi et al. 2013; Li et al. 2014) for orbit and polynomial and harmonics coefficients for clock. Since the new augmentation data can be updated at a very low rate, the PPP users no longer need to receive such data from the server system as frequently as the case with current PPP systems. Therefore the above mentioned concerns can be addressed. The new method for real-time PPP correction

updates will be useful to applications that are susceptible to correction data loss such as vehicular navigation. It will also be of value to applications for reducing the communication cost of correction data, which is particularly critical for real-time PPP applications using low-cost mobile devices. In this paper, the concept of the new real-time PPP system will be described from system architecture, methods to numerical examples as well as the future work.

2 A New Real-Time PPP System

The real-time PPP system architecture based on the new correction update method is illustrated in Fig. 1, which also consists of three major system components similar to current PPP systems but their functions are different.

In the new PPP system, the server system is responsible for the generation of real-time precise satellite orbit and clock initial parameters (IPs) using GNSS observations from a network of globally distributed reference receiver stations. The initial parameters consist of initial conditions and additional crucial data for orbit and key coefficients for clock. With such initial parameters provided at selected reference time and sent to PPP users, precise orbit can be derived through numerical integration and precise clock can be obtained through extrapolation by PPP users at any epochs before next update from the server system. In this way, the update rate of the augmentation data transmitted from the server system to PPP users can be significantly lowered. Table 1 shows those initial parameters and potential update rate for each parameter. The communication system is similar to current real-time PPP systems but it differs in the data content and update rate. The user system is different from the current real-time PPP systems, which requires the user system to generate high update rate (e.g. 1–2 min for orbit and 1–10 s for clock) satellite orbit and clock corrections using the low update rate satellite orbit and clock initial parameters before precise position determination using PPP techniques. Since the precise orbit/clock is no longer sent in the form of corrections with respect to the broadcast orbit/clock which must be updated frequently, but through sets of initial parameters which can be updated much less frequently, the new real-time PPP system offers some appealing advantages. With significantly reduced update rate on initial parameters, the requirements on continuous wireless connection are also relaxed (Li et al. 2015). The new real-time PPP system will also be less susceptible to temporary poor network connection and communication satellite signal blockage in challenging environments, such as when a receiver is operating in urban canyons and under tree canopy (Leandro et al. 2011; Mozo et al. 2012). The communication cost and data service charge for real-time PPP based on with the new correction update method will be reduced as
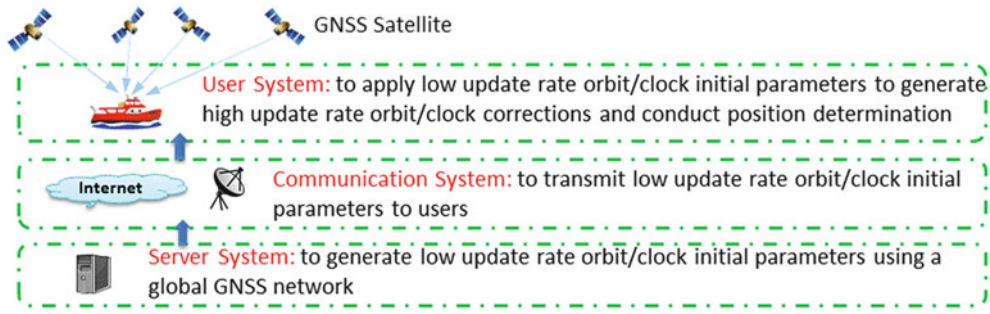
Fig. 1 PPP system architecture based on new correction update method

Table 1 Precise satellite orbit and clock initial parameters (n: satellite number)

	Item	Parameter specification	Update rate
Satellite orbit IPs	Satellite position	X, Y, Z for each satellite: 3n	1–3 h
	Satellite velocity	X, Y, Z for each satellite: 3n	1–3 h
	Satellite SRPs	5–9 SRP for each satellite: 5–9n	24 h
	EOPs	2 linear coefficients for pole, UT1 and nutation and procession	24 h
Satellite clock IPs	Polynomial terms	3 polynomial terms for each satellite: 3n	1–3 h
	Periodical terms	8 periodical terms for each satellite: 8n	1–3 h

SRP solar radiation parameter, *EOP* Earth rotation parameter (Dick and Richter 2011)

well which is beneficial to many applications such as precise positioning using low-cost mobile devices. In the remaining of the section, the methods for the generation of satellite orbit and clock initial parameters by the server system and position determination using satellite and clock initial parameters by the user system are described.

2.1 Satellite Orbit and Clock Initial Parameter Generation

For a satellite in space, given the orbit initial parameters (position $\mathbf{r}$, velocity $\dot{\mathbf{r}}$, and SPR $\mathbf{p}$) at a reference time t_0, the succeeding orbit at any time t, $\mathbf{r}(t)$, can be obtained by integrating the accelerations $\ddot{\mathbf{r}}$ in Eq. (1), as illustrated in Eq. (2) (Montenbruck and Gill 2000).

$$\ddot{\mathbf{r}}(t) = -GM \frac{\mathbf{r}}{|\mathbf{r}|^3} + a\left(t, \mathbf{r}, \dot{\mathbf{r}}, \mathbf{p}, \dots\right) \qquad (1)$$

$$\mathbf{r}(t) = \mathbf{r}(t_0) + \int_{t_0}^{t} \left[\dot{\mathbf{r}}(t_0) + \int_{t_0}^{t} \ddot{\mathbf{r}}(t)dt \right] dt \qquad (2)$$

The satellite position $\tilde{\mathbf{r}}_k$ at a specific time epoch t_k can be obtained by the following expression in a discrete form:

$$\tilde{\mathbf{r}}_k = \mathbf{h}\left(t_k, r_0, \dot{r}_0, \mathbf{p}\right) \qquad (3)$$

where $\mathbf{h}$ is a nonlinear integral function. The optimal estimates of the initial parameters can be obtained by least-squares adjustment or Kalman filtering of the following observation equations using an arc of observed orbits.

$$\mathbf{v}_k = \mathbf{r}_k - \mathbf{h}\left(t_k, \mathbf{x}_0\right) = \mathbf{r}_k - \tilde{\mathbf{r}}_k, \quad \mathbf{P}_k \qquad (4)$$

where $\mathbf{x}_0 = \begin{bmatrix} \mathbf{r}_0^T & \mathbf{v}_0^T & \mathbf{p}^T \end{bmatrix}^T$ is satellite orbit initial parameter vector at reference time t_0, $\mathbf{v}_k$ is the error (residual) vector of the predicted orbits relative to the observed one $\mathbf{r}_k$, $\mathbf{P}_k$ is the weight matrix of the observed equations which will be determined based on the accuracy of the observed orbit $\mathbf{r}_k$. For GNSS satellites, the acceleration of gravitation by the Earth, the sun, the moon, solar radiation, solid tides and ocean tides are at the magnitude of 1.0e-9 1.0 m/s^2 (Li 2016). Even the smallest one (ocean tides) could cause several centimeter orbit errors over 24 h prediction. To ensure the accuracy of the derived orbit, the forces of gravitation, solar radiation and tides exerted on the satellites that result in acceleration should be well modeled. Note that the satellite orbit integral processing is all done in the inertial system. However the observed orbits are usually described in an Earth-fixed system. Thus, one needs to first transform the satellite positions from the Earth-fixed frame into those in the inertial frame, and then estimate the initial parameters and determine the satellite positions in the inertial system. After that, the satellite position is transformed back to the Earth-fixed system from the inertial system.

The satellite clock initial parameters are estimated using the precise clock data in the same arc based on the least-

squares or Kalman filtering. The application of a linear or quadratic polynomial model is mainly decided based on whether the frequency drift of the satellite clock is noticeable or not. In fact, different satellite clocks have different characteristics of frequency drift. Besides, the pervasiveness and prominence of the periodic characteristics in most GNSS clocks indicate that these variations should be explicitly modeled in all high-accuracy applications as follows (Senior et al. 2008; Heo et al. 2010):

$$dt^s(t) = dt_s^s(t) + dt_p^s(t) + \psi(t) \tag{5}$$

where dt_s^s is the standard polynomial clock model component; dt_p^s is the periodic signals component; ψ is the generic random noise process, which is modelled as zero–mean Gaussian white noise processes. In the GPS satellite clocks, periodic signals with period of 3 h, 4 h, 6 h and 12 h were observed, which is in agreement with the results presented in Senior et al. (2008). The results of a dynamic frequency stability analysis of the GPS satellite clocks indicate that the period of the periodic signals are stable over the course of several months, suggesting that the period can be modelled as (almost) constant or as a slowly varying state. Thus, for the general GPS satellite clock, the periodic signals component of the extended clock model includes fours periods, which are modelled as constant.

2.2 Position Determination Using Satellite and Clock Initial Parameters

The work at the user system with the new method includes two parts. One is the generation of high update rate satellite orbit and clock corrections at desired epochs by numerical integration and extrapolation techniques using the low update rate satellite orbit and clock initial parameters sent from the server system. The other is similar to current systems, that is, the application of the orbit and clock corrections to mitigate the orbit and clock errors in GNSS observations. The required orbit numerical integration has been discussed in the preceding section which will increase the computational load for the user system. Zhang et al. (2008) have indicated that a three-day numerical integration takes only around 0.6 s on a 600-MHz processor with floating point unit. Considering that multi-core processors at GHz level have been widely used in mobile devices nowadays, it should not be a concern particularly considering the growing computing power of modern GNSS receivers and mobile devices. Zhang et al. (2008) have also demonstrated that it is practically feasible to derive the orbit arc without significant degradation in accuracies, as long as the used numerical integrators, force models and EOP are the same or highly similar to those used in the precise orbital determination by the server system.

As to clock extrapolation techniques, Huang et al. (2013) show promising results particularly taking into account of increased clock stability on newer GNSS satellites. The orbit/clock correction accuracies at end users therefore can be comparable to those directly sent from the server system in existing PPP systems, although the update rate of the initial parameters in the new PPP system is much lower.

3 Experiment and Results

To demonstrate the performance of the new real-time PPP system, the International GNSS Service (IGS) Real-Time Service (RTS) orbits and clocks on DOY 103, 2014 are obtained by combining IGS01 stream and broadcast ephemeris and used as the precise orbits and clocks generated by the server system. The low update rate orbit and clock initial parameters at the server system are estimated using IGS rapid precise ephemerides on the preceding day. The high update rate GPS satellite orbit and clock corrections at the user system are generated using orbit and clock initial parameters from the server system. The initial parameters at three different update rates (1 h, 2 h and 3 h) are applied to assess their impacts on positioning performance.

A comparison between the high update rate GPS satellite orbit and clock corrections generated by the user system using orbit and clock initial parameters from the server system and the high update rate IGS RTS orbit and clock corrections are first made. Table 2 contains the averaged RMS values of the user generated GPS orbit and clock corrections with respect to IGS final orbit and clock products. The averaged RMS value for satellite orbits is calculated by projecting 3D orbits into the Line-Of-Sight (LOS) direction. The RMS value for satellite clocks is calculated using the clock correction differences with respect to the IGS final clock product but with the mean value removed since it can be absorbed by the related ambiguity parameter and will not affect the user position determination. In this case, the RMS value is equal to the standard derivation (Li et al. 2015). The results in Table 2 indicate that the accuracy of the user generated orbit correction is relatively stable over the 3 h prediction (with a difference smaller than 3 cm) and is similar

Table 2 Average RMS of user generated and RTS orbit and clock corrections

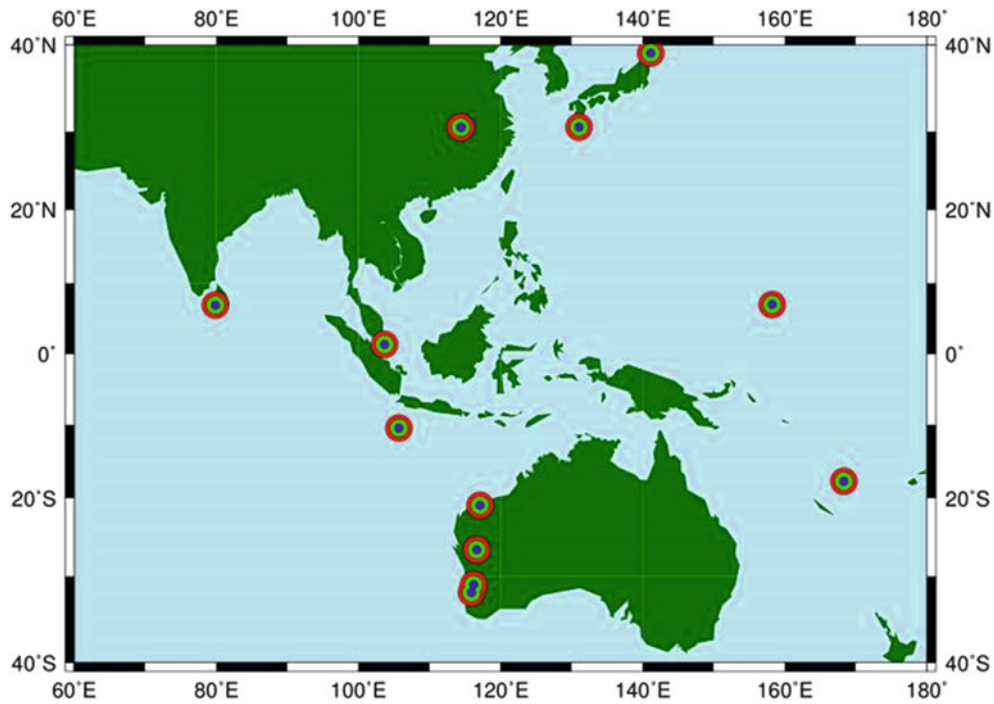| Satellite type	Orbit			Clock		
	1 h	2 h	3 h	1 h	2 h	3 h
GPS-IIA	1.2	1.3	1.3	13.5	25.0	32.5
GPS-IIR	2.3	2.5	2.7	6.9	9.2	11.0
GPS-IIR-M	2.5	2.8	2.9	4.2	6.7	10.4
GPS-IIF	2.1	2.6	2.8	4.7	9.4	14.2
GPS RTS		2.3			6.9	

Fig. 2 Distribution of testing stations for PPP

to RTS products. As for the user generated satellite clock corrections, their accuracy is stable over 1–2 h prediction for GPS IIF, IIR and IIR-M satellites and compatible to IGS RTS. But the clock on GPS IIA is not as stable as the clocks on GPS IIF/IIR/IIR-M satellites with much worse accuracy. The above is consistent to the analysis on satellite clock stability in Hesselbarth and Wanninger (2008) who show that GPS-IIF satellite clock has the best stability while GPS-IIR/IIR-M satellite clock ranks the second overall by analyzing modified Allan deviation of the satellite clock.

Static PPP processing at 12 stations distributed in the Asian-Pacific region as shown in Fig. 2 is then conducted to assess positioning performance with the new method based on ionosphere-free code and carrier phase measurements with a sampling interval of 30s and the high update rate orbit and clock corrections generated by the user system. At each station, 24 h of observation data are collected. For the purpose of comparison, PPP processing that the user directly applies IGS RTS high update rate (1 min for orbit and 10 s for clock) orbit and clock corrections is also conducted. The corresponding positioning errors are summarized in Table 3.

The results in Table 3 show that the decrease of the update rate for orbit and clock initial parameters for generating high update rate orbit and clock corrections by the user system will cause degradation in positioning accuracy when

Table 3 Positioning errors (cm) over different convergence periods

Update rate	Position components	Convergence period					
		1 h	2 h	3 h	4 h	5 h	6 h
1 h (initial parameters)	N	5.9	2.5	2.7	2.1	1.9	1.6
	E	17.2	7.9	8.7	6.1	5.7	5.2
	U	22.2	10.5	7.2	6.3	5.6	5.3
2 h (initial parameters)	N	9.4	1.9	3.1	2.6	2.7	1.9
	E	17.2	8.0	8.8	6.1	5.7	5.2
	U	24.7	9.3	7.1	12.0	10.2	7.5
3 h (initial parameters)	N	9.6	3.0	5.7	6.0	4.3	4.3
	E	17.2	12.2	12.4	14.2	9.0	8.5
	U	25.3	12.2	12.8	5.6	10.8	10.1
60s (RTS orbit) 10s (RTS clock)	N	4.8	2.2	1.7	1.9	1.7	1.7
	E	8.9	4.3	5.8	5.7	5.4	4.3
	U	9.3	5.1	4.8	4.9	5.4	5.4

compared to the case that directly applies high update rate orbit and clock corrections sent from the server system. Selection of appropriate update rate for initial parameters with respect to positioning accuracy requirements is therefore necessary which should be further investigated. The results however are encouraging since decimeter level accuracy, for instance, is obtainable with less than 1 h convergence and even centimeter level obtainable after 3 h convergence. This is very promising for many precise positioning applications.

4   Conclusions and Recommendations

A new method for real-time PPP correction update has been proposed in this paper and its performance has also been demonstrated by numerical results. The new method can reduce the update rate of the augmentation data to be transmitted from the server system to the users in a real-time PPP system. As a result, it will result in increased system availability as well as reduced communication cost since the new system will be less sensitive to the latency and outage of the augmentation data from the server system and less susceptible to connectivity restrictions. Further research on the new method is required including the investigation of appropriate update rate for orbit and clock initial parameters for applications with different accuracy requirements and the improvement of high update rate satellite orbit and clock corrections using low update rate satellite orbit and clock initial parameters in the user system. Positioning performance in kinematic mode should also be investigated.

References

Bisnath S, Gao Y (2009) Precise point positioning: a powerful technique with a promising future, innovation, GPS World, April 2009

Choi K, Ray J, Griffiths J, Bae T (2013) Evaluation of GPS orbit prediction strategies for the IGS ultra-rapid products. GPS Solut 17(3):403–412

Dick WR, Richter B (2011) International earth rotation and reference systems service (IERS), Annual Report 2008–09. Verlag des Bundesamts für Kartographie und Geodäsie, Frankfurt am Main

Gao Y (2006) GNSS solutions: precise point positioning and its challenges. Inside GNSS, November 2006

Gao Y, Chen K (2005) Performance analysis of precise point positioning using real-time orbit and clock products. J Global Positioning Syst 3(1–2):95–100

Gao Y, Zhang W, Li Y (2015) Methods and systems for performing global navigation satellite system (GNSS) orbit and clock augmentation and position determination. Patent pending

Heo YJ, Cho J, Heo MB (2010) Improving prediction accuracy of GPS satellite clocks with periodic variation behavior. Meas Sci Technol 21:073001. doi:10.1088/0957-0233/21/7/073001

Herring TA, King RW, McClusky SC (2010) GAMIT Reference Manual Release 10.4, 28 October

Hesselbarth A, Wanninger L (2008) Short-term stability of GNSS satellite clocks and its effects on precise point positioning. In: Proceedings of ION GNSS 2008, 16–19 September 2008, Savannah, pp 1855–1863

Huang G, Zhang Q, Xu G (2013) Real-time clock offset prediction with an improved model. GPS Solut 18(1):95–104

Leandro R, Landau H, Nitschke M, Glocker M, Seeger S, Chen X, Deking A, BenTahar M, Zhang F, Ferguson K, Stolz R, Talbot N, Lu G, Allison T, Brandl M, Gomez V, Cao W, Kipka A (2011) RTX positioning: the next generation of cm-accurate real-time GNSS positioning. In: Proceedings of ION GNSS 2011, 20–23 September 2011, Portland, pp 1460–1475

Li Y (2016) Real-time ambiguity-fixed precise point positioning using global and regional reference networks. University of Calgary, UCGE Report 20460

Li Y, Gao Y (2013) Navigation performance using long-term ephemeris extension for mobile device. In: Proceedings of ION GNSS 2012, 16–20 September 2013, Nashville, pp 1642–1651

Li Y, Gao Y, Li B (2014) An impact analysis of arc length on orbit prediction and clock estimation for PPP ambiguity resolution. GPS Solut 19(2):201–213

Li Y, Nie Z, Chen S, Gao Y (2015) Multiple constellation navigation performance using long-term ephemeris extension with backward error representation. In: Proceedings of ION Pacific PNT Meeting, 20–23 April 2015, pp 117–130

Montenbruck O, Gill E (2000) Satellite orbits-models, methods and applications. Springer

Mozo A, Calle D, Navarro P, Píriz R, Rodríguez D, Tobías G (2012) Demonstrating in-the-field real-time precise positioning. In: Proceedings of the ION GNSS+, 16–20 September 2013, Nashville, pp 1642–1651

Senior K, Ray JR, Beard RL (2008) Characterization of periodic variations in the GPS satellite clocks. GPS Solut 12(3):211–225

Weber G, Dettmering D, Gebhard H (2005) Networked transport of RTCM via internet protocol (NTRIP). A window on the future of geodesy. Springer

Zhang W, Venkatasubramanian V, Liu H, Phatak M, Han S (2008) SiRF InstantFix-II technology, Proceedings of ION GPS, 16–19 September 2008, Savannah, pp 1840–1847

Towards Reliable and Precise BeiDou Positioning with Stochastic Modelling

Bofeng Li and Qingzhi Hao

Abstract

The China's BeiDou system is the first global satellite navigation system to broadcast the three frequency signals for full constellation. A lot of studies have been done recently for positioning and navigation by using BeiDou three frequency signals, but mostly based on the GPS-like empirical stochastic model. This paper aims to study the stochastic modelling of BeiDou observations and then analyze its impact on the ambiguity resolution and precision positioning. To generalize the stochastic model, the satellite-dependent precisions, cross correlations between arbitrary two frequencies and time correlations for each frequency are set up. The results indicate that comparing with empirical stochastic model, the realistic stochastic model can improve the ambiguity resolution and positioning precision. Besides, the derived variance matrix of parameters with realistic stochastic model can objectively reflect the actual precisions of parameter estimates, which is rather important for solution evaluation in real applications.

1 Introduction

An adjustment equation system includes typically the functional and stochastic model. The functional model describes the relationship between observations and parameters, while the stochastic model the observation precisions and their correlations. The stochastic model is specified by the variance matrix of observations. Once the functional model is appropriately set up, one can obtain the unbiased least squares estimator with an arbitrary positive-definite variance matrix, but not the minimum variance estimator unless the correct variance matrix is applied (Koch 1999; Li et al. 2011). Therefore, the stochastic model is very important, attracting more and more research attentions.

In Global Navigation Satellite Systems (GNSS) applications, the adequate stochastic model is a pre-condition for reliable ambiguity resolution and precise positioning (Teunissen et al. 1998; Liu 2002). Refining GNSS stochastic model is a long-term aspiration (Wang et al. 2002; Tiberius and Kenselaar 2000; Li et al. 2008).

The China's BeiDou is the first GNSS system that all orbiting satellites broadcast three frequency signals. Since the Interface Control Document of China's BeiDou system was released, many folks have been intensifying their efforts to explore BeiDou's capability for ambiguity resolution and positioning (Wang and Rothacher 2013; Shi et al. 2013; He et al. 2014). However, all this performance is based on the empirical stochastic model from knowledge of GPS stochastic model. The discrepancy between BeiDou and GPS stochastic model will definitely affect the objective evaluation of BeiDou's ambiguity resolution and positioning. Actually, this discrepancy exists due to the BeiDou's satellite constellation, signal quality and rudimentary receiver level

B. Li (✉) • Q. Hao
College of Surveying and Geo-Informatics, Tongji University, Shanghai, China
e-mail: bofeng_li@tongji.edu.cn

different from GPS. Hence, it is necessary to study the BeiDou's stochastic modelling.

This paper dedicates to refining the stochastic model of BeiDou three frequency observations and then preliminarily analyse its impact on ambiguity resolution and precise positioning by comparing with empirical stochastic model that we used currently. As a case study, we use the three frequency observations collected by Trimble receivers on a short baseline. The comparisons are specified by whether taking into account the following factors in stochastic model, i.e., precision elevation-dependence, cross correlation and time correlation.

2   GNSS Model and Its Solutions

2.1   DD Observation Model

For short baseline double difference (DD) observations, the clock errors and initial phase biases of both receiver and satellite are totally eliminated, and the atmospheric biases are so small to be ignored. The single-epoch observation equations of f-frequency DD phase and code read

$$\mathrm{E}\left(\begin{bmatrix} \phi \\ p \end{bmatrix}\right) = \begin{bmatrix} e_f \otimes G \ \Lambda \otimes I_s \\ e_f \otimes G \ \ \ \ \ 0 \end{bmatrix}\begin{bmatrix} b \\ a \end{bmatrix} \qquad (1)$$

where $\phi = \left[\phi_1^T, \ldots, \phi_f^T\right]^T$ is the vector of f-frequency observed-minus-computed DD phase observations; $\phi_j = \left[\phi_j^1, \ldots, \phi_j^s\right]^T$ is the DD phase observation vector of s satellite pairs on frequency j. The code observations p and p_j have the same structures to ϕ and ϕ_j, respectively. G is the design matrix to baseline b. $\Lambda = \mathrm{diag}\left(\left[\lambda_1, \ldots, \lambda_f\right]\right)$ with λ_j the wavelength of frequency j, corresponding to DD integer ambiguities $a = \left[a_1^T, \ldots, a_f^T\right]^T$. The symbols '$\otimes$' and E denote the Kronecker product of two matrices and the expectation operator, respectively; I_s denotes the ($s \times s$) identity matrix and e_f the f-column vector with all elements of ones.

The compact form of mixed integer model (1) reads

$$y = Aa + Bb + \epsilon_y, \ Q_y = \mathrm{blkdiag}\left(Q_\phi, Q_p\right) \quad (2)$$

where $y = \left[\phi^T, p^T\right]^T \in \mathbb{R}^m$ with $m = 2fs$; $A = [1, \ 0]^T \otimes \Lambda \otimes I_s$ and $B = e_{2f} \otimes G$. $a \in \mathbb{Z}^n$ with $n = fs$ and $b \in \mathbb{R}^3$ are integer and real parameters, respectively. ϵ_y is the random noise assumed to be normal distribution with zero mean and variance matrix of Q_y, where Q_ϕ and Q_p are the variance matrices of DD phase and code observations. blkdiag is the operator of block diagonal concatenation of matrices.

2.2   Float and Fixed Solutions

In general, a three-step procedure is employed to solve model (2) based on least squares criterion.

Step 1: Float Solution The integer property of a is disregarded, and the so-called float solution is obtained,

$$\begin{bmatrix} \hat{a} \\ \hat{b} \end{bmatrix} = \begin{bmatrix} Q_{\hat{a}} \ Q_{\hat{a}\hat{b}} \\ Q_{\hat{b}\hat{a}} \ Q_{\hat{b}} \end{bmatrix}\begin{bmatrix} A^T Q_y^{-1} y \\ B^T Q_y^{-1} y \end{bmatrix} \qquad (3)$$

where

$$\begin{bmatrix} Q_{\hat{a}} \ Q_{\hat{a}\hat{b}} \\ Q_{\hat{b}\hat{a}} \ Q_{\hat{b}} \end{bmatrix} = \begin{bmatrix} A^T Q_y^{-1} A \ A^T Q_y^{-1} B \\ B^T Q_y^{-1} A \ B^T Q_y^{-1} B \end{bmatrix}^{-1}$$

Step 2: Integer Estimation The float ambiguity estimate $\hat{a}$ is used to compute its integer counterpart, denoted as

$$\check{a} = I(\hat{a}) \qquad (4)$$

with $I : \mathbb{R}^n \mapsto \mathbb{Z}^n$ the integer mapping from the reals to the integers. Different choices of mapping function correspond to different integer estimation methods. Of all choices, integer least squares is optimal (Teunissen 1999).

Step 3: Fixed Solution The float baseline solution is updated using the fixed integer parameters,

$$\check{b} = \hat{b} - Q_{\hat{b}\hat{a}} Q_{\hat{b}}^{-1}(\hat{a} - \check{a}) \quad Q_{\check{b}} = Q_{\hat{b}} - Q_{\hat{b}\hat{a}} Q_{\hat{b}}^{-1} Q_{\hat{a}\hat{b}}, \qquad (5)$$

In general, $Q_{\check{b}} \ll Q_{\hat{b}}$ reveals that fixed solution is more precise than float solution. However, this inequality holds true only when the success rate is sufficiently close to 1. If the success rate is not sufficiently high, the fixed solution $\check{b}$ is not necessarily more precise (Verhagen et al. 2013; Li et al. 2014).

3   Stochastic Model Estimation

3.1   Formulation of Unknown Variance Model

The following assumptions are made on the unknown variance matrix. The unknown variance is assigned to individual satellite. The cross correlation is set up between arbitrary two frequencies for phase and code respectively. The time correlation is assigned to each observation type. Based on these assumptions, the variance matrix of K-epoch undifference

observations is then symbolized as

$$\boldsymbol{Q}_y = \boldsymbol{Q}_T \otimes \boldsymbol{Q}_C \otimes \boldsymbol{Q}_E \qquad (6)$$

where the matrices $\boldsymbol{Q}_T$, $\boldsymbol{Q}_C$=blkdiag($\boldsymbol{Q}_{C,\phi}, \boldsymbol{Q}_{C,p}$) and $\boldsymbol{Q}_E$ are defined as follows:

$$\boldsymbol{Q}_T = \begin{bmatrix} 1 & \sigma_{[1]} & \dots & \sigma_{[K-1]} \\ \sigma_{[1]} & 1 & & \sigma_{[K-2]} \\ & \vdots & \ddots & \vdots \\ \sigma_{[K-1]} & \sigma_{[K-2]} & \cdots & 1 \end{bmatrix} \qquad (7)$$

$$\boldsymbol{Q}_{C,\phi} = \begin{bmatrix} \sigma_{\phi_1}^2 & \sigma_{\phi_1\phi_2} & \sigma_{\phi_1\phi_3} \\ \sigma_{\phi_1\phi_2} & \sigma_{\phi_2}^2 & \sigma_{\phi_2\phi_3} \\ \sigma_{\phi_1\phi_3} & \sigma_{\phi_2\phi_3} & \sigma_{\phi_3}^2 \end{bmatrix} \qquad (8)$$

and

$$\boldsymbol{Q}_E = \mathrm{diag}\left(\left[\sigma_1^2, \dots, \sigma_s^2\right]\right) \qquad (9)$$

where the $K \times K$ Toeplits matrix $\boldsymbol{Q}_T$ represents the time correlation. The diagonal entries of $\boldsymbol{Q}_{C,\phi}$ capture the frequency-specific phase precisions, while the off-diagonals the between-frequency (cross) correlations. $\boldsymbol{Q}_E$ captures the satellite-specific precisions, which may be expressed with an elevation-dependent function (Li 2016)

$$\sigma_s = c_0 / (\sin\theta_s + c_1) \qquad (10)$$

where c_0 and c_1 are two parameters of elevation-dependent function. They differ from observation types. θ_s is the elevation of satellite s.

The DD observations are formed from the between-receiver SD observations by multiplying the transformation matrix $\boldsymbol{I}_K \otimes \boldsymbol{I}_{2f} \otimes \boldsymbol{D}^T$. $\boldsymbol{D}^T$ is difference matrix, for instance, $\boldsymbol{D}^T = [-\boldsymbol{e}_{s-1}, \boldsymbol{I}_{s-1}]$ with first satellite as pivot. In terms of error propagation law, the variance matrix of DD observations follows

$$\boldsymbol{Q}_y = 2\boldsymbol{Q}_T \otimes \boldsymbol{Q}_C \otimes \left(\boldsymbol{D}^T \boldsymbol{Q}_E \boldsymbol{D}\right) \qquad (11)$$

where the scalar '2' stands for transformation from undifference to between-receiver single difference.

3.2 LS-VCE for Estimating Stochastic Model

To estimate the unknown variance and covariance components, we refer to least squares variance component estimation (LS-VCE) method due to its superior properties

(Teunissen and Amiri-Simkooei 2008). We implement LS-VCE after integer ambiguities are fixed. The observation model becomes

$$\mathrm{E}\left(\boldsymbol{y} - \boldsymbol{A}\breve{\boldsymbol{a}}\right) = \boldsymbol{B}\boldsymbol{b}, \ \boldsymbol{Q}_y = \boldsymbol{Q}_0 + \sum_{k=1}^{p} \sigma_k \boldsymbol{U}_k \qquad (12)$$

where $\boldsymbol{Q}_y$ is decomposed into the known part $\boldsymbol{Q}_0$ and the unknown part specified by p unknown variances and covariances σ_k and their associated cofactor matrices $\boldsymbol{U}_k$. The LS-VCE normal equation reads

$$\boldsymbol{N}\hat{\boldsymbol{\sigma}} = \boldsymbol{\omega} \qquad (13)$$

where $\hat{\boldsymbol{\sigma}} = \left[\hat{\sigma}_1, \dots, \hat{\sigma}_p\right]^T$ and the entries of normal matrix $\boldsymbol{N}$ and vector $\boldsymbol{\omega}$ are

$$n_{kl} = \mathrm{tr}\left(\boldsymbol{U}_k \boldsymbol{Q}_y^{-1} \boldsymbol{P}_B^{\perp} \boldsymbol{U}_l \boldsymbol{Q}_y^{-1} \boldsymbol{P}_B^{\perp}\right) \qquad (14)$$

$$\omega_k = \breve{\epsilon}^T \boldsymbol{Q}_y^{-1} \boldsymbol{U}_k \boldsymbol{Q}_y^{-1} \breve{\epsilon} - \mathrm{tr}\left(\boldsymbol{U}_k \boldsymbol{Q}_y^{-1} \boldsymbol{P}_B^{\perp} \boldsymbol{Q}_0 \boldsymbol{Q}_y^{-1} \boldsymbol{P}_B^{\perp}\right) \qquad (15)$$

with project matrix $\boldsymbol{P}_B^{\perp} = \boldsymbol{I} - \boldsymbol{B}\left(\boldsymbol{B}^T \boldsymbol{Q}_y^{-1} \boldsymbol{B}\right)^{-1} \boldsymbol{B}^T \boldsymbol{Q}_y^{-1}$. Obviously, LS-VCE needs iterative computations since the unknown variance matrix $\boldsymbol{Q}_y$ is involved in normal equation. Usually, giving initial values of unknowns denoted by $\sigma_k^0, (k = 1, \dots, p)$, one computes the more precise unknowns. The iteration continues until the obtained unknowns between two consecutive iterations are stationary.

Many variance and covariance unknowns are involved in unknown variance matrix, which may lead to instable estimates or even negative variances and nonsense correlation coefficients. To stabilize the VCE solutions and reduce the computation complexity, a stepwise estimation procedure is advised:

- Estimate two parameters of elevation-dependent function for each observation type;
- Estimate the cross correlation coefficients for phase and code, respectively;
- Estimate the time correlation coefficients for phase and code of each frequency as a function of time lags.

4 Real Data Processing and Analysis

Two Trimble receivers with NetR9 antennas were employed to collect three frequency BeiDou data on a short baseline of 4.27 m. The baseline coordinates are precisely known. Two 24-hour datasets were collected with sampling interval

Table 1 The estimated parameters of elevation-dependent precision model for three frequency observations. The unit $\hat{c}_0$ is meter for code and millimeter for phase

	B1		B2		B3	
	$\hat{c}_0$	$\hat{c}_1$	$\hat{c}_0$	$\hat{c}_1$	$\hat{c}_0$	$\hat{c}_1$
Phase	0.72	0.15	0.72	0.04	0.67	0.15
Code	0.37	0.18	0.33	0.38	0.25	0.27

Table 2 The estimated 6 cross correlation coefficients

ϱ_{ϕ_1,ϕ_2}	ϱ_{ϕ_1,ϕ_3}	ϱ_{ϕ_2,ϕ_3}	ϱ_{p_1,p_2}	ϱ_{p_1,p_3}	ϱ_{p_2,p_3}
-0.33	-0.35	-0.38	0.06	0.08	0.53
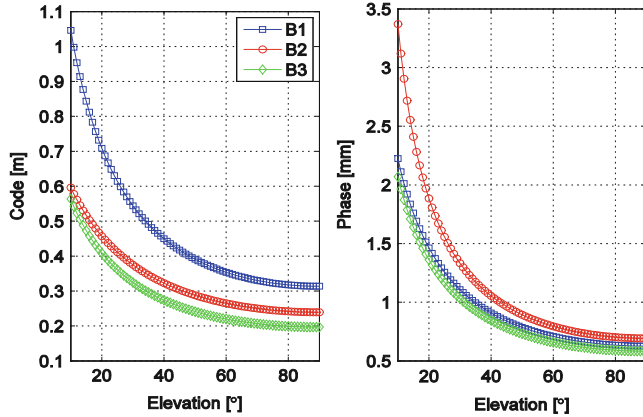
Fig. 1 The observation precisions as function of elevations
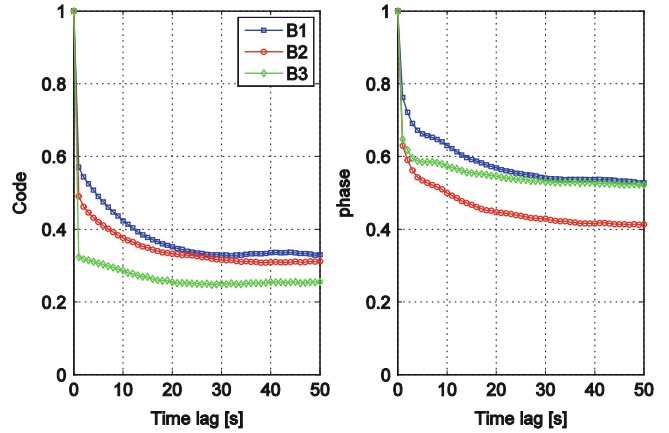
Fig. 2 The time correlation coefficients as function of time lags

of 1 s. Following the proposed VCE procedure, the realistic BeiDou stochastic model was estimated by using the first dataset, where the single epoch ambiguity resolution was successfully implemented by using LAMBDA method (Teunissen 1995). The impacts of realistic stochastic model were investigated on ambiguity resolution and positioning based on the second dataset by comparing with empirical stochastic model.

4.1 Estimation of Realistic Stochastic Model

We first study the observation precisions and their elevation dependence. Given the data window $K = 200$, we estimate the parameters c_0 and c_1 of elevation-dependent function for all observation types. Total 432 sets of parameters, i.e., 432 data windows, are obtained. The mean of parameters over all sets are as the final estimates, shown in Table 1. With estimated parameters, $\hat{c}_0$ and $\hat{c}_1$, the elevation-dependent precisions are illustrated in Fig. 1. The results show that the observation precisions are elevation-dependent for all three frequency phase and code. For code, B1 is worst and B3 is most precise. For phase, B1 and B3 have comparable precisions while B2 is much worse than them especially for lower elevations.

With fixing observation precisions obtained previously, we estimate 6 cross correlation coefficients for each data window. The mean cross correlation coefficients of all 432 sets are finally obtained, presenting in Table 2. The negative

cross correlations exist for phase with correlation coefficients -0.33, -0.35 and -0.38 for (B1, B2), (B1, B3) and (B2, B3). Such moderate correlations should be properly considered in data processing. For code, B3 is significantly correlated with B2 and the mean correlation coefficient is as large as 0.53.

Figure 2 shows the time correlation coefficients of all observation types as function of time lags. The time correlations differ significantly from phase and code as well as frequencies. The time correlation coefficients are ordered in descending by B1, B2 and B3 for code while by B1, B3 and B2 for phase over all time lags. For 1 s time lag, the time correlations of phase are much larger than those of code. In general, the time correlations have a quick decrease for smaller time lags, while slow decrease for larger time lags.

4.2 Positioning with Realistic Stochastic Model

With realistic stochastic model estimated based on the first dataset, we will investigate its impacts on ambiguity resolution (AR) and positioning by using the second dataset. First, the single-frequency observations are used to conduct the single epoch AR, where the realistic and empirical stochastic models specified by elevation-dependent and -independent precisions are applied, respectively. In elevation-independent model, the precisions of undifferenced phase and code are empirically taken by 2 mm and 0.2 m, respectively. Based on the whole dataset, all integer ambiguities are correctly fixed as references. Comparing with these integer references, the percentages of successful AR are obtained for realistic and

Table 3 The single-frequency baseline solutions with elevation-dependent and empirical stochastic model

		B1			B2			B3		
		N	E	U	N	E	U	N	E	U
Realisitic [mm]	Mean	0.7	−0.0	−0.4	0.5	−0.5	−2.4	0.0	−0.8	−0.5
	STD	2.6	2.1	5.9	2.9	2.2	6.2	2.5	2.2	5.8
	RMS	2.7	2.1	5.9	2.9	2.2	6.6	2.5	2.2	5.8
Empirical [mm]	Mean	1.3	0.2	1.3	0.6	−0.4	−1.4	−0.4	−1.5	−1.6
	STD	3.1	2.3	6.4	3.3	2.4	7.1	3.0	2.3	6.3
	RMS	3.4	2.3	6.5	3.4	2.4	7.2	3.0	2.7	6.5
RMS improvement	[%]	21.2	9.0	10.3	14.7	7.7	7.8	15.8	17.3	10.4

empirical stochastic model, respectively. Here the percentage of successful AR is defined as the fraction of the number of epochs with correct AR relative to the total number of epochs. With realistic stochastic model, the percentages of successful AR are 99.7, 99.8% and 99.8% for B1, B2 and B3, respectively; while with empirical stochastic model, they are 98.6, 99.8% and 99.8%. The results are comparable between two stochastic models only a very slight improvement is received by B1 with realistic model. The reason is that the baseline is too short such that the incorrect stochastic model has very little impact on AR.

In addition, we analyze the single epoch baseline solutions with two stochastic models. Excluding the epochs with wrong integer solutions, we compute the statistics, mean, standard deviation (STD) and root mean square error (RMS) by using the baseline errors. Baseline error is here defined as the difference of baseline solution from its true value. The results are presented in Table 3. For such short baseline, the millimeter accuracy baseline solution is achievable with single-frequency observations. Although the baseline solutions are very accurate even with empirical stochastic model, they are still improved by about 10–20%, shown in last row of Table 3.

To investigate the impact of cross correlation on positioning, B2 and B3 code observations are used to solve baseline epoch by epoch, where B2 and B3 is strongly correlated with correlation coefficient 0.53 in Table 2. Two stochastic models are designed, identified by whether the cross correlation with $\varrho_{p_2 p_3} = 0.53$ is taken into account or not. For two stochastic models, we compute the LS baseline solutions and their theoretical precisions (formal STDs) in north (N), east (E) and up (U) directions epoch by epoch. The baseline solutions are practically same for two stochastic models with differences in level of 10^{-12} mm though they are not shown here. In other words, the cross correlation has no impact on baseline solutions in case of $\sigma_{p_2} \approx \sigma_{p_3}$ see Li (2016) for proof.

However, the cross correlation has serious impact on the derived formal STDs of baseline solutions. That is the formal STDs with realistic stochastic model of $\varrho_{p_2 p_3} =$
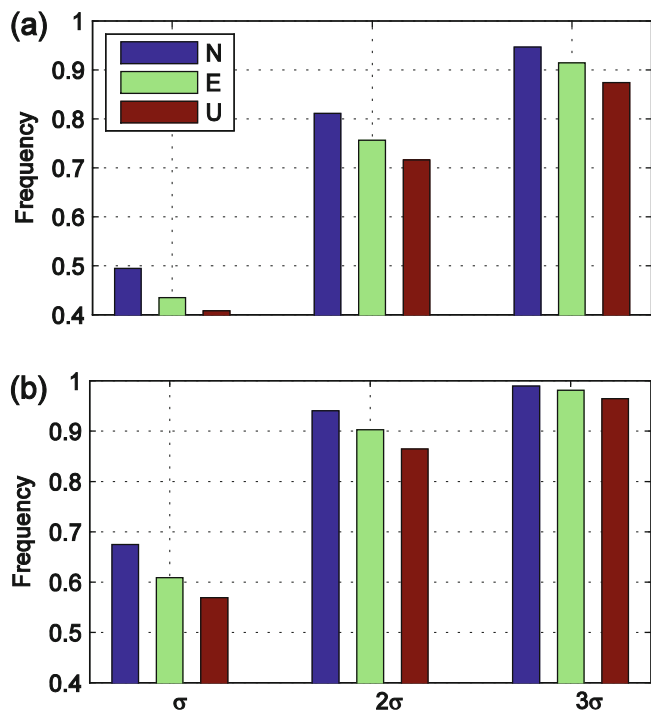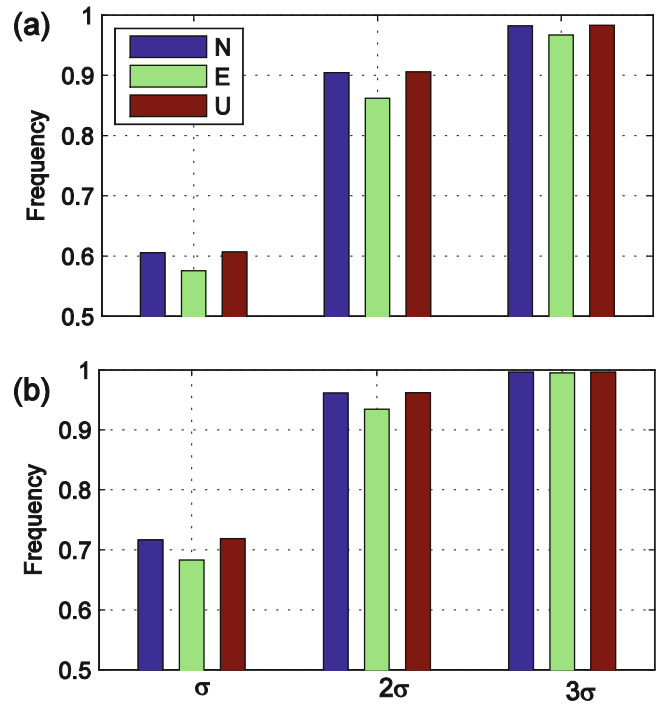

Fig. 3 The frequencies of baseline errors insides the confidence intervals defined by scaled their formal STDs with two stochastic models specified by ignoring (**a**) and considering (**b**) **cross correlations**, respectively

0.53 can reflect the actual precisions of baseline solutions, while those with empirical stochastic model of $\varrho_{p_2 p_3} = 0$ are usually too optimal (smaller). To verify this point, we compute the frequency of baseline errors inside an interval defined by their corresponding formal STDs. Let the baseline error at epoch k as $\hat{\epsilon}_k$ and its associate formal STD $\hat{\sigma}_k$. In principle, the probability of baseline error inside the interval $[-\beta\hat{\sigma}_k, \beta\hat{\sigma}_k]$ is $P(\beta) = \int_{-\beta}^{\beta} \frac{1}{\sqrt{2\pi}} e^{-x^2/2} dx$, and therefore $P(1) = 0.683$, $P(2) = 0.955$ and $P(3) = 0.997$. For all m epochs, we count the number of epochs for which the baseline error is inside the given interval, say, n. Then the frequency n/m should approximate the theoretical probability very well if the formal STD is realistic. With $\beta = 1, 2$ and 3,

the frequencies of baseline errors with two stochastic models are shown in Fig. 3. Obviously, the frequencies with realistic stochastic model of considered cross correlation are more close to the theoretical values. In other words, the formal STD with considered cross correlation is more reasonable to evaluate the baseline solutions.

Finally, we demonstrate the impact of time correlation on positioning. We solve the baseline by using B1 code observations of two consecutive epochs. Two stochastic models are examined, identified by whether considering the time correlation with $\varrho_{[1]} = 0.58$ sampled from Fig. 2. We compute the baseline solutions with two stochastic models for every two epochs, and total obtain 43,200 baseline solutions for each stochastic models. Again the baseline solutions (not shown here) are very close between both stochastic models. It makes sense and can be explained as follows. Let the observations of two consecutive epochs y_1 and y_2, the design matrices A_1 and A_2 and the variance matrices Q_1 and Q_2. Due to very small sampling interval of 1 s, it is adequate that $A_1 \approx A_2 \equiv A$ and $Q_1 \approx Q_2 \equiv Q$. It is easy to derive the normal equation as $2A^T Q^{-1} A\hat{b} = A^T Q^{-1} (y_1 + y_2)$ and $\frac{2}{1+\rho_{[1]}} A^T Q^{-1} A\hat{b} = \frac{1}{1+\rho_{[1]}} A^T Q^{-1} (y_1 + y_2)$ when ignoring and considering the time correlation, respectively. These two normal equations are exactly the same for solving the baseline $\hat{b}$.

Let us focus on analysis of formal STDs obtained with realistic stochastic model by considering the time correlations. Similar to analyzing the cross correlation, we compute the frequencies of baseline errors inside the confidence intervals defined by the formal STDs. The results are shown in Fig. 4. Again, the frequencies with realistic stochastic model of considering time correlations are more close to the theoretical probabilities than those with empirical stochastic model of ignoring time correlations.

To further verify the point that the formal STDs obtained with realistic stochastic model of considering time correlations can reflect the actual precisions of baseline errors. We compute the actual STD of baseline errors themselves. Let baseline solution series as $\hat{x}_1, \ldots, \hat{x}_n$. Due to the time correlation of observations, the time-close solutions are correlated as well. To eliminate the impact of time correlation, we use a new series $\hat{x}_k, \hat{x}_{k+\tau}, \hat{x}_{k+2\tau}, \ldots$ sampled from the original series with interval of τ to compute the actual STDs of baseline errors. With $\tau = 300s$ as example, we compute actual STDs of baseline errors. The results are shown in Fig. 5, comparing with the formal STDs obtained with realistic and empirical stochastic model by considering and ignoring time correlations. As expected, the formal STDs obtained with realistic stochastic model match with the actual STDs very well; whereas the formal STDs with empirical

Fig. 4 The frequencies of baseline errors insides the confidence intervals defined by scaled their formal STDs with two stochastic models specified by ignoring (**a**) and considering (**b**) **time correlations**, respectively

stochastic model are overall smaller, namely, too optimal but not realistic.

5 Concluding Remarks

We have preliminarily studied the stochastic modelling of three frequency BeiDou signals and analyzed its impacts on the ambiguity resolution and precise positioning. Based on the results from a short baseline of Trimble receivers, the conclusions are summarized as follows. With the realistic stochastic model, the percentage of successful AR can be improved; the accuracy of single-frequency single-epoch baseline solutions can be improved by 10–20%. Both cross and time correlations have ignorable impacts on the baseline solutions. However, they have significant impact on the variance matrix and then formal STDs of baseline solutions. The formal STDs with considering cross and time correlations can objectively reflect the actual precisions of baseline solutions. This is important, since in real applications, one has to use the formal STDs to evaluate the baseline solutions. Without taking into account the cross and time correlations, it always derives too smaller but not realistic formal STDs of baseline solutions.

Fig. 5 Comparison of three types of precisions of baseline errors. 'Empirical' and 'Realistic' denote the formal STDs of baseline errors obtained with empirical and realistic stochastic model of ignoring and considering time correlation, respectively. 'Actual' denotes the actual STDs of baseline errors based on the baseline errors themselves
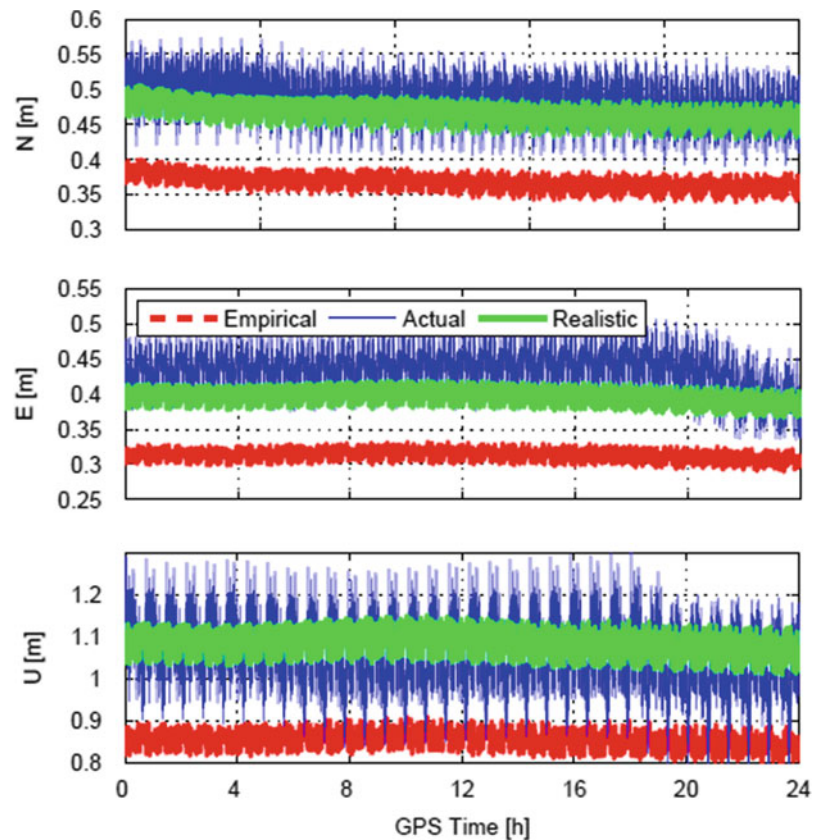
References

He H, Li J, Yang Y, Xu J, Guo H, Wang A (2014) Performance assessment of single- and dual-frequency BeiDou/GPS single-epoch kinematic positioning. GPS Solut 18(3):393–403

Koch K (1999) Parameter estimation and hypothesis testing in linear models, 2nd edn. Springer, Berlin

Li B (2016) Stochastic modeling of triple-frequency BeiDou signals: estimation, assessment and impact analysis. J Geod. doi:10.1007/s00190-016-0896-7

Li B, Shen Y, Xu P (2008) Assessment of stochastic models for GPS measurements with different types of receivers. Chi Sci Bull 53(20):3219–3225

Li B, Shen Y, Lou L (2011) Efficient estimation of variance and covariance components: a case study for GPS stochastic model evaluation. IEEE Trans Geosci Remote Sens 49(1):203–210

Li B, Verhagen S, Teunissen PJG (2014) Robustness of GNSS integer ambiguity resolution in the presence of atmospheric biases. GPS Solut 18:283–296

Liu X (2002) A comparison of stochastic models for GPS single differential kinematic positioning. In: ION GPS 2002, Portland

Shi C, Zhao Q, Hu Z, Liu J (2013) Precise relative positioning using real tracking data from COMPASS GEO and IGSO satellites. GPS Solut 17(1):103–119

Teunissen PJG (1995) The least-squares ambiguity decorrelation adjustment: a method for fast GPS integer ambiguity estimation. J Geod 70:65–82

Teunissen PJG (1999) An optimality property of the integer least-squares estimator. J Geod 73(11):587–593

Teunissen PJG, Amiri-Simkooei AR (2008) Least-squares variance component estimation. J Geod 82:65–82

Teunissen PJG, Jonkman NF, Tiberius CCJM (1998) Weighting GPS dual frequency observations: bearing the cross of cross-correlation. GPS Solut 2(2):28–37

Tiberius C, Kenselaar F (2000) Estimation of the stochastic model for GPS code and phase observation. Surv Rev 35(277):441–454

Verhagen S, Li B, Teunissen PJG (2013) Ps-LAMBDA: ambiguity success rate evaluation software for interferometric applications. Comput Geosci 54:361–376

Wang K, Rothacher M (2013) Ambiguity resolution for triple-frequency geometry-free and ionosphere-free combination tested with real data. J Geod 87(6):539–553

Wang J, Satirapod C, Rizos C (2002) Stochastic assessment of GPS carrier phase measurements for precise static relative positioning. J Geod 76(2):95–104

PPP Carrier Phase Residual Stacking for Turbulence Investigations

Franziska Kube and Steffen Schön

Abstract

Microwave space-geodetic observations such as Global Navigation Satellite Systems (GNSS) or Very Long Baseline Interferometry (VLBI) are delayed in the neutral atmosphere. In order to improve the quality of these techniques for precise applications like reference frame realisation, we need to get more knowledge about the temporal and spatial refractivity variations in the neutrosphere. In addition to the annually to hourly long periodic variations, which can be considered within the adjustment process, micro-scale meteorological phenomena in the range of minutes to sub-seconds affect space-geodetic observations as well. Thus, induced phase fluctuations of wavefronts passing through the turbulent medium form a significant error source for electromagnetic wave propagation.

In order to identify high-frequency atmospheric effects, we analysed 1 Hz high-rate GPS observations from the continuous operating GNSS station at the Geodetic Observatory Wettzell and derived post-fit carrier phase residuals for several days with a Kalman-Filter based Precise Point Positioning (PPP) approach. Since undifferenced carrier phase observations contain a superposition of several effects, the computed power-law behaviour of the residuals might not follow the theoretically predicted stochastical behaviour for refractivity fluctuations. Hence, the influence of multipath was identified. A residual stacking was performed, and the reduced residuals were analysed with regard to turbulence characteristics.

Keywords

Atmospheric turbulence • GNSS PPP • Multipath • Receiver clock modelling • Satellite clock interpolation

1 Introduction

Atmospheric delay caused by the dry (hydrostatic) and wet (non-hydrostatic) components of the troposphere is one of the major error sources in space-geodetic techniques, such as GNSS and VLBI. The long periodic behaviour is mainly caused by the local meteorological conditions and has already been studied thoroughly within the last decades.

The short periodic components are caused by turbulent fluctuations of the water vapour content and thus of the refractive index field within in the first few kilometers above the ground, i.e., the atmospheric boundary layer (Stull 2009). They induce phase fluctuations which restrict the attainable accuracy for microwave-based observation techniques on the one hand and should therefore be treated by appropriate means. Results of using fully populated covariance matrices in order to take correlation due to tropospheric turbulence into account, are published e.g. by Kermarrec and Schön (2014) and Schön and Brunner (2008). However, up to now, they are not considered within the stochastic model of the GNSS or VLBI data analysis for reference frame solutions. On the other hand, phase fluctuations reveal

F. Kube (✉) • S. Schön
Institut für Erdmessung (IfE), Leibniz Universität Hannover, Schneiderberg 50, 30167 Hannover, Germany
e-mail: kube@ife.uni-hannover.de

valuable information about the turbulent media through which the signal has travelled and thus can be used to enhance the modelling of neutrospheric refraction. The impact of these refractivity fluctuations on electromagnetic waves are described by turbulence theory, e.g. Wheelon (2001) and Tatarskii (1971).

Another short periodic effect, namely ionospheric scintillation will not been considered in our investigations. The first order effect of ionospheric refraction is cancelled out by using the ionospheric-free linear combination, since this effects scales with the wavelength of the carrier. Additionally, diffractive effects are present and do not cancel out when scintillations are present (Carrano et al. 2013). However at mid-latitudes, ionospheric effects are smaller and disturbances occur less often than at high latitudes or in the equatorial region (Aarons 1982). In addition, no space weather alert was announced for the period of our investigations (NOAA 2016).

The main objective of this paper is to detect the impact of atmospheric turbulence within the processing of GNSS observation with PPP. For this purpose, a very short introduction into atmospheric turbulence theory is given in the first part. As shown by Vennebusch et al. (2011), the stochastic behaviour of PPP derived zenith wet delay (ZWD) time series indicates turbulence. We focus here on the carrier phase residuals. They contain a superposition of several effects such as residual receiver and satellite clock variations, receiver noise, and multipath and thus have to be treated carefully. Especially the latter is strongly site-specific and represents a major error source in GNSS positioning. In order to reduce the effect of multipath, a robust multipath stacking as described in Fuhrmann et al. (2015) was performed and the residuals were corrected for the multipath effect. The PPP analysis and the residual stacking is described in the second part. In the last part, the resulting residual time series were analysed with selected statistical methods in order to identify atmospheric turbulence.

2 Short Review of Turbulence Theory

2.1 Atmospheric Turbulence

Fluctuations of the refractivity index field can be described by separating the refractive index n at a fixed location into two components

$$n = n_0 + \Delta n \qquad (1)$$

with a steady state component n_0 and a random component Δn which is a function of time and space. The latter one is characterised by rapid fluctuations, which are generated by a complex superposition of swirls (called "eddies") of different sizes and random, chaotic motions (Stull 2009).

Due to this random behaviour no deterministic description has been found yet.

However, the net effect of eddy motions can be described statistically via the spectrum of irregularities, which indicates the amount of total turbulence kinetic energy associated with the different scales of turbulence elements ("eddies"). The turbulence spectrum is divided in different parts. Most important for this investigation is the inertial subrange since in this part isotropic turbulence dominates and thus eddies behave randomly. It is usually expressed in terms of the Kolmogorov spectrum or the von Karman spectrum. The latter one reads (Wheelon 2001, pp. 37 ff):

$$\Phi_n(\kappa) = \frac{0.033 C_n^2}{\left(\kappa^2 + \kappa_0^2\right)^{\frac{11}{6}}} \propto \kappa^{-\frac{11}{3}}, \quad 0 < \kappa < \kappa_s. \qquad (2)$$

Here, C_n^2 is the so-called refractivity structure constant, $\kappa = 2\pi/l$ indicates the wavenumber corresponding to eddy size l, κ_0 and κ_S are the wavenumbers corresponding to the inner and outer scale lengths l_0 and L_0, respectively. Typical values for C_n^2 can be found in literature (Treuhaft and Lanyi 1987; Wheelon 2001; Gradinarsky 2002).

2.2 Stochastic Behaviour of Atmospheric Turbulence

The von Karman spectrum, given in Eq. (2) follows a so-called power-law behaviour with an exponent $\alpha = -11/3$ (Agnew 1992). This indicates that atmospheric turbulence is characterised as a non-stationary stochastic process and thus should not be expressed in terms of (auto-)correlation functions or power spectral densities. An appropriate quality measure is the temporal structure function $D_T(\tau)$ of a quantity T (Wheelon 2001):

$$D_T(\tau) = \left\langle \left[T(t + \tau) - T(t) \right]^2 \right\rangle, \qquad (3)$$

with $\langle \cdot \rangle$ denoting an ensemble average and τ indicating the time lag between two values of T. The temporal differencing removes data trends and thus generates a difference process which is usually stationary even if the original time series is non-stationary.

Graphical visualisation of structure functions in loglog-plots enables easily to associate the slope of the structure function to the power-law exponent and hence identify the underlying stochastic process and its properties in a qualitative and phenomenological way. In terms of power-law processes the structure function can be expressed as

$$D_T(\tau) = c \cdot \tau^\alpha, \qquad (4)$$

with a constant c and the power-law index α. Turbulence theory predicts a smooth transition from $\alpha = {}^2\!/_3$ for 2D turbulence to $\alpha = {}^5\!/_3$ for 3D turbulence (Wheelon 2001). For larger time lags the structure function approaches an asymptotic value of $2 \cdot \sigma_T$, i.e., twice the variance of T. For these time lags with zero slope, the data is considered as being uncorrelated. Similar expression can be found for the power spectrum and Allan variance (Allan 1987).

3 PPP for Turbulence Investigations

3.1 PPP Setup and Analysis

A daily PPP analysis was performed for the station *WTZR* at Wettzell Geodetic Observatory, Germany, for 17 consecutive days in 2011 using a precise point positioning software developed at the Institut für Erdmessung. We chose this time (VLBI CONT11 campaign) and station in order to study the variability of water vapour in the atmosphere and the resulting refraction effects with two techniques in the radio frequency domain (GPS and VLBI) in parallel. We used a Kalman Filter approach (see Table 1 for settings) to generate ionosphere-free (L3) 1 Hz GPS carrier phase residuals.

3.2 PPP Carrier Phase Residual Stacking

The L3 phase residuals show variations of about ± 80 mm and an elevation dependent behaviour, see Fig. 1a exemplary for 1 day and selected satellites.

Apart from turbulence effects, the phase residuals contain superpositions of several effects, such as residual receiver and satellite clock variations, receiver noise, residuals from the imperfect receiver and satellite antenna models, and multipath. In order to reduce their impact and to study turbulence in detail, we pursued the following strategy:

1. We applied a receiver clock modelling (solution *CLK-MOD1*) instead of an epoch wise clock estimation (solution *CLKMOD0*) since the GNSS receiver at Wettzell is connected to a stable hydrogen maser (Weinbach and Schön 2011, 2015).

2. In order to reduce potential satellite clock errors, we used high-rate satellite clock corrections (solution *SATCLK5s*) instead of 30 s clock corrections (solution *SATCLK30s*) (Bock et al. 2009).

3. Finally, a statistically robust multipath stacking map was generated (Fuhrmann et al. 2015) which was used as correction, see Fig. 2a (solution *MP*). Congruent cells with an azimuth resolution of 2° at the local horizon and elevation resolution of 1° were computed. Robust estimation means rigorous statistical assessments in terms of outlier detection and significance evaluation of the stacked values. The minimum number of residuals in one stacking cell was set to 15. In addition to the days during the VLBI CONT11 campaign, we computed PPP L3 phase residuals for other 40 days in 2011. Overall 57 days of PPP analysis yield 44,159,885 L3 phase residuals, with 196,6060 outlier (0.4%) and 260 residuals (0.0006%) in cells with less than 15 residuals. As expected, the multipath stacking map shows smaller variations and standard deviations at higher elevation and vice versa, see Fig. 2a, b. The pattern at elevations lower than 30° between 60° and 100° azimuth may be attributed to multipath. A similar elevation dependent pattern was found by Rost and Wanninger (2009). The higher standard deviation in the sector between 150° and 190° azimuth at 45° elevation cannot be fully explained. Since the mean values in this area is close to zero, the deviation might result from vegetational or constructional changes and not from multipath. The repeatability of the residual stacking was considered by computing the mean stacked values for randomly chosen 40 days. This was performed 20 times and the mean deviation to the final 57-days stacking

Table 1 PPP analysis settings

Processing time interval	DoY 257-273 2011 (VLBI CONT11) & Sundays DoY 072:7:359 2011
Elevation cut-off angle	5°
Observation weighting	Elevation dependent $sin^2(E)$
Sampling rate	1 s
EOP/Satellite orbits & -clocks	CODE final orbits (15 min)
	CODE.CLK (high-rate 5 s and high-rate 30 s), linearly interpolated to 1 s (Bock et al. 2009)
Satellite antenna	Absolute antenna model from IGS08.atx
Receiver antenna	Individual absolute calibration
Troposphere a priori model	Saastamoinen model (Saastamoinen 1973), pressure values from local meteorological station
Mapping function	VMF1 (Vienna mapping function) (Böhm et al. 2006)
Troposphere modelling	Random walk with process noise of 15 $mm\!/\!\sqrt{h}$ (Tralli and Lichten 1990)
Static coordinates modelling	Random constant
Carrier phase ambiguities modelling	Random constant
Receiver clock model	2-state-model (van Dierendonck et al. 1984; Weinbach and Schön 2011)
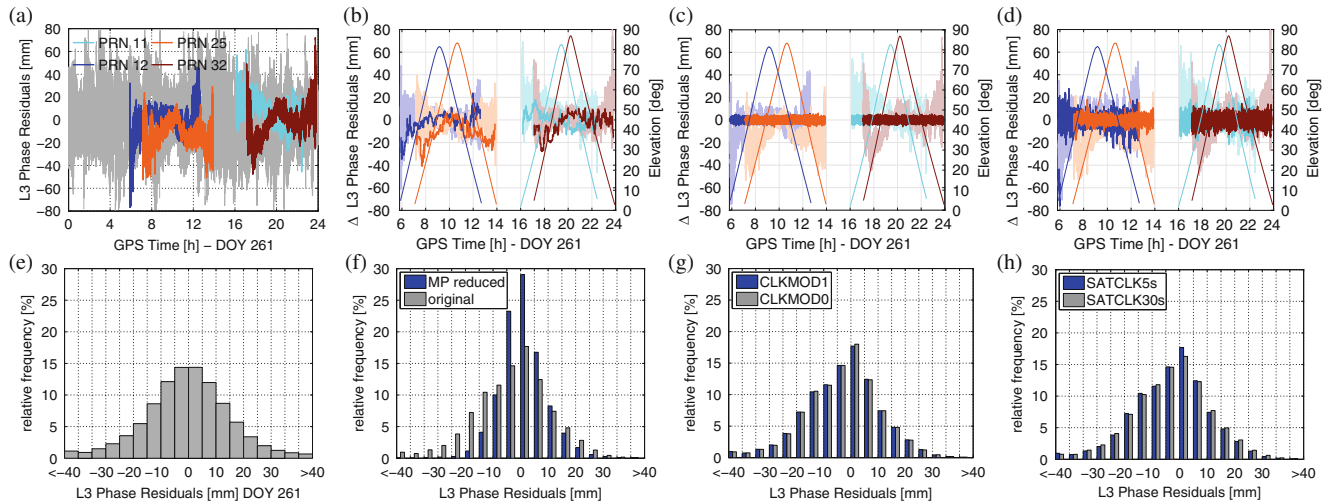
Fig. 1 WTZR PPP L3 phase residuals for DoY 261 2011 for different solutions and differences (*first row*) and their distribution (*second row*). *First column*: Phase residuals after applying receiver clock modelling and using high-rate satellite clock corrections for all visible PRN (*CLKMOD1, SATCLK5s*). Selected satellites are highlighted. *Second to fourth column*: Residuals for selected satellites (transparent in background) and differences to solution in first column are presented.

Second column: Additionally multipath stacking was performed and the computed mean stacked values were reduced from the original residuals (*CLKMOD1, SATCLK5s, MP*). *Third column*: No receiver clock modelling was performed (*CLKMOD0, SATCLK5s*). *Fourth column*: 30 s satellite clock corrections were used instead of high-rate clock corrections (*CLKMOD1, SATCLK30*)
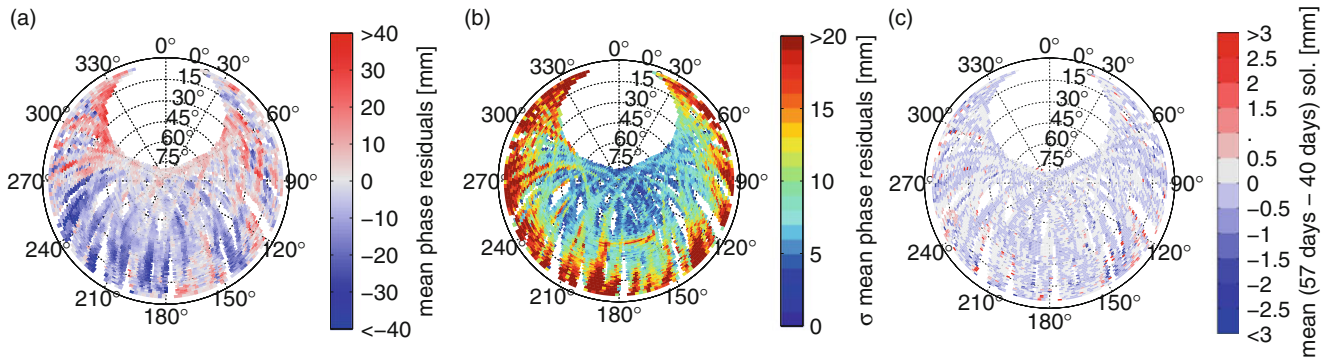
Fig. 2 PPP L3 phase residuals stacking map (**a**) with corresponding standard deviation (**b**) and repeatability (**c**). Overall 57 days of PPP residuals were stacked

solution is depicted in Fig. 2c. The differences are mainly within ±0.5 mm which indicates a good performance of the multipath stacking scheme.

The residuals with and without applying the three strategies, the differences to the solution applying all, and the residual distributions are depicted in Fig. 1, respectively. Using high-rate satellite clock corrections and modelling the receiver clock significantly reduces the variance of the

residual time series, see Fig. 1c, d. The histograms also show less values exceeding ±20 mm, when using 5 s satellite clock corrections, see Fig. 1h. After removing the computed mean stacked values from the original residuals (solution *MP*), variations over the whole elevation range are removed and the histogram shows less values exceeding ±15 mm, see Fig. 1b, f. Compared to Fig. 1c and d, Fig. 1b shows the long periodic variations of multipath effects.
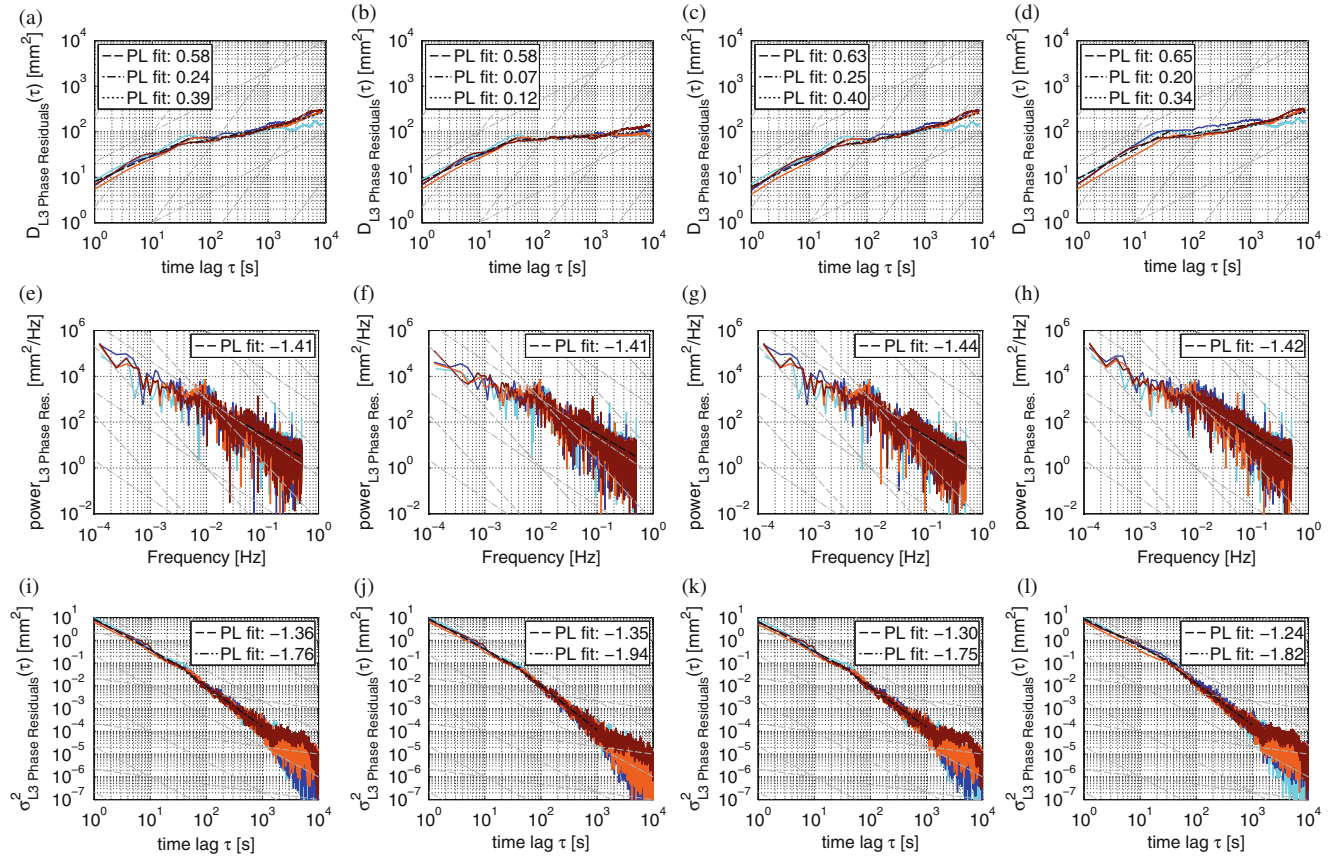
Fig. 3 Statistics of computed PPP L3 phase residuals and reduced residuals for selected satellites. The PRN colour codes are the same as in Fig. 1. Power-law relations as listed in Table 2 are plotted as grey lines. *First line*: temporal structure function, *second line*: power spectrum, *third line*: Allan variance. *First column*: Residuals from processing with receiver clock modelling using high-rate satellite clock correc-

tion (*CLKMOD1*, *SATCLK5s*), *second column*: additional multipath reduction (*CLKMOD1*, *SATCLK5s*, *MP*), *Third column*: residuals from processing without receiver clock modelling (*CLKMOD0*, *SATCLK5s*), *fourth column*: residuals from processing with receiver clock modelling but without using high-rate satellite clocks (*CLKMOD1*, *SATCLK30s*)

4 Stochastic Behaviour of PPP Residuals

In order to identify refractivity fluctuations in the resulting phase residuals, dedicated analysis tools are applied such as temporal structure functions (Fig. 3a–d), power spectrum (Fig. 3e–h) or the Allan variance (Fig. 3i–l).

The prevailing turbulent regime is then characterised by the shape of the temporal structure function yielding typical slopes in a loglog-plot, cf. Sect. 2.2 and Table 2. In addition, the slope of power spectrum or Allan variance can be used as indicator for turbulence processes (Thompson et al. 2001).

Since undifferenced carrier phase residuals contain a superposition of several unmodelled effects, the computed slopes from the original residuals will not clearly show the theoretical values. In order to minimize distortions of the temporal structure functions, power spectra and Allan variances, respectively, offset and trend of the individual residual time series have been removed. The slopes are

computed for the mean statistic quality measure of selected satellites on DoY 261 2011, see Fig. 3.

The results show 2–3 segments with different dominant power-law, i.e. a first segment for up to $45 \ldots 100\,\mathrm{s}$, and a second, and maybe third segment beyond. For time lags up to $\sim 45\,\mathrm{s}$ (small τ), the slopes nearly reach the expected values for 2D turbulence for the structure functions, power spectra and Allan variances, respectively. There are slight changes resulting from applying different solution strategies in the computed power-law behaviour for these time lags. For longer time lags (second segment), the influence of multipath stacking is most significant. No segment shows a dominant power-law corresponding to a 3D turbulence.

For time lags up to $\sim 45\,\mathrm{s}$, a slope of $\sim 2/3$ can be observed in the temporal structure function. When not applying receiver clock modelling and using 30 s satellite corrections, the slopes are marginally closer to the theoretical value for these time lags, see Fig. 3c, d. Probably more medium periodic effects persist in this case. Reducing the residuals

Table 2 Power-law relations for turbulence

Quantity	Exponent	
	3D turbulence (very small τ)	2D turbulence (small τ)
(Temporal) structure function	$\frac{5}{3}$	$\frac{2}{3}$
Power spectrum	$-\frac{8}{3}$	$-\frac{5}{3}$
Allan variance	$-\frac{1}{3}$	$-\frac{4}{3}$

for the multipath effect mainly changes the slope for larger time lags. The slope nearly reaches 0 in the reduced residuals. Hence, long periodic effects are successfully reduced by the performed multipath stacking and reduction, see Fig. 3a, b.

In the power spectrum of phase residuals a slope of $\sim -\frac{5}{3}$ is noticeable for periods up to $\sim$100 s. A peak in the spectrum appears at $\sim$20 s and $\sim$100 s in all four power spectra. The reason is not yet identified and has to be investigated in future work. For lower frequencies the slopes reduce but there is no significant influence from multipath stacking, see Fig. 3e–h.

The Allan variance shows a continuous $\sim -\frac{4}{3}$ behaviour for periods up to $\sim$45 s for all solution strategies. Using high-rate satellite clock correction and modelling the receiver clock seems to have minor impact on the power law behaviour, see Fig. 3k, l, whereas multipath stacking changes the slope for larger periods up to $\sim$1,000 s. It is changing to a more steep negative slope of ~ -1.9 for the multipath reduced residuals, indicating an approach to white phase noise (theoretical values -2) see Fig. 3j.

5 Summary

We performed 57 days of daily 1 Hz PPP analysis in order to generate a large number of residuals for statistically robust multipath stacking. The mean values were reduced from the original residuals and the resulting reduced residuals were analysed with regard to turbulent effects. In addition, we used high-rate satellite clock corrections and modelled the receiver clock in order to reduce their impact on the phase residuals. Statistic measures, such as temporal structure function, power spectrum and Allan variance were used to identify turbulence in the residual time series. The results show, that multipath stacking mainly changes the slope (in loglog-plot) for all three quantities for larger periods helping to identify the breakpoint between coloured and white noise. For smaller time lags τ, the slopes are nearly unchanged. Their values can be interpreted as an indication for 2D turbulence for time lags up to $\sim$45 s. Receiver clock modelling and the usage of high-rate clock correction seems to have minor impact on the computed power law behaviour. Further investigations will concentrate on Kalman filter settings and the simulation of turbulence effects in order to explain the peaks in the power spectra and to analyse in which step

of geodetic data processing atmospheric turbulence can be observed. In order to remove high-frequency multipath alternative stacking schemes, e.g. observation-domain sidereal filtering as presented by Atkins and Ziebart (2015) has to be considered in future analysis.

References

Aarons J (1982) Global morphology of ionospheric scintillations. Proc IEEE 70(4):360–378. doi:10.1109/PROC.1982.12314

Agnew DC (1992) The time-domain behavior of power–law noises. Geophys Res Lett 19(4):333–336. doi:10.1029/91GL02832

Allan DW (1987) Time and frequency (time-domain) characterization, estimation, and prediction of precision clocks and oscillators. IEEE Trans Ultrason Ferroelectr Freq Control 34(6):647–654. doi:10.1109/T-UFFC.1987.26997

Atkins C, Ziebart M (2015) Effectiveness of observation-domain sidereal filtering for GPS precise point positioning. GPS Solutions 20(1):111–122. doi:10.1007/s10291-015-0473-1

Bock H, Dach R, Jäggi A, Beutler G (2009) High-rate GPS clock corrections from CODE: support of 1 Hz applications. J Geodesy 83:1083–1094

Böhm J, Werl B, Schuh H (2006) Troposphere mapping functions for GPS and very long baseline interferometry from European Centre for medium-range weather forecasts operational analysis data. J Geophys Res 111(B2)

Carrano CS, Groves K, McNeil W, Doherty P (2013) Direct measurement of the residual in the ionosphere-free linear combination during scintillation. In: International technical meeting (ITM) of the Institute of Navigation, San Diego, CA, January 28–30, 2013, pp 585–596

Fuhrmann T, Luo X, Knöpfler A, Mayer M (2015) Generating statistically robust multipath stacking maps using congruent cells. GPS Solutions 19(1):83–92

Gradinarsky L (2002) Sensing atmospheric water vapor using radiowaves. Dissertation, School of Electrical Engineering, Chalmers University of Technology

Kermarrec G, Schön S (2014) On the Mátern covariance family: a proposal for modeling temporal correlations based on turbulence theory. J Geodesy 88(11):1061–1079. doi:10.1007/s00190-014-0743-7

NOAA (2016) Space Weather Prediction Center. National Oceanic and Atmospheric Administration. http://www.swpc.noaa.gov/products/alerts-watches-and-warnings. Accessed 26 Aug 2016

Rost C, Wanninger L (2009) Carrier phase multipath mitigation based on GNSS signal quality measurements. J Appl Geod 3(2):81–87. doi:10.1515/JAG.2009.009

Saastamoinen J (1973) Contributions to the theory of atmospheric refraction. B Geod 107:13–34. doi:10.1007/BF02522083

Schön S, Brunner FK (2008) Atmospheric turbulence theory applied to GPS carrier-phase data. J Geodesy 82:47–57. doi:10.1007/s00190-007-0156-y

Stull RB (2009) An introduction to boundary layer meteorology. Springer, Dordrecht

Tatarskii VI (1971) The effects of the turbulent atmosphere on wave propagation. National Technical Information Service, Springfield

Thompson AR, Moran JM, Swenson GW (2001) Interferometry and synthesis in radio astronomy, 2nd edn. Wiley, New York

Tralli DM, Lichten SM (1990) Stochastic estimation of tropospheric path delays in global positioning system geodetic measurements. B Geod 64:127–159. doi:10.1007/BF02520642

Treuhaft RN, Lanyi GE (1987) The effect of the dynamic wet troposphere on radio interferometric measurements. Radio Sci 22(2):251–265

van Dierendonck AJ, McGraw JB, Brown RG (1984) Relationship between Allan variances and Kalman filter parameters. In: Proceedings of the 16th annual PTTI meeting 1984

Vennebusch M, Schön S, Weinbach U (2011) Temporal and spatial stochastic behaviour of high-frequency slant tropospheric delays from simulations and real GPS data. Adv Space Res 47(10):1681–1690. doi:10.1016/j.asr.2010.09.008

Weinbach U, Schön S (2011) GNSS receiver clock modeling when using high-precision oscillators and its impact on PPP. Adv Space Res 47(2):229–238

Weinbach U, Schön S (2015) Improved GPS-based coseismic displacement monitoring using high-precision oscillators. Geophys Res Lett 42(10):3773–3779. doi:10.1002/2015GL063632

Wheelon AD (2001) Electromagnetic scintillation I: geometrical optics. Cambridge University Press, Cambridge

On Removing Discrepancies Between Local Ties and GPS-Based Coordinates

S. Schön, H. Pham, and T. Krawinkel

Abstract

Local ties are vectors that link reference points of different space geodetic instruments at co-located stations. Discrepancies between local ties and solutions from space geodetic techniques weaken the determination of reference frames. Terrestrially determined local ties and GPS-derived coordinates differences can disagree at the cm-level due to suboptimal GPS processing.

In this paper, we propose a post-processing correction strategy to reduce apparent height differences which occur when, unnecessarily, tropospheric delay are estimated between co-located stations or tropospheric constraints between co-located stations are not taken into account. A site-dependent correction factor is determined which stays constant over time and thus can be calibrated. The correction strategy is successfully applied to co-located stations in the pillar network of our institute where the local tie is well-controlled. We find that height discrepancies between levelling survey and post-processed GPS results can be reduced from the centimeter-level to some millimeters. This holds also true for co-located GPS stations of the EUREF Permanent Network.

Keywords

GPS • Local ties • Tropospheric delay

1 Introduction

Local ties are vectors that link reference points of different space geodetic instruments at co-located sites. These vectors are often determined by terrestrial geodetic measurements or local GPS surveys. Unfortunately, these local measurements disagree with results from regional or global GPS solutions. Approximately 37% of the 3D coordinate discrepancies (mean value of combined space geodetic techniques) are larger than 10 mm (Altamimi et al. 2011) weakening the determination of the reference frame.

Reasons for the discrepancies can be found in deficiencies in the determination of the local tie vector as well as site-dependent errors in the space geodetic techniques as discussed in Sarti et al. (2012). Steigenberger et al. (2012) investigated the differences between the GPS antenna array at Wettzell with respect to different antenna calibration models. Brockmann et al. (2010) analyzed differences between local ties and co-located double stations in the Swiss AGNES network focusing on antenna calibration models and processing strategies. Wilkinson et al. (2012) studied the local ties between GPS stations at Herstmonceux indicating seasonal variations on short baselines.

Another reason for disagreements between local ties and GPS-based coordinates can be the different and sometimes suboptimal processing strategies (observation type, troposphere modeling) applied for local and global GPS networks as will be shown in this paper and also stated in Brockmann et al. (2010). In fact, two cases of suboptimal processing

S. Schön • H. Pham (✉) • T. Krawinkel
Institut für Erdmessung (IfE), Leibniz Universität Hannover, Schneiderberg 50, 30167 Hannover, Germany
e-mail: krawinkel@ife.uni-hannover.de; huekiem@gmx.de

can be distinguished: (1) the short baseline between co-located stations may be processed applying the ionosphere-free linear combination and estimating troposphere parameters (L3T), e.g. if it is included in a one-step analysis of a regional or global network also containing long baselines. This yields noisier coordinates due to the about 3 times noisier L3 observable, and apparent height deviations due to the unnecessary estimation of tropospheric delays absorbing further site-specific effects. (2) Apparent height discrepancies between co-located stations can also be obtained when tropospheric constraints are not considered, e.g. the co-located stations are linked via long baselines (L3T) to other network stations allowing differences in the troposphere estimates between the co-located stations.

The contribution of this paper is a proposal of an easy-to-use post-processing correction strategy to reduce these apparent height deviations and thus reduce discrepancies between local ties and GPS-based coordinates.

The remainder of the paper is organized as follows: Sect. 2 explains our proposal considering different network scenarios. In Sect. 3, we present the GPS processing scheme applied to two different case studies. Section 4 discusses the results from a dedicated experiment at the Institut für Erdmessung (IfE) where the local tie is well known. Furthermore, we extend our study to co-located GNSS stations in the EUREF Permanent Network (EPN, Bruyninx et al. 2012) showing the benefits of the proposed correction strategy.

2 Methodology

The basic idea behind our proposal is that on very short baselines or between co-located stations, respectively, there is no relative tropospheric delay expected thanks to identical conditions at both stations (Krawinkel et al. 2014). If, nevertheless, troposphere parameters are estimated, their deviations from zero lead to apparent height changes due to the high mathematical correlations between these parameters (Beutler et al. 1989). The relation between

the estimated height coordinate and the corresponding troposphere parameter was analytically evaluated by, inter alia, Beutler et al. (1989) and Santerre (1991). It has a constant ratio of approximately $1{:}-3$, i.e. a deviation in the tropospheric delay of $+1$ mm relates to $–3$ mm in the height coordinate. Applying this relation, the mathematical effect of the height discrepancy Δh_{L3T-L3} between co-located stations stemming from two different solution, namely L3 and L3T, can be corrected as follows:

$$\Delta h_{L3T,corr} = \Delta h_{L3T} - \delta_U^T \, \Delta Trop \qquad (1)$$

with $\Delta h_{L3T,corr}$, Δh_{L3T} corrected and original differences of the height estimates of an L3T solution, respectively, and $\Delta Trop$ the relative tropospheric delay between the two co-located stations obtained from the L3T solution. The ratio δ_U^T can be determined either analytically or empirically. In the first case, the simulation strategy by Santerre (1991) is used. Depending on the elevation cutoff angle, geographic location and additional observation masking a ratio of $1{:}-3.5$ to $1{:}-3$ is obtained. The empirical method is based on processing results of the short baseline. Here, δ_U^T is derived from the ratio between the difference of height estimates from the L3T (U_{L3T}) and the L3 (U_{L3}) solution of the short baseline, and the corresponding troposphere estimate from L3T:

$$\delta_U^T = \frac{U_{L3T} - U_{L3}}{\Delta Trop} \qquad (2)$$

If no external effects like e.g. snow coverage occur, this ratio changes only slightly over time and thus can be calibrated.

Feasible scenarios to link local and global network coordinates or short and long baselines, respectively, are shown in Fig. 1. They represent the scenarios that are considered to validate the proposal in experiments conducted at IfE in 2011 and in analyses of co-located EPN stations. The long baselines amount up to hundreds of kilometers, and short baselines up to 100 m.

Fig. 1 Network scenarios: (**a**) local reference station LREF is linked via long baseline to REF, station STA2 is connected to LREF via short baseline (*red*); (**b**) two local stations LREF and STA2 are linked to one reference station REF via two long baselines (*blue*); (**c**) two local stations LREF and STA2 are connected to two different reference stations REF1 and REF2 via long baselines
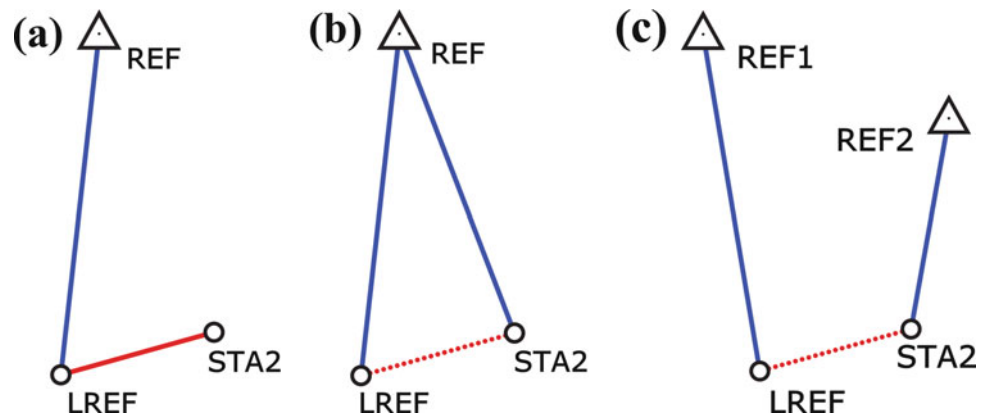
3   GNSS Processing

For both case studies, we use the Bernese GNSS Software 5.2 (BSW52, Dach et al. 2015). All computations are based on double differences where station coordinates and troposphere parameters are estimated. We use IGS (International GNSS Service, Dow et al. 2009) final orbits and differential code biases from CODE (Center for Orbit Determination in Europe). For troposphere modeling, we apply the Niell (dry and wet) model (Niell 1996), the troposphere parameters are estimated as piecewise linear functions with a temporal resolution of one hour. Observations with low elevation angles (cutoff angle: 3°) are used to improve the estimation of tropospheric zenith path delays and thus the height component. Additionally, horizontal tropospheric gradients are estimated on long baselines to take into account azimuthal asymmetries of the local troposphere at low elevations. We apply an elevation-dependent weighting $w(z) = \cos(z)$ of the observations, where z is the zenith angle of the satellite. The coordinates of the reference stations were held fixed to their nominal values. The ambiguities of the L3 and L3T cases were resolved using a wide-lane narrow-lane strategy.

The first case study is based on dedicated data from 2011. Two local stations LREF and STA2 (cf. Fig. 1) were mounted on two pillars separated by ca. 20 m on the rooftop at IfE, Germany, equipped with identical receivers (JAVAD Delta TRE-G3T) and two Leica antennas (AT504GG at STA2, AR25.R3 LEIT at LREF). We chose three different IGS stations, namely Warnemünde, Germany (WARN), Westerbork, the Netherlands (WSRT) and Wettzell, Germany (WTZR), successively as regional reference station REF. The analysis contains 5 days of data (DoY 339–343) in 2011. Individual absolute phase center offsets and variations determined at IfE were available for the antennas of STA2 and LREF, while IGS type mean values were used for the reference stations. The nominal height difference between LREF and STA2 is known from precision leveling (13.0 mm).

The second case study includes six pairs of co-located EPN stations listed in Table 1. For the long baseline analysis the centrally located EPN station POTS (Potsdam, Germany) is selected as reference station REF. For most antennas only the type mean values of the phase center offsets and variations (PCO, PCV) are available. Some co-located stations are equipped with different antenna types, the receiver types and settings being moreover inhomogeneous (cf. Table 1). In addition different cutoff angles are applied in the receiver (often 0° or 5°). The given local tie information in topocentric coordinates with origin in the corresponding local reference station are mostly obtained from GPS campaigns in combination with trilateration measurements. Exceptions are the station pair KRA1/KRAW where only precise leveling is available, and PENC/PEN2 where no local tie information is accessible.

One week of GPS data (DoY 124–130) in 2014 was chosen for the analysis. No remarkable effects such as adverse weather conditions or increased ionosphere activity were expected for this period.

4   Results

4.1   Experiments at IfE

For an optimal solution for *scenario (a)* (Fig. 1a), first the two baselines are processed independently, i.e. baseline LREF-STA2 as L1 and LREF-REF as L3T. This is due to the fact that we cannot compute a one-step network solution using different observables for different baselines in BSW52. The normal equation systems of both baselines are then combined fixing the coordinates of station REF. The obtained coordinate solution for STA2 is optimal because the most precise L1 observations can be exploited for the short baseline. Tropospheric parameters should not be estimated since no physical tropospheric signal remains in the double differences of the short baseline. Additionally, the short baseline is also processed as L3 and L3T so that we can calculate the height correction using Eq. (2).

The resulting height discrepancies of the short baseline LREF-STA2 with respect to the results from precision leveling are depicted in Fig. 2, mean values and scatters over the one week data set are given in Table 2.

The L1 height difference of 12.8 mm fits very well the nominal height difference of 13.0 mm stemming from precise leveling, whereas the L3T height difference of 9.6 mm differs by 3.4 mm. This offset can be compensated by determining the parameter δ_U^T analytically as described in Sect. 2. Here, we found a ratio of 1:–3.2 (Krawinkel et al. 2014). Taking the determined tropospheric delays of ca. 0.7 mm and applying Eq. (1), the height component of the L3T solution is improved in both the mean value and the scatter, cf. Fig. 2 and Table 2.

In *scenario (b)* (Fig. 1b), stations LREF and STA2 are connected to the IGS stations (REF) independently via long baselines as L3T (L3T WARN, L3T WSRT, L3T WTZR) since tropospheric effects cannot be eliminated on long baselines by only using double differenced observations. Assuming that the same physical tropospheric delay should be obtained for both long baselines (*tropospheric constraint*), the height coordinate can be improved by determining a correction term from Eq. (1), where $\Delta Trop$ is the difference of the estimated tropospheric delays of LREF and STA2. For each of the three IGS stations, the resulting mean corrected height and its scatter are shown in Table 2. A correction by δ_U^T reduces the systematic deviation of L3T. A dependency of

Table 1 Information about co-located EPN stations used for data analysis

Station	City, County	Basel. length [m] [km]	Ant. calib. [LREF] [STA2]	Antenna type (radome) [LREF] [STA2]	Receiver type [LREF] [STA2]	Local tie [m] North East Up	Tie epoch Method
BOGO BOGI	Borowa Poland	107 550	Type Type	ASH700936C_M (SNOW), ASH701945C_M (SNOW)	TPS EUROCARD, JAVAD TRE_G3T DELTA	−106.374 −8.753 −9.734	2001 GPS
HERT HERS	Halisham, United Kingdom	136 900	Type Type	LEIAT504GG (NONE), LEIAR25.R3 (NONE)	LEICA GRX1200GGPRO, SEPT POLARX3ETR	−18.432 135.036 −6.851	2008 GPS
JOZE JOZ2	Jozefoslaw, Poland	84 550	Type Type	TRM14532.00 (NONE), LEIAT504GG (NONE)	TRIMBLE 4000SSI, LEICA GRX1200GGPRO	62.416 55.666 11.103	2001 GPS
KRA1 KRAW	Krakow, Poland	3 550	Type Type	TRM57971.00 (NONE), ASH701945C_M (SNOW)	TRIMBLE NETR5, ASHTECH UZ-12	– – −0.0062	2014 LEV
PENC, PEN2	Penc, Hungary	33 680	Indiv. Indiv.	LEIAT504GG (LEIS), LEIAR25.R4 (LEIT)	LEICA GRX1200GGPRO, LEICA GRX1200 + GNSS	– – –	
ZIMM, ZIM2	Zimmerwald, Switzerland	19 740	Type Indiv.	TRM29659.00 (NONE), TRM59800.00 (NONE)	TRIMBLE NETRS, TRIMBLE NETR5	−0.422 −18.766 0.094	2007 GPS
[REF] POTS	Potsdam, Germany	–	Indiv.	JAV_RINGANT_G3T (NONE)	JAVAD TRE_G3TH DELTA		

Column 2 indicates the country and city, column 3 the baseline length between the local stations in [m] and w.r.t. the reference station POTS in [km], columns 4–6 describe the equipment used including the antenna calibration type (type mean or absolutely individual), columns 7–8 indicate the local tie in [m] its epoch and the observable used for its determination (GPS, Leveling LEV)
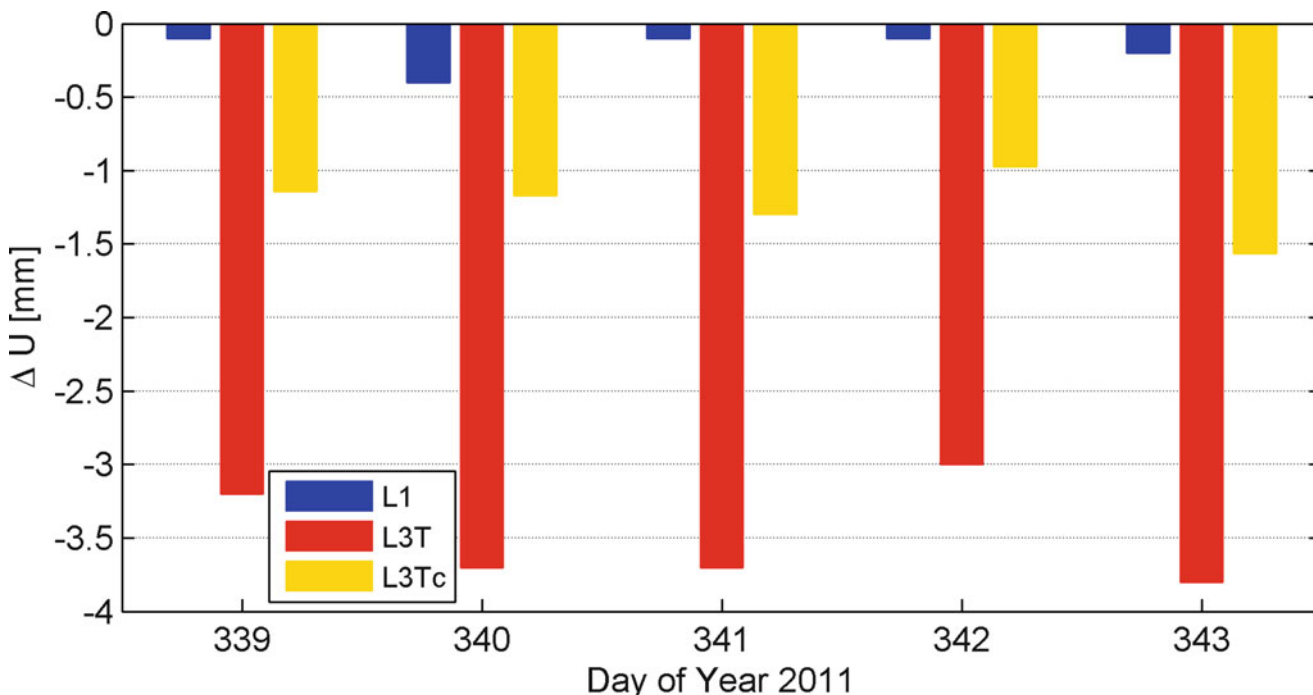
Fig. 2 Discrepancies in the up component to local tie in scenario (**a**) from experiments at IfE in local topocentric system: baseline LREF-STA2 as L1 (*blue*); baseline LREF-STA2 as L3T (*red*) corrected L3T time series (*yellow*)

Table 2 Discrepancies in [mm] between local tie (height difference from precise leveling, uncertainty smaller 0.3 mm) and GPS-derived coordinates from scenario a) and b) when using different GNSS observables as well as applying the correction term $\delta_U^T \Delta Trop$

REF	L1	L3T	L3Tc
a) LREF	-0.1 ± 0.1	-3.4 ± 0.4	-1.3 ± 0.2
b) WEST		-1.7 ± 1.8	-1.8 ± 0.4
b) WTZR		-2.5 ± 1.8	-0.7 ± 1.2
b) WARN		-4.9 ± 1.4	-1.3 ± 0.4

the solution on the chosen reference station is visible. Thus, also for *scenario (b)*, the apparent height deviation can be reduced.

Using our post-processing correction strategy, all baselines in the network can be solved as L3T solutions independently from their length. The correlations of the baselines in the stochastic model are then taken into account during the GPS analysis. However, the difference between L1 and L3 solution remains as a systematic offset that cannot be remedied yet.

In *scenario (c)*, the two local stations LREF and STA2 are connected to two different reference stations REF1 and REF2 via two long baselines (Fig. 1c) evaluated as L3T solutions. The experiment shows that the apparent change in the height coordinate cannot be repaired by the proposed correction since similar troposphere conditions at both reference sites are not present. In addition station-specific effects may

occur that further influence the validity of the tropospheric constraint. Thus, an improvement for this scenario is not possible.

4.2 EPN Coordinate Solutions

The short baselines of six exemplary local station pairs in the EPN network are evaluated as L3T in *scenario (a)* (L3T short: LREF-STA2), and as L3T via two long baselines (L3T long: REF-LREF, REF-STA2) in *scenario (b)* with POTS as reference station REF. In addition, the L1 short and L3 short solution of baseline LREF-STA2 are processed.

As an example, Fig. 3 shows the (apparent) relative tropospheric delay of one day at station PEN2 relative to PENC. Here, the daily mean differs from the expected value of zero. This deviation leads to apparent height changes because of the high correlation between station height and tropospheric delay.

Analyses of the co-located EPN stations confirm that the ratio between the height difference of L3 and L3T and the estimated (daily mean) tropospheric delay (Eq. 1) stays relatively constant over time, cf. Table 3.

The discrepancies between local ties and GPS-based coordinates are computed in a local topocentric coordinate system of station LREF depicted in Fig. 4. Since no local tie information are available for PENC/PEN2 the actual difference is plotted. The local L1 solution is assumed as reference; the
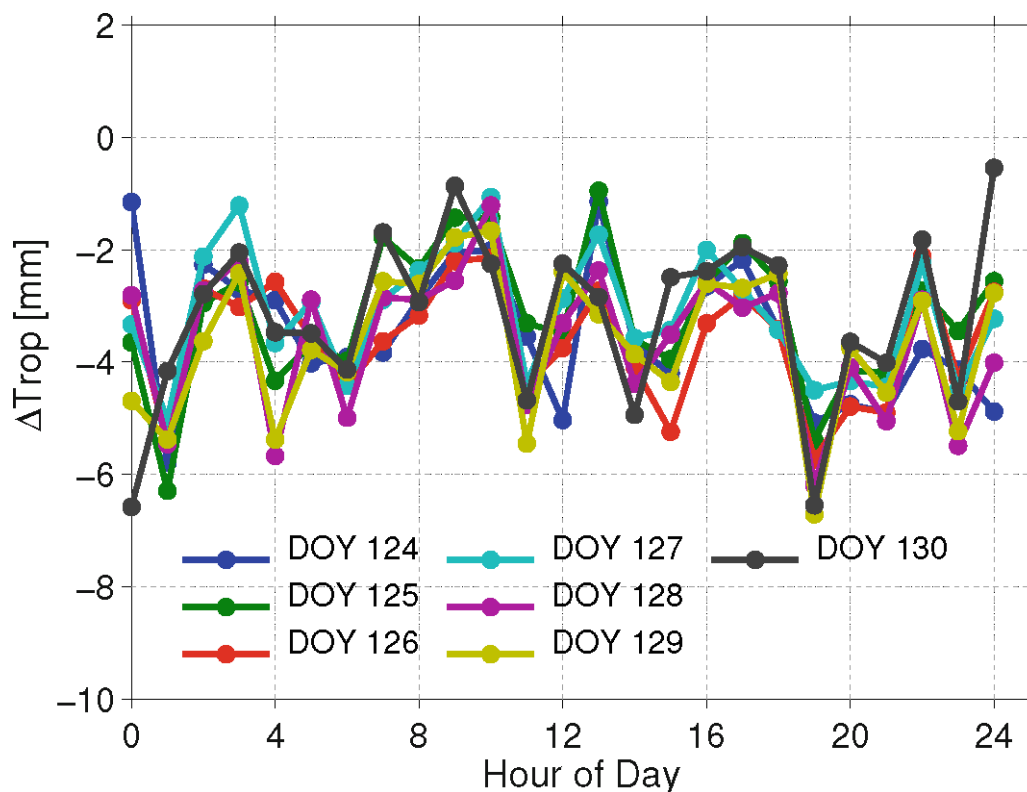
Fig. 3 Relative tropospheric delay of PEN2 wrt PENC (short baseline) of one day with an estimation interval of one hour

Table 3 Relation between troposphere and height estimates determined from Eq. (2)

DoY2014	BOGI	HERS	JOZ2	KRAW	PEN2	ZIM2
124	−3.3	−3.0	−2.7	−2.9	−2.9	−2.3
125	−3.0	−3.0	−2.7	−2.9	−2.9	−2.4
126	−2.9	−3.0	−2.7	−2.9	−2.9	−2.4
127	−3.1	−3.1	−2.7	−2.8	−2.9	−2.5
128	−3.1	−3.1	−2.6	−2.9	−2.9	−2.9
129	−3.0	−3.0	−2.7	−2.9	−2.9	−2.7
130	−3.0	−2.9	−2.7	−2.9	−2.9	−2.9
Mean	−3.1	−3.0	−2.7	−2.9	−2.9	−2.6

station pair is used since the identical equipment and individual absolute antenna calibration values are available. For KRAW/KRA1 only a leveled height difference is available.

The results in Fig. 4 confirm that the L1 solution matches the local ties well, especially in case of the leveled height difference at KRAW. The coordinate time series on short baselines (in particular for L1) stay stable for all stations. However, also offsets are visible. They may be attributed to antenna changes, receiver changes and updates as reported in the site log of the stations. In addition, the difference between local tie epoch (Table 3, last column) and the GPS mea-

surement epoch is sometimes more than 10 years, in which changes may occur. Furthermore, a general uncertainty on the local tie definition may persist.

The results for the L3 short and L3T short solutions show additional offsets as also reported by Steigenberger et al. (2012) or Brockmann et al. (2010). They are due to the noisier ionosphere-free linear combination, and the amplification of non-modeled elevation dependent systematics by estimating additional troposphere parameters.

The height differences between the co-located stations obtained with L3T long solutions in *scenario (b)* show larger day-to-day variations at the mm-level for the horizontal components, at the 1–2 cm-level for the height component, and for some station pairs additional offsets.

Finally, the height correction from Eq. (1) is applied to the L3T long solution using the empirically determined mean relation from Table 3. It leads to a smoother height time series (L3Tc) in comparison to the original L3T long solution, and improved results for the height component. For HERS and PEN2 the corrected height is even at the level of the L1 short and L3 short solutions.

Thus, the proposed post-processing correction strategy can contribute to improve the height coordinates and to reduce the discrepancies between local ties.
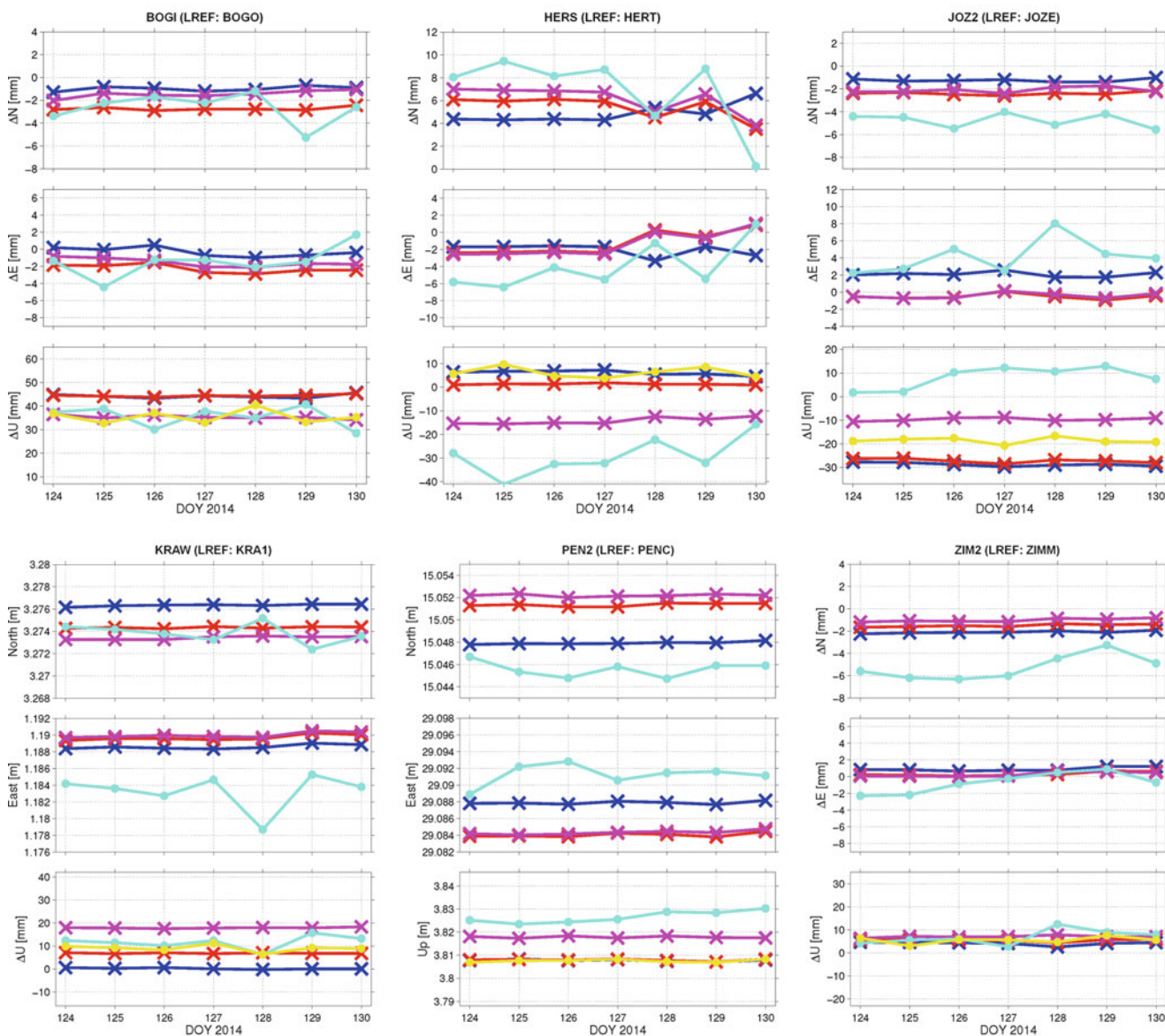
Fig. 4 Discrepancies between local ties and GPS-based coordinates in a local topocentric coordinate system of the station LREF. The range of the coordinate axes are identical for all stations, i.e. 12 mm for North, 16 mm for East and 55 mm for Up. The different time series are color-coded as follows: L1 short (*blue*), L3 short (*red*), L3T short (*magenta*), L3T long (*cyan*), L3T long corrected (*yellow*)

5   Conclusions

In this paper, a post-processing correction strategy was proposed to reduce apparent height differences between post processed GPS data and terrestrial measurements like levelling. These discrepancies occur when unnecessarily tropospheric delays are estimated between co-located stations, or when tropospheric constraints between co-located stations are not taken into account.

The strategy is based on the analytical relation between tropospheric delay and station height of approximately 1:–3. The correction factor δ_U^T can be derived either analytically or empirically from the analysis of short baselines. It is site-dependent but stays relatively constant over time and for that reason can be calibrated. The correction strategy was successfully applied to co-located stations reducing height discrepancies from the cm-level to some millimeters. As a benefit, all baselines in a regional network can be solved as L3T solutions independently from their baseline length. However, the difference between L1 and L3 solution remains as a systematic offset that cannot be remedied yet.

References

Altamimi Z, Collilieux X, Metivier L (2011) ITRF2008: an improved solution of the international terrestrial reference frame. J Geodesy 85(8):457–473

Beutler G, Bauersima I, Botton S, Gurtner W, Rothacher M, Schild-knecht T (1989) Accuracy and biases in the geodetic application of the Global Positioning System. Manuscripta Geodaetica 14:28–35

Brockmann E, Ineichen D, Schär S, Schlatter A (2010) Use of double stations in the Swiss Permanent GNSS Network AGNES Proceeding EUREF 2010. 6 pp

Bruyninx C, Habrich H, Söhne W, Kenyeres A, Stangl G, Völksen C (2012) Enhancement of the EUREF permanent network services and products. Geodesy Planet Earth IAG Symp 136:37–35

Dach R, Lutz S, Walser P, Fridez P (eds) (2015) Bernese GNSS Software Version 5.2. User manual, Astronomical Institute, University of Bern, Bern Open Publishing

Dow JM, Neilan RE, Rizos C (2009) The International GNSS Service in a changing landscape of Global Navigation Satellite Systems. J Geodesy 83:191–198

Krawinkel T, Lindenthal N, Schön S (2014) Scheinbare Koordinatenän-derungen von GPS-Referenzstationen: Einfluss von Auswertestrate-gien und Antennenwechseln. ZfV 139:252–263

Niell AE (1996) Global mapping functions for the atmosphere delay at radio wavelengths. J Geophys Res 101(B2):3227–3246

Santerre R (1991) Impact of GPS satellite sky distribution. Manuscripta Geodaetica 16:28–53

Sarti P, Abbondanza C, Altamimi Z (2012) Local ties and co-location sites: some considerations after the release of ITRF2008. In: Altamini Z, Collilieux X (eds) Reference frames for applications in geosciences, IAG Symposia, vol 138. Springer, Heidelberg, pp 75–80

Steigenberger P, Hugentobler U, Schmid R, Hessels U, Klügel T, Seitz M (2012) GPS-Specific local effects at the geodetic observatory Wettzell. In: Altamini Z, Collilieux X (eds) Reference frames for applications in geosciences, IAG Symposia, vol 138. Springer, Hei-delberg, pp 125–130

Wilkonson M, Appleby G, Sherwood R, Smith V (2012) Monitoring site stability at the Space Geodesy Facility, Herstmonceux, UK. In: Altamini Z, Collilieux X (eds) Reference frames for applications in geosciences, IAG Symposia, vol 138. Springer, Heidelberg, pp 95–102

Receiver Antenna Phase Center Models and Their Impact on Geodetic Parameters

Tobias Kersten and Steffen Schön

Abstract

Evaluating the impact of receiver antenna phase centre corrections (PCCs) in geodetic positioning and timing applications in a general way is quite challenging, because several estimation concepts, implementation philosophies as well as different sets of PCCs exist and interact with each other and their contributions are not identifiable.

In this paper, the authors present a methodology, based on investigations of Geiger (GPS-techniques applied to geodesy and surveying. Lecture notes in earth sciences, vol 19. Springer, New York, pp 210–222, 1988) and Santerre (Manuscr Geodaet 16:28–53, 1991), to classify PCCs and forecast their impact on all geodetic parameters, i.e. not only the position but also the receiver clock and troposphere parameter in a phase based precise point positioning (PPP) approach. In a first step, we introduce the mathematical model and generic PCC patterns. In the second step, simulation studies are carried out. Findings are evaluated by empirical studies using differences of PPP results to isolate the impact of different patterns. In parallel, the software impact is analysed since every software handles the observation modelling and parameter estimation differently, e.g., Kalman filter versus least squares approach. We show that all geodetic parameters are affected by PCC and that the impact on the parameters can be even amplified compared to the magnitude of the generic patterns.

1 Introduction

The comparability of phase centre corrections (PCC) obtained from different calibration institutions (Wübbena et al. 1996; Seeber et al. 1997; Zeimetz and Kuhlmann 2008; Bilich and Mader 2012; Moore and Ridell 2016), where some institutions using independent calibration strategies, is still an issue in the International GNSS Service (IGS). Becker et al. (2010) showed that for several antennas PCC

obtained from chamber and robot antenna calibrations agree below 1 mm. However, challenges exist as shown by Aerts (2011) and Aerts and Moore (2013) for other individual calibration sets with variations up to 6–8 mm. Discrepancies between individual and type mean calibrations of up to 4 mm could be verified. Furthermore, differences of individual and type mean PCC values are reported in regional and global networks, (Sidorov and Teferle 2012; Steigenberger et al. 2013). Differences of individual and type mean calibration values introduce systematic discrepancies of up to 10 mm in the up component and up to 4 mm in the horizontal component in European Permanent Network (EPN), (Baire et al. 2014). Therefore, generic patterns are used as a method to analyse the difference of PCC patterns and to study their impact on geodetic parameter estimation, consequently.

T. Kersten (✉) • S. Schön
Institut für Erdmessung (IfE), Leibniz Universität Hannover, Schneiderberg 50, Hannover, Germany
e-mail: kersten@ife.uni-hannover.de

PCC can be compared directly (cf. IGS comparison strategy as shown in Schmid et al. 2015; Kersten and Schön 2013; Bilich et al. 2012). However, even more important seems the impact on the estimated parameters, like e.g. coordinates, tropospheric delays as well as clock parameters or ambiguities. This impact depends on the geometric shape of the PCC difference, the processing strategy of positioning applied as well as the geographic location. The authors propose to categorize the pattern of PCC differences and subsequently their impact on all geodetic parameters in precise point positioning (PPP) by generic patterns and simulation studies. The method is based on investigations initially introduced by Geiger (1988) and Santerre (1991).

The paper is organized as follows: In the first part several generic antenna patterns are presented. Next, the obtained simulation results are compared with those from different PPP software packages. There, the influence of different processing strategies (Kalman filter versus common least squares approach) is studied that propagates generic PCC patterns differently to the estimated parameters (position, receiver clock and troposphere). To this end, generic patterns are added to real, absolutely and individual calibrated PCCs.

2 Simulation Strategy

The relationship between PCC as well as differences of PCCs and estimated geodetic parameters is given by the least-squares solution

$$\Delta \mathbf{x} = (\mathbf{A^T P A})^{-1} \mathbf{A^T P r}(\theta, \lambda) \tag{1}$$

with the unknown vector $\Delta \mathbf{x}$ containing the estimated parameters, the Jacobi- or Designmatrix $\mathbf{A}$, the weight matrix $\mathbf{P}$, the generic patterns (or PCCs), $\mathbf{r}(\theta, \lambda)$ along the line-of-sight (LOS) to the satellite with zenith distance θ and azimuth angle λ in the antennas body-frame. In this contribution, the vector

$$\Delta \mathbf{x} = \begin{bmatrix} \Delta N \ \Delta E \ \Delta U \ \delta_{rec} \ \delta_{trop} \end{bmatrix}^T \tag{2}$$

contains the horizontal components ΔN, ΔE, and the vertical component ΔU of the estimated position as well as the troposphere delay δ_{trop}, and the receiver clock parameters δ_{rec}.

To qualify the impact of the receiver antenna PCCs on the estimates, different sets of generic patterns are used to characterize different kind of PCC patterns or differences of PCCs. The simulation strategy proposed by Geiger (1988) and Santerre (1991) was used, assuming continuous satellite sky distribution and expressing all terms in Eq. (1) by integrals. The initial formulas by Geiger and Santerre were extended to improve on the one hand the approximation of the northern hole in the sky distribution and on the other hand to take into account different observation weighting models like identical-, $\cos \theta$ and $\cos^2 \theta$.

3 Generic Patterns

Generic PCC patterns, that are described as error functions in Geiger (1988), are adequate to analyse and get access to the impact of PCC on geodetic parameters. In Fig. 1 four different generic patterns are shown, that can be interpreted as a component on the real receiver antenna PCC pattern.

A typical turnstile (cross dipole) pattern is described by

$$\mathbf{r}(\theta, \lambda) = A \cdot \cos(\theta) \tag{3}$$

with the amplitude A and the zenith distance θ. Figure 1a indicates that this generic pattern is completely independent from the azimuth angle and depends on the amplitude and zenith distance only. Because of the pure zenith angle dependency, inaccurate antenna orientations does not matter.

Modelling the error function of a micro-strip antenna as shown in Fig. 1b yields

$$\mathbf{r}(\theta, \lambda) = A \cdot \sin(\theta) \cdot \cos(\lambda - a_0) \tag{4}$$

where the orientation of the antenna is modelled by a_0 and the azimuth angle by λ.

Furthermore, an 1-wire ($n = 1$, Fig. 1c) or a 4-wire ($n = 4$, Fig. 1d) helix antenna is described by

$$\mathbf{r}(\theta, \lambda) = A \cdot \sin(\theta) + D \cdot \cos(\theta) \cdot \cos(n \cdot \lambda - 4\theta - n \cdot a_0) \tag{5}$$

with an additional amplitude D.

Table 1 summarizes the most prominent patterns and parameter values used in this study to describe differences in the PCC of ionosphere free linear combination (L3). The patterns are part of actual PCC patterns as determined from receiver antenna PCC comparisons at the Institut für Erdmessung (IfE). The considered magnitudes and shapes for L3 PCC are also reported in other studies (Aerts 2011; Aerts and Moore 2013) where similar differences between chamber and robot calibrations are obtained for different sets of receiver antenna models. Differences in the up-component of the phase centre offset (PCO) values result in differential PCC patterns similar to the generic pattern of Fig. 1a, differences in the horizontal PCO to those of Fig. 1b. If variations in azimuth are taken into account, generic patterns like the 1-wire helix and 4-wire helix (cf. Fig. 1c, d) are adequate as first approximation.

Fig. 1 Generic patterns to analyse the impact of different PCC patterns, (**a**) turnstile, (**b**) micro-strip, (**c**) 1-wire helix and (**d**) 4-wire helix
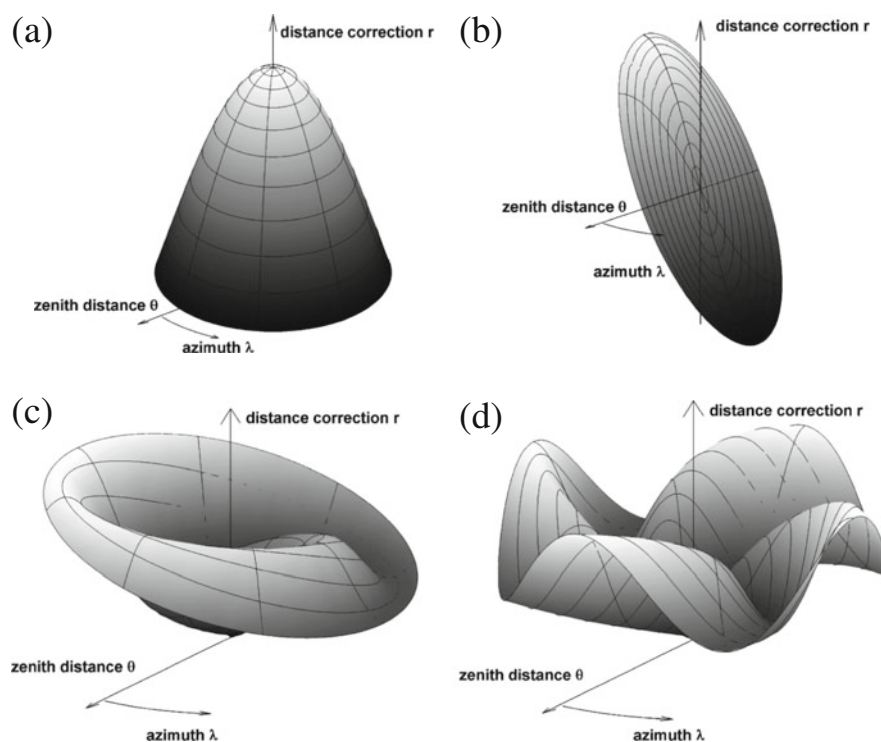
4 Evaluation and Comparison with PPP

4.1 Methodology

The simulation strategy is evaluated by taking the difference of two PPP runs (performed in static mode with 24 h sessions), where the reference solution is determined without and the second run with additional generic patterns (cf. Fig. 2 and Table 1). Results obtained from different software packages are compared to the simulation strategy (model) in Fig. 3.

Setup The first PPP solution is based on a 24 h data set with an 30 s data sampling and a cut-off angle of 3°. The data was recorded on DOY339, in 2011 with a Leica AR25.R3 antenna and a Javad TRE_G3T receiver on the laboratory network of the IfE located at a mean latitude of 54°. The solutions for DOY339 are confirmed by repeatability checks of consecutive days (DOY340 and DOY341). The Leica antenna is individually and absolutely calibrated by IfE by using the Hannover Concept of antenna calibration, developed by IfE and Geo++® during joint research projects, (Wübbena et al. 1996; Seeber et al. 1997; Wübbena et al. 1997, 2000). This calibration facility is accepted in the IGS (Dow et al. 2009) and provides PCC patterns with azimuth and elevation dependent values independently from any reference antenna or place and time of calibration.

Parameters For the second PPP processing, the original azimuth and elevation dependent PCC pattern was manipulated with sets of generic patterns (cf. Table 1). For seek of simplicity, since we are interested in the ionosphere-free linear combination (L3), both L1 and L2 patterns are manipulated here with the same generic pattern, so that also for L3 the same generic pattern is used. The troposphere was corrected using the Hopfield model and zenith path delay (ZPD) parameters are estimated as piece-wise linear function with parameter spacing of 2 h. No gradients were estimated.

The obtained PPP solutions are subtracted from the reference solution. They show only the impact of generic patterns on coordinates, receiver clock and tropospheric delay, respectively. This is true, since the same observation data is used and the impact of the observation noise is eliminated by subtraction. Additionally, first studies show, that the float ambiguity parameters are affected additionally.

The obtained results for the first five parameters (position, receiver clock, troposphere) are summarised in Fig. 3 for the different software packages.

Software Several software packages were used to obtain the different PPP solutions and access the effect of PCC patterns due to different implementation strategies or processing schemes. In this contribution, results using the Bernese 5.2 Software (Dach et al. 2015), CSRS-PPP from Natural Resources Canada's CSRS (Canadian Spatial Reference

(a) 1-wire helix (A=D=5 mm)

(b) 4-wire helix (A=5 mm,D=5 mm)

(c) 4-wire helix (A=20 mm,D=5 mm)

(d) 1-wire helix (A=D=5 mm)

(e) 4-wire helix (A=5 mm,D=5 mm)

(f) 4-wire helix (A=20 mm,D=5 mm)
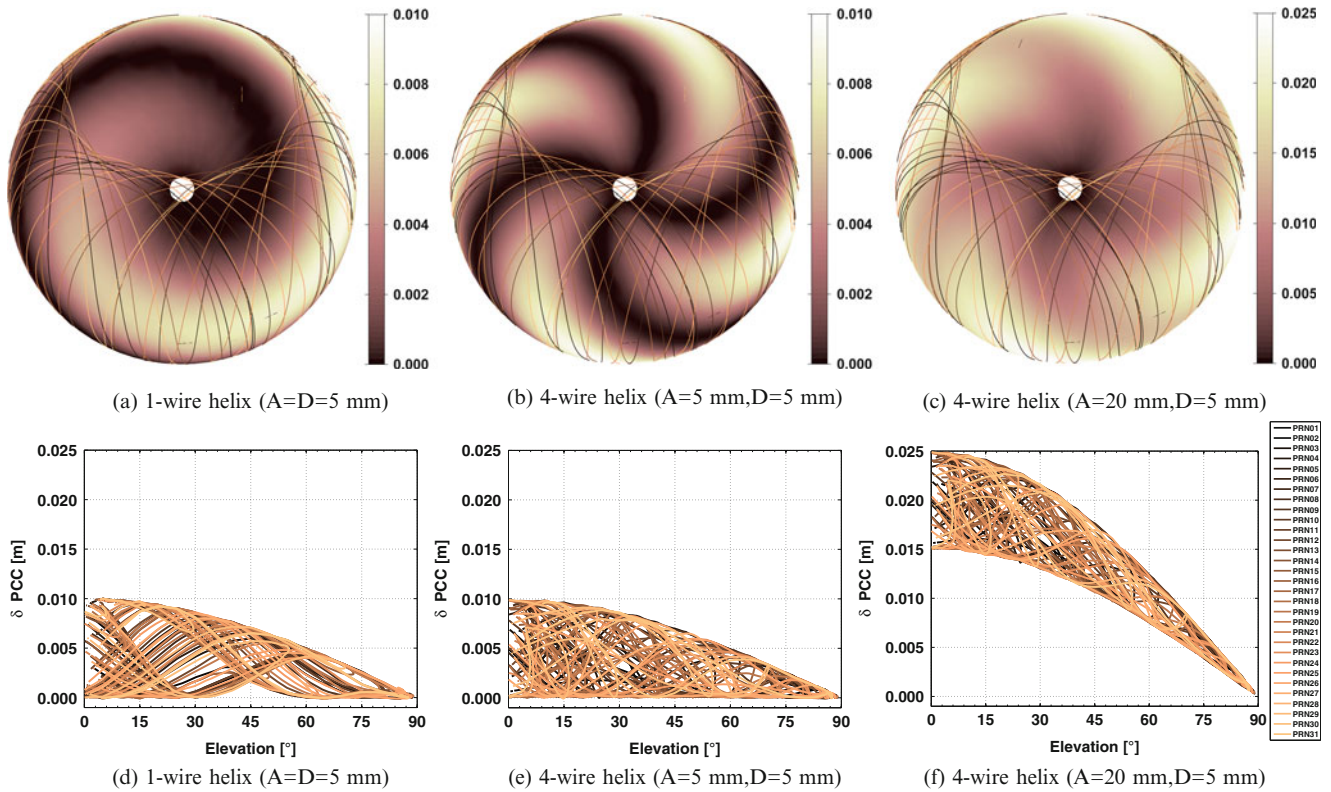
Fig. 2 Sampling of PCC pattern by a real satellite sky distribution. Identical skyplot traces in (**a**–**c**) lead to different PCC representations in the observation domain versus elevation as shown in (**d**–**f**)

Table 1 Configurations of generic patterns used in the study to analyze the impact on geodetic parameters

Identifer	Name	Generic pattern	Parameter values
P1	Turnstile	$\mathbf{r}(\theta, \lambda) = A \cdot \cos(\theta)$	$A = 1\,cm$
P2	Micro-strip	$\mathbf{r}(\theta, \lambda) = A \cdot \sin(\theta) \cdot \cos(\lambda - a_0)$	$A = 1\,cm$
P3	1-wire helix	$\mathbf{r}(\theta, \lambda) = A \cdot \sin(\theta) + D \cdot \cos(\theta) \cdot \cos(\lambda - 4\theta - 1a_0)$	$A = D = 0.5\,cm$
P{4/5}	4-wire helix	$\mathbf{r}(\theta, \lambda) = A \cdot \sin(\theta) + D \cdot \cos(\theta) \cdot \cos(4\lambda - 4\theta - 4a_0)$	$A = \{0.5\,cm/2\,cm\}, D = 0.5\,cm$

System) (MacLeod and Tetreault 2014) and GPS-Toolkit (GPSTk) (Conn et al. 2012) are compared in Fig. 3 with each other.

In addition, a second Bernese analysis was processed using (1) different observation weightings ($\cos z$ vs. equal weighting) as well as (2) different tropospheric mapping functions (global mapping function (GMT) vs. Niell model (Saastamoinen zenith path delay (ZPD) with Niell mapping function)), (Niell 1996; Boehm et al. 2006). These results are summarised in Fig. 4.

4.2 Impact of Simple Generic Patterns

As expected, the turnstile generic pattern only affects the height component, indicated by the first bar in Fig. 3a–e. In Fig. 3 the bars (2–5) show the typical behaviour, expected for the generic pattern of a micro-strip model, where only the

horizontal component is affected by the introduced generic pattern. The orientation a_0 is varied from 0° to 35° (5) in 10° steps.

In both cases (turnstile and micro-strip) the magnitude in position domain (10 mm) equals the amplitude in the observation domain (10 mm). Thus, neither an amplification nor a reduction of possible discrepancies in PCC pattern of these types occur when analysing the parameters.

The Fig. 3 also indicates, that all software packages (expect GPS Toolkit) agree at the sub-millimetre level with respect to the values from simulations (model). In the case of GPSTk, the studies shown that exact the half of the amplitude in the observation domain is transferred to the horizontal position domain. From Fig. 3 it can be noted additionally, that GPSTk show differences between the expected model values for receiver clock and troposphere parameter.

Additionally, further studies (Hiemer et al. 2015) showed that the observation weighting has no significant impact on
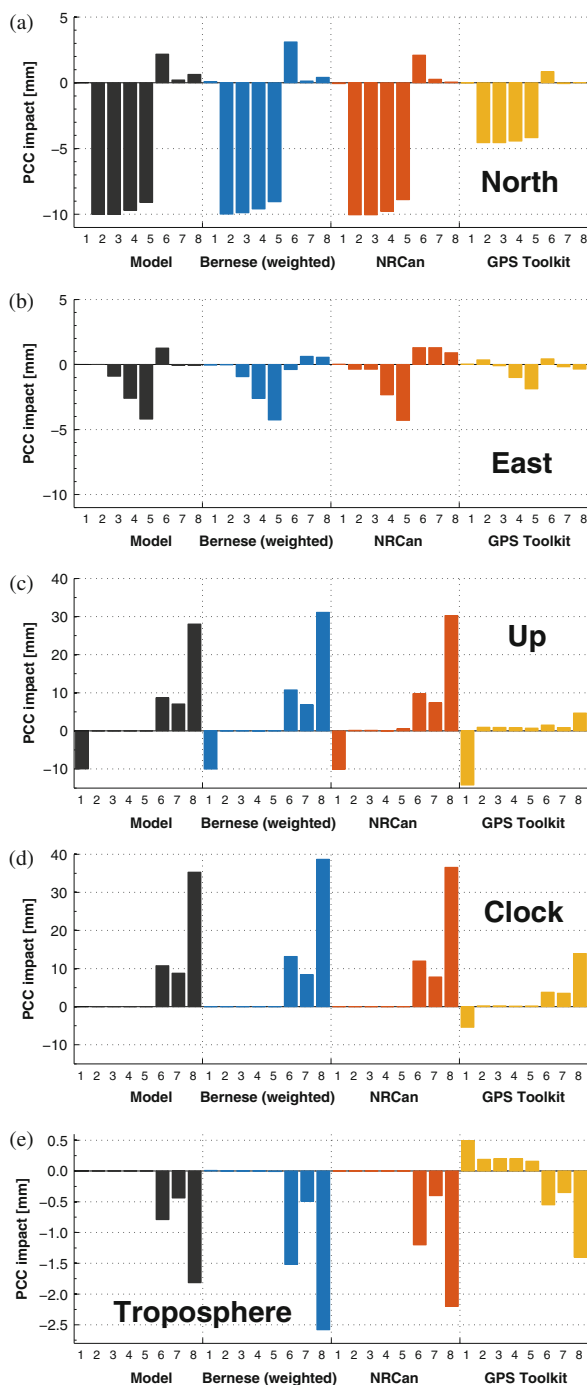
Fig. 3 Differences between solutions obtained with different software packages. The subfigures show solutions for (**a–c**) the north-, east- and up-component, (**d**) the estimated receiver clock and (**e**) the troposphere parameters. The numbers define the kind of generic patterns: (*1*) turnstile, (*2-5*) micro-strip with orientations a_0 from 0°i to 30°, (*6*) 1-wire helix, (*7*) 4-wire helix and (*8*) 4-wire helix with higher amplitude. Bernese results are obtained using $\cos z$ weighting, while the model and the other products run with equal weighted observation weighting

this comparison for turnstile and micro-strip antennas as depicted in Fig. 3.

4.3 Impact of Complex Patterns

Comparison for Several Software Packages Contrary to the previous results, patterns of 1-wire and 4-wire helix affect all geodetic parameters cf. Fig. 3, bars 6–8. Due to high correlations between up component, clock and troposphere parameters, they are most sensitive for elevation dependent patterns. Different software solutions show similar qualitative pattern but vary about few millimetre, except for GPSTk where the variations are more important. It is very important to note that the impact of generic patterns on the up component (ΔU) and clock parameter (δ_{rec}) can reach values of approx 40 mm, much larger than the pattern itself (25 mm), compare Fig. 3 bar 6 and 7 (magnitude of 10 mm for 1-wire and 4-wire helix) with bar 8 where a magnitude of 25 mm for the 4-wire helix occurs. Thus, an amplification of PCC differences of this type are obtained.

Comparison for Different Processing Strategies In Fig. 4 the findings for complex patterns with two different processing strategies are summarised. The simulation of complex patterns for 4-wire helix antenna (II, III) with amplitudes of $A = D = 5$ mm agrees very well with the results from Bernese for all components. However, differences occur for different amplitudes, e.g. in the case of 4-wire (III) with $A = 20$ mm and $D = 5$ mm, differences of 3–5 mm in the up component and receiver clock parameter are clearly detectable, cf. Fig. 4c, d. The troposphere parameter is challenging since the discrepancies differ between 1 mm and 4 mm depending on the chosen amplitude (A versus D), cf. Fig. 4e. Furthermore, the agreement between data and simulation of 4-wire helix antenna is better than for the 1-wire model. This is mostly depending on the non-symmetrical distribution of the 1-wire helix generic pattern, cf. Fig. 2a vs. Fig. 2c. This emphasizes that the parametrization of the satellite sky distribution has an important impact on this simulation strategy and has to be modelled as precisely as possible. Therefore, an adequate distribution function to parametrise the satellite sky distribution for different geographic latitudes has to be improved.

5 Conclusions

The analysis shows, that the improved theoretical model of generic PCC patterns gives valuable and qualitative information on the impact of variations of the PCC patterns on the
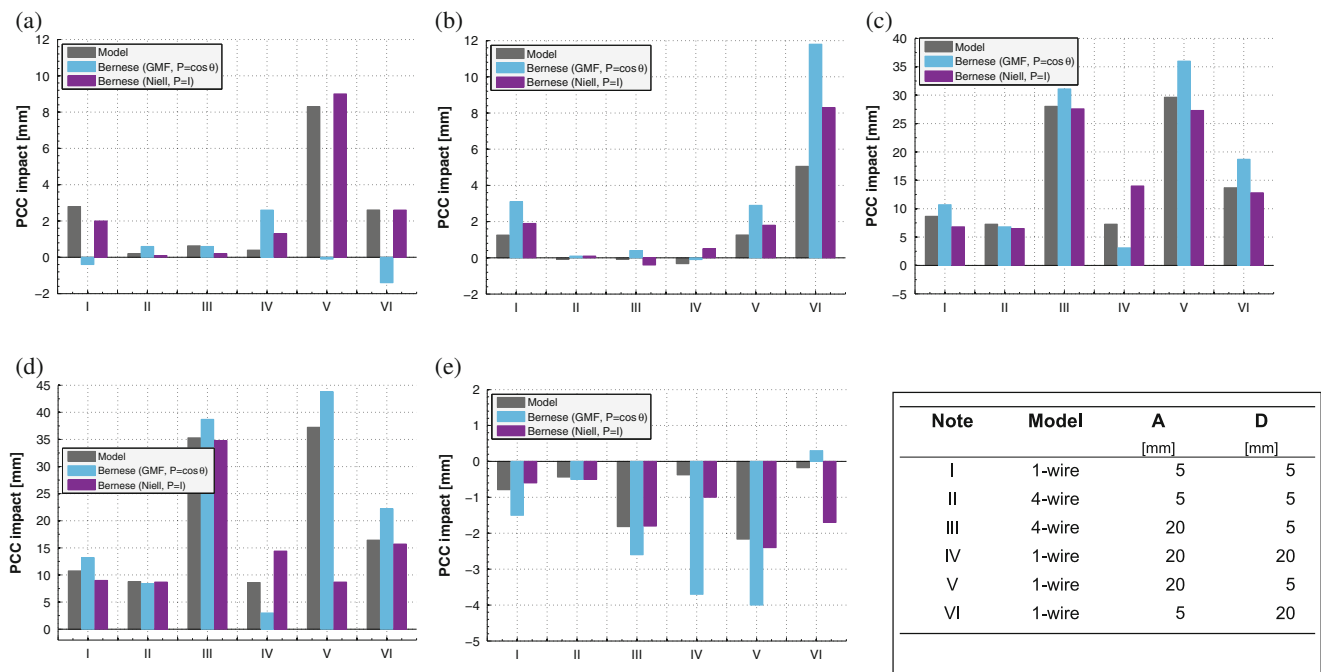
Fig. 4 Additional studies with Bernese using 1-wire and 4-wire generic patterns with GMF-Model and elevation weighted ($P = \cos\theta$) as well as unweighted ($P = I$) observations with Niell. (**a**) North component. (**b**) East component. (**c**) Up component. (**d**) Receiver clock parameter. (**e**) Tropospheric parameter

estimated geodetic parameters. It should be stressed, that all geodetic parameters should be analysed including e.g. clock parameters and tropospheric delays as well as ambiguities, since besides positioning also time and frequency transfers as well as meteorological studies are important fields of GNSS. The values obtained from the simulations are generally smaller than those obtained from software packages.

The analysis showed that not only the magnitude of a PCC pattern but especially its shape is critical for a classification of the impact on geodetic parameters. Patterns $A\cos\theta$ and $A\sin\theta\cos(\lambda - a_0)$ are 1:1 transferred to the vertical and horizontal coordinates, respectively. The user should be aware that more complex pattern, like e.g., n-wire helix affect all parameters and the magnitude in the parameter domain can be amplified by up to 68 % compared to that of the pattern. This can be the case, when type mean values are used instead of individual PCCs.

References

Aerts W (2011) Comparison of UniBonn and Geo++® calibration for LEIAR25.R3 antenna 09300021. Technical report, Royal Observatory of Belgium

Aerts W, Moore M (2013) Comparison of UniBonn and IGS08 antenna type means. White paper, International GNSS Service - Antenna Working Group IGS-AWG. EMail: IGS-AWG-393

Baire Q, Legrand CBB, Pottiaux E, Aerts W, Defraigne P, Bergeot N, Chevalier JM (2014) Influence of different GPS receiver antenna calibration models on geodetic positioning. GPS Solutions 18(4):529–539

Becker M, Zeimetz P, Schönemann E (2010) Anechoic Chamber calibrations of phase center variations for new and existing GNSS signals and potential impacts in IGS processing. In: IGS workshop 2010 and vertical rates symposium, June 28–July 2, Newcastle upon Tyne, United Kingdom of Great Britain

Bilich A, Mader G (2012) GNSS absolute antenna calibration at the national geodetic survey. In: IGS workshop 2012, University of Warmia and Mazury, July 23–27. Poster, Olsztyn

Bilich A, Schmitz M, Görres B, Zeimetz P, Mader G, Wübbena G (2012) Three-method absolute antenna calibration comparison. In: IGS workshop 2012, University of Warmia and Mazury, Olsztyn, July 23–27

Boehm J, Niell AE, Tregoning P, Schuh H (2006) Global mapping function (gmf): a new empirical mapping function based on numerical weather model data. Geophys Res Lett 33(7):4

Conn T, Gaussiran T, Harris RB, Mach JLR, Munton D, Renfro B, Tolman B, Craddock T, Vermeer M (2012) The GPS toolkit - a user's guide for scientists, engineers and students. The University of Texas at Austin. GPSTk Revision 1038

Dach R, Lutz S, Walser P, Fridez P (eds) (2015) Bernese GNSS software version 5.2. Astronomical Institute, Universtiy of Bern, Bern Open Publishing. doi:10.7892/boris.72297

Dow JM, Neilan R, Rizos C (2009) The international GNSS service in a changing landscape of global navigation satellite systems. J Geod 83(3–4):191–198. doi:10.1007/s00190-008-0300-3

Geiger A (1988) Modeling of phase centre variation and its influence on GPS-positioning. In: GPS-techniques applied to geodesy and surveying. Lecture notes in earth sciences, vol 19. Springer, New York, pp 210–222

Hiemer L, Kersten T, Schön S (2015) On the impact of GPS phase center corrections on geodetic parameters: analytical formulation and empirical evaluation by PPP. In: Geophysical research abstracts, EGU General Assembly 2015, vol 17, Vienna

Kersten T, Schön S (2013) On adequate comparison of antenna phase center variations. In: AGU fall meeting, San Francisco, CA, Dec 09–13. Abstract #G13B-0950

MacLeod K, Tetreault P (2014) NRCan precise point positioning (PPP) service. In: Civil GPS service interface committee, Tampa Convention Center, Sept 8

Moore M, Ridell A (2016) Geoscience Australia antenna calibration facility. In: International GNSS service (IGS) workshop, Sydney, NSW, Feb 08–12

Niell AE (1996) Global mapping functions for the atmosphere delay at radio wavelengths. J Geophys Res 101(b2):3227–3246

Santerre R (1991) Impact of GPS satellite sky distribution. Manuscr Geodaet 16:28–53

Schmid R, Dach R, Collilieux X, Jäggi A, Schmitz M, Dilssner F (2015) Absolute IGS antenna phase center model igs08.atx: status and potential improvements. J Geod 90(4):343–364

Seeber G, Menge F, Völksen C, Wübbena G, Schmitz M (1997) Precise GPS positioning improvements by reducing antenna and site dependent effects. In: Advances in positioning and reference frames. International association of geodesy symposia, vol 118. Springer, Berlin/Heidelberg, pp 237–244

Sidorov D, Teferle F (2012) Antenna phase center calibration effects on sub-daily and daily position estimates. In: IGS workshop 2012, University of Warmia and Mazury, Olsztyn, July 23–27

Steigenberger P, Hugentobler U, Schmid R, Hessels U, Klügel T, Seitz M (2013) GPS-specific local effects at the geodetic observatory Wettzell. In: Reference frames for applications in geosciences, vol. 138 International association of geodesy symposia, pp 125–130. Springer, Berlin/Heidelberg. doi:10.1007/978-3-642-32998-2_20

Wübbena G, Menge F, Schmitz M, Seeber G, Völksen C (1996) A new approach for field calibration of absolute antenna phase center variations. In: The Institute of Navigation (ION GPS 1996), Kansas City, Sept 17–20, pp 1205–1214

Wübbena G, Schmitz M, Menge F, Seeber G, Völksen C (1997) A new approach for field calibration of absolute antenna phase center variations. Navigation 44(2):247–256

Wübbena G, Schmitz M, Menge F, Böder V, Seeber G (2000) Automated absolute field calibration of GPS antennas in real-time. In: The Institute of Navigation (ION GPS 2000), Sept 19–22. Institute of Navigation (ION), Salt Lake City, pp 2512–2522

Zeimetz P, Kuhlmann H (2008) On the accuracy of absolute GNSS antenna calibration and the conception of a new anechoic chamber. In: Proceedings of the FIG working week 2008 - integrating generations, Stockholm, June 14–19, p 16

Singular Spectrum Analysis for Modeling Geodetic Time Series

Q. Chen and N. Sneeuw

Abstract

Geodetic time series obtained via space-geodetic techniques, e.g. site displacements from continuous GPS observations and aggregated basin water storages from GRACE, display a seasonal behavior. Much focus has been given to separate such periodic signal from other signals buried in the geodetic time series, e.g. linear or non-linear trends. Conventionally, these seasonal signals are retrieved with constant amplitudes by the classical least squares estimation approach. Recently, singular spectrum analysis (SSA) has been successfully applied to extract the time variable seasonal signals from the GPS time series.

This study aims to extend the application of SSA to other geodetic time series. Through two examples, i.e. water level time series from satellite altimetry and GRACE-derived basin averaged equivalent water height time series, the capabilities of SSA to separate the non-linear trend from seasonal signals are demonstrated. In addition, it is shown that the so-called **w**-correlation analysis is beneficial in determining the optimal embedding window size, which is a key parameter during SSA analysis.

Keywords

Geodetic time series • Non-linear trend • Seasonal signals • Singular spectrum analysis

1   Introduction

Over the last two decades, investigation of surface mass loading via space-geodetic techniques has shown that many of the mass fluxes display a seasonal behavior, especially a composition of annual plus semiannual signals (Dong et al. 2002). Much attention has been given to separate these periodic signals from other signals in the geodetic time series,

e.g. linear or nonlinear trends. Conventionally, these seasonal signals are modeled by sums of sinusoids with annual plus semiannual cycles using the classical least squares estimation approach. However, only constant amplitudes and phases can be obtained in this parametric approach. In reality, true seasonal signals are not constant from year to year. For example, water storage changes show strong peaks due to floods or droughts. Recently, several studies have endeavored to determine the time-varying periodic variations using non-parametric approaches (e.g. Freymueller 2009; Chen et al. 2013) or model based approaches (e.g. Davis et al. 2012). Among them, Chen et al. (2013) successfully applied singular spectrum analysis (SSA) to time-variable seasonal signals modeling for GPS time series. Comparing to the least squares as well as the Kalman filtering approach (Davis et al. 2012), SSA shows both its advantages and disadvantages (Chen et al. 2013, 2015)

In geodesy, data-driven methods, such as PCA (Principal Component Analysis), are of significant interests because

Q. Chen (✉)
Institute of Geodesy, University of Stuttgart, Geschwister-Scholl-Str. 24D, 70174 Stuttgart, Germany

Faculty of Science, Technology and Communication, University of Luxembourg, Luxembourg City, Luxembourg
e-mail: qiang.chen@gis.uni-stuttgart.de

N. Sneeuw
Institute of Geodesy, University of Stuttgart, Geschwister-Scholl-Str. 24D, 70174 Stuttgart, Germany

of their parameter free and straightforward implementation characteristics. These approaches are normally used to smooth or model multivariate geodetic time series, e.g. multivariate GPS time series (Dong et al. 2006). As an extension of PCA, Rangelova et al. (2012) utilized M-SSA (multi-channel singular spectrum analysis) to investigate the main time-variable mass variations from GRACE data. In comparison to these approaches, SSA, as a special case of M-SSA, is designed to analyze univariate time series. This feature facilitates its application to univariate geodetic time series, for example, single-coordinate GPS time series (Chen et al. 2013). On the basis of Chen et al. (2013), this study is dedicated to extend the application of SSA to other univariate geodetic time series. In addition to extracting seasonal signals, other features of SSA, e.g. non-linear trend extraction, will also be investigated.

The paper is accordingly organized as follows: in Sect. 2 we shortly outline the methodology of SSA, following which in the same section we discuss few aspects related to its application. Section 3 is the data analysis part, where we show two examples of applying SSA to the lake level time series from satellite altimetry and GRACE-derived equivalent water height time series. Finally, we summarize our study and draw conclusions in Sect. 4.

2 Methodology

2.1 Singular Spectrum Analysis

Following the description of SSA from Broomhead and King (1986) and Vautard and Ghil (1989), the main procedure of the technique can be summarised as follows:

1. Given a centered time series x_t ($1 \leq t \leq N$), the first step is to construct a covariance matrix. We follow the algorithm proposed by Vautard and Ghil (1989) to compute the covariance matrix C_{VG}, which is based on the lagged-covariance matrix of the process x_t. With a maximum lag (or window size), M, the matrix C_{VG} has a Toeplitz structure, i.e., constant diagonals corresponding to equal lags:

$$C_{\mathrm{VG}} = \begin{pmatrix} c_0 & c_1 & c_2 & \cdot & \cdots & c_{M-1} \\ c_1 & c_0 & c_1 & \cdot & \cdots & \cdot \\ c_2 & c_1 & c_0 & \cdot & \cdots & \cdot \\ \cdot & c_2 & c_1 & c_0 & \cdots & \cdot \\ \vdots & \vdots & \vdots & \vdots & \vdots & \vdots \\ \cdot & \cdot & \cdot & \cdot & \cdot & c_1 \\ c_{M-1} & \cdot & \cdot & \cdot & c_1 & c_0 \end{pmatrix}, \quad (1)$$

where entries c_j, $0 \leq j \leq M-1$, are the covariance of x at lag j. Its unbiased estimates are:

$$c_j = \frac{1}{N-j} \sum_{i=1}^{N-j} x_i x_{i+j}, \qquad 0 \leq j \leq M-1. \quad (2)$$

2. We apply eigenvalue decomposition to C_{VG} in order to obtain the eigenvalues, λ_k, and eigenvectors (also called EOFs), E^k, of this matrix. These are then sorted in descending order of λ_k, where index $k = 1, 2, \ldots, M$. The kth principal component (PC) is

$$a_i^k = \sum_{j=1}^{M} x_{i+j} E_j^k, \qquad 0 \leq i \leq N-M. \quad (3)$$

3. We reconstruct each component, i.e. reconstructed component (RC), of the original time series as given by

$$x_i^k = \begin{cases} \frac{1}{i} \sum_{j=1}^{i} a_{i-j}^k E_j^k & 1 \leq i \leq M-1 \\[2ex] \frac{1}{M} \sum_{j=1}^{M} a_{i-j}^k E_j^k & M \leq i \leq N-M+1 \\[2ex] \frac{1}{N-i+1} \sum_{j=i-N+M}^{M} a_{i-j}^k E_j^k & N-M+2 \leq i \leq N. \end{cases}$$

$$(4)$$

4. According to Plaut and Vautard (1994), harmonic oscillations can be identified in terms of the three fundamental properties: (1) two consecutive eigenvalues are nearly equal; (2) the two corresponding time sequences described by EOFs are nearly periodic, with the same period and in quadrature; (3) the associated PCs are in quadrature.

2.2 Aspects of Application of SSA

In the practical implementation of the SSA algorithm, one most important aspect is to select the optimal lag-window size M which depends not only on the length of the data but also on the desired periodic cycles. Both empirical and mathematical rules exist in the literature to suggest how to make a proper choice of the lag-window size M. For instance, a 2-year or 3-year window size is demonstrated to be appropriate by Chen et al. (2013) using both simulated and observed weekly GPS time series. Here we suggest another useful tool, i.e. the **w**-correlation analysis proposed by Golyandina and Zhigljavsky (2013), to optimize the lag-window size. The **w**-correlation analysis evaluates
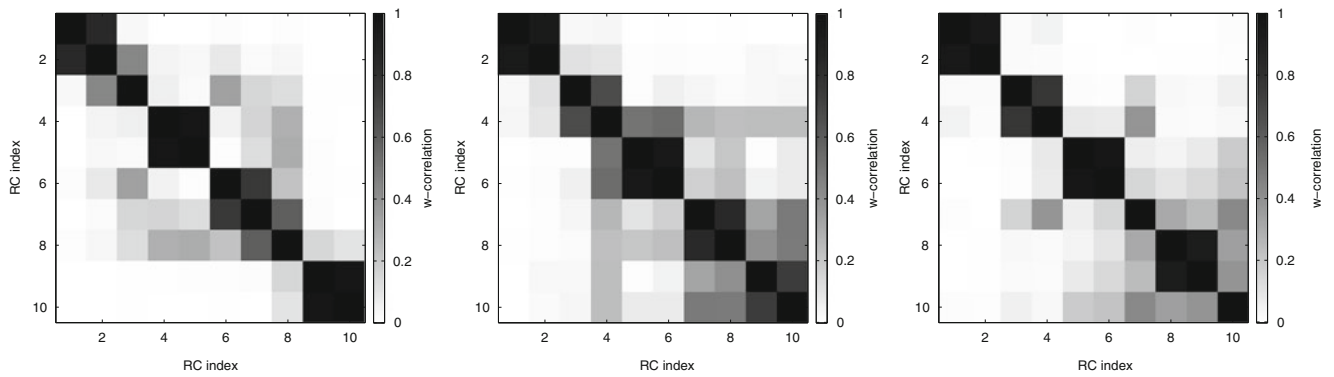
Fig. 1 The **w**-correlation analysis of the first ten RCs form the water level time series using a 3-year window size ($M = 108$, *left*), a 4-year window size ($M = 144$, *middle*) and a 5-year window size ($M = 180$, *right*). Different separabilities are shown with different lag-window sizes

Fig. 2 The observed water level time series of Lake Urmia (Tourian et al. 2015) and the interpolated time series
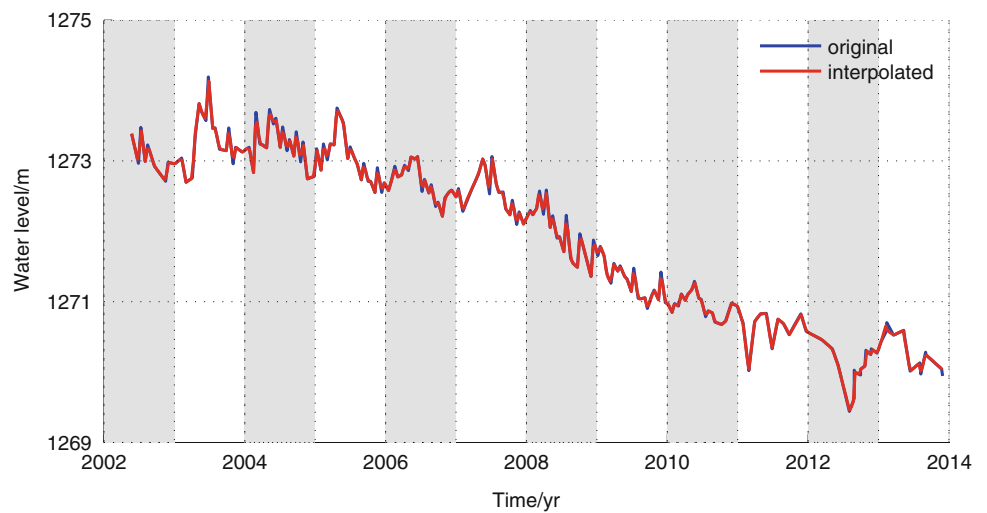
correlations between the obtained RCs so as to define whether a weak or strong separability exists. One example for the **w**-correlation analysis is illustrated in Fig. 1 using the lake level time series from Sect. 3.1. Clearly, better separabilities are observed using a 5-year window size for the first ten modes and strong separabilities of signals are preferable in practice.

Another important aspect related to the application of SSA is to deal with gaps in geodetic time series. For the gaps due to irregular sampling, we resample the data into regular sampling (see Sect. 3.1). While for the gaps due to missing data in the evenly sampling, one solution is to fill the gaps using interpolation techniques and apply SSA afterwards. An alternative approach is suggested by Schoellhamer (2001), which has been demonstrated to be advantageous by Chen et al. (2013) (see also Sect. 3.2). In the use of the Schoellhamer (2001)'s approach, missing observations are filled with NaN values and computing Eqs. (2) and (3) is done by ignoring these filled NaN values. Specifically, a scale factor related to the number of missing data is applied to compensate the missing value when computing PCs. The Schoellhamer (2001)'s approach has been demonstrated to be a special case of a more rigorous approach suggested very recently by Shen et al. (2015).

3 Application of SSA to Geodetic Time Series

3.1 Lake Level Time Series

The lake level time series used in this section comes from Tourian et al. (2015) which was derived for monitoring the desiccation of Lake Urmia in Iran. The data spanning from 2002.4 to 2013.9 was derived from three different satellite altimetry orbit configurations launched by European Space Agency (ESA), namely, ENVISAT (ENVIromental SATellite), EVISAT extended and CryoSat-2. Each satellite orbit configuration has its own sampling rate, for example, a 35-day repeat period for ENVISAT and a 30-day repeat cycle for ENVISAT extended. In addition, both descending and ascending tracks were used to derive lake level changes. All these factors make the whole dataset into an irregularly sampled time series (Tourian et al. 2015). Thus, it is necessary to resample the data and it is accordingly interpolated with the piecewise cubic spline interpolation into time series with a 10-day sampling interval. The original water level time series and the interpolated one are shown in Fig. 2 which display a very

clear non-linear trend together with different periodicities and noise. The following analysis will show capabilities of SSA to capture the non-linear trend and separate the oscillations.
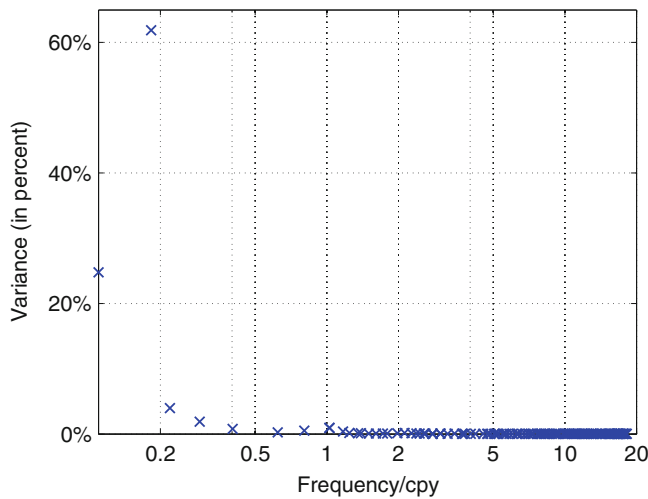
Fig. 3 Eigenvalues versus the dominant frequency associated with their corresponding EOFs

Based on the experiences from Chen et al. (2013) as well as the **w**-correlation analysis shown in Fig. 1, a 5-year window size ($M = 180$) is selected and applied. In terms of the methodology presented in Sect. 2, the corresponding eigenvalue spectrum plot is firstly shown in Fig. 3. It is shown in Fig. 3 that the long term trend signal appears in the first four modes which dominate the whole data and correspond to up to 92.5 % of the total variance. Annual signals appear in the fifth and sixth modes corresponding only up to 1.85 % energy and no significant semi-annual signals occur in the time series.

According to the eigenspectrum shown in Fig. 3 as well as suggestions by Plaut and Vautard (1994), corresponding EOFs and PCs are grouped and shown in Fig. 4. The first four modes clearly illustrate the long-term trends with different frequencies and the fifth and sixth modes correspond to the annual signals. The latter four modes correspond to other irregular oscillations with no origins to our knowledge which might be due to colored noise (Allen and Smith 1996).

In terms of variance contributions, the first six modes contribute up to 94.35 % of the total variance and therefore these first six modes are reconstructed and displayed in Fig. 5. The first two RCs clearly display the long-term trend while the third and fourth RCs seem to show two long-term

Fig. 4 The first ten EOFs and PCs are grouped in terms of the eigenspectrum
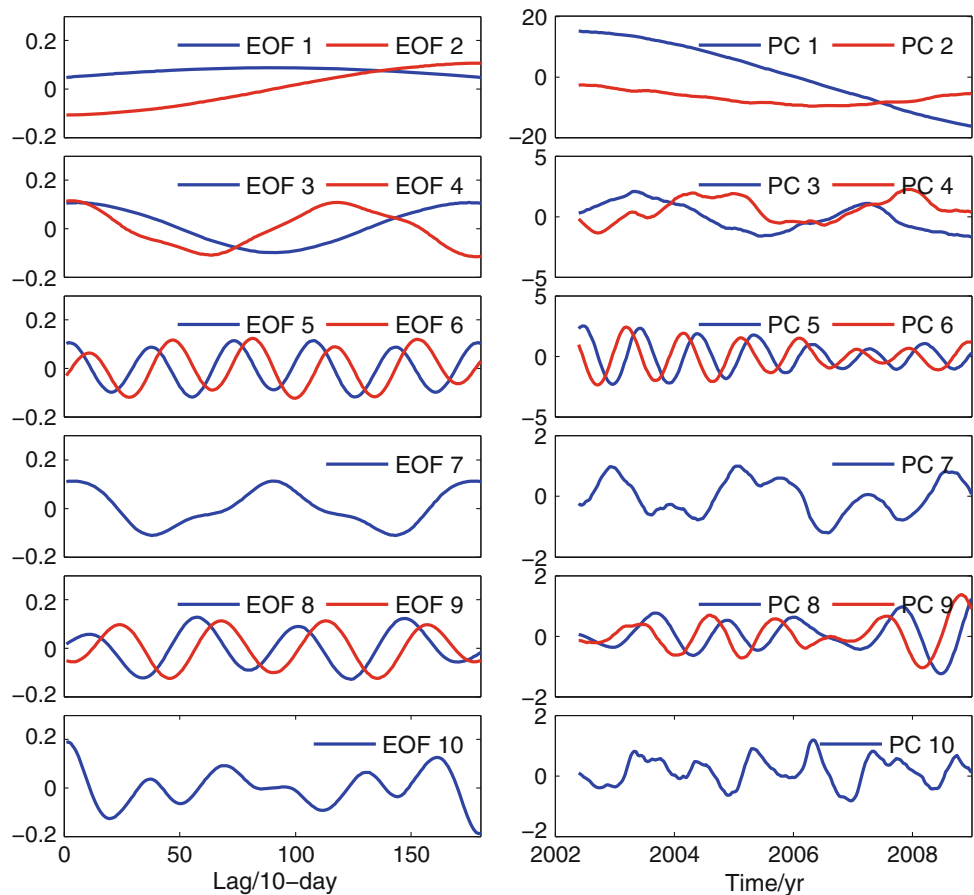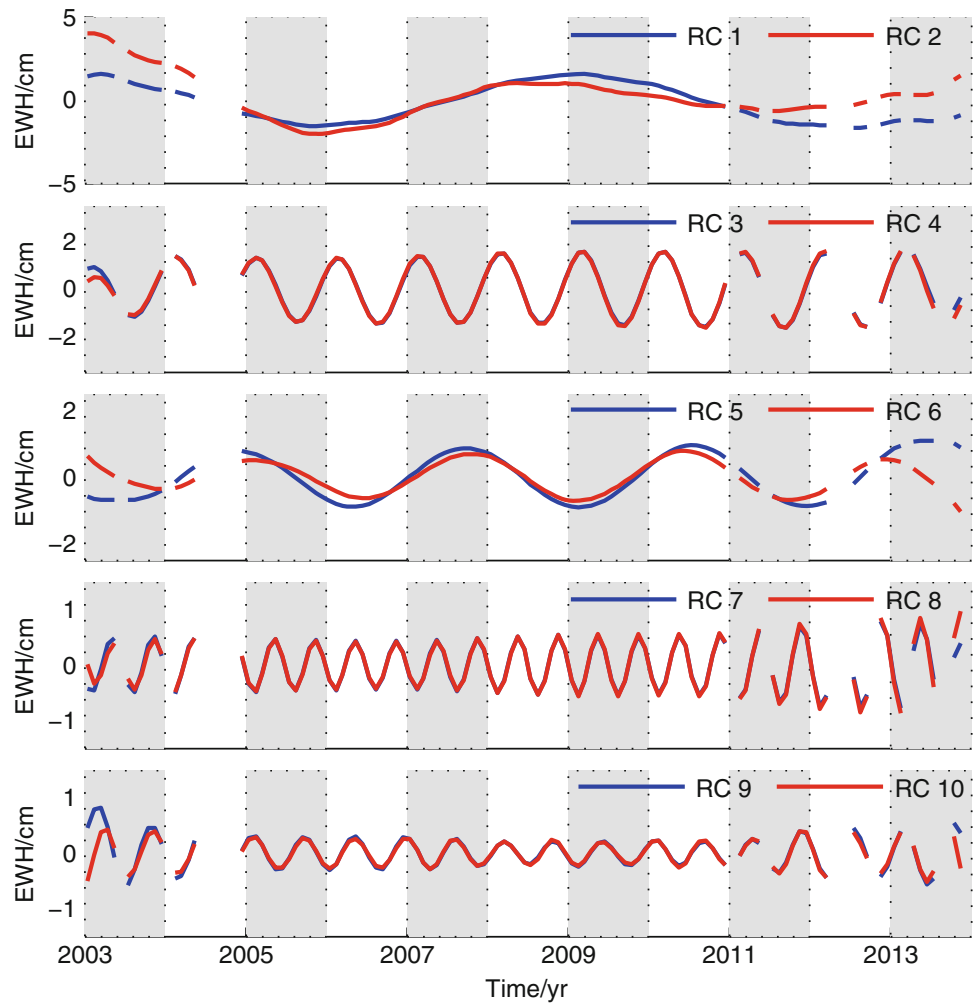
Fig. 5 The first six reconstructed components
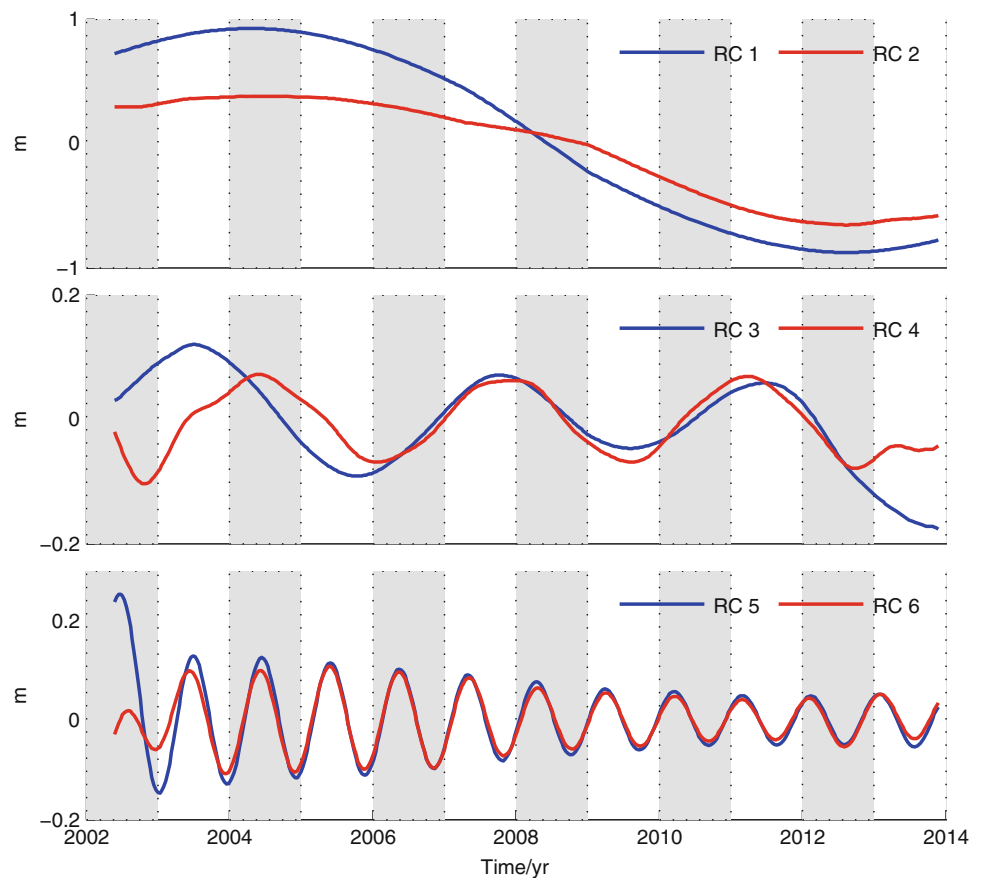
Fig. 6 Comparison of RCs with respect to the original time series. Plots with *magenta and red curves* are shifted for plotting purposes
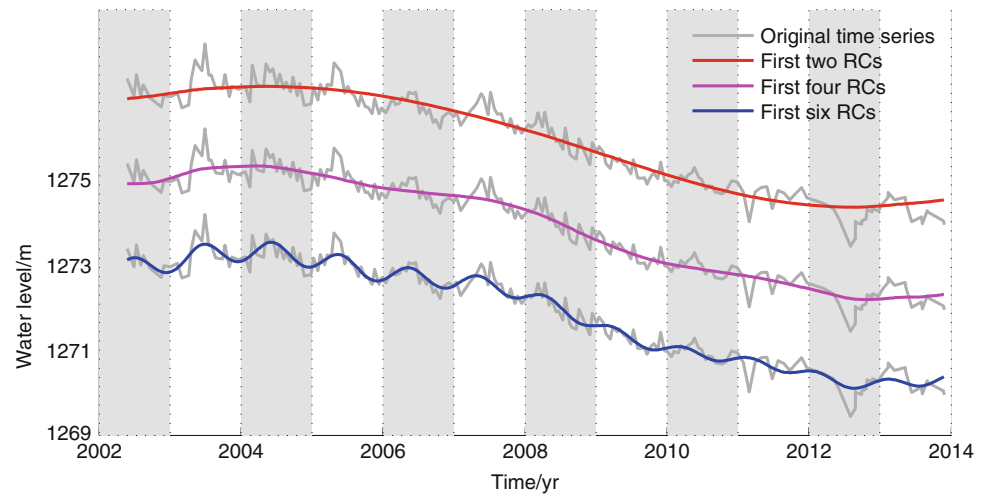
oscillations with a period around 4 years which deserve a further investigation of their origin. However, this further investigation is out of the scope of this section. The amplitude modulated annual signals are obviously represented with decreasing amplitudes which might be caused by the desiccation of Lake Urmia (Tourian et al. 2015).

Figure 6 shows the summation of the first six RCs with respect to the original time series. The blue curve in Fig. 6 fits the original time series very well capturing both the non-

linear trend as well as the periodic signals. Furthermore, it is also found that the red curve representing the long-linear trend follows the whole time series closely, which demonstrates the ability of SSA to separate the long-term trend from the periodic variabilities and noise.

SSA is not compared with other mode-based techniques, e.g. the classical least squares method and the Kalman filter approach (Chen et al. 2013; Davis et al. 2012), due to the existence of the non-linear trend which is hard to be

represented by a simple mathematic model. Nevertheless, future work will focus on this aspect to compare SSA with other potential techniques or to examine the significance of those captured signals using, for example, Monte-Carlo SSA (Allen and Smith 1996).

3.2 Basin Averaged Equivalent Water Height Time Series

With the advent of the GRACE mission, equivalent water height (EWH) time series, especially area or basin averaged ones, are of remarkable interest for geodesists to study hydrological loading processes. These time series normally display a strong seasonal signal together with a linear or non-linear trend depending on location (e.g., Rangelova et al. 2012). It is always of central importance to separate these components so as to facilitate the understanding of their origins (see Davis et al. 2012; Rangelova et al. 2012). In particular, Rangelova et al. (2012) demonstrated the usage of M-SSA combined with a 700 km Gaussian filter on the weekly GRACE gravity spherical harmonic coefficients to derive basin averaged seasonal total water storages. This section aims to show an alternative procedure which applies SSA to extract non-linear and seasonal signals from the basin averaged total water storage time series.

It is worth mentioning that, before performing SSA, we firstly derive the equivalent water height and then compute the basin averages to obtain the basin scale equivalent water height time series. The Congo basin which is located in west equatorial Africa with a basin size of 3693×10^3 km^2 is adopted here as an example. To be more detailed in the procedure of deriving the equivalent water height time series, the combination of the destriping filter (Swenson and Wahr 2006) and a 500 km Gaussian filter is applied to the monthly GFZ RL05a spherical harmonic coefficients (Dahle et al.

2014). The months with regularized solutions, e.g. June to November in 2004, are removed so that a few gaps exist in the time series, see Fig. 7.

As mentioned before, Schoellhamer (2001)'s approach is used here for dealing with gaps in the course of the SSA analysis. Via the **w**-correlation analysis, a window size of 5-year is deployed here in this example. We skip to show the corresponding eigenvalue spectrum, EOFs and PCs here due to limited pages. Nevertheless, clearly shown in Fig. 8, long-term trends appear in the first two reconstructed modes and strong annual signal patterns occur in the third and fourth components. These four modes dominate the whole time series contributing up to 71.8 % in terms of variance. Inter-annual patterns (a 3-year cycle) which were also seen by Schmidt et al. (2008) and Rangelova et al. (2012) are observed in the fifth and sixth modes with a contribution of 8.4 % variance. The same finding as Schmidt et al. (2008) for the Congo basin here is that semi-annual signals do not play a significant role contributing only 4.0 % variance. An approximate 1.5-year oscillation pattern also appears in the ninth and tenth modes which requires further investigation of its origin.

The comparison of the reconstructed components with respect to the derived equivalent water height is displayed in Fig. 9. The blue curve consists of the first eight RCs with a contribution of 84.2 % to the total variance and it fits the original time series closely with a correlation of 0.9. The red curve indicating the non-linear trend also sees the minimum and the peak which were also shown in Rangelova et al. (2012). By a careful visual inspection, the pattern shown in Fig. 9 has significant similarities with the Fig. 9b shown in Rangelova et al. (2012), which in a way verifies the analysis presented here.

The above analysis confirms that gaps are not a problem in the SSA analysis and the modified SSA algorithm proposed by Schoellhamer (2001) could adequately handle time series

Fig. 7 The derived equivalent water height time series of the Congo Basin
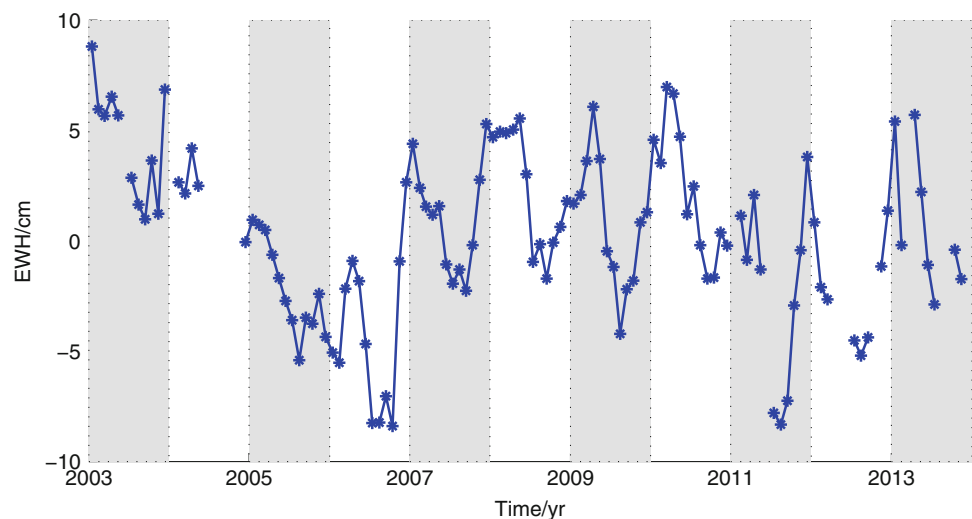
Fig. 8 The first ten reconstructed components of the equivalent water height time series from the Congo basin

Fig. 9 Comparison of RCs with respect to the original time series in the Congo basin. Plots with *magenta and red curves* are shifted for plotting purposes
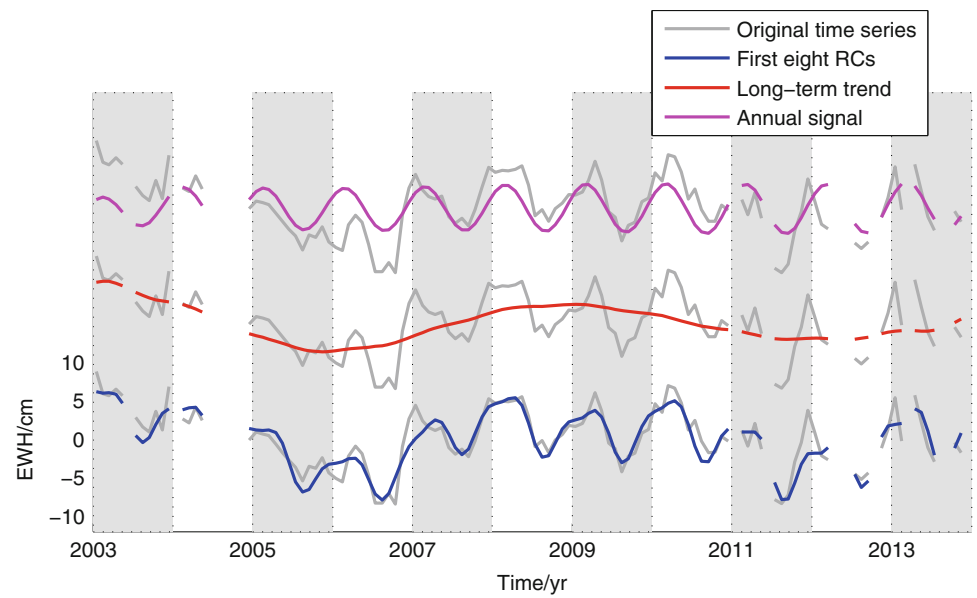
with missing data. Nevertheless, it is worth pointing out that SSA fails to capture few peaks of the equivalent water height time series in Congo. This might be a potential weakness of SSA.

4   Conclusion

In this study, we further investigate the capabilities of SSA for modeling geodetic time series. Two exemplary time series with clear long-term trends together with other periodic variabilities, e.g. annual variations, are used for demonstration. By applying SSA to them, it is shown that SSA has the ability to separate non-linear trends and long-term variations from the seasonal oscillations.

The lag-window size is a key parameter in SSA and we have demonstrated that the **w**-correlation analysis is helpful in determining the optimal lag-window size. A 5-year window size which is found to be optimal, is applied in both examples.

References

Allen M, Smith L (1996) Monte Carlo SSA: detecting irregular oscillations in the presence of colored noise. J Climate 9(12):3373–3404. DOI 10.1175/1520-0442(1996)009<3373:MCSDIO>2.0.CO;2

Broomhead D, King GP (1986) Extracting qualitative dynamics from experimental data. Physica D 20:217–236. DOI 10.1016/0167-2789(86)90031-X

Chen Q, van Dam T, Sneeuw N, Collilieux X, Weigelt M, Rebischung P (2013) Singular spectrum analysis for modeling seasonal signals from GPS time series. J Geodyn 72:25–35. DOI 10.1016/j.jog.2013.05.005

Chen Q, Weigelt M, Sneeuw N, van Dam T (2015) On time-variable seasonal signals: comparison of SSA and Kalman filtering based approach. In: International Association of geodesy symposia, vol 142. Springer, Berlin, pp 1–6. DOI 10.1007/1345_2015_4

Dahle C, Flechtner F, Gruber C, König D, König R, Michalak G, Neumayer KH (2014) GFZ RL05: an improved time-series of monthly GRACE gravity field solutions. In: Flechtner F, Sneeuw N, Schuh WD (eds) Advanced technologies in earth sciences. Springer, Berlin, pp 29–39

Davis JL, Wernicke BP, Tamisiea ME (2012) On seasonal signals in geodetic time series. J Geophys Res 117(B1):B01403. DOI 10.1029/2011JB008690

Dong D, Fang P, Bock Y, Cheng MK, Miyazaki S (2002) Anatomy of apparent seasonal variations from GPS-derived site position time series. J Geophys Res 107(B4):2075. DOI 10.1029/2001JB000573

Dong D, Fang P, Bock Y, Webb F, Prawirodirdjo L, Kedar S, Jamason P (2006) Spatiotemporal filtering using principal component analysis and Karhunen-Loeve expansion approaches for regional GPS network analysis. J Geophys Res 111(B3):B03405. DOI 10.1029/2005JB003806

Freymueller J (2009) Seasonal position variations and regional reference frame realization. In: Drewes H (ed) Geodetic reference frames, IAG symp, vol 134. Springer, Berlin, pp 191–196. DOI 10.1007/978-3-642-00860-3_30

Golyandina N, Zhigljavsky A (2013) Singular spectrum analysis for time series. Springerbriefs in statistics. Springer, Berlin

Plaut G, Vautard R (1994) Spells of low-frequency oscillations and weather regimes in the northern hemisphere. J Atmos Sci 51(2):210–236. DOI 10.1175/1520-0469(1994)051<0210:SOLFOA>2.0.CO;2

Rangelova E, Sideris M, Kim J (2012) On the capabilities of the multi-channel singular spectrum method for extracting the main periodic and non-periodic variability from weekly GRACE data. J Geodyn 54:64–78. DOI 10.1016/j.jog.2011.10.006

Schmidt R, Petrovic S, Güntner A, Barthelmes F, Wünsch J, Kusche J (2008) Periodic components of water storage changes from GRACE and global hydrology models. J Geophys Res 113(B8):B08419. DOI 10.1029/2007JB005363

Schoellhamer DH (2001) Singular spectrum analysis for time series with missing data. Geophys Res Lett 28(16):3187–3190. DOI 10.1029/2000GL012698

Shen Y, Peng F, Li B (2015) Improved singular spectrum analysis for time series with missing data. Nonlinear Process Geophys 22(4):371–376. DOI 10.5194/npg-22-371-2015

Swenson S, Wahr J (2006) Post-processing removal of correlated errors in GRACE data. Geophys Res Lett 33:L08402. DOI 10.1029/2005GL025285

Tourian M, Elmi O, Chen Q, Devaraju B, Roohi S, Sneeuw N (2015) A spaceborne multisensor approach to monitor the desiccation of Lake Urmia in Iran. Remote Sens Environ 156:349–360. DOI 10.1016/j.rse.2014.10.006

Vautard R, Ghil M (1989) Singular spectrum analysis in nonlinear dynamics, with applications to paleoclimatic time series. Physica D 35(3):395–424. DOI 10.1016/0167-2789(89)90077-8

Impact of Limited Satellite Visibility on Estimates of Vertical Land Movements

Azimuth-Dependent Masking in the Bernese GNSS Software 5.2

K.E. Abraha, F.N. Teferle, A. Hunegnaw, and R. Dach

Abstract

The number of Global Navigation Satellite System (GNSS) satellites and their geometry directly affect the quality of positioning and derived satellite products. Accordingly, the International GNSS Service (IGS) recommends GNSS antennas to be installed away from natural and man-made surfaces and structures, which may affect the incoming signals through severe multipath or obstructions. Following these recommendations, continuous GNSS (cGNSS) stations are generally located in low multipath environments with minimal signal obstructions. However, some applications require GNSS antennas to be installed at specific locations in order to measure local processes. In support of sea level studies, cGNSS stations are established at or close to tide gauges in order to accurately monitor the local vertical land movements experienced by the sea level sensors. However, the environment at the tide gauge might not be optimal for GNSS observations due to the aforementioned station-specific effects, which may degrade the quality of coordinate solutions. This study investigates the impact of severe signal obstructions on long-term position time series for some selected stations. A masking profile from an actually obstructed site is extracted, simulated and applied to unobstructed IGS sites. To investigate these effects, we implemented a new feature called azimuth-dependent elevation masking in the Bernese GNSS Software version 5.2. We present our preliminary results on the use of this new feature to study the impact of different obstruction scenarios on long-term GNSS position time series and vertical land movement estimates. The results show that a certain obstruction, with the effect being highly dependent on its severity and azimuthal direction, affects all coordinate components with the effect being more significant for the Up component. Moreover, it causes changes in the rate estimates and increases the rate uncertainty with the effect being site-specific.

Keywords

Azimuth-dependent masking • Global navigation satellite systems • Vertical land movements

K.E. Abraha (✉) • F.N. Teferle • A. Hunegnaw
Geophysics Laboratory, University of Luxembourg, Luxembourg
L-1359, Luxembourg
e-mail: kibrom.abraha@uni.lu

R. Dach
Astronomical Institute, University of Bern, Sidlerstrasse 5, CH-3012 Bern, Switzerland

1 Introduction

Mis-modelling of multipath signals and orbit dynamics, radiation pressure modelling deficiencies, satellite antenna modelling errors and hydrologic loading are some of the factors which cause spurious signals in GNSS position time series and lead to erroneous interpretations of geophysical

signals (Ge 2005; King and Watson 2010; Goebell and King 2011; Griffiths and Ray 2012; Rodriguez-Solano et al. 2014). These low-frequency spurious signals can be caused either due to un-modelled long period signals or propagation of sub-daily signals into the time series (Penna et al. 2007). It is a well-known fact that the way systematic errors propagate or GNSS positioning accuracy is dependent on the distribution of the observable satellites in the sky (Santerre 1991). Over time, the commissioning and decommissioning of satellites, as well as maneuvers, will change the constellation and, hence, the geometry. These dynamical events are well handled by the International GNSS Service (IGS) Analysis Centers (ACs) such as the Center for Orbit Determination in Europe (CODE), which make this information publicly available (Dach et al. 2015, p. 166).

On the ground, man-made and natural objects can obstruct the satellite signals and can cause a compromised geometry. To avoid this, GNSS antennas are usually installed away from objects of possible obstructions. For high-precision applications the IGS and other organizations provide specific recommendations for site selections[1] for GNSS antennas which take this into account. However, some applications require the installation of GNSS antennas at specific locations, which may not be ideal for GNSS observations, in order to precisely measure local processes. For example, sea level studies require vertical land movements to be measured at or close to tide gauges (TG) in order to avoid costly levelling links between the antenna and the TG benchmarks. TGs are often located in harbours, providing an environment which may not be favourable to the GNSS observations due to a number of effects (Teferle et al. 2003; Woodworth et al. 2009). Other examples of GNSS antennas being sited in less favourable locations may be found when monitoring mountain slopes prone to land slides (Gili et al. 2000; Wang et al. 2015). In these locations, obstructions can be a dominant factor, which affects the satellite sky distribution by limiting the number of visible satellites and leading to a non-uniform spatial distribution, which in turn limits the GNSS positioning accuracy. Figure 1 shows examples of satellite sky plots for some severely obstructed sites from the global networks of the IGS (Dow et al. 2009), Tide Gauge Benchmark Monitoring (TIGA) (Schöne et al. 2009) and the UNAVCO Plate Boundary Observatory (PBO)[2] working groups.

Different studies have already been presented on the impacts of local obstructions such as topography on GNSS positioning (Chen et al. 2009; Ji et al. 2010; Han et al. 2012). However, the impact of obstructions on long-term monitoring applications such as the observation of vertical land movement (VLM) has not been fully investigated so
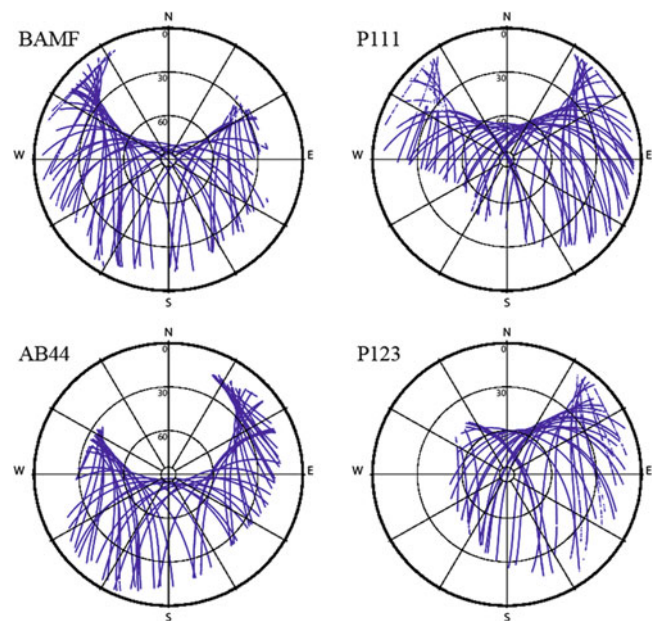
Fig. 1 Skyplots of stations with severe obstructions from the IGS(BAMF), TIGA(P111, P123), UNAVCO/PBO (AB44) networks. See Fig. 5 for their locations

far. To better understand this effect, we have implemented a new feature called azimuth-dependent masking in the Bernese GNSS Software Version 5.2 (BSW52, Dach et al. 2015). This provides an azimuth-dependent elevation cut-off option to the software. Besides its usage to study the effect of obstructions on GNSS derived products, this feature can also be used to remove observations with a certain azimuth if the data in that direction are believed to be systematically noisy. In the latter, the feature should be used carefully as it could make things worse since it causes an asymmetric pattern and allows the nominally lower systematic noise in the other azimuthal directions to have more weight.

The implementation of the new feature in BSW52 is presented in Sect. 2. The GNSS data processing strategies, simulation of obstruction scenarios and results on the effects of the obstructions on GNSS repeatability and rate estimates are presented in Sect. 3. Finally, Sect. 4 concludes the study.

2 Azimuth-Dependent Masking Implementation in BSW52

The azimuth-dependent masking is implemented by providing azimuth-dependent elevation cut-off information for stations of interest using a fixed-column format as shown in Fig. 2. The current version of the masking information file (version 1.00) has a resolution of 10° and 1° in azimuth and elevation, respectively. Zero degree elevation values are

```
AZIMUTH DEPENDENT MASKING: BSW5.2                    07-JAN-2015
----------------------------------------------------------------

FORMAT VERSION: 1.00
RESOLUTION: 10

TYPE 001: MASK ALONG THE HORIZON
--------------------------------

Station name       sat/sys  0  1  2  3  4  5  6  7  8  9 10 11 12 13 14 15 16 17 18 19 20 21 22 23 24 25 26 27 28 29 30 31 32 33 34 35
****************   ***      ** ** ** ** ** ** ** ** ** ** ** ** ** ** ** ** ** ** ** ** ** ** ** ** ** ** ** ** ** ** ** ** ** ** ** **
P111 21763S001     GPS      0  0  0  0  0  0  0  0  0  0  0  0  0 12 20 25 44 54 52 50 54 56 57 57 53 47 37  0  0  0  0  0  0  0  0  0
P123 21774S001     GPS      0  0  0  0  0  0  0  0  0  0  0  0  0  0  0 26 21 28 30 40 41 48 46 49 50 51 49 49 52 54 54 48 46  0  0  0
AB44 00000M000     GPS     15 15 16 22 24 26 26 21 17 20 21 23 25 25 24 20 17 13 13 11 11 13 11 11 16 28 29 29 34 35 35 32 24 19 16 14
ONSA 10402M004     GPS      0  0  0  0 10 11  9  0  0  0  0  0  0  0  0  0  0  0  0  0  0  0  0  0  0  0  0  0  0  0  0 27 24 25  0  0  0
```

Fig. 2 Fixed-column formatted file containing masking information. In this Figure, the masking informations listed in the columns are from a synthetic obstruction scenario for ONSA and real extracted profiles for the other stations (Sect. 3.1 describes how the profiles are extracted)
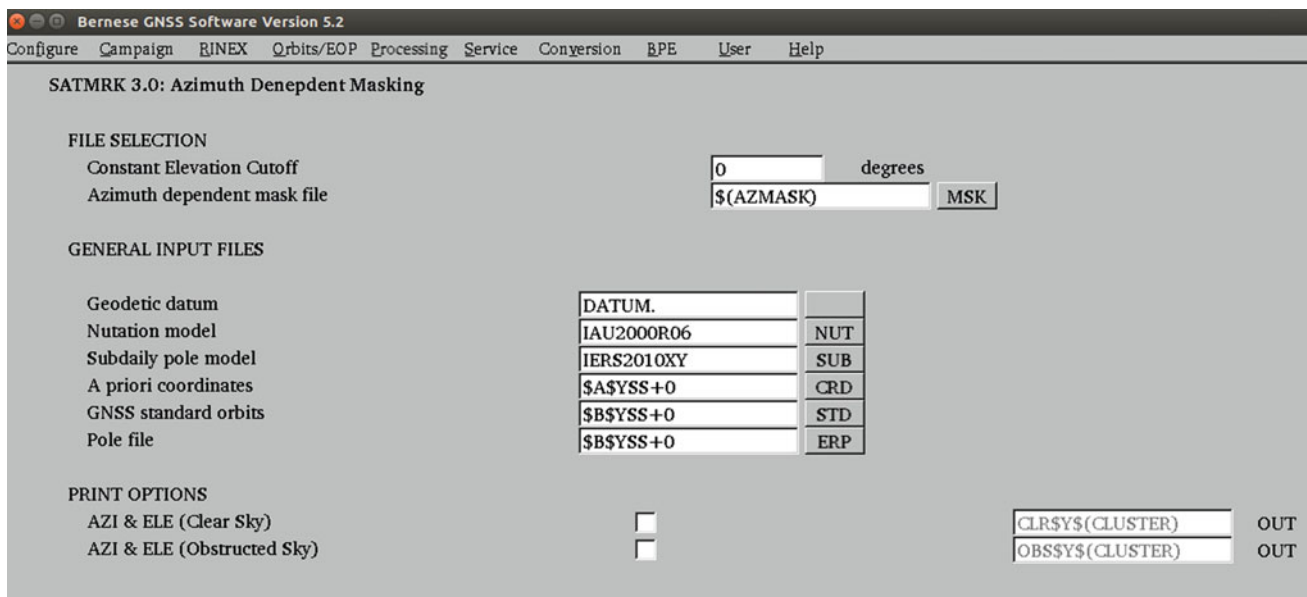
Fig. 3 Graphical User Interface (GUI) of the new feature added to implement the azimuth-dependent masking in BSW52

given to observations whose azimuths are not obstructed. The "TYPE 001" section of the fixed-column file format contains the masking information with the station names and DOMES number as a first column ("station names"). The second column ("sat/sys") allows to choose satellite systems to be masked for a particular azimuth. A blank character in the second column is given to mask all satellites from any system. The last column (0 . . . 35) is where the elevation cut-off angles are listed. This divides the whole horizon into 36 sectors to simulate the mask with a resolution of 10°. The masking information is routinely read as:

Defining the horizon as *azi(i)* with a resolution of 10° (*for i*, $i = 0°, 360°, 10°$);

$$if (azimuth \leq azi (i + 1) \& azimuth > azi (i)) \text{ then}$$

$$\text{Elevation cut-off} = elev (i)$$

where *azimuth* is the current azimuth of a given satellite. *azi(i)* and *azi(i+1)* are the start and end of the azimuth, respectively, *elev(i)* is the elevation cut-off between azimuths *azi(i)* and *azi (i+1)*.

For example Fig. 2 shows for ONSA elevation cut-offs of 10°, 11° and 9° are used for the azimuths between (40° and 50°], (50° and 60°] and (60° and 70°], respectively. In addition, elevation cut-offs of 27°, 24° and 25° are used as a mask for azimuths between (300° and 310°], (310° and 320°] and (320° and 330°], respectively. In the rest of the azimuths, all observations from 0° elevation are used.

Figure 3 shows the additional panel added to the MENU of the BSW52 to implement the new feature. "Azimuth dependent mask file" is the option where one has to enter the masking file name described in Fig. 2 as an input. The other options are the inputs for the general files which are used to estimate the positions, elevation and azimuths of the satellites with respect to the receivers. The masking information is implemented after the RINEX files have been converted into the BSW52-formatted observations and before forming baselines [for Precise double-differenced Network Positioning (PNP)] as in Fig. 4.

3 Results

This section presents the processing strategy, simulations of obstruction scenarios and results on the effect of obstructions for GNSS repeatability and rate estimates.
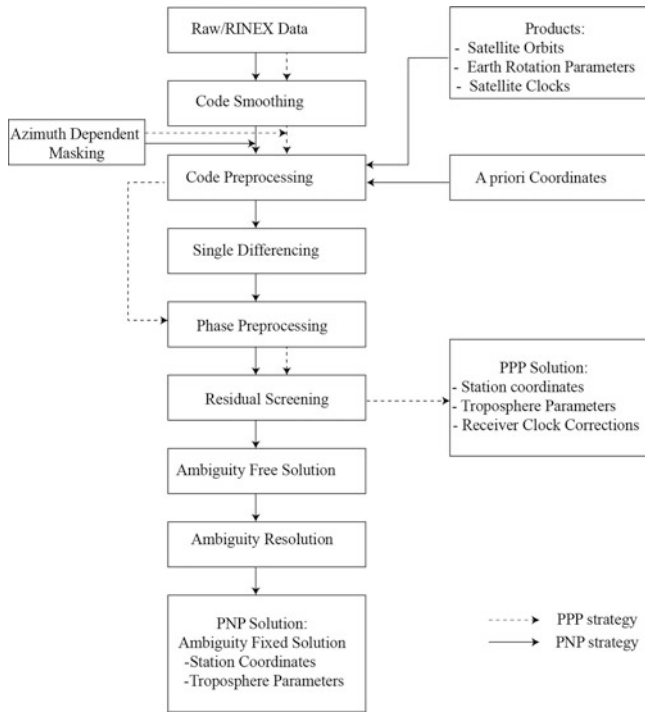
Fig. 4 Simple PPP (*dotted arrows*) and PNP (*solid arrows*) processing strategies with the new masking feature

3.1 GNSS Data and Processing Strategies

For this experiment we used a PPP (Zumberge et al. 1997) processing strategy. As it is based on a single station only, the effects of a certain obstruction on a specific station can easily be assessed. In addition to this, the computational burden and the independence of the network configuration makes PPP somewhat more advantageous than the more conventional PNP strategy. The PPP solutions are computed by fixing the CODE final satellite orbits, Earth Orientation Parameters (EOP) and satellite clocks (Dach et al. 2016). A sampling rate of 30 s for the preprocessing and 3 min for the final parameter estimation are used and elevation dependent weighting is applied. An elevation cut-off of 3° is used as standard cut-off angle for both solutions. Station coordinates, troposphere parameters and receiver clocks are the estimated parameters for every station. Though the implemented obstruction scenario affects all the aforementioned parameters, we only present the effect on the position time series, specifically on the Up coordinate component and rate estimates, in this study. It should be mentioned that, for this specific study we make use of Global Positioning System (GPS) observations only.

We have processed two PPP solutions for a global network of selected IGS stations from 2008 to 2014 (Fig. 5). The first solution is based on the real (unobstructed) observations while the second one is based on the same observations but with the applied P123 obstruction scenario which can be regarded as a severe scenario. The two solutions are computed using the same strategy, models and products except the implemented obstruction scenario and the consistency between the solutions is guaranteed. To investigate the effect
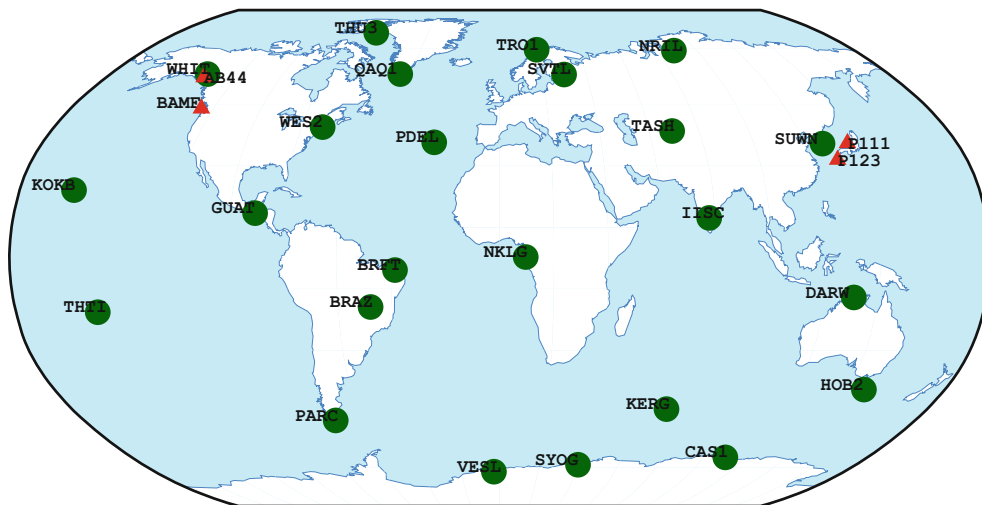
Fig. 5 Map of stations used: stations in Fig. 1 (*red triangles*) and global stations (*green dots*) used for the PPP solutions

Fig. 6 Up difference time series for selected stations (Fig. 2, green stations). *Green dots* and *red line* are the daily Up differences and the rate of the difference time series, respectively. The values on the *upper right corner* are the rate estimates and their associated uncertainty (assuming randomness of the differences)

the skyplots of the actual and simulated observations are stacked together for a given period and the obstruction profile is extracted from the comparison.

The obtained observation masks are then written into the fixed-column format as in Fig. 2 and applied to un-obstructed IGS sites (green dots in Fig. 5) to investigate the impact of the limited satellite visibility on the coordinate time series and rate estimates. In the PPP processing strategy the obstructions are implemented as in the flow chart shown in Fig. 4. Throughout the discussion, this obstruction scenario will be termed as the P123 scenario. In-terms of the amount of data missing, this scenario is as severe as a constant 20° elevation cut-off across the horizon and the percentages of data missing range from 27 to 42% (Table 1). As Table 1 (column 1) shows, the observation rate varies from station to station which in effect makes some stations to be over-masked relative to others. It should be noted that the observation rate is estimated by comparing the possible (computed using GPSSIM) and completed number of observations starting from elevation of 0°.

3.2 Effects of Obstructions on Coordinate Time Series and Rate Estimates

Figure 6 shows the coordinate difference time series of the Up component for 11 selected stations from the global network. The figure shows that the effect varies from station to station. The mean coordinate (Up) differences are less than 5 mm for nearly 65% of the stations. However it reaches from 5 to 15 mm for some stations. The rate estimates for the difference time series range from 0.89 mm/yr (IISC) to −0.57 mm/yr (PDEL).

As expected the effect of the obstruction scenario depends on how severe they are and where the obstructing objects are located relative to the GNSS antenna. There is a latitude-dependency which can vary from station to station. In general, we showed that a certain obstruction produces a coordinate bias, increases the day-to-day scatter (Figs. 6 and 7) and a bias in the rate estimates (Fig. 8). Naturally with short time series this effect is substantially larger (not shown).

Figure 7 depicts the RMS of the Up coordinate differences due to the P123 scenario for all stations. Stations in the Northern Hemisphere mid-latitudes and equatorial regions are more affected than the stations from the northernmost and southern hemisphere regions. This effect is correlated with the nature of the P123 scenario as the mask is more severe in the southern horizon than the northern horizon. This will have less effect for stations in the Southern Hemisphere as the "constellation hole", where observations are not possible due to the 55° inclination of the orbital planes, exists in the northern part of the horizon. However, as observations in a certain azimuthal direction are ignored (masked), the

of the obstructions, position differences time series between the unobstructed and obstructed solutions are computed. We assume that all common signals and biases will cancel from the difference, highlighting the effect of the obstruction scenario. Having said that, we do expect some effects from slightly different receiver clock and tropospheric delay estimates as the obstruction affects them as well.

Overall, we have simulated several artificial obstruction scenarios (no results shown here) and extracted real scenarios from stations with severe obstructions (Fig. 1). However, here we only present the results of obstruction profile extracted from P123. To extract the profile, synthetic observations are simulated using the GPSSIM tool in BSW52. GPSSIM uses a model identical to the main parameter estimation program GPSEST where "zero tests" are thus possible if the same options are used in both the simulation and processing routines (Dach et al. 2015, p. 443). Finally,

Fig. 7 RMS of up component coordinate differences
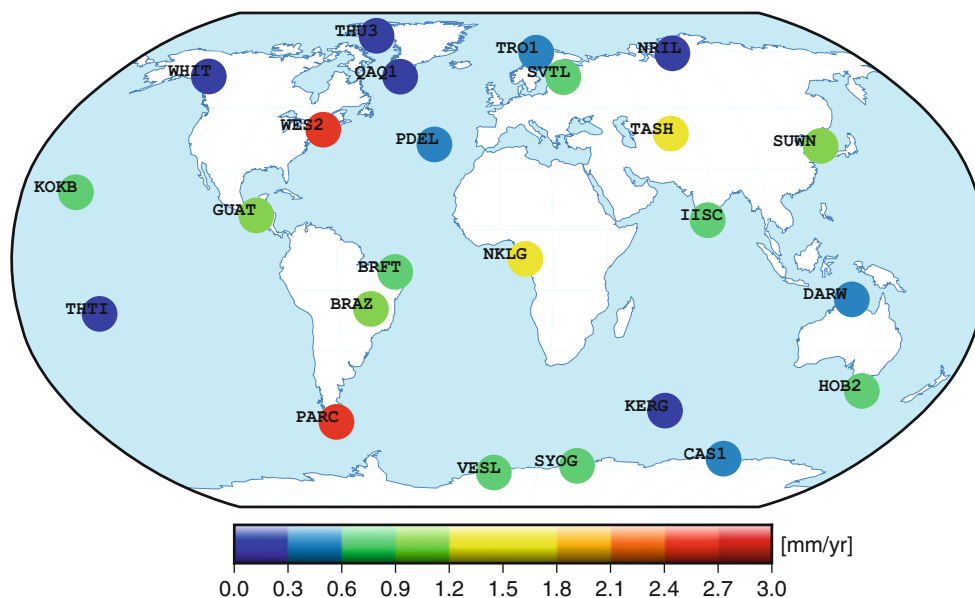
Fig. 8 Up component absolute rate differences

quality of the masked observations may vary from station to station. For some stations noisy data e.g. due to high multipath and water vapour, might be masked while the masked observations are less noisy or good for others. The more of site-specific nature in Figs. 7 and 8 can be related to this. Moreover, some of the sites (e.g. WES2 station) are over-masked due to their low observation rates (Table 1) of unknown reasons. In general, the RMS of the coordinate differences ranges between 0.8 and 1.8 mm, 1.7 and 8 mm, and 5 and 12 mm for the North, East and Up components, respectively.

Overall, the Up component is more affected than the horizontal components which can also be seen from the repeatability (WRMS) differences in Table 1. The repeatability of the time series are analysed for both solutions where outliers were rejected for all components with a criteria of three times the WRMS. The WRMS and rates are then estimated by fitting a model which includes annual and semi-annual signals. In addition, offsets are also corrected. The WRMS differences are at the sub-millimetre (below 1 mm) for the North component while they range between 0.6 and 3 mm for the East and between 1.7 and 8 mm for the Up components.

Table 1 Total Number of observations before masking (TotalObs, columns 2), Percentage of data missing due to P123 scenario (Missing, column 3), Weighted root-mean-square (WRMS) difference statistics for North, East and Up components (columns 4 to 6), Up rate differences (Rate, column 7) and Up rate uncertainty differences (Uncer, column 8)

Station	TotalObs (%)	Missing (%)	North (mm)	East (mm)	Up (mm)	Rate (mm/yr)	Uncer (mm/yr)
BRAZ	91.6	31.6	0.27	1.71	3.03	0.90	0.30
BRFT	86.8	27.3	0.27	2.59	1.92	0.77	0.06
CAS1	99.2	42.3	0.62	1.88	4.80	0.51	0.20
DARW	95.6	28.6	0.29	1.61	4.70	0.34	0.54
GUAT	94.3	42.2	0.15	2.60	4.86	0.98	0.42
HOB2	95.2	35.4	0.23	1.02	2.00	0.77	0.15
IISC	77.1	38.0	0.19	2.40	4.58	0.77	0.42
KERG	77.1	26.2	0.17	1.08	2.86	0.03	0.13
KOKB	89.5	36.2	0.24	1.97	8.26	0.85	0.81
NKLG	97.6	32.9	0.45	2.50	3.18	1.35	0.35
NRIL	93.4	37.0	0.52	0.64	1.77	0.20	0.20
PARC	98.5	36.6	0.47	1.92	3.23	2.60	0.20
PDEL	94.1	36.0	0.08	0.77	4.79	0.34	0.40
QAQ1	91.9	33.5	0.35	1.07	2.02	0.03	0.20
SUWN	74.6	29.1	0.16	0.56	4.60	1.00	0.30
SVTL	91.0	36.2	0.23	0.86	2.50	0.60	0.30
SYOG	85.9	41.3	0.79	2.11	3.61	0.67	0.20
TASH	95.8	42.5	0.27	1.26	4.89	1.21	0.42
THTI	85.0	27.2	0.53	1.48	2.94	0.01	0.20
THU3	96.0	36.8	0.76	0.75	1.92	0.24	0.20
TRO1	95.4	34.5	0.75	0.99	1.81	0.42	0.20
VESL	94.8	42.1	1.09	3.05	2.13	0.70	0.34
WES2	72.9	38.3	0.24	1.66	7.10	2.52	0.50
WHIT	94.9	35.5	0.27	1.13	1.19	0.06	0.20

The effect of the obstruction on the North and East rates is negligible. However, the rate differences for the Up component are more obvious with the effect being more site-specific than latitude-dependent for this specific scenario. This is confirmed by Fig. 8 and Table 1 which show the absolute rate differences for the Up component reach ±1 mm/yr in general with the differences reaching ±2 mm/yr for some stations. A comparison of the Up rate uncertainties between the two solutions also shows that the uncertainty differences for the Up rates range between ±0.06 and ±0.8 mm/yr. The last column of Table 1 lists the rate uncertainty differences for the Up component which are calculated as: rate uncertainty of the unmasked time series subtracted from the rate uncertainty of the masked time series. The values are all positive (in sign) which indicates an increased rate uncertainty for all stations. It should be noted that, the estimated rate uncertainties are likely to be optimistic as they are estimated without taking the stochastic properties of the time series into account (Santamaría-Gómez et al. 2011). One might expect a certain obstruction scenario to cause a position differences or bias as it causes a satellite geometer

change. In effect, the way systematic errors propagate will also be different. The causes of the rate change due to a constant (non-variable in time) obstruction can be related to the variations of the number of observations (e.g. due to satellite commissioning/decommissioning, eclipses . . .), tropospheric variations and site-specific systematic errors (such as multipath) reductions. The effects of the obstructions on all estimated parameters is under investigation and will be reported as a future work.

4 Conclusions

The effect of obstructions on GPS time series and rate estimates has been investigated using a global network of IGS stations covering the period 2008 to 2014. To study the effect, a new feature called azimuth-dependent masking, which allows azimuth-dependent elevation cut-off, was added to the Bernese GNSS Software 5.2. This feature can be used to remove observations in a certain azimuth if they are believed to be systematically noisy. Besides it can be used to simulate different obstruction scenarios and study their effects on GNSS products. This paper focused on the latter and simulates an obstruction scenario extracted from an actually obstructed station. The effect on GPS coordinate repeatability and rate estimates was assessed. Accordingly, an investigation of the effect of signal obstructions using a simulated scenario has been performed. The preliminary results confirm that the effect of the obstruction is to a large degree site-specific and latitude-dependent. The obstructing objects cause a compromised satellite geometry, increase scatter of the position time series and introduce coordinate and rate biases.

Using the obstruction profile of P123, a severely obstructed station in Japan, we showed that the obstruction has a visible effect on all components with the effect being largest for the Up component. The obstruction causes data missing which ranges from 27 to 42% which varies from station to station and to some extent latitude-dependent. In-turn, it causes the WRMS differences, which are at the sub-millimetre level for the North component, range between 0.6 and 3 mm for the East and between 1.7 and 8 mm for the Up components, respectively. The effect on the rates for the North and East components is minimal while the effect being largest for the Up component, reaching ±1 mm/yr for most stations and ±2 mm/yr for the worst cases. The rate bias due to a constant masking can be related to the observation evolution and geometry change (as the way systematic errors propagate varies accordingly) and tropospheric evolution (as the obstruction adversely affects this parameter as well). A more detailed analysis on the rate bias, on the effects of different obstruction scenarios from different azimuthal directions on all estimated parameters

and the benefits from a multi-GNSS constellation will be part of future work.

References

Chen HC, Huang YS, Chiang KW, Yang M, Rau RJ (2009) The performance comparison between GPS and BeiDou-2/COMPASS: a perspective from Asia. J Chin Inst Eng 32:679–689

Dach R, Lutz S, Walser P, Pierre F (eds) (2015) Bernese GNSS software version 5.2. User manual, Astronomical Institute, University of Bern, Bern Open Publishing. doi:10.7892/boris.72297; ISBN: 978-3-906813-05-9

Dach R, Schaer S, Arnold D, Orliac E, Prange L, Susnik A, Villiger A, Jäggi A (2016) CODE final product series for the IGS. Published by Astronomical Institute, University of Bern. http://www.aiub.unibe.ch/download/CODE; doi:10.7892/boris.75876

Dow JM, Neilan RE, Rizos C (2009) The international GNSS service in a changing landscape of global navigation satellite systems. J Geod 83(3–4):191–198. doi:10.1007/s00190-008-0300-3

Ge M (2005) Impact of GPS satellite antenna offsets on scale changes in global network solution. Geophys Res Lett 32(6). doi:10.1029/2004gl022224

Gili JA, Corominas J, Rius J (2000) Using global positioning system techniques in landslide monitoring. Eng Geol 55(3):167–192

Goebell S, King MA (2011) Effects of azimuthal multipath asymmetry on long GPS coordinate time series. GPS Solutions 15:287–297. doi:10.1007/s10291-011-0227-7

Griffiths J, Ray JR (2012) Sub-daily alias and draconitic errors in the IGS orbits. GPS Solutions 17(3):413–422. doi:10.1007/s10291-012-0289-1

Han JY, Wu Y, Liu RY (2012) Determining the optimal site location of GNSS base stations. Bol Ciênc Geod, sec Artigos, Curitiba, 18(1):154–169

Ji S, Chen W, Ding X, Chen Y, Zhao C, Hu C (2010) Potential benefits of GPS/GLONASS/Galileo integration in an urban canyon – Hong Kong. J Navig 63:681–693. doi:10.1017/s0373463310000081

King MA, Watson CS (2010) Long GPS coordinate time series: multipath and geometry effects. J Geophys Res. 115:B04403. doi:10.1029/2009JB006543

Penna NT, King MA, Stewart MP (2007) GPS height time series: short-period origins of spurious long-period signals. J Geophys Res 112:B02402. doi:10.1029/2005JB004047

Rodriguez-Solano CJ, Hugentobler U, Steigenberger P, Bloßfeld M, Fritsche M (2014) Reducing the draconitic errors in GNSS geodetic products. J Geod 88(6):559–574. doi: 10.1007/s00190-014-0704-1

Santamaría-Gómez A, Bouin MN, Collilieux X, Wöppelmann G (2011) Correlated Errors in GPS Position Time Series: Implications for velocity estimates. J Geophys Res 116(B1). doi:10.1029/2010jb007701

Santerre R (1991) Impact of GPS satellite sky distribution. Manuscr Geodaet 16:28–53

Schöne T, Schön N, Thaller D (2009) IGS Tide Gauge Benchmark Monitoring Pilot Project (TIGA): scientific benefits. J Geod 83:249–261. doi:10.1007/ s00190-008-0269-y

Teferle FN, Bingley R, Dodson A, Apostolidis P, Staton G (2003) RF interference and multipath effects at continuous GPS installations for long-term monitoring of tide gauges in UK harbours. In: Proceedings of 16th international technical meeting of the satellite division of the institute of navigation ION GPS-GNSS 2003, Portland, Oregon, September 9–12, 2003, Institute of Navigation: 2082–2092

Wang G, Bao Y, Cuddus Y, Jia X, Serna J, Jing Q (2015) A methodology to derive precise landslide displacement time series from continuous GPS observations in tectonically active and cold regions: a case study in Alaska. Nat Hazards 77:1939–1961. doi:10.1007/s11069-015-1684-z

Woodworth PL, Teferle FN, Bingley RM, Shennan I, Williams SDP (2009) Trends in UK mean sea level revisited. Geophys J Int 176(22):19–30. doi: 10.1111/j.1365-246X.2008.03942.x

Zumberge J, Heflin M, Jefferson D, Watkins M, Webb F (1997) Precise point positioning for the efficient and robust analysis of GPS data from large networks. J Geophys Res 102(B3):5005

Noise Filtering Augmentation of the Helmert Transformation for the Mapping of GNSS-Derived Position Time Series to a Target Frame

Miltiadis Chatzinikos and Christopher Kotsakis

Abstract

The generation of position time series in geodetic networks is often based on the successive forward implementation of the Helmert transformation (HT) to daily/weekly solutions using the transformation parameters obtained from a separate least-squares adjustment over a selected set of reference stations. An overlooked problem with this approach is that the estimation noise of the daily/weekly solutions is fully absorbed into the transformed station positions, or even amplified if we consider the additional uncertainty of the estimated Helmert parameters. Its filtering is therefore a desirable task which could enhance the geophysical content of geodetic time series to be analyzed in a global secular frame. To accommodate the need for such filtering, we present in this paper an epoch-wise stacking approach for the HT-based alignment of a series of daily/weekly frames to a common secular frame via an integrated estimation process. The resulting transformation formulae differ from the classic HT solution in terms of Kalman-like corrections, and they lead to an improved solution in the sense of minimizing the error variances of the transformed positions in the target frame.

1   Introduction

Position time series (PTS) for geodetic and geophysical applications are commonly derived by aligning daily or weekly solutions of GNSS networks to a realization of the International Terrestrial Reference System (e.g. ITRF2008, IGb08, DTRF2008). One of the standard approaches for the alignment procedure relies on the estimation of Helmert transformation (HT) parameters between successive solutions of the observed network and the desired terrestrial reference frame (TRF) for the problem at hand. For its implementation a subset of high-quality reference stations with accurately known positions and velocities in the desired frame should be selected and included ahead in the epoch-wise adjustment of the underlying network. The transformation parameters are obtained on the basis of those reference stations by least-squares estimation techniques, and then they are used to map the GNSS-derived positions of all network stations to the target TRF for further scientific inference in a time series analysis context.

The aforesaid methodology is often used for studying the temporal behavior of linear and nonlinear station displacements in geodetic networks with respect to well-defined

M. Chatzinikos (✉)
Department of Geodesy and Surveying, Aristotle University of Thessaloniki, Thessaloniki, Greece

Royal Observatory of Belgium, 3 avenue Circulaire, 1180 Brussels, Belgium
e-mail: Miltiadis.Chatzinikos@oma.be

C. Kotsakis
Department of Geodesy and Surveying, Aristotle University of Thessaloniki, Thessaloniki, Greece

Earth monitoring frames (e.g. Tregoning and van Dam 2005; Bastos et al. 2010; van Dam et al. 2012; Collilieux et al. 2010, 2012). Its main advantage is the ability to preserve the information content of the GNSS measurements in the sense that the network geometry will not be deformed during the transformation procedure. Yet, a number of drawbacks exist in the HT approach which may degrade the accuracy of the transformed positions and could diminish the geophysical "interpretability" of the derived PTS. For instance, the choice of the reference stations affects the estimated Helmert parameters due to the so-called network effect, and thus it influences the behavior of temporal variations in the transformed positions (Collilieux et al. 2010; Bastos et al. 2010). Another nuisance is the aliasing of unmodeled loading signals from the original daily/weekly solutions to the estimated Helmert parameters. This is mainly attributed to the secular character of the target TRF, and it is also affected by the spatial distribution of the reference stations. Both of these problems have been extensively discussed in the geodetic literature and various modeling schemes have been proposed to mitigate their effects during the estimation of HT parameters in GNSS networks (Collilieux et al. 2012).

Nevertheless, an important aspect which has been somewhat overlooked in the previous context is that the HT approach does not filter the random errors of the original daily/weekly solutions, and it could even amplify their propagated effect to the transformed positions in the target TRF (see Sect. 2). These errors are highly correlated among the network stations and their signatures are comparable to, if not stronger than, the geodynamical displacements of station positions that need to be detected from the GNSS measurements. Moreover, such random errors may accumulate a strong constituent of temporally correlated noise in the derived PTS, as a result of their systematic projection to a common frame under the Helmert transformation model. Their filtering is therefore a desirable task which not only would improve the frame alignment process per session (or, more precisely, the statistical accuracy of the transformed positions in the target TRF) but it could also enhance the geophysical content of geodetic time series to be analyzed in a global secular frame (van Dam et al. 2012).

Considering the previous remarks, the aim of this paper is to augment the HT approach with a noise filtering step in support of PTS formation in geodetic networks. Our rationale follows the recent work by Kotsakis et al. (2014, 2015) where the mapping problem of a network solution to a known TRF was rigorously solved via a stacking process by exploiting the noise covariance structure of all relevant input data. This led to more general transformation formulae which involve easy-to-compute corrections to the classic HT-based solution in a Kalman filtering fashion (see Sect. 3). Despite their distorting effect on the network figure, these corrections provide an improved solution in the sense of minimizing the error variances of the transformed positions, and thus offering better estimates for their temporal changes (linear trend, seasonal variations) in the target frame. It should be kept in mind, after all, that the (standard) HT approach preserves not the true but the erroneous geometry of the underlying network which is estimated from geodetic data and it is always coupled with spatially correlated random errors. Hence, its distortion during the transformation procedure – due to the filtering of these errors – should not be hastily interpreted as a degradation of the data information, since it may lead to an improved estimate of the true network geometry at each considered epoch.

Our goal here is to expose the modeling aspects of the aforementioned noise filtering within the HT approach by applying it to a time series of epoch frames for their alignment to a common secular frame. To assess its performance with real data, a case study is also presented in a regional GNSS network using weekly solutions over a period of seven years (2007–2014).

2 Frame Alignment Via Helmert Transformation: Standard Approach

Traditionally, the alignment of geodetic frames relies both on the inversion and the forward implementation of the Helmert transformation model (Collilieux et al. 2012)

$$X = X' + G\,\theta \tag{1}$$

The vectors X and X' correspond to different frame realizations for the same set of stations at the same epoch, whereas the vector θ contains the transformation parameters, namely 3 translations, 3 small orientation angles and 1 differential scale factor (or a subset of those parameters). The matrix G is constructed by the Jacobian of the Euclidean similarity transformation using the known positions of the "initial" frame realization (X') or some other approximate values which are close to them.

For the PTS formation in geodetic networks, the standard HT approach is implemented in two steps. Firstly, the transformation parameters for each daily/weekly solution are obtained by the weighted least-squares estimator

$$\widehat{\theta}\,(t_i) = \left(G_i^T W_i G_i\right)^{-1} G_i^T W_i \left(X\,(t_i) - X'\,(t_i)\right) \tag{2}$$

which is applied over a selected group of reference stations with prior known positions in the target frame (e.g. ITRF). The latter are propagated to the solution epoch by their known velocities in the usual linear manner, that is $X\,(t_i) = X\,(t_o) + (t_i - t_o)\,\dot{X}$. Conversely, the vector $X'\,(t_i)$ contains the positions of the reference stations as obtained from the epoch adjustment of the underlying network. Both

of these vectors are associated with known covariance (CV) matrices, denoted by $\boldsymbol{\Sigma}_{X_i}$ and $\boldsymbol{\Sigma}_{X'_i}$, which can be utilized to form the weight matrix $\boldsymbol{W}_i$ for estimating the HT parameters at each considered epoch.

To avoid the aliasing of unmodeled loading effects from the daily/weekly solutions to the estimated Helmert parameters, a number of de-aliasing strategies have been proposed in the geodetic literature (e.g. Collilieux et al. 2012). These strategies include the use of a subnet of reference stations with uniform areal density, the deliberate downweighting of the height component in the matrix $\boldsymbol{W}_i$, the omission of the scale factor from the frame transformation procedure, and the prior incorporation (or simultaneous estimation) of loading corrections for the reference station positions. Also, to prevent possible errors in the adopted long-term frame or inconsistencies with the input daily/weekly solutions which may affect the transformed PTS, it is recommended that the secular positions and velocities of the reference stations are estimated anew, along with the epoch Helmert parameters, via a unified stacking of the available data, instead of obtaining them directly by an external long-term solution; for more details see Collilieux et al. (2012) and the references given therein.

In the second and final step, each daily/weekly solution is mapped to the target frame via Eq. (1) using the transformation parameters from the previous step. This involves both the reference and non-reference stations and it can be expressed by the combined equation

$$\begin{bmatrix} \widehat{\boldsymbol{x}}^{\text{st}}(t_i) \\ \widehat{\boldsymbol{z}}^{\text{st}}(t_i) \end{bmatrix} = \begin{bmatrix} \boldsymbol{X}'(t_i) \\ \boldsymbol{Z}'(t_i) \end{bmatrix} + \begin{bmatrix} \boldsymbol{G}_i \\ \tilde{\boldsymbol{G}}_i \end{bmatrix} \widehat{\boldsymbol{\theta}}(t_i) \qquad (3)$$

where the superscript "st" is used to distinguish the above result from its filtered counterpart that will be presented in the next section. The vector $\boldsymbol{Z}'(t_i)$ refers to the estimated positions of the non-reference stations and it is jointly obtained with $\boldsymbol{X}'(t_i)$ from the epoch adjustment of the GNSS measurements. The cross-correlation of these vectors is neglected in the standard HT approach which does not provide any theoretical optimality for the statistical accuracy of the transformed positions in the target frame! This of course does not mean that Eq. (3) loses its usefulness for practical applications, yet it is obvious that the noise of the daily/weekly solutions is always absorbed in full to the derived PTS. Actually, if we consider the uncertainty contribution from the estimated Helmert parameters, then the error variances of the transformed positions may be even larger than the initial error variances of $\boldsymbol{X}'(t_i)$ and $\boldsymbol{Z}'(t_i)$ – a fact which exposes the inherent weakness of Eq. (3) to recover with sufficient accuracy the geodynamical variations of station positions in the target frame.

3 Frame Alignment via Helmert Transformation: Epoch Stacking Approach

An alternative scheme for the alignment of daily/weekly GNSS solutions to an existing long-term frame can be derived by the least-squares inversion of the stacked system of "epoch observation equations"

$$\boldsymbol{X}(t_i) = \boldsymbol{x}(t_i) + \boldsymbol{v}_{X_i} \qquad (4a)$$

$$\boldsymbol{X}'(t_i) = \boldsymbol{x}(t_i) - \boldsymbol{G}_i\,\boldsymbol{\theta}(t_i) + \boldsymbol{v}_{X'_i} \qquad (4b)$$

$$\boldsymbol{Z}'(t_i) = \boldsymbol{z}(t_i) - \tilde{\boldsymbol{G}}_i\,\boldsymbol{\theta}(t_i) + \boldsymbol{v}_{Z'_i} \qquad (4c)$$

in conjunction with the "data" weight matrix

$$\boldsymbol{P}_i = \begin{bmatrix} \boldsymbol{\Sigma}_{X_i} & 0 & 0 \\ 0 & \boldsymbol{\Sigma}_{X'_i} & \boldsymbol{\Sigma}_{X'_i Z'_i} \\ 0 & \boldsymbol{\Sigma}_{Z'_i X'_i} & \boldsymbol{\Sigma}_{Z'_i} \end{bmatrix}^{-1} \qquad (5)$$

where the meaning of all terms was either previously explained or is easily deduced in the present context. The above formulation relies on the same modeling principle as the standard HT approach to relate each daily/weekly solution with a secular TRF by taking into account the prior (noisy) positions of the reference stations. The difference in the current approach is that the Helmert parameters and the transformed positions of all network stations are simultaneously estimated, at each epoch, within a single-step procedure.

The least-squares solution of the previous stacking model was analytically derived by Kotsakis et al. (2014) and it can be expressed in terms of the following estimators:

$$\widehat{\boldsymbol{\theta}}(t_i) = \left(\boldsymbol{G}_i^T \left(\boldsymbol{\Sigma}_{X_i} + \boldsymbol{\Sigma}_{X'_i} \right)^{-1} \boldsymbol{G}_i \right)^{-1}$$
$$\boldsymbol{G}_i^T \left(\boldsymbol{\Sigma}_{X_i} + \boldsymbol{\Sigma}_{X'_i} \right)^{-1} \left(\boldsymbol{X}(t_i) - \boldsymbol{X}'(t_i) \right) \qquad (6)$$

and

$$\begin{bmatrix} \widehat{\boldsymbol{x}}(t_i) \\ \widehat{\boldsymbol{z}}(t_i) \end{bmatrix} = \begin{bmatrix} \widehat{\boldsymbol{x}}^{\text{st}}(t_i) \\ \widehat{\boldsymbol{z}}^{\text{st}}(t_i) \end{bmatrix} - \begin{bmatrix} \boldsymbol{\Sigma}_{X'_i} \\ \boldsymbol{\Sigma}_{Z'_i X'_i} \end{bmatrix}$$
$$\left(\boldsymbol{\Sigma}_{X_i} + \boldsymbol{\Sigma}_{X'_i} \right)^{-1} \left(\widehat{\boldsymbol{x}}^{\text{st}}(t_i) - \boldsymbol{X}(t_i) \right) \qquad (7)$$

where $\widehat{x}^{\text{st}}(t_i)$ and $\widehat{z}^{\text{st}}(t_i)$ correspond to the transformation solution according to the standard HT approach, see Eq. (3). The Helmert parameters retain the same values with the ones implied by the classic estimator of Eq. (2), a fact which is expected since the stacking process does not add new information for the estimation of those parameters. Conversely, the transformed positions differ from the classic estimates of Eq. (3) by additive corrections which are computed via Wiener-type filtering of the post-fit residuals $\widehat{x}^{\text{st}}(t_i) - X(t_i)$. The latter reflect the daily/weekly geodynamical displacements of the reference stations relative to their known linear trend in the secular frame, and they are always contaminated by the full noise of the initial GNSS-derived positions $X'(t_i)$ (and also by the noise of the known secular positions $X(t_i)$). The key element in Eq. (7) is the exploitation of these residuals to facilitate the filtering of the daily/weekly solution noise from the transformed positions of all network stations. Note the role of the cross CV matrix $\Sigma_{Z'_i X'_i}$ which allows the noise filtering procedure to be carried at the non-reference stations, in contrast to the CV matrix $\Sigma_{Z'_i}$ which does not affect the least-squares solution of the stacking model.

From a statistical perspective, the PTS from Eq. (7) have smaller error variances compared to the standard HT approach (Kotsakis et al. 2014) and they can theoretically reveal with higher accuracy the temporal behavior of the network positions in the target frame. This of course presumes that the used CV matrices reflect in a realistic way the stochastic behavior of the random errors in the available data $(X(t_i), X'(t_i), Z'(t_i))$. Even so, one can justly claim that the noise filtering step may obscure the assessment of physical station displacements since the Kalman-like corrections in Eq. (7) could also remove a part of the (unmodeled) loading signals that exist in the original GNSS measurements. Indeed, in the context of the stacking model given in Eq. (4a)–(4c), the non-secular station displacements could be aliased not only to the Helmert parameters but also to the noise vectors of the daily/weekly solutions. This unwanted effect is most likely to occur at the reference stations, especially if the input noise of their epoch positions is much larger than the noise of their prior secular positions in the sense that $\Sigma_{X'_i}\left(\Sigma_{X_i} + \Sigma_{X'_i}\right)^{-1} \simeq I$; see Eq. (7). A partial loss of geophysical signal(s) should thus be expected in the transformed PTS, which is a characteristic problem for any alignment scheme between a series of *epoch frames* and a *secular frame*.

The aforementioned aliasing could be avoided if the reference stations are free of any seasonal variations and the non-secular displacements occur only at the non-reference stations. Obviously, this condition cannot be fulfilled in

practice and the aliasing effect should be mitigated by adding suitable loading corrections to the previous stacking model, in conformity with the general recommendations given in Collilieux et al. (2010, 2012). This aspect, however, will not be further elaborated or tested in the present paper.

4 Case Study of a Hellenic Network

To investigate the behavior of the "augmented" transformation in Eq. (7) we performed some preliminary tests for the weekly alignment of a regional GNSS network to the ITRF2008 frame (Altamimi et al. 2011). Our tests refer to the Hellenic network that was used by Chatzinikos (2013) for studying the crustal deformation field in Greece, which consists of four sub-networks with a total of 122 permanent stations. Weekly GNSS observations over a seven-year period (2007–2014) were processed in a subset of 23 stations of the above network, including 16 IGS reference stations in Europe (see Fig. 1), using the Bernese software ver. 5.0 (Dach et al. 2007). The reason for retaining a smaller number of Hellenic stations in our analysis is to avoid the stochastic mismodeling in the estimation of combined weekly solutions from overlapping subnetworks due to the (inconsistent) hypothesis of linear independence in the phase double differences at the common stations (e.g. Biagi and Sansò 2012). In this way we can ensure more realistic weekly CV matrices ($\Sigma_{X'_i}$, $\Sigma_{Z'_i}$, $\Sigma_{Z'_i X'_i}$) without too optimistic values for the estimated position variances.

A series of 362 weekly free-net solutions were computed in the test network, and they were then aligned to ITRF2008 following both options of the HT approach which were described in previous sections. The ITRF2008 positions of the reference stations, along with their full CV matrices, were linearly propagated to the epochs of the weekly solutions using the initial positions and velocities (and their respective CV matrices) that were retrieved from the sinex file *ITRF2008-TRF-IGS.SNX* at ftp://itrf.ign.fr/pub/itrf/itrf2008. Each frame alignment scheme, i.e. with and without the use of the noise filtering step, was implemented via the 6-parameter version of the Helmert transformation model (no scale factor is used). Two sets of PTS were finally derived in ITRF2008 for all network stations, which have been compared in terms of their linear trend and nonlinear variability.

Firstly, the station velocities were estimated by a least-squares linear fit to both sets of transformed PTS. Their values reflect the secular motion of the network stations in ITRF2008 (as inferred by the analyzed GNSS data in the

Fig. 1 The GNSS regional
network used in the frame
alignment tests (*black squares*:
IGS reference stations, *red
circles*: non-reference Hellenic
stations)
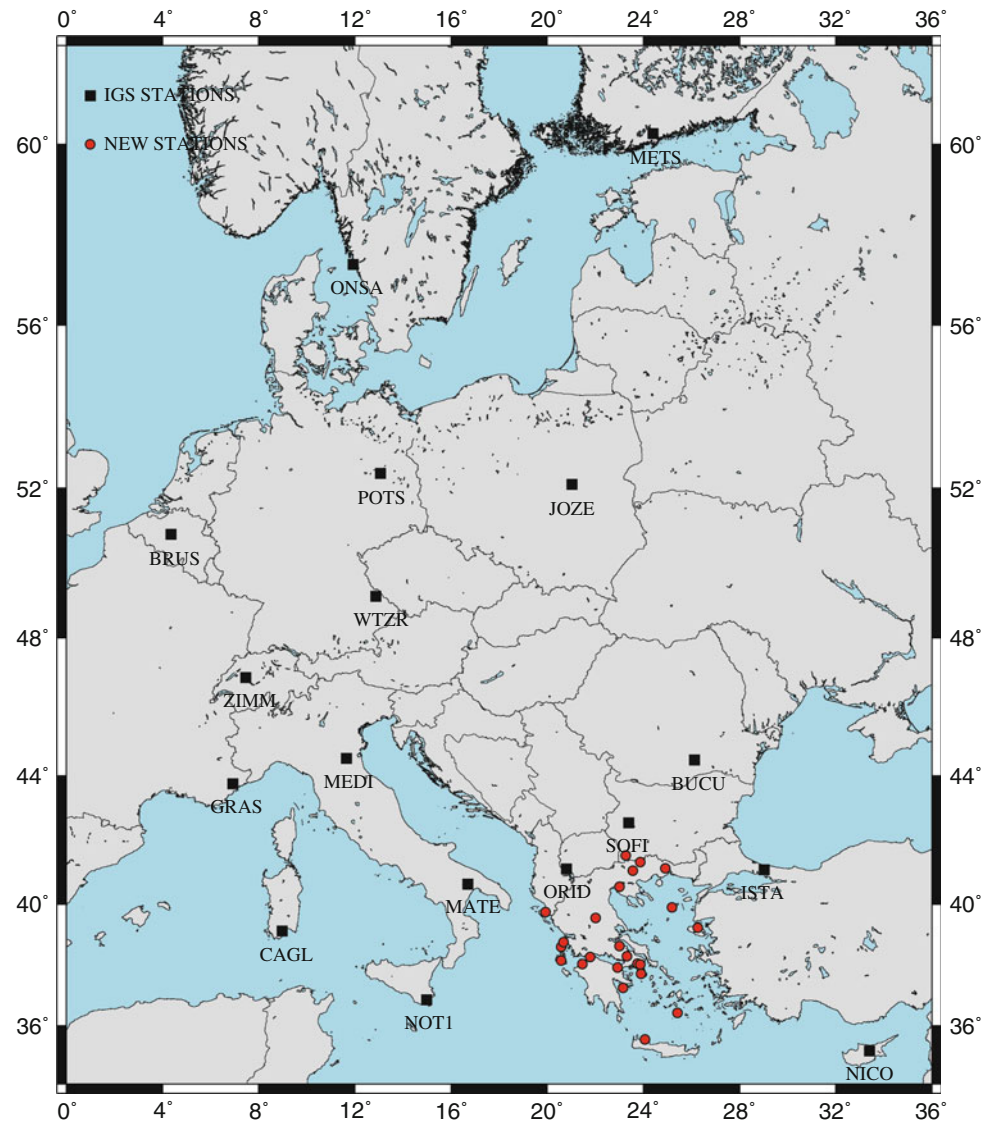
period 2007–2014) and they appear to have varying magnitudes between the tested alignment schemes. The differences vary mostly at the sub-mm per year level and they are depicted in Fig. 2, separately for the horizontal and vertical components. The large velocity differences (1–1.5 mm/year) shown at a few reference stations originate by undetected jumps/discontinuities in their weekly positions, which have been effectively filtered by the augmented transformation in Eq. (7). Note also a systematic offset of 0.3–0.5 mm/year that appears at all *non-reference stations* between their estimated horizontal velocities from each alignment scheme. This suggests that the propagated noise of the weekly solutions causes a small bias to the linear trend of the transformed PTS by the standard HT approach, yet more extensive analysis is

required to verify this distorting effect in regional GNSS networks. The few non-reference stations showing large differences in their horizontal velocities (see right side in Fig. 2) are the ones having smaller data records (ranging from one to three years) compared to the rest of the Hellenic GNSS stations which cover the entire 2007–2014 period.

After the removal of the linear trend from the transformed PTS, the remaining residuals reflect a mixture of temporally correlated noise (due to the propagated errors of the original weekly solutions in the target frame) and nonlinear geodynamical displacements originating from unmodeled loading effects in the weekly GNSS measurements. Some examples of residual PTS that were obtained in our test network by the frame alignment schemes are given in Fig. 3. The
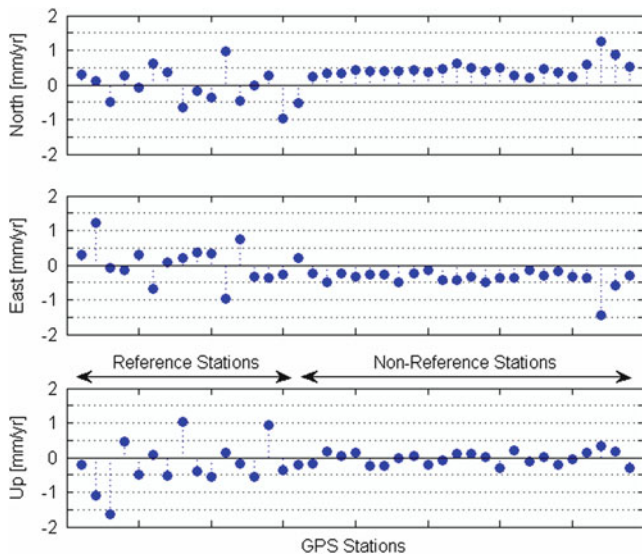
Fig. 2 Differences of the estimated station velocities from the transformed PTS after applying the standard and the augmented HT approaches for the weekly alignment to ITRF2008

same figure also shows the time series plots of the Kalman-like corrections which were computed in the context of the "augmented" transformation. The particular plots refer to the Hellenic station *SPAN* (located in the Lefkada island) and the IGS station *NOT1* (located in Noto, Italy), and they reveal the effect of noise filtering during the implementation of Eq. (7).

The augmented HT approach reduces the root-mean-square (RMS) of the residual PTS in the test network, as should be expected due to the noise filtering of the input weekly solutions. In Fig. 4 we give the RMS values of the horizontal and vertical components of the residual PTS at each station from each alignment scheme. The RMS reduction ranges from 2–3% up to 65% depending on the actual station and the position component. The largest decrease occurs in the east and vertical components of the reference stations, whose nonlinear variability drops by 0.5–4 mm (in the RMS sense) compared to the standard HT approach. Conversely, the non-reference stations (all of which are located within the Hellenic area) show smaller RMS reduction in their residual PTS, which does not exceed 1–2 mm in all three spatial components.
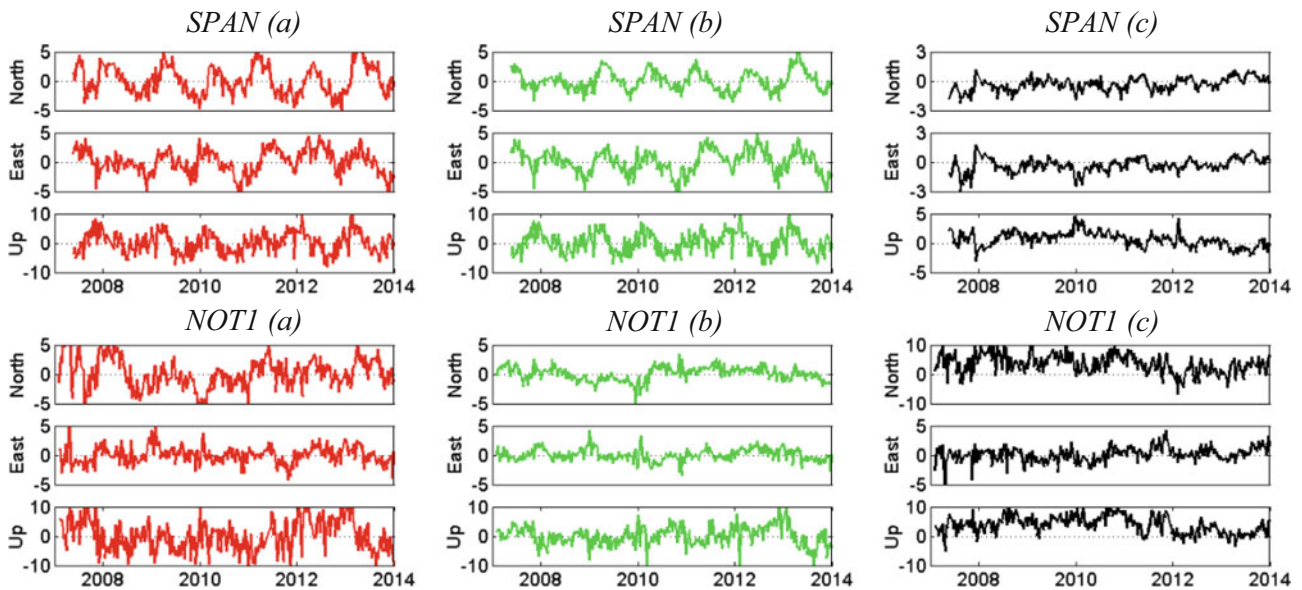
Fig. 3 Residual PTS (in mm) at the *SPAN* and *NOT1* stations as obtained by: (**a**) the standard HT approach and (**b**) the augmented HT approach. The time series plots shown in the third column correspond to the Kalman-like corrections that were computed at each epoch according to Eq. (7)
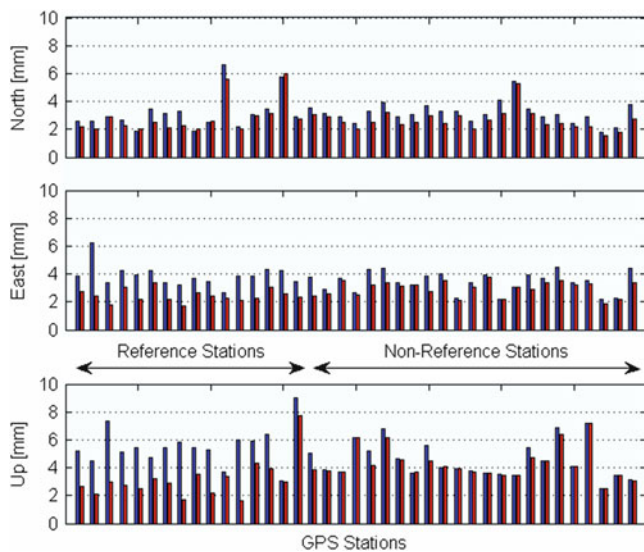
Fig. 4 RMS of the residual PTS (after linear trend removal) in the test network, after applying the standard HT approach (*blue*) and the augmented HT approach (*red*) for the weekly alignment to ITRF2008

The previous results give only a preliminary idea about the performance of the augmented HT approach. Obviously, a more detailed analysis is still required to assess its strengths (and weaknesses) in the context of geodetic applications and geophysical investigations.

5   Summary: Conclusions

Neglecting the (spatially correlated) noise of daily/weekly GNSS solutions during their alignment to a secular frame diminishes the accuracy of the transformed positions and it weakens the geophysical content of the derived PTS. This is, in fact, one of the inherent drawbacks in the standard HT approach which is often applied to generate position time series with respect to Earth monitoring frames (e.g. ITRF). The implementation of this approach relies on the forward transformation of daily/weekly solutions using the estimated Helmert parameters from a separate least-squares adjustment step, thus causing the transfer of their full noise into the target frame without any intermediate filtering. To overcome this limitation, we presented in this paper an *epoch-wise stacking approach* for the alignment of a series of epoch frames to a common secular frame via a least-squares estimation process. The derived transformation formulae differ from

the classic HT solution in terms of additive Kalman-like corrections which depend on the noise characteristics of (1) the daily/weekly solutions and (2) the prior reference positions. Their advantage is that they lead to transformed PTS with smaller noise variances in the target frame and higher robustness against the effect of undetected outliers in the epoch solutions. To achieve its full potential the presented methodology should be combined with well-known de-aliasing strategies (e.g. Collilieux et al. 2012) in order to reduce the expected aliasing of the (unmodeled) loading signals not only to the Helmert parameters, but also to the filtered noise of the daily/weekly solutions.

References

Altamimi Z, Collilieux X, Métivier L (2011) ITRF2008: an improved solution of the international terrestrial reference frame. J Geod 85:457–473

Bastos L, Bos M, Fernandes RM (2010) Contribution of GPS measurements to plate tectonics–overview and recent developments. In: Xu G (ed) Sciences of geodesy-I: advances and future directions. Springer, Berlin, pp 155–184

Biagi L, Sansò F (2012) Some pitfalls to be avoided in combining simultaneous GNSS networks. IAG symposia, vol. 137. Springer, Berlin, pp 335–340

Chatzinikos M (2013) Study of the earth's crust displacements in the area of Greece analyzing GNSS data. PhD Thesis, School of Rural and Surveying Engineering, Aristotle University of Thessaloniki, Greece

Collilieux X, Altamimi Z, Coulot D, van Dam T, Ray J (2010) Impact of loading effects on determination of the International Terrestrial Reference Frame. Adv Space Res 45:144–154

Collilieux X, van Dam T, Ray J, Coulot D, Metivier L, Altamimi Z (2012) Strategies to mitigate aliasing of loading signals while estimating GPS frame parameters. J Geod 86(1):1–14

Dach R, Hugentobler U, Fridez P, Meindl M (2007) Bernese GPS software version 5.0. Astronomical Institute, University of Bern, Switzerland

Kotsakis C, Vatalis A, Sanso F (2014) On the importance of intra-frame and inter-frame covariances in frame transformation theory. J Geod 88(12):1187–1201

Kotsakis C, Vatalis A, Sanso F (2015) The Helmert transformation approach in network densification revisited. IAG Symposia Series, Springer, Heidelberg, vol. 146. Proceedings of the IAG International Symposium on Reference Frames for Applications in Geosciences, Kirchberg, Luxemburg, 13–17 Oct 2014

Tregoning P, van Dam T (2005) Effects of atmospheric pressure loading and seven parameter transformations on estimates of geocenter motion and station heights from space geodetic observations. J Geoph Res 110:B03408. doi:10.1029/2004JB003334

van Dam T, Collilieux X, Wuite J, Altamimi Z, Ray J (2012) Nontidal ocean loading: amplitudes and potential effects in GPS height time series. J Geod 86(11):1043–1057

Geodetic Modelling of Atmospheric Variables

Assessing GPS + Galileo Precise Point Positioning Capability for Integrated Water Vapor Estimation

Marco Mendonça, Ryan M. White, Marcelo C. Santos, and Richard B. Langley

Abstract

Although conventionally used for positioning, navigation, and timing, GNSS observations constitute a useful tool for atmospheric remote sensing. By quantifying and analyzing the influence of the atmosphere on the propagating electromagnetic signals, we can infer a significant amount of information for further understanding Earth's atmosphere as well as its relationship with satellite positioning activities. For some industrial sectors that require high accuracy and reliability, such as oil exploration, dredging, and aviation, the understanding of how GNSS satellite signals propagate across the atmosphere is crucial information. Among several improvements related to GNSS, the increasing number of in-orbit Galileo satellites opens a new window of opportunities for atmospheric research. Users can achieve improved satellite geometry and take advantage of Galileo signal characteristics, such as improved signal strength. In this study, the usage of Galileo signals for neutral atmospheric delay (NAD) estimation is assessed along with its integration with signals from the already established GPS constellation. Using the University of New Brunswick's GNSS Analysis and Positioning Software (GAPS) precise point positioning suite, the NAD values are estimated and integrated with in situ measurements of pressure, temperature, and humidity, allowing us to estimate the integrated water vapor (IWV) of the atmosphere above a GNSS station. As a reference for the estimation assessment, existing IWV values from radiosondes are used. Preliminary results show that the Galileo + GPS NAD estimations are close to those of GPS at the 2-centimeter level. The recently-released multi-GNSS processing online version of GAPS is now able to provide users with a useful tool for atmospheric research.

Keywords

Atmospheric studies • Galileo • GAPS • Geodesy • IWV • Multi-GNSS • NAD

1 Introduction

The integration of different satellite constellations for any given positioning-oriented purpose is a challenge (Montenbruck et al. 2014; Dow et al. 2009). When using two or more systems with different reference frames for both position and time, a series of biases and statistical models should be considered in order to achieve a satisfactory synergy. In this study, the integration between the Global Positioning System (GPS) and Galileo is assessed in the scope of the neutral atmospheric delay estimation by the calculation of integrated water vapor (IWV).

In an attempt to validate the IWV estimated via the integration of the aforementioned systems and the Vienna Mapping Function 1 (VMF1) gridded product, this study uses radiosonde data provided by the Department of Atmospheric

M. Mendonça (✉) • R.M. White • M.C. Santos • R.B. Langley
Department of Geodesy and Geomatics Engineering, University of New Brunswick, P.O. Box 4400, Fredericton, NB, Canada E3B 5A3
e-mail: marco.mendonca@unb.ca
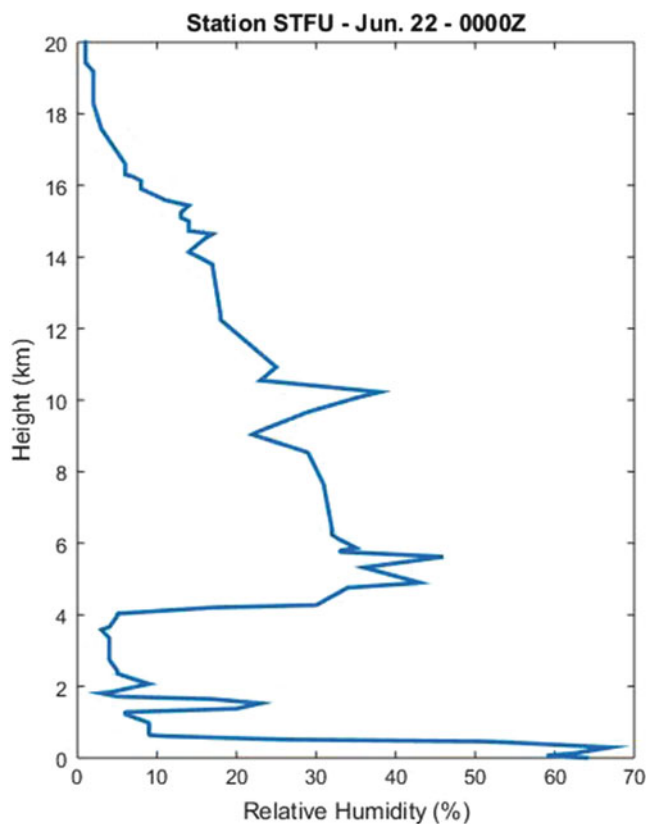
Fig. 1 Example of radiosonde relative humidity profiling

Sciences of the University of Wyoming[1] (UWYO) and compares these values with the same parameters estimated using the precise point positioning (PPP) technique utilized by the GNSS Analysis and Positioning Software (GAPS). An example of a relative humidity vertical profile as calculated using a radiosonde and provided by UWYO is presented in Fig. 1.

When considering the expected biases and errors encountered during the integration of different constellation observables, it is possible to see that the integration will not only provide a direct benefit to the solution in terms of accuracy of the IWV estimation, but will also increase the robustness and availability of the solution, since more satellites can be observed and subsequently integrated into the mathematical model.

Several studies have been conducted considering the impact of new GNSS satellites in atmospheric remote sensing activities. Li et al. (2015a, b) studied the impact of the Beidou constellation in IWV estimation, concluding that this constellation is ready for being integrated into tropospheric parameters estimation, as well high-precision GNSS activities. Rohm et al. (2014) showed that, although PPP is inferior in accuracy to double-differencing

positioning, it still provides a high consistency solution, agreeing to radiosonde references up to the centimeter level. Li et al. (2015a) studied the integration of different GNSS constellations, arriving to the conclusion that even for real time applications, the integration of different systems is achievable and beneficial for GNSS and meteorology applications.

Considering the aforementioned, this study aims to analyze the integration between GPS and Galileo on a PPP solution regarding the IWV estimation product. This paper is organized in order to present the dataset used and processing parameters, followed by the IWV estimation technique, data analysis, conclusions, and future work.

2   Data

For use in this investigation, 4 days of four globally-distributed International GNSS Service (IGS) Multi-GNSS Experiment (MGEX) tracking stations were selected at locations within 10 km of radiosondes launched daily at 0000Z and 1200Z. Their approximate locations are shown in Fig. 2.

These selected stations provide receivers with Galileo tracking capability as well as radiosonde data availability for the time interval of each station's 24-hour GNSS observation period. While dual-frequency observables are available from the 11 current Galileo satellites, observation periods are rather inconsistent due to their limited number. Additionally, simultaneous observability of a minimum of four Galileo satellites is currently limited to 4 h (at best) with, in most situations, relatively poor satellite geometric distribution. These conditions hinder any accurate estimation of IWV using Galileo-only processing at this time. For the processing of GPS observables, standard IGS final clock (5-minute) and orbit products have been utilized. For Galileo observable processing, clock (5-minute) and orbit products from the Center for Orbit Determination in Europe (CODE) made available through the IGS MGEX campaign have been utilized (Montenbruck et al. 2014). While observables were logged at a 30-second sampling interval at each of the selected stations, processing was performed at a 5-minute interval as to avoid interpolation of satellite clock corrections, including the subsequent estimation of IWV. All of the aforementioned products are available from the IGS FTP servers with a latency of approximately 2 weeks (Dow et al. 2009).

In order to appropriately combine observables from different constellations, additional system-dependent corrections must be applied. These corrections include estimated inter-system biases (ISBs), differential code biases (DCBs), and

Fig. 2 Location of the selected GNSS stations and radiosonde launching sites

antenna phase-centre offsets. In GAPS modified algorithm, ISBs are estimated in order to account for the varying antenna differential delays experienced when tracking multi-constellation observables. A random-walk with a process noise of 0.10 m/$\sqrt{h}$ is subsequently applied in order to properly constrain ISB parameters. As the IGS MGEX orbit and clock products reflect the use of the E1/E5a iono-free linear combinations also used in GAPS, no DCB corrections to Galileo observables are currently required. Differing antenna phase-centre offsets, on the other hand, must be considered when combining multi-constellation observables. While standard IGS ANTEX phase-centre offsets (PCOs) and variations (PCVs) are used for GPS observables, GAPS applies generic Galileo IOV and FOC satellite PCO corrections as recommended by the IGS MGEX campaign (http://mgex.igs.org/IGS_MGEX_Status_GAL.html). At this time, no corrections for PCVs are considered as no data is yet available.

The residual wet component (as well as a trace of the dry component) of the neutral atmospheric delay (D_{ZW}) is estimated within GAPS sequential least-squares filter and constrained with a random-walk process noise of 5 mm/$\sqrt{hr}$. VMF1 (ECMWF) was utilized as the a priori NAD prediction model and reduced to a vertical delay through use of the Vienna mapping functions. Observables used in processing include the iono-free linear combination of the GPS legacy L1/L2 and Galileo Open Service E1/E5a signals. A 10° elevation angle cutoff threshold was applied as was a GDOP cutoff threshold of 20 to avoid outliers caused by poor geometry. Additionally, both Earth body tides and ocean tidal loading corrections were applied to modeled parameters during processing. The station coordinates were left unconstrained at the beginning of the processing and then propagated between days.

3   IWV Estimation

In order to assess the impact of using Galileo observables in a PPP solution, the chosen dataset was processed with GAPS using GPS-only and GPS + Galileo strategies. Estimates resulting from GPS-only and GPS + Galileo processing are subsequently analyzed and compared to each other to see if the multi-GNSS solution is able to provide satisfactory results in terms of inferring total NAD. As a second step, the wet component of the delay (D_{ZW}), along with troposphere mean temperature (T_m) from VMF1 model, water vapor specific constant (R_w), and atmospheric refractivity constants (k_2', k_3) are used to estimate IWV (Sapucci et al. 2005):

$$\text{IWV} = D_{ZW} \frac{10^6}{R_w \left[k_2' + \frac{k_3}{T_m} \right]}, \tag{1}$$

where the constants k_2' and k_3 are, respectively, 22.1 ± 2.2 (in Kelvin per hectopascal (K/hPa)) and $3.739 \pm 0.012 \times 10^5$ (K^2/hPa) (Davis et al. 1985).

Once IWV is determined, a comparison is performed against in situ radiosonde precipitable water sounding. The difference is then summarized and analyzed to assess the interoperability between GPS and Galileo for such an application as well as to determine the appropriateness of the least-squares algorithm used in GAPS to estimate the wet delay.

4   Data Analysis

Even though the Galileo constellation is still in its infancy, integration of Galileo observables with those of GPS is currently achievable and shows satisfactory results in
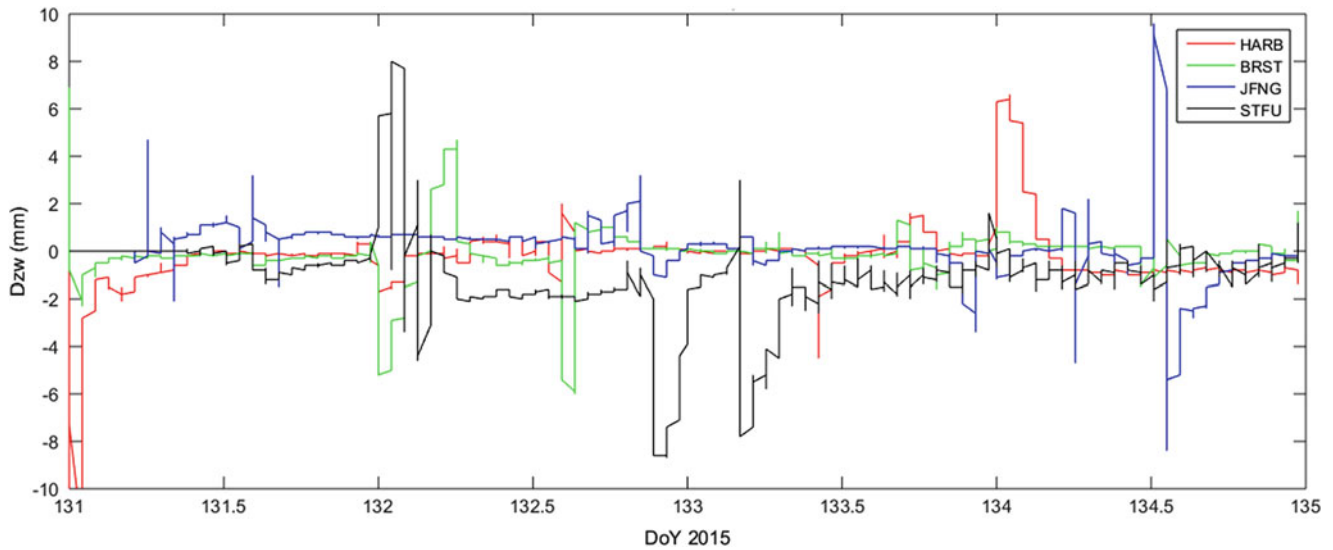
Fig. 3 Time series of the difference between GPS-only and GPS + Galileo D_{ZW} estimates between DOY 131 and 135, 2015
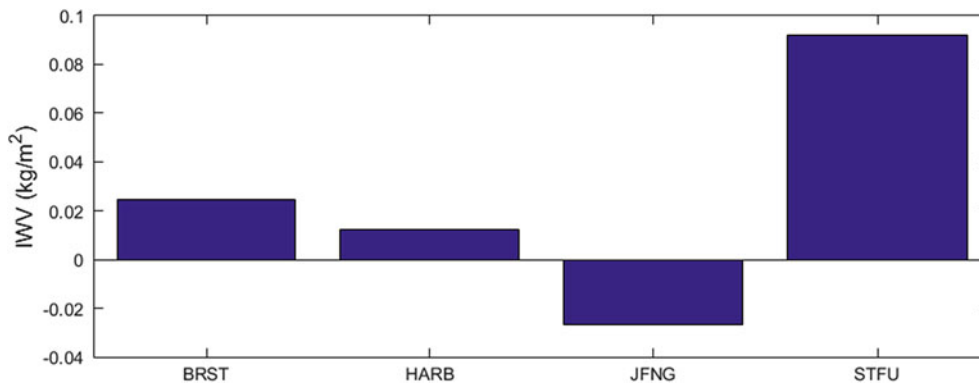
Fig. 4 Discrepancy between GPS-only minus GPS + Galileo IWV

terms of position and atmospheric parameter estimation. By analyzing the differences between GPS-only and GPS + Galileo D_{ZW} estimates, it can be seen that the differences between each are, on average, within 1 mm of the estimated D_{ZW} (station STFU) with a minimum difference of 0.08 mm (station JFNG). This represents approximately 0.16 and 0.013 kg/m^2 of precipitable water in the atmosphere, respectively. A maximum difference of about 1 cm occurred at station JFNG at 1200Z on day-of-year (DOY) 134, representing a discrepancy in the precipitable water estimate of approximately 1.7 kg/m^2. Figure 3 summarizes the analysis of the entire dataset. With the exception of station STFU, all the GPS minus GPS + Galileo solutions are below the millimeter level on average and 1.5 mm of standard deviation. For STFU, the average is 2.2 mm and a standard deviation of 2.8 mm.

Although occasional outliers exist, the average difference remains within the expected noise of Galileo observ-

able integration when considering the sporadic availability of Galileo satellites and the use of experimental Galileo orbit and clock products. To investigate if these outliers are due to the integration algorithm or, perhaps, with the tropospheric delay estimation, radiosonde sounding data are used as a benchmarking tool for further comparison of estimated precipitable water. Figure 4 shows the discrepancy between GPS-only minus GPS + Galileo IWV. Figure 5 shows error bars for each station related to the difference between the GPS + Galileo PPP-based estimation of IWV and the radiosonde-measured IWV.

It is possible to see that the error in both estimates are close in terms of bias and dispersion from the radiosonde estimates (Fig. 5). This, again, indicates a success in terms of the system integration being that GPS + Galileo estimations are, on average, closer to the radiosonde IWV measurements than GPS-only solutions, but points towards a necessary investigation of the D_{ZW} estimation algorithm for both methods.
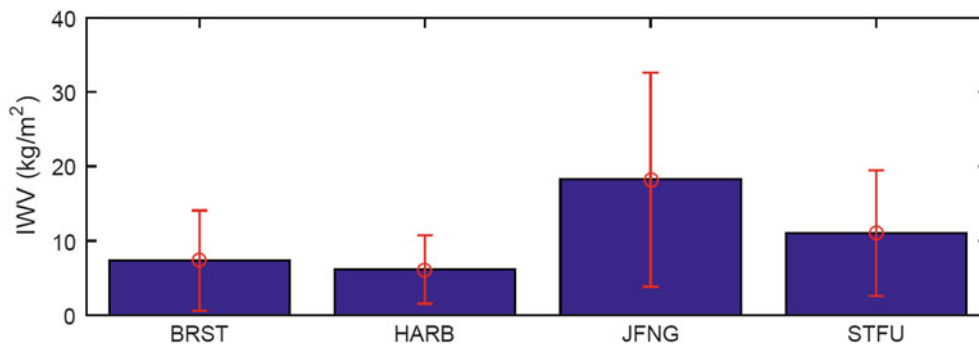
Fig. 5 Error bars for each station related to the difference between the PPP-based estimation of IWV and the radiosonde-measured IWV

It is important to stress that the immaturity of the Galileo products combined with challenges in finding a reasonable geometry contribute to occasional spikes in the solution. In spite of the fact that their source is hard to track without proper geometry and orbit repeatability, from the analyzed dataset it is possible to conclude that they are occasional and not a recurrent problem in the integration.

5 Conclusions

Results show that the Galileo + GPS IWV estimates are close to those of GPS-only at a level of 0.13 kg/m^2 of precipitable water. This demonstrates that both systems can be successfully used together to improve data quality, specifically in challenging environments where satellite geometry can be an issue. Although the selected datasets were obtained from sites with unobstructed surroundings to eliminate other possible error sources, it is safe to say that users can, by now, begin to take advantage of the Galileo GNSS, particularly in the case of estimation of atmospheric parameters. For atmospheric research, Galileo-only processing is still not currently feasible as the constellation as-is provides very large DOP values due to the limited number of observable satellites as well as the limited availability of a minimum of four simultaneously-observable satellites. However, with the anticipated launch of several more full-operational-capability satellites in the coming year, Galileo will soon become a useful tool for atmospheric parameter estimation and IWV determination.

Another point to be emphasized is that GAPS is able to integrate both constellations, estimate the wet component of the troposphere delay and calculate the IWV parameter. This implementation is a novelty among the free online PPP software suites currently available to the research community.

6 Future Work

As previously mentioned, the Galileo constellation remains at an early stage in its development. Following successful completion of the Galileo In-Orbit-Validation (IOV) campaign and the salvage mission to restore the two Galileo satellites affected by the orbit injection anomaly of 2014, the constellation is rapidly progressing towards Full-Operation-Capability. As more and more satellites are added to the constellation, satellite availability and geometry will improve significantly, thus enhancing the performance of GPS + Galileo and Galileo-only atmospheric parameter estimation through use of the PPP estimation technique. Additional improvements to the IGS MGEX Galileo orbit and clock product line are sure to follow, further enhancing the accuracy potential of atmospheric parameters like IWV. Future research will investigate this potential enhancement in accuracy by including each new Galileo satellite as they become available as well as utilizing new and improved Galileo products as they are introduced.

Further work will also need to be done in order to optimize the GAPS NAD estimation algorithm in order to account for biases seen between its integrated IWV estimates and those of the radiosonde data. Alternative estimation routines will be investigated as will use of various NAD prediction models and mapping functions.

References

Davis JL, Herring TA, Sapiro II, Rogers AEE, Elgered G (1985) Geodesy by radio interferometry: effects of atmospheric modelling errors on estimate of baseline length. Radio Sci 2:1593–1607

Dow JM, Neilan RE, Rizos C (2009) The international GNSS service in a changing landscape of global navigation satellite systems. J Geod 83(3–4):191–198

Li M, Li W, Shi C, Zhao O, Su X, Qu L, Liu Z (2015a) Assessment of precipitable water vapor derived from ground-based BeiDou observations with Precise Point Positioning approach. Advances in Space Research 55(1):150–162. doi:10.1016/j.asr.2014.10.010, ISSN 0273-1177

Li X, Dick G, Lu C, Ge M, Nilsson T, Ning T, Wickert J, Schuh H (2015b) Multi-GNSS meteorology: real-time retrieving of atmospheric water vapor from BeiDou, Galileo, GLONASS, and GPS observations. IEEE Trans Geosci Remote Sens 53:12

Montenbruck O, Steigenberger P, Khachikyan R, Weber G, Langley RB, Mervart L, Hugetobler U (2014) IGS-MGEX: preparing the ground for multi-constellation GNSS science. InsideGNSS 9(1):42–49

Rohm W, Yuan Y, Biadeglgne B, Zhang K, Le Marshall J (2014) Ground-based GNSS ZTD/IWV estimation system for numerical weather prediction in challenging weather conditions. Atmos Res 138:414–426. doi:10.1016/j.atmosres.2013.11.026, ISSN 0169-8095

Sapucci LF, Machado LAT, da Silveira RB, Fisch G, Monico JFG (2005) Analysis of relative humidity sensors at the WMO radiosonde intercomparison experiment in Brazil. J Atmos Ocean Technol 22(6):664–678

Atmospheric Precipitable Water in Somma-Vesuvius Area During Extreme Weather Events from Ground-Based GPS Measurements

U. Tammaro, U. Riccardi, F. Masson, P. Capuano, and J.P. Boy

Abstract

In this paper, we analyze the tropospheric delay observed on some ground-based CGPS stations in a dense small regional network and its time evolution during extreme weather conditions. In particular, we studied two severe weather events occurring in the Campanian Region (Italy) on October 12, 2012 and December 2, 2014, reaching 42 and 28 mm rainfall during about 1 h at Naples (MAFE) and Gragnano (GRAG) stations respectively. The main concern of this study is the retrieval of the precipitable water (PW) from co-located GPS and meteorological stations. We investigate the correlation between PW and rain amount at ground level. We analyse phase residuals for each visible GPS satellite using sky plots of the phase residuals along the GPS satellites tracks, showing that the two phenomena are shown in the phase residual plots. Moreover, we compare PW data retrieved from observed meteorological data and from models (GPT2 and ECMWF), evidencing that there is a need for co-located CGPS and weather stations to improve the assessment of water content in the troposphere.

Keywords

Precipitable water • Tropospheric delay • GPT2 • ECMWF • GPS

1 Introduction

The extensive use of permanent GNSS stations, currently operating for geodetic purposes, offers a tool for a dense and reliable remote sensing of atmospheric water vapour (WV) (e.g. Bevis et al. 1994; Song and Grejner-Brzezinska 2009). We analyse the tropospheric delay observed on some continuous CGPS (Continuous Differential Global Positioning System) stations of the NeVoCGPS (Neapolitan Volcanoes Continuous GPS) network managed by Istituto Nazionale di Geofisica e Vulcanologia (INGV) for volcanic monitoring and we discuss its time evolution during extreme weather events. We focus mainly on the study of the wet component of the atmospheric delay of the GPS signals and the computation of the precipitable water (PW) by using co-located GPS and meteorological stations. Four new stations have been installed in September 2014 in joint venturing with EOST (Ecole et Observatoire des sciences de la Terre), aimed at densifying the existing NeVoCGPS network and trying a high-resolution modelling of the PW in the Somma-Vesuvius area, Italy.

A number of scientific topics, other than the obvious weather forecast and atmospheric general circulation models, can benefit from an improvement of our ability to map at

U. Tammaro (✉)
Istituto Nazionale di Geofisica e Vulcanologia, Sezione "Osservatorio Vesuviano", Naples, Italy
e-mail: umberto.tammaro@ingv.it

U. Riccardi
Dipartimento di Scienze della Terra, dell'ambiente e delle Risorse (DiSTAR), University "Federico II" of Naples, Naples, Italy

F. Masson • J.P. Boy
IPGS/EOST Université de Strasbourg/CNRS, Strasbourg, France

P. Capuano
Department of Physics "E.R. Caianiello", University of Salerno, Salerno, Italy

local scale the WV content in the troposphere all around a prominent topographic area of interest, such as an active volcano. Because of the peculiar topography of Mt. Vesuvius, the use of satellite geodetic techniques, for monitoring purposes, as the DInSAR (Differential SAR Interferometry), for instance, may significantly suffer from a poor knowledge of atmospheric heterogeneities.

In the following sections, we will first introduce the methodology used. Then, we describe the data set and network processing. In the fourth section, we present and discuss the results. Finally, we draw our conclusions and ongoing activities.

2 Methodology

The zenith tropospheric delay (ZTD) is the sum of two terms, hydrostatic (ZHD) and wet (ZWD) delay:

$$ZTD = ZHD + ZWD \tag{1}$$

both hydrostatic and wet delays are projected by means of "mapping functions", which allows mathematically modelling the elevation dependence of the delays. We use the new empirical slant delay model GPT2 (Lagler et al. 2013), as implemented in GAMIT 10.5 (Herring et al. 2010), to compute the a priori ZHD functions. GPT2 is based on 10 years (2001–2010) of global monthly mean profiles for pressure, temperature, specific humidity, and geopotential from ERA-Interim (Dee et al. 2011), discretized at 37 pressure levels, providing the interpolated meteorological parameters at any site on the Earth on a $1° \times 1°$ grid. We use Saastamoinen formulas (Saastamoinen 1973) as modified by Davis et al. (1985) to calculate ZHD from GPT2. For more accurate modelling of ZHD, we use atmospheric pressure from sensors of four weather stations.

Subtracting the hydrostatic delay (ZHD) from ZTD, we obtain the wet delay (ZWD) leading us to assess the PW. Then ZWD is converted to PW using formulas given by Bevis et al. (1994). Furthermore, to test the significance of our results, we compare the PW retrieved from observed meteorological data with PW time series coming from both GPT2 and the operational ECMWF model. In the latter case, we use the model obtained by Boy and Chao (2005). The ECMWF operational model, available at a horizontal resolution of about 15 km, vertical resolution variable from 91 to 137 levels and 3-hourly samples, is used to re-compute the surface pressure on the real Earth surface, by propagating the pressure from the orography to the surface. In particular, the total water vapor (wv) is computed using the following relation:

$$wv = \int_{ps}^{0} q \frac{dp}{g_m} \tag{2}$$

where, q is the specific humidity, P_S is the surface pressure, g_m is the constant model gravity ($g_m = 9.80665$).

3 Data Set and Network Processing

The permanent GPS network (Fig. 1) used in this study consists of 14 sites. Ten stations belong to the continuously operating NeVoCGPS network (Tammaro et al. 2013), managed by INGV, and four GPS stations co-managed by EOST and INGV installed from 2014 to 2015 in Somma-Vesuvius area (Fig. 1). The network covers an area of about 500 km^2, from centre of Naples to Sorrento peninsula. The highest relief in this area is the Somma-Vesuvius volcano, which is about 1,200 m high and covers a surface area of 165 km^2 (Principe et al. 1987). The density of GPS stations, for the whole network, is about one station every 30 km^2, instead, on Vesuvius, it increases to one station every 15 km^2.

We process two datasets of continuous GPS and meteorological data from four weather stations (Fig. 1) by means of the software GAMIT/GLOBK v. 10.5 (Herring et al. 2010).

We compute the "ionofree" linear combinations (LC) in order to obtain the positions of the GPS stations in ITRF2008
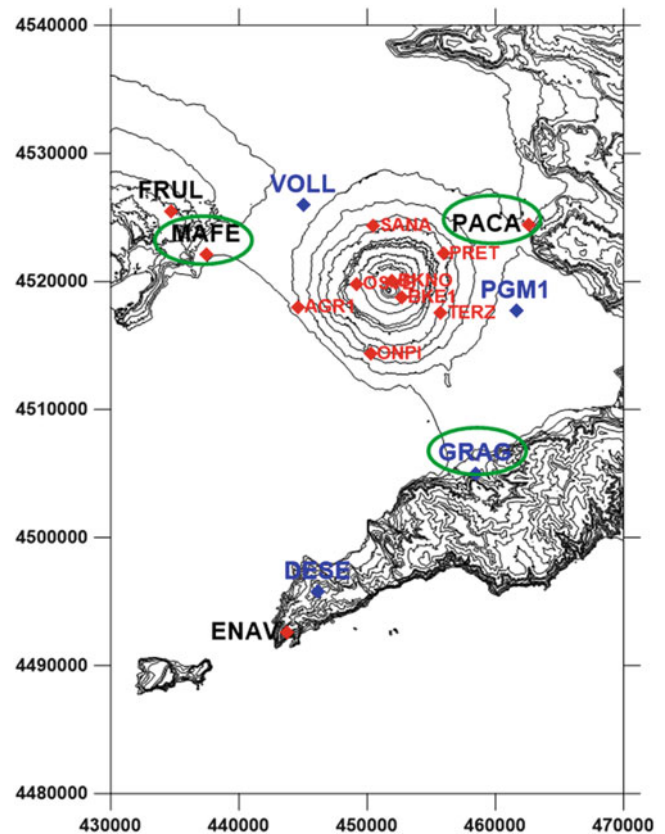
Fig. 1 Neapolitan volcanic area and GPS network. The *green ellipses* indicate the CGPS equipped with "meteo" sensors. *Blue* and *red diamonds* denote EOST and NeVoCGPS stations respectively

frame (Altamimi et al. 2011) using daily sessions, a cut off angle of 5°, and IGS precise ephemeris. We use eight IGS (Dow et al. 2009) stations (AJAC, MATE, NOT1, POTS, GRAS, GRAZ, WTRZ, ZIMM) for the frame referencing. The final coordinates are obtained by constraining the fiducial GPS stations to their ITRF2008 coordinates by means of a Kalman filter procedure implemented in GLOBK (Herring et al. 1990). We do a second run with loose constraints of 1 m on the coordinates to assess hourly ZTD (Haase et al. 2003).

Pressure, humidity, temperature values and rainfall amounts are collected at the meteorological stations. Moreover, we assimilate data from a remote station (baseline length > 200 km), called MATE (in Matera, Italy), to avoid correlation of the delay parameters in the small regional network (Duan et al. 1996).

PW is calculated with "sh_metutil" script, available in GAMIT software package. The utility "*metutil*" extracts the zenith delay estimates from the daily solutions, applies corrections for the hydrostatic delay (Saastamoinen 1972) and converts the residual wet delay to precipitable water.

The daily GAMIT solutions, besides the quasi-observation, contain the parameters of the piecewise-linear model estimated from the data, hence, the zenith total delay (ZTD) is obtained by interpolation. The outputs of *metutil* are the zenith wet delay (ZWD), precipitable water (PW) as well as North–south and East–west gradients, with combined errors.

$$PW = \frac{ZWD * 10^6}{\rho * R_v * \left(\frac{K_3}{T_m} + K_2'\right)} \quad (3)$$

where ρ is the density of liquid water, R_v is the specific gas constant for water vapor (Askne et al. 1987), T_m is a weighted mean temperature of the atmosphere as well as K_3, K_2' are physical constants (Bevis et al. 1994). For both the hydrostatic corrections and evaluation of weighted mean temperature T_m, the input pressure and temperature values can be the "a priori" ones (from the GPT2 model) or the observed data from the RINEX meteorological files.

The values of the constants ρ, R_v are well determined, and their experimental uncertainties have no potential impact on the PW (Bevis et al. 1994). The uncertainties in PW (σ_{PW}) derive from uncertainties in T_m as well as in the physical constants.

$$\sigma_{PW} = \frac{\sigma_{ZTD} * 10^6}{\rho * R_v * \left(\frac{K_3}{T_m} + K_2'\right)} \quad (4)$$

4   Results and Discussion

On October 12, 2012 (Fig. 2) and December 2, 2014, two severe weather events occurred in the Campania Region, reaching 42 and 28 mm rainfall during about 1 h at Naples (MAFE) and Gragnano (GRAG) stations respectively.

The first phenomenon can be followed in the 4-h snapshots from MeteoSat (Fig. 3). The thunderstorm reaches Naples city at 07:00 UTC (09:00 Local Time). The second event, although smaller in terms of rainfall (28 mm/h) than the previous one, can be quite clearly tracked in the 1-h snapshots of MeteoSat (Fig. 4). The raining phenomenon, moving to the SE, passes over Naples (MAFE) at 9–10 (UTC) and at 16–17 attains Gragnano (GRAG) and Palma Campania (PACA).

In order to investigate the correlation between PW and rain amount at ground level, we look at those GPS stations (GRAG, MAFE, PACA) closest to the core of precipitation and which are equipped with rain gauges. In particular, we analyse phase residuals for each visible GPS satellite and sky plots of the phase residuals along the GPS satellites tracks. The residuals are the one-way (undifferenced) phase residuals of the LC ionofree combination in terms of delay accumulated in the line of sight between the satellite and the antenna.

Aimed at checking the significance of the residuals retrieved during a not so severe (<30 mm) rainfall event, we consider the thunderstorm occurred on December 2, 2014. This phenomenon, although smaller (28 mm/h) than the previous one, is well tracked by MeteoSat and it can be envisaged in the phase residuals (Fig. 6). Rainfall, moving to the SE, passes over Naples (MAFE) at 9–10 (UTC) and at 16–17 reaches Gragnano (GRAG) and Palma Campania (PACA). Figure 6 shows the time series of the phase residuals around 09:00 UTC at MAFE station, around 16:00 UTC at GRAG and PACA stations. There is an evident correlation in time between the amplitude of the residuals and the intensity of rainfall: a significant scatter appears on MAFE station (satellite 11, 14) between 10:00 and 11:00, on GRAG and on PACA spanning 16:00–17:00 UTC. We can also follow this phenomenon by correlating the satellite images with the 4-h snapshots phase residuals. Figure 7 shows the 4-h snapshots of LC residuals (MAFE station) of the day 336 encompassing raining event as well as during the day 334, which was dry one.
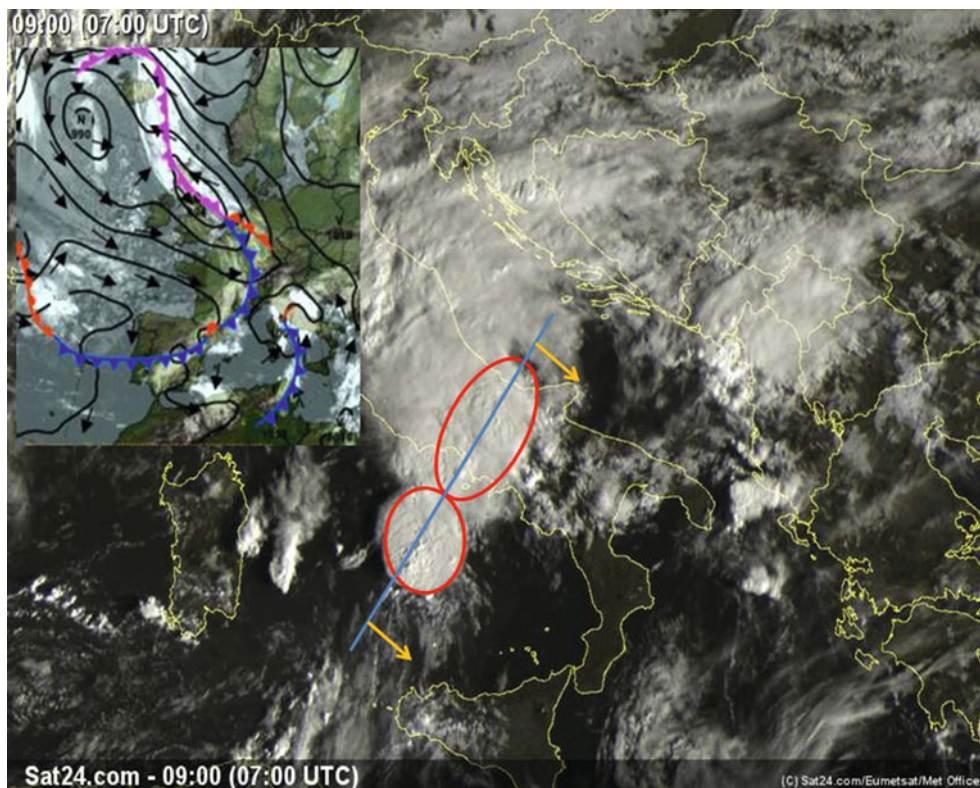
Fig. 2 Campania region (Italy). On October 12, 2012 07:00 UTC 09:00 LT, a cold front coming from Tyrrhenian Sea and moving towards South-East hits the South of Italy breaking out a heavy thunderstorm with large rain amount concentrated in a very short time span. Rain amount: 45–50 mm in $\approx$50 min (Naples station)

During the second raining event, we compare PW data retrieved from observed meteorological data, GPT2 model as well as ECMWF (Boy and Chao 2005); the vertical resolution of the ECMWF model is given by the number of vertical model levels (91 up to 2013/06/24 and 137 afterwards). The ECMWF data have a sampling rate of 3 h, while GPT2 and observed data are sampled at 1 h. Therefore, we have performed a decimation of the data to reduce them to a common sampling rate (3 h).

For GRAG station, the Fig. 8a shows the time history (during December 2014) of PW evaluated from the observed data. Indeed, we observe a very clear correlation between the evolution of the PW retrieved from the GPS delays and the rain. This is in agreement with what was noticed by Benevides et al. (2015), namely the events of intense rain occur after a build-up of PW and initiate a sharp reduction in PW during the following hours. Figure 8b shows PW residuals, namely PW from observed meteorological data minus

modelled ones, for December 2, 2014 (dashed rectangle in Fig. 8a). Positive residuals indicate that observed data are larger than the modelled ones and vice versa for negative residuals. In general, we observe that the residuals of GPT2 are larger than ECMWF. A few hours before the severe events, the positive residuals of both models increase. This clearly indicates that during the rain events statistical models with low resolution, like GPT2, but also operational ones at higher resolution, could be ineffective in the PW retrieval. There is, therefore, a need for co-located CGPS and Meteo stations to improve the assessment of water content in the troposphere.

Figure 5 shows the time series of the phase residuals around 7:00 UTC at MAFE station for the event occurred in 2012. Residuals normally show an increase in fluctuations when elevation angles decrease mainly due to the distance, longer than the zenithal distance, travelled by the wave through the troposphere and related mismodellings of the
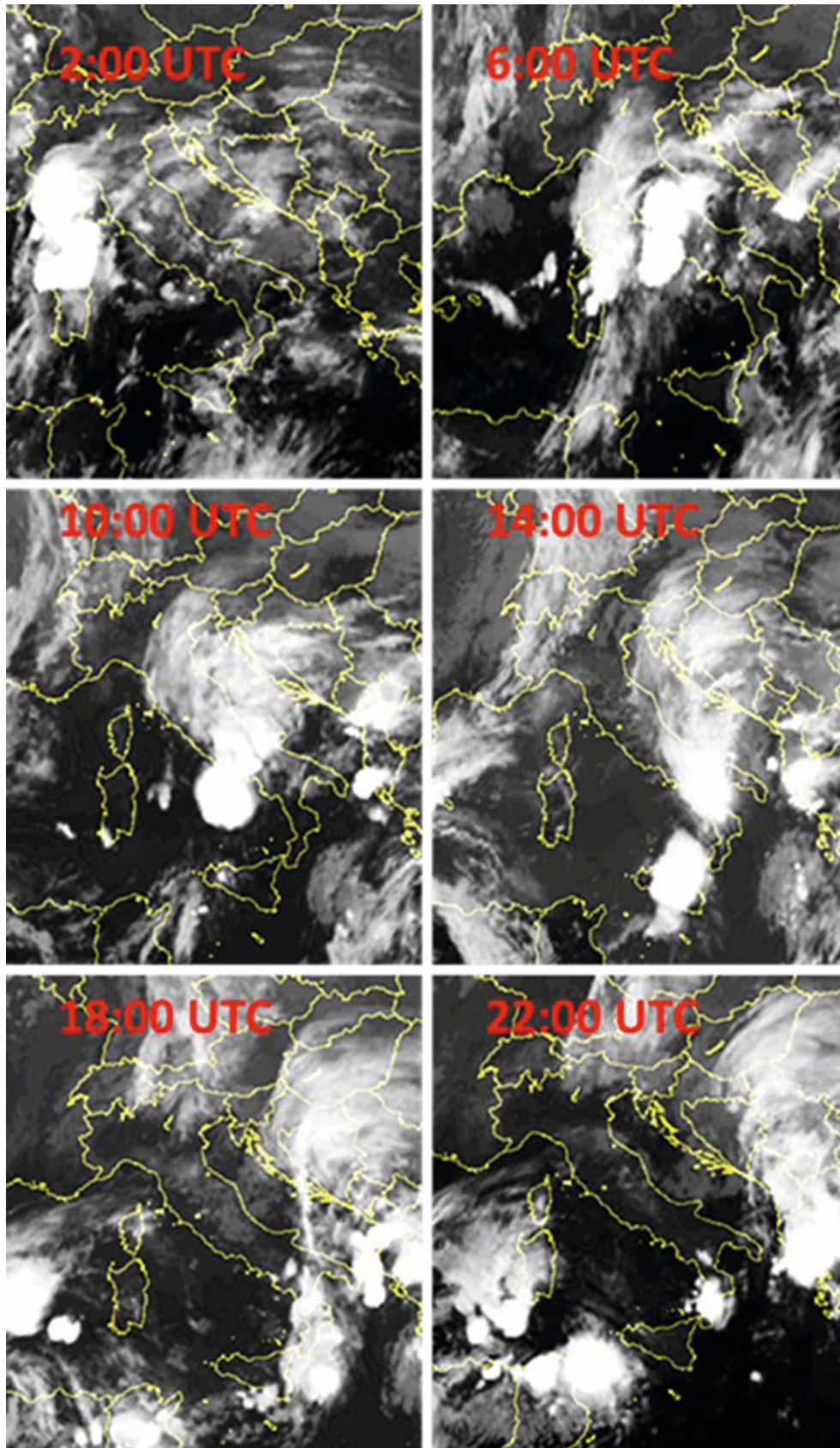
Fig. 3 Four-hour snapshots from MeteoSat radio sensors acquired on October 12, 2012. A severe thunderstorm attains Naples city at 07:00 UTC (09:00 Local Time)
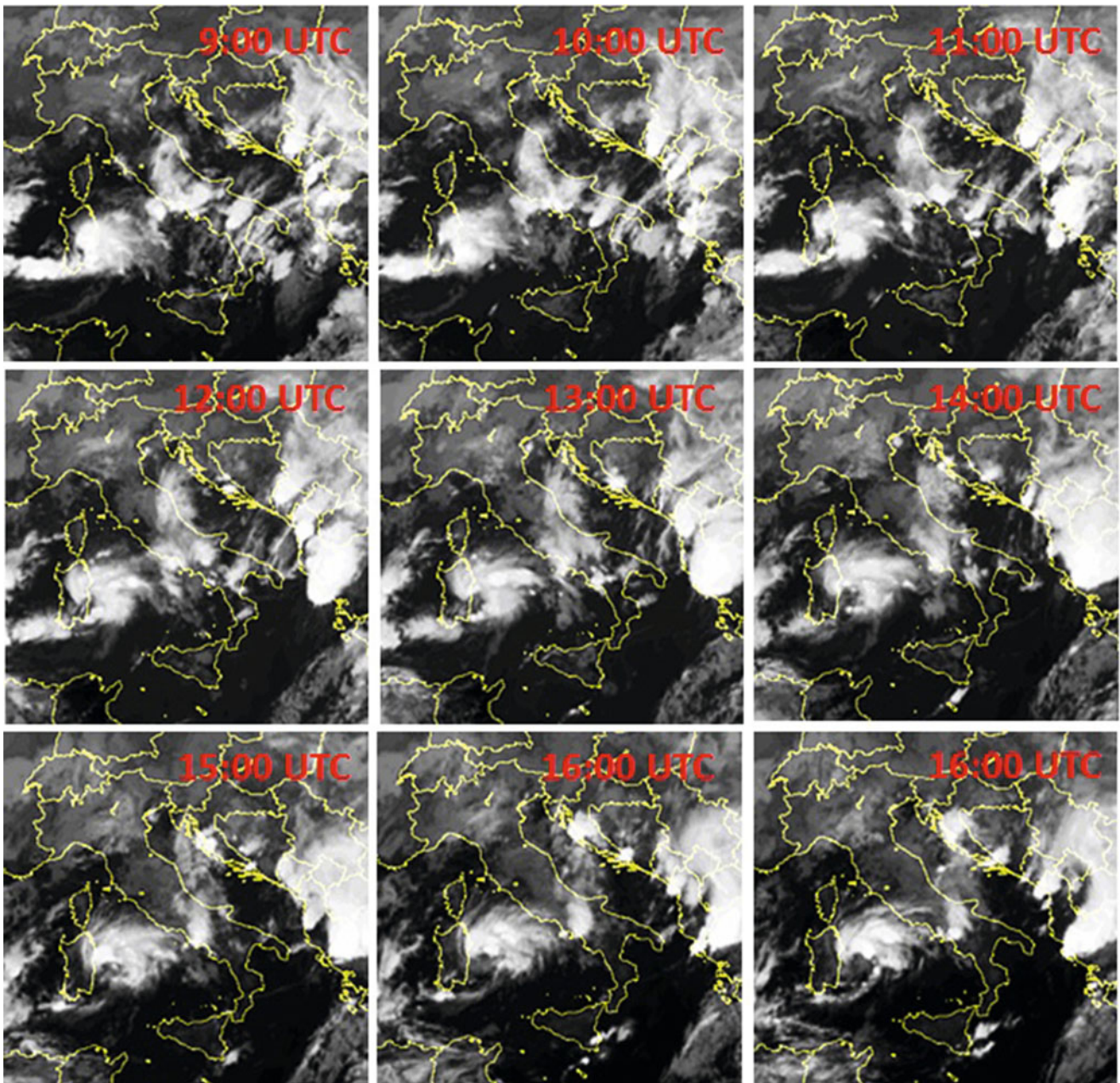
Fig. 4 Four-hour snapshots from MeteoSat radio sensors acquired on December 2, 2014
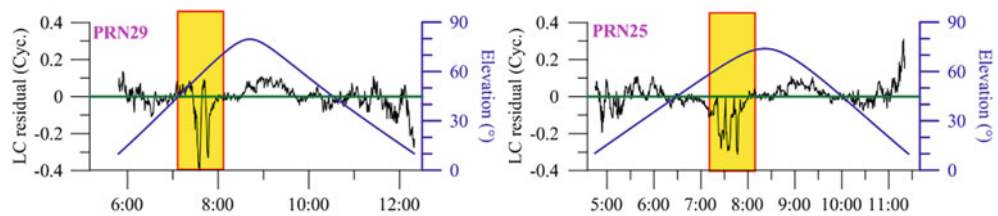
Fig. 5 October 12, 2012: phase residuals (*black curve*) computed at MAFE station, and elevation angle (*blue line*); PRN indicates the satellite number
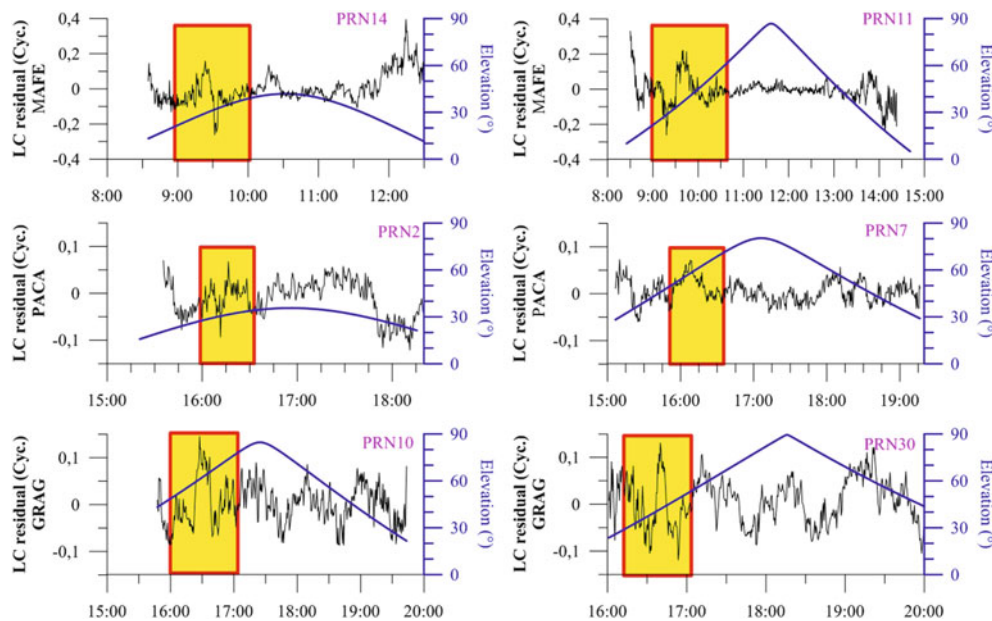
Fig. 6 December 2, 2014: phase residuals (*black curve*) computed at MAFE, GRAG and PACA stations, and elevation angle (*blue line*); PRN indicates the satellite number

atmosphere. During the main rainfall from 07:00 to 08:00 UTC, the phase residuals, at MAFE GPS station, are large and variable in time. Interesting results come out when a significant scatter appears on satellites 25 and 29 seen at high elevation (Fig. 5). Compared to the averaged values of the residuals at MAFE station, the residuals observed during the rainfall are two or three times larger. These large residuals are independent from the elevation of satellites, therefore they should not be due to multipath. Further to the study by Solheim et al. (1999), Champollion et al. (2004) hypothesize that the most significant part of the residuals could be due to liquid water in the troposphere in the form of rain, ice and clouds.

5   Conclusions and Future Perspective

We have analysed GPS and meteorological data collected during two severe weather events occurred in Campania Region. For both events, we detect an evident correlation in time between the amplitude of the residuals and the rainfall. We have also shown that it is possible to follow the spatial evolution of the phenomenon through the analysis of the phase residuals computed at different GPS stations in a dense network.

GPS and meteorological data evidence, as expected, that rainfall is associated with an ongoing accumulation of Water Vapour. Moreover, the use of multi-sensors GNSS and Meteo stations at different altitudes would enable a retrieval of PW vertical profile. Finally, our study confirms that a dense GNSS network co-located with some selected meteorological stations is a useful tool for monitoring PW and its temporal variability. As a future perspective, a tomographic 3D mapping of the water content in the troposphere could turn useful to better understand the humidity distribution in an area like Mt. Somma-Vesuvius characterized by a complex orography.
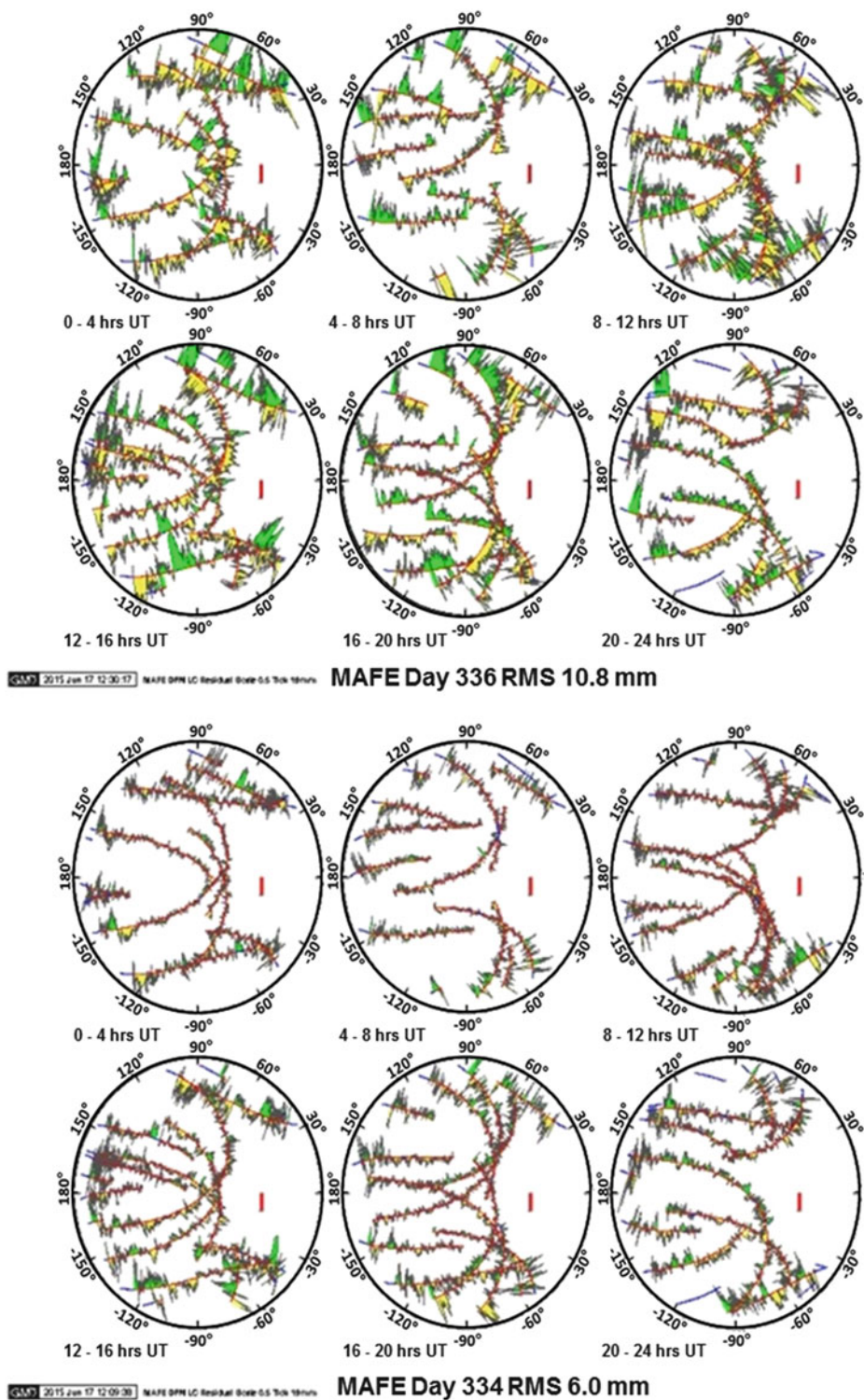
Fig. 7 Four-hour snapshots of LC residuals (MAFE station). Snapshots of the day 336 encompassing the raining event (*top*). Snapshots showing a "normal" behaviour during dry days (*down*). Snapshots made with GMT (Wessel and Smith 1998)
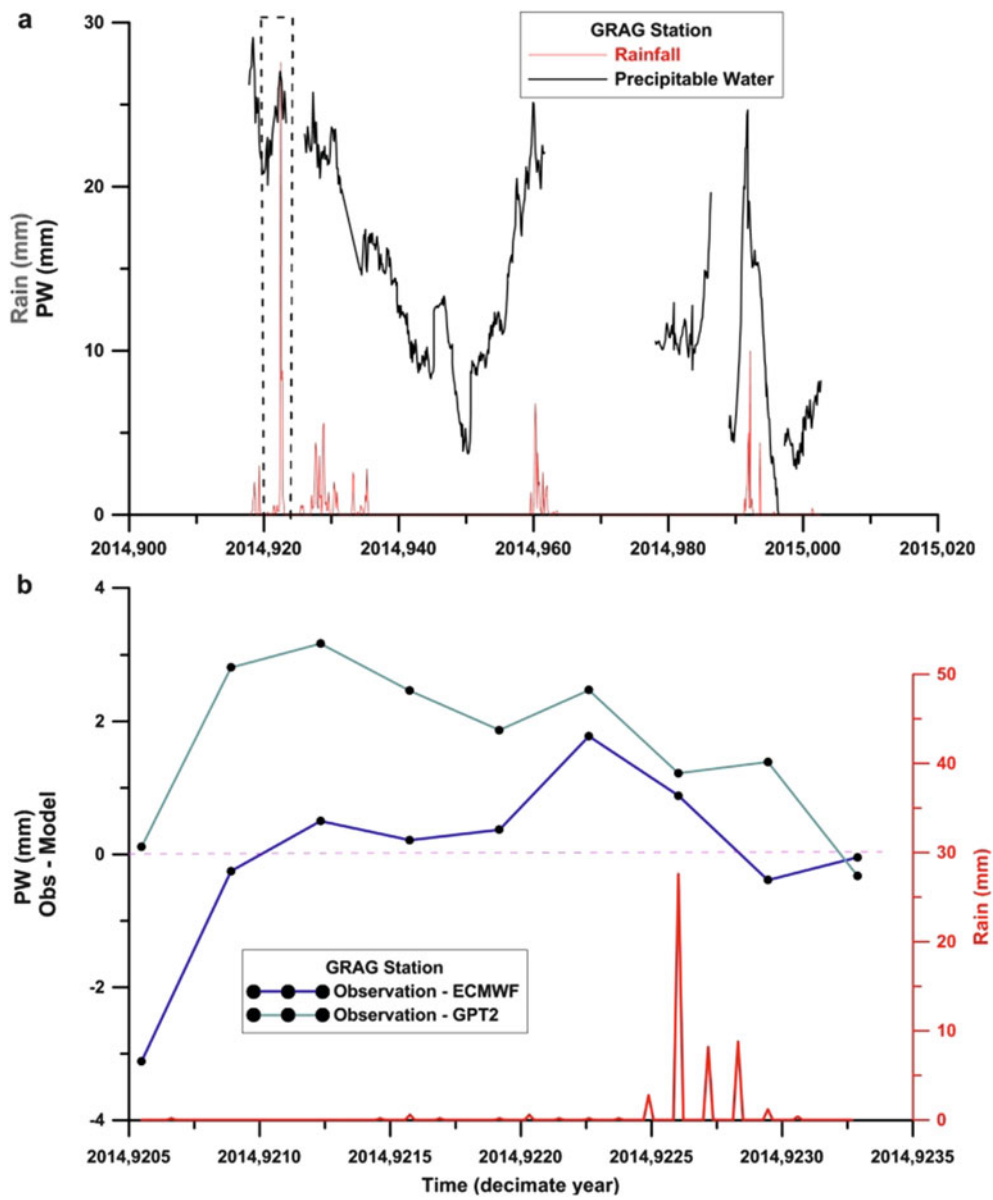
Fig. 8 Hourly precipitable water (PW) retrieved from the observed data (*black line*) and cumulated rain values (*red line*) during December 2014; the *dashed rectangle* indicates the day December 2, 2014 (**a**). PW residuals (i.e. observed minus GPT2 and ECMWF models) during December 2, 2014 event (encircled in *dashed rectangle*); here the residuals have 3 h sampling rate (**b**)

References

Altamimi Z, Collilieux X, Métivier L (2011) ITRF2008: an improved solution of the international terrestrial reference frame. J Geodesy 85(8):457–473. doi:10.1007/s00190-011-0444-4

Askne J, Nordius H (1987) Estimation of tropospheric delay for microwaves from surface weather data. Radio Sci 22(3):379–386

Benevides P, Catalao J, Miranda PMA (2015) On the inclusion of GPS precipitable water vapour in the nowcasting of rainfall. Nat Hazards Earth Syst Sci 15:2605–2616. doi:10.5194/nhess-15-2605-2015

Bevis M, Businger S, Chiswell S, Herring TA, Anthes RA, Rocken C, Ware RH (1994) GPS meteorology: mapping zenith wet delays onto precipitable water. J Appl Meteorol 33:379–386

Boy J-P, Chao BF (2005) Precise evaluation of atmospheric loading effects on Earth's time-variable gravity field. J Geophys Res 110, B08412. doi:10.1029/2002JB002333

Champollion C, Masson F, Van Baelen J, Walpersdorf A, Chéry J, Doerflinger E (2004) GPS monitoring of the tropospheric water vapor distribution and variation during the 9 September 2002 torrential precipitation episode in the Cévennes (southern France). J Geophys Res 109, D24102. doi:10.1029/2004JD004897

Davis JL, Herring TA, Shapiro II, Rogers A, Elgered G (1985) Geodesy by radio interferometry: effects of atmospheric modeling errors on estimates of baseline length. Radio Sci 20(6):1593–1607

Dee D et al (2011) The ERA-Interim reanalysis: configuration and performance of the data assimilation system. Q J Roy Meteorol Soc 137:553–597. doi:10.1002/qj.828

Dow JM, Neilan RE, Rizos C (2009) The International GNSS Service in a changing landscape of Global Navigation Satellite Systems. J Geodesy 83:191–198. doi:10.1007/s00190-008-0300-3

Duan J, Bevis M, Fang P, Bock Y, Chiswell SR, Businger S, Rocken C, Solheim FS, Van Hove T, Ware R, McClusky S, Herring TA, King RW (1996) GPS meteorology: direct estimation of the absolute value of precipitable water. J Appl Meteorol 35:830–838

Haase J, Ge M, Vedel H, Calais E (2003) Accuracy and variability of GPS tropospheric delay measurements of water vapor in the western Mediterranean. J Appl Meteorol 42:1547–1568

Herring TA, Davis JL, Shapiro II (1990) Geodesy by radio interferometry: the application of Kalman filtering to the analysis of very long baseline interferometry data. J Geophys Res 95(B8):12561–12581

Herring TA, King RW, McClusky SC (2010) GAMIT reference manual. Release 10.4. Massachusetts Institute of Technology, Cambridge. http://www-gpsg.mit.edu/~simon/gtgk/

Lagler K, Schindelegger M, Böhm J, Krásná H, Nilsson T (2013) GPT2: empirical slant delay model for radio space geodetic techniques. Geophys Res Lett 40(6):1069–1073. doi:10.1002/grl.50288

Principe C, Rosi M, Santacroce R, Sbrana A (1987) Explanatory notes to the geological map. In: Santacroce R (ed) Somma-Vesuvius, Quaderni de "La Ricerca Scientifica", CNR, 114 (Progetto finalizzato Geodinamica, Monografie finali, 8), pp 11–52. ISSN: 0556-9664. CNR, Rome

Saastamoinen J (1972) Atmospheric corrections for the troposphere and stratosphere in radio ranging of satellites. In: Henriksen SW, Mancini A, Chovitz BH (eds) The use of artificial satellites for geodesy. Geophys. Monogr. Ser., vol 15. Amer. Geophys. Union, Washington, DC, pp 247–251

Saastamoinen J (1973) Contributions to the theory of atmospheric refraction. Bull Geod 107:13–34. doi:10.1007/BF02521844

Solheim FS, Vivekanandan J, Ware RH, Rocken C (1999) Propagation delays induced in GPS signals by dry air, water vapor, hydrometeors, and other particulates. J Geophys Res 104:9663–9670. doi:10.1029/1999JD900095

Song DS, Grejner-Brzezinska DA (2009) Remote sensing of atmospheric water vapor variation from GPS measurements during a severe weather event. Earth Planets Space 61:1117–1125

Tammaro U, De Martino P, Obrizzo F, Brandi G, D'Alessandro A, Dolce M, Malaspina S, Serio C, Pingue F (2013) Somma Vesuvius volcano: ground deformations from CGPS observations (2001–2012). Ann Geophys 56(4):S0456. doi:10.4401/ag-6462

Wessel P, Smith WH (1998) New, improved version of generic mapping tools released. EOS Trans Am Geophys Union 79(47):579

Water Vapor Radiometer Data in Very Long Baseline Interferometry Data Analysis

Tobias Nilsson, Benedikt Soja, Maria Karbon, Robert Heinkelmann, and Harald Schuh

Abstract

We investigate the possibilities to use data from water vapor radiometers (WVR) to calibrate the wet tropospheric delays in geodetic Very Long Baseline Interferometry (VLBI) observations. We test three methods: (1) direct calibration using WVR measurements aquired in the directions of the VLBI observations, (2) estimating zenith wet delays and gradients from the WVR data and use these to correct the VLBI data, and (3) including the WVR measurements as additional observations in the VLBI data analysis. Furthermore, in all cases we model the WVR calibration errors in the data analysis. We test the three methods using data from the continuous VLBI campaigns CONT02–CONT14. We find clear improvements when applying methods 1 and 3 for CONT05 campaign, however, the results are degraded for the other campaigns.

1   Introduction

The atmosphere is a major error source for space geodetic techniques such as Very Long Baseline Interferometry (VLBI). The propagation delay of the atmosphere must be corrected in the data analysis in order to avoid errors in the results. This delay is commonly divided into a hydrostatic delay, which is mainly caused by the dry gases in the atmosphere, and a wet delay, which is the excess delay caused by water vapor. The hydrostatic delay can be accurately estimated from surface pressure measurements (Saastamoinen 1972; Davis et al. 1985). However, the wet delay cannot be modeled that easily with high accuracy. Thus the common way of handling the wet delay, ℓ_w, is to parametrize it as the zenith wet delay (ZWD), ℓ_w^z, and horizontal north and east,

gradients, G_n and G_e, which are then estimated in the data analysis (Nilsson et al. 2013):

$$\ell_w = m_w(\epsilon)\, \ell_w^z + m_g(a, \epsilon)\, [G_n \cos(a) + G_e \sin(a)] \quad (1)$$

where m_w and m_g are the wet and gradient mapping functions and a and ϵ denotes the azimuth and the elevation angle, respectively. This method has the disadvantage that the number of estimated parameters increase significantly, what results in increased formal uncertainties of all estimates. An alternative way is to use an external instrument to measure the wet delay. For this way to work properly, the external delays need to be very accurate, what is difficult to achieve.

One possible instrument for providing external information on the wet delay is a water vapor radiometer (WVR). There have been several studies of using WVR data in VLBI data analysis, for example Elgered et al. (1991), Kuehn et al. (1991), Emardson and Jarlemark (1999), Nothnagel et al. (2007), and Bar-Sever et al. (2007). The results of these studies are, however, inconclusive: some results indicate that using WVR data improves the VLBI estimates (e.g., station position repeatabilities), while other results indicate

T. Nilsson (✉) • M. Karbon • B. Soja • R. Heinkelmann • H. Schuh
Department 1: Geodesy and Remote Sensing, Helmholtz Centre Potsdam, GFZ German Research Centre for Geosciences, 14473 Potsdam, Germany
e-mail: nilsson@gfz-potsdam.de

that the estimates get worse. A problem is likely that the WVR observation are corrupted by, e.g. calibration errors. Furthermore, most WVR operating close to VLBI telescopes only measure at elevation angles >20° in order to avoid picking up radiation from the ground, while VLBI commonly measures at lower elevation angles. Thus the low elevation angles either have to be excluded or the WVR observations need to be extrapolated to low elevation angles, what will introduce errors. Another issue with WVR is that it does not produce reliable data during rain.

In this work we study the application of using WVR to calibrate the wet delay, and compare it to the classical approach of estimating the wet delay in the data analysis. In particular, we investigate if it is possible to find an optimum compromise of correcting for the wet delay, i.e., determining it from both VLBI and WVR data. We test whether it is possible to use the VLBI data to calibrate the WVR, i.e. the wet delay is corrected using the WVR observations and the calibration error of the WVR is estimated in the VLBI data analysis. By strongly constraining the temporal variation of the calibration error, the rapid variations in the wet delay (time scale of seconds up to 1 h) will be determined by the WVR while the variations at longer time scales will be determined by the VLBI data. Another possibility is to include the WVR observations of the wet delay as external observations in the VLBI data analysis, and estimate the ZWD and gradients as usual. The WVR observations will thus improve the precision of the determined ZWD and gradients, thus the precision of the other parameters can be expected to improve as well. Another advantage of this approach is that there will be no problems when there are no WVR observations, e.g., at low elevation angles or during rain.

2 Data Analysis

2.1 VLBI Data Analysis

In this work we analyzed data from the continuous VLBI campaigns CONT02 (observed 16–31 October, 2002, with 8 stations), CONT05 (12–27 September, 2005, 11 stations), CONT08, (12–26 August, 2008, 11 stations), CONT11 (15–29 October, 2011, 13 stations), and CONT14 (6–20 May, 2014, 17 stations). These campaigns were designed to show the current state-of-the-art of geodetic VLBI. They all were 15 days long, and the station networks were larger than for standard 24 h geodetic VLBI sessions. Interesting for our study is that several stations have been operating WVR during these campaigns, especially during CONT05.

The VLBI data were analyzed with the GFZ version of the Vienna VLBI Software (Böhm et al. 2012), VieVS@GFZ. For the modeling we basically followed the IERS 2010 Conventions (Petit and Luzum 2010), except that we also corrected for non-tidal atmospheric loading (Petrov and Boy 2004). For the parameter estimation we used the newly implemented Kalman filter module, VIE_KAL (Nilsson et al. 2015; Soja et al. 2015), analyzing each 1-day session individually. The station coordinates, radio source coordinates, and the Earth orientation parameters were estimated as constant offsets over the session, while the clock parameters, the ZWD, and the gradients were estimated as random walk processes.

2.2 WVR Data

A WVR measures the thermal radiation from the sky, i.e the sky brightness temperature, at two (or more) frequencies. Typically one frequency is close to the 22.235 GHz water vapor line, while the other is around 30 GHz. The brightness temperature is dependent on the amount of water vapor, liquid water, and oxygen in the atmosphere. Thus we can combine the brightness temperatures to infer the wet delay (Elgered 1993; Nilsson et al. 2013):

$$l_w = c_b \left[\left(\frac{f_2}{f_1} \right)^2 T_b'(f_1) - T_b'(f_2) - T_{bg,ox} \right] \qquad (2)$$

Here T_b' represent the linearized brightness temperatures, f_1 and f_2 the two frequencies, and $T_{bg,ox}$ the contribution from oxygen and the cosmic microwave background radiation. The conversion coefficient c_b and $T_{bg,ox}$ can be estimated from pressure and temperature measurements by empirical models (Jarlemark 1997). In this work we used the wet delay as provided by the stations, hence the retrieval algorithms (e.g. the models for c_b and $T_{bg,ox}$) were different for each WVR.

The availability of WVR data during the CONT campaigns is shown in Table 1. We can see that the amount of WVR data varies greatly between the campaigns. In CONT05 special efforts were made to have WVR operated

Table 1 Availability of WVR data for the various CONT campaigns

| Station | CONT | | | | |
	02	05	08	11	14
ONSALA60	V	V	SM	SM	SM
WETTZELL	SM	SM	SM	–	–
TSUKUB32	–	Z	Z	Z	–
KOKEE	SM	SM	–	–	–
ALGOPARK	–	Z	–	–	–
HARTRAO	–	SM	–	–	–

The letters in the tables indicate the observing mode used by the WVR: following the VLBI schedule (V), sky-mapping mode (SM), and zenith only observations (Z)

at the VLBI stations. Thus there are six stations with WVR. In later campaigns no such effort was made, thus there are only WVR data from the stations regularly operating a WVR, like ONSALA60. The operational mode of the WVR also varied. In CONT02 and CONT05, the WVR at the ONSALA60 station was following the VLBI schedule whenever possible (i.e., for observations at elevation angles above 18°), plus occasionally additional observations for the tip-curve calibration. The most common mode used was, however, the so-called sky-mapping mode. This means that the WVR operates in a repeated cycle of, e.g., 60 observations spread uniformly across the sky. Furthermore, the WVR at TSUKUB32 and ALGOPARK only made observations in the zenith direction. The observing mode of course puts limits on how the WVR data can be used to calibrate the VLBI data. In this work we tested the following three methods:

1. Direct Calibration In this method the wet delays are fixed to those measured by the WVR. This is the most direct method of applying WVR calibration to the VLBI data, however it requires that the WVR always measures in the same direction as the VLBI telescope. As discussed above, such data are only available at the ONSALA60 station during the CONT02 and CONT05 campaigns. Thus this method could only be tested for this station during these campaigns. For all other stations, no WVR calibration was applied and the wet delays were estimated by ZWD and gradients as usual. The VLBI observations of ONSALA60 which had no corresponding useful WVR observation (e.g., due to low elevation angle or rain) were excluded from the data analysis when applying this method.

2. WVR ZWD and Gradients In the cases when a WVR was operated in sky-mapping mode, we could try to estimate the wet delays of the VLBI observations by interpolate/extrapolate the WVR measurements to the directions and time epochs of the VLBI observations. One way to do this is to estimate ZWD and gradients from the WVR data, then use these parameters to calculate the wet delays of the VLBI observations. We did the estimation of the tropospheric parameters with a Kalman filter, using the same stochastic modeling as in the VLBI data analysis. The Kalman filter estimates the ZWD and gradients from WVR at the time epochs of the WVR measurements; these were then interpolated to the epochs of the VLBI observations. However, to avoid large errors due to interpolation for time periods with no WVR measurements (e.g. during rain), we only performed interpolation when there was at least one WVR measurement within 5 min before or after the VLBI observation. The other VLBI observations were excluded from the data analysis. For WVR only measuring in the zenith direction, estimation of gradients is, however, impossible.

For these stations, only the ZWD were estimated from the WVR data, and the ZWD were then fixed to these values in the VLBI data analysis while gradients were still estimated.

3. WVR Data as Additional Observations The third method is to keep the estimation of ZWD and gradients for all stations, and simply include the WVR measurements as additional observations of the wet delay.

WVR Calibration Errors As noted in the introduction an issue is that the WVR data are not error free, e.g., there could be calibration errors. For example, there could be errors in the empirical models used for calculating c_b and $T_{bg,ox}$ (Eq. (2)). If $T_{bg,ox}$ is wrong, it will introduce an error in the wet delay approximately proportional to the amount of air-masses observed, while an error in c_b will cause an error proportional to the wet delay. Thus, since the WVR do not observe at low elevation angles, we can as a first order approximation assume that the errors in c_b and $T_{bg,ox}$ both causes errors in the wet delays proportional to $1/\sin(\epsilon)$, where ϵ is the elevation angle. Furthermore, when using a WVR (or another method) to measure the wet delay instead of estimating it in the VLBI data analysis, it is more important that the pressure measurements used to calculate the hydrostatic delay are correct. When a ZWD is estimated, the hydrostatic delay error caused by a pressure offset will mostly affect the ZWD, hence the effect on the other parameters is relatively limited. This is not the case when no ZWD is estimated. All the three mentioned error sources can to some extent, for all three methods, be taken into account by estimating a term for each WVR proportional to $1/\sin(\epsilon)$ in the VLBI data analysis. In this work, we modeled these terms as random walk processes with low process noise, in order to allow for some long-term variations but not short-term ones.

We made solutions both with and without the estimation of the calibration error. However, since the solutions, for which no calibration error was estimated, were clearly worse than those with this error estimated, we only show the results from the solutions with estimation of the calibration error.

3   Results

3.1   Direct Calibration

As already noted, due to the availability of suitable data we only applied this method to the ONSALA60 station and in the CONT02 and CONT05 campaigns. As an example, the baseline repeatabilities for the CONT05 period is shown in Fig. 1. Plotted are the standard solution as well as the solution with WVR calibration. Because the VLBI observations at

ONSALA60 without corresponding WVR observations were excluded when applying WVR calibration, we also show a synchronized solution: a standard solution but with these observations also excluded. This provides a standard solution containing the same VLBI data as in the solution with WVR calibration, what is good for comparison and for assessment of how much the quality is degraded by excluding these observations.

We can note from Fig. 1 that the best repeatabilities are obtained when applying the WVR calibration, followed by the standard solution and the synchronized solution. This shows that the WVR data was able to improve the VLBI results in this case. The mean improvement in terms of mean repeatability and number of baselines with improved repeatbility in CONT02 and CONT05 is shown in Table 2. We can note that, whereas these parameters are improved by the WVR calibration in CONT05 there is a degradation observed in CONT02, as less then 50% of the baselines improved (i.e. more than 50% got worse). Part of this degradation can be explained by the fact that some

observations are excluded in the WVR calibrated solution. However there is still some degradation (i.e. less than 50% of baselines improved) seen relative to the synchronized solution. A reason could be that there are errors in the WVR data which are not corrected by the estimated calibration term.

3.2 WVR ZWD and Gradients

Figure 2 shows the baseline length repeatabilities for CONT05 when applying the second method for WVR calibration, i.e. using ZWD and gradients calculated from the WVR data. Also here two standard solutions are shown as references, one with all data and one synchronized solution where observations from time periods with no WVR data were excluded. We can see that in this case the repeatabilities get significantly worse when using WVR calibration. The main reason is that the gradients were estimated from WVR. If only the ZWD from the WVR are used and gradients are estimated in the VLBI analysis, we obtain similar repeatabilities as in the standard VLBI analysis. Since the WVR uses an elevation cut-off angle of 20°, and the effect of gradients on the wet delay is largest at low elevation angles, the accuracy of the WVR gradients may not be good enough. Furthermore, it should be noted that the gradients are only a first order approximation of the horizontal variations. Thus gradients from WVR might not be consistent with gradients determined with a 5° cut-off elevation angle (what is used by VLBI).

Fig. 1 Baseline length repeatabilities for the CONT05 campaign. Shown are the results when applying direct WVR calibration (method 1) as well as two standard VLBI solutions, one using all data (Standard) and one using the same data as in the WVR calibrated solution (Sync.). Shown are also the differences between the WVR calibrated solution and the standard solutions

Table 2 Mean difference in baseline length repeatability between the solution applying direct WVR calibration (method 1) and the standard/synchronized VLBI solution (Mean), and the percentage of baselines which have a reduced repeatability when applying the WVR calibration (Imp. BL)

	WVR-Standard		WVR-Sync.	
	Mean (mm)	Imp. BL (%)	Mean (mm)	Imp. BL (%)
CONT02	1.1	29	0.5	46
CONT05	−1.0	85	−1.1	91

Fig. 2 Baseline length repeatabilities for the CONT05 campaign. Shown are the results when using ZWD and gradient to calibrate the wet delay (method 2) as well as two standard VLBI solutions, one using all data (Standard) and one using the same data as in the WVR calibrate solution (Sync.). Shown are also the differences between the WVR calibrated solution and the standard solutions

3.3 WVR Data as Additional Observations

The baseline length repeatabilities obtained for the CONT05 and CONT08 campaigns when using the WVR measurements as additional observations in the VLBI data analysis are shown in Fig. 3. In Table 3 the statistics of the mean improvement in the repeatability and the percentage of baselines with improved repeatability are shown. We can note a clear improvement relative to the standard solution for CONT05, while the results generally get worse for the other CONT campaigns. One reason could be that the WVR data quality for some reason is better in CONT05 than in other CONT campaigns. Furthermore, a reason for the worse results for later CONT campaigns could be that the VLBI

Table 3 Mean difference in baseline length repeatability between the solution including the WVR data as additional observations (method 3) and the standard VLBI solution (Mean), and the percentage of baselines where the repeatability is lower when applying the WVR calibration (Imp. BL)

	WVR-Standard	
	Mean (mm)	Imp. BL (%)
CONT02	0.9	39
CONT05	−1.8	75
CONT08	0.6	18
CONT11	0.4	36
CONT14	0.4	20

data from these campaigns are of higher quality, thus the standard approach is working better.

Another issue could be the relative weighting of the WVR and VLBI data. In this work we used the formal errors reported in the respective data files, however, this may not be optimal. We have made tests where we additionally down-weighted the WVR data, and this improved the results in most cases. In the future we will continue these investigations and try to find the optimum weighting factors for the WVR data.

4 Conclusions

The baseline length repeatabilities are improved for CONT05 when applying WVR calibration (method 1 and 3), however, no improvement can be seen for the other campaigns. This indicates that there is some potential to use WVR data to calibrate the wet delay. However more investigations are needed to properly understand and correct the errors in the WVR data.

One issue could be that the modeling applied for the WVR calibration error is not accurate enough. There could be errors present which are not proportional to $1/\sin(\epsilon)$, e.g. an error in the gain calibration would give an error which is almost independent of the elevation angle. In the future we will extend the model for the WVR error to see if the results improves.

Another issue could be the hydrostatic delay gradients. What is sensed by VLBI are the total gradients, i.e., the sum of the wet and hydrostatic ones, while WVR is only sensitive to the wet gradients. Thus, when we apply WVR calibration we assumed that the hydrostatic gradients were zero. This is not necessarily true, although the wet gradients are typically larger and more variable than the hydrostatic ones, the hydrostatic gradients are not negligible. In the future we will study the possibility to use hydrostatic gradients calculated from numerical weather models.

Fig. 3 Baseline length repeatabilities for the CONT05 (*top*) and CONT08 (*bottom*) campaigns. Shown are the results when including the WVR data as additional observations in the VLBI data analysis (method 3) and the standard VLBI solution. Shown are also the differences between them

References

Bar-Sever YE, Jacobs CS, Keihm S, Lanyi GE, Naudet CJ, Rosenberger HW, Runge TF, Tanner AB, Vigue-Rodi Y (2007) Atmospheric media calibration for the deep space network. Proc IEEE 95(11):2180–2192. doi:10.1109/JPROC.2007.905181

Böhm J, Böhm S, Nilsson T, Pany A, Plank L, Spicakova H, Teke K, Schuh H (2012) The new Vienna VLBI software. In: Kenyon S, Pacino MC, Marti U (eds) IAG scientific assembly 2009. International Association of Geodesy symposia, no. 136. Springer, Buenos Aires, pp 1007–1011. doi:10.1007/978-3-642-20338-1_126

Davis JL, Herring TA, Shapiro II, Rogers AEE, Elgered G (1985) Geodesy by radio interferometry: Effects of atmospheric modeling errors on estimates of baseline length. Radio Sci 20(6):1593–1607

Elgered G (1993) Tropospheric radio-path delay from ground based microwave radiometry. In: Janssen M (ed) Atmospheric remote sensing by microwave radiometry, chap 5. Wiley, New York

Elgered G, Davis JL, Herring TA, Shapiro II (1991) Geodesy by radio interferometry: Water vapor radiometry for estimation of the wet delay. J Geophys Res 95(B4):6541–6555. doi:10.1029/90JB00834

Emardson TR, Jarlemark POJ (1999) Atmospheric modelling in GPS analysis and its effect on the estimated geodetic parameters. J Geodesy 73:322–331

Jarlemark POJ (1997) Analysis of temporal and spatial variations in atmospheric water vapor using microwave radiometry. Ph.D. Thesis, Technical Report 308, School Electrical Computer Engineering, Chalmers University of Technology, Göteborg, Sweden

Kuehn CE, Himwich WE, Clark TA, Ma C (1991) An evaluation of water vapor radiometer data for calibration of the wet path delay in very long baseline interferometry experiments. Radio Sci 26(6):1381–1391. doi:10.1029/91RS02020

Nilsson T, Böhm J, Wijaya DD, Tresch A, Nafisi V, Schuh H (2013) Path delays in the neutral atmosphere. In: Böhm J, Schuh H (eds) Atmospheric effects in space geodesy. Springer, Heidelberg, pp 73–136. doi:10.1007/978-3-642-36932-2_3

Nilsson T, Soja B, Karbon M, Heinkelmann R, Schuh H (2015) Application of Kalman filtering in VLBI data analysis. Earth Planets Space 67(136):1–9. doi:10.1186/s40623-015-0307-y

Nothnagel A, Cho J, Roy A, Haas R (2007) WVR calibration applied to European VLBI observing sessions. In: Tregoning P, Rizos C (eds) Dynamic planet, IAG scientific assembly 2005. International Association of Geodesy symposia no. 130. Springer, Cairns, pp 152–157. doi:10.1007/978-3-540-49350-1_24

Petit G, Luzum B (eds) (2010) IERS Conventions (2010). IERS Technical Note 36, Verlag des Bundesamts für Kartographie und Geodäsie, Frankfurt am Main, Germany

Petrov L, Boy JP (2004) Study of the atmospheric pressure loading signal in VLBI observations. J Geophys Res 109:B03405, doi:10.1029/2003JB002500

Saastamoinen J (1972) Atmospheric correction for the troposphere and stratosphere in radio ranging of satellites. In: Henriksen SW, et al. (eds) The use of artificial satellites for geodesy, vol 15. AGU, Washington, D.C., pp 247–251

Schuh H, Behrend D (2012) VLBI: A fascinating technique for geodesy and astrometry. J Geodyn 61:68–80. doi:10.1016/j.jog.2012.07.007

Soja B, Nilsson T, Karbon M, Zus F, Dick G, Deng Z, Wickert J, Heinkelmann R, Schuh H (2015) Tropospheric delay determination by Kalman filtering VLBI data. Earth Planets Space 67(144):1–16. doi:10.1186/s40623-015-0293-0

Land Subsidence Detected by Persistent Scatterer Interferometry Using ALOS/PALSAR Data from the Nakagawa Lowland in the Central Kanto Plain, Japan

Shoichi Hachinohe and Yu Morishita

Abstract

The Nakagawa lowland is located in the central part of the Kanto Plain; the largest plain in Japan. During the 1960s, major land subsidence occurred, exceeding 10 cm/year, as a result of over pumping of shallow and deep groundwaters in this area. In recent times, following the regulation of pumping by national and local governments, the amount of land subsidence in this area has decreased sharply. However, in the Nakagawa lowland, subsidence exceeding 1 cm/year is still ongoing in some areas, and is more pronounced during dry years in which the amount of groundwater use increases. In this study, we examined the local characteristics of land subsidence through persistent scatterer interferometry using ALOS/PALSAR data obtained from April 2006 to April 2011. On the basis of this analysis, we confirmed that subsidence was concentrated along the western margin of an incised buried valley, in which average displacement rates exceed 10 mm/year. The characteristics of this subsidence zone are suggestive of a geological structure that is buried beneath the alluvial plains, which is affected by groundwater pumping that targets the basal gravel layers of buried valley-fills. In addition, we detected a patched zone of around 0.3 km^2 in the study area, in which average displacement rates exceed 15 mm/year. We estimated that this zone was formed by consolidation settlement of soft ground as a result of residential landfill.

1 Introduction

In the fifth assessment report of the intergovernmental panel on climate change [IPCC 2013], the generation of extreme weather was predicted to accompany ongoing global warming. In the Kanto district of Japan, which contains around 30% of the country's population, it has also been proposed that climate change will not only generate an unexpected scale of torrential rainfall, but also extensive water shortages as a result of specific dry weather conditions that are now more frequent [Japan Meteorological Agency 2013]. When an extensive water shortage occurs, the water supplied by rivers is substantially decreased, and so the amount of extracted groundwater increases. Various studies have shown a spatial and temporal correlation between water pumping and land subsidence [*e.g.* Constan et al. 2016; Ishitsuka et al. 2014; Ferretti et al. 2000]. During previous decades, whenever water shortages have occurred in the Kanto district, the land subsidence area has experienced broad expansion [Morita 2015]. Thus, it may be expected that, if large-scale water shortages occur again in the

S. Hachinohe (✉)
Research Institute, Center for Environmental Science in Saitama, Kazo, Saitama, Japan
e-mail: hachinohe.shoichi@pref.saitama.lg.jp

Y. Morishita
Geospatial Information Authority of Japan, Tsukuba, Ibaraki, Japan

Fig. 1 Location of the study area and Saitama prefecture on a topography map of Kanto district
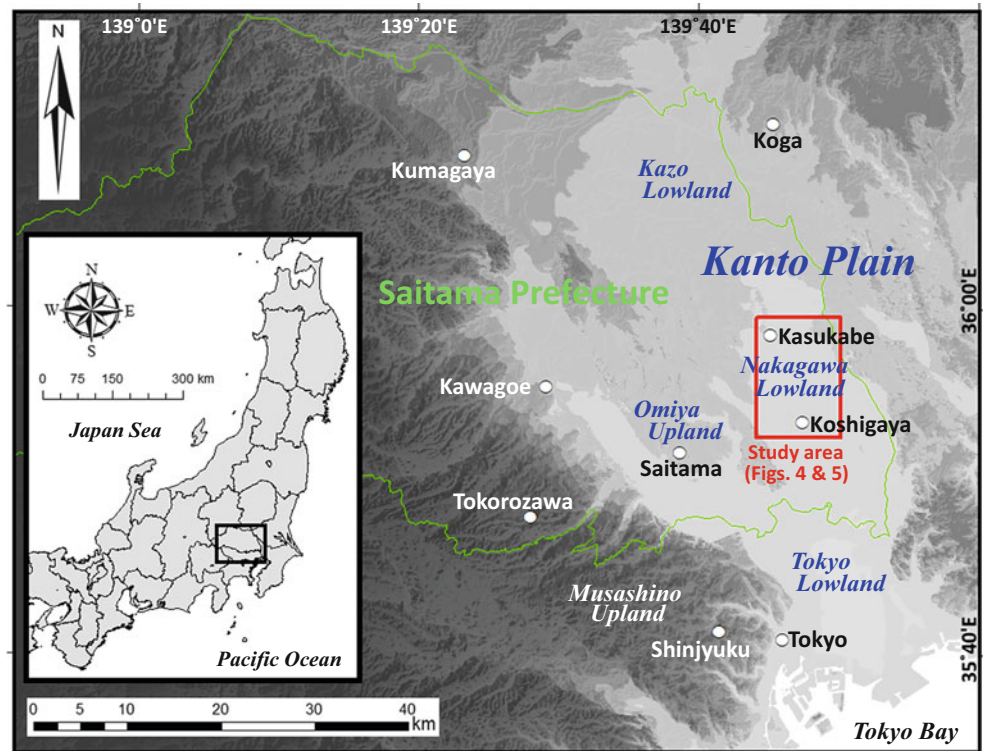
near future, a similar amount, or even larger scale of land subsidence may be seen in this area.

In recent years, analyses of land surface displacements through remote sensing using data from satellites and aircraft have made significant contributions to various fields, including the earth sciences [*e.g.* Bekaert et al 2015; Hooper et al 2012; Zebker et al. 1994] and disaster prevention [*e.g.* Ozawa and Fujita 2013]. In particular, as a result of the improvements in quantities and qualities of data obtained by Synthetic Aperture Radar (SAR) and the establishment of correction methods various types of errors, scientists have been able to precisely detect the movement of land surface. In this research, in order to evaluate the local characteristics of land subsidence in the Nakagawa lowland (Fig. 1), in which the likelihood of land subsidence is high during water shortages in the near future, we perform and examine persistent scatterer interferometry (PSI) using ALOS PALSAR (L-band) SAR data acquired by JAXA.

2 Study Area

Land subsidence became a major problem in almost all the alluvial plains in Japan after World War II, due to an increase in the amount of groundwater extraction that occurred in line with the economic recovery. The Tokyo bayside region has experienced the most significant land subsidence over the past 80 years, with the total subsidence having exceeded 4 m by 1970 [Endo 2009]. In the Kanto plain (Fig. 1), various types of pumping regulations have been imposed by national and local governments since the 1950s. Under these restrictions, groundwater levels in this area recovered dramatically from the end of the 1960s to the early 1970s, while land subsidence rates also improved [Hachinohe et al. 2014]. However, the areas in which the land subsidence was concentrated shifted from Tokyo city center to suburban areas, including the Kazo lowland, the Musashino upland [Hayashi 2004]. Therefore, it appears that these phenomena have been produced by the movement of concentrated groundwater use from the southern part of the Kanto plain to the surrounding satellite cities, as a result of the expansion of urbanization.

Figure 2a shows the distribution of annual land subsidence in Saitama prefecture, north of Tokyo, in 1975, as shown by leveling measurements. As shown in this figure, we can confirm that land subsidence is concentrated in the Kazo lowland, the Musashino upland, the Nakagawa lowland and the Omiya upland (Figs. 1 and 2). Although the subsidence trends become less pronounced over time, as shown in Fig. 2b, c, subsidence in the Kazo lowland and the Nakagawa lowland is still ongoing. The land subsidence in the Nakagawa lowland has been detected through SAR observations by Tobita et al. 2005 and Deguchi et al. 2009. Tobita et al. 2005 measured a maximum vertical subsidence

Fig. 2 Changes in land subsidence areas and annual subsidence in Saitama prefecture, north of Tokyo, Japan [from Hachinohe et al. 2014]
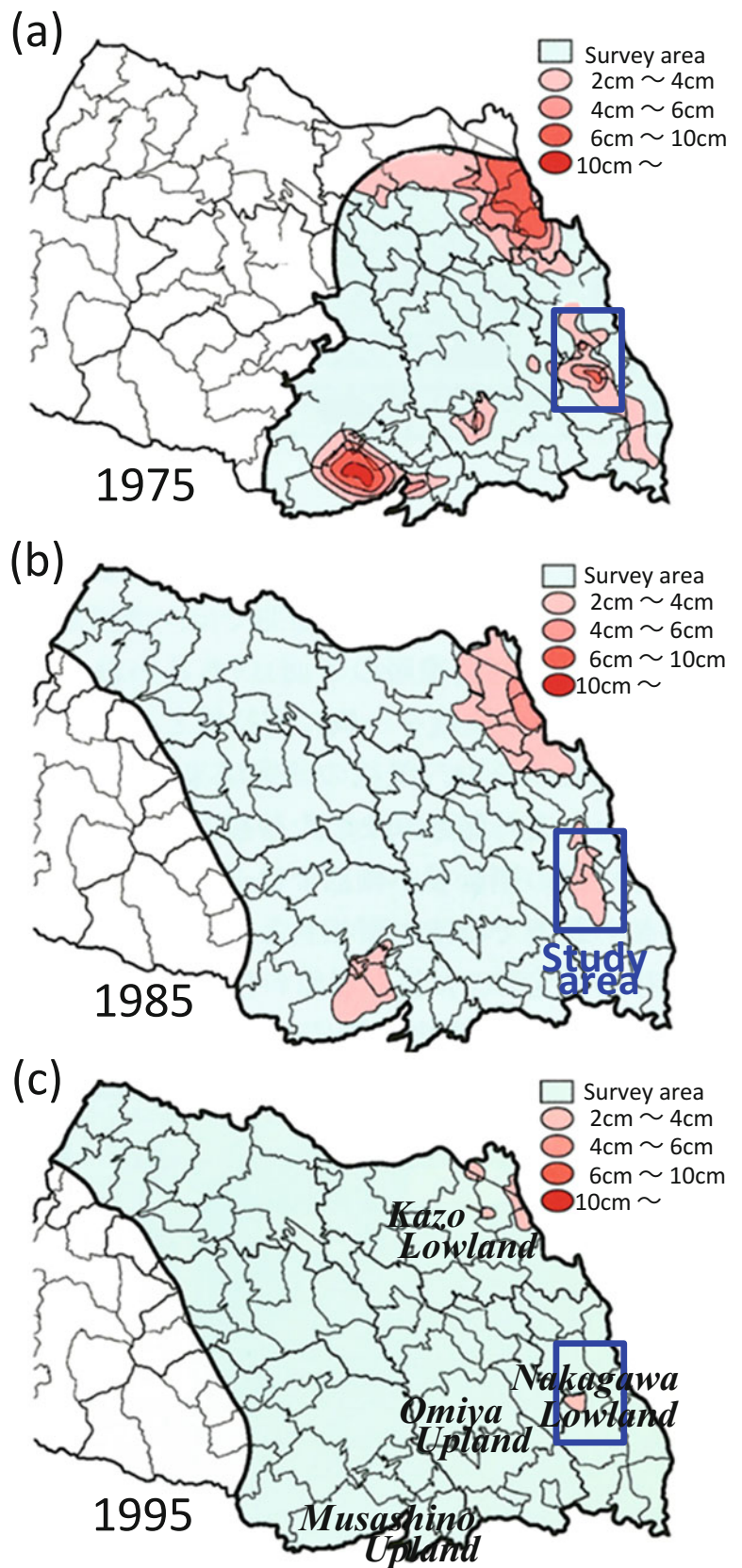
of around 4 cm over about 3 years from January 1995 to March 1998, using JERS-1 and GPS positioning data. Deguchi et al. 2009 measured a maximum line-of-sight (LOS) displacement of around 5 cm over five and a half years from January 2003 to June 2008 using ENVISAT data.

3   SAR Methodology

The Japan Aerospace Exploration Agency (JAXA) launched their Advanced Land Observing Satellite (ALOS) in 2006, and observational data were obtained up until 2011. In this study, we carried out persistent scatterer interferometry (PSI) by DORIS [Kampes et al. 2003] and StaMPS/MTI [Hooper et al. 2012] within the Nakagawa lowland using SAR data from ALOS. The PSI method is an analytical technique that allows the calculation of rates of displacement of a target on the land surface through the extraction of points that have stable phase characteristics over time (PS), such as roads and buildings. As an external digital elevation model (DEM), we used Base map information with an interval of 10 m which is constructed and distributed in free by Geospatial Information Authority of Japan (GSI) (http://fgd.gsi.go.jp/download/menu.php). SAR can detect only one-dimensional displacements between the satellite and a target on the land surface in the direction of the LOS. However, in satellite-based SAR observations, it is possible to observe the same location on the Earth's surface from the two directions of the ascending and the descending orbits. We can calculate quasi-vertical and quasi-east–west components of a displacement rate on a plane determined by ascending and descending LOS vectors from the two LOS displacement rates (Fig. 3) [Fujiwara et al. 2000; Kobayashi et al. 2015; Huang et al. 2016]. For this study area, ALOS/PALSAR data exist on paths 405 and 406 of the ascending orbit and path 58 of the descending orbit, with the data sets of each path comprising 24, 22 and 23 images, respectively (Table 1). We first calculated average displacement rates in the LOS direction using the data sets from these three paths, for 4 years from 2007 to 2010. A huge number of PS points were detected in this area, and so we thinned out the data at 200 m-intervals before analysis [*e.g.* Fujiwara et al. 2000]. Tropospheric noise reduction using a numerical weather model provided by Japan Meteorological Agency (JMA) was applied [Kobayashi et al. 2014]. In order to reduce the influences of any orbital errors, a correction to flatten the phase inclination of the entire study area was applied. The average of the phases in the area where no displacement is seen (shown in Fig. 4) is set to zero as a reference.
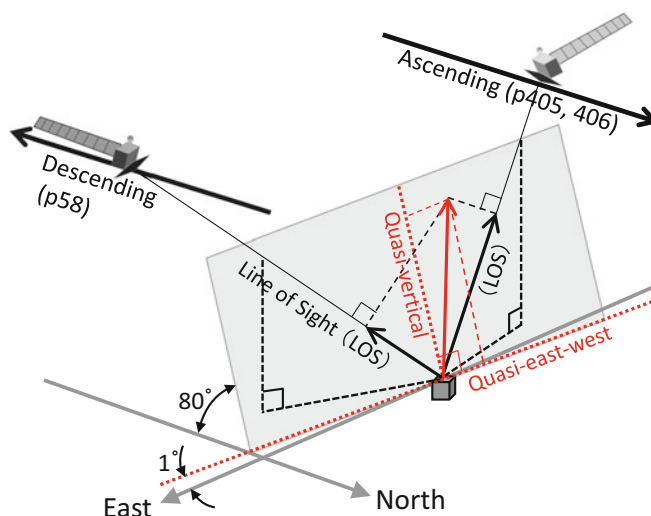
Fig. 3 Schematic diagram of quasi-vertical displacement analysis. The red arrow indicates a displacement vector obtained from and explaining two (ascending and descending) LOS displacements on a plane determined by the two LOS directions. The reason why not "pure" but "quasi-" vertical and east–west components are obtained is that the plane is slightly tilting to the south and horizontally rotating

Table 1 ALOS/PALSAR datasets used for PSI analysis in this study

Path	Row	Orbit	Data set number	Offnadir angle
405	700–710	Ascending	24	34.3°
406	700–710	Ascending	22	34.3°
58	2890–2990	Descending	23	34.3°

4   Results and Discussion

Figure 4 shows the distribution map of quasi-vertical displacement rates (V_v, Fig. 3) from paths 405 and 58. The quasi-vertical displacement rates represent the true vertical ones because no large north–south displacement seems to exist in this area. This figure shows those areas are undergoing strong subsidence (colored in blue and light blue) as well as those areas that are more stable (colored in orange and red). The spatial distribution of the strongly subsiding area was approximately consistent with the results obtained from ENVISAT data by Deguchi et al. 2009. Figure 5a, b shows results overlain on (a) a geomorphological map and on (b) the topographic map of the valley-fill base [Komatsubara et al. 2014] of this area, respectively. As shown in Fig. 5a, almost all the subsidence points, which are indicated by blue and light blue squares, are located within the backmarsh area. In contrast, we confirm that the stable points, indicated by red and orange squares, are distributed across the natural levees (hatched with dotted symbols) and in some parts of

Fig. 4 Average rates of quasi-vertical displacement (V_v) and a reference point (35.920N, 139.773E) in the study area
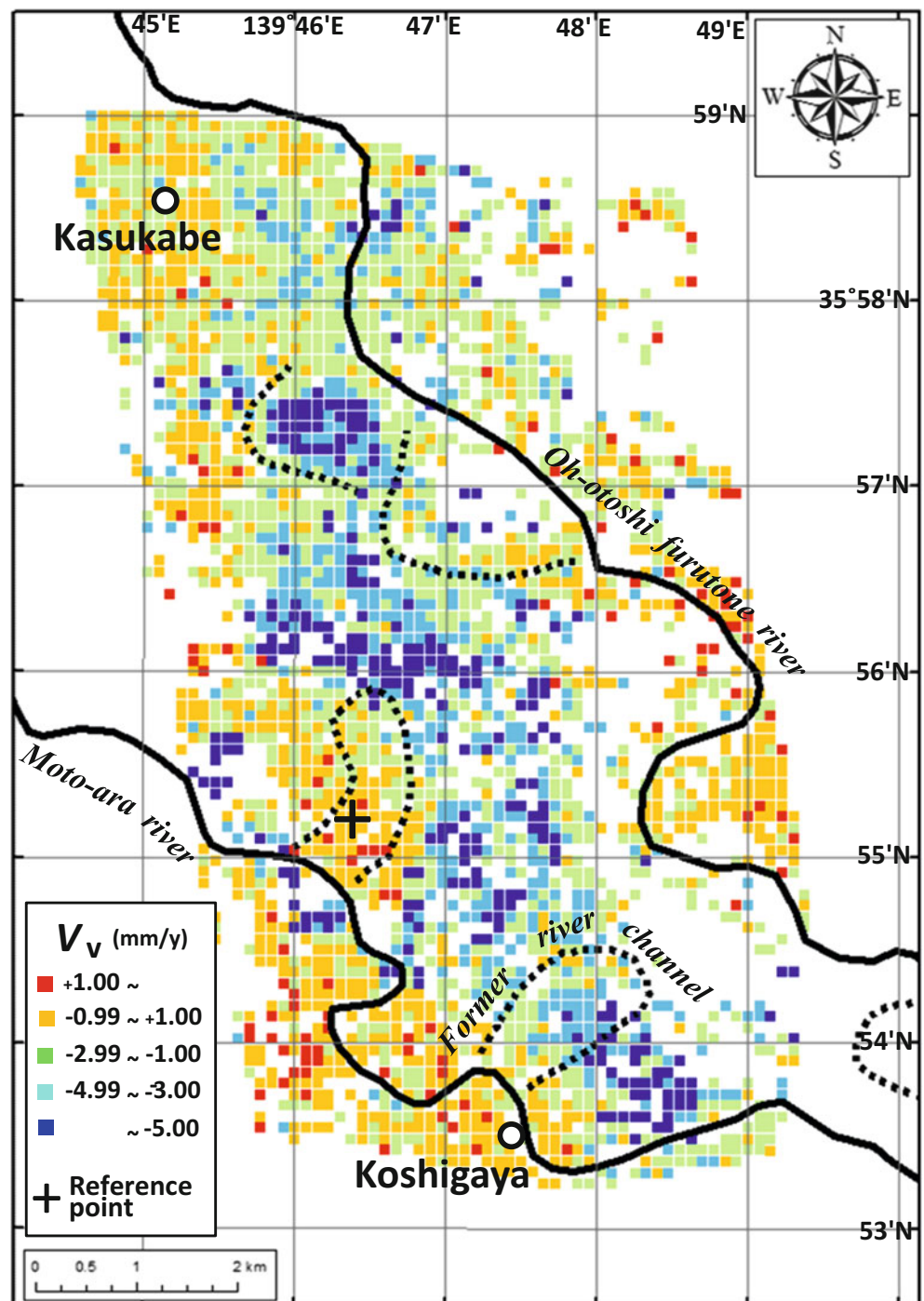
the backmarsh (hatched with horizontal thin lines), indicated as zones A, B, C and D. On the basis of Fig. 5b, we confirm that zones A-D are located above the buried terraces which are distributed around −20 m in elevation. Further,

it can be seen that the subsidence areas, whose average displacement rates exceed 10 mm/year, are distributed along the western margin of the buried valley bottom, as well as in the backmarsh area near the surface. It should be noted
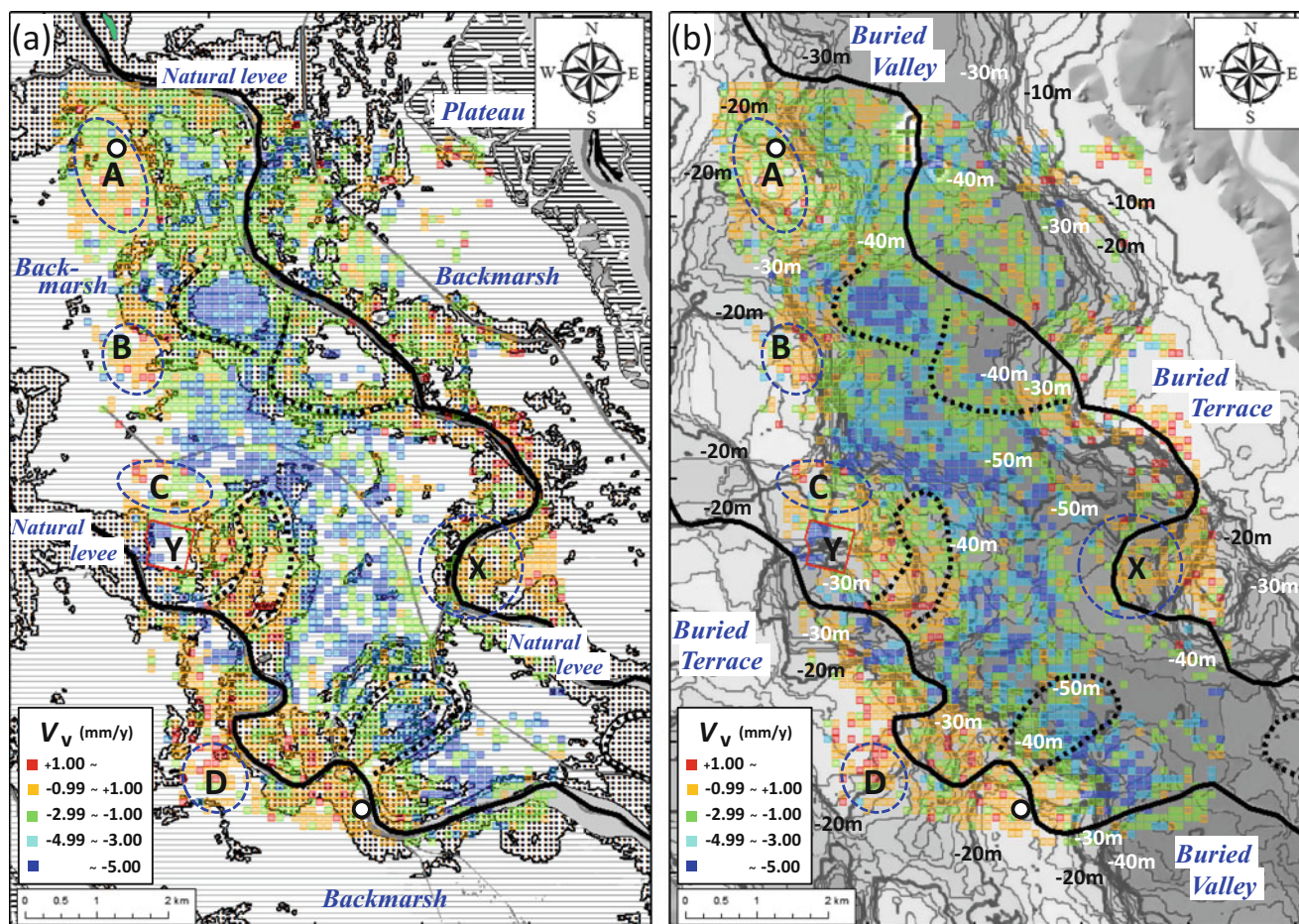
Fig. 5 Average rates of quasi-vertical displacement (V_v) on (**a**) a geomorphological map, and (**b**) a topographic map of the valley-fill base [Komatsubara, 2014] in the study area. The base map was made base on the land condition map "Noda" and "Omiya" (GSI)

Table 2 Sedimentary system and lithofacies of the latest Pleistocene to Holocene incised-valley fills under the central part of Nakagawa lowland [from Nakanishi et al. 2011]

Depositional system	Sedimentary facies	Lithofacies	Elevation (m)	
			Min.	Max.
Delta	Modern river floodplain	Mud	+5	−30
	Modern river channel	Sand		
	Salt marsh and shallow marine	*Mud*		
Estuary	*Tidal influenced shallow marine*	*Mud*	−25	−35
	Tidal flat	*Mud*		
Meandering river	*Meandering river floodplain*	*Mud*	−30	−40
	Meandering river channel	Sand		
Braided river	Braided river channel	Gravel	−35	−45

that some areas inside the buried valley are stable, such as zone X, but almost all of these areas are located on natural levees according to the land classification shown in Fig. 5a. The incised-valley fills under the Nakagawa lowland were formed during the last glacial age [Kimura et al. 2006; Tanabe et al. 2008]. The alluvial sediments are classified into

the following seven facies in ascending order: Braided river channel fills; meandering river floodplain sediments; tidal flat sediments; tide-influenced transgressive shallow marine sediments; upward-shallowing marine sediments; salt marsh sediments; and modern river channel fill and floodplain sediments (Table 2) [Nakanishi et al. 2011]. The braided

Fig. 6 Average rates of LOS displacement (V_{LOS}) given by PSI analysis in the area surrounding the strongest subsidence zone (zone Y). (PSI data: P406/R700-710)
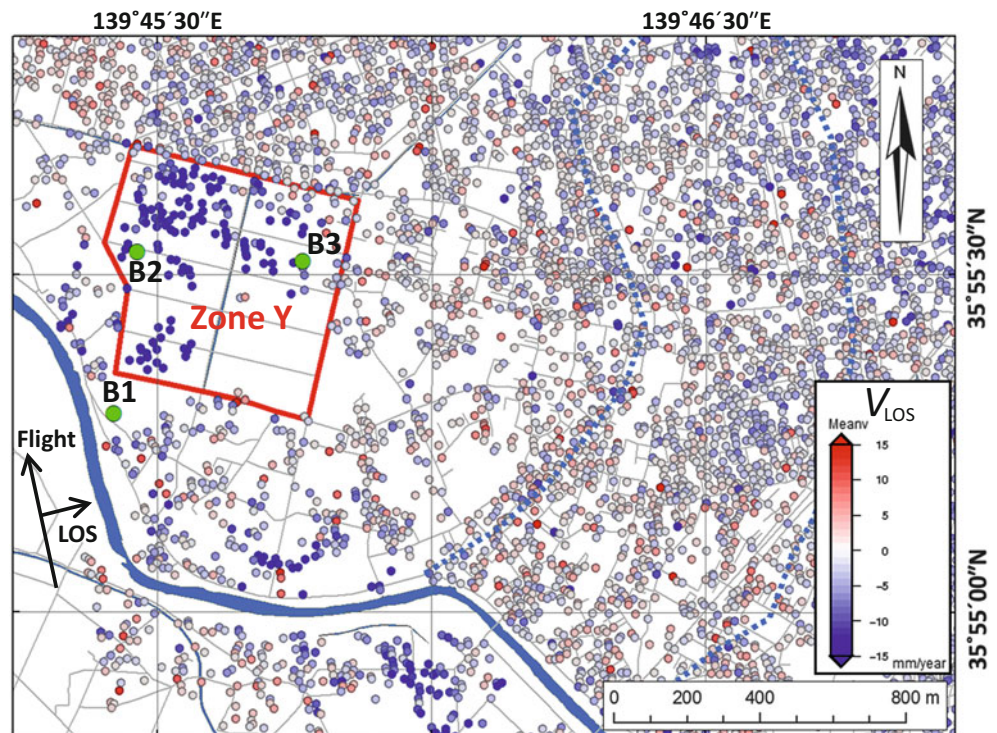
river channel fills consist of gravels that are 2–3 cm in diameter, which form the basis of a good aquifer in this area. The meandering river floodplain sediments lie just above the aquifer, and consist of silt with plant fragments and fine sand. Thus, it suggests that withdrawal of groundwater from the gravel layer which is distributed around −40 m in elevation triggered downward motion of the mud layers right above the gravel layer.

In addition, we detected strong subsidence with an average displacement rate exceeding 15 mm/year above the buried terraces in the western margin of the study area, shown by zone Y in Figs. 5 and 6. Figure 6 shows the PSI analysis results from path406, between August 2006 and April 2011. It is clear that the zone Y shows a remarkable subsidence tendency compared with the surrounding area. Figure 7 illustrates drill logs with N-values provided by the standard penetration test (SPT N-values) in zone Y. In Fig. 6, the average rate of LOS displacement at the B3 site is larger than that at the B1 site. However, the thickness of the unconsolidated silt layer at the B3 site is thinner than at the B1 site. Therefore, we estimate that the most

significant subsidence occurred in the layer shallower than 15 m beneath the ground surface in this area. Figure 8a, b illustrates temporal changes in land use within zone Y. Figure 8a shows the land use situation 11 years before the SAR data acquisition. From this figure, we can confirm that paddy fields were distributed across the entire area of zone Y. Thus, on the basis of Figs. 7 and 8a, it is clear that an unconsolidated silt layer is distributed thickly beneath the surface in this area, and that the groundwater level exists a depth of around 1 m. Figure 8b shows the land use distribution 4 years before the SAR data acquisition. This shows that the construction of urban developments had begun and that a regulating reservoir had been built to the south. Generally, when construction takes place on soft ground, civil engineers preempt any land subsidence by preloading the ground and pumping up the groundwater. In this study area, it is supposed that preconsolidation of the shallow ground was carried out by the preloading of landfills and the drainage of shallow groundwater by the regulating reservoir. Hence, it is assumed that the strongest subsidence detected by the PSI analysis in zone Y is a phenomenon related to

Fig. 7 Drill logs with SPT N-values around zone Y. GL: elevation of ground surface, GW: elevation of groundwater
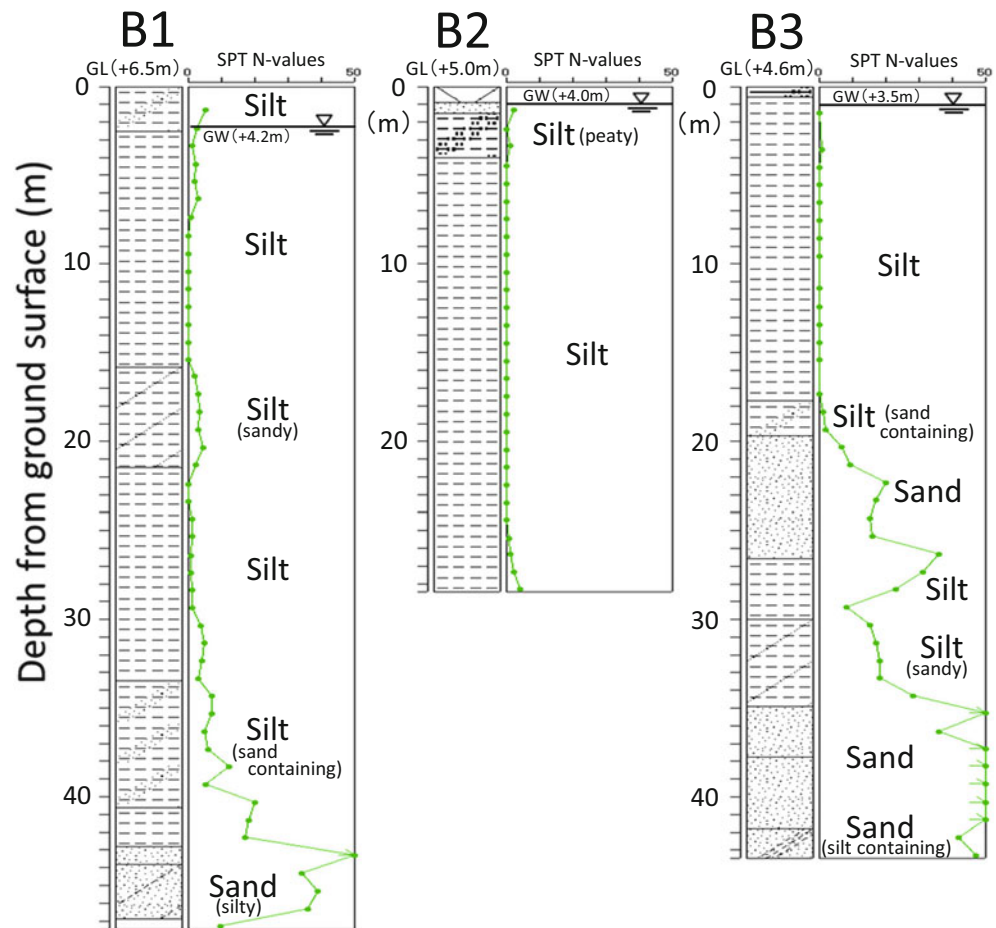
the final stage of preconsolidation during construction upon reclaimed land.

5 Conclusions

In the Kanto Plain, subsidence areas, with average displacement rates exceeding 10 mm/year, are distributed along the western margin of a buried valley bottom (from −40 m to −50 m in elevation) and on the backmarsh near the surface. These subsidence zones are believed to be caused by the presence of a geological structure of valley fills beneath the alluvial plain and by groundwater pumping that targets the basal gravel layer at the bottom of the valley fills. Average displacement rates exceeding 15 mm/year were detected in a patchy zone (zone Y: Approximately 0.3 km^2), and likely occurred as a result of consolidation settlement on soft ground following preloading by residential landfill.

Fig. 8 Land use situation in 1995 to 2002 at zone Y (Aerial photos: (**a**) Saitama Pref. 1995-A-33B-54, (**b**) Saitama Pref. 2002)
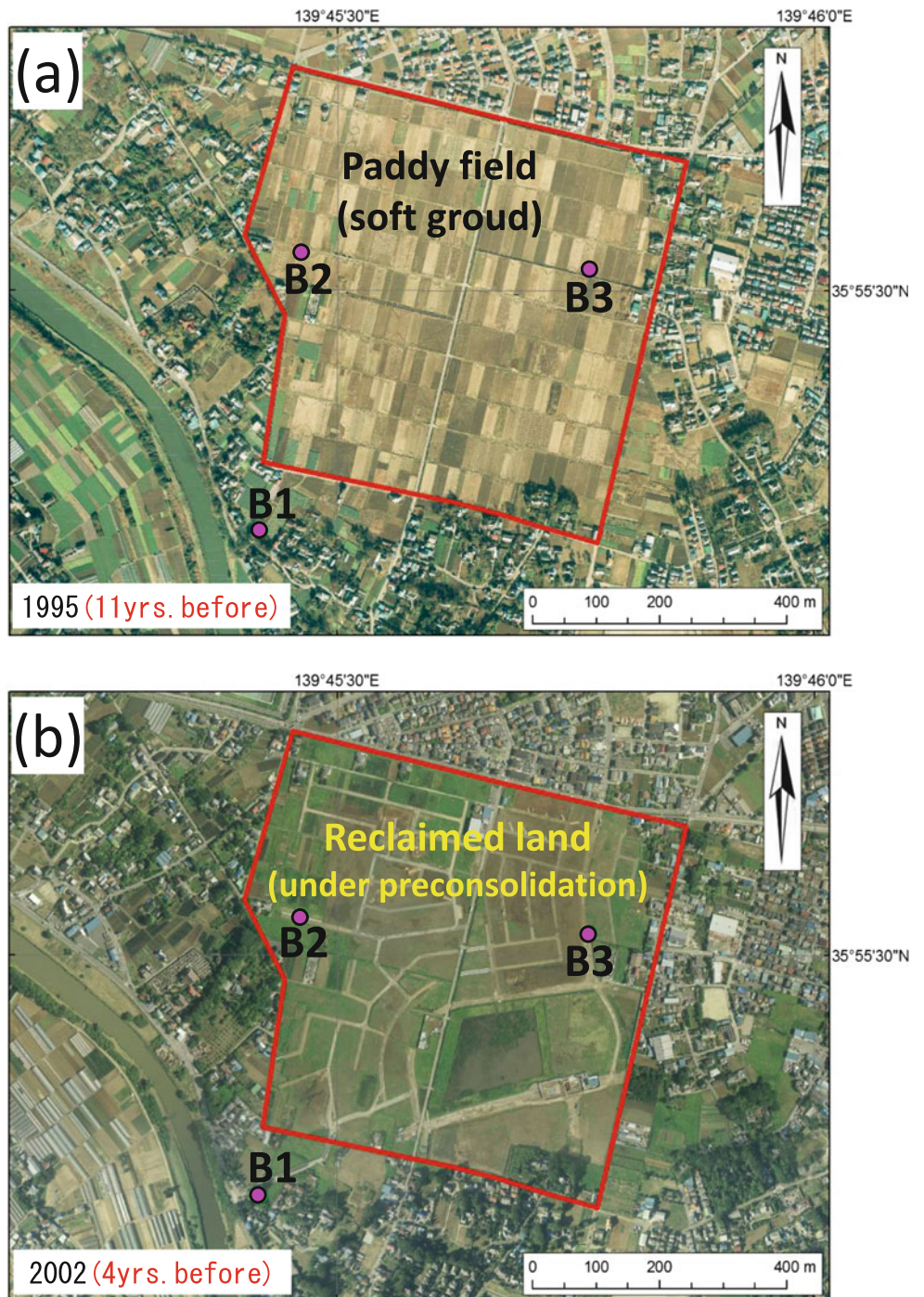
References

Bekaert DPS, Hooper A, Wright TJ (2015) Reassesing the 2006 Guerrero slow-slip event, Mexico: implications for large earthquakes in the Guerrero Gap. J Geophys Res Solid Earth 120:1357–1375. doi:10.1002/2014JB011557

Constan A, Armenteros AM, Fernandez F, Rosillo S, Delgado JM, Bekaert DPS, Sousa JJ, Gil AJ, Cuenca MC, Hanssen RF, Zaldivar J, Galdeano CS (2016) Multi-temporal InSAR evidence of ground subsidence induced by groundwater withdrawal: the Montellano aquifer (SW Spain). Environ Earth Sci 75:242. doi:10.1007/s12665-015-5051-x

Deguchi T, Rokugawa S, Matsushima J (2009) Long-term ground deformation measurement by time series analysis for SAR interferometry. J Remote Sens Soc Japan 29:418–428 (in Japanese with English abstract)

Endo T (2009) Historical review of groundwater withdrawal management in the southern Kantoh Regions with reference to one by the Tokyo Metropolitan Government. Proc Symp Jpn Soc Eng Geol 1–25 (in Japanese)

Ferretti A, Prati C, Rocca F (2000) Nonlinear subsidence rate estimation using permanent scatterers in differential SAR interferometry. IEEE Trans Geosci Remote Sens 38(5):2202–2212

Fujiwara S, Nishimura T, Murakami M, Nakagawa H, Tobita M, Rosen PA (2000) 2.5-D surface deformation of M6.1 earthquake near Mt Iwate detected by SAR interferometry. Geophys Res Lett 27:2049–2052

Hachinohe S, Hayashi T, Wada E, Osada M (2014) Ground of Saitama prefecture. In: Shin Kanto no Jiban. Maruzen Co Ltd., Japanese Geotechnical Society, pp 81–96 (in Japanese)

Hayashi T (2004) Change of groundwater environment and groundwater quality in the central part of the Kanto plain. J Jpn Assoc Hydro Sci 34:217–226 (in Japanese with English abstract)

Hooper A, Bekaert D, Spaans K, Arikan M (2012) Recent advances in SAR interferometry time series analysis for measuring crustal deformation. Tectonophysics 514–517:1–13. doi:10.1016/j.tecto.2011.10.013

Huang M-H, Tung H, Fielding E, Huang H-H, Liang C, Huang C, Hu J-C (2016) Multiple fault slip triggered above the 2016 Mw 6.4 MeiNong earthquake in Taiwan. Geophys Res Lett 43:7459–7467. doi:10.1002/2016GL069351

IPCC (2013) Climate change 2013: the physical science basis. In: Stocker TF et al (eds) Contribution of Working Group I to the Fifth Assessment Report of the Intergovernmental Panel on Climate Change. Cambridge University Press, Cambridge, United Kingdom and New York, NY, USA, p 1535

Ishitsuka K, Fukushima Y, Tsuji T, Yamada Y, Matsuoka T, Giao PH (2014) Natural surface rebound of the Bangkok plain and aquifer characterization by persistent scatterer interferometry. Geochem Geophys Geosyst 15:965–974. doi:10.1002/2013GC005154

Japan Meteorological Agency (2013) Global Warming Projection 8: 88 (in Japanese)

Kampes B, Hanssen R, Perski Z (2003) Radar interferometry with public domain tools. Proc. Fringe 2003, p 6

Kimura K, Ishihara Y, Miyachi Y, Nakashima R, Nakanishi T, Nakayama T, Hachinohe S (2006) Sequence stratigraphy of the latest Pleistocene-Holocene incised valley fills from the Tokyo and Nakagawa Lowland, Kanto Plain, central Japan. Mem Geol Soc Jpn 59:1–18 (in Japanese with English abstract)

Kobayashi T, Ishimoto M, Tobita M, Yarai H (2014) A tool for reduction of atmosphere-related noises included in an InSAR image, incorporating a numerical weather model. Bull GSI 125:31–38 (in Japanese)

Kobayashi T, Morishita Y, Yarai H (2015) Detailed crustal deformation and fault rupture of the 2015 Gorkha earthquake, Nepal, revealed from ScanSAR-based interferograms of ALOS-2. Earth Planets Space 67:201. doi:10.1186/s40623-015-0359-z

Komatsubara J (2014) Basal topography of the latest Pleistocene – Holocene valley fills under the Arakawa Lowland, Nakagawa Lowland and Tokyo Lowland, central Japan. In: Integral research and application of the subsurface geology "the central Kanto Plain", Miscellaneous Map Series. Geol. Surv. Japan, vol 40, AIST, pp 51–55 (in Japanese with English abstract)

Morita M (2015) Present state of land subsidence in the northern Kanto Plain. J Groundwater Hydrol 57:29–36 (in Japanese)

Nakanishi T, Tanabe S, Kimura K, Nakashima R, Uchiyama M, Shibata Y (2011) Sedimentary facies, diatom assemblages, physical properties and radiocarbon ages of the latest Pleistocene to Holocene incised valley fills under the central area of the Nakagawa Lowland, Kanto Plain, central Japan. Bull Geol Surv Jpn 62:47–84 (in Japanese with English abstract)

Ozawa T, Fujita E (2013) Local deformations around volcanoes associated with the 2011 off the Pacific coast of Tohoku Earthquake. J Geophys Res 118:390–405. doi:10.1029/2011JB009129

Tanabe S, Nakanishi T, Kimura K, Hachinohe S, Nakayama T (2008) Basal topography of the Alluvial under the northern area of the Tokyo Lowland and Nakagawa Lowland, central Japan. Bull Geol Surv Japan 59(11/12):497–508 (in Japanese with English abstract)

Tobita M, Munekane H, Matsuzaka S, Kato M, Yarai H, Murakami M, Fujiwara S, Nakagawa H, Ozawa T (2005) Studies on InSAR data processing technique. J Geospatial Inf Auth Jpn 106:37–49 (in Japanese)

Zebker HA, Rosen PA, Goldstein RM, Gabriel A, Werner CL (1994) On the derivation of coseismic displacement fields using differential radar interferometry: the Landers earthquake. J Geophys Res 99(B10):19617–19634

A New Velocity Field of Greece Based on Seven Years (2008–2014) Continuously Operating GPS Station Data

Stylianos Bitharis, Aristeidis Fotiou, Christos Pikridas, and Dimitrios Rossikopoulos

Abstract

Greece is characterized by complex and intense geodynamics, because it is located between the collision boundaries of two tectonic plates (Africa-Nubia and Eurasia), with major active tectonic features such as the Hellenic Arc, the Anatolian fault in North Aegean Trough and the Kefalonia fault in the Ionian Sea. GPS is a well-established tool for geophysical research purposes, because it is able to provide continuous measurements for monitoring displacements of the Earth's crust. The aim of the present study is to create a modern and improved geodetic velocity field for Greece using GPS observations from continuously operating reference stations. The new set of geodetic velocities is derived from the processing of 7 years (2008–2014) of daily GPS data, using 155 stations distributed in the broader Greek territory and 30 IGS-EPN GPS stations. The GAMIT/GLOBK software package was used to process the GPS measurements. The results are expressed in the ITRF2008 reference frame. The analysis showed that the northern region of Greece is the most stable and has identical movement with the Eurasian plate in contrast with the region of the southern part and the Aegean Sea. According to the results, the estimated horizontal geodetic velocities show completely different pattern between northern and southern Greece with significant differences both in magnitude and direction. The derived site values were used for a velocity grid creation in order to predict velocities within the Greek area and to enforce proper realization of GNSS reference systems in Greece.

1 Introduction

The Greek territory and mainly the Aegean Sea is one of the most deforming areas at the Eurasian Plate with a long history in geodetic methods for crustal displacement monitoring. The majority of previous studies are based on campaign-style measurements with triangulation technique and GPS at the early years (Billiris et al. 1991; Davies et al. 1997; Fotiou et al. 2003) or by exploiting only the advantages of satellite geodesy some years later (Rossikopoulos et al. 1998; McClusky et al. 2000; Doukas et al. 2004; Reilinger et al. 2006; Hollenstein et al. 2008; Floyd et al. 2010 and Müller et al. 2013). In all these studies the inhomogeneous horizontal velocity field is demonstrated, which if ignored on long term the datum definition becomes unrealistic.

The official Hellenic Geodetic Reference System of 1987 (HGRS87) and the geocentric Hellenic Terrestrial Reference System of 2007 (HTRS07) are both static datums. In particular, the HGRS87 is derived from combination of satellite and terrestrial observations carried out between 1964 and 1987. The HTRS07 is a realization of ETRS89 given by the HEPOS (HEllenic POsitioning System) reference stations.

S. Bitharis (✉) • A. Fotiou • C. Pikridas • D. Rossikopoulos
Department of Geodesy and Surveying, Aristotle University of Thessaloniki, Thessaloniki, Greece
e-mail: stylbith@gmail.com

The HTRS07 reference epoch is 2007.5, the mean epoch of the national GPS campaign at 2,470 benchmarks, in order to determine the official transformation model between HTRS07 and HGRS87 (Katsampalos et al. 2009).

In a recent study (Chatzinikos et al. 2013), where continuous Global Positioning System (cGPS) data only is used, the need of a semi kinematic datum in Greece including a velocity model is highlighted. In the present study a denser network of GPS sites, which was reprocessed and extended to 7-year time span, is expected to improve the datum realization and transformations. Consequently, if we predict the value of a geodetic velocity vector $\mathbf{V}_i$ at any i location in Greece, based on a high accuracy grid, we have the benefit to shift the coordinates at an epoch $\mathbf{X}_i(t)$ to a previous epoch $\mathbf{X}_i(t_o)$, by the equation:

$$\mathbf{X}_i(t) = \mathbf{X}_i(t_o) + (t - t_o)\mathbf{V}_i \qquad (1)$$

2   GPS Data and Analysis

In our study we do not combine GPS surveys from other studies, but analyze and process 30-sec daily cGPS data, from 155 stations which are well established in the whole Greek territory, with very good distribution (Bitharis 2015). Noteworthy is the fact that in the used Hellenic Permanent GNSS Network (HPNet) the included sites are operated by Leica SmartNet Greece, National Observatory of Athens (NOA, Ganas et al. 2011), National Cadastre and Mapping Agency (NCMA) of Greece, National Technical University of Athens (NTUA) and Hermes GNSS Network of Aristotle University of Thessaloniki (AUTh, Fotiou et al. 2010; Fotiou and Pikridas 2012). Finally, the HPNet consists of four subnetworks, as shown in Table 1, with additionally 30 IGS-EPN common sites to all sub-networks, in order to be combined with other global solutions.

The analysis was performed using the GAMIT/GLOBK release 10.5 (Herring et al. 2010) software suite at 24-h sessions, with the three-step approach as recommended. Firstly, the raw data processed in order to estimate daily loosely constrained solutions of site positions, where orbital

Table 1 Classification of HPNet sub-networks

Sub-network	Organizations/Agencies	Span (year)	No. of sites
HEPOS Subnetwork	NCMA	2008–2010	46
NTUA Subnetwork	NTUA	2008–2011	18
North Subnetwork	Leica SmartNet Greece, NOA, AUTh	2008–2014	47
South Subnetwork	Leica SmartNet Greece, NOA, AUTh	2008–2014	44

and Earth Orientation Parameters (EOP) were held fixed to IGS final and IERS Bulletin A values with weights. The weighting strategy is dictated by the network scale and the a-priori Earth rotation tables, thus the EOPs are constrained as recommended for a continental scale analysis (Herring et al. 2010). In our strategy we estimate Zenith Total Delay (ZTD) adjusted every 2-hour interval using Vienna Mapping Function 1 (VMF1) (Boehm et al. 2006). Concerning the Solid Earth Tides, the IERS2003 conventions were followed. In addition, the FES2004 ocean loading model (Lyard et al. 2006) and the Atmospheric Pressure Loading corrections (Tregoning and van Dam 2005) were applied.

In the second step, all the individual sessions of the four local sub-networks were combined, using a seven-parameter Helmert transformation to estimate site coordinates in ITRF2008 from individual daily solution. The geodetic velocities were estimated by time series analysis fitting the linear and the extended model (Nikolaidis 2002). The computed WRMS values, almost the same, in each fitting were 2.0, 2.2 and 4.8 mm in East, North and Up component respectively. The differences between the derived velocities from the linear and the extended model, are less than 1 mm/year for a data span greater than 2.5 years. The extended model is described by the following equation:

$$y(t_i) = \alpha + \beta t_i + \sum_{k=1}^{n}(c_k \sin(2k\pi t_i)$$
$$+ d_k \cos(2k\pi t_i)) + \sum_{k=1}^{n_g} g_k H(t_i - T_{g_k}) + v_i \qquad (2)$$

where, α and β are position and velocity of the monitoring station, c_k and d_k describe periodic motions, the term

$$z(t_i) = \sum_{k=1}^{n_g} g_k H(t_i - T_{gk}) \qquad (3)$$

is used to describe the discontinuities caused by the earthquakes and equipment changes, with magnitudes g_k at epochs T_{gk} and H is the Heaviside step function. The raw time series helps to detect outliers and discontinuities occur in site coordinates derived from various sources and having an impact on long time series.

In the last step, after outliers removal, station coordinates and velocities are estimated by a Kalman filtering sequential approach (Dong et al. 1998). The realization of the frame is estimated by the minimization of the deviations between positions and velocities relative to ITRF2008 (Altamimi et al. 2011; Rossikopoulos 2013) applying the 7-parameter Helmert transformation. Thus, the datum definition is implemented using inner constraints to coordinates and their velocities in 24 IGS stations, with a three-dimensional a-posteriori
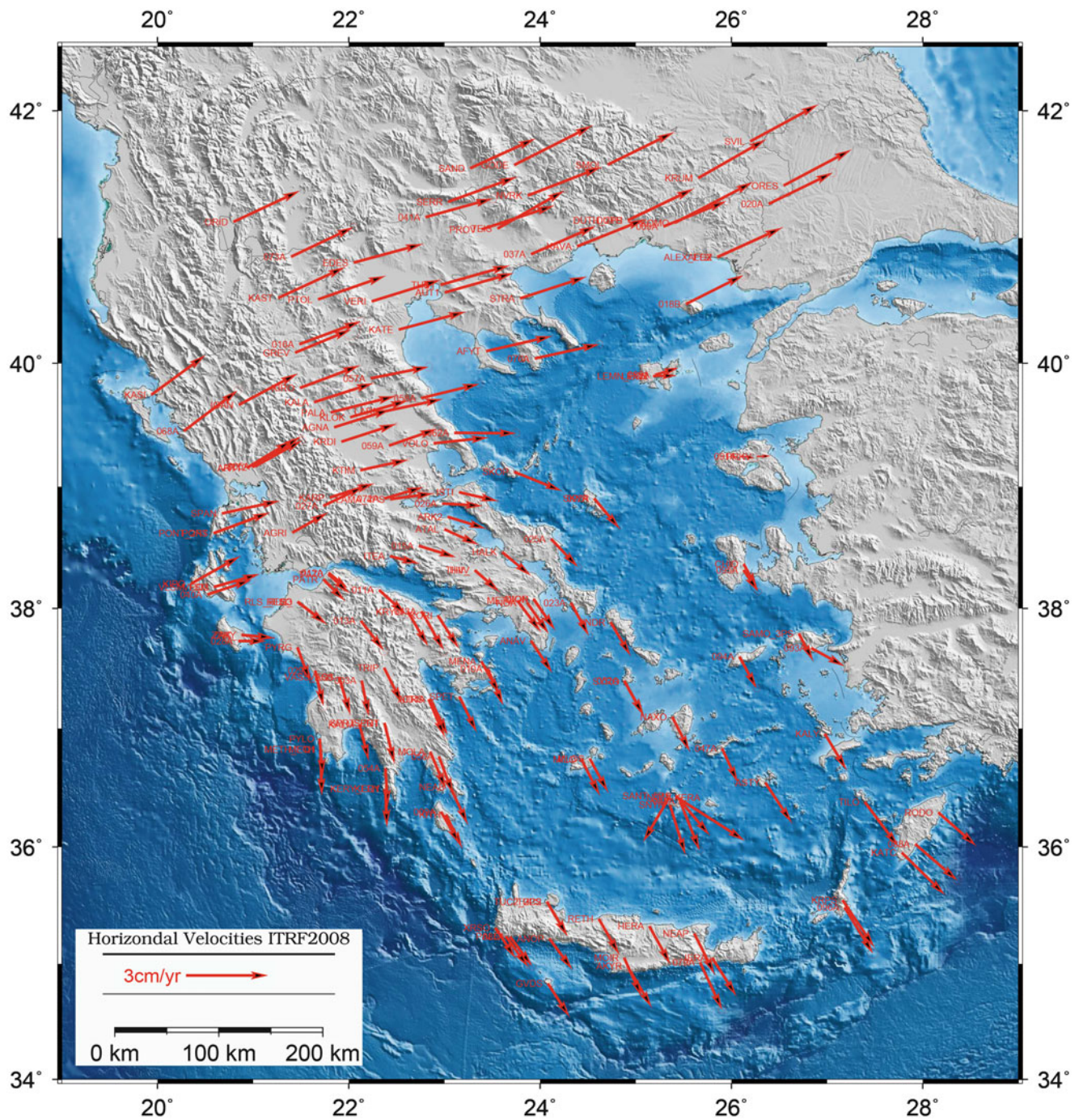
Fig. 1 Horizontal velocities relative to ITRF2008 in Greek area

RMS error of 2 mm and 0.6 mm/year respectively. In more detail, the WRMS for each component (East, North, Up) resulted in 2.0, 2.2, 4.4 mm for the position and 0.6, 0.5, 0.7 mm/year for the velocities. The majority of selected stations are located in the European plate and two stations in the Arabian plate.

Figure 1 depicts the station velocities of the processed permanent GPS sites relative to ITRF2008 in Greek area. Comparing Figs. 1 and 2 it should be noted that the velocities

of the most IGS sites in the European plate, are almost the same with those in the northern part of Greece. More over in Fig. 2 the 24 used IGS stations are given with their velocities relative to ITRF2008.

It is worth to mention that there is a significant correlation between the standard deviation and the duration of time occupation. The standard deviations of horizontal velocities are ~3.5 times smaller than the velocities on vertical component as shown in Fig. 3.
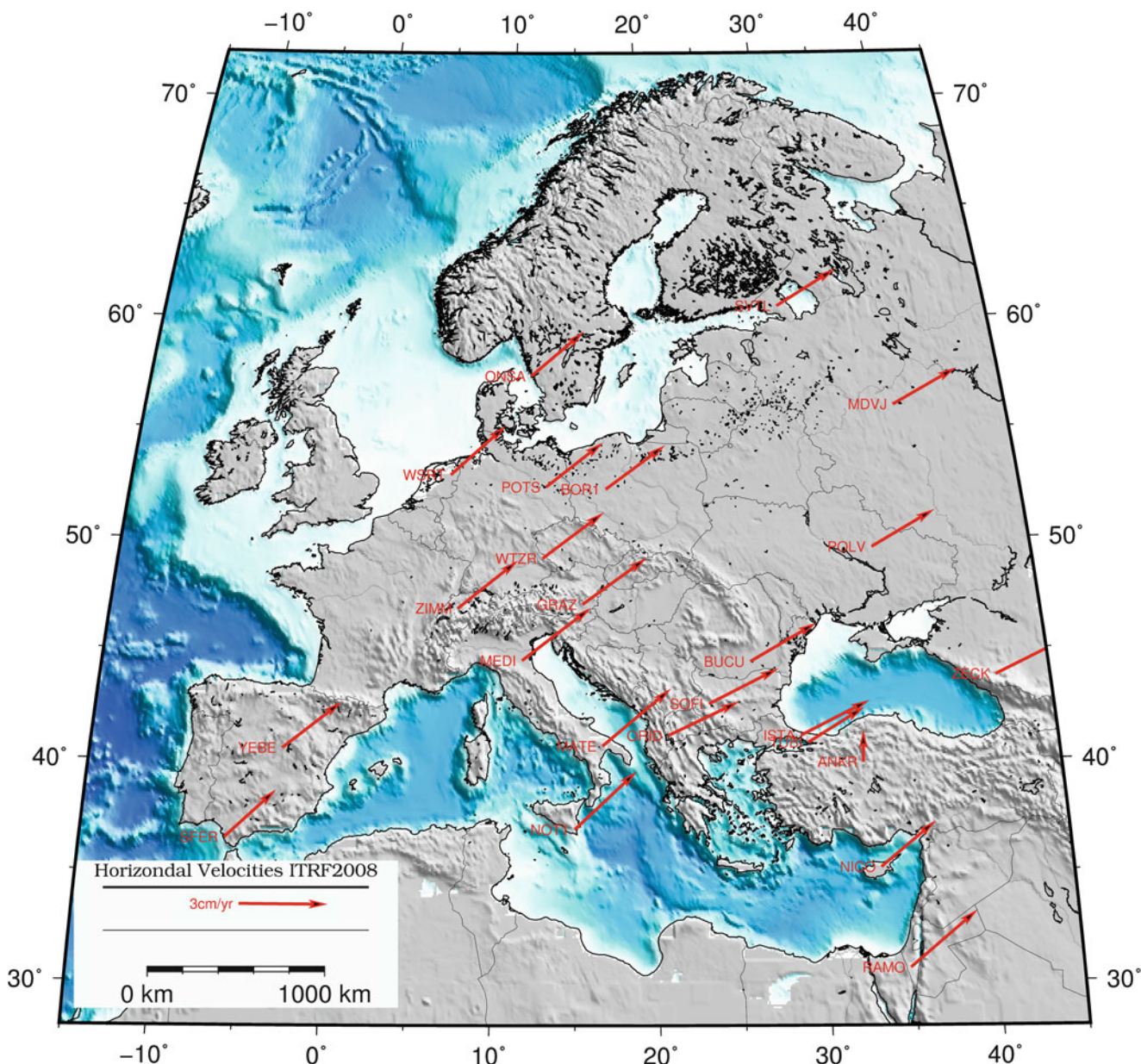
Fig. 2 Horizontal velocities of 24 IGS stations relative to ITRF2008

In Fig. 3 a set of points with greater standard deviation is obvious as compared with the remaining points. These points belong to the HEPOS subnetwork, shown in Table 1, with a small data time span of 5 days per year from 2008 to 2010.

2.1 Horizontal Velocities in Greece Relative to the Eurasia Plate

The velocities could be expressed with respect to the Eurasia plate, following the methodology described in detail by Boucher and Altamimi (2011). The European Terrestrial Reference System (ETRS89) realizations are based on the removal of the European plate velocity, coincident with International Terrestrial Reference System (ITRS) at the reference epoch 1989 and fixed to the stable part of Eurasian plate (Gurtner et al. 2008).

The ETRF provides a homogenous velocity field in central Europe with minimum velocities (less than 1 mm/year). However, in deformation zones as in Greece and Italy the velocities could be greater than 1 cm/year (Altamimi 2012). In most geophysical studies the ETRF approach is preferred as the behavior of the Earth's crust in the study area is more clearly represented. According to the results in our study the velocities in ETRF2000 (Fig. 4) are compatible with previous studies (e.g., McClusky et al. 2000; Chatzinikos
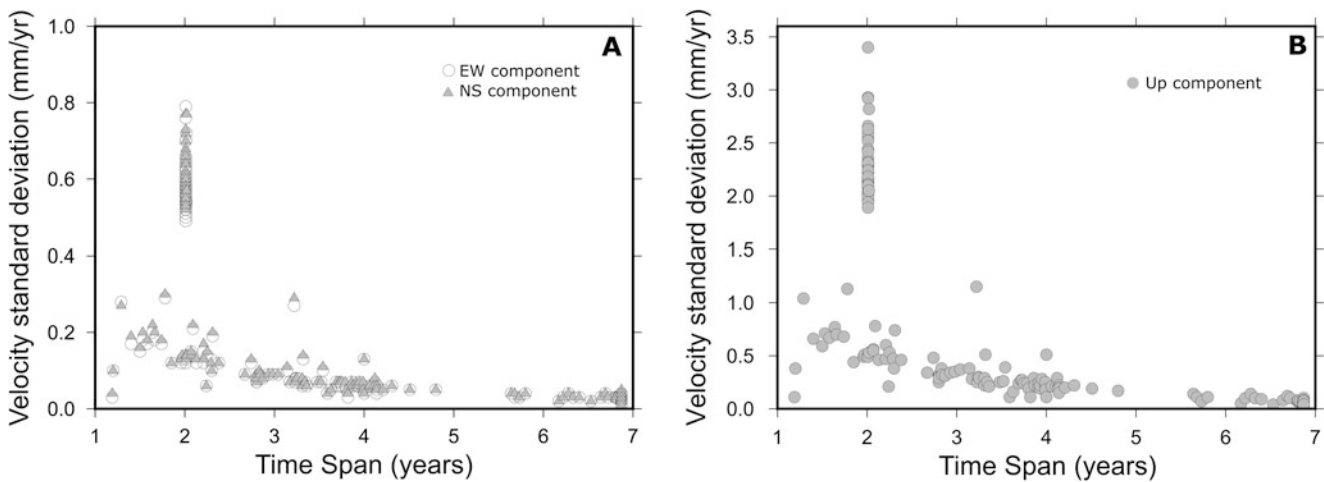
Fig. 3 Standard deviation of geodetic velocities per component as a function of observation time span (years). The horizontal velocity uncertainties are provided on the *left part* (**a**) and the vertical on the *right part* (**b**)

et al. 2013; Kenyeres et al. 2014). The advantage of the present study is that due to a significant densification of the GPS network in Greece and the corresponding long time span of data processing the horizontal velocity field has been more accurately estimated. However, in this paper, a detailed comparison among relative studies with respect to the Eurasia plate is not presented.

3 A New Horizontal Velocity Field in Greece

Given the distribution of the GPS sites and the inhomogeneous variation of velocities, the geographical boundaries of the new model is defined strictly in Greek territory with cell dimension $0.3° \times 0.3°$ (Lon. × Lat.), using the bi-cubic spline interpolation with Generic Mapping Tools software (Wessel et al. 2013; Rossikopoulos 2001). In general, cubic splines, which provide a smooth surface that passes exactly through the input points (velocities of GPS sites), could be a suitable model. After an extensive analysis with various interpolation methods, the bi-cubic spline interpolation proved more efficient in terms of the smaller RMS error, i.e. 0.3 mm/year, for the horizontal predicted velocities. For distances greater than 100 km from each GPS station, the model does not provide velocities because unrealistic values could be obtained (Fig. 5).

The widely known intense geophysical activity at the Santorini volcano affected our geodetic velocity estimation especially at the vertical component. To avoid any bias, stations at Santorini volcano were excluded from our model.

This special case enforces us to do a separate study in the near future.

From the estimated velocity vectors we can characterize the different displacement fields (inhomogeneous velocity areas) mainly between north and south part of Greece. The northern region is the most stable and co-moves with the Eurasian plate in contrast with the southern part and the Aegean Sea. As a conclusion, a geodetic datum without a velocity model cannot serve as a uniform spatial framework for accurate surveying and mapping applications in medium or large areas.

3.1 Model Validation with Previous Studies

Our model was evaluated with one of the most recent studies which is by far the largest global velocity solution, the Global Strain Rate Model (GSRM v.2.1 (Kreemer et al. 2014). GSRM is a synthetic model, which includes velocities from the literature and the scope of this work is to serve plate motion and strain rate studies in plate boundary zones. We isolated 699 velocity values in our study area and compared them with the predicted velocities from our model at the same locations. The horizontal differences are illustrated in Fig. 6.

As shown in Fig. 6, large differences are found at the area of Corinthian Gulf and along the coast line of Turkey, mainly due to lack of proper number of cGPS sites and large geodynamic activity existed there as well. For all other areas the (horizontal) vectors differences do not exceed 2.5 mm/year.

Fig. 4 Horizontal velocities relative to ETRF2000 in Greek area

4   Conclusions

The significant crustal deformations in Greece impose that datum related to geodetic positioning and the associated surveying applications could not be ignored, as the used official Greek datum (HGRS87), with an age of over 30 years, and the latest geocentric system HTRS07 are both static. We computed a new horizontal velocity field for Greece, expressed in the ITRF2008 and/or in ETRF2000, using 7 years of cGPS data from a well distributed and dense permanent GPS network of 155 sites. In GPS data processing the GAMIT/GLOBK software package was used with recommended parameters and extensive time-series analysis was performed. The new velocity grid was estimated using the appropriate interpolation method of bi-cubic splines,

Fig. 5 Continuous geodetic velocity model in Greece expressed in the ITRF2008. The *red-black* vectors represent the initial velocities on GPS stations whereas the *color bar* indicates the magnitude of the predicted horizontal velocities

in order to provide velocity anywhere within the Greek area. One of the future goals is the inclusion of more GPS data in areas with specific geodynamic activity, as it is the Corinthian Gulf and the Santorini volcano. The presented model could be the official horizontal velocity model in Greece, providing accurate solutions of permanent Greek GNSS networks and datum transformation in almost any modern international terrestrial frame.
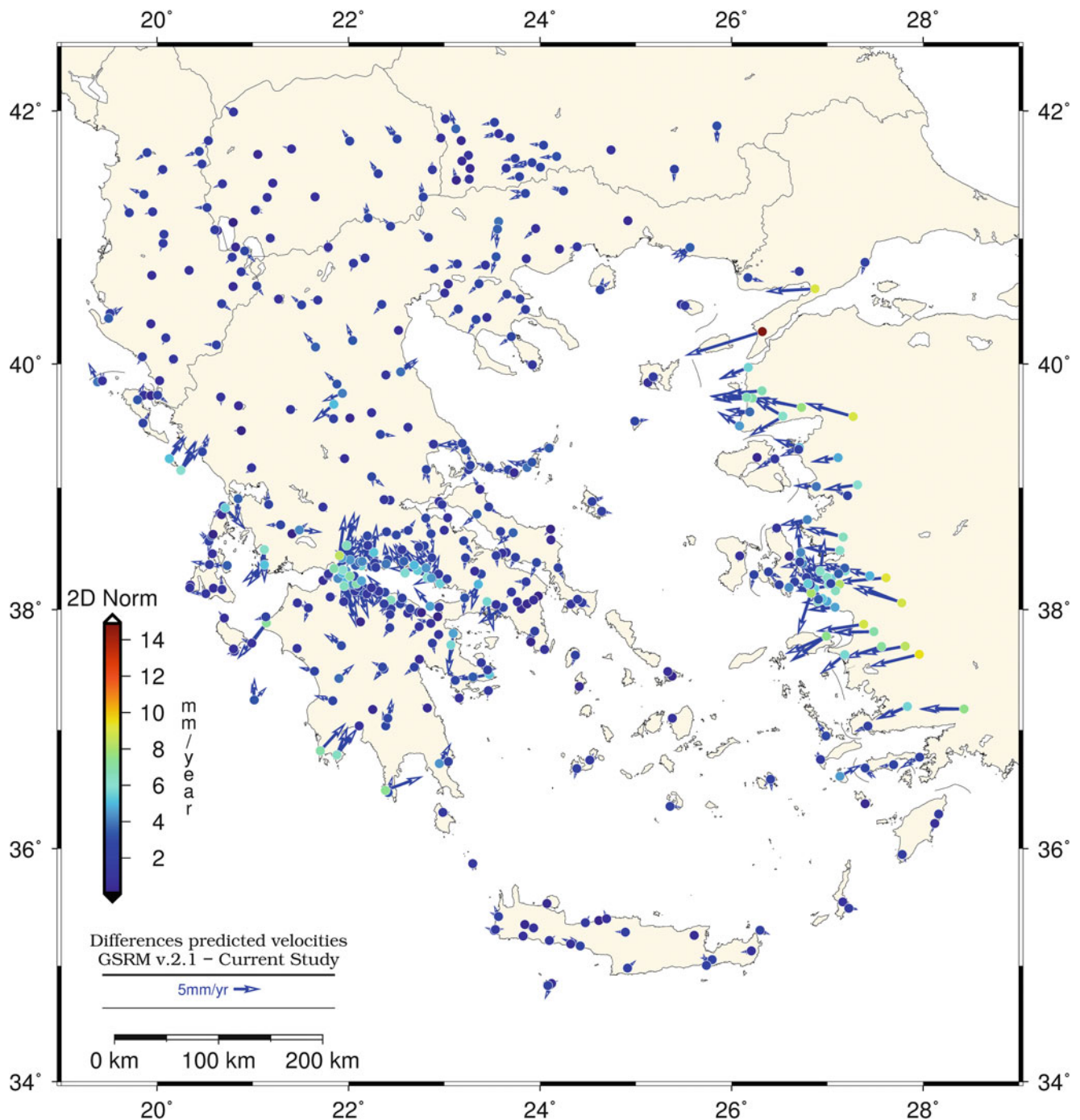
Fig. 6 Differences between new velocity model in Greece and GSRM v.2.1

References

Altamimi Z (2012) ITRS, ETRS89, their relationship and realization. In: Proceedings of the EUREF symposium, Paris Saint-Mandé, France

Altamimi Z, Collilieux X, Métivier L (2011) ITRF2008: an improved solution of the international terrestrial reference frame. J Geod 85(8):457–473. doi:10.1007/s00190-011-0444-4

Billiris H, Paradissis D, Veis G, England P, Featherstone W, Parsons B, Cross P, Rands P, Rayson M, Sellers P, Ashkenazi V, Davison M, Jackson J, Ambraseys N (1991) Geodetic determination of tectonic deformation in central Greece from 1900 to 1988. Nature 350(6314):124–129. doi:10.1038/350124a0

Bitharis S (2015) Process of GPS permanent stations data and estimation of velocity field in Greek area. Master Thesis, Department of Geodesy and Surveying, Aristotle University of Thessaloniki (in Greek)

Boehm J, Werl B, Schuh H (2006) Troposphere mapping functions for GPS and very long baseline interferometry from European Centre for Medium-Range Weather Forecasts operational analysis data. J Geophys Res Solid Earth 111(2):1–9. doi:10.1029/2005JB003629

Boucher C., Altamimi Z. (2011), Memo: Specifications for reference frame fixing in the analysis of a EUREF GPS campaign, Version 8, http://etrs89.ensg.ign.fr/memo-V8.pdf

Chatzinikos M, Fotiou A, Pikridas C, Rossikopoulos D (2013) The realization of a semi-kinematic datum in Greece including a new velocity model. In: Rizos C, Willis P (eds) IAG 150 years. Springer, Berlin/Heidelberg, pp 1–9. doi:10.1007/1345_2015_93

Davies R, England P, Parsons B, Billiris H, Paradissis D, Veis G (1997) Geodetic strain of Greece in the interval 1892–1992. J Geophys Res 102(B11):24571. doi:10.1029/97JB01644

Dong D, Herring TA, King RW (1998) Estimating regional deformation from a combination of space and terrestrial geodetic data. J Geod 72(4):200–214. doi:10.1007/s001900050161

Doukas I, Fotiou A, Ifadis IM, Katsambalos K, Lakakis K, Petridou-Chrysohoidou N, Pikridas C, Rossikopoulos D, Savvaidis P, Tokmakidis K, Tziavos IN (2004) Displacement field estimation from GPS measurements in the Volvi area. In: Proceedings of FIG 27th working week "The Olympic Spirit in Surveying", Athens, Greece, 22–27 May 2004

Floyd MA, Billiris H, Paradissis D, Veis G, Avallone A, Briole P, McClusky S, Nocquet J-M, Palamartchouk K, Parsons B, England PC (2010) A new velocity field for Greece: implications for the kinematics and dynamics of the Aegean. J Geophys Res Solid Earth 115(10):1–25. doi:10.1029/2009JB007040

Fotiou A, Pikridas C (2012) GPS and geodetic applications, 2nd edn. Ziti Publishing, Thessaloniki

Fotiou A, Kagiadakis V, Pikridas C, Rossikopoulos D (2003) Geodetically derived displacements and crustal deformation analysis: application in the volvi area. In: Proceedings of the 11th international symposium on deformation measurements. FIG commission 6, Santorini, Greece, 25–28 May 2003

Fotiou A, Pikridas C, Rossikopoulos D, Spatalas S, Tsioukas V, Katsougiannopoulos S (2010) The Hermes GNSS NtripCaster of AUTh. Bull Geodesy Geophys LXIX(1):35–43

Ganas A, Chousianitis K, Drakatos G, Papanikolaou M, Argyrakis P, Kolligri M, Petrou P, Batsi E, Tsimi C (2011) NOANET: high-rate GPS network for seismology and geodynamics in Greece. In: Geophysical research abstracts, vol 13 (EGU General Assembly 2011)

Gurtner W, Ihde J, Luthardt J (2008) Realization of ETRS89: alternatives and future concepts. In: EUREF symposium. Brussels, Belgium, 18–20 June 2008

Herring TA, King RW, McClusky SC (2010) Documentation of the GAMIT GPS analysis software release 10.4. Department of Earth and Planetary Sciences, Massachusetts Institute of Technology, Cambridge, Massachusetts, pp 1–171

Hollenstein C, Müller MD, Geiger A, Kahle HG (2008) Crustal motion and deformation in Greece from a decade of GPS measurements, 1993–2003. Tectonophysics 449(1–4):17–40. doi:10.1016/j.tecto.2007.12.006

Katsampalos K, Kotsakis C, Gianniou M (2009) Hellenic Terrestrial Reference System 2007 (HTRS07): a regional realization of ETRS89 over Greece in support of HEPOS. In: 2009 EUREF symposium, presentation. Retrieved from http://ikee.lib.auth.gr/record/211975

Kenyeres A, Horváth T, Caporali A, Brockmann E, Droščak B, Franke P, Garayt B, Gianniou M, Georgiev I, Hansen D, Huisman L, Jumare I, Nagl J, Pihlak P, Ryczywolski M, Stangl G, Valdes M (2014) Global reference frame densification based on the integration of regional and national active GNSS Network products. IGS Workshop 2014, Pasadena, USA

Kreemer C, Blewitt G, Klein EC (2014) A geodetic plate motion and global strain rate model. Geochem Geophys Geosyst 15:3849–3889. doi:10.1002/2014GC005407

Lyard F, Lefevre F, Letellier T, Francis O (2006) Modelling the global ocean tides: modern insights from FES2004. Ocean Dyn 56(5–6):394–415. doi:10.1007/s10236-006-0086-x

McClusky S, Balassanian S, Barka A, Demir C, Ergintav S, Georgiev I, Gurkan O, Hamburger M, Hurst K, Kahle H, Kastens K, Kekelidze G, King R, Kotzev V, Lenk O, Mahmoud S, Mishin A, Nadariya M, Ouzounis A, Paradissis D, Peter Y, Prilepin M, Reilinger R, Sanli I, Seeger H, Tealeb A, Toksöz MN, Veis G (2000) Global Positioning System constraints on plate kinematics and dynamics in the eastern Mediterranean and Caucasus. J Geophys Res 105(B3):5695. doi:10.1029/1999JB900351

Müller MD, Geiger A, Kahle HG, Veis G, Billiris H, Paradissis D, Felekis S (2013) Velocity and deformation fields in the North Aegean domain, Greece, and implications for fault kinematics, derived from GPS data 1993–2009. Tectonophysics 597–598:34–49. doi:10.1016/j.tecto.2012.08.003

Nikolaidis R (2002) Observation of geodetic and seismic deformation with the global positioning system. University of California, San Diego

Reilinger R, McClusky S, Vernant P, Lawrence S, Ergintav S, Cakmak R, Ozener H, Kadirov F, Guliev I, Stepanyan R, Nadariya M, Hahubia G, Mahmoud S, Sakr K, ArRajehi A, Paradissis D, Al-Aydrus A, Prilepin M, Guseva T, Evren E, Dmitrotsa A, Filikov SV, Gomez F, Al-Ghazzi R, Karam G (2006) GPS constraints on continental deformation in the Africa-Arabia-Eurasia continental collision zone and implications for the dynamics of plate interactions. J Geophys Res Solid Earth 111(5):1–26. doi:10.1029/2005JB004051

Rossikopoulos D (2001) Modeling alternatives in deformation measurements. In: Carosio A, Kutterer H (eds) First international symposium on robust statistics and fuzzy techniques in geodesy and GIS. ETH Zurich

Rossikopoulos D (2013) Time-depended geodetic networks and the reference frame definition problem. In: Arabelos D, Kaltsikis C, Spatalas S, Tziavos IN (eds) THALES. Volume in honor of Professor Emeritus Michael E. Contadakis. Publication of Faculty of Rural and Surveying Engineering, Aristotle University of Thessaloniki, pp 266–287

Rossikopoulos D, Fotiou A, Livieratos E, Baldi P (1998) A rigorous analysis of GPS data to detect crustal deformations. Application in the area of the Ionian Sea. Tectonophysics 294(3–4):271–280. doi:10.1016/S0040-1951(98)00105-X

Tregoning P, van Dam T (2005) Atmospheric pressure loading corrections applied to GPS data at the observation level. Geophys Res Lett 32(22):1–4. doi:10.1029/2005GL024104

Wessel P, Smith WHF, Scharroo R, Luis J, Wobbe F (2013) Generic mapping tools: improved version released. Eos Trans AGU 94(45):409–410. doi:10.1002/2013EO450001

SPINA Region (South of Iberian Peninsula, North of Africa) GNSS Geodynamic Model

B. Rosado, I. Barbero, A. Jiménez, R. Páez, G. Prates, A. Fernández-Ros, J. Gárate, and M. Berrocoso

Abstract

As it is well known, GNSS data analysis is a powerful tool to study geodynamic processes. However, observational methodologies and data analysis results should be adapted to determine local or even regional effects. It is particularly important in tectonic plate boundary areas when looking for subduction zone limits.

When using Continuous GNSS (CGNSS) observing receiver networks, a set of precise topocentric coordinates (e, n, u) for each place, will be available. Furthermore time series formed by the daily positions will produce the sites temporal variations. If those time series are long enough, horizontal components (e, n) use to show linear behaviors if there are no other geodynamic effect affecting the tectonic plates movement. Anyway the height component (u) uses to show periodical but not linear effects. But often time series are disturbed by different processes, as local subsidence, periodic dilatation compression effects, GNSS signal interferences, etc.

This paper shows a detailed topocentric coordinates time series study for sites belonging to what we call the SPINA network, which stands for South of the Iberian Peninsula, North of Africa Region. To avoid the above mentioned local effects, a priori quality control is carefully performed. Solutions are obtained by processed positioning with respect to a IGS reference station and by PPP processing (Precise Point Positioning), using the Bernese software. Results will be compared and combined. Then, a designed methodology, using filter processes, harmonic adjustments and wavelets will be applied. As final product we expect to get horizontal displacement model to describe the regional geodynamic main characteristics.

Keywords

Boundary zone tectonic plates • Regional crustal deformation

B. Rosado • I. Barbero • A. Jiménez • R. Páez • G. Prates •
A. Fernández-Ros • M. Berrocoso
Laboratorio de Astronomía, Geodesia y Cartografía, Facultad de
Ciencias, Universidad de Cádiz, Cádiz, Spain
e-mail: belen.rosado@uca.es

G. Prates
Centro de Estudos Geográficos, IGOT, Universidade de Lisboa,
Lisboa, Portugal

Instituto Superior de Engenharia, Universidade do Algarve, Faro,
Portugal

1 Introduction

Earth surface deformation observation and study is important to investigate local tectonic movements in geodynamic active areas. Some processes can be identified from GPS data time

A. Fernández-Ros
Instituto Hidrográfico de la Marina, Cádiz, Spain

J. Gárate
Grupo de Investigación RNM314 Geodesia y Geofísica, Cádiz, Spain

series. For this reason, during the last decade a number of continuous processing systems for observations taken by Global Positioning System (GPS) networks have been implemented worldwide (Fernandes et al. 2003; Kulkarni et al. 2006; Mancilla et al. 2013).

In this work, the analyzed GPS data correspond to 60 continuously recording GPS (CGPS) stations located in the southern region of the Iberian Peninsula and Northern Africa, what we call SPINA network. The main goal is to present a detailed topocentric coordinates time series study for these sites.

The methodology applied on this paper for CGPS coordinate time series analysis is based on wavelet analysis, once the coordinate time series are cleaned for outliers and periods of bad data are identified and removed. Then, the wavelet transform was applied to the GPS time series to reduce scattering and separate noise and signal (Mallat 2008). Next, a mathematical model for the station movement is applied to determine sites' velocities, in order to provide useful information for further geodynamic interpretations. From this processing, we present sites' velocities determined by GPS, from which the surface deformation model is given. Finally, we compare the results obtained in our final solution with results provided by other geodetic and geophysical models.

2 Site Description

We have analyzed data from 60 continuously recording GPS (CGPS) stations located in the southern region of the Iberian Peninsula and Northern Africa.

The CGPS stations are included in some different organizations: the Portuguese RENEP: *Rede Nacional de Estaçoes Permanentes* (for National Continuous Network), the Andalusian RAP: *Red Andaluza de Posicionamiento* (for Andalusian Positioning Network), the Murcia Region CGPS Networks, and the Valencia Region ERVA: *Red Estaciones de Referencia de Valencia* (for Valencian Reference Stations Network). Some other CGPS included in IGS and EUREF were analyzed to be used as fiducial points to determine velocities with respect to ITRF as well as to the stable Eurasian Plate (ETRF).

Figure 1 shows the location of each CGPS stations. Different colors are used for different networks. We used position time series derived from daily observations, processed positioning with respect to the IGS station located in Villafranca, VILL (40°15′N, 3°34′W), in Madrid, to get

site displacements. We called SPINA (South of the Iberian Peninsula and North Africa) this set of CGPS.

Time series start in the beginning of 2005 and finish at the end of 2014. For those sites installed after 2005, we built the longest time series available.

3 Data Processing

3.1 Wavelet Analysis

The wavelet technique permits to study the signal at different resolutions to improve the search of different frequencies. The wavelet transform decomposes a signal using functions (wavelets) well localized in both physical space (time) and spectral space (frequency), generated from each other by translation and dilation (Kumar et al. 2002).

The Continuous Wavelet Transform (CWT) tries to express a signal x(t) continuous in time, by an expansion of proportional coefficients to the inner product between the signal and different scaled and translated versions of a function prototype, Eq. (1) (Ramírez et al. 2005).

$$CWT(a,b) = \frac{1}{\sqrt{a}} \int_{-\infty}^{+\infty} x(t)\varphi\left(\frac{t-b}{a}\right) dt \qquad (1)$$

The objective of wavelet analysis is to define these powerful wavelet basis functions and find efficient methods for their computation. It can be shown that every application using the Fast Fourier Transform (FFT) can be formulated using wavelets to provide more localized temporal (or spatial) and frequency information. Thus, instead of a frequency spectrum, for example, one gets a wavelet spectrum. In signal processing, wavelets are very useful for processing nonstationary signals.

The Discrete Wavelet Transform (DWT) uses filter banks for the construction of the multi-resolution time-frequency plane. DWT analyzes the signal at different frequency bands with different resolutions by decomposing the signal into an approximation and detail information. The decomposition of the signal into different frequency bands obtained by successive high pass $g(n)$ and low pass $h(n)$ filtering of the time domain signal (Fig. 2). DWT processes data on a variable time-frequency plane that matches progressively the lower frequency components to coarser time resolutions and the high-frequency components to finer time resolutions, thus achieving a multi-resolution analysis (Percival and Walden 2000).
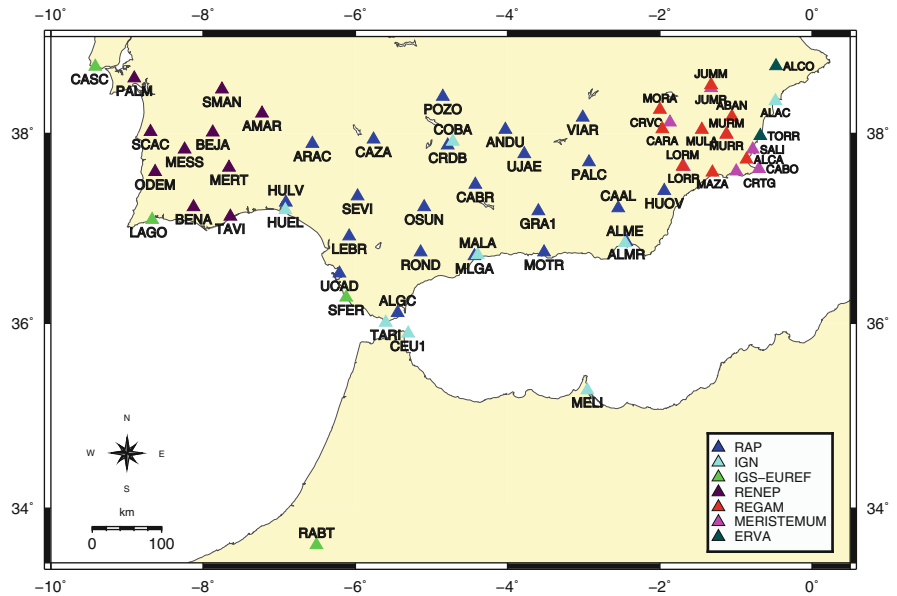
Fig. 1 Map of SPINA GPS Sites. Different colors indicate the different networks: the Andalusian RAP: Red Andaluza de Posicionamiento (for Andalusian Positioning Network), the Portuguese RENEP: Rede Nacional de Estaçoes Permanentes (for National Continuous Network), the Murcia Region CGPS Networks (REGAM and MERISTEMUM), and the Valencia Region ERVA: Red Estaciones de Referencia de Valencia (for Valencian Reference Stations Network), and some others CGPS included in IGS and EUREF
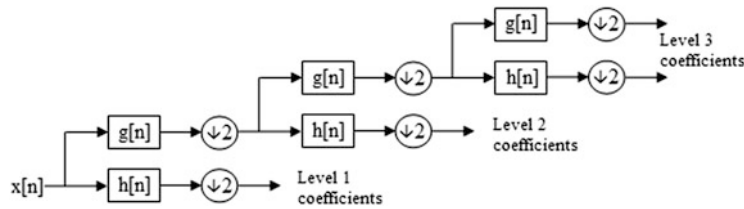
Fig. 2 Diagram of signal decomposition. The original signal *x* passes through two complementary filters: a low-pass filter (G) determined by *g(n)* coefficients to obtain the low-frequency of the signal; and a high-pass filter (H) represented by *h(n)* coefficients to estimate the high-frequency of the signal

3.2 Harmonic Analysis

A complete time series analysis, in order to get a more accurate velocity field, is made by using algorithm 2 (Kierulf et al. 2008):

$$
\begin{aligned}
x(t) = a + bt + \sum_{j=1}^{2} \left(A_j \sin\left(\omega_j t\right) + B_j \cos\left(\omega_j t\right) \right) \\
+ \sum_{j=1}^{n} C_j H\left(t - T_j\right)
\end{aligned}
\tag{2}
$$

where *x* is the height value, *t* the time, ω_1 and ω_2 the angular frequency of an annual and semi-annual harmonic

constituent, and A_j and B_j their respective amplitudes of the sine and cosine parts. The coefficients C_j are the magnitude of offsets described by the Heaviside function (Eq. 3)

$$
H(t) = \{0 \; t < 0, 1 \; t \geq 0\}
\tag{3}
$$

and the time of the offset T_j, *n* is the number of jumps included. In the least squares fit of Eq. (2) to the individual time series, we solved for the offset *a*, the rate *b*, the coefficients A_j and B_j of the annual and semi-annual harmonic constituents. Moreover, we solved for the magnitude C_j of obvious jumps in the time series identified either from log-file information or visually in the time series.

Fig. 3 Daily position time series for the SEVI CGPS station for 2-sigma filter, shown as a *blue line*. Time series are obtained by processed positioning with respect to the VILL station using the Bernese software. We have applied wavelet analysis, which is shown as a *red line*. We have also taken into account the estimated displacement rate obtained by harmonic analysis. *Green lines* indicate the IRTF frame discontinuity
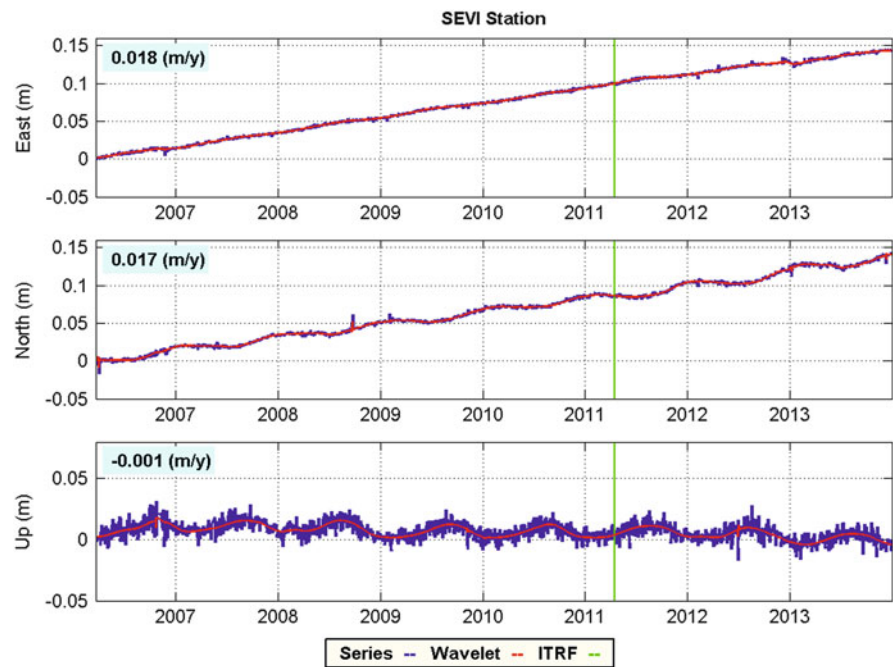
Fig. 4 Daily position time series for the SEVI CGPS station for 2-sigma filter, shown as a *blue line*. Time series are obtained by PPP processing using the Bernese software. We have applied wavelet analysis, which is shown as a *red line*. We have also taken into account the estimated displacement rate obtained by harmonic analysis. *Green lines* indicate the ITRF frame discontinuity
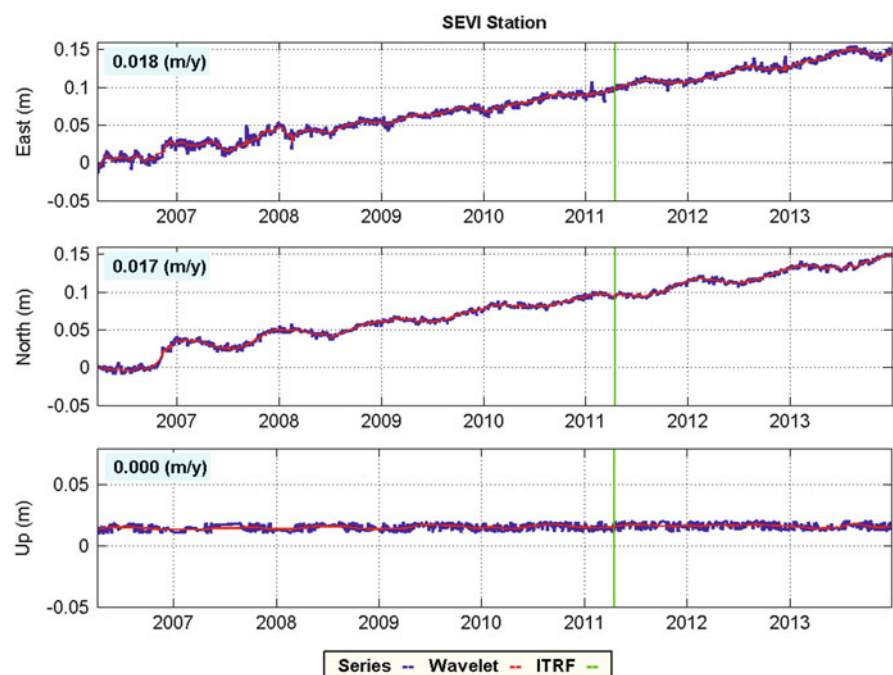
4 Displacement of GPS Stations

The data for all stations have been processed using the scientific BERNESE v5.0 GPS software, developed by the Astronomy Institute of the University of Bern, Switzerland (Dach et al. 2011).

Figures 3 and 4 show daily position time series for the SEVI CGPS station for 2-sigma filter, shown as a blue line. In Fig. 3 time series have been obtained by pro-

cessed positioning with respect to the VILL station and Fig. 4 presents time series obtained by PPP processing, using the Bernese software. Both figures wavelet analysis was applied, which is shown as a red line. We have also taken into account the estimated displacement rate obtained by harmonic analysis. Green lines indicate the ITRF frame discontinuity.

In these figures, a ripple with an annual periodicity is observed in the up component and, more emphasized, in the north component. This is due to the station is built

Fig. 5 Horizontal displacement rates at GPS sites in the south of the Iberian Peninsula and North Africa, estimated from GPS time-series data with 95% confidence level error ellipses
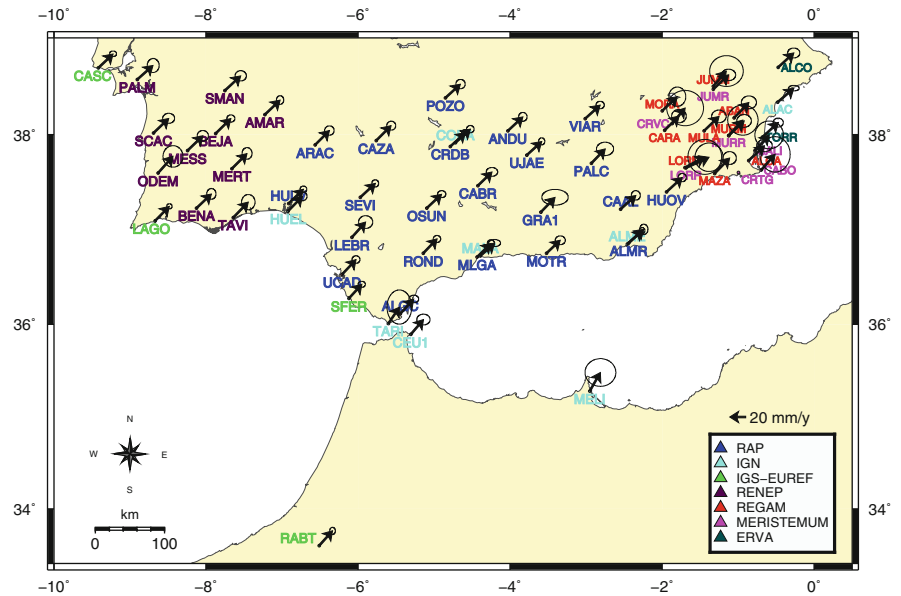
Fig. 6 Residuals velocities relative to the IGS reference station located in Villafranca (VILL), estimated from GPS time-series data with 95% confidence level error ellipses
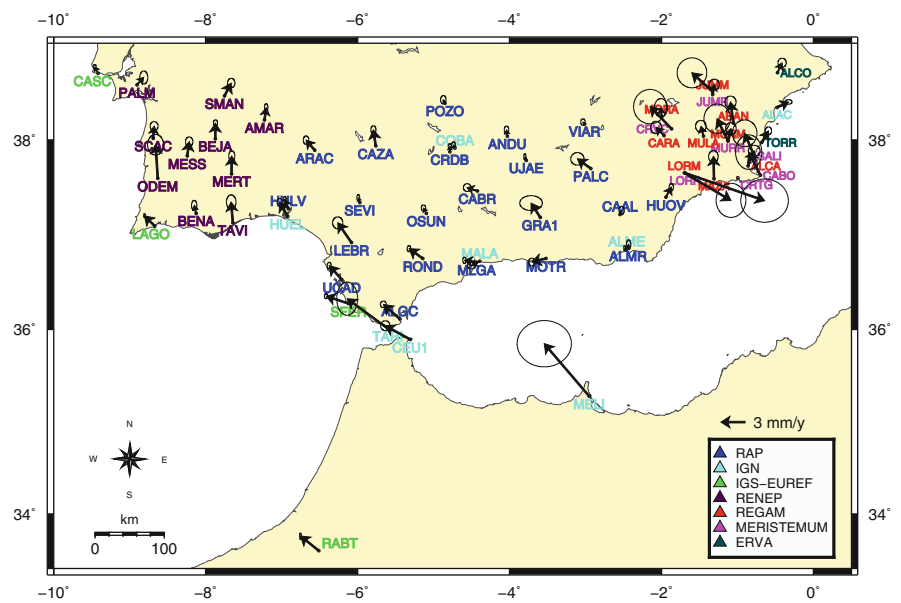
on a high building, oriented as the north-south direction (with a difference of 10°). This fact makes the effect on the expansion-contraction of the building is more pronounced in the north-south direction.

The main result of this work is shown in Figs. 5 and 6, where horizontal surface deformation velocity is presented. Figure 5 shows horizontal displacement rates at GPS sites in the south of the Iberian Peninsula and North Africa, estimated from GPS time-series data (January 2005–January 2014). Figure 6 presents the GPS site velocities with respect to the IGS reference station located in Villafranca VILL. All GPS solutions are realized in the ITRF 2005 global reference frame.

5 Cluster Analysis

Finally, cluster analysis has been applied to detect groups of stations with similar behaviour. We have used this statistical model looking for new tools which allow us to identify displacement models even if we have not a complete view of the regional geology. In such a way we can interact with geophysics to look for causes justifying particular behaviours. In this work, agglomerative hierarchical clustering algorithm or AGNES (agglomerative nesting) (Kaufman and Rousseeuw 1990) was applied to the estimated displacement rate obtained by harmonic analysis. We

Fig. 7 Geographical
representation of the stations
classified by similar behaviours
in their coordinate variations
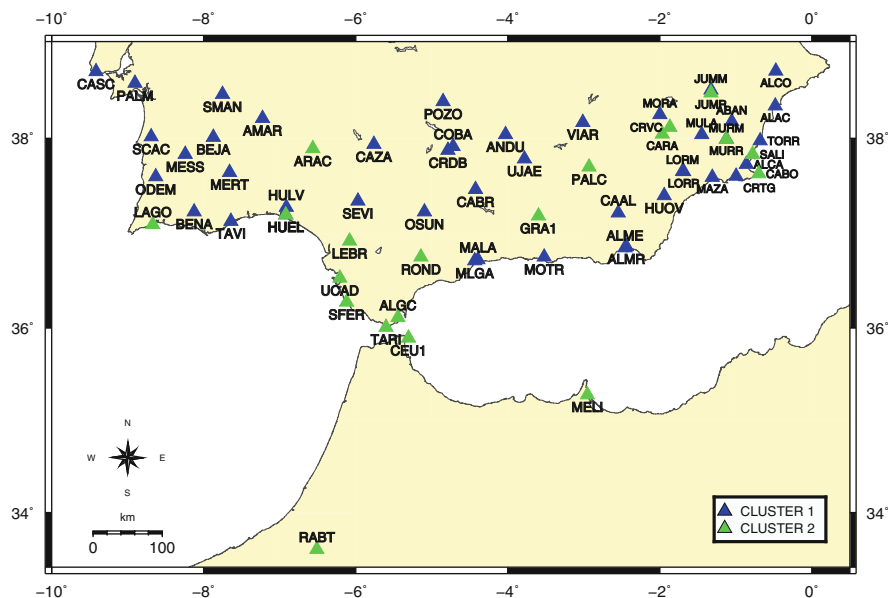
also consider Manhattan distance, Eq. (4) (Chattopadhyay et al. 2013):

$$d(i, j) = |x_{i1} - x_{j1}| + |x_{i2} - x_{j2}| + \cdots + |x_{ip} - x_{jp}| \quad (4)$$

where $i = (x_{i1}, x_{i2}, \ldots, x_{ip})$ and $j = (x_{j1}, x_{j2}, \ldots, x_{jp})$ are two p-dimensional data objects.

These techniques have been used as a complement of the knowledge geophysical data such as the boundaries of tectonic plates, which can be used to support the validity of those limits and also to detect and correct inconsistencies. Lorca station has been excluded from analysis because of its particular displacing model due to the 2011 Lorca Earthquake (González et al. 2012). Figure 7 presents the stations classified by similar behaviours in their coordinate variations.

6 Discussion and Conclusions

In this study, a CGPS coordinate time series analysis strategy for the determination of horizontal model deformation has been introduced and evaluated. This strategy incorporates a preliminary study of the coordinate time series to clean for utliers. Then, the wavelet transform was applied to the GPS time series to reduce scattering and separate noise and signal, and a mathematical model for the station movement is applied to determine sites' velocities. The GPS network used in this study included 60 continuous GPS stations (CGPS) located in the southern region of the Iberian Peninsula and northern Africa.

Figure 5 shows horizontal displacement rates at GPS sites in this region. Our re-sults in this figure show average velocities of 2 cm/year in a NNE direction in the region. Figure 6 presents the GPS site velocities with respect to the IGS reference station VILL. We clearly observe four differents zones: South-East of Iberian Peninsula, South of Iberia and North of Africa, North of Andalusia and South of Portugal.

In the South-East of the Iberian Peninsula, we appreciate a significant motion for stations located in Lorca (LORR and LORM), due to the 2011 Lorca Earthquake. The general trend is in the NE-SW direction, except for station HUOV, TORR, ALAC and ALCO. These results are consistent with Khazaradze et al. (2014) and Koulali et al. (2011).

We also detect other transitions zones. There is a transition zone which direction varies from NW to SE, with increasing values towards the south of the Iberian Peninsula. Deformations in the region of Northern Anadalusia are associated with the convergence of the Eurasian plate. We appreciated a significant behaviour in GRA1, PALC, CARA, MORA and JUMM stations.

References

Chattopadhyay AK, Mondal S, Chattopadhyay T (2013) Independent component analysis for the objective classification of globular clusters of the galaxy NGC 5128. Comput Stat Data Anal 57:17–32

Dach R, Hugentobler U, Walser P (2011) Bernese GPS software version 5.0. Astronomical Institute, University of Bern, Bern

Fernandes RMS, Ambrosius BAC, Noomen R, Bastos L, Wortel M, Spakman W, Govers R (2003) The relative motion between Africa and Eurasia as derived from ITRF2000 and GPS data. Geophys Res Lett 30(16):1828. doi:10.1029/2003GL017089

González PJ, Tiampo KF, Palano M, Cannavó F, Fernández J (2012) The 2011 Lorca earthquake slip distribution controlled by groundwater crustal unloading. Nat Geosci 5:821–825

Kaufman L, Rousseeuw PJ (1990) Finding groups in data: an introduction to cluster analysis. Wiley, New York

Khazaradze G, Echeverría A, Asensio E (2014) Present-day crustal deformation field of the Iberian Peninsula estimated by GPS measurements. Física de la Tierra 26:25–46

Kierulf HP, Plag HP, Bingley RM, Teferle N, Demir C, Cingoz A, Yildiz H, Garate J, Davila JM, Silva CG, Zdunek R, Jaworski L, Martinez-Benjamin JM, Orus R, Aragon A (2008) Comparison of GPS analysis strategies for high-accuracy vertical land motion. Phys Chem Earth 33:194–204

Koulali A, Ouazar D, Tahayt A, King RW, Vernant P, Reilinger RE, McClusky S, Mourabit T, Davila JM, Amraoui N (2011) New GPS constraints on active deformation along the Africa–Iberia plate boundary. Earth Planet Sci Lett 308:211–217

Kulkarni MN, Radhakrishnan N, Rai D (2006) Global positioning system in disaster monitoring of Koyna Dam, western Maharashtra. Surv Rev 37(292):490–497

Kumar KV, Miyashita K, Jianxin L (2002) Secular crustal deformation in central Japan, based on the wavelet analysis of GPS time-series data. Earth Planets Space 54:133–139

Mallat S (2008) A wavelet tour of signal processing. Elsevier, Amsterdam. ISBN: 13:978-0-12-374370-1

Mancilla FDL, Stich D, Berrocoso M, Martín R, Morales J, Fernández-Ros A, Páez R, Pérez-Peña A (2013) Delamination in the Betic Range: deep structure, seismicity, and GPS motion. Geology 41(3):307–310

Percival DB, Walden AT (2000) Wavelet methods for time series analysis. Cambridge University Press, Cambridge

Ramírez ME, Jiménez Y, González MJ, Berrocoso M, Sánchez-Francisco M (2005) A new data analysis technique in the study of mutual event lightcurves. Astron Astrophys 448:1197–1206

Continuous Kinematic GPS Monitoring of a Glacier Lake Outburst Flood

Cornelia Zech, Tilo Schöne, Julia Neelmeijer, and Alexander Zubovich

Abstract

Natural glacier events such as ice avalanches, debris flows or glacier lake outburst floods (GLOF) may have hazardous impacts on the downstream area of the glacier and can cause severe destructions. The Inylchek Glaciers in Kyrgyzstan, are one of the largest non-polar glacier systems in the world. Each year, an ice-dammed lake is formed (Lake Merzbacher) by melt-water which drains predominantly every year suddenly within a few days causing a destructive flood. To understand the mechanism of the GLOF, a network of continuously operating GPS stations at the Inylchek Glaciers provide daily horizontal and vertical positions of the ice-dam in front of the Merzbacher Lake. Irrespective of the general motion during the year, the ice-dam is strongly influenced by the formation and outburst of the lake. Especially the vertical position and surface velocities increase shortly before the GLOF supporting the assumption that the ice-dam adjacent to the lake becomes afloat. After the GLOF, e.g. in 2014, the elevation decreases rapidly by 20 m within 8 days. In 2015, the GLOF changes in timing, magnitude and available lake water volume but the motion pattern of the ice-dam is similar compared to the year before. These comparable results have the potential to develop an early warning system for the glacier-dammed lake outburst flood.

Keywords

Early warning system • Glacier lake outburst flood • Inylchek Glacier • Kinematic GPS glacier monitoring • Kyrgyzstan

1   Introduction

Glacial lakes can arise from retreating glaciers and are filled by melt-water. If the melt-water is blocked by moraines or ice-dams and accumulates over a certain timespan, the risk of a sudden drainage, called Glacier Lake Outburst Flood (GLOF) or Jökulhlaup referred to the Icelandic term

is strongly increasing. These GLOFs may have a catastrophic impact on the downstream area of the glacier as the abrupt release of water and the transportation of debris can cause severe destructions on villages and the environment. However, the complexity to predict the time of the outburst makes these floods a serious hazard. Over the past years, the research has been increased to understand the mechanism, timing and magnitude of these events. Various glacier lakes have been subject for many intensive field campaigns. Huss et al. (2007) and Sugiyama et al. (2008) described the outburst events at the ice-dammed lake at the Gornergletscher in Switzerland with a main focus on the triggering and drainage mechanism. Walder et al. (2006) investigated the Hidden Creek Lake in Alaska concerning the mechanical behaviour of the ice-dam at different positions with a surveying total station and Russell et al. (2011) described

C. Zech (✉) • T. Schöne • J. Neelmeijer
Helmholtz Centre Potsdam, GFZ German Research Centre for Geosciences, Potsdam, Germany
e-mail: czech@gfz-potsdam.de

A. Zubovich
Central-Asian Institute for Applied Geosciences (CAIAG), Bishkek, Kyrgyzstan

discharge mechanism, volume, magnitude and frequency of the outburst events at the Russell Glacier in West Greenland. Furthermore, Maas et al. (2012) developed a new approach to monitor the GLOF with automatic cameras and detecting a rapid loss in the water level with digital pictures. But as these glacial lakes are usually located in remote areas with limited access, continuous data about GLOFs are still sparse. Moreover, to transfer the knowledge from one glacier to another glacier is challenging as the topographic setting and drainage mechanism can change completely.

In this paper, we focus on the GLOF of the ice-dammed Lake Merzbacher at the Inylchek Glaciers. The ice-dam's behaviour has been monitored with a continuously operated GPS station over the last years including the complete outburst events of 2014 and 2015. The results of the GPS monitoring in combination with extracted lake level outlines from remote sensing data and the potential to develop an early warning system are subject of this paper.

2 Monitoring of the GLOF at the Inylchek Glaciers

2.1 Field Site

The Inylchek Glaciers (42°11′N 79°50′E) are located in East Kyrgyzstan close to the border to China in the Central Tian Shan mountain range. The glacier system stretches over 60 km from east to west at altitudes from 2,900 to 7,400 m a.s.l. (Hagg et al. 2008). The Lake Merzbacher is a pro-glacial ice-dammed lake (Mayer et al. 2008, Mayr et al. 2014; Glazirin 2010) that is formed during the melting period predominantly by melt-water from the Northern Inylchek (Glazirin 2010). Additional water is provided from the Southern Inylchek as assumed by Mavlyudov (1997), especially by calving from the ice-dam (Mayer et al. 2008). While most parts of the Southern Inylchek Glacier stream follow the main valley to the glacier terminus, other parts from the ice turn into the valley of the northern tributary and block the water flow from the northern stream in the form of a calving ice front (see Fig. 1). After Hutchinson (1957) the topographic setting of the pro-glacial lake can be classified as a lake located in the tributary valley, surrounded by hills and dammed by the glacier in the main valley. GLOFs occur almost every summer with a complete discharge of the lake through subglacial channels or followed by a second GLOF in case the lake was not empty (Glazirin 2010; Kingslake and Ng 2013). The lake drainage trigger mechanism is still not completely understood. In general, Tweed and Russell (1999) proposed different types of triggering for ice-dammed lakes. While some of them cannot be identified at the Lake

Merzbacher, others seem to be likely and should be further investigated. The overspill or overflow of lake water over the ice-dam have neither been described in the literature nor visually observed for this lake. The Glen Mechanism (Glen 1954) where the lake's water depth is proposed to be the drainage initiation mechanism seems to be more promising. Glen (1954) and Tweed and Russell (1999) argue that lake drainage would occur at water depth of approx. 120–200 m when the hydrostatic pressure of the water (horizontal stress component) will exceed the vertical comprehensive stress component and thus cause a hole in the ice to enlarge. But the usual water depth at the Lake Merzbacher does not exceed more than 80–100 m (Glazirin 2010; Ng and Liu 2009). Therefore, ice-dam floatation where water penetrates underneath the ice-dam and separates the ice from its bed or enhanced subglacial cavity formation due to increased glacier velocities seem to be more realistic and will be further discussed in this paper.

2.2 Data and Methods

Since 1902 the behaviour of the Lake Merzbacher has raised the interest of many researchers and the outbursts have been monitored and documented during different expeditions (e.g., Merzbacher 1905; Demchenko 1934). Recent activities include the usage of various aerial and terrestrial sensors over the last years to improve the understanding of the glacier's behaviour. While Neelmeijer et al. (2014) and Shangguan et al. (2015) used remote sensing data to examine general characteristics of the Inylchek Glacier in terms of surface kinematics and mass changes, Mayer et al. (2008) focused on the post-drainage ice-dam response derived from GPS campaign data and Aster images. Kingslake and Ng (2013) used different hydrological models to investigate the predictability of the timing of the GLOFs. However, regarding the short duration within the outburst flooding occurs, all of these studies are hampered by sparse data availability during the GLOF phase: in case of remote sensing, data is acquired at the shortest repeat cycle of 11 days (TerraSAR-X) and regarding field campaigns data could only be taken for a limited amount of days, which usually do not cover the immediate time before and after the drainage.

To overcome such problems, in 2009 the German Research Centre for Geosciences (GFZ) and the Central Asian Institute of Applied Geosciences (CAIAG) jointly installed the Global Change Observatory Central Asia at the Inylchek Glaciers with Remotely Operated Multi-Parameter Stations (Schöne et al. 2013) providing meteorological, hydrological, GPS and seismic data as well as optical cameras that support the monitoring of the GLOF. The
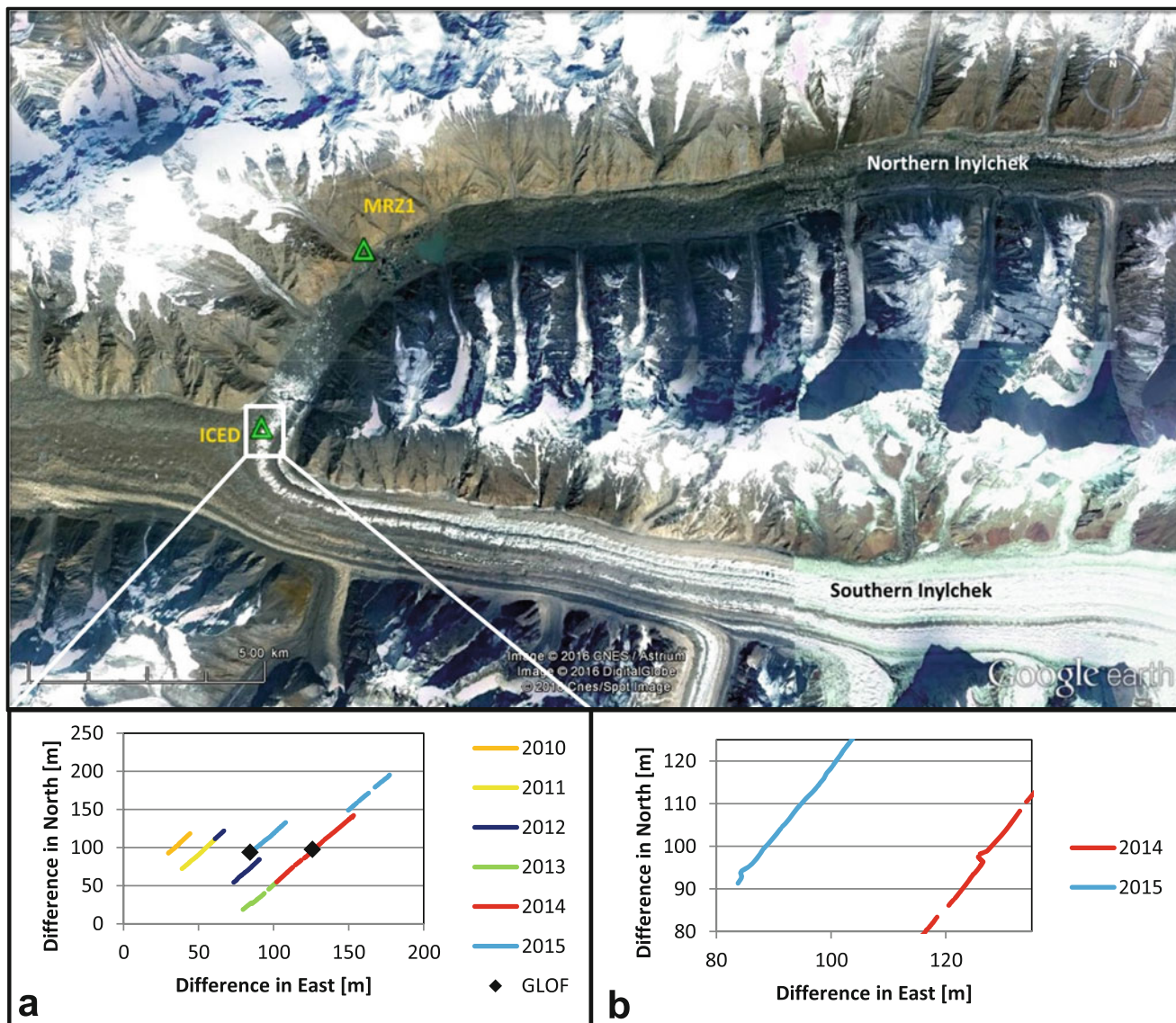
Fig. 1 Inylchek Glaciers with northern and southern tributary showing the locations of the GNSS monitoring stations MRZ1 and ICED marked with *green triangles*. (**a**) Tracks of the moving ICED station for the years 2010–2015 with different initial position for each year. 2010: *Orange*, 2011: *Yellow*, 2012: *Dark blue*, 2013: *Green*, 2014: *Red*, 2015: *Light blue*. (**b**) Horizontal movement of ICED showing the change of direction around the GLOF for 2014 (*red*) and 2015 (*light blue*). Courtesy Google Earth, Digital Globe 2016, CNES/Astrium, Cnes/SpotImage 2016

main station (MRZ1) located on a stable rock at the slope of the surrounding mountains (see Fig. 1), is capable of transmitting data in near real-time via a satellite communication system. To directly investigate the behaviour of the ice-dam, a continuously operating GPS station (ICED) has been installed providing 1 Hz GPS data. The equipment of the station is fixed on a metal construction and put on the surface of the ice-dam. The design of the metal construction allows the station to directly follow the movement of the

ice (floating on the ice) towards the Lake Merzbacher but prevents the station to turn over. The data is processed with the kinematic positioning software TRACK (Herring et al. 2009) with MRZ1 held fixed as the reference station and ICED as the kinematic station. Daily horizontal and vertical positions of ICED for all available data were estimated from the GPS observables. The accuracy of the daily positions is 0.5–0.8 cm for the horizontal component and 1.6–2.5 cm for the vertical component. Before and after the GLOF

when rapid movements of the ICED occur, the accuracy decreases to 0.9–1.3 cm for the horizontal component and 2.2–2.8 cm for the vertical component. This accuracy is sufficient to compare the results for all years. As the station moves towards the heavily crevassed part of the ice-dam, it was relocated back to a safe position every year. In the first years (2010–2013) the relocation was not recorded by the GPS and in 2014 the elevation difference was only marginal. But in 2015, the station was moved by 140.4 m backwards to a new position with an elevation difference of 7.6 m and therefore, a simple offset (difference of old and new elevation) is applied to the GPS time series accounting for the relocation. Unfortunately in the first years, the ICED station stopped data sampling during the winter time due to power failures and could only be reactivated after the expeditions in summer time which were after the outburst events in 2010, 2011 and 2012. In 2013, the station was visited shortly before the GLOF but data sampling was only possible after the GLOF. 2014 was the first year the data acquisition was successful for a complete season. Therefore, we mainly focus on the data for 2014 and 2015. To monitor relative lake level changes, pictures from the optical camera at the main station MRZ1 are used. We define the beginning of the discharge of the lake as the GLOF date.

To compare our results with previous measurements, results from the expedition in 2005 described in Mayer et al. (2008) are used. GPS measurements within a period of 10 days were carried out at several positions on the ice-dam including a few days before and several days after the GLOF.

2.3 Extraction of Lake Level Outlines by Remote Sensing Data

In order to compare the characteristics of Lake Merzbacher between the years 2005, 2013, 2014 and 2015, lake level outlines have been extracted from various remote sensing data. Namely, imagery from Landsat 7 and Landsat 8 in terms of optical satellite data and imagery from TerraSAR-X/TanDEM-X and Sentinel-1A in terms of radar satellite data were used to manually digitize lake outlines at their maximum extent. Additionally, a high spatial resolution (10 m) digital elevation model (DEM) was generated from a TanDEM-X scene acquired on 18. November 2013 by applying the InSAR technique using the GAMMA software (Werner et al. 2000). At this time of the year, the area of Lake Merzbacher was empty and almost water-free, which allows the extraction of the lake bathymetry from the DEM in high resolution. As the position of the ice-dam in November 2013 was at its most southern location of the observed time period, it does not extend within the derived lake outlines of the following years. As a consequence, the 2013 bathymetry can be used to improve the estimation of all lake outlines.

This was achieved by overlaying the manually digitized lake outlines on the contour field in order to extract the respective closest matching contour lines, which were then taken as the final lake outline. Only at the location of the ice-dam margin the lake outlines were left as digitized to use the outlines derived from the remote sensing data and not from the DEM. The thus refined lake outlines were then used to calculate the maximum surface area of Lake Merzbacher in the various years. In combination with the DEM, the lake volumes were estimated as well. As the manual extraction of the lake outline was hampered by several factors like spatial resolution, cloud cover (within optical data) and layover and foreshortening effects (within radar data) the derived outline never fitted a contour line entirely. We thus estimated lake areas and volumes of each year for the two respective bordering contours as well, to evaluate the impact of a potential ±2 m lake level uncertainty.

3 Results

3.1 Vertical Motion of the ICED Station

The elevation change of ICED can be separated into two parts: One part is the time shortly before and after the GLOF and the second part is the time when ICED is dominated by the general motion of the glacier. Figure 2 shows the elevation change for the years 2010–2015 compared to air temperatures. In all years, the elevation slightly increases or is nearly stable during the winter time (from October
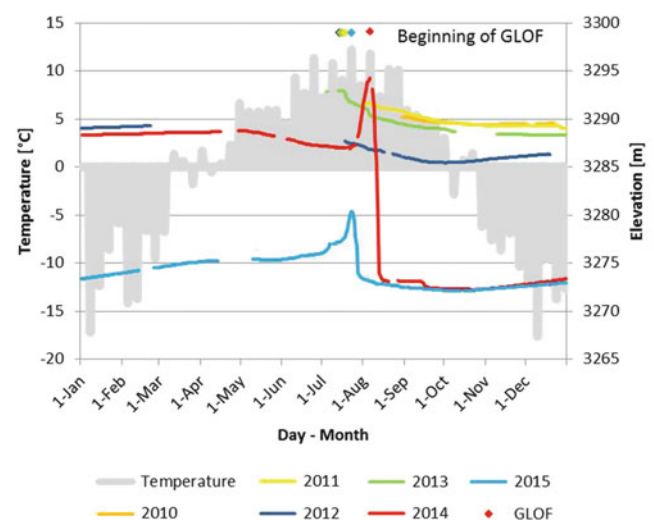

Fig. 2 Elevation changes of the station ICED for the years 2010–2015 compared to average air temperatures values for 2014 and 2015. The different elevation for each year is the result of varying initial positions. The disturbance of the elevation time series of 2015 is the result of the relocation on July 8th 2015. GLOF dates (beginning of discharge) are marked with *diamonds*

till end of April) when the air temperatures are below 0°C. While the elevation is nearly stable and does not change more than 0.7 m from October till December in 2010, 2011 and 2013, the elevation slightly increases by 0.8 m in 2012 and 2015 and by 1.0 m in 2014. With beginning of May, when the air temperatures start to increase above 0°C, the elevation of the ICED station decreases, which is especially observable in 2014. In 2015, this elevation decrease is less pronounced. Shortly prior and after the GLOF, the GPS time series show a substantial change in the ice-dam's behaviour. In 2014, the elevation increases rapidly before the GLOF by 6.0 m within 8 days and in 2015 by 2.8 m within 6 days. In both years, the discharge of the lake observed by the optical camera started at the same time when the elevation of ICED reached its maximum. On June 8th 2015 (approx. 2 weeks before the GLOF), the ICED station was manually moved to a new position resulting in an elevation difference of 7.6 m. Figure 2 shows the offset corrected elevation time series for 2015 but the relocation is still clearly visible as the elevation increase changes abruptly. Before the relocation, the increase in elevation already started but after the station was moved backwards (further away from the ice-margin), the elevation increase started later. After the GLOF, the elevation rapidly decreases by 20.7 m within 8 days in 2014 and 6.6 m within 6 days in 2015, respectively. In 2013, the elevation decrease was less dominant, only 1.1 m within 6 days. After the rapid loss, the elevation continues to decrease but this is less pronounced.

3.2 Horizontal Motion and Surface Velocities of the ICED Station

The horizontal motion of the ICED station follows the main movement of the glacier stream towards the calving ice-dam front (Fig. 1a). During winter time in 2014 and 2015, the surface velocities are 29% smaller than in summer time and are nearly constant. With beginning of May, when air temperatures rise above 0°C, the surface velocities increase (Fig. 3). Shortly before the GLOF, the surface velocities decrease and are highly variable. This behavior is synchronous to the rapid elevation increase and a change in horizontal motion from north-east towards north-west (Fig. 1b). After the outburst of the lake, the ice masses can stretch unhampered and the station moves back to its original direction of movement with increased surface velocities. The change of direction from north-west back to north-east is synchronous again with the elevation decline. During winter time, the velocities decrease and become nearly constant.
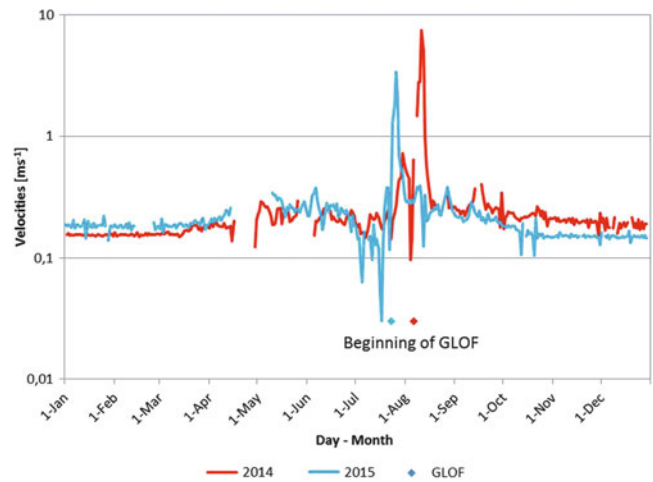
Fig. 3 Surface velocities of the station ICED printed on a log scale for the years 2014 and 2015 and GLOF dates marked with *diamonds*

Table 1 Lake surface area and volumes (bold)

Year	2005	2013	2014	2015
Surface Area (km²)	**3.73**	**2.57**	**3.22**	**2.77**
Surface Area −2 m (km²)	*3.58*	*2.48*	*3.06*	*2.62*
Surface Area +2 m (km²)	*3.91*	*2.66*	*3.36*	*2.94*
Lake Volume (km³)	**0.14**	**0.08**	**0.11**	**0.09**
Lake Volume −2 m (km³)	*0.13*	*0.07*	*0.10*	*0.08*
Lake Volume +2 m (km³)	*0.14*	*0.08*	*0.12*	*0.09*

Additionally, changes of the lake surface area and volumes are given would the lake level altitude be either 2 m higher or lower (in italics)

3.3 Lake Levels

The calculated lake surface areas and lake volumes of the Merzbacher Lake are shown in Table 1. Focussing on the recent years, the lake volume in 2013 is 27% and in 2015 is 18% less than the lake volume in 2014. To compare our results, especially the vertical displacement and the lake volumes with the data observed in 2005 by Mayer et al. (2008), the lake volume for 2005 was additionally calculated and is 21% higher than the lake volume in 2014. To evaluate the impact of lake level uncertainties, lake levels and volumes of ±2 m were calculated. Although the absolute values vary, the relative relation between the years does not change and is still in the same order. Therefore, it is feasible to use the calculated lake levels and volumes although these values are derived from images shortly before the GLOF. However, the calculated lake volumes are slightly lower than the flood volumes of 0.13 km³ for 1981 calculated with a hydrological model by Mayr et al. (2014) and 0.13–0.28 km³ for 1981–1996 estimated by Ng and Liu (2009) from data at the Chinese Xiehela river-gauging station which
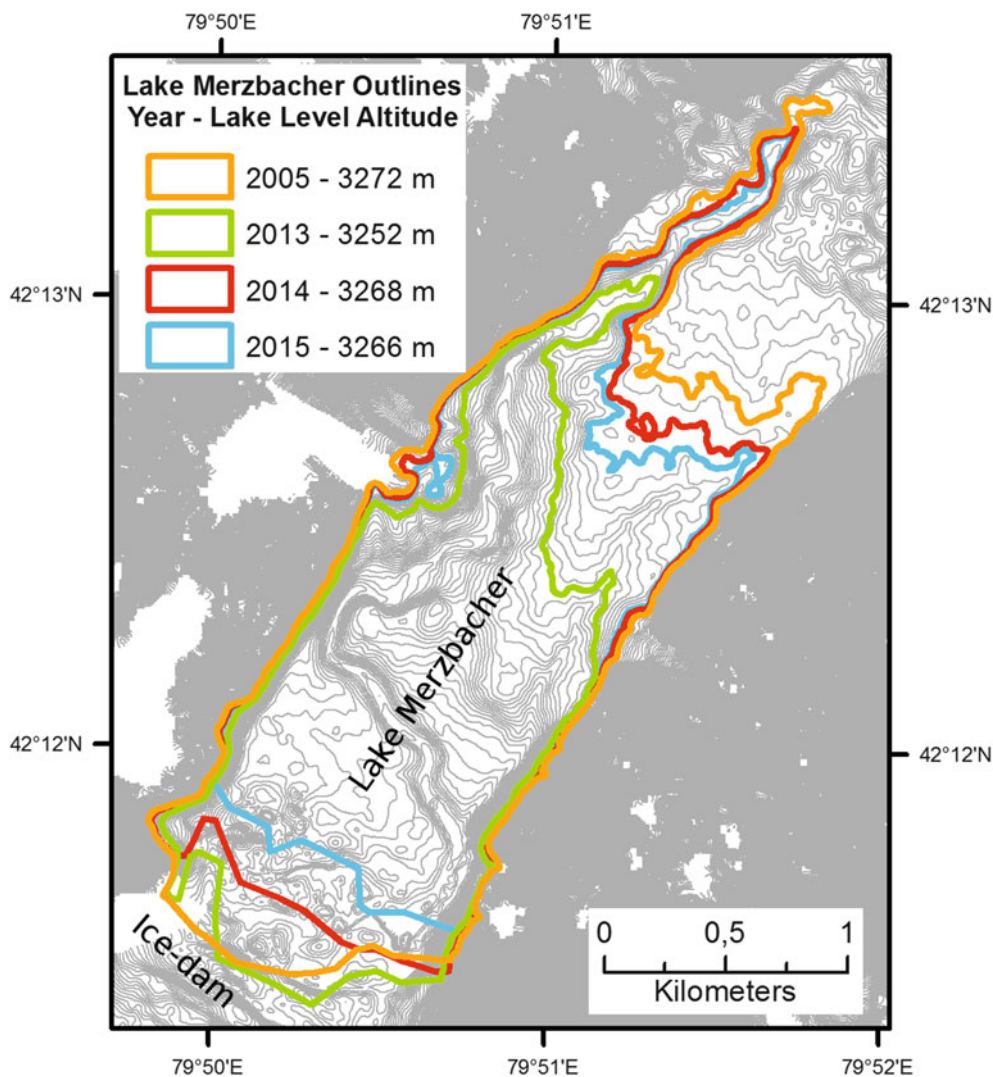
Fig. 4 Bathymetry of Lake Merzbacher shown with 2 m contour intervals. The maximal lake extends for the years 2005, 2013, 2014 and 2015 are highlighted in different colours

is approx. 150 km downstream (Kundzewicz et al. 2015) but are still in the same comparable range. The calculated lake volumes in this study rely on the visible extend of the lake, it does not include temporarily stored water inside the glacier or underneath the ice-dam. Additionally, the calculation of outburst flood volumes can be superimposed by normal catchment discharge, especially if the river-gauging station is some distance downstream of the lake (Wortmann et al. 2013).

Figure 4 shows the corresponding lake level outlines. These outlines can be seen as the maximum extend of the lake as we used remote sensing data close to the GLOF date. Obviously, the lake outline in 2013 is much smaller than especially in 2014 and 2005, and likewise were the lake volumes. Additionally, the ice-margin has varied over the years. Especially in 2014 and 2015 the ice-dam advanced further towards the lake.

4 Discussion

The results from the GPS data analysis show a clear seasonality of the ice-dam and the influence of the Lake Merzbacher. During the winter time, the behaviour of the ice-dam reflects a normal condition of the glacier where winter velocities are in general smaller than summer velocities (Mayer et al. 2008). With beginning of May and temperatures above 0°C, melting is enhanced supporting basal sliding of the ice as a result of increased water pressure in the glacier system (Bartholomaus et al. 2011). But the water pressure at this time is not sufficient to support an increase of the elevation. In combination with higher ice flux and mass transport towards the lake due to intensive calving and loss of ice at the ice-margin, this enhanced sliding is reflected in the increased surface velocities (Funk and Röthlisberger 1989)

and a slightly elevation decrease. Before the lake starts to fill generally in early May and the counter pressure of the forming lake is still low, respectively, the ice-margin could advance further towards the forming lake. Especially in 2014, the ice-margin advanced further from the position in 2013 (Fig. 4) and the elevation decrease is more pronounced compared to 2015. We assume that this different behaviour can be the result of a later formation of the lake in 2015 (visual observation from the pictures recorded at the main station) and thus less calving and less mass transport to the lake.

Shortly before the GLOF, the elevation increases rapidly suggesting that water penetrated underneath the ice-dam. When the pressure in this subglacial stored water is high enough, basal separation is possible thus resulting in an uplift of the ice (Sugiyama et al. 2008). This uplift indicates a temporary flotation of the ice-dam (Huss et al. 2007) due to a buoyancy force that bends the ice upwards (Nye 1976). In correlation to the uplift and due to the pressure of the increasing lake volume, the surface velocities decrease and the ice-dam cannot move further on towards the calving ice-dam front and has to spread away from the main flow direction (Fig. 1b). In 2015, the uplift is 53% less compared to 2014 and the outburst of the lake occurred earlier with a 14% smaller lake surface. Russell et al. (2011) experienced a similar behaviour at Russell Glacier, West Greenland and assumed that a larger GLOF can weaken the ice-dam and more cavities can arise in the vicinity of the calving ice-dam front that the next GLOF can occur earlier in the year and at lower lake levels. These generated cavities decrease the density of the ice which hampers the ice-dam to withstand the pressure of the water. This decreased density supports an earlier lake drainage initiation (Tweed and Russell 1999).

Directly after the outburst is initiated, the rapid elevation decrease is the result of the discharge of the water underneath the ice which forced the ice-dam to become afloat. Mayer et al. (2008) assumed that the elevation decrease is additionally supported by a reduction of the existing subglacial channels the lake's water drained through and which were enlarged by melt-widening from the discharging water (Tweed and Russell 1999). Furthermore, when the water has drained, the counter-pressure of the water does no longer exist and the ice masses can stretch unhampered resulting in an additional elevation decrease. The station moves back to its original direction of movement with increased surface velocities.

Some days after the GLOF, we hypothesize that several of these channels collapse resulting in sudden changes in the movement of the ice-dam causing discontinuous velocities and elevation changes which continues for a few weeks after the GLOF (Zech et al. 2015).

Mayer et al. (2008) observed a maximal total vertical displacement at the ice-dam in 2005 of 17.7 m which is 15% less than the uplift in 2014. Although the calculated lake surface area is 14% greater for 2005, the results are still in the same order. The different displacement values may be the result of different locations at the ice-dam (no exact position is given in Mayer et al. (2008)). It is most likely that faults that cut the ice-dam from surface to bottom exist as the surface of the ice-dam is highly crevassed in that area. Thus, areas separated by faults behave differently in terms of uplift magnitude (Walder et al. 2006). These results show clear evidence that flotation in combination with subglacial cavity formation of different scales depending on the distance towards the ice-margin (bigger cavities in the vicinity of the ice-margin and smaller cavities further away) seem to be a reasonable triggering mechanism. A similar interpretation that flotation and the existence of subglacial cavities support the drainage mechanism was given by Mayer et al. (2008) for the outburst event in 2005. Additionally, Tweed and Russell (1999) described that the formation of cavities at the glacier-margin due to an increase in velocity which occurs before the GLOF, may be responsible for the triggering of the outburst. However, a sound statement about the trigger mechanism is challenging because of the lack of information about the ice and the lake and their interaction. Still, a combination of more than one drainage trigger mechanism is reasonable and may be the result of varying environmental conditions, e.g. fluctuations in ice-dam thickness or changing quantity of water supply. While the amount of water supply would be costly to measure in-situ by inducing sensors in boreholes at the ice-dam, fluctuations in the ice-dam thickness could be easily retrieved from repeating TanDEM-X acquisitions.

5   Early Warning Capabilities

The ice-dam's behaviour in 2014 and 2015, especially the raise and decline of the elevation is very similar and differ only in timing and magnitude. Although the comparison of only 2 years might not be sufficient for a reliable statement, we assume that subsequent outburst events are similar every year as the geophysical processes do not change completely. In both years, the elevation of the ICED station rapidly increased from less than 0.1 m/day up to 1.1 m/day in 2014 and 0.7 m/day in 2015 resulting in an uplift of the ice-dam. The initiation of the uplift is accompanied by a rapid elevation increase (values greater than 0.2 m/day). This uplift with respect to time (which we define as the elevation gradient) is shown in Fig. 5. To compare the 2 years, the elevation gradients have been shifted to match at the same GLOF date. Once the elevation gradient starts to decrease again, the drainage will start within the next day. The GLOF occurs when the elevation gradients get negative as the elevation decrease coincides with the drainage initiation. This elevation gradient could be used as the initiation threshold
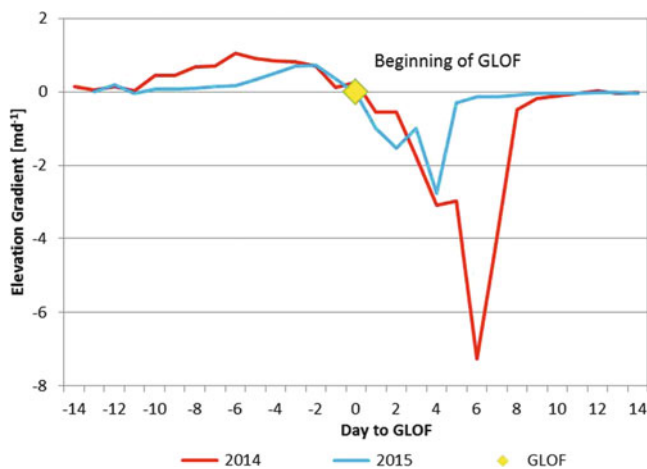
Fig. 5 Elevation gradients for the GLOFs in 2014 and 2015. The elevation gradients have been shifted to match at the same GLOF date

that the GLOF will occur within the next days and offer the possibility to forecast the outburst time.

Another possibility to monitor the lake level directly is the usage of optical geodetic cameras but the predictability is strongly dependent on good weather conditions. Additionally, the image processing should be made directly on the station as the transmission of Bitmap data is more cost effective. But an automatic image processing may fail during bad weather conditions. With a continuous monitoring of the ice-dam's behaviour in combination with a real-time or near real-time data communication, it is possible to develop an early warning system.

6 Conclusion

The monitoring of the GLOF at the Inylchek Glaciers with a continuously operating GPS station gives the opportunity to investigate the behaviour of the interaction between the ice-dam and Lake Merzbacher for the complete year. While previous studies rely on campaign data for a short period or data acquired once a year, we presented a unique data set for two complete years. The behaviour of the ice-dam within the complete year especially around the GLOF was investigated. A few days before the GLOF, the elevation and surface velocities increase supporting the assumption that the ice-dam adjacent to the lake becomes afloat and water penetrates underneath the ice-dam. A few hours before the GLOF, the elevation gradient decreases again and the elevation reaches its maximum which coincides with the outburst of the lake. After the outburst, the elevation decreases rapidly by 20 m in 2014 and, additionally, the surface velocities increase significantly. A continuous monitoring in combination with a near real-time data communication has the potential to develop an early warning system for the Merzbacher GLOF.

References

Bartholomaus TC, Anderson RS, Anderson SP (2011) Growth and collapse of the distributed subglacial hydrologic system of Kennicott Glacier, Alaska, USA, and its effects on basal motion. J Glaciol 57(206):985–1002. doi:10.3189/002214311798843269
Demchenko MA (1934) Glaciers of the Central Tien Shan – Inylchek Glacier, Reznichenko Glacier and others on investigation of Ukrainian research expedition. In: Proceedings of the first All-Union Geographical Congress, issue 3 (in Russian)
Funk M, Röthlisberger H (1989) Forecasting the effects of a planned reservoir which will partially flood the tongue of Unteraargletscher in Switzerland. Ann Glaciol 13:76–81
Glazirin GE (2010) A century of investigations on outburst of the ice-dammed lake Merzbacher (Central Tien Shan). Aust J Earth Sci 103(2):171–179
Glen JW (1954) The stability of ice-dammed lakes and other water-filled holes in glaciers. J Glaciol 2:316–318
Hagg W, Mayer C, Lambrecht A, Helm A (2008) Sub-debris melt rates on Southern Inylchek Galcier, Central Tian Shan. Geogr Ann Ser A Phys Geogr 90:55–63. doi:10.1111/j.1468-0459.2008.00333
Herring TA, King RW, McClusky SC (2009) Documentation for the GAMIT/GLOBK GPS processing software release 10.3. Massachusetts Institute of Technology, Cambridge
Huss M, Bauder A, Werder M, Funk M, Hock R (2007) Glacier-dammed lake outburst events of Gornersee, Switzerland. J Glaciol 53(181):189–200
Hutchinson GE (1957) A treatise on limnology, vol 1. Wiley, New York
Kingslake J, Ng F (2013) Quantifying the predictability of the timing of jökulhlaups from Merzbacher Lake, Kyrgyzstan. J Glaciol 59(217)
Kundzewicz ZW, Merz B, Vorogushyn S, Hartmann H, Duethmann D, Wortmann M, Huang S, Su B, Jiang T, Krysanova V (2015) Analysis of changes in climate and river discharge with focus on seasonal runoff predictability in the Aksu River Basin. Environ Earth Sci 73(2):501–516. doi:10.1007/s12665-014-3137-5
Maas HG, Mulsow C, Wendt A, Casassa G (2012) Pilot studies with a photogrammetric glacier lake outburst flood early warning system, international archives of the photogrammetry. Remote Sens Spat Inf Sci 39(B5):523–527
Mavlyudov BR (1997) Drainage of the ice-dammed Mertzbacher Lake, Tien Shan. Materiay Glyatsiologicheskikh Issledovannii (Data of Glaciological Studies) 81:61–65 (In Russian)
Mayer C, Lambrecht A, Hagg W, Helm A, Scharrer K (2008) Post-drainage ice dam response at Lake Merzbacher, Inylchek Glacier, Kyrgyzstan. Geogr Ann Ser A Phys Geogr 90(1):1–10

Mayr E, Juen M, Mayer C, Usubaliev R, Hagg W (2014) Modeling Runoff from the Inylchek glaciers and Filling of Ice-Dammed Lake Merzbacher, Central Tian Shan. Geografiska Annaler: Series A 96(4):609–625. doi:10.1111/Geoa.12061

Merzbacher G (1905) In: Murray J (ed) The Central Tian-Shan Mountains (1902–1903), 1st UK edition. London, p 294

Neelmeijer J, Motagh M, Wetzel HU (2014) Estimating spatial and temporal variability in surface kinematics of the Inylchek glacier, Central Asia, using TerraSAR-X Data. Remote Sens 6:9239–9259. doi:10.3390/rs6109239

Ng F, Liu S (2009) Temporal dynamics of a Jökulhlaup system. J Glaciol 55(192):651–665. doi:10.3189/002214309789470897

Nye JF (1976) Water flows in glaciers: Jökulhlaups, tunnels and veins. J Glaciol 17(76):181–207

Russell AJ, Carrivick JL, Ingeman-Nielsen T, Yde JC, Williams M (2011) A new cycle of jökulhlaups at Russell Glacier, Kangerlussuaq, West Greenland. J Glaciol 57(202):238–246

Schöne T, Zech C, Unger-Shayesteh K, Rudenko V, Thoss H, Wetzel HU, Gafurov A, Illigner J, Zubovich A (2013) A new permanent multi-parameter monitoring network in Central Asian high mountains – from measurements to data bases. Geosci Instrum Method Data Syst 2:97–111. doi:10.5194/gi-2-97-2013, www.geosci-instrum-method-data-syst.net/2/97/2013/

Shangguan DH, Bolch T, Ding YJ, Kröhnert M, Pieczonka T, Wetzel HU, Liu SY (2015) Mass changes of Southern and Northern Inylchek Glacier, Central Tian Shan, Kyrgyzstan, during 1975 and 2007 derived from remote sensing data. Cryosphere 9:703–717

Sugiyama S, Bauder A, Huss M, Riesen P, Funk M (2008) Triggering and drainage mechanism of the 2004 glacier-dammed lake outburst in Gornergletscher, Switzerland. J Geophys Res 113, F04019. doi:10.1029/2007JF000920

Tweed FS, Russell AJ (1999) Controls on the formation and sudden drainage of glacier-impounded lakes: implications for Jökulhlaup characteristics. Prog Phys Geogr 23(1):79–110

Walder JS, Trabant DC, Cunico M, Fountain AG, Anderson SP, Anderson RS, Andrew M (2006) Local response of a glacier to annual filling and drainage of an ice-marginal lake. J Glaciol 52(178):440

Werner CL, Wegmüller U, Strozzi T, Wiesmann A (2000) Gamma SAR and interferometric processing software. In: Proceedings of ERS-ENVISAT symposium, Gothenburg, Sweden

Wortmann M, Krysanova V, Kundzewicz ZW, Su B, Li X (2013) Assessing the influence of the Merzbacher Lake outburst floods on discharge using the hydrological model SWIM in the Aksu headwaters, Kyrgyzstan/NW China. Hydrol Process 28:6337–6350. doi:10.1002/hyp.10118

Zech C, Schöne T, Neelmeijer J, Zubovich A, Galas R (2015) Geodetic monitoring networks: GNSS-derived glacier surface velocities at the Global Change Observatory Inylchek (Kyrgyzstan). doi:10.1007/1345_2015_38

Water in Central Asia: Reservoir Monitoring with Radar Altimetry Along the Naryn and Syr Darya Rivers

Tilo Schöne, Elisabeth Dusik, Julia Illigner, and Igor Klein

Abstract

Water is a scarce resource in many regions of the world. In all Central Asian countries, the society depends on the availability of water either for hydro-power generation or irrigation. Since the collapse of the Soviet Union and the separation into independent countries, water resources management became a critical and political issue. Public information on water resources is now unavailable for many lakes and reservoirs and the data exchange about in- and outflows or actual storage volumes is limited. While the initial purpose of radar altimetry has been to measure sea surface topography and sea level changes, it proved to be a suitable tool for inland water body monitoring and to partially provide data about lake and reservoir level changes. Using this technology, the water levels of the Toktogul, Kairakum and Shardara Reservoirs and Lake Aydarkol have been extracted from 1995 onward. Using external information the derived water levels have been converted into water volume changes. This study shows that since 2011 the available water volume decreased and the water from the Toktogul and Shardara Reservoirs are overused. In 2015 the stored water volume of the Toktogul Reservoir was almost at its lowest possible amount. Merely the Kairakum Reservoir with a smaller storage capacity is replenished every year. Likewise, a decrease of water level and volume of Lake Aydarkol is clearly visible for the past years.

T. Schöne (✉) • J. Illigner
Helmholtz Zentrum Potsdam, GeoForschungsZentrum GFZ, Potsdam, Germany
e-mail: tschoene@gfz-potsdam.de; julia@gfz-potsdam.de

E. Dusik
Deutsche Gesellschaft für Internationale Zusammenarbeit (GIZ) GmbH, Bishkek, Kyrgyzstan
e-mail: elisabeth.dusik@giz.de

I. Klein
Deutsches Zentrum für Luft- und Raumfahrt e.V. (DLR), Weßling, Germany
e-mail: igor.klein@dlr.de

1 Introduction

In the arid to semi-arid region of Central Asia, water resources are vital for the growing population. After the collapse of the Soviet Union in 1991, many rivers are now of transboundary nature. The Aral Sea's main sources – the Amu Darya and Syr Darya River with their tributaries – cross six independent countries: Kazakhstan, Kyrgyzstan, Tajikistan, Turkmenistan, Uzbekistan and northern Afghanistan. Their water is intensively used, albeit, often with conflicting claims between the countries to generate hydroelectric power in winter and to have

water available for irrigation during the summer months (Giese et al. 2004; Eschment 2011; Sehring and Diebold 2012). Overexploitation and mismanagement of water resources in the past decades have led to an increasing water scarcity in the region (De Martino et al. 2005; UNECE 2011). Long-term effects of global climate change are likely to aggravate the situation even further. To counteract these challenges, information on (regional) water availability is needed for sustainable planning and management of water resources in Central Asia (Abdullayev and Rakhmatullaev 2014). To assist such processes, independent and freely available information on water parameters, e.g. lake and reservoir volumes, are in high demand (WWAP 2012). Over the past two decades, radar altimetry (RA) became a suitable tool for monitoring inland water bodies. New altimetric missions and recent reprocessing of data, acquired during previous missions, allow a construction of time series of lake and reservoir levels back to 1992. Such data support studies of natural changes in the water availability as well as of changes in reservoir storage (Song et al. 2015; Crétaux et al. 2016).

2 Geographical Settings

The Amu Darya and the Syr Darya River with their tributaries are Central Asia's lifelines and the main source of water in the region. Both rivers have their origins in the Tien Shan and Pamir Mountains in Kyrgyzstan, Tajikistan and Northern Afghanistan. The Syr Darya is formed by the confluence of the Naryn River and the Kara Darya River in the Fergana Valley. Starting here the river crosses Tajik and Uzbek territory and flows into the northern end of the Aral Sea in Kazakhstan. The Amu Darya is formed by the confluence of the Vakhsh and Panj River on the border of Tajikistan and Afghanistan. It flows along the Afghan-Uzbek border, crosses the eastern part of Turkmenistan and empties into the southern end of the Aral Sea in Uzbekistan. In total, the Aral Sea Basin covers an area of 1.55 Mio. km^2 and extends over six countries (Eschment 2011).

Both rivers are mainly fed by glacier and snow melt in the high mountains of Central Asia. Hence, the availability of water resources is closely linked to seasonal changes and may vary significantly from year to year. Around 86% of the Aral Sea Basin's water resources are formed in the countries on the upper reaches of both rivers (Kyrgyzstan,

Tajikistan and northern Afghanistan). However, only 17% of the Basin's water resources are used by the upstream countries, while 83% are abstracted by the countries in the lower reaches of both rivers (Kazakhstan, Turkmenistan and Uzbekistan) (Sehring 2007; Sehring and Diebold 2012).

During the time of the Soviet Union (1922–1991), numerous reservoirs and hydro-facilities were built along both rivers to control water flow and have water available when needed. A joint water-energy system was established between the five countries to regulate the supply of water and energy. The reservoirs were mainly operated to provide the downstream countries with water for irrigation in summer and only used for hydro-power production in peak times. In exchange, the upstream countries received gas and coal to cover their needs for electricity and heating. With the collapse of the Soviet Union the established water-energy system broke down. Lacking own fossil fuels, the upstream countries Kyrgyzstan and Tajikistan gradually changed their reservoirs' operation mode from irrigation support to hydropower production during winter time (Eschment 2011).

The three major reservoirs along the Syr Darya River and the Naryn River – the Toktogul Reservoir, the Kairakum Reservoir and the Shardara Reservoir (Fig. 1) – started their operation between the late 1950s and the early 1970s. The Toktogul Reservoir is located at the Naryn River in Kyrgyzstan with a total capacity of 19.5 km^3 (FAO 1997). Since the collapse of the Soviet Union, it is mainly operated to produce hydropower in winter and is consequently replenished in spring and summer. The down-stream Kairakum and the Shardara Reservoirs are operated in a counter-regulatory mode and replenish in autumn and winter to provide water for irrigation in the growing season. Their total capacity amounts to 4.2 km^3 and to 5.7 km^3 respectively (FAO 1997).

In 1969, an emergency situation at the Shardara Reservoir led to the release of water into the Arnasay Lowland in Uzbekistan to prevent breaking of the dam and avoid flooding downstream of the Syr Darya river basin. In the subsequent years, the area was repeatedly flooded and the artificial Aydar Arnasay Lake System was formed. It covers an area of 3,500 km^2 and consists of three brackish water lakes, of which Lake Aydarkol (Fig. 1) has the largest size (1,050 km^2) (UNECE 2011). The highly saline water cannot be used for irrigation without further treatment and the lakes mainly serve as a recreational area and for industrial fishing.
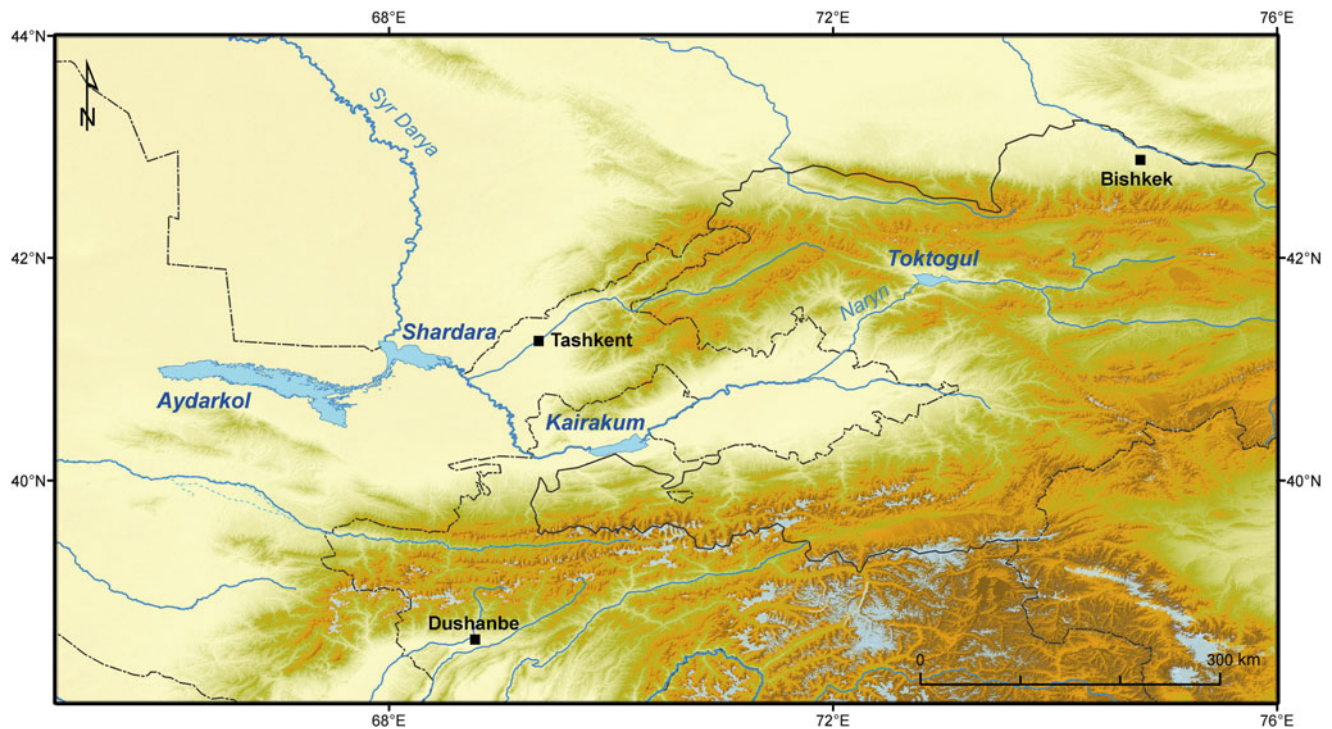
Fig. 1 Study area in Central Asia. The Toktogul (Kyrgyzstan), Kairakum (Tajikistan), and Shardara (Kazakhstan) Reservoirs and Lake Aydarkol (Uzbekistan) are situated along the Naryn and Syr Darya River System

3   Reservoir and Lake Height Estimation

Since the launch of the first satellite radar altimeters (RA) (Fu and Cazenave 2001) various studies demonstrated the potential for the continuous monitoring of inland water bodies (e.g., Koblinsky et al. 1993; Birkett 1994, 1995; Crétaux and Birkett 2006). In past years different databases have been developed providing time series of altimetric heights or volumes, e.g., HYDROWEB (www.legos.obs-mip.fr/soa/ hydrologie/hydroweb/, Crétaux et al. 2011), the River & Lake project of ESA (tethys.eaprs.cse.dmu.ac.uk/RiverLake, River and Lake Product Handbook 2009), or DAHITI (dahiti.dgfi.tum.de, Schwatke et al. 2015). These databases concentrate on selected lakes, reservoirs and rivers with global distribution.

With the launch of ERS-1 in 1991 and TOPEX/Poseidon in 1992 satellite-derived heights became continuously available on either 35-day or 10-day repeat orbits. Due to the orbital parameters only a limited number of inland water bodies can be sensed by RA. Some large water bodies are crossed by multiple missions, which allow to combine water level time series with higher temporal resolution. Since RA has been primarily designed for open ocean application, the nadir-looking radar beam illuminates a footprint larger than 2 km in diameter. This limits the ability to track small water bodies. The so-called Brown Model (Brown 1977) best describes the returning waveform over the open
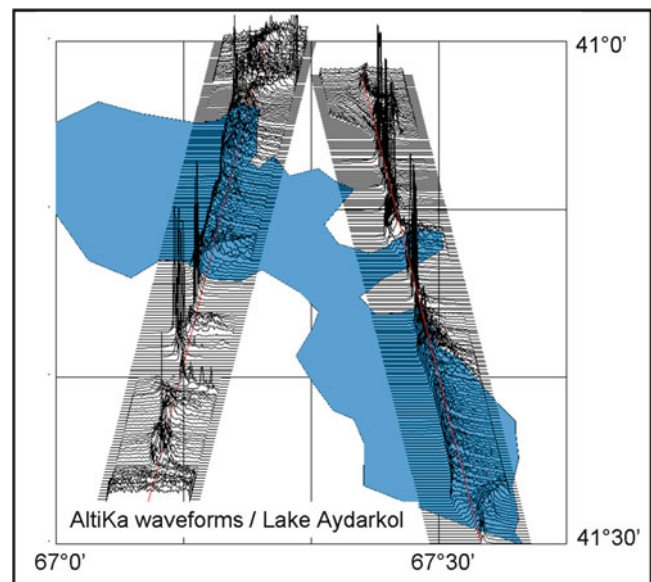
Fig. 2 SARAL/AltiKa waveforms (*black*) over the Lake Aydarkol (*blue*). Waveforms outside the reservoir are spiky, i.e. not ocean-like. Also waveforms near the shore-line show a complex return structure. As soon as the footprint is fully over water, the waveforms become ocean-like

ocean. Over smaller inland water bodies, the reflecting signal departs from the "ideal" model; the resulting waveform is deteriorated (Fig. 2). Thus, other functional models are applied to extract the travel time and the surface properties.

This process, called 'retracking', fits more complex tailored mathematical models to the waveform to derive improved range estimates, and thus, water level heights (e.g., Martin et al. 1983; Rodriguez 1988; Laxon 1994).

With the recently finished reprocessing of ERS-1 and ERS-2 (REAPER 2014) the majority of radar altimeter products now already contain a basic set of retrackers, namely OCOG/ICE1 (Wingham et al. 1986), ICE2 (Legresy and Remy 1997), and some others (Vignudelli et al. 2011, and references therein). These retracking functions cover a much wider range of possible waveform shapes than the Brown model. A few studies concluded that the ICE1 retracker performs with sufficient accuracy over inland waters (Frappart et al. 2004; da Silva et al. 2010; Calmant et al. 2013; Sulistioadi et al. 2014).

Prior to any processing all RA missions needs careful inter-calibration for system biases. These offsets are satellite-dependent and are derived from global multi-mission crossover analyses over the open ocean using the standard OCEAN (Brown model) retracker (e.g., REAPER 2014). In addition the different retracking functions reflect only partially the physics of the illuminated surface and the mid-point definition for range retrieval is different. Consequently the analysis of satellite passes using different retracker functions yields to offsets between the heights derived by the OCEAN retracker and heights derived with other retrackers (e.g., Calmant et al. 2013). In cases, when different retrackers for different missions have to be used, these corrections should be estimated and applied to the individual time series. Typically the reference mission in radar altimetry is Topex/Poseidon, which only provides the OCEAN retracker. The difference between the OCEAN and ICE1 retracker for all missions has been tested over Lake Issykul (Northern Kyrgyzstan). The biases found and applied are SARAL/AltiKa: −16 cm, ENVISAT: −25 cm, ERS-1: −28 cm, ERS-2: −45 cm. It should be noted, that the differences between the retrackers may also be corrected by estimating biases in overlapping periods.

4 Reservoir Monitoring for Toktogul, Kairakum, Shardara, and Lake Aydarkol

To construct time series of reservoir heights, the Altimeter Database and Processing System (ADS) (http://adsc.gfz-potsdam.de/ads, Schöne et al. 2010) is used. The ADS provides 1-Hz and high-rate harmonized and inter-calibrated radar altimetry data, including the retracking corrections of the original geophysical data records (GDR). To construct combined time series from different missions, the most recent satellite orbits and geophysical corrections are

applied. To find optimal solutions, different retrackers for individual missions were tested. Criteria in our selection process have been the number of valid measurements per pass and the number of valid passes. This confirms the finding by other authors (e.g., Frappart et al. 2004; da Silva et al. 2010; Calmant et al. 2013; Sulistioadi et al. 2014) that the ICE1 retracker (Wingham et al. 1986) gives the best performance over inland water bodies. In this study the ERS-1 altimeter measurements have been neglected since the orbit was shifted several times (3-/35-/501-days repeat orbit) during its mission life-time leading to a varying coverage.

Time series of reservoir heights from 1995 onward have been constructed using the ICE1 retracker for ERS-2, ENVISAT, SARAL/AltiKa, and Jason-2 and the OCEAN retracker for TOPEX and Jason-1. For CryoSat-2 the standard range information is used. High-rate data are used and an outlier-corrected median height, referenced to the EIGEN-6C3-static geoid model (Förste et al. 2013) was computed. In case of multi-mission time series corrections have been applied by constraining the time series on overlapping times to a common reference. These corrections mainly account for the difference between the geoid and the lake's geopotential surface, which is a function of the density distribution in mountainous areas.

For the Toktogul Reservoir data from ERS-2, ENVISAT and SARAL/AltiKa, and CryoSat-2 is available. Although nominal passes of TOPEX, Jason-1 and Jason-2 crosses the Toktogul Reservoir, only TOPEX gives a few but unreliable data. The time series has reliable results for 1995 until 2008 and from 2010 onward. Due to the failure of ENVISAT, the gap between 2008 and 2010 cannot be filled and no external data is available to fill the gap. The time series show pronounced annual cycles with varying high- and low-stands. Overall, three maximum replenishments (peaks) of the reservoir can be identified over the observation period and, starting at the highstand in 2011 a sharp decline with a typical annual cycle is observed.

For the Kairakum Reservoir reliable height estimates are derived from ERS-2, ENVISAT, SARAL/AltiKa and Jason-2. Measurements prior to year 2000 have higher internal RMS. The Shardara Reservoir and Lake Aydarkol are crossed by all missions. For both water bodies, surface heights can be estimated with a 10-day temporal resolution. The derived time series for all reservoirs and Lake Aydarkol show a pronounced annual signal. The time series of Lake Aydarkol also shows the slow flooding of the Arnasay Lowland after 1995 forming the lake system and since 2002 a slow decline in water storage volume. As mentioned above Lake Aydarkol is not part of the water storage system.

5   Reservoir Volumetric Curves

The discharge volume, i.e. the available downstream water volume, is an essential parameter for assessing the hydrology of lakes and reservoirs (Crétaux et al. 2016). This parameter, however, cannot be extracted from radar altimetry alone. The volumes is influenced by various factors, like the inflow from different sources, precipitation, evaporation, withdrawals for
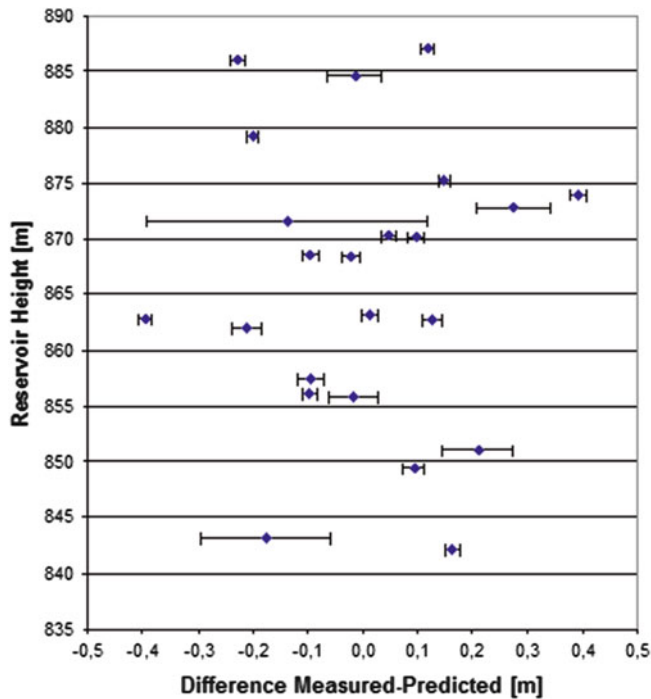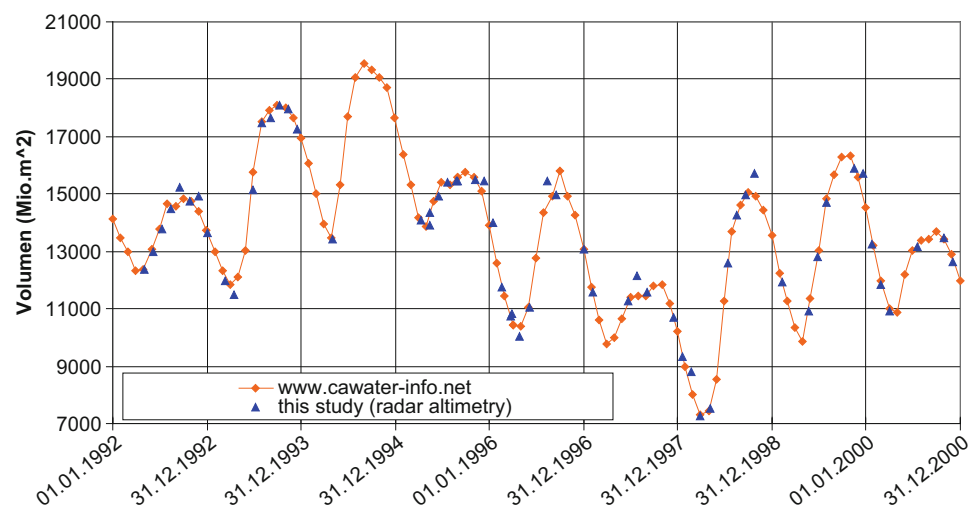

Fig. 3 For the Toktogul Reservoir using a polynomial representation of the volume-height relationship leads to very small differences between observed and predicted height. The results are consistent over the height range observed. Heights are given in Meter above the EIGEN-6C3-static geoid model (Förste et al. 2013), the error bars are the RMS of RA

agriculture, groundwater percolation, seepage, and, in case of reservoirs, the operational regime. In most cases none of these parameters is available. Reasons may be found in the lack of appropriate in-situ measurements (gauging stations) or difficulties in data exchange, since information is often considered as political sensitive and of national and/or economic interest.

The desired quantity is the total water volume, which is a function of the water level and bathymetry/topography of the reservoir or lake (Håkanson 1977). In absence of this information, remote sensing provides the area extent of the water body (e.g., Duan and Bastiaanssen 2013; Klein et al. 2014; Crétaux et al. 2016). With a series of area information for different water levels, the water volume change in reference to the lowest observed water height can be approximated.

For the Toktogul Reservoir sparse external volume information is made available by the reservoir operator (www.energo-es.kg). The best results for the height-volume relationship is obtained by a polynomial fit (Volume $[10^6 \text{ m}^3] = 0.966*h^2 - 1,456.553*h + 547,827.459$, $R^2 = 0.9998$). The external information does not cover the full reservoir level range (highest historical level was above 900 m), but a significant part of it. To evaluate our formula and to access the quality the external volume data is reconverted to heights and compared to the RA-derived heights (Fig. 3). Over the observed range of 842–887 m no obvious trend or shift exists. This confirms that RA can measure Toktogul Reservoir levels to better than 30 cm. In addition historical monthly volume information is available from www.cawater-info.net (after authorization) between 1984 and 2000 (Fig. 4). The RA-derived reservoir volumes agree well with the historical data.

The study by Klein et al. (2014) provide time series of surface water extents for the Shardara Reservoir between 1986 and 2012 for three selected months (April, July, September) each year. The series was derived from two different spec-
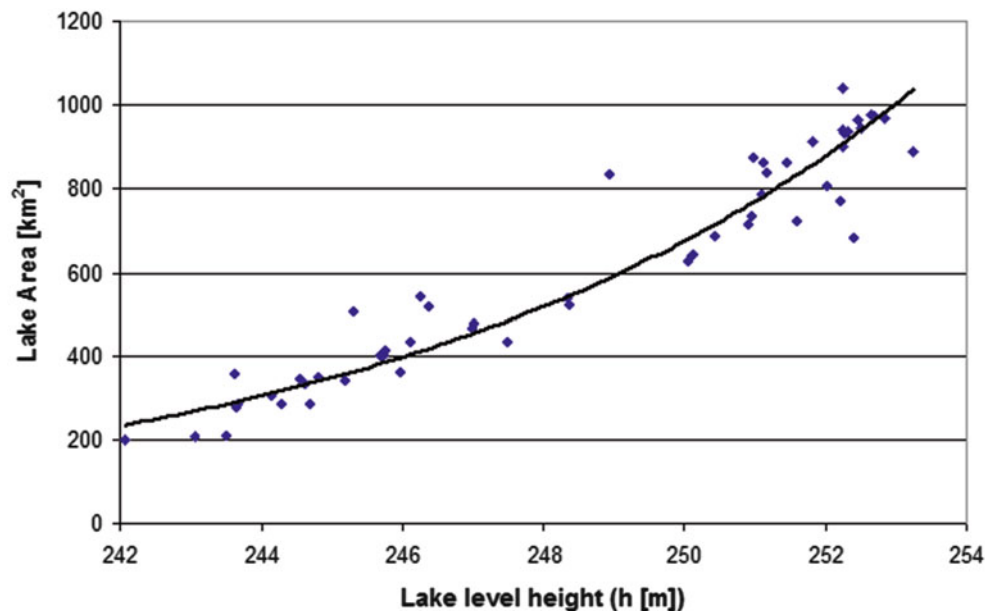

Fig. 4 Comparison of RA-derived volumes of the Toktogul Reservoir with end-of-month values from www.cawater-info.net. The RMS is 486 Mio. m³ (for clarity we haven't interpolated cawater-info data, pairs within 15 days to the month-end are used)

Fig. 5 Hypsometry of the Shardara Reservoirs area extents from Klein et al. (2014) and the altimetric-derived surface heights from this study. It is best described by LakeArea [km²] = 2.983941049*10¹²*e^(0.1322066*h). There are only a few measurements with larger deviations. This function is used to convert altimetric height changes to volume changes using a truncated cone formula

tral sensors with medium spatial resolution. Water surfaces derived from Advanced Very High Resolution Radiometer (AVHRR) with a spatial resolution of 1 km cover the time interval 1986–1999 and feature an overall accuracy of 83%. The Moderate-resolution Imaging Spectroradiometer (MODIS) provides results with spatial resolution of 250 m and an overall accuracy of 91% between 2000 and 2012. More than 50 pairs of RA heights and area extents are available (Fig. 5). To construct the time series, we assume the remote sensing information to be mid-month. From RA either the nearest pass was selected or the height was interpolated from the pass before and after. We tested a polynomial, exponential and linear fit to the data. The exponential fit gives the highest correlation ($R^2 = 0.93$) for the area-height relationship. The computed area is used to convert RA reservoir levels to volumes.

The volume-height relationship (Volume=LakeArea*Δh) for Lake Aydarkol is based on an average lake surface area of 1,050 km² (www.worldlakes.org/lakedetails.asp?lakeid= 10192) and for the Kairakum Reservoir of 520 km² (www. worldlakes.org/lakedetails.asp?lakeid=8616).

6 Volume Changes and Water Regimes

Our analysis of the water volumes and water regimes (Fig. 6) in the reservoirs is based on net volume changes.

For the Toktogul Reservoir data about in- and outflow is available from www.cawater-info.net for 1980–2000. After the Soviet Union collapse in 1991 the reservoir opera-

tion changed from irrigation mode to power mode. During autumn/winter water is used for hydro-power electric supply and higher outflows are observed which may reach peak values of 800 m³/s, with a winter inflow of about 200 m³/s. During spring/summer the inflow increases to 1,000 m³/s (with peaks of 1,500 m³/s), and an outflow of 200 m³/s. The maximum water volume of the reservoir was observed in 2002 with 9 km³. From the altimetric time series (Fig. 6) four periods of reservoir lowstands occurred in 1998, 2002, 2007 and 2015, with the latter being the absolute RA-observed minimum (no reliable data exist between 2007 and early 2011, but 2007 is reported with an exceptionnel lowstand (Libert et al. 2008)). For the lowstand in 2002 it can be seen that at least two consecutive years with high inflows are needed to fully replenish the reservoir. The spring/summer time of 2015 has been the first period since 2011, where the replenishment was larger than the previous outflow. To further investigate the volume changes, we analyze the annual maximum/minimum (mainly April/October) volumes (Fig. 7). Between 1995 and 2007 the relatively constant winter volume outflow is 5 km³. In contrast, the replenished net-volume is highly variable over the years. The water regime is balanced only for a few years, but most of the time the inflow is slightly lower than the outflow volume (it should be noted that these values are net values as they represent the difference between in- and outflow only). For 2004–2007 and 2010–2014 all years have low inflow volumes. Very high outflows are measured in 2013 (6.6 km³) and 2014 (7.3 km³) leading to the reservoir lowstand. The situation changed in
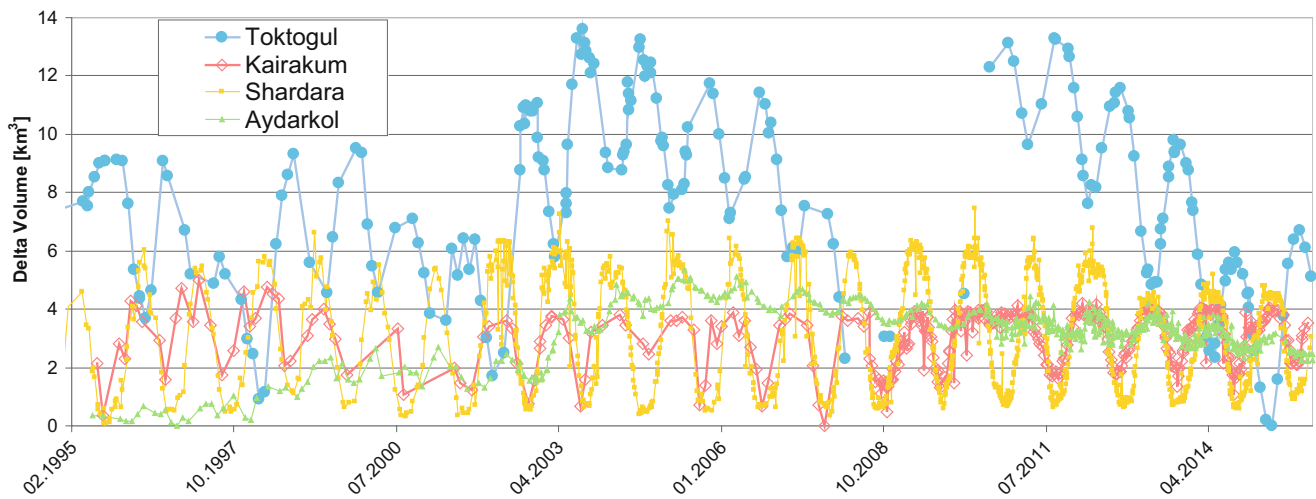
Fig. 6 The RA-derived volume changes in [km^3]. The baseline (= zero volume change) refer always to the lowest observed reservoir/lake level

Fig. 7 The reservoir volume of the Toktogul versus the discharge/replenishment volumes for each season. The discharge is relatively constant while the replenishment volumes are highly variable. The time series is extended backward with volume data from www.cawater-info.net
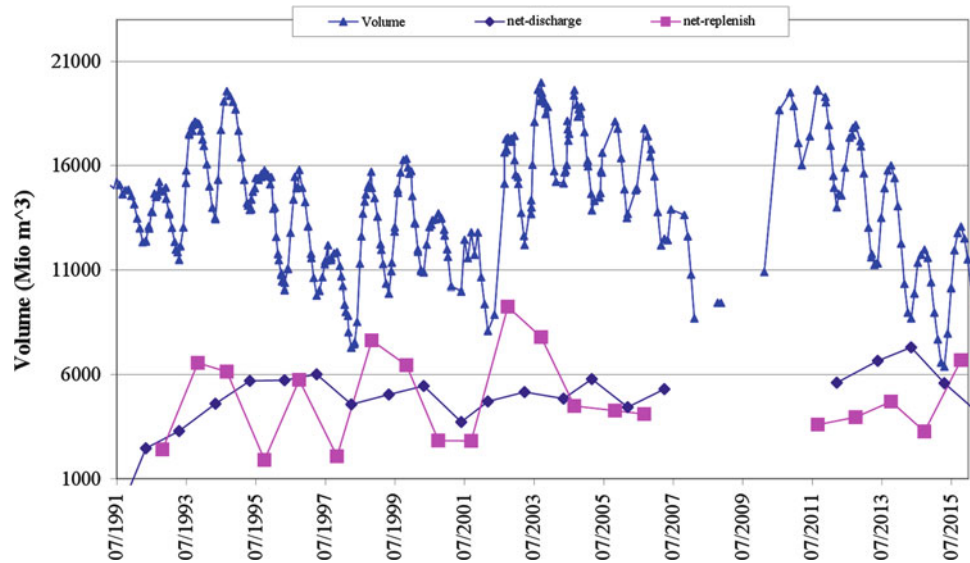

2015, but the reservoir volume is only slightly larger than in 2014.

The Kairakum Reservoir is mainly used for irrigation (UNECE 2007). During the winter discharge from the Toktogul Reservoir, the reservoir is replenished to its maximum capacity between October and January, followed by an extended period with constantly high water levels between January and June. Increased outflow is monitored between June and September. The available water storage of the Kairakum Reservoir decreases from about 4 km^3 in 2008 to now 2 km^3 (Fig. 6). Any excess water in winter continues downstream to the Shardara Reservoir with it's much higher capacity of 6 km^3. The multi-purpose reservoir serves to prevent harmful winter floods in the lowlands, hydropower generation, and to provide water in the irrigation season (UNECE 2007). Water is released between June to October, here for a slightly longer period compared to the Kairakum

Reservoir. The Shardara Reservoir shows a more pronounced and longer period with low stored volumes between October and December, and is replenished until March. The highstand period is March till June. Compared to the Kairakum Reservoir the replenishment is slightly delayed.

Water levels of Lake Aydarkol are available from 1995 onward. As part of the Aydar Arnasay Lake System, Lake Aydarkol is directly connected with the Shardara Reservoir. Between 1995 and 2005 annually about 1 km^3 of excess water was stored to prevent winter flooding in the plains below the Shardara Reservoir. After the construction of the Koksarai Reservoir the excess water is now directed to Koksarai (pers. comm. Alexandr Nikolayenko). Since 2005 the stored volume of Lake Aydarkol slowly decreases although some excess water is still released into the lake and leads to an annual cycle in stored water volumes.

Fig. 8 Sum of the monthly reservoir/lake volumes. Only values are displayed where all 3 (or 4) volumes are available
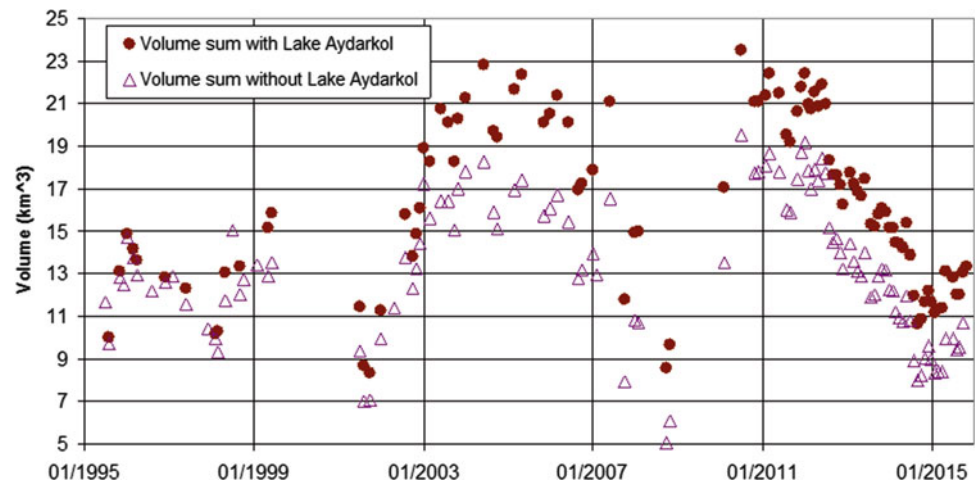
The Toktogul Reservoir dominates the operational regime of the whole system along the Naryn and Syr Darya River (Keith and McKinney 1997). Especially since 2011 when the water level of the Toktogul Reservoir decreased rapidly the volume variations of the Kairakum and Sharadara Reservoirs became smaller and also the water level of Lake Aydarkol decreased.

The missing outflow information of the Shardara Reservoir makes the interpretation of the water regime difficult. All volume changes are summed up on a monthly basis (Fig. 8). The periods of 1995–1999 and 2003–2007 show reasonable constant total volumes, but fast increase/decrease for 2001/2002 and 2007/2008, respectively. After 2011 the total storage now decrease for 4 years and falls back to it's 1995/1999 level, where the Toktogul Reservoir and Lake Aydarkol provided less to the total stored water volume. Unknown to this analysis is the effect of the hydro-power oriented Kambarata-2 Reservoir which became operational in 2010 (Sehring and Diebold 2012) and may regulate the inflow to the Toktogul Reservoir.

7 Summary

Radar altimetry is a suitable tool for monitoring water storage volume changes in the remote areas of Central Asia. With accuracies better than 30 cm RMS per satellite pass, lakes and reservoirs can be monitored independently of any ground network. In this study, the volume changes of the reservoirs Toktogul, Kairakum and Shardara and Lake Aydarkol have been derived and analyzed for their changes since 1995.

Between 2011 and 2015 the Toktogul Reservoir lost 75% of its possible water storage volume. The water volume in 2015 was on the same level as prior to 1987 when the reservoir started to become operational. As the first major downstream reservoir, the Kairakum Reservoir replenishes to its maximum every year. However, the water volume

variations decreased from 4 km^3 to 2 km^3 since 2008. There is currently no explanation for this change. Until 2010 the Shardara Reservoir provided the available capacity of 6 km^3. Since 2011 the reservoir's annual highstands slowly decrease. The reason remains unclear, but is probably due to the operation of the Koksarai Reservoir. The very high winter discharge volumes from Toktogul in 2013 and 2014 should have supported the replenishment of the Shardara Reservoir, but is not visible in the derived data. Lake Aydarkol slowly filled between 1995 and 2002, and reached a maximum water level in 2005. In the past years, the lake level lowers but still shows seasonal cycles driven by summer evaporation.

References

Abdullayev I, Rakhmatullaev S (2014) Data management for integrated water resources management in Central Asia. J Hydroinf 16(6):1425–1440

Birkett CM (1994) Radar altimetry: a new concept in monitoring lake level changes. EOS, Trans Am Geophys Union 75(24):273–275

Birkett CM (1995) The contribution of TOPEX/POSEIDON to the global monitoring of climatically sensitive lakes. J Geophys Res 100(C12):25179–25204. doi:10.1029/95JC02125

Brown GS (1977) The average impulse response of a rough surface and its application. IEEE Trans Antennas Propag 25:67–73

Calmant S, da Silva JS, Moreira DM, Seyler F, Shum CK, Crétaux JF, Gabalda G (2013) Detection of Envisat RA2/ICE-1 retracked radar altimetry bias over the Amazon basin rivers using GPS. Adv Space Res 51(8):1551–1564. doi:10.1016/j.asr.2012.07.033

Crétaux JF, Birkett C (2006) Lake studies from satellite radar altimetry. C R Geosci 338:1098–1112

Crétaux JF, Jelinski W, Calmant S et al (2011) SOLS: A lake database to monitor in the near real time water level and storage variations from remote sensing data. Adv Space Res 47:1497–1507

Crétaux J-F, Abarca-del-Río R, Bergé-Nguyen M et al (2016) Lake volume monitoring from space. Surv Geophys 37(2):269–305. doi:10.1007/s10712-016-9362-6

da Silva JS, Calmant S, Seyler F, Filho OCR, Cochonneau G, Mansur WJ (2010) Water levels in the Amazon basin derived from the ERS 2 and ENVISAT radar altimetry missions. Remote Sens Environ 114(10):2160–2181. doi:10.1016/j.rse.2010.04.020

De Martino L et al (2005) Environment and security: transforming risks into cooperation – Central Asia – Ferghana/Osh/Khujand area. enrin.grida.no/environment-and-security/ferghana-report-eng.pdf. Accessed 16 May 2016

Duan Z, Bastiaanssen WGM (2013) Estimating water volume variations in lakes and reservoirs from four operational satellite altimetry products and satellite imagery data. Remote Sens Environ 134:403–416

Eschment B (2011) Wasserverteilung in Zentralasien. Ein unlösbares Problem?. Studie der Friedrich Ebert Stiftung. http://library.fes.de/pdf-files/id/08201.pdf. Accessed 30 Sept 2015)

Food and Agriculture Organization of the United Nations (FAO) (1997) Irrigation in the countries of the Former Soviet Union in figures, FAO Water Reports No. 15, Rome

Förste C, Bruinsma S, Abrykosov O, Flechtner F, Dahle C, Neumayer K-H, Barthelmes F, König R, Marty J-C, Lemoine J-M, Biancale R (2013) EIGEN-6C3 – The newest high resolution global combined gravity field model based on the 4th release of the GOCE direct approach. In: Book of abstracts. The IAG Scientific Assembly 2013, 150th Anniversary of the IAG (Potsdam 2013), Potsdam

Frappart F, Cazenave A, Seyler F, Calmant S (2004) Comparison of the envisat waveform retrackers over inland waters. In: Lacoste H, Ouwehand L (eds) Proceedings of the 2004 Envisat & ERS Symposium (ESA SP-572). 6–10 September 2004, Salzburg, Austria. Published on CD-Rom

Fu LL, Cazenave A (2001) Satellite altimetry and earth sciences. In: A Handbook of techniques and applications, International geophysics series, vol 69. Academic, San Diego

Giese E, Sehring J, Trouchine A (2004) Zwischenstaatliche Wassernutzungskonflikte in Zentralasien. http://www.uni-giessen.de/fbz/zentren/zeu/forschung/publikationen/publi2/disc18/at_download/file. Accessed 16 May 2016

Håkanson L (1977) On lake form, lake volume and lake hypsographic survey. Geografiska Ann Ser A, Phys Geogr 59(1/2):1–30. doi:10.2307/520579

Keith J, McKinney DC (1997) Options analysis of the operation of the Toktogul reservoir. USAID Environmental Policy and Technology (EPT) Issue Paper No. 7. Almaty. www.ce.utexas.edu/prof/mckinney/papers/aral/Issue7.pdf. Accessed 16 May 2016

Klein I, Dietz A, Gessner U, Galayeva A, Myrzakhmetov A, Künzer C (2014) Evaluation of seasonal water body extents in Central Asia over the past 27 years derived from medium-resolution remote sensing data. Int J Appl Earth Obs Geoinf 26:335–349. doi:10.1016/j.jag.2013.08.004

Koblinsky CJ, Clarke RT, Brenner AC, Frey H (1993) Measurements of river level variations with satellite altimetry. Water Resour Res 29(6):1839–1848. doi:10.1029/93WR00542

Laxon S (1994) Sea ice altimeter processing scheme at the EODC. Int J Remote Sens 15(4):915–924

Legresy B, Remy F (1997) Surface characteristics of the Antarctic ice sheet and altimetric observations. J Glaciol 43(144):197–206

Libert B, Orolbaev E, Steklov Y (2008) Water and energy crisis in Central Asia. China Eurasia Forum Q 6(3):9–20. http://kms2.isn.ethz.ch/serviceengine/Files/RESSpecNet/105566/ichaptersection_singledocument/205999F7-B0A4-4A96-838F-4B2D64902A7E/en/02_wecca2008089-20.pdf. Accessed 16 May 2016

Martin TV, Zwally HJ, Brenner AC, Bindschadler RA (1983) Analysis and retracking of continental ice sheet radar altimeter waveforms. J Geophys Res 88:1608–1616

REAPER (2014) https://earth.esa.int/web/guest/document-library/browse-document-library/-/article/reaper-product-handbook-for-ers-altimetry-reprocessed-products

River and Lake Product Handbook v3.5 (2009) Available at http://tethys.eaprs.cse.dmu.ac.uk/RiverLake/rl_docs/Product-Handbook-3-05.doc . Accessed 28 Sept 2015

Rodriguez E (1988) Altimetry for non-Gaussian oceans: height biases and estimation of parameters. J Geophys Res 93:14107–14120

Schöne T, Esselborn S, Rudenko S, Raimondo J-C (2010) Radar altimetry derived sea level anomalies – the benefit of new orbits and harmonization. In: Flechtner F et al (eds) System earth via geodetic-geophysical space techniques, Advanced technologies in earth sciences. Springer, Heidelberg. doi:10.1007/978-3-642-10228-8_25

Schwatke C, Dettmering D, Bosch W, Seitz F (2015) DAHITI - an innovative approach for estimating water level time series over inland waters using multi-mission satellite altimetry. Hydrol Earth Syst Sci 19:4345–4364. doi:10.5194/hess-19-4345-2015

Sehring J, Diebold A (2012) From Glaciers to the Aral Sea – water unites. Trescher Verlag GmbH, Berlin

Sehring J (2007) Irrigation reform in Kyrgyzstan and Tajikistan. Irrig Drain Syst 21(3-4):277–290. Available at: http://link.springer.com/10.1007/s10795-007-9036-0

Song C, Huang B, Ke L (2015) Heterogeneous change patterns of water level for inland lakes in High Mountain Asia derived from multi-mission satellite altimetry. Hydrol Process 29:2769–2781. doi:10.1002/hyp.10399

Sulistioadi YB, Tseng K-H, Shum CK, Hidayat H, Sumaryono M, Suhardiman A, Setiawan F, Sunarso S (2014) Satellite radar altimetry for monitoring small river and lakes in Indonesia. Hydrol Earth Syst Sci Discuss 11:2825–2874. doi:10.5194/hessd-11-2825-2014

United Nations Economic Commission for Europe (UNECE) (2007) Dam safety in Central Asia: capacity-building and regional cooperation. Water Series No. 5. http://www.unece.org/fileadmin/DAM/publications/oes/WaterSeriesNo.5_E.pdf. Accessed 30 Sept 2015

United Nations Economic Commission for Europe (UNECE) (2011) Second assessment of transboundary rivers, lakes and groundwaters, UNECE, Geneva. http://www.unece.org/fileadmin/DAM/env/water/publications/assessment/English/ECE_Second_Assessment_En.pdf. Accessed 30 Sept 2015

Vignudelli S, Kostianoy AG, Cipollini P, Benveniste J (eds) (2011) Coastal altimetry. Springer, Heidelberg. doi:10.1007/978-3-642-12796-0

Wingham DJ, Rapley CG, Griffiths H (1986) New techniques in satellite altimeter tracking systems. In: Proceedings of IGARSS'86 Symposium, Zürich, 8–11 Sept 1986, ESA SP-254, pp 1339–1344

WWAP (World Water Assessment Programme) (2012) The United Nations world water development report 4: managing water under uncertainty and risk. Paris, UNESCO. http://unesdoc.unesco.org/images/0021/002156/215644e.pdf. Accessed 16 May 2016

Erratum to: A Method of Airborne Gravimetry by Combining Strapdown Inertial and New Satellite Observations via Dynamic Networks

J. Skaloud, I. Colomina, M.E. Parés, M. Blázquez, J. Silva, and M. Chersich

Erratum to: International Association of Geodesy Symposia,
10.1007/1345_2016_229

In the references section of this chapter, author's name Mansi has been misspelled as Mansi X, instead of Mansi, A.H.

This has now been corrected.

The updated online version of the original chapter can be found under
DOI 10.1007/1345_2016_229

J. Skaloud
Geodetic Engineering Laboratory (TOPO), EPFL, Station 18, CH-1015 Lausanne, Switzerland
e-mail: jan.skaloud@epfl.ch

I. Colomina • M. Blázquez
GeoNumerics, Av. de Carl Friedrich Gauss 11, E-08860 Castelldefels, Spain

M.E. Parés
CTTC, Av. de Carl Friedrich Gauss 7, E-08860 Castelldefels, Spain

J. Silva
DEIMOS Engenharia, Av. Dom João II-2 41, 1998-023 Lisboa, Portugal

M. Chersich
ESRI Italia c/o EUCENTRE, Via Ferrata 1, 27100 Pavia, Italy

Associate Editors

List of Reviewers

Adelheid Weise	Akbar Shabanloui	Alessandro Caporali
Alexander Braun	Alexander Horvath	Alvaro Santamaría-Gómez
Ambrus Kenyeres	A.C.O. Cancoro de Matos	Andreas Iddink
Andreas Kvas	Andrew Newman	Angelyn W. Moore
Annette Eicker	Athanasios Dermanis	Balaji Devaraju
Beate Klinger	Ben Chao	Bernard Ducarme
C.K. Shum	Carine Bruyninx	Carla Braitenberg
Charles Meertens	Chopo Ma	Christoph Dahle
Christopher Neil Crook	Christopher S. Jacobs	Chuntao Chen
Claudia Tocho	David Becker	David Bekaert
David Crossley	David Gordon	David Wiese
Denizar Blitzkow	Dennis Odijk	Diethard Ruess
Elena Mazurova	Elena Rangelova	Elisabeth Mayr
Erricos C. Pavlis	Felix Norman Teferle	Fritz K. Brunner
Georgios S. Vergos	Giorgio Spada	Graham Appleby
Guenter Stangl	Hans Neuner	Hans-Georg Scherneck
Harald Schuh	Herbert Wilmes	Holger Steffen
Jaakko Mäkinen	Jacek Paziewski	Jan Krynski
Jean-Claude Raimondo	Jean-Paul Boy	Jeffrey T. Freymueller
Jen-Yu Han	Jennifer Bonin	Jian Sun
Joao Agria Torres	Joao Catalao	Johannes Boehm
John C. Ries	John Lillibridge	Julie Elliott
Junbo Shi	Juraj Janak	Kefei Zhang
Laura Sánchez	Leonid F. Vitushkin	Lucia Plank
Luciana Fenoglio-Marc	Luisa M. C. Bastos	Manabu Hashimoto
Maorong Ge	Marcelo Santos	M.A. Moraes de Mendonca
Marianne Greff-Lefftz	Martin Lidberg	Martina Barandun
Martina Sacher	Mathis Blosfeld	Mehdi Eshagh
Michael Moore	Michael Schindelegger	Michal Sprlak
Mike Chin	Miquel Garcia-Fernandez	Mirko Reguzzoni
Nicole Capitaine	Oliver Francis	Pavel Novak
Pawel Wielgosz	Petr Holota	Pieter NAM Visser
Przemyslaw Dykowski	Rene Forsberg	Riccardo Barzaghi
Richard Gross	Robert Tenzer	Roelof Rietbroek
Roland Pail	Ronni Grapenthin	Rosa Pacione
Róbert Cunderlík	Rüdiger Haas	Silvio R.C. de Freitas
Srinivas Bettadpur	Sten Bergstrand	Steve Paul Coss
Sunil Bisnath	Thomas Artz	Thomas Fuhrmann

Thomas Herring
Timothy Bartholomaus
Umberto Riccardi
Vojtech Pálinkáš
Wei Feng
Yan Ming Wang
Yoichi Fukuda

Thomas Hobiger
Tobias Nilsson
Vassilios Grigoriadis
Volker Klemann
Wu Chen
Yanming Feng
Zinovy M. Malkin

Thomas Jahr
Tomasz Hadas
Vicki Childers
Walter Zuern
Xiaoying Cong
Yasuhiro Koyama

Author Index

A
Abraha, K.E., 269–276
Abtout, A., 89–95
Ågren, J., 137–142
Ampatzidis, D., 3–8, 11–15
Artz, T., 181–186

B
Balidakis, K., 195–202
Barbero, I., 331–336
Berrocoso, M., 331–336
Bitharis, S., 321–328
Blázquez, M., 111–121
Böhm, J., 17–23, 163–168
Bonvalot, S., 25–28, 63–67
Bořík, M., 39–44
Boudin, F., 171–178
Boy, J.-P., 89–95, 171–178, 293–301
Bruinsma, S., 63–67

C
Calvo, M., 123–129, 131–135, 147–152
Capuano, P., 293–301
Chatzinikos, M., 277–283
Chen, Q., 261–268
Chersich, M., 111–121
Cimbaro, S.R., 53–61
Colomina, I., 111–121

D
Dach, R., 269–276
Dusik, E., 349–356

E
Engfeldt, A., 137–142

F
Fagiolini, E., 189–194
Falk, R., 25–28
Fernández-Ros, A., 331–336
Flechtner, F., 3–8
Fotiou, A., 321–328

G
Gao, Y., 223–228
Gárate, J., 331–336
Girdiuk, A., 163–168
Glaser, S., 3–8, 11–15

H
Hachinohe, S., 311–320
Halsig, S., 181–186
Hamidi, R., 89–95
Hamoudi, M., 89–95
Hao, Q., 229–235
Hector, B., 123–129
Heinkelmann, R., 3–8, 195–202, 303–308
Hinderer, J., 89–95, 123–129, 131–135, 155–160, 171–178
Holota, P., 47–52
Hunegnaw, A., 269–276

I
Iddink, A., 181–186
Illigner, J., 349–356
Issawy, E., 89–95

J
Jiménez, A., 331–336

K
Karbon, M., 303–308
Kersten, T., 253–258
Khodabandeh, A., 215–220
Klein, I., 349–356
König, R., 3–8, 11–15, 189–194
Korakitis, R., 33–37
Kotsakis, C., 277–283
Krásná, H., 17–23
Krawinkel, T., 245–252
Kube, F., 237–242

L
Lambert, S., 147–152
Langley, R.B., 287–291
Lederer, M., 77–85